REPORT DOCUMENTATION PAGE

Form Approved
OMB NO. 0704-0188

1. AGENCY USE ONLY (Leave Blank)	2. REPORT DATE	3. REPORT TYPE AND DATES COVERED
	02/15/08	Final (03-01-05 - 12-31-07)

4. TITLE AND SUBTITLE
Theoretical and Computational Studies of Stability, Transistion and Flow Control in High-Speed Flows

5. FUNDING NUMBERS
FA9550-05-1-0179

6. AUTHOR(S)
Dr Anatoli Tumin

7. PERFORMING ORGANIZATION NAME(S) AND ADDRESS(ES)
Dept. of Aerospace and Mechanical Engineering, University of Arizona, Tucson, AZ 85721

8. PERFORMING ORGANIZATION REPORT NUMBER

9. SPONSORING / MONITORING AGENCY NAME(S) AND ADDRESS(ES)
AFOSR /NA
875 North Randolph Street
Suite 325, Room 3112
Arlington, VA 22203-1768

10. SPONSORING/MONITORING AGENCY REPORT NUMBER
AFRL-SR-AR-TR-08-0144

11. SUPPLEMENTARY NOTES
The views, opinions and/or findings contained in this report are those of the author(s) and should not be construed as an official Department of the Army position, policy or decision, unless so designated by other documentation.

12 a. DISTRIBUTION / AVAILABILITY STATEMENT
Approved for public release; distribution unlimited.

12 b. DISTRIBUTION CODE

13. ABSTRACT (Maximum 200 words)

A comprehensive study of stability and receptivity of hypersonic boundary layers has been carried out. The main results of the project:
1. Mathematical method of the multimode decomposition for three-dimensional perturbations in compressible boundary layers has been developed. The method provides analysis of experimental and computational results for modes of discrete and continuous spectra.
2. Theory of boundary-layer receptivity was developed for roughness-induced perturbations in incompressible and compressible boundary layers.
3. The transient growth phenomenon in compressible boundary layers over flat plate, sphere, and sharp cone has been studied. The work was accompanied by development of solvers for these geometries.

14. SUBJECT TERMS	15. NUMBER OF PAGES
	304
	16. PRICE CODE

17. SECURITY CLASSIFICATION OR REPORT	18. SECURITY CLASSIFICATION ON THIS PAGE	19. SECURITY CLASSIFICATION OF ABSTRACT	20. LIMITATION OF ABSTRACT
UNCLASSIFIED	UNCLASSIFIED	UNCLASSIFIED	UL

NSN 7540-01-280-5500

Standard Form 298 (Rev.2-89)
Prescribed by ANSI Std. 239-18
298-102

Theoretical and Computational Studies of Stability, Transition and Flow Control in High-Speed Flows

Principal Investigator: A. Tumin

February 14, 2008

Contents

1 Introduction **3**

2 Biorthogonal eigenfunction system and its application to the receptivity problem and to the multimode decomposition **7**

2.1 Introduction 7
2.2 Three-dimensional normal modes in a compressible boundary layer 10
2.3 Receptivity to 3D actuators placed on the wall 29
2.3.1 Roughness-induced perturbations in incompressible boundary layer . 29
2.3.2 Roughness-induced perturbations in a compressible boundary layer . 44
2.4 Nonparallel flow effects on roughness-induced perturbations in boundary layers 53
2.4.1 Periodic-in-time actuators placed on the wall 68
2.5 Multimode decomposition of perturbations in a compressible boundary layer 79
2.5.1 Introduction 79
2.5.2 Outline of the method 81
2.5.3 Application of the decomposition to DNS results 91
2.6 Biorthogonal eigenfunction system for supersonic inviscid flow past a flat plate 119
2.7 Biorthogonal eigenfunction system in the triple-deck limit 140

3 Three-dimensional wave packets in a compressible boundary layer **153**

3.1 Introduction 153
3.2 Initial-value problem for three-dimensional perturbations in a compressible boundary layer 155
3.3 Three-dimensional wave packets 183

4 Transient growth of perturbations in compressible boundary layers **207**

4.1 Introduction 207
4.2 Spatial transient growth, problem formulation 210
4.3 Spatial transient growth in a compressible boundary layer over a flat plate . 227
4.4 Spatial transient growth in a boundary layer over a sphere 231
4.5 Transient growth phenomenon in a boundary layer over a sharp cone 237
4.6 Transient growth phenomenon in a boundary layer past a blunt cone 250

5 Conclusions **251**

A Appendices to Chapter 2 **252**
A.1 The matrix elements, Section 2.2 252
A.2 The biorthogonal eigenfunction system, Section 2.2 257
A.3 Numerical method, Section 2.2 260
A.4 The non-zero elements of matrices in Eqs. (2.96) and (2.100), Section 2.5.2 . 263
A.5 Correspondence between solutions of the adjoint problems, Eqs. (2.106) and (2.107), Section 2.5.2 266
A.6 Fundamental solutions in the triple-deck limit, Section 2.7 266

B Appendices to Chapter 3 **274**
B.1 Biorthogonal system of eigenfunctions, Section 3.2 274

C Appendices to Chapter 4 **277**
C.1 Matrices for compressible flow past a sphere, Section 4.4 277
C.2 Matrices for compressible flow past a sharp cone, Section 4.5 282
C.3 Matrices for compressible flow past a blunt cone 286

Chapter 1

Introduction

The potential of sustained hypersonic flight to revolutionize military and commercial activity is well recognized, and is reflected in recent initiatives such as the National Aerospace Initiative. High-speed vehicles will substantially impact military strategy by providing new defensive options such as a rapid on-demand global strike capability with much shorter response times than currently possible. Furthermore, the development of new technologies based on air-breathing propulsion can be leveraged to considerably reduce the cost of access-to-space, the benefits of which are both military as well as commercial.

However, daunting technical challenges remain in realizing such vehicles. The harsh environment imposed by the envelope of such future missions is manifested in the severe anticipated thermo-mechanical loads and various propulsion-related requirements. Although the diversity of the physical phenomena encountered is broad, several key limiting issues have been identified as primary challenges, including both local and global constraints such as, for example, cowl lip loading and airframe balance. A scrutiny of the problems identified reveals the pervasive importance of several basic fluid dynamic phenomena. One of these, and possibly the least understood, is that of high-speed transition.

The impact of hypersonic boundary layer transition on airbreathing propulsion design, on extended range re-entry systems, and on tactical missile design has been outlined by Dr. Key Y. Lau and Dr. Kevin G. Bowcutt (Phantom Works, The Boeing Company) in their talk at AFOSR Contractors Meeting in Unsteady Aerodynamics and Hypersonics (September 10-11, 2002). Particularly, in the summary of the talk, they pointed out that there is a need of a better understanding of roughness-induced transition and boundary layer trip design. The latter is associated with the requirement of robust, turbulent boundary layer flow for inlet operability on missiles and on small-scale flight test vehicles. The boundary-layer transition on small vehicles is dominated by bypass mechanisms because the forebody of tactical missiles and small vehicles is too short to cause natural transition, and tripping is required. This outline illustrates the manifold role of roughness-induced perturbations as the cause of the transition and a means for flow control.

In the present report, the main results stemming from research supported by AFOSR grant are presented. The theoretical and computational studies of stability, transition and flow control have been carried out in close contact with AFRL at WPAB with an emphasis

on the roughness-induced transition prediction due to the transient growth mechanism, and on the roughness-induced flow control.

The principal investigator is thankful to Prof. E. Reshotko, Prof. X. Zhong, Dr. E. Forgoston, Dr. S. Zuccher, Dr. X. Wang, Mr. C. Chiquete, Mr. P. Gaydos, Mr. I. Shalaev, and Mr. M. Veirgutz for their significant input into this three-year project.

The results have been published in 9 journal papers and in 17 conference papers.

Journal publications

1. P. Gaydos, and A. Tumin, Multimode Decomposition in Compressible Boundary Layers, AIAA Journal, Vol. 42, pp. 1115-1121, 2004.

2. E. Forgoston, and A. Tumin, Initial Value Problem for Three-Dimensional Disturbances in a Hypersonic Boundary Layer, Physics of Fluids , Vol. 17, No. 8, Paper No. 084106, 14 pages, 2005.

3. A. Tumin, and E. Reshotko, Receptivity of a Boundary-Layer Flow to a Three-Dimensional Hump at Finite Reynolds Numbers, Physics of Fluids, Vol. 17, No. 9, Paper No. 094101, 8 pages, 2005.

4. S. Zuccher, A. Tumin, and E. Reshotko, Parabolic Approach to Optimal Perturbations in Compressible Boundary Layers, J. Fluid Mechanics, Vol. 556, 2006, pp. 189-216, 2006.

5. A. Tumin, Biorthogonal Eigenfunction System in Triple-deck Limit, Studies in Applied Mathematics, Vol. 117, 2006, pp. 165-190

6. E. Forgoston, and A. Tumin, Three-Dimensional Wave Packets in a Compressible Boundary Layer, Physics of Fluids, Vol. 18, No. 10, Paper No. 104103, 2006.

7. S. Zuccher, I. Shalaev, A. Tumin, and E. Reshotko, Optimal Disturbances in the Supersonic Boundary Layer Past a Sharp Cone, AIAA Journal, Vol. 45, No. 2, 2007, pp. 366-373.

8. A. Tumin, X. Wang, and X. Zhong, Direct Numerical Simulation and the Theory of Receptivity in a Hypersonic Boundary Layer, Physics of Fluids, Vol. 19, No. 1, Paper 014101, 2007.

9. A. Tumin, Three-Dimensional Spatial Normal Modes in Compressible Boundary Layers, Journal of Fluid Mechanics, Vol. 586, 2007, pp. 295-322.

Conference publications

1. A. Tumin and E. Reshotko, Optimal Disturbances in the Boundary Layer Over a Sphere, 34th AIAA Fluid Dynamics Conference and Exhibit, Portland OR, AIAA Paper 2004-2241, 2004.

2. E. Forgoston and A. Tumin, Initial-Value Problem for a Three-Dimensional Disturbance in a Hypersonic Boundary Layer, 34th AIAA Fluid Dynamics Conference and Exhibit, Portland OR, AIAA Paper 2004-2243, 2004.

3. E. Forgoston and A. Tumin, Three-Dimensional Wave Packet in a Hypersonic Boundary Layer 43rd Aerospace Sciences Meeting and Exhibit, Reno NV, AIAA Paper 2005-0099, 2005.

4. A. Tumin, Biorthogonal Eigenfunction System in the Triple-deck Limit, 43rd Aerospace Sciences Meeting and Exhibit, Reno NV, AIAA Paper 2005-0524, 2005

5. S. Zuccher, A. Tumin, and E. Reshotko, Optimal Disturbances in Compressible Boundary LayersComplete Energy Norm Analysis, 4th Theoretical Fluid Mechanics Conference, AIAA Paper 2005-5314, Toronto ON, June 2005.

6. E. Forgoston, A. Tumin, and D. Ashpis, Distributed Blowing and Suction for the Purpose of Streak Control in a Boundary Layer Subjected to a Favorable Pressure Gradient, 4th Theoretical Fluid Mechanics Conference, AIAA Paper 2005-5195, Toronto ON, June 2005.

7. F. G. Ergin, M. Choudhari, P. Fischer, and A. Tumin, Transient Growth: Experiments, DNS, and Theory, Proceedings, 4th International Symposium on Turbulence and Shear Flow Phenomena, Williamsburg VA, Vol. 2, pp. 583-588, June 27-29, 2005.

8. A. Tumin, X. Wang, and X. Zhong, Direct Numerical Simulation and the Theory of Receptivity in Hypersonic Boundary Layers, 44th Aerospace Sciences Meeting and Exhibit, Reno NV, AIAA Paper 2006-1108, 2006.

9. A. Tumin, Three-Dimensional Spatial Normal Modes in Compressible Boundary Layers, 44th Aerospace Sciences Meeting and Exhibit, Reno NV, AIAA Paper 2006-1109, 2006.

10. A. Tumin, Receptivity of Compressible Boundary Layers to Three-Dimensional Wall Perturbations, 44th Aerospace Sciences Meeting and Exhibit, Reno NV, AIAA Paper 2006-1110, 2006.

11. S. Zuccher, I. Shalaev, A. Tumin, and E. Reshotko, Optimal Disturbances in a Boundary Layer Past a Sharp Cone, 44th Aerospace Sciences Meeting and Exhibit, Reno NV, AIAA Paper 2006-1113, 2006.

12. I. Shalaev and A. Tumin, Stability of Three-Dimensional Mixing Layers, 36th AIAA Fluid Dynamics Conference, San Francisco, AIAA Paper 2006-3882, June 5-8, 2006.

13. E. Forgoston, M. Veirgutz, and A. Tumin, Numerical and Asymptotical Study of Three-Dimensional Wave Packets in a Compressible Boundary Layer, 36th AIAA Fluid Dynamics Conference, San Francisco, AIAA Paper 2006-3223, June 5-8, 2006.

14. E. Reshotko, and A. Tumin, Application of Transient Growth Theory to Bypass Transition, in G.E.A. Meier, K.R. Sreenivasan, H.J. Heinemann, eds., IUTAM Symposium on One Hundred Years of Boundary Layer Research, Springer, 2006, pp. 83-93.

15. C. Chiquete, and A. Tumin, Biorthogonal Eigenfunction System for Supersonic Inviscid Flow Past a Flat Plate, 37th AIAA Fluid Dynamics Conference, Miami FL, AIAA Paper 2007-3982, 2007.

16. A. Tumin, Outlook for Theoretical Modeling of Isolated Roughness-Induced Perturbations in Turbulent Boundary Layers, 37th AIAA Fluid Dynamics Conference, Miami FL, AIAA Paper 2007-3993, 2007 [Invited]

17. A. Tumin, Nonparallel Flow Effects on Roughness-Induced Perturbations in Boundary Layers, 46th Aerospace Sciences Meeting and Exhibit, Reno NV, AIAA Paper 2008-0504, 2008.

Chapter 2

Biorthogonal eigenfunction system and its application to the receptivity problem and to the multimode decomposition

2.1 Introduction

The conventional linear stability theory of boundary layers deals with the quasi-parallel flow approximation when the characteristic scale of the perturbations, λ (wavelength), is much smaller than the longitudinal scale of the mean flow, L: i. e. $\lambda \ll L$. In this approximation, the solution of the linearized Navier-Stokes equations is considered in the form of normal modes

$$q(x, y, z, t) = \hat{q}(y) \exp(i(\alpha x + \beta z - \omega t)), \tag{2.1}$$

where x, y, and z are the Cartesian coordinates, and coordinate y stands for distance from the wall; t is the time; α and β are the x- and z-components of the wavenumber, respectively. The analysis can be carried out within the scope of the temporal or spatial approach.

In the case of temporal analysis, the wavenumber of the perturbation is considered as a real parameter and the complex frequency has to be determined. For incompressible boundary layer flow, [GS78] showed that there are normal modes of discrete and continuous spectra. Later on, [SG81] proved that the solution of the initial-value problem [Gus79] can be presented as an expansion into these normal modes. Their weights can be found from the initial data with the help of the eigenfunctions of the adjoint problem. There is an orthogonality condition between the eigenfunctions of the direct and adjoint problems, and the sets of eigenfunctions are called a biorthogonal eigenfunction system. Recently, this result was extended to the cases of two- [FT03] and three-dimensional [FT05] perturbations in compressible boundary layers.

In the case of a spatial framework, frequency is prescribed as a real parameter. For two-dimensional mean flow with coordinate x in the downstream direction, β is a real parameter,

and the complex wavenumber, α, has to be found. The corresponding biorthogonal eigenfunction system for spatially growing disturbances was introduced independently by [ZST80] and [SG81] for two-dimensional perturbations in incompressible boundary layers. In addition to discrete modes (Tollmien-Schlichting-type modes), there are four branches of continuous spectra. The modes of two branches have arbitrary large growth rates in the downstream direction (they may be interpreted as upstream decaying modes). This indicates that a spatial Cauchy problem is ill-posed. [TF83b] suggested considering spatial initial-value problems having finite growth rates in the downstream direction. In the case of incompressible flow, the initial data require velocity and pressure perturbations, together with some of derivatives with respect to x. The constraint on the initial data providing finite growth rates in the downstream direction means that the short-scale upstream perturbations are not presented in the initial data. Under this condition, the Laplace transform with respect to x can be utilized. When additional *a priori* information is available, the spatial initial-value problem can be solved with partial inflow data. For example, [Tum03] illustrated by an example that when the downstream boundary is far away (in the length scale of the upstream perturbations) one can assume that the solution can be expanded into downstream modes only, and the spatial initial-value problem is solvable with only velocity perturbations as the initial data. Apparently, recovering the whole flow field from one velocity component is impossible, even under the assumption that only downstream modes are involved in the solution. However, if it is known that the main input into the perturbations is associated with a finite number of specific modes, one can still find their amplitudes. For example, two unstable discrete modes coexist in a laminar wall jet. Therefore, [TACZ96] assumed that experimental data were comprised of the unstable modes only and found their amplitudes and phases from experimental data for one velocity component only. Afterwards, the quality of the decomposition could be checked by comparing the experimental data with data obtained with the help of the utilized normal modes and their recovered weights. [GT04] illustrated this approach by an example of two-dimensional perturbations in a compressible boundary layer. One can recognize that decomposition of experimental data should depend on the quality of the assumptions. In compressible boundary layers, results of measurements could be contaminated by acoustic perturbations that can penetrate into the boundary layer. Therefore, in order to provide a reasonable accuracy of the decomposition aimed at a discrete mode, one also needs data for the external acoustic field [Gay04].

An analysis of compressible [TF83b] and incompressible [ZT87] boundary layers using the Laplace transform with respect to the streaming coordinate, x, demonstrated the completeness of the biorthogonal eigenfunction system for two-dimensional perturbations. Three-dimensional spatially growing/decaying perturbations in an incompressible boundary layer were considered by [Tum03]. A biorthogonal eigenfunction system for three-dimensional perturbations in compressible boundary layers was formally introduced by [Tum83] without analysis of the spatial initial-value problem, which is necessary to establish an expansion of the solution into normal modes of discrete and continuous spectra.

The biorthogonal eigenfunction system turned out to be a powerful tool for solving receptivity problems for boundary layers and for internal flows [ZST80, Fed82, TF83a, Tum83,

TF84, Fed84, ZF87, Fed88, Hil95, Tum96, TA97, Tum98, FK02, Fed03a, Fed03b]. Originally, the method was utilized for analysis of discrete modes (Tollmien-Schlichting-like modes) only. After clarification of uncertainties associated with the continuous spectra [Tum03], the method was also applied to the analysis of roughness-induced perturbations [TR04b, TR05, Tum06b]. It was proven [TA97, Tum06a] that the receptivity solution based on the biorthogonal eigenfunction expansion is equivalent to the method used by [AR90], whereas in the triple-deck limit the method leads to the results by [SSB77] and [Ter81].

Another emerging application of the biorthogonal eigenfunction system is associated with the progress being made in computational fluid dynamics (CFD), which provides an opportunity for reliable simulation of such complex phenomena as boundary layer receptivity and laminar-turbulent transition [MZ01, MZ03a, MZ03b, MZ05, ZM02, EFN04, EFS05, WZ05, WZ07]. In addition to experimental observations, CFD provides complete information about the flow field that cannot be measured in real experiments. However, this increase in available information does not furnish a physical insight to the problem because the leading mechanisms still remain hidden behind a messy disturbance field. Sometimes a flow possesses several discrete modes that are equally significant in the transition process, and it might be desirable to distinguish the dynamics of each mode in the complex non-steady flow field. Consequently, the problem of flow fields decomposing into normal modes arises. [GT04] demonstrated how the biorthogonal eigenfunction system could be applied to an analysis of CFD data for two-dimensional perturbations in a compressible boundary layer. In order to find the amplitudes of the normal modes comprising the perturbations, it is necessary to provide velocity components, temperature, pressure, and some of their derivatives at one crossection only. The orthogonality relation for the eigenfunctions of the direct and adjoint problems provides a straightforward tool to filter out amplitudes of the modes. [TWZ07] applied the technique to analyze perturbations generated in a high-speed boundary layer by blowing–suction through a slot on the wall. Amplitudes of stable and unstable discrete modes were filtered out from the CFD results and compared with the solution of the receptivity problem. Their work illustrates how the biorthogonal eigenfunction system could be used to gain insight on the details of the flow field that would have remained hidden without the advanced analysis. Future progress of the computational efforts will be associated with three-dimensional perturbations [WZ07], and an extension of the multimode decomposition method is required.

2.2 Three-dimensional normal modes in a compressible boundary layer

The objective of this section is to solve the spatial initial-value problem for three-dimensional perturbations in a compressible boundary layer, and to establish decomposition of the solution into the normal modes of the discrete and continuous spectra.

Spatial Cauchy problem

We consider a compressible two-dimensional boundary layer in Cartesian coordinates, where x and z are the downstream and spanwise coordinates, respectively, and coordinate y corresponds to the distance from the wall. We write the governing equations (the linearized Navier-Stokes equations) for a periodic-in-time perturbation, $\sim \exp(-i\omega t)$, in the matrix form

$$\frac{\partial}{\partial y}\left(\mathbf{L}_0\frac{\partial \mathbf{A}}{\partial y}\right)+\mathbf{L}_1\frac{\partial \mathbf{A}}{\partial y}=\mathbf{H}_1\mathbf{A}+\mathbf{H}_2\frac{\partial \mathbf{A}}{\partial x}+\mathbf{H}_3\frac{\partial \mathbf{A}}{\partial z}, \tag{2.2}$$

where vector $\mathbf{A}$ has 16 components

$$\begin{aligned}\mathbf{A}(x,y,z)=&(u,\partial u/\partial y,v,\pi,\theta,\partial\theta/\partial y,w,\partial w/\partial y,\partial u/\partial x,\partial v/\partial x,\\&\partial\theta/\partial x,\partial w/\partial x,\partial u/\partial z,\partial v/\partial z,\partial\theta/\partial z,\partial w/\partial z)^T.\end{aligned} \tag{2.3}$$

$\mathbf{L}_0,\mathbf{L}_1,\mathbf{H}_1,\mathbf{H}_2$, and $\mathbf{H}_3$ are 16×16 matrices (their definitions are given in Appendix A.1); u,v,w,π, and θ represent three velocity components, pressure, and temperature perturbations, respectively; and the superscript T in (2.3) and in what follows stands for transposed. The mean flow is assumed to be parallel (quasi-parallel approximation). Solution of (2.2) is subject to the following boundary conditions

$$y = 0: \qquad u=v=w=\theta=0, \tag{2.4}$$

$$y \to \infty: \qquad |A_j|\to 0, \qquad (j=1,\ldots,16). \tag{2.5}$$

We consider the spatial Cauchy problem for (2.2) assuming that the initial data, $\mathbf{A}_0(y,z)$, at $x=0$ corresponds to the solution having a finite growth rate in the downstream direction.

After Fourier transform with respect to the coordinate z and Laplace transform with respect to x,

$$\mathbf{A}_{p\beta}(y)=\int_0^\infty e^{-px}\int_{-\infty}^{\infty}e^{-i\beta z}\mathbf{A}(x,y,z)\,dz\,dx, \tag{2.6}$$

we arrive at the following system of ordinary differential equations:

$$\frac{d}{dy}\left(\mathbf{L}_0\frac{d\mathbf{A}_{p\beta}}{dy}\right)+\mathbf{L}_1\frac{d\mathbf{A}_{p\beta}}{dy}-\mathbf{H}_1\mathbf{A}_{p\beta}-p\mathbf{H}_2\mathbf{A}_{p\beta}-i\beta\mathbf{A}_{p\beta}=-\mathbf{H}_2\mathbf{A}_{0\beta}, \tag{2.7}$$

where

$$\mathbf{A}_{0\beta}(y) = \int_{-\infty}^{\infty} e^{-i\beta z}\mathbf{A}_0(y,z)\,dz. \tag{2.8}$$

The homogeneous part of (2.7) can be recast as an equation for vector $\mathbf{z}$ comprised of the first eight elements of vector $\mathbf{A}_{p\beta}$ as follows:

$$\frac{d\mathbf{z}}{dy} = \mathbf{H}_0\mathbf{z}, \tag{2.9}$$

where $\mathbf{H}_0$ is 8×8 matrix.

There are eight fundamental solutions, $\mathbf{z}_1, ..., \mathbf{z}_8$, of the homogeneous system of equations (2.9). Outside the boundary layer ($y \to \infty$), $\mathbf{H}_0$ is a matrix of constant coefficients, and thus each fundamental solution has an exponential asymptotic behavior $\sim \exp(\lambda_j y)$, where $\lambda_1, ..., \lambda_8$ are determined from the characteristic equation

$$\det \|\mathbf{H}_0 - \lambda\mathbf{I}\| = 0, \tag{2.10}$$

that can be recast as follows:

$$\left(b_{11} - \lambda^2\right)^2 \times \left[\left(b_{22} - \lambda^2\right)\left(b_{33} - \lambda^2\right) - b_{23}b_{32}\right] = 0, \tag{2.11}$$

where

$$b_{11} = H_0^{21}, \tag{2.12a}$$
$$b_{22} = H_0^{42}H_0^{24} + H_0^{43}H_0^{34} + H_0^{46}H_0^{64} + H_0^{48}H_0^{84}, \tag{2.12b}$$
$$b_{23} = H_0^{42}H_0^{25} + H_0^{43}H_0^{35} + H_0^{46}H_0^{65} + H_0^{48}H_0^{85}, \tag{2.12c}$$
$$b_{32} = H_0^{64},\ b_{33} = H_0^{65}, \tag{2.12d}$$

with H_0^{ij} denoting the (i,j) element of matrix $\mathbf{H}_0$. The roots of (2.11) are (we substitute $p = i\alpha$)

$$\begin{aligned}
\lambda_{1,2}^2 &= \lambda_{7,8}^2 = b_{11} = \alpha^2 + \beta^2 + iRe\,(\alpha - \omega)\,, \\
\lambda_{3,4}^2 &= (b_{22} + b_{33})/2 + \frac{1}{2}\sqrt{(b_{22} - b_{33})^2 + 4b_{23}b_{32}}, \\
\lambda_{5,6}^2 &= (b_{22} + b_{33})/2 - \frac{1}{2}\sqrt{(b_{22} - b_{33})^2 + 4b_{23}b_{32}}.
\end{aligned} \tag{2.13}$$

The root branches are chosen to have $\mathrm{Real}(\lambda_1, \lambda_3, \lambda_5, \lambda_7) < 0$, and we define a matrix of fundamental solutions,

$$\mathbf{m} = \|\mathbf{z}_1, \ldots, \mathbf{z}_8\|\,. \tag{2.14}$$

We use a lower case $\mathbf{z}$ for vectors having 8 components, whereas vectors having 16 components will be denoted by a capital $\mathbf{Z}$. By the definition of the components in (2.3), one can find all the components of the fundamental solutions $\mathbf{Z}$ if the fundamental solutions $\mathbf{z}$ are known.

The non-homogeneous system given by (2.7) has a solution expressed in the form

$$\mathbf{A}_p = \mathbf{M}\mathbf{Q}(y) + \mathbf{G}, \tag{2.15}$$

where $\mathbf{M}$ is the matrix of fundamental solutions comprised of vectors $\mathbf{Z}_j$ ($j = 1, \ldots, 8$), and the vector of coefficients $\mathbf{Q}(y)$ has to be found. Vector $\mathbf{G}(y)$ is defined as follows:

$$\begin{aligned} &G_1 = ... = G_8 = 0, \\ &G_9 = -F_9; ..., G_{16} = -F_{16}, \end{aligned} \tag{2.16}$$

where F_j are components of the vector $\mathbf{F}(y) = -(\mathbf{H}_2\mathbf{A}_{0\beta})$. After substituting (2.15) into (2.7), we arrive at the following equations for $\mathbf{Q}$

$$\begin{aligned} 2\mathbf{L}_0\frac{d\mathbf{M}}{dy}\frac{d\mathbf{Q}}{dy} + \mathbf{L}_0\mathbf{M}\frac{d^2\mathbf{Q}}{dy^2} + \frac{d\mathbf{L}_0}{dy}\mathbf{M}\frac{d\mathbf{Q}}{dy} + \mathbf{L}_1\mathbf{M}\frac{d\mathbf{Q}}{dy} + \\ \mathbf{L}_1\frac{d\mathbf{G}}{dy} - \mathbf{H}_1\mathbf{G} - p\mathbf{H}_2\mathbf{G} - i\beta\mathbf{H}_3\mathbf{G} = \mathbf{F}. \end{aligned} \tag{2.17}$$

Let us consider the individual equations of Eq. (2.17). Denoting z_{ij} to be ith component of vector $\mathbf{z}_j$, Q_j to be the jth component of vector $\mathbf{Q}$, and F_j to be the jth component of vector $\mathbf{F}$, then the first, third, fifth, sixth, and seventh equations of Eq. (2.17) are, respectively,

$$z_{1j}\frac{dQ_j}{dy} = 0, \tag{2.18a}$$

$$z_{3j}\frac{dQ_j}{dy} = F_3, \tag{2.18b}$$

$$z_{5j}\frac{dQ_j}{dy} = 0, \tag{2.18c}$$

$$z_{6j}\frac{dQ_j}{dy} - pF_{11} = F_6, \tag{2.18d}$$

$$z_{7j}\frac{dQ_j}{dy} = 0, \tag{2.18e}$$

where the index summation rule is imposed, and the explicit form of the matrix elements (see Appendix A.1) is taken into account. Using Eq. (2.18b), and the definitions $Z_{10j} = pz_{3j}$ and $Z_{14j} = i\beta z_{3j}$, the second and eighth equations of Eq. (2.17) are, respectively,

$$z_{2j}\frac{dQ_j}{dy} + (m+1)\frac{dG_{10}}{dy} + (m+1)pF_3 + pH_2^{29}F_9 - i\beta(m+1)F_12 = F_2, \tag{2.19a}$$

$$z_{8j}\frac{dQ_j}{dy} + (m+1)i\beta F_3 + (m+1)\frac{dG_{14}}{dy} + pG_{12} = F_8. \tag{2.19b}$$

The fourth equation of Eq. (2.17) is recast as

$$L_0^{43}\frac{dz_{3j}}{dy}\frac{dQ_j}{dy} + \frac{d}{dy}\left(L_0^{43}z_{3j}\frac{dQ_j}{dy}\right) + z_{4j}\frac{dQ_j}{dy} - pH_2^{4,10}G_{10} = F_4. \tag{2.20}$$

The third equation of Eq. (2.9) yields

$$\frac{dz_{3j}}{dy} = H_0^{31} z_{1j} + H_0^{33} z_{3j} + H_0^{34} z_{4j} + H_0^{35} z_{5j} + H_0^{37} z_{7j}. \tag{2.21}$$

After substitution of Eq. (2.21) into (2.20) and taking into account Eqs. (2.18), we arrive at

$$z_{4j} \frac{dQ_j}{dy} = \left[F_4 - L_0^{43} H_0^{33} F_3 - \frac{d\left(L_0^{43} F_3\right)}{dy} + p H_2^{4,10} G_{10} \right] \left(1 + L_0^{43} H_0^{34}\right)^{-1}. \tag{2.22}$$

Therefore, we have the following algebraic system of equations for dQ_j/dy:

$$\mathbf{m} \frac{d\mathbf{Q}}{dy} = \boldsymbol{\varphi}, \tag{2.23}$$

where vector $\boldsymbol{\varphi}$ has the following eight components

$$\varphi_1 = 0, \tag{2.24a}$$

$$\varphi_2 = F_2 - (m+1) \frac{dG_{10}}{dy} - (m+1) p F_3 - p H_2^{29} F_9 + i\beta (m+1) F_{12}, \tag{2.24b}$$

$$\varphi_3 = F_3, \tag{2.24c}$$

$$\varphi_4 = \left[F_4 - L_0^{43} H_0^{33} F_3 - \frac{d\left(L_0^{43} F_3\right)}{dy} + p H_2^{4,10} G_{10} \right] \left(1 + L_0^{43} H_0^{34}\right)^{-1}, \tag{2.24d}$$

$$\varphi_5 = 0, \tag{2.24e}$$

$$\varphi_6 = F_6 + p F_{11}, \tag{2.24f}$$

$$\varphi_7 = 0, \tag{2.24g}$$

$$\varphi_8 = F_8 - (m+1) i\beta F_3 - (m+1) \frac{dG_{14}}{dy} - p G_{12}. \tag{2.24h}$$

One can solve the algebraic equations (2.23) and write down the solution of (2.7) for the first eight components as follows

$$\mathbf{A}_{p\beta} = \sum_{j=1}^{8} \left(a_j + \int_{y_j}^{y} \frac{dQ_j}{dy}\, dy \right) \mathbf{z}_j, \tag{2.25}$$

where the constants a_j and y_j are determined using the boundary conditions. Using properties of determinants, we obtain the following solution:

$$\begin{aligned} \mathbf{A}_{p\beta} = {} & \left(a_1 + \int_0^y \frac{dQ_1}{dy}\, dy \right) \mathbf{z}_1 + \int_\infty^y \frac{dQ_2}{dy}\, dy\, \mathbf{z}_2 + \left(a_3 + \int_0^y \frac{dQ_3}{dy}\, dy \right) \mathbf{z}_3 \\ & + \int_\infty^y \frac{dQ_4}{dy}\, dy\, \mathbf{z}_4 + \left(a_5 + \int_0^y \frac{dQ_5}{dy}\, dy \right) \mathbf{z}_5 + \int_\infty^y \frac{dQ_6}{dy}\, dy\, \mathbf{z}_6 \\ & + \left(a_7 + \int_0^y \frac{dQ_7}{dy}\, dy \right) \mathbf{z}_7 + \int_\infty^y \frac{dQ_8}{dy}\, dy\, \mathbf{z}_8, \end{aligned} \tag{2.26}$$

where

$$
\begin{aligned}
a_1 &= \frac{c_2 E_{2357} + c_4 E_{4357} + c_6 E_{6357} + c_8 E_{8357}}{E_{1357}}, \\
a_3 &= \frac{c_2 E_{1257} + c_4 E_{1457} + c_6 E_{1657} + c_8 E_{1857}}{E_{1357}}, \\
a_5 &= \frac{c_2 E_{1327} + c_4 E_{1347} + c_6 E_{1367} + c_8 E_{1387}}{E_{1357}}, \\
a_7 &= \frac{c_2 E_{1352} + c_4 E_{1354} + c_6 E_{1356} + c_8 E_{1358}}{E_{1357}}, \\
c_j &= \int_0^\infty \frac{dQ_j}{dy} dy, \\
E_{ijkl} &= \det \left\| \begin{array}{cccc} z_{1i} & z_{1j} & z_{1k} & z_{1l} \\ z_{3i} & z_{3j} & z_{3k} & z_{3l} \\ z_{5i} & z_{5j} & z_{5k} & z_{5l} \\ z_{7i} & z_{7j} & z_{7k} & z_{7l} \end{array} \right\|_{y=0}.
\end{aligned}
$$

Although the result (2.26) formally looks the same as in [FT05] (see Section 3.2), the derivatives dQ_j/dy are found from a different set of algebraic equations.

The inverse Laplace transform,

$$\mathbf{A}_\beta(x, y; \beta) = \frac{1}{2\pi i} \int_{p_0 - i\infty}^{p_0 + i\infty} \mathbf{A}_{p\beta}(y; p, \beta) e^{px}\, dp, \tag{2.27}$$

will be determined by the poles corresponding to the roots $E_{1357} = 0$, and by the branch cuts associated with the equations $\mathrm{Real}(\lambda_1, \lambda_3, \lambda_5, \lambda_7) = 0$. The structure of the branch-cuts is the same as in the case of two-dimensional perturbations (Section 2.5.2). They represent perturbations of the continuous spectra: vorticity, entropy, and acoustic modes. The constraint on the initial data ensures that there is such p_0 that the solution is analytic at $\mathrm{Real}(p) \geq p_0$ and the path of integration in (2.27) lies in the domain of analyticity of $\mathbf{A}_{p\beta}$.

The result (2.27) is recast as a sum of integrals along the sides γ^+ and γ^- of each left-hand-side branch in the complex plane p that represent input from the continuous spectra, and a sum of the residue values corresponding to the input from the discrete spectrum,

$$\mathbf{A}_\beta = -\frac{1}{2\pi i} \sum_m \Big(\int_{\gamma_m^+} \mathbf{A}_{p\beta} e^{px}\, dp + \int_{\gamma_m^-} \mathbf{A}_{p\beta} e^{px}\, dp \Big) + \sum_n \mathrm{Res}_n(\mathbf{A}_{p\beta} e^{px}). \tag{2.28}$$

The three-dimensional character of the perturbations leads to overlapping of the two branches corresponding to the vorticity modes, similar to the cases of spatial [Tum03] and temporal [FT05] analysis of three-dimensional perturbations. The latter is reflected by the double root in (2.13).

In principle, the assumption about a finite growth rate of the solution (2.28) admits inclusion of a portion from the upstream modes into the initial data [TF83b, Tum03]. However, the typical applications of the method are associated with downstream modes only, and the upstream modes are excluded from the consideration.

Similar to the analysis of the initial-value problem, the integrals along the branch cut sides can be written as one integral of the difference $\mathbf{A}^+_{p\beta} - \mathbf{A}^-_{p\beta}$, where superscripts + and − indicate values evaluated at sides γ^+ and γ^-, respectively. Although the coefficients c_j in (2.26) are different from those defined in the Section 3.2, all formulas for $\mathbf{A}^+_{p\beta} - \mathbf{A}^-_{p\beta}$ remain the same for the spatial Cauchy problem under consideration. Particularly, for branch cuts corresponding to the acoustic waves, $\lambda_{3,4} = \pm ik$, where $k > 0$, we find

$$\begin{aligned}\mathbf{A}_{c,4} = \mathbf{A}^+_{p\beta} - \mathbf{A}^-_{p\beta} = \\ \left(\frac{c_2 E_{1275}}{E_{1753}E_{1754}} + \frac{c_3 E_{1753}}{E_{1753}E_{1754}} + \frac{c_4 E_{1754}}{E_{1753}E_{1754}} + \frac{c_6 E_{1756}}{E_{1753}E_{1754}} + \frac{c_8 E_{7185}}{E_{1753}E_{1754}}\right) \\ \times \left(E_{5734}\mathbf{z}_1 + E_{1754}\mathbf{z}_3 + E_{7153}\mathbf{z}_4 + E_{7134}\mathbf{z}_5 + E_{1534}\mathbf{z}_7\right).\end{aligned} \tag{2.29}$$

All functions on the right-hand side (2.29) are evaluated at the γ^+ side of the branch cut, where $\mathbf{z}_3 \sim \exp(+iky)$.

In the region of overlapping vorticity modes, we can use the result for the initial-value problem to represent $\mathbf{A}^+_{p\beta} - \mathbf{A}^-_{p\beta}$ as a sum of stand-alone modes corresponding to $\lambda_{1,2} = \lambda_{7,8} = \pm ik$ $(k > 0)$

$$\mathbf{A}^+_{p\beta} \;-\; \mathbf{A}^-_{p\beta} = \mathbf{A}_{c,1} + \mathbf{A}_{c,5}, \tag{2.30}$$

where

$$\begin{aligned}\mathbf{A}_{c,1} = \left(\frac{c_1 E_{1753}}{E_{1753}E_{2753}} + \frac{c_2 E_{2753}}{E_{1753}E_{2753}} + \frac{c_4 E_{4753}}{E_{1753}E_{2753}} + \frac{c_6 E_{6753}}{E_{1753}E_{2753}} + \frac{c_8 E_{8753}}{E_{1753}E_{2753}}\right) \\ \times \left(E_{2753}\mathbf{z}_1 - E_{1753}\mathbf{z}_2 + E_{1275}\mathbf{z}_3 + E_{1723}\mathbf{z}_5 + E_{1253}\mathbf{z}_7\right)\end{aligned} \tag{2.31}$$

and

$$\begin{aligned}\mathbf{A}_{c,5} = \left(\frac{c_1 E_{1253}}{E_{2753}E_{2853}} + \frac{c_4 E_{5234}}{E_{2753}E_{2853}} + \frac{c_6 E_{2563}}{E_{2753}E_{2853}} + \frac{c_7 E_{7253}}{E_{2753}E_{2853}} + \frac{c_8 E_{8253}}{E_{2753}E_{2853}}\right) \\ \times \left(E_{7853}\mathbf{z}_2 + E_{2785}\mathbf{z}_3 - E_{2783}\mathbf{z}_5 - E_{2853}\mathbf{z}_7 + E_{2753}\mathbf{z}_8\right).\end{aligned} \tag{2.32}$$

We call modes (2.31) and (2.32) vorticity modes A and B, respectively. Here notation γ^+ corresponds to the branch–cut side where $\mathbf{z}_1$ and $\mathbf{z}_7$ have asymptotics as $\sim \exp(+iky)$.

In the case of steady supersonic perturbations, there is an overlapping of two vorticity modes and the entropy mode with $\lambda_{5,6} = \pm ik$ $(k > 0)$. For this case, we can also use the result for the initial-value problem,

$$\mathbf{A}^+_{p\beta} \;-\; \mathbf{A}^-_{p\beta} = \mathbf{A}_{c,1} + \mathbf{A}_{c,2} + \mathbf{A}_{c,5}, \tag{2.33}$$

where $\mathbf{A}_{c,1}$ and $\mathbf{A}_{c,5}$ are given by (2.31), (2.32), and

$$\mathbf{A}_{c,2} = \left(\frac{c_1 E_{1283}}{E_{2853} E_{2863}} - \frac{c_4 E_{2834}}{E_{2853} E_{2863}} + \frac{c_5 E_{2853}}{E_{2853} E_{2863}} + \frac{c_6 E_{2863}}{E_{2853} E_{2863}} - \frac{c_7 E_{2783}}{E_{2853} E_{2863}} \right) \times \left(E_{8563} \mathbf{z}_2 + E_{2856} \mathbf{z}_3 + E_{2863} \mathbf{z}_5 - E_{2853} \mathbf{z}_6 - E_{2563} \mathbf{z}_8 \right). \tag{2.34}$$

In (2.34), the side γ^+ also means that $\mathbf{z}_5 \sim \exp(+iky)$.

In the case of steady subsonic perturbations, there is an overlapping of four modes. This case has not been considered yet elsewhere. Similarly to the other cases, one can derive

$$\mathbf{A}^+_{p\beta} \; - \; \mathbf{A}^-_{p\beta} = \mathbf{A}_{c,1} + \mathbf{A}_{c,2} + \mathbf{A}_{c,3} + \mathbf{A}_{c,5}, \tag{2.35}$$

where $\mathbf{A}_{c,3}$ is defined as follows

$$\mathbf{A}_{c,3} = \left(\frac{c_1 E_{6218}}{E_{2863} E_{2468}} - \frac{c_3 E_{2863}}{E_{2863} E_{2468}} + \frac{c_4 E_{2468}}{E_{2863} E_{2468}} - \frac{c_5 E_{6528}}{E_{2863} E_{2468}} - \frac{c_7 E_{6728}}{E_{2863} E_{2468}} \right) \times \left(E_{6348} \mathbf{z}_2 - E_{2468} \mathbf{z}_3 - E_{2863} \mathbf{z}_4 - E_{2834} \mathbf{z}_6 + E_{2463} \mathbf{z}_8 \right). \tag{2.36}$$

In addition, we should address the discrete spectrum, which is associated with poles originating from zeros, p_n, of the equation $E_{1357}(p_n) = 0$. Their input into (2.28) is presented by the residue values

$$\begin{aligned} \mathrm{Res}_n \left(\mathbf{A}_p e^{px} \right) = \frac{e^{p_n x}}{\left(\frac{\partial E_{1357}}{\partial p} \right)} [& \mathbf{z}_1 \left(c_2 E_{2357} + c_4 E_{4357} + c_6 E_{6357} + c_8 E_{8357} \right) \\ + \; & \mathbf{z}_3 \left(c_2 E_{1257} + c_4 E_{1457} + c_6 E_{1657} + c_8 E_{1857} \right) \\ + \; & \mathbf{z}_5 \left(c_2 E_{1327} + c_4 E_{1347} + c_6 E_{1367} + c_8 E_{1387} \right) \\ + \; & \mathbf{z}_7 \left(c_2 E_{1352} + c_4 E_{1354} + c_6 E_{1356} + c_8 E_{1358} \right)], \end{aligned} \tag{2.37}$$

where the right-hand side is evaluated at $p = p_n$. Taking into account that $E_{1357} = 0$, one can derive from (2.37)

$$\mathrm{Res}_n \left(\mathbf{A}_p e^{px} \right) = e^{p_n x} \frac{\left(c_2 E_{1257} + c_4 E_{1457} + c_6 E_{1765} + c_8 E_{1578} \right)}{\left(\frac{\partial E_{1357}}{\partial p} \right) E_{1457}} \times \left(\mathbf{z}_1 E_{4357} + \mathbf{z}_3 E_{1457} + \mathbf{z}_5 E_{1347} + \mathbf{z}_7 E_{1354} \right). \tag{2.38}$$

The result (2.38) represents a discrete mode that is comprised of four fundamental solutions, $\mathbf{z}_1$, $\mathbf{z}_3$, $\mathbf{z}_5$, and $\mathbf{z}_7$, decaying outside the boundary layer. This result and the results for the continuous spectra were verified with the help of Mathematica [Wol99].

One can see that input into the inverse Laplace transform (2.28) from the integrals along branch cuts [(2.29), (2.31), (2.32), (2.34), (2.36)], and the residue values evaluated at the poles (2.38) are written as stand-alone modes (vector functions) with coefficients depending on the initial conditions $\mathbf{A}_0(y, z)$,

$$\mathbf{A}_\beta (x, y) = \sum_\nu d_\nu \mathbf{A}_{\alpha_\nu}(y) e^{i\alpha_\nu x} + \sum_j \int_0^\infty d_j(k) \mathbf{A}_{\alpha_j}(y) e^{i\alpha_j(k) x} \, dk. \tag{2.39}$$

Here, $\sum_\nu$ and $\sum_j$ denote sums over the discrete spectra and branches of the continuous spectra, respectively. The coefficients d_ν and d_j also can be found from the initial data, $\mathbf{A}_0(y,z)$, using the biorthogonal eigenfunction system $\{\mathbf{A}_{\alpha\beta}, \mathbf{B}_{\alpha\beta}\}$ defined in Appendix A.2. The solution (2.39) provides the background for the multimode decomposition that will be discussed later in this section.

Recapitulation of spectra

Continuous spectra

Although one can find properties of continuous spectra for perturbations in compressible boundary layers elsewhere [TF83b, BM92, GT04], for the sake of clarity, we briefly recapitulate these properties.

The structure of the 3D continuous spectra is similar to the 2D case discussed in [GT04] (see Section 2.5.2). As in the 2D case, there are 7 branches. Three-dimensionality leads to two vorticity modes, A and B (see the previous subsection with the spatial Cauchy problem formulation) stemming from the vector character of the quantity. There are branches associated with the upstream modes that are of no interest to the present work. Figure 2.1(a) shows branches of the downstream modes in the complex plane $\alpha = -ip$ (p is the Laplace variable in the previous subsection) at Mach number $M = 5.95$, Reynolds number $Re = 1500$, $\beta = 10^{-4}$, and frequency parameter $F = \omega\mu_e/\rho_e U_e^2 = 10^{-4}$, where the subscript e stands for the flow parameters at the edge of the boundary layer. In what follows, we use the specific heat ratio $\gamma = 1.4$, and assume that viscosity is a function of the temperature in accordance with Sutherland's law. Results in figure 2.1 were obtained at Prandtl number $Pr = 0.72$, the free-stream stagnation temperature $T_0 = 470K$, and bulk viscosity parameter $e = 0.8$ (see Appendix A.1). One can see two horizontal branches representing the slow (SA) and fast (FA) acoustic waves. In the limit of high Reynolds numbers, the branch points correspond to phase velocities $c = 1 \pm 1/M$. The vorticity and entropy modes are indistinguishable in the scale of figure 2.1(a), but they are not identical, as one can see from figure 2.1(b). However, there is an overlapping of the modes at $\omega = 0$. In the limit of high Reynolds numbers, the branch points of the vorticity and entropy modes are $\alpha \approx \omega$. One can find more details about the branch points for 3D perturbations in [BM92].

In the case of 3D perturbations, the modes of continuous spectra are comprised of five fundamental solutions. Some of them are oscillating outside the boundary layer as $\sim \exp(\pm iky)$, whereas the others are decaying. Figures 2.2(a,b) and 2.3(a,b) show real, u_r, and imaginary, u_i, parts of the streamwise velocity perturbations of the vorticity, entropy and two acoustic modes in the case of a boundary layer over a flat plate with temperature factor $T_w/T_{ad} = 0.1$, where T_w and T_{ad} are the wall temperature and the temperature of the adiabatic wall, respectively. We use the length scale $H = (\mu_e x/\rho_e U_e)^{1/2}$, where x is the distance from the leading edge. The continuous spectrum parameter in these examples is $k = 1$. The other parameters are the same as in figure 2.1, except the spanwise wavenumber, which is $\beta = 0.16$. The solutions are normalized by the wall condition $du/dy(0) = 1$. One can see that the vorticity and entropy modes do not penetrate the boundary layer at these parameters, whereas the

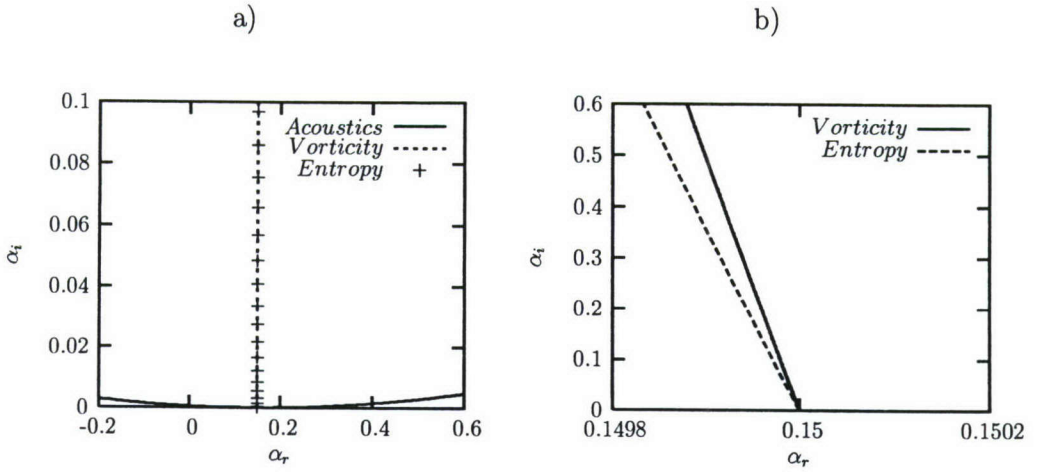

Figure 2.1: Branch cuts in the upper half-plane, α. $M = 5.95$, $F = 10^{-4}$, $Re = 1500$, $\beta = 10^{-4}$.

acoustic modes have velocity perturbations significantly larger than outside the boundary layer. This phenomenon is the reason why the quality of perturbation measurements in high-speed boundary layers depends on the level of the acoustic perturbations originated in boundary layers over wind–tunnel walls.

Figure 2.4 shows branches of the continuous spectra in the complex plane, α, for a subsonic boundary layer at Mach number $M = 0.5$, $Re = 1500$, $F = 10^{-4}$, and $\beta = 10^{-4}$. In the limit $M \to 0$, the branch cuts corresponding to the acoustic modes degenerate into the imaginary axis of α. In the limit $Re \to \infty$, the acoustic branch cuts form a cross with the midpoint at $\alpha = -M^2\omega/(1 - M^2)$ [Fed82, ZT87].

Slow and fast discrete modes

As was found by [Mac69], the discrete spectrum of perturbations in supersonic boundary layers is more complicated than in the subsonic case. [FK01] noticed that at high Mach numbers (when the so-called second Mack's mode exists) there are two discrete modes (stable and unstable) that could be synchronized at some downstream coordinate, x, depending on the flow parameters and the perturbation frequency. Because at small Reynolds numbers one discrete mode is synchronized with the slow acoustic mode, whereas the other mode is synchronized with the fast acoustic mode, [Fed03a] suggested calling them slow and fast discrete modes, respectively. The synchronization means that these discrete modes could be generated by acoustic waves interacting with the leading edge of a flat plate.

Both the slow and fast discrete modes could be involved in the laminar-turbulent transition scenario. For example, the decaying mode could be generated by the entropy or vorticity modes of the continuous spectra. At the point of synchronism between the fast and slow modes, the decaying mode can give rise to the unstable mode (switching of the modes),

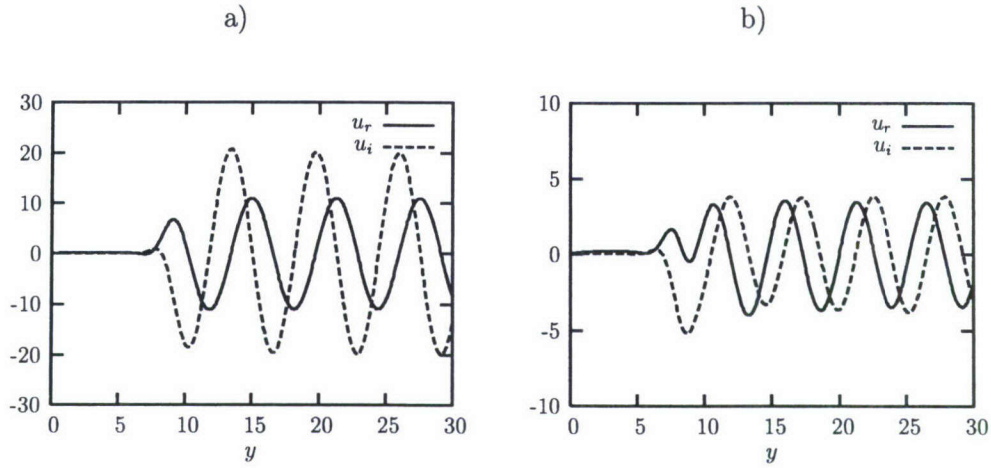

Figure 2.2: Streamwise velocity perturbation of vorticity mode A (a) and entropy mode (b). $M = 5.95$, $T_w/T_{ad} = 0.1$, $F = 10^{-4}$, $Re = 1500$, $\beta = 0.16$, $k = 1$.

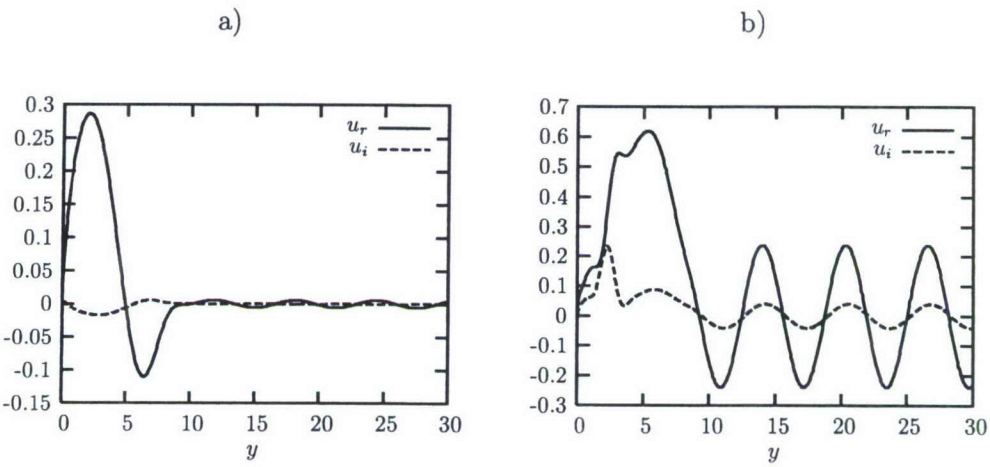

Figure 2.3: Streamwise velocity perturbation of the fast (a) and slow (b) acoustic modes. $M = 5.95$, $T_w/T_{ad} = 0.1$, $F = 10^{-4}$, $Re = 1500$, $\beta = 0.16$, $k = 1$.

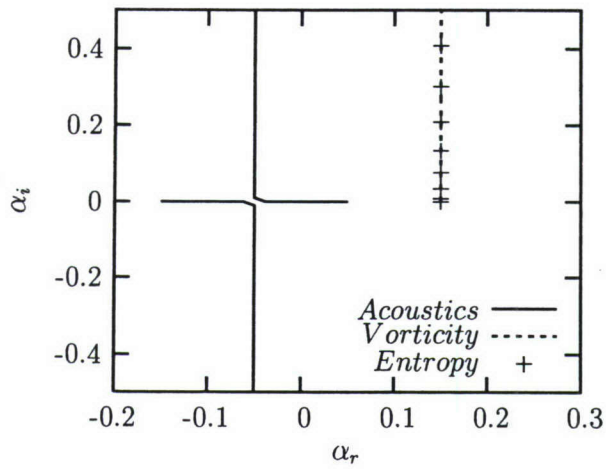

Figure 2.4: Branch cuts at $M = 0.5$, $F = 10^{-4}$, $Re = 1500$, $\beta = 10^{-4}$.

which may lead to the transition. The scenario suggested by [FK01] means that both the stable and unstable modes are of interest for understanding transition mechanisms. Later on, switching of the modes was observed in direct numerical simulations of perturbations in high-speed boundary layers [MZ03b].

In order to clarify the terminology and to illustrate the motivation for analysis of stable discrete modes, we provide an example of slow and fast discrete modes in a boundary layer of a calorically perfect gas over a flat plate. The free-stream stagnation temperature T_0= 470K, the edge Mach number $M = 5.6$, the Prandtl number $Pr = 0.71$, and we employ Stokes' hypothesis ($e = 0$ in the matrix elements of Appendix A.1).

Here is an example of a boundary layer on an adiabatic wall. In the limit of two-dimensional perturbations, we choose a small spanwise wavenumber, $\beta = 5.7 \times 10^{-5}$. The local Reynolds number, $Re = 704$. Figure 2.5 shows the map of eigenvalues obtained with the help of the spectral collocation method. The frequency parameter is $F = 150 \times 10^{-6}$. One can see the discretized continuous spectra. There are two horizontal branches corresponding to the slow and fast acoustic modes, and a vertical branch corresponding to the vorticity and entropy modes. Also, one can see fast (F) and slow (S) discrete modes. Figure 2.6(a,b) illustrates real, α_r, and imaginary, α_i, parts of the downstream wavenumber α versus the frequency. Lines SA and FA in figure 2.6(b) represent slow and fast acoustic modes with phase velocities $c = 1 \mp 1/M$, respectively. Figure 2.6(b) also shows the line corresponding to the phase velocity $c = 1$ that represents vorticity and entropy perturbations moving with the free stream. One can see that at $\omega \to 0$ the discrete modes S and F are synchronized with the slow (SA) and the fast (FA) acoustic modes. This synchronization means that there is a channel of coupling between the acoustic and discrete modes.

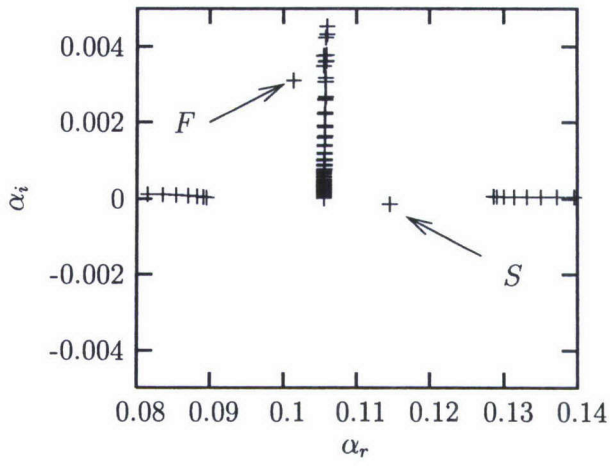

Figure 2.5: Eigenvalue map. $M = 5.6$, $F = 150 \times 10^{-6}$, $Re = 704$, $\beta = 5.77 \times 10^{-5}$.

At $\omega \approx 0.12$, the mode F is synchronized with the vorticity mode ($c = 1$). This synchronization is accompanied by discontinuity in α_i. As was discussed by [FT03], the discrete mode coalesces with the continuous spectrum from one side of the branch cut and reappears on the other side at another point. Mathematically, the pole associated with mode F approaches one side of the branch cut on the complex p plane. At the same time, another pole, located on the lower Riemann sheet, approaches the branch cut from the opposite side. As the pole on the plane coalesces with the branch cut, it moves to the upper Riemann sheet while, simultaneously, the pole that was on the lower Riemann sheet moves into the complex p plane at another point. The discontinuity of α_i at the point of synchronism between a discrete mode with the vorticity/entropy modes could also be noticed in plots published by other authors [Mac69, EB93]. Usually, the discontinuity looks like a wiggle on the plots, and it has not been interpreted as a discontinuity. [BM92] reported coalescence of discrete modes with the vorticity/entropy branch cut in the complex plane α, but they did not report the reappearance of a discrete mode from another side.

There is a synchronism between mode F and mode S at $\omega \approx 0.13$. However, there is no coalescence of the eigenvalues. A model of two-mode synchronism considered in [FK91] and [FK01] explains branching of the modes at the point of synchronism. At this point, one of the modes becomes unstable, whereas the other one moves toward positive α_i. Although in this example the modes have the same value of $c_r \approx \omega/\alpha_r$ at $\omega \approx 0.13$, the minimum of $|\alpha_F - \alpha_S|$ exists in the vicinity of $\omega \approx 0.11$, and this is actually the point of the modes' branching. The synchronism between mode F and the vorticity/entropy modes accompanied by the synchronism between modes F and S suggests that there is a scenario associated with excitation of mode F by vorticity/entropy modes, and mode F can give rise to the

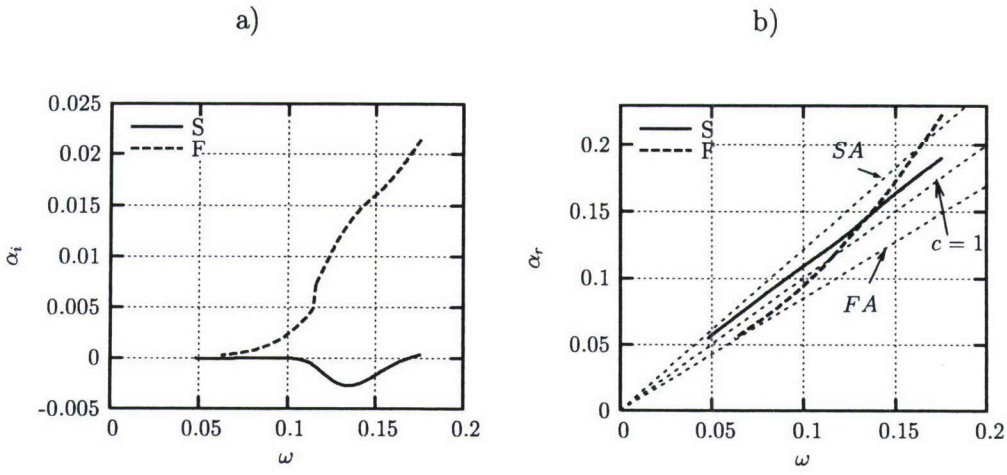

Figure 2.6: Imaginary (a) and real (b) parts of the wavenumber. $M = 5.6$, $Re = 704$, $F = 150 \times 10^{-6}$, $\beta = 5.77 \times 10^{-5}$.

unstable mode S at the point of their synchronism. The aforementioned properties of discrete spectrum are typical for high Mach number ($M > 4$) and an adiabatic wall.

Effect of three-dimensionality on the discrete modes can be depicted as follows. Figure 2.7(a,b) illustrates α_r and α_i for mode S as functions of frequency at three wavenumbers $\beta = 5.77 \times 10^{-5}$, 4.62×10^{-2}, and 9.24×10^{-2}. One can see from figure 2.7 that there is no significant effect on α_r, and that α_i has two minima. The first minimum (at lower ω) demonstrates that the mode is more unstable in the case of three-dimensional perturbations, whereas the magnitude of the second minimum decreases with an increase of β. Usually, these two peaks are associated with Mack's mode 1 and mode 2, respectively. This terminology originated from Mack's analysis of inviscid perturbations [Mac69]. He found that an increase of Mach number is accompanied by an increase of distinct unstable discrete modes. Using asymptotic analysis, [GF89] showed that each amplified inviscid mode represents a separate solution. At finite Reynolds numbers, the structure of the discrete spectrum is different. Results in figure 2.7 correspond to one discrete normal mode, and the minima in α_i are only the footprints of Mack's mode 1 and mode 2.

Decomposition of three-dimensional perturbations

Examples when all components of the vector $\mathbf{A}_0$ are available

Recently, the multimode decomposition was successfully applied by [TWZ07] to an analysis of CFD data in the case of two-dimensional perturbations (see Section 2.5.3). The results of the spatial Cauchy problem subsection and the orthogonality relation (A.6) provide a tool for decomposition of three-dimensional perturbations into normal modes of discrete and continuous spectra. To illustrate application of the method to three-dimensional perturbations,

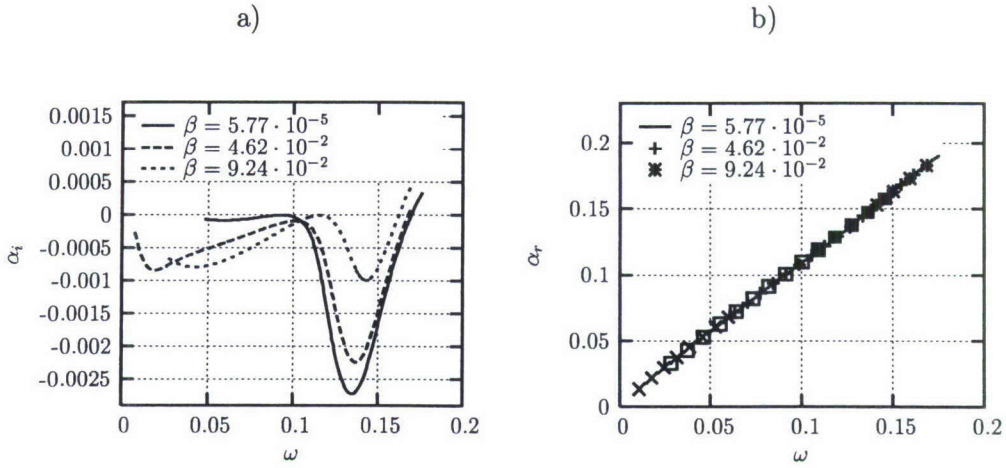

Figure 2.7: Imaginary (a) and real (b) parts of the wavenumber as functions of the frequency at $\beta = const$. Mode S. $M = 5.6$, $Re = 704$.

we emulate the 'CFD' data by superposition of modes from discrete and continuous spectra, and use the orthogonality condition in order to decompose the perturbation and to recover weights of the modes.

In the first example, we consider superposition of mode S, mode F, and a vorticity mode A in the boundary layer over a flat plate at $M = 5.95$, $T_w/T_{ad} = 0.1$. The frequency parameter $F = 10^{-4}$, the Reynolds number $Re = 1895$, and the spanwise wavenumber $\beta = 0.16$. The parameter k of the vorticity mode is equal to one. The eigenfunctions of these modes are normalized by the wall condition $\partial u/\partial y(0) = 1$.

Figure 2.8(a) shows superposition results of two discrete modes with weights $C_S = 1$ and $C_F = -1$ for the slow and fast modes, respectively. Decomposition with the help of the orthogonality relation (A.6) leads to the restored values of the coefficients $C_S = 0.999996 + i\,5.55698 \times 10^{-7}$ and $C_F = -1.00001 + i\,1.78601 \times 10^{-6}$.

Figure 2.8(b) shows results when, in addition to the discrete modes as in figure 2.8(a), there is a vorticity mode with weight $C_V = 2$. For this case, the decomposition with the help of the orthogonality relation (A.6) leads to the coefficients $C_S = 0.999999 + i\,1.21594 \times 10^{-6}$ and $C_F = -1.00002 - i\,3.90897 \times 10^{-6}$.

Examples of decomposition when the perturbations were composed of the mode S ($C_S = 1$), mode F ($C_F = -1$), and an acoustic wave are shown in figure 2.9(a,b). Figure 2.9(a) illustrates the case when the fast acoustic wave was used with $C_{FA} = 2$, $k = 1$, while the example with the slow acoustic wave ($C_{SA} = 2$, $k = 1$) is shown in figure 2.9(b). Results of the decomposition for the case corresponding to figure 2.9(a) were $C_S = 0.999966 - i\,4.79233 \times 10^{-6}$ and $C_F = -1.00008 + i\,6.22089 \times 10^{-5}$. For the example corresponding to figure 2.9(b), we found $C_S = 0.999948 - i\,1.70326 \times 10^{-4}$ and $C_F = -0.999860 + i\,1.87548 \times 10^{-4}$.

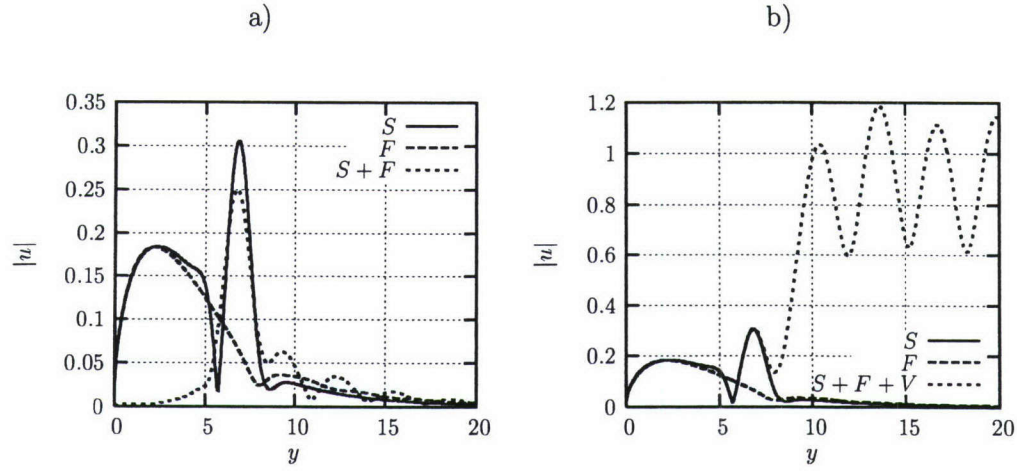

Figure 2.8: Superposition of mode S, mode F, and fast acoustic mode ($k = 1$): a) $C_S = 1$, $C_F = -1$, $C_V = 0$; b) $C_S = 1$,$C_F = -1$, $C_V = 2$. $M = 5.95$, $T_w/T_{ad} = 0.1$, $F = 10^{-4}$, $Re = 1895$, $\beta = 0.16$.

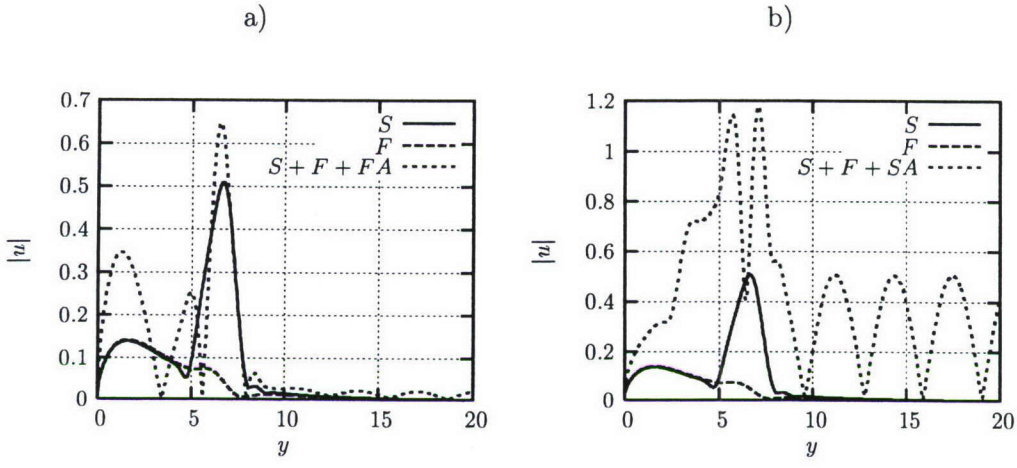

Figure 2.9: Superposition of mode S, mode F, and acoustic modes ($k = 1$). a) Two discrete modes and fast acoustic mode; b) Two discrete modes and slow acoustic mode. $M = 5.95$, $T_w/T_{ad} = 0.1$, $F = 10^{-4}$, $Re = 2300$, $\beta = 0.16$, $C_S = 1$, $C_F = -1$,$C_{FA} = 2$, $C_{SA} = 2$.

An example with partial data available

Similarly to the analysis of two-dimensional perturbations in Section 2.5.2, one can consider decomposition of three-dimensional perturbations when only partial information is available, as happens when experimental data are used. To proceed with the decomposition, one has to make an assumption about the modes that had input into the measured function. The accuracy of the assumption can be checked *a posteriori* by comparing the measured function to that constructed with the weights found from the decomposition.

Decomposition of steady three-dimensional perturbations into modes of continuous spectra is a more complicated problem because there are overlapping vorticity, entropy, and pressure (subsonic flow) modes of the continuous spectra. In the case of incompressible flow [Tum03], the expansion into vorticity modes of the continuous spectra was approximated by a sum of the finite number of the modes with unknown coefficients that were found from a system of algebraic equations. The same algorithm, in principle, could be utilized for decomposition of perturbations into the vorticity modes of the continuous spectra in a compressible boundary layer. To illustrate the application, we consider a steady perturbation corresponding to optimal transiently growing disturbances at Mach number $M = 3$. We emulate the 'measured' velocity components and temperature perturbations by the solutions of the linearized boundary layer equations over a flat plate with an adiabatic wall [TR03]. The Reynolds number is based on the free-stream velocity and the Blasius scale H is equal to 301.64. The spanwise wavenumber, β, is equal to 0.45.

For the purpose of this analysis, we assume that there is no influence from the upstream modes, and we carry out the decomposition only into two vorticity modes, A and B [see Eqs. (2.31) and (2.32)] and entropy modes. For this type of perturbations (counter-rotating streamwise vortices), we assume that input from the acoustic branch cuts is negligible, and they are not included in the decomposition algorithm. For the present example, the continuous spectrum is discretized by 400 modes on the interval $k \in (0, 4)$.

Overlapping of the entropy and vorticity modes leads to significant complication of the algorithm. In order to avoid the overlapping, we used eigenfunctions of the continuous spectra at small ω. Figure 2.10(a) shows weight, $|C|$, for mode A obtained at $\omega = 10^{-4}$, 10^{-5}, and 5×10^{-6} to illustrate convergence as $\omega \to 0$. For the numerical decomposition into modes of the continuous spectra, in what follows, we use $\omega = 5 \times 10^{-6}$. The magnitudes of the weights for modes A and B and for entropy modes are shown in Figure 2.10(b). Figures 2.11(a,b) and 2.12 demonstrate a comparison of the x-, y-, z-velocity components, and temperature 'measured' and composed with the found weights for the vorticity and entropy modes. Similarly to the incompressible case [Tum03], one can see that there is a discrepancy between the 'measured' and composed data of order $1/Re$.

Discussion of the results

The spatial Cauchy problem was solved for three-dimensional perturbations in compressible boundary layers. Although the numerical examples and the matrix elements in Appendix A.1 were given for two-dimensional boundary layers, all the results of the spatial Cauchy

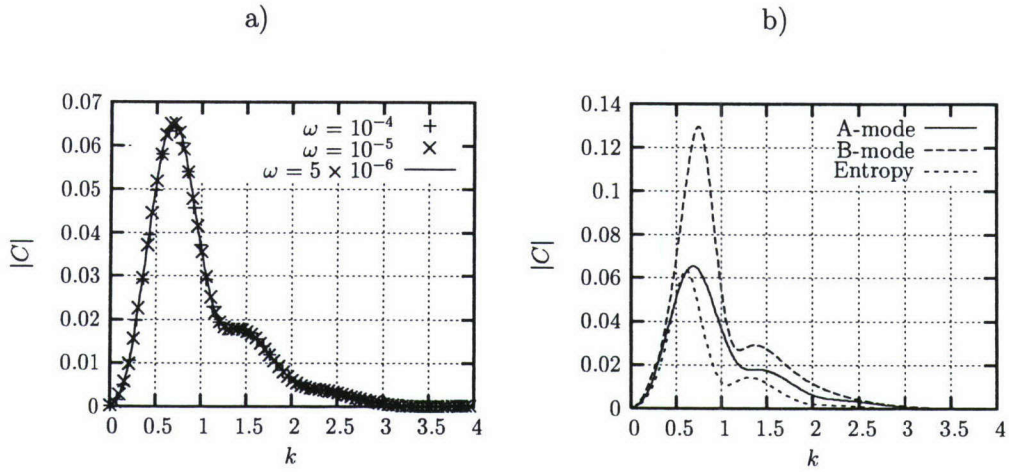

Figure 2.10: Vorticity and entropy modes in the multimode decomposition when three velocity components and temperature are 'measured': a) Vorticity mode A at $\omega = 10^{-4}$, 10^{-5}, and 5×10^{-6}; b) Vorticity modes A and B and entropy mode at $\omega = 5 \times 10^{-6}$. $M = 3$, $Re = 301.64$, $\beta = 0.45$.

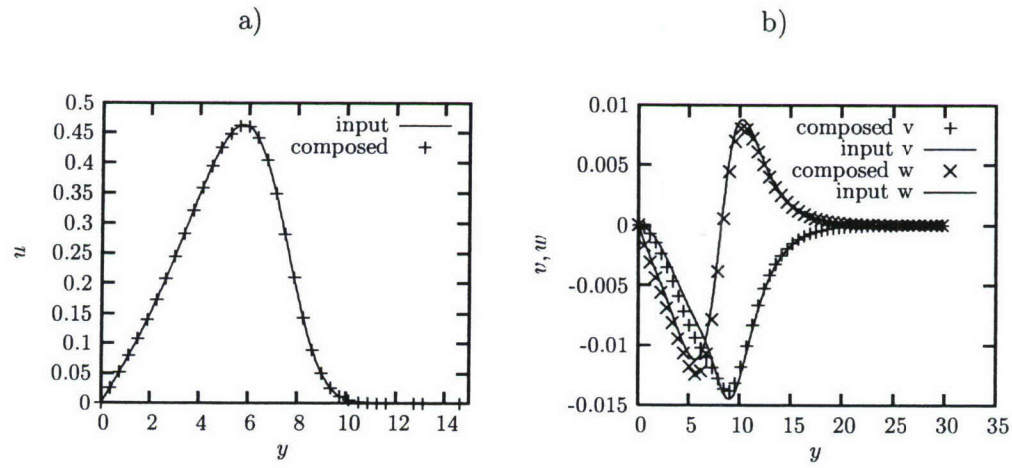

Figure 2.11: Comparison of 'measured' (input) and composed velocity components. $M = 3$, $Re = 301.64$, $\beta = 0.45$.

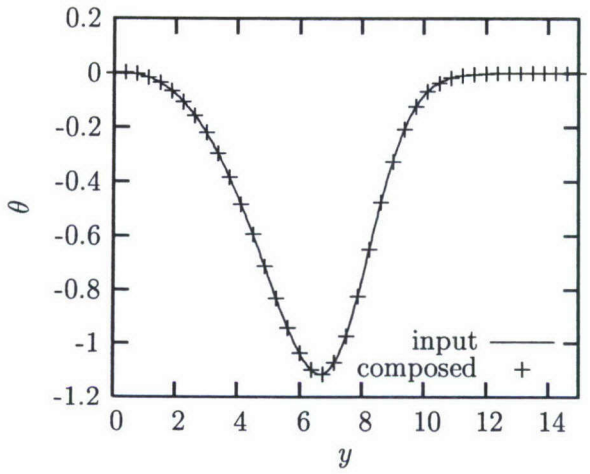

Figure 2.12: Comparison of 'measured' (input) and composed temperature perturbations. $M = 3$, $Re = 301.64$, $\beta = 0.45$.

problem section are valid [after minor adjustments in (2.24)] for three-dimensional boundary layers when the mean flow profiles are independent of the spanwise coordinate, z. These results provide a tool to decompose perturbations given only at a local station, x, into modes of continuous and discrete spectra. In order to be able to distinguish the modes, one needs amplitude and phase distributions for pressure, temperature, and velocity components, together with some of their derivatives with respect to the coordinate x. This is possible in computational studies of perturbations introduced into boundary layers. The latter might be helpful to elucidate underlying mechanisms that are important in laminar-turbulent transition scenarios. For example, we discussed the synchronism of discrete modes F and S. One of them might be unstable, and it could be responsible for transition to turbulence. The other decaying mode might be synchronized with vorticity and entropy modes. It means that there exists a channel: 'vorticity/entropy modes' $\rightarrow$ 'decaying discrete mode' $\rightarrow$ 'unstable discrete mode' $\rightarrow$ 'transition to turbulence' [FK01]. In conventional computational studies, one could observe the generation of the instability mode only in the far field, where the unstable mode dominates the other modes of discrete and continuous spectra. However, the significant element of the scenario - the decaying mode - could not be attained in the analysis. The present method allows evaluation of the amplitude of the decaying modes in order to provide a more rigorous background for interpretation of CFD results (see Section 2.5.3).

Decomposition of perturbations when only partial information is available is an ill-posed problem. Nevertheless, one can apply a regularization procedure to recover the flow field. Actually, the assumption that the flow field is composed of downstream modes only is an

example of regularization leading to decomposition based on measured velocity components and temperature only. We expect that developed methods of regularizations for ill-posed problems [TA77, TGSY95] may allow a further reduction of measured data under reasonable assumptions.

Although the considered examples are associated with the cases when the solution is comprised of the downstream modes only, the orthogonality condition (A.6) allows distinguishing upstream modes in the initial data as well. The main constraint on the initial data is that it must be orthogonal to short-scale upstream modes in order to provide finite downstream growth rate for the solution, and to carry out the inverse Laplace transform.

The solution in the present work is based on the parallel flow approximation. This approximation is valid when the length scale of interest is much smaller than the characteristic scale of the unperturbed flow in the downstream direction. Results of the present work are also based on the assumption that the normalization constant Γ in (A.6) is not equal to zero. [FK02] showed that the constant is equal to zero at the branching point of two discrete modes, and the nonparallel flow effects are to be taken into account in order to resolve the singularity. Analysis of discrete and continuous spectra by [TWZ07] demonstrated that the normalization constant tends to zero also in the case of synchronism between the discrete mode and the continuous spectra (Section 2.5.3). Therefore, an extension of the theoretical model by [FK02] is required when one needs to resolve the mode close to a point of synchronism with the continuous spectra.

Another issue that we find worthwhile to address in this discussion is the terminology used for discrete modes in high-speed boundary layers. Historically, the terminology was introduced by [Mac69]. In his inviscid analysis of perturbations, Mack discovered the existence of new instability modes. At finite Reynolds numbers (see our example in the spectra recapitulation part, there is only one unstable mode having signatures of Mack's mode 1 and mode 2 (see figure 2.7*a*). Mathematically, this is a single mode associated with a pole in the solution (2.26), and the pole is moving around the complex plane in such a way that one can see two peaks in the imaginary part of α. [[BM92] also emphasized that there exists only one unstable eigenvalue, α, for a given β.] These two peaks are associated with Mack's mode 1 and 2. The first peak demonstrates that three-dimensional perturbations grow faster than two-dimensional, whereas the second peak has the opposite trend. One should keep in mind that the terminology based on Mack's modes addresses different behaviors of the same unstable mode at low and high frequencies.

2.3 Receptivity to 3D actuators placed on the wall

2.3.1 Roughness-induced perturbations in incompressible boundary layer

This section is based on the paper published in collaboration with E. Reshotko [TR05].

Tiny roughness elements might be responsible for laminar-turbulent transition associated with the transient growth mechanism of perturbations introduced into the boundary-layer flow [Res01, RT00]. Extensive theoretical analyses of optimal disturbances in incompressible and compressible flows [TR01, TR03] led to correlations for transition Reynolds numbers consistent with the available experimental data [RT04] related to roughness-induced transition. From the theoretical studies, optimal transient growth is associated with streamwise vortices. To investigate the transient growth mechanism experimentally, an array of roughness elements was used in [Whi02, WE97]. Although the experimental results agree qualitatively with the theoretical ones, there are quantitative differences that will be discussed later. In order to resolve the discrepancy and to complete the transient growth scenario, one has to solve the receptivity problem, i.e., find the flow perturbation generated by an array of humps.

Boundary-layer flows in the presence of three-dimensional (3D) humps have been investigated extensively with the help of asymptotic methods [SSB77, BL85, Bog86, Bog87, Bog88] in the limit $\varepsilon = R_L^{-1/8} \to 0$, where R_L is the Reynolds number based on the characteristic length of the oncoming boundary layer, L, and the freestream velocity, U_∞. The asymptotic methods are very helpful for an overall understanding of flow structure and for the purpose of deriving the governing parameters, whereas the quantitative results might be questionable at finite Reynolds numbers. Therefore, it would be preferable to solve the receptivity problem with the help of a method that is applicable to the case of finite Reynolds numbers.

The flow response to a small roughness element on the wall is a particular example of the general receptivity problem. Usually, the term "receptivity" is used for the generation of instability modes only. Because the method applied in the present work originated as a method for solving receptivity problems in boundary layers at finite Reynolds numbers, we would like to outline its origin and how it was verified by comparison with other methods (we do not present a review of the receptivity problem, and the list of references includes only some of the earliest papers and the papers relevant to the verification of the method used in the present work).

[Mor69, Res76] clarified the important role of receptivity in the laminar-turbulent transition process. These papers motivated intensive investigations of various mechanisms responsible for excitation of unstable Tollmien-Schlichting (TS) waves. A partial listing of the vast bibliography on the topic is presented in [Cho98, SRK02, Fed03a].

Theoretical models may be categorized according to their underlying principles as follows: (i) the asymptotic analysis of the linearized Navier-Stokes equations at large Reynolds numbers ($R_L \to \infty$); (ii) the finite Reynolds-number approach based on a combination of analytical models with numerical representation of normal modes; and (iii) direct numerical

simulation. In what follows, we shall address only (i) and (ii).

The first results on the generation of TS waves within the scope of asymptotic methods (the triple-deck theory) were obtained by Terentev [Ter81, Ter84, Ter85] for an actuator on the plate surface. The first theoretical model on the generation of spatially growing TS waves at finite Reynolds numbers was suggested by Gaster [Gas65]. He considered a localized periodic-in-time forcing on the wall and outlined how to evaluate the TS wave amplitude. [AP79] published experimental data on the excitation of TS waves by acoustic waves interacting with a roughness element and suggested a theoretical model, which incorporated simultaneously solving of the direct and adjoint Orr-Sommerfeld equations. In succeeding years, this approach led to the formulation of the biorthogonal eigenfunction system [ZST80, TF83a, TF83b, TF84, Fed84], which turned out to be a powerful technique in solving receptivity problems for spatially developing perturbations. The bulk of the results obtained with this approach were presented by [Fed82].

However, the aforementioned results at finite Reynolds numbers suffered due to uncertainty in the path of integration in the inverse Fourier transform at supercritical frequencies of the forcing, and the hypothesis by [BR82] was adopted in order to include the unstable discrete mode into the downstream solution. Using the triple-deck theory, [Ter84] justified the hypothesis of [BR82]. [AR90] revisited the problem of a vibrating ribbon in a boundary layer at finite Reynolds numbers and resolved the question concerning the contour in the inverse Fourier transform. The result provided a rigorous basis for the analysis of receptivity problems at finite Reynolds numbers. Later on, [Cro92, CS92] extended the analysis to the problem of acoustic waves scattering into TS waves on localized irregularities.

Up to the point where the solution of the problem is presented as an inverse Fourier transform, the finite Reynolds number approach [AR90, Cro92, CS92] and the method based on the biorthogonal eigenfunction system [TA97] are identical. The difference is only in evaluation of the contributions from the poles and from integrals associated with the continuous spectrum. In [AR90, Cro92, CS92], the pole contribution was evaluated in a straightforward manner, whereas solution of the adjoint problem in [ZST80, TF83a, TF83b, TF84, Fed84] served as a convenient filter to evaluate the contribution. It was proved in [TA97] that results of the receptivity problem solution for a localized actuator on the wall obtained within the scope of the biorthogonal eigenmode expansion and with the finite Reynolds-number approach [AR90] are identical.

In this section, the biorthogonal eigenfunction system is applied to the problem of flow perturbation due to a three-dimensional hump (an array of humps) placed on the wall. Due to some obstacles in the extension of the biorthogonal eigenfunction technique to the 3D stationary perturbations, the method had not been applied yet to this type of problem. Recently, however, these issues were resolved in [Tum03]. This makes it possible to revisit the problem of the 3D humps with the help of the biorthogonal eigenfunction expansion.

Problem formulation

We consider a steady two-dimensional incompressible boundary layer in the parallel flow approximation. The coordinate x corresponds to the distance along the surface, y is the

distance from the wall, and the coordinate z represents the distance in the spanwise direction. A localized hump of shape $y_w(x,z) = hf(x,z)$ is placed on the wall, where h stands for the height of the hump and $\max_{x,z}(f) = 1$. The value of h is assumed to be small enough (less than the viscous sublayer thickness [SSB77], $h_{cr} = \epsilon^5 L$) to employ the linearized Navier-Stokes equations and the linearized boundary conditions on the wall

$$y = 0: \qquad u = -hf(x,z)\,U'_w, \quad v = w = 0 \tag{2.40}$$

where (u,v,w) are the perturbation velocity components, $U(y)$ is the undisturbed flow velocity profile, and $U'_w = (dU/dy)_{y=0}$. Far from the hump ($y \to \infty$), the perturbations are assumed to be decaying.

Formal solution

We introduce the vector-function $\mathbf{A} = (u, \partial u/\partial y, v, p, w, \partial w/\partial y, \partial u/\partial x, \partial v/\partial x, \partial w/\partial x)^T$ comprised of nine components, where p stands for the pressure perturbation. The superscript T stands for "transposed". After Fourier transform with respect to x and z, the linearized Navier-Stokes equations are written in the form [Tum03]

$$E\frac{d\mathbf{A}_v}{dy} = H_1\mathbf{A}_v + i\alpha_v H_2\mathbf{A}_v \tag{2.41}$$

where E, H_1, and H_2 are 9×9 matrices (their definitions are given in [Tum03]); α_v is the Fourier transform variable corresponding to the coordinate x; and $\mathbf{A}_v$ is the Fourier transform of $\mathbf{A}$. Actually, Eq. (2.41) represents the continuity equation and three momentum equations supplemented by the definitions of $\partial u/\partial y$, $\partial w/\partial y$, $\partial u/\partial x$, $\partial v/\partial x$, and $\partial w/\partial x$ via the other components. The boundary conditions are the following:

$$\begin{aligned} y &= 0: \qquad A_{v1} = \hat{u}_w(\alpha_v,\beta), \quad A_{v3} = A_{v5} = 0 \\ y &\to \infty: \qquad |A_{vj}| \to 0 \end{aligned} \tag{2.42}$$

where

$$\begin{aligned} \hat{u}_w(\alpha_v,\beta) &= -hU'_w\rho(\alpha_v,\beta) \\ \rho(\alpha_v,\beta) &= \frac{1}{(2\pi)^2}\int_{-\infty}^{+\infty}\int_{-\infty}^{+\infty} f(x,z)\,e^{-i\alpha_v x - i\beta z}dxdz \end{aligned} \tag{2.43}$$

The system of ODE (2.41) has six fundamental solutions, $\mathbf{Z}_1(y), ..., \mathbf{Z}_6(y)$. Their asymptotic behavior outside the boundary layer can be easily found as $\sim \exp(\lambda_j y)$, with complex numbers λ_j, $j = 1, ..., 6$

$$\begin{aligned} \lambda_1 &= -\sqrt{\alpha_v^2+\beta^2}, \quad \lambda_2 = \sqrt{\alpha_v^2+\beta^2} \\ \lambda_{3,5} &= -\sqrt{\alpha_v^2+\beta^2+iR\alpha_v} \\ \lambda_{4,6} &= \sqrt{\alpha_v^2+\beta^2+iR\alpha_v} \end{aligned} \tag{2.44}$$

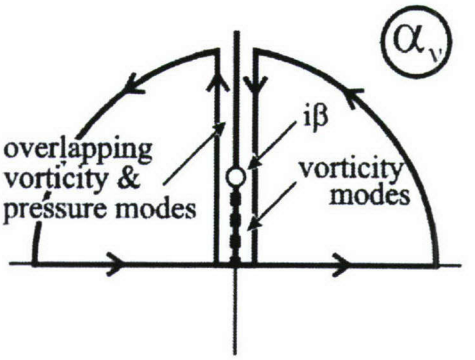

Figure 2.13: The integration path in an evaluation of the inverse Fourier transform with respect to α_v.

where R is the Reynolds number.

In the general case, three fundamental solutions are decaying outside the boundary layer, whereas the other three solutions are exponentially growing. To be specific, we choose $\mathbf{Z}_1(y)$, $\mathbf{Z}_3(y)$, and $\mathbf{Z}_5(y)$ as the decaying solutions. Therefore, the solution of system (2.41) satisfying the boundary conditions (2.42) can be written as follows:

$$\begin{aligned}
\mathbf{A}_v(y;\alpha_v,\beta) &= \frac{\hat{u}_w}{E_{135}}\left(z_{33}z_{55}-z_{35}z_{53}\right)_{y=0}\mathbf{Z}_1(y) \\
&+ \frac{\hat{u}_w}{E_{135}}\left(z_{35}z_{51}-z_{31}z_{55}\right)_{y=0}\mathbf{Z}_3(y) \\
&+ \frac{\hat{u}_w}{E_{135}}\left(z_{31}z_{53}-z_{33}z_{51}\right)_{y=0}\mathbf{Z}_5(y) \qquad (2.45)\\
E_{135} &= \det\begin{pmatrix} z_{11} & z_{13} & z_{15} \\ z_{31} & z_{33} & z_{35} \\ z_{51} & z_{53} & z_{55} \end{pmatrix}_{y=0}
\end{aligned}$$

where z_{ij} stands for ith component of the jth vector. Finally, the formal solution corresponding to the spanwise wave number β will be written as

$$\mathbf{A}_\beta(x,y) = \int_{-\infty}^{+\infty} \mathbf{A}_v(y)\, e^{i\alpha_v x} d\alpha_v \qquad (2.46)$$

After the inverse Fourier transform with respect to β, one can find dependence on the coordinate z, as well.

Up to this point, our analysis is equivalent to the finite Reynolds-number approach [AR90, Cro92, CS92]. The inverse transform (2.46) can be evaluated numerically in a straightforward manner, or one can use an integration path over the upper half of the complex α_v plane, $(x > 0)$, as is shown in figure 2.13. The result will be recast as a sum of integrals along

the branch-cuts (only one branch-cut exists for stationary perturbations) and the residue values originating from the pole singularities (there are no pole singularities in the stationary perturbation case). In the present method, we employ the result in [Tum03] that solution (2.46) can be recast as a sum of normal modes of the continuous spectrum (pressure and vorticity modes), and the coefficients can be determined with the help of the orthogonality condition between the direct and adjoint eigenmodes.

Biorthogonal eigenfunction system

For the sake of clarity, the definition and properties of the biorthogonal eigenfunction system are briefly recapitulated. We introduce the following biorthogonal eigenfunction system $\{\mathbf{A}_\alpha(y), \mathbf{B}_\alpha(y)\}$:

$$\begin{aligned} & E\frac{d\mathbf{A}_\alpha}{dy} = H_1\mathbf{A}_\alpha + i\alpha H_2\mathbf{A}_\alpha \\ & y = 0: \qquad A_{\alpha 1} = A_{\alpha 3} = A_{\alpha 5} = 0 \\ & y \to \pm\infty: \quad |A_{\alpha j}| < \infty, \quad (j = 1, ..., 9) \end{aligned} \tag{2.47}$$

$$\begin{aligned} & -E\frac{d\mathbf{B}_\alpha}{dy} = H_1^T\mathbf{B}_\alpha + i\alpha H_1^T\mathbf{B}_\alpha \\ & y = 0: \qquad B_{\alpha 2} = B_{\alpha 4} = B_{\alpha 6} = 0 \\ & y \to \pm\infty: \quad |B_{\alpha j}| < \infty, \quad (j = 1, ..., 9) \end{aligned} \tag{2.48}$$

where α is a complex number and the subscript 'α' indicates the corresponding solution. With the help of the analysis of the fundamental solutions from [Tum03], we arrive at the conclusion that the eigenvalues α belong to the discrete or continuous spectrum. In the case of the continuous spectrum, α are found from equations $\lambda_j^2 = -k^2$, $j = 1, ..., 6$, where k is a real parameter ($k > 0$) and λ_j, $j = 1, ..., 6$ are defined in Eq. (2.44). The corresponding solutions, $\alpha(k)$, represent the branch-cuts in the complex plane on figure 2.13.

Actually, Eq. (2.48) defines the complex conjugate of the conventional adjoint problem (in the numerical implementation, we use only the complex conjugate solution). The system of equations in the direct problem (2.47) can be recast as follows:

$$\frac{d\mathbf{z}}{dy} = H_0\mathbf{z} \tag{2.49}$$

whereas the adjoint problem (2.48) can be recast as

$$\begin{aligned} & -\frac{d\mathbf{Y}}{dy} = H_0^T\mathbf{Y} \\ & y = 0: \quad Y_2 = Y_4 = Y_6 = 0 \\ & y \to \infty: \quad |Y_j| < \infty, \quad (j = 1, ..., 6) \end{aligned} \tag{2.50}$$

Elements of the matrix H_0 are given in [Tum03]. One can find the following relationship

between the solutions of (2.48) and (2.50):

$$\begin{aligned} &B_{\alpha 1} = Y_1, \quad B_{\alpha 2} = Y_2, \quad B_{\alpha 3} = Y_3, \\ &B_{\alpha 4} = Y_4, \quad B_{\alpha 5} = Y_5, \quad B_{\alpha 6} = Y_6, \\ &B_{\alpha 7} = i\alpha B_{\alpha 2}, \quad B_{\alpha 8} = -\frac{i\alpha B_{\alpha 4}}{R}, \\ &B_{\alpha 9} = i\alpha B_{\alpha 6} \end{aligned} \tag{2.51}$$

Modes of the continuous spectra outside the boundary layer have asymptotic behavior $\sim \exp(\pm iky)$. There are downstream and upstream modes [Tum03]. Because we are going to consider perturbations downstream from the hump, only downstream modes will be taken into account. Among these downstream modes, one can recognize pressure modes with the streamwise wave number

$$\alpha = i\sqrt{k^2 + \beta^2}, \quad k > 0 \tag{2.52}$$

The pressure modes have a pressure perturbation not equal to zero outside the boundary layer, whereas the vorticity perturbation is equal to zero. As a result of the 3D character of the problem, there are two types of vorticity modes with the streamwise wave number

$$\alpha = -\frac{iR}{2}\left(1 - \sqrt{1 + \frac{4\left(k^2 + \beta^2\right)}{R^2}}\right) \tag{2.53}$$

The vorticity modes have a zero pressure perturbation outside the boundary layer and a non-zero vorticity perturbation. In order to distinguish between the two types of vorticity modes, they were referred to as modes "A" and "B", respectively, in [Tum03]. The following orthogonality relation is valid [Tum03]:

$$\langle H_2 \mathbf{A}_\alpha, \mathbf{B}_{\alpha'} \rangle \equiv \int_0^\infty \sum_{j,m=1}^{9} H_2^{jm} A_{\alpha j} B_{\alpha' m} dy = Q\Delta_{\alpha,\alpha'} \tag{2.54}$$

where $\Delta_{\alpha,\alpha'}$ is the Kronecker symbol if α or α' belongs to the discrete spectrum; $\Delta_{\alpha,\alpha'} = \delta(\alpha - \alpha')$ is a delta-function if both α and α' belong to the continuous spectrum. Coefficient Q on the right-hand side of (2.54) depends on normalization of $\mathbf{A}_\alpha(y)$ and $\mathbf{B}_\alpha(y)$.

Contribution of the modes in the formal solution

It was shown in [Tum03] that the eigenfunction system is complete, i.e., a spatially growing/decaying solution of linearized Navier-Stokes equations can be presented as an expansion into the eigenfunction system. In the case of steady perturbations, it means that solution (2.46) can be presented as follows:

$$\mathbf{A}_\beta = \sum_j \int_0^\infty c_j(k) \mathbf{A}_\alpha(y) e^{i\alpha_j(k)x} dk \tag{2.55}$$

where $\sum_j$ stands for summation over the downstream pressure and vorticity modes and α_j corresponds to the downstream pressure or vorticity modes from Eqs. (2.52) and (2.53), respectively.

With the help of the orthogonality condition (2.54), one can find from Eq. (2.55) at some distance x

$$c_j(k)e^{i\alpha_j x} = \frac{\langle H_2\mathbf{A}_\beta, \mathbf{B}_{\alpha_j}\rangle}{Q_j} \tag{2.56}$$

If we consider the dot-product of Eq. (2.41) and $\mathbf{B}_{\alpha_j}$ and integrate with respect to y over the interval $[0,\infty)$, we arrive at the following relationship:

$$\langle H_2\mathbf{A}_v, \mathbf{B}_{\alpha_j}\rangle = \frac{\left(A_{v1}B_{\alpha_j 1}\right)_{y=0}}{i\left(\alpha_j - \alpha_v\right)} = \frac{\hat{u}_w\left(\alpha_v,\beta\right)B_{\alpha_j 1,w}}{i\left(\alpha_j-\alpha_v\right)} \tag{2.57}$$

where $B_{\alpha_j 1,w}$ is the first component of vector $\mathbf{B}_{\alpha_j}$ evaluated at $y=0$.

Substitution of the formal solution (2.46) into Eq. (2.56) together with Eq. (2.57) leads to the following result

$$c_j(k) = -\frac{B_{\alpha_j 1,w}}{Q_j}\int_{-\infty}^{+\infty}\frac{e^{i(\alpha_v-\alpha_j)x}\hat{u}_w\left(\alpha_v,\beta\right)}{i\left(\alpha_v-\alpha_j\right)}d\alpha_v \tag{2.58}$$

By closing the path of integration in the upper half-plane, one can find the coefficient as the residue value at $\alpha_v = \alpha_j$

$$c_j(k) = -\frac{2\pi}{Q_j}\hat{u}_w\left(\alpha_j,\beta\right)B_{\alpha_j 1,w} = \frac{2\pi h}{Q_j}U_w'\rho\left(\alpha_j,\beta\right)B_{\alpha_j 1,w} \tag{2.59}$$

Finally, substitution of coefficients $c_j(k)$ into Eq. (2.55) provides the solution of the receptivity problem.

Numerical examples

For the purpose of illustration, we consider an array of humps (figure 2.14). In this case, we use a Fourier series instead of the Fourier transform with respect to the spanwise coordinate, z. In the first example, the parameters are chosen in accordance with experimental conditions [WE97] in a boundary layer over a flat plate. The roughness strip was placed at $x_{rough} = 300$ mm. The distance between the centers of the dots was equal to $L_z = 19$ mm. The unit Reynolds number was equal to $U_\infty/\nu = 627 \times 10^3$ m^{-1}. It was found that the base flow parameters fit the Blasius solution, with the virtual origin at $x_0 = 58$ mm. Therefore, the Blasius length scale is $H = \sqrt{\nu(x_{rough}-x_0)/U_\infty} = 0.621$ mm. The corresponding Reynolds number, $R = U_\infty H/\nu$, is equal to 390. The roughness strip was composed of dots of diameter $D = 6.35$ mm ($D/H = 10.23$) and having a height of $h = 0.47$ mm. One can recognize that the height ($h/H = 0.757$) is too large to use the linearized boundary conditions (2.40). Therefore, the linearized analysis can only qualitatively approximate the experiment.

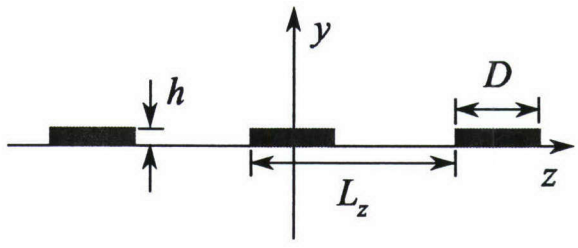

Figure 2.14: The array of humps.

Because $2\pi H/L_z = 0.205$, we are considering the following spanwise wave numbers: $\beta_n = n \times 0.205$, $n = 1, 2, ..., 12$. For the purpose of illustration, we exclude input from $\beta = 0$. This allows exclusion of the pressure modes from consideration because they have $\mathrm{Im}(\alpha) \geq \beta$, and one can choose a distance x downstream from the hump where the input of the pressure modes will be small in comparison with the input from vorticity modes "A" and "B". Integrals with respect to the parameter k were evaluated numerically on the interval $0 < k < 12$ (similarly to [Tum03]) with 250 modes on the interval. The number of modes was chosen after convergence tests with up to 500 modes on the interval.

Figures 2.15 and 2.16 demonstrate the results of the summation of the first 12 terms of the Fourier series for the velocity perturbations downstream from the roughness strip at a distance equal to $5.51D$ (corresponding to 35 mm). Figure 2.15 shows contours of the streamwise velocity perturbation in the $y-z$ plane. One can see the wake region downstream from the hump and high-speed streaks aside the hump. Velocity perturbation in the high-speed streaks is above 10^{-3}, whereas the velocity perturbation in the wake region is about -4×10^{-3}. A vector plot of the flow field in the $y-z$ plane is shown in figure 2.16. One can see that there is a pair of counter-rotating streamwise vortices. This topology of the flow field is associated with very small humps represented by the linearized boundary conditions (2.40), and it is in agreement with the result obtained within the triple-deck asymptotic analysis [TR04b]. Recently, [FC04] carried out a numerical simulation of the flow accurately resolving the shape of the hump. Their results revealed that there is a pair of two counterrotating streamwise vortices in the near field. The difference between the linear solution and the numerical result is attributed to the nonlinear character of the receptivity problem. Energies of the first six spanwise Fourier harmonics, $E_n = \int_0^\infty u_n^2(y)\, d(y/H)$, evaluated with the streamwise velocity perturbation at $z = 0$ are shown in figure 2.17. At the end of the interval, $(x - x_{rough})/H = 120$, harmonics $n = 1$, 2, 3, and 5, as one can see from figure 2.17, are the dominating ones, whereas the experimental [WE97] and computational [FC04] data demonstrate that the harmonics are ordered as 3, 4, 1 and 2.

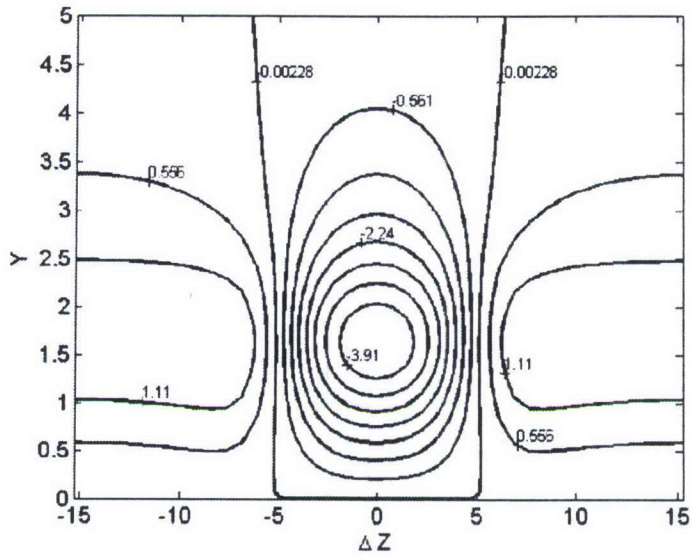

Figure 2.15: Contours of the streamwise velocity perturbation downstream ($\Delta x = 5.51$) from the hump (dot) in steps of 0.558 from -3.91 to +1.11 (the values are multiplied by 10^3). The length scale is equal to $H = 0.621$ mm.

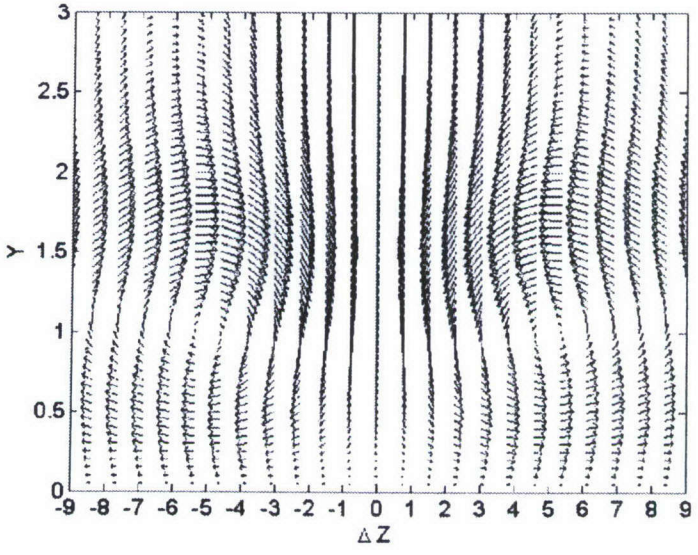

Figure 2.16: The vector plot corresponding to figure 2.15 in the $y - z$ plane. The length scale is equal to $H = 0.621$ mm.

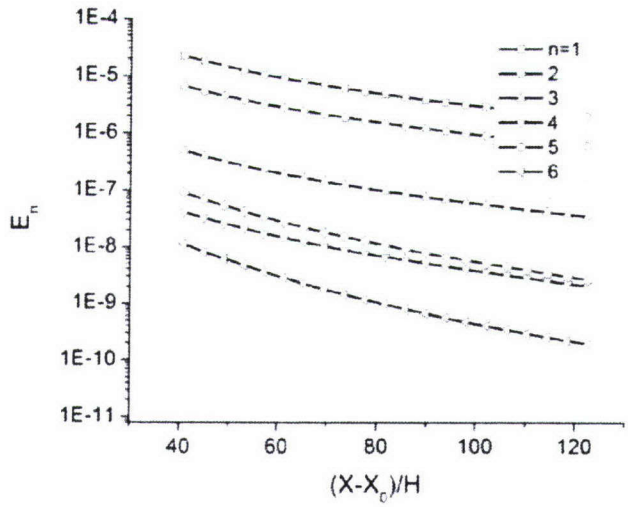

Figure 2.17: Energies of the spanwise Fourier harmonics versus the downstream coordinate $(x - x_{rough})$ at parameters corresponding to [WE97].

Another example is associated with the numerical simulation of flow behind an array of roughness elements by Joslin and Grosch [JG95]. They solved nonlinear equations for perturbations, but the boundary conditions were linearized as in Eq. (2.40). The goal of [JG95] was to simulate the experimental conditions of [GGJ94], where a hump was located in a boundary layer over a flat plate at 400 mm from the leading edge. For purposes of the numerical simulation, the array of humps was chosen with a spanwise period of $L_z = 50$ mm. The local Reynolds number based on the displacement thickness, R_{δ^*}, was equal to 1200 and the local displacement thickness, δ^*, was equal to 1 mm. The shape of the hump chosen for the computations was defined by the following equation [JG95]

$$h(x,z) = a\cos^3\left(\frac{\pi\Delta x}{l_x}\right)\cos^3\left(\frac{\pi\Delta z}{l_z}\right) \tag{2.60}$$

where Δx and Δz are measured from the center of the hump, amplitude $a = 0.1$, $l_x = 15.9$, and $l_z = 13$ (all these parameters are scaled with the displacement thickness, δ^*, as it was chosen in [JG95] in order to simplify comparisons). In this example, $2\pi\delta^*/L_z = 0.126$, and, similarly to the previous example, we include only the first 12 harmonics with $\beta_n = n \times 0.126\,(n = 1, 2, ..., 12)$. Because the closest velocity field in the $y - z$ plane was reported at dimensionless $x = 503$ ($\Delta x = 103$ downstream from the hump), we solve the receptivity problem and find the flow field at this distance in accordance with the method described above. Although for this distance (about 100 displacement thicknesses) nonparallel flow effects have to be taken into account, our results are based on the parallel flow approximation. The height of the hump ($0.1\delta^*$) is still large for the linear receptivity problem, and it should

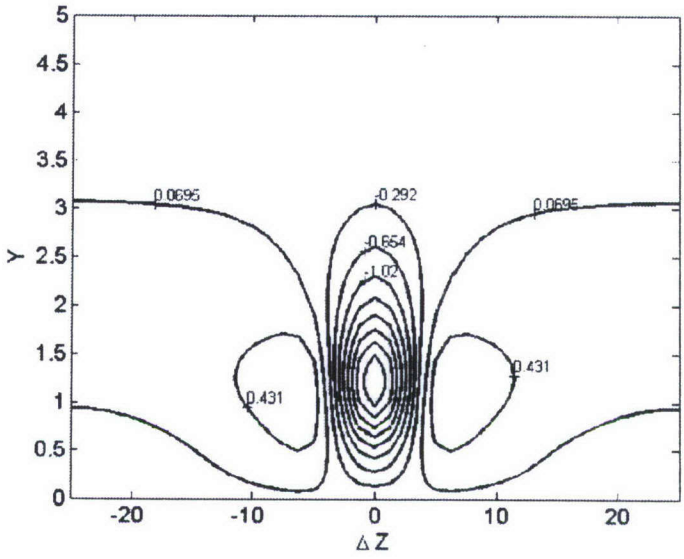

Figure 2.18: Contours of the streamwise velocity perturbation downstream from the hump ($\Delta x = 103$) as in [JG95] in steps of 0.362 from -2.83 to + 0.431 (the values are multiplied by 10^4). The length scale is equal to $\delta^* = 1$ mm.

be taken into account in the following comparisons with computational results.

Figure 2.18 shows contours of the streamwise velocity perturbation in the $y - z$ plane. One can see the wake region downstream from the hump and high-speed streaks aside the hump. Velocity perturbation in the high-speed streaks is about $+0.5 \times 10^{-4}$, whereas the velocity perturbation in the wake region is about -3×10^{-4}. These values are different from those reported in [JG95] ($+0.48 \times 10^{-3}$ and -1.69×10^{-3} respectively). Contours of $\sqrt{v^2 + w^2}$ in the $y-z$ plane are shown in figure 2.19. Our results correspond to a maximum value about 9×10^{-6}, whereas the authors of [JG95] report 2.62×10^{-5}. A vector plot of the flow field in the $y - z$ plane is shown in figure 2.20. The linear theory gives only a pair of counter-rotating streamwise vortices, whereas the vector plot in [JG95] has a more complicated structure. Energies of the first six spanwise Fourier harmonics, $E_n = \int_0^\infty u_n^2(y)\, d(y/\delta^*)$, evaluated with the streamwise velocity perturbation at $z = 0$ are shown in figure 2.21. In this case, one can see that harmonics $n = 2$ and 3 overcome the first one at $(x - x_{rough}) \geq 6 l_x$.

In the following example, we consider the same flow parameters corresponding to figures 2.18-2.21, but the shape of the hump is replaced by a rectangle having $l_x = 15.9$ and $l_z = 13$. The height of the hump is the same, $a = 0.1$. Figure 2.22 shows contours of the streamwise velocity in the $y-z$ plane at $\Delta x = 103$. One can see that there are two relatively high-speed streaks in the wake region. Comparison of the results in figures 2.18 and 2.22 illustrate the hump geometry effect.

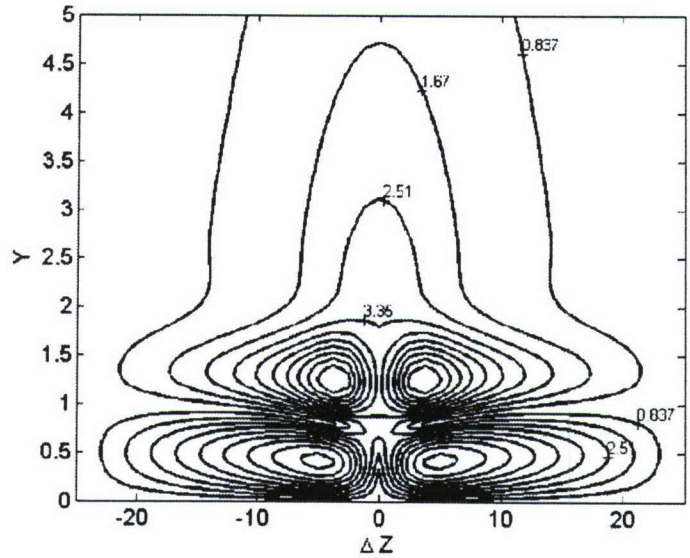

Figure 2.19: Contours of $\sqrt{v^2 + w^2}$ in the $y-z$ plane downstream from the hump ($\Delta x = 103$) as in [JG95] in steps of 0.837 from 0.837 to 8.37 (the values are multiplied by 10^6). The length scale is equal to $\delta^* = 1$ mm.

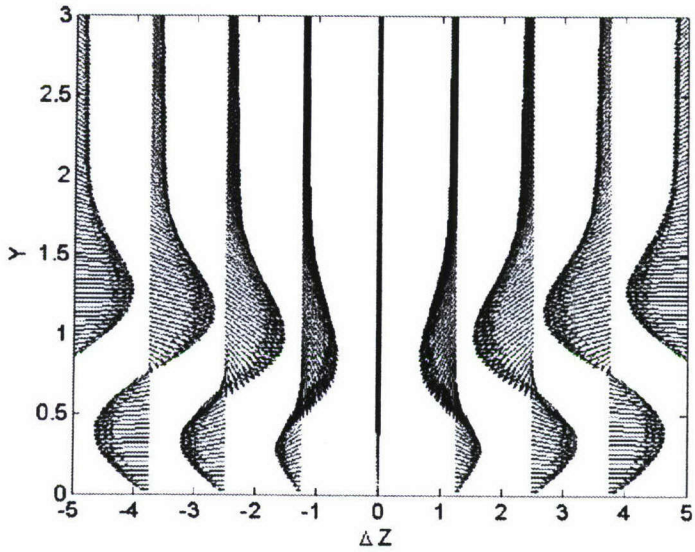

Figure 2.20: The vector plot corresponding to figures 2.18 and 2.19 in the $y - z$ plane. The length scale is equal to $\delta^* = 1$ mm.

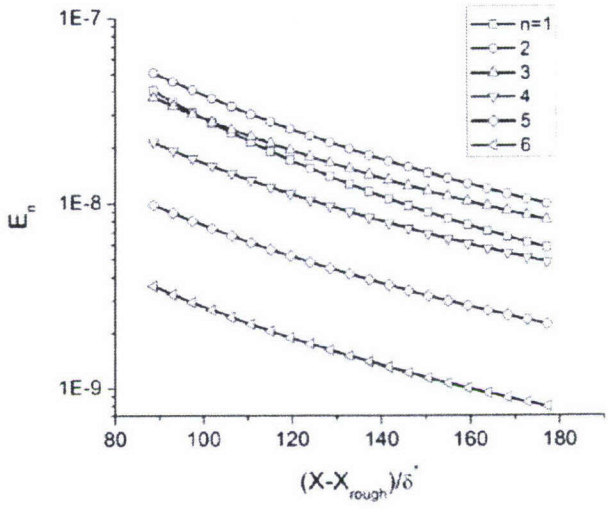

Figure 2.21: Energies of the spanwise Fourier harmonics versus the downstream coordinate $(x - x_{rough})$ at parameters corresponding to [JG95].

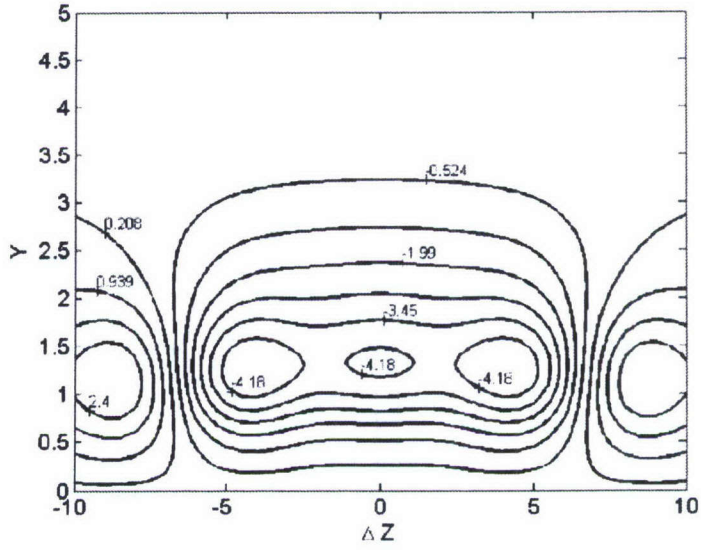

Figure 2.22: Contours of the streamwise velocity perturbation downstream from the rectangular hump ($\Delta x = 103$) in steps of 0.731 from -4.18 to +2.4 (the values are multiplied by 10^4). The length scale is equal to $\delta^* = 1$ mm.

Discussion

The linear receptivity of the boundary-layer flow to a 3D hump has been solved with the help of the biorthogonal eigenfunction system. This approach provides a convenient tool to filter out the amplitude of a normal mode representing the flow field. Only the formal solution (2.55) of the elliptic boundary value problem for the perturbations had to be found in order to filter out the modes of interest. As a result, the flow field in the $y-z$ plane could be computed locally on a conventional computer.

The triple-deck asymptotic analysis [SSB77, BL85, Bog86, Bog87, Bog88] of perturbations in the vicinity of a three-dimensional hump revealed that the linearized boundary conditions are applicable only when the height of the hump is much smaller than the viscous sublayer thickness, i.e., $h << h_{cr} = \epsilon^5 L$. For example, h_{cr}/δ^* is 0.13 and 0.11 in [FC04] and [JG95], respectively. If the height is comparable with the viscous sublayer thickness h_{cr} or larger, the governing equations in the vicinity of the hump are also nonlinear (boundary-layer equations), whereas in the main and the outer decks (the main and the outer parts of the boundary layer, respectively) the governing equations are linear. In the considered examples, we compared the results of the linear theory with the computational results at heights, h/δ^*, equal to 0.44 and 0.1 (heights of roughness elements considered in [FC04] and [JG95], respectively). As expected, these heights are too large to be treated within the scope of the linear theory, and our results illustrate the discrepancy between the linear theory and the computations stemming from the nonlinear character of the receptivity problem.

In both cases [FC04, JG95], the choice of parameters was motivated by available experimental data [WE97, GGJ94] that were limited by the desirable accuracy in measurements of small velocity perturbations. Because the numerical simulations [FC04, JG95] require supercomputing, we do not have parametric studies of flow past roughness elements in order to explore effects of the roughness shape. One should expect that the results can be strongly affected by the geometry. For example, [AS87] observed a pair of counter-rotating streamwise vortices (standing vortices in their terminology) behind a hemisphere placed on the wall, whereas they were not observed behind a half teardrop obstacle. The theoretical model developed in the present work may serve as a tool to explore the geometry effects at the limit of small heights.

In order to incorporate the influence of roughness-induced perturbations into the transition prediction theory [RT04], effects of roughness geometry, compressibility and temperature factors should be included. For this purpose, the developed theoretical model has to be extended to the case of compressible boundary layers, and the initial amplitude of the perturbation has to be derived from the receptivity analysis.

The flow field behind the hump possesses a pair of streamwise vortices that bring down the high-speed fluid, whereas the streamwise velocity perturbation in the wake is negative. One can expect that far away from the hump, the velocity perturbation may change its sign due to the downwash motion induced by the streamwise vortices. We have solved linearized boundary layer equations with inflow obtained from the linear receptivity problem [TR04b] in order to explore the possibility of the velocity sign reversal. However, observed weak transient growth was caused by a mismatch in the inflow data, and the corrected results

did not demonstrate the effect, and the perturbation decayed gradually with the distance from the hump. Numerical results [FC04, JG95] and experimental data [WE97] revealed that transient growth can be observed downstream from an array of humps for some spanwise Fourier harmonics. It might be that the effect is associated with the strong nonlinear receptivity mechanism responsible for the near-field perturbation in the computations and the experiment.

2.3.2 Roughness-induced perturbations in a compressible boundary layer

Recently, formulation of the biorthogonal eigenfunction system was extended to the case of three-dimensional perturbations in compressible boundary layers in Ref. [Tum06c]. This extension allows revisiting the receptivity problems with a three-dimensional source of perturbations placed on the wall when a continuous spectrum is of interest as well. It might be an oscillating membrane installed on the surface, a three-dimensional roughness element, periodic-in-time blowing and suction through a hole, wall-temperature perturbations, etc.

At the present time, there are only some limited results on the receptivity to three-dimensional perturbations in compressible boundary layers at finite Reynolds numbers. Tumin [Tum83] considered the vibrating surface of an infinite swept wing. Fedorov [Fed88] applied the biorthogonal eigenfunction technique to crossflow receptivity with a roughness element placed on a swept wing wall. Manuilovich [Man89], Crouch [Cro93], Choudhari [Cho94b], and Ng and Crouch [NC99] analyzed crossflow receptivity in three-dimensional incompressible boundary layers within the scope of the finite Reynolds number approach. Balakumar and Malik [BM92] analyzed the receptivity of supersonic boundary layers to a point source of blowing and suction on the wall. In addition to the discrete modes, they also included input from the continuous spectra in the consideration.

The objective of the section is to solve the receptivity problem when three-dimensional perturbations in a compressible boundary layer are generated by an actuator (periodic-in-time or stationary) placed on the wall by using the biorthogonal eigenfunction system considered in T06.

Problem formulation and formal solution

We consider a steady two-dimensional compressible boundary layer in the parallel flow approximation. The coordinate x corresponds to the distance along the surface, y is the distance from the wall, and the coordinate z represents the distance in the spanwise direction. We consider two problems: blowing-suction through the wall with the amplitude function $v_w(x,z)$, and a localized hump $y_w(x,z) = f(x,z)$ placed on the wall. The height of the hump and the intensity of the blowing-suction are assumed to be small enough to employ the linearized Navier-Stokes equations and the linearized boundary conditions on the wall.

We introduce the vector-function

$$\begin{aligned}\mathbf{A}(x,y,t) = (&u, \partial u/\partial y, v, \pi, \theta, \partial\theta/\partial y, w, \partial w/\partial y,\\ &\partial u/\partial x, \partial v/\partial x, \partial\theta/\partial x, \partial w/\partial x, \partial u/\partial z, \partial v/\partial z, \partial\theta/\partial z, \partial w/\partial z)^T\end{aligned} \tag{2.61}$$

comprised of 16 components, where (u,v,w) are the perturbation velocity components, θ is the temperature perturbation, and π represents the pressure perturbation. The superscript T stands for 'transpose'. The linearized Navier-Stokes equations for a periodic-in-time perturbation, $\sim \exp(-i\omega t)$, are written in the form [Tum06c]

$$\frac{\partial}{\partial y}\left(\mathbf{L}_0\frac{\partial \mathbf{A}}{\partial y}\right) + \mathbf{L}_1\frac{\partial \mathbf{A}}{\partial y} = \mathbf{H}_1\mathbf{A} + \mathbf{H}_2\frac{\partial \mathbf{A}}{\partial x} + \mathbf{H}_3\frac{\partial \mathbf{A}}{\partial z}, \tag{2.62}$$

where $\mathbf{L}_0, \mathbf{L}_1, \mathbf{H}_1, \mathbf{H}_2$, and $\mathbf{H}_3$ are 16×16 matrices (their non-zero elements are presented in Appendix A of [Tum06c]). Solution of (2.62) is subject to the following boundary conditions on the wall and outside the boundary layer

$$y = 0: \quad u = -q_h f(x,z) U'_w, \quad v = q_v v_w(x,z), \quad w = 0, \quad \theta = 0, \tag{2.63a}$$

$$y \to \infty: \quad |A_j| \to 0, \tag{2.63b}$$

where $U'_w = (dU/dy)_{y=0}$ is the derivative of the unperturbed flow velocity profile. For the case of a hump, $q_h = 1$, $q_v = 0$, and $\omega = 0$, whereas for blowing–suction on the wall, $q_h = 0$, $q_v = 1$, and $\omega \neq 0$.

Because the boundary layer is assumed independent of the coordinate z, one can employ the Fourier transform with respect to z. For simplicity, we assume that the perturbation frequency is subcritical, i.e. the perturbation decays downstream from the actuator. In this case, one can employ the Fourier transform with respect to x as well:

$$\mathbf{A}_v(\alpha_v, y, \beta) = \int_{-\infty}^{+\infty}\int_{-\infty}^{+\infty} \mathbf{A}(x,y,z)\, e^{-i\alpha_v x - i\beta z} dz dx. \tag{2.64}$$

In the case of a supercritical frequency, one has to employ the Briggs method in order to include the unstable (exponentially growing downstream mode) into the inverse Fourier transform [AR90, BM92].

Vector–function $\mathbf{A}_v(\alpha_v, y, \beta)$ satisfies the following equation and the boundary conditions

$$\frac{d}{dy}\left(\mathbf{L}_0 \frac{d\mathbf{A}_v}{dy}\right) + \mathbf{L}_1 \frac{d\mathbf{A}_v}{dy} = \mathbf{H}_1 \mathbf{A}_v + i\alpha_v \mathbf{H}_2 \mathbf{A}_v + i\beta \mathbf{H}_3 \mathbf{A}_v, \tag{2.65}$$

$$y = 0: \quad A_{v1} = -q_h U'_w \varphi(\alpha_v, \beta), \quad A_{v3} = q_v \rho(\alpha_v, \beta), \quad A_{v5} = 0, \quad A_{v7} = 0, \tag{2.66a}$$

$$y \to \infty: \quad |A_{vj}| \to 0, \qquad (j = 1, ..., 16); \tag{2.66b}$$

where

$$\varphi(\alpha_v, \beta) = \int_{-\infty}^{+\infty}\int_{-\infty}^{+\infty} f(x,z)\, e^{-i\alpha_v x - i\beta z} dz dx, \tag{2.67a}$$

$$\rho(\alpha_v, \beta) = \int_{-\infty}^{+\infty}\int_{-\infty}^{+\infty} v_w(x,z)\, e^{-i\alpha_v x - i\beta z} dz dx. \tag{2.67b}$$

Equation (2.65) has four fundamental solutions decaying outside the boundary layer [Tum06c]. One can solve the inhomogeneous boundary-value problem as follows:

$$\mathbf{A}_v = C_1 \mathbf{Z}_1 + C_3 \mathbf{Z}_3 + C_5 \mathbf{Z}_5 + C_7 \mathbf{Z}_7, \tag{2.68}$$

where $\mathbf{Z}_1, \mathbf{Z}_3, \mathbf{Z}_5$, and $\mathbf{Z}_7$ are the decaying fundamental solutions. The coefficients C_j in (2.68) are found from the boundary conditions (2.66a) on the wall. The formal solution for the Fourier harmonic, $\mathbf{A}_\beta(x, y, \beta)$, can be written as follows:

$$\mathbf{A}_\beta(x, y, \beta) = \frac{1}{2\pi} \int_{-\infty}^{+\infty} \mathbf{A}_v(\alpha_v, y, \beta)\, e^{i\alpha_v x} d\alpha_v \tag{2.69}$$

The original problem for perturbations of a prescribed frequency ω is an elliptic one. It was shown in [Tum03] and [Tum06c] that if the downstream boundary is located far away, and one can neglect its upstream influence, the solution of the linearized Navier–Stokes equations can be expanded into the normal modes of continuous and discrete spectra.

$$\mathbf{A}_\beta(x, y, \beta) = \sum_j \int_0^\infty C_j(k) \mathbf{A}_{\alpha\beta}(y, k) e^{i\alpha_j(k)x} dk + \sum_m C_m \mathbf{A}_{\alpha_m\beta}(y)\, e^{i\alpha_m x}. \tag{2.70}$$

The first term in (2.70) represents summation over the modes of the continuous spectrum, and the second term represents input of the discrete modes. $\mathbf{A}_{\alpha_m\beta}$ in (2.70) are solutions of the direct eigenvalue problem. Together with the solution of the adjoint problem, $\mathbf{B}_{\alpha\beta}$, they represent the biorthogonal eigenfunction system $\{\mathbf{A}_{\alpha\beta}, \mathbf{B}_{\alpha\beta}\}$ (see [Tum06c]). There is the following orthogonality relation:

$$\langle \mathbf{H}_2 \mathbf{A}_{\alpha\beta}, \mathbf{B}_{\alpha'\beta} \rangle \equiv \sum_{j=1}^{16} \int_0^\infty \left(\mathbf{H}_2 \mathbf{A}_{\alpha\beta}\right)_j B_{\alpha'\beta j} dy = Q \Delta_{\alpha,\alpha'}, \tag{2.71}$$

where $\Delta_{\alpha,\alpha'}$ is the Kronecker delta if α or α' belongs to the discrete spectrum, and $\Delta_{\alpha,\alpha'} = \delta(\alpha - \alpha')$ is the delta function if both α and α' belong to the continuous spectrum. The coefficient Q on the right-hand side of (2.71) depends on the normalization of $\mathbf{A}_{\alpha\beta}(y)$ and $\mathbf{B}_{\alpha\beta}(y)$. The orthogonality relation (2.71) provides a tool to find coefficients C_j and C_m in the formal solution (2.69).

Contribution of the modes to the formal solution

With the help of the orthogonality relation (2.71), one can find the input of a mode to the formal solution

$$C e^{i\alpha x} = \frac{\langle \mathbf{H}_2 \mathbf{A}_\beta, \mathbf{B}_{\alpha\beta} \rangle}{Q_j}. \tag{2.72}$$

If we consider a dot product of $\mathbf{B}_{\alpha\beta}$ and (2.65), and integrate with respect to y over the interval $[0, \infty)$, we arrive at the following identity (we take into account explicit forms of matrices L_0, L_1):

$$\begin{aligned} &\left[L_0^{43} A_{v3} \frac{dB_{\alpha\beta 4}}{dy} - A_{v3} B_{\alpha\beta 3} - A_{v1} B_{\alpha\beta 1} \right]_{y=0} + \left\langle \mathbf{A}_v, \frac{d}{dy}\left(\mathbf{L}_0^T \frac{d\mathbf{B}_{\alpha\beta}}{dy} \right) \right\rangle \\ &- \left\langle \mathbf{A}_v, \mathbf{L}_1^T \frac{d\mathbf{B}_{\alpha\beta}}{dy} \right\rangle = \langle \mathbf{A}_v, \mathbf{H}_1^T \mathbf{B}_{\alpha\beta} \rangle + i\alpha_v \langle \mathbf{A}_v, \mathbf{H}_2^T \mathbf{B}_{\alpha\beta} \rangle + i\beta \langle \mathbf{A}_v, \mathbf{H}_3^T \mathbf{B}_{\alpha\beta} \rangle, \end{aligned} \tag{2.73}$$

where L_0^{43} stands for the element of matrix $\mathbf{L}_0$ having indices $(4,3)$. Taking into account the adjoint equation and the boundary conditions (2.66), one can derive

$$\langle \mathbf{H}_2 \mathbf{A}_v, \mathbf{B}_{\alpha\beta} \rangle = q_v \rho(\alpha_v, \beta) \frac{\left[L_0^{43} \frac{dB_{\alpha\beta 4}}{dy} - B_{\alpha\beta 3} \right]_{y=0}}{i(\alpha_v - \alpha)} + \frac{q_h \varphi(\alpha_v, \beta) \left[B_{\alpha\beta 1} \right]_{y=0} U'_w}{i(\alpha_v - \alpha)} \tag{2.74}$$

We substitute (2.69) into (2.72) and utilize (2.74) to find

$$\begin{aligned} Ce^{i\alpha x} = \frac{1}{2\pi} \frac{q_v}{Q} \int_{-\infty}^{+\infty} e^{i\alpha_v x} \rho(\alpha_v, \beta) \frac{\left[L_0^{43} \frac{dB_{\alpha\beta 4}}{dy} - B_{\alpha\beta 3} \right]_{y=0}}{i(\alpha_v - \alpha)} d\alpha_v \\ + \frac{1}{2\pi} \frac{q_h U'_w}{Q} \int_{-\infty}^{+\infty} e^{i\alpha_v x} \varphi(\alpha_v, \beta) \frac{\left[B_{\alpha\beta 1} \right]_{y=0}}{i(\alpha_v - \alpha)} d\alpha_v. \end{aligned} \tag{2.75}$$

By closing the path of the integrals in the upper half-plane, we find the coefficient as the residue value at the pole $\alpha_v = \alpha$

$$C = q_v \rho(\alpha, \beta) G_v + q_h \varphi(\alpha, \beta) G_h, \tag{2.76a}$$

$$G_v = \frac{1}{Q} \left[L_0^{43} \frac{dB_{\alpha\beta 4}}{dy} - B_{\alpha\beta 3} \right]_{y=0}, \tag{2.76b}$$

$$G_h = \frac{U'_w}{Q} \left[B_{\alpha\beta 1} \right]_{y=0}. \tag{2.76c}$$

The coefficients G_v and G_h in (2.76a) are independent of the blowing-suction distribution or the hump shape.

Receptivity to an array of roughness elements

For the purpose of illustration, we consider an array of humps placed at distance x_0 from the leading edge of a flat plate (in this case, the Fourier transform with respect to z is replaced by the Fourier series). The geometry of the humps is the same as in [JG95]:

$$f(x,z) = a \cos^3\left(\frac{\pi \Delta x}{l_x}\right) \cos^3\left(\frac{\pi \Delta z}{l_z}\right), \tag{2.77}$$

where Δx and Δz are measured from the center of the hump, amplitude $a = 0.172$, $l_x = 27.36$, and $l_z = 22.37$. The spacing between the humps is $L_z = 86.04$. All lengths are scaled with the Blasius scale. The local Reynolds number is $Re = 697.37$. In this example, $2\pi/L_z = 0.073$, and we include only the first 12 harmonics with $\beta_n = n \times 0.073$. Recently, this configuration was analyzed theoretically by Tumin and Reshotko [TR05] (see Section 2.3) within the scope of the receptivity theory for incompressible flow. In this section, we repeat the results of 2.3, assuming that the Mach number was equal to 0.02.

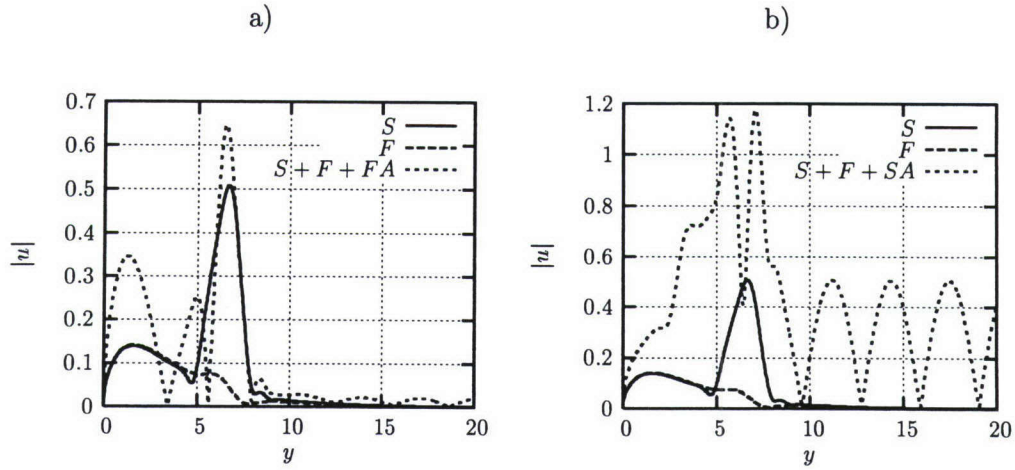

Figure 2.23: Convergence test for the streamwise velocity perturbation at $M = 0.5$ and $T_w/T_{ad} = 1$ at $\omega \to 0$, $x - x_0 = 6.48 l_x$.

Flat plate, M=0.5. In the case of subsonic steady perturbations, there is an overlapping of the two vorticity modes A and B, similarly to the incompressible flow case [Tum03]. In addition, at $\omega = 0$, there is an overlapping of the vorticity modes with the entropy mode. These three modes overlap with the pressure mode at $\mathrm{Im}(\alpha) > |\beta|$ (see [Tum03] and [Tum06c]). Because all these modes decay downstream, one can choose a distance where the pressure modes could be neglected. A numerical evaluation of the integrals in (2.70) associated with the vorticity and entropy modes was done with the help of the trapezoidal formula on a finite interval $[0, k_{max}]$ with 500 steps and $k_{max} = 5$. Overlapping of the vorticity and entropy modes complicates the problem because it requires special treatment. In order to avoid the complication, the eigenfunctions were computed at a small non-zero frequency ω. Figure 2.23 shows the convergence test for the streamwise velocity component at $\omega \to 0$. One can see that the real parts of the streamwise velocity component, $u_r = \mathrm{Real}(u)$, are indistinguishable at $\omega = 10^{-4}$, 10^{-5}, and 5×10^{-6}. The imaginary part, $u_i = \mathrm{Im}(u)$, is very small at $\omega = 5 \times 10^{-6}$ (at $\omega = 0$ it has to be equal to zero). Frequency $\omega = 5 \times 10^{-6}$ was used in the following examples at $M = 0.5$.

A vector plot of the perturbation in the (y, z) plane at distance $x - x_0 = 6.48 l_x$ for the case of an adiabatic wall is shown in figure 2.24*a*, and contours of $u \times 10^5$ are shown in figure 2.24*b*. One can see that the flow structure is similar to the one obtained in Section 2.3: there is a pair of counter-rotating streamwise vortices, there is a wake region downstream from the hump, and there are high-speed streaks on both sides of the hump.

Figure 2.25 illustrates levels of the velocity and temperature perturbations at $x - x_0 = 6.48 l_x$ when the temperature factor, T_w/T_{ad}, is equal to 0.5. One can see that the temperature increases in the wake region, there are cold streaks at the both sides of the hump, and there is a cold streak above the hump. We attribute this cold streak to the displacment of cold

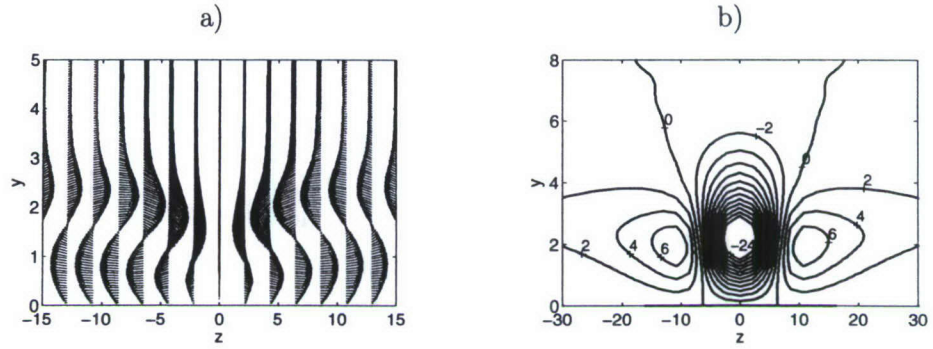

Figure 2.24: a) Vector plot of v and w at $x - x_0 = 6.48l_x$. b) Contour plot of $u \times 10^5$ at $x - x_0 = 6.48l_x$ with step 2 from the starting level -24. Adiabatic wall. $M = 0.5$.

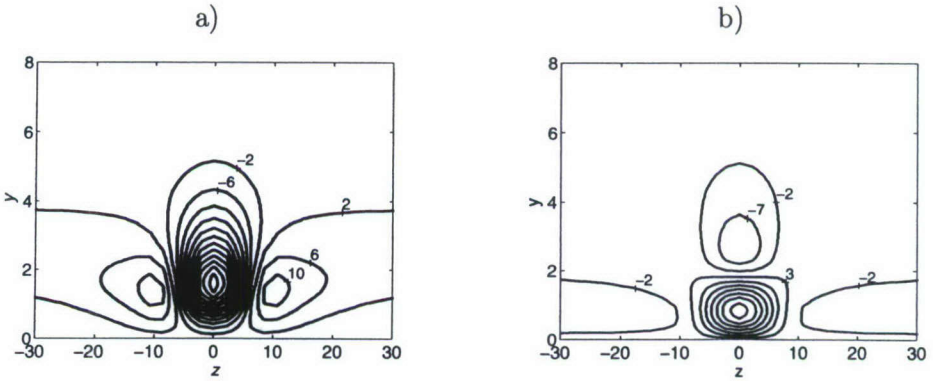

Figure 2.25: a) Contour plots of u and θ at $x - x_0 = 6.48l_x$; a) $u \times 10^5$ with step 4 from the starting level -46; b) $\theta \times 10^5$ with step 5 from the starting level -7. $T_w/T_{ad} = 0.5$, $M = 0.5$.

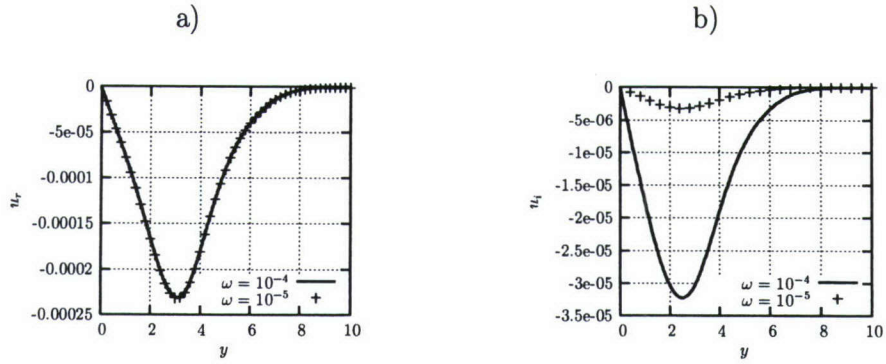

Figure 2.26: Convergence test for the streamwise velocity perturbation at $M = 2$ and $T_w/T_{ad} = 1$ at $\omega \to 0$. $x - x_0 = 6.48 l_x$.

gas by the hump.

Flat plate, M=2. In the case of a supersonic boundary layer, in addition to the vorticity and entropy modes, we have to include also input from the acoustic branch cuts. In what follows, we use interval $[0, k_{max}]$ with 1000 steps and $k_{max} = 10$. As in the previous example, we consider a small nonzero frequency in order to avoid overlapping of the vorticity and the entropy modes in the numerical implementation. Figure 2.26 illustrates the convergence test for the streamwise velocity component when $\omega \to 0$. The imaginary part of the streamwise velocity perturbation is very close to zero at $\omega = 10^{-5}$. This value was chosen for the numerical evaluations.

Temperature perturbation in the (z, y) plane at $x - x_0 = 6.48 l_x$ is shown in figure 2.27. One can see the Mach waves generated by the roughness element located at $z = 0$ and by the neighboring elements. In order to show more detail, streamwise velocity and temperature perturbation profiles at $z = 0$ and $z = 40$ are shown in figure 2.28. One can see that there are three regions at $z = 0$ where the amplitudes of the perturbations are relatively large. The first region is located inside the boundary layer. The second region, at $y \approx 110$, is associated with the Mach wave generated by the roughness element. The other region, at $y \approx 60$, is associated with the Mach waves generated by the left and right neighboring roughness elements in the array. The streamwise velocity and temperature perturbations inside the boundary layer are shown in figure 2.29.

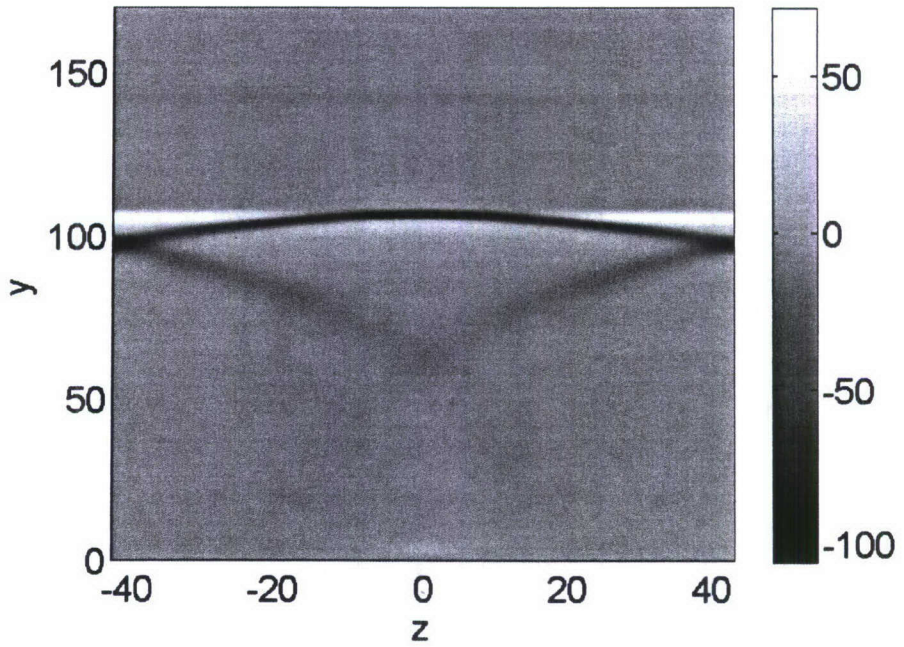

Figure 2.27: Contour plot of $\theta \times 10^5$ at $x - x_0 = 6.48 l_x$. $M = 2$, $T_w/T_{ad} = 1$.

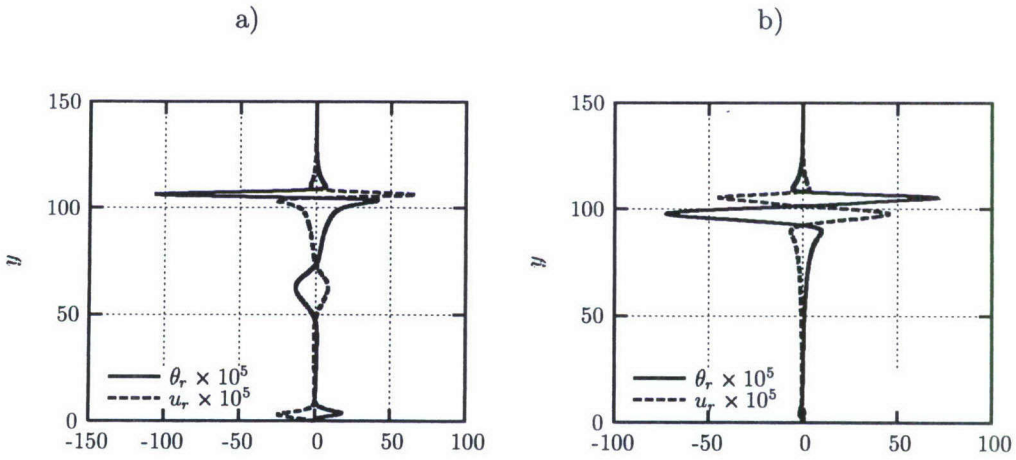

Figure 2.28: Temperature and streamwise velocity perturbations at $x - x_0 = 6.48 l_x$, $M = 2$, $T_w/T_{ad} = 1$. a) $z = 0$, b) $z = 40$.

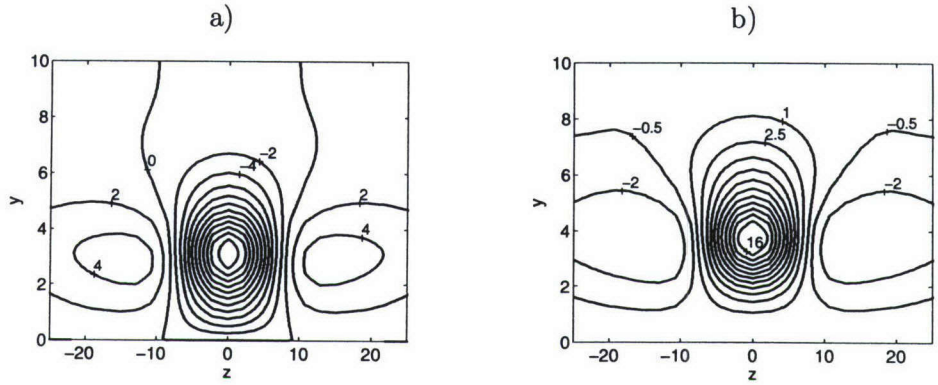

Figure 2.29: a) Contour plots of u and θ at $x - x_0 = 6.48 l_x$ a) $u \times 10^5$ with step 2 from the starting level -22; b) $\theta \times 10^5$ with step 1.5 from the starting level -2. $T_w/T_{ad} = 1$, $M = 2$.

2.4 Nonparallel flow effects on roughness-induced perturbations in boundary layers

The non-parallel flow effects on receptivity are important when the source of the disturbances is distributed on a scale larger than the boundary-layer thickness. Choudhari [Cho94a] and Bertolotti [Ber00] developed methods that can be used for analysis of the receptivity when the nonparallel flow effects are to be included. The nonparallel flow effects on development of unstable discrete modes on a length scale that is much larger than the boundary-layer thickness have been studied within the scope of the method of multiple scales [Bou72, Gas74, SN75, SN77, PN79, Gap80, Nay80, EH80, TF82]. Another method that allows inclusion of the nonparallel flow effects on TS waves is based on the parabolized stability equations [Her97]. To our knowledge, nonparallel flow effects on modes of the continuous spectra have not been addressed yet.

Governing equations

We consider a compressible two-dimensional boundary layer in the Cartesian coordinates, where x and z are the downstream and spanwise coordinates, respectively, and coordinate y corresponds to the distance from the wall. We write the governing equations (the linearized Navier-Stokes equations) for a periodic-in-time perturbation (the frequency is equal to zero in the case of a roughness-induced perturbation), $\sim \exp(-i\omega t)$, in the matrix form

$$\frac{\partial}{\partial y}\left(\mathbf{L}_0\frac{\partial \mathbf{A}}{\partial y}\right)+\mathbf{L}_1\frac{\partial \mathbf{A}}{\partial y}=\mathbf{H}_1\mathbf{A}+\mathbf{H}_2\frac{\partial \mathbf{A}}{\partial x}+\mathbf{H}_3\frac{\partial \mathbf{A}}{\partial z}+\mathbf{H}_4\mathbf{A}, \tag{2.78}$$

where vector $\mathbf{A}$ has 16 components

$$\begin{aligned}\mathbf{A}(x,y,z)=&(u,\partial u/\partial y,v,\pi,\theta,\partial\theta/\partial y,w,\partial w/\partial y,\partial u/\partial x,\partial v/\partial x,\\&\partial\theta/\partial x,\partial w/\partial x,\partial u/\partial z,\partial v/\partial z,\partial\theta/\partial z,\partial w/\partial z)^T.\end{aligned} \tag{2.79}$$

$\mathbf{L}_0,\mathbf{L}_1,\mathbf{H}_1,\mathbf{H}_2,\mathbf{H}_3$, and $\mathbf{H}_4$ are 16×16 matrices (their definitions are given in Appendix of [Tum08]); u,v,w,π, and θ represent three velocity components, pressure, and temperature perturbations, respectively; and the superscript T in (2.79) stands for transposed. Matrix $\mathbf{H}_4$ originates from the nonparallel character of the flow.

We utilize the Fourier transform with respect to the coordinate z

$$\mathbf{A}_\beta(x,y)=\int_{-\infty}^{\infty}e^{-i\beta z}\mathbf{A}(x,y,z)\,dz. \tag{2.80}$$

In the quasi-parallel flow approximation, the solution of the linearized Navier-Stokes equations can be expanded into normal modes of the discrete and continuous spectra [Tum07]

$$\mathbf{A}_\beta(x,y)=\sum_\nu d_\nu A_{\alpha_\nu\beta}(y)\,e^{i\alpha_\nu x}+\sum_j\int_0^\infty d_j(k)\,A_{\alpha_j\beta}(y)\,e^{i\alpha_j(k)x}dk. \tag{2.81}$$

Here, Σ_ν and Σ_j denote sums over the discrete spectrum and branches of the continuous spectra, respectively. The coefficients d_ν and d_j are to be found from the receptivity problem solution [Tum06b].

The following biorthogonal eigenfunction system $\{\mathbf{A}_{\alpha\beta}, \mathbf{B}_{\alpha\beta}\}$ was formulated in [Tum07]:

$$\frac{d}{dy}\left(\mathbf{L}_0\frac{d\mathbf{A}_{\alpha\beta}}{dy}\right) + \mathbf{L}_1\frac{d\mathbf{A}_{\alpha\beta}}{dy} = \mathbf{H}_1\mathbf{A}_{\alpha\beta} + i\alpha\mathbf{H}_2\mathbf{A}_{\alpha\beta} + i\beta\mathbf{H}_3\mathbf{A}_{\alpha\beta}, \tag{2.82}$$

$$y = 0: \quad A_{\alpha\beta1} = A_{\alpha\beta3} = A_{\alpha\beta5} = A_{\alpha\beta7} = 0,$$

$$y \to \infty: \quad |A_{\alpha\beta j}| < \infty,$$

$$\frac{d}{dy}\left(\mathbf{L}_0^T\frac{d\mathbf{B}_{\alpha\beta}}{dy}\right) - \mathbf{L}_1^T\frac{d\mathbf{B}_{\alpha\beta}}{dy} = \mathbf{H}_1^T\mathbf{B}_{\alpha\beta} + i\alpha\mathbf{H}_2^T\mathbf{B}_{\alpha\beta} + i\beta\mathbf{H}_3^T\mathbf{B}_{\alpha\beta}, \tag{2.83}$$

$$y = 0: \quad B_{\alpha\beta2} = B_{\alpha\beta4} = B_{\alpha\beta6} = B_{\alpha\beta8} = 0,$$

$$y \to \infty: \quad |B_{\alpha\beta j}| < \infty.$$

Actually, (2.83) defines the complex conjugate of the conventional adjoint problem.

The eigenfunction system $\{\mathbf{A}_{\alpha\beta}, \mathbf{B}_{\alpha\beta}\}$ has an orthogonality relation given as

$$\langle \mathbf{H}_2\mathbf{A}_{\alpha\beta}, \mathbf{B}_{\alpha'\beta}\rangle \equiv \int_0^\infty (\mathbf{H}_2\mathbf{A}_{\alpha\beta}, \mathbf{B}_{\alpha'\beta})dy = \Gamma\Delta_{\alpha\alpha'}, \tag{2.84}$$

where Γ is a normalization constant; $\Delta_{\alpha\alpha'}$ is a Kronecker delta if either α or α' belongs to the discrete spectrum; $\Delta_{\alpha\alpha'}$ is a Dirac delta function if both α and α' belong to the continuous spectrum. Because Eq. (2.83) represents the complex conjugate of the conventional problem, the dot product $(,)$ in (2.84) does not involve complex conjugation.

Weakly nonparallel flow analysis

Discrete mode

For the purpose of clarity, we begin with an outline of analysis for a discrete mode in a weakly nonparallel boundary layer (see, for example, [Nay80]).

In a weakly nonparallel flow, one can employ the method of multiple scales by introducing fast (x) and slow ($X = \varepsilon x, \varepsilon \ll 1$) scales. The mean flow profiles depend on y and X only, whereas the perturbation will depend on both length scales. In the case of a discrete mode, solution of the linearized Navier-Stokes equation is presented in the form

$$\mathbf{A}_\beta(x, X, y) = \left[D_\nu(X)\,\mathbf{A}_{\alpha_\nu\beta}(X, y)\,e^{i\int\alpha_\nu(X)dx} + \varepsilon\mathbf{A}^{(1)}_{\alpha_\nu\beta}(X, y)\,e^{i\int\alpha_\nu(X)dx} + \ldots\right], \tag{2.85}$$

where $\mathbf{A}_{\alpha_\nu\beta}$ is an eigenfunction satisfying Eq. (2.82), and function $D_\nu(X)$ has to be determined. After substitution of Eq. (2.85) into Eq. (2.78), we arrive in order $O(\varepsilon)$ at an inhomogeneous equation for $\mathbf{A}^{(1)}_{\alpha_\nu\beta}$ having the same leading operator as in Eq. (2.82) (the terms associated with matrix $\mathbf{H}_4$ have order of magnitude $O(\varepsilon)$). Taking the dot product of the equation with the adjoint solution, $\mathbf{B}_{\alpha_\nu\beta}$, satisfying Eq. (2.83) and evaluating integral

of the result with respect to y from 0 to ∞, we arrive at an ordinary differential equation for D_ν:

$$i\alpha_{np} = \frac{d\ln D_\nu}{dx} = -\Gamma^{-1}\left[\left\langle \mathbf{H}_2\frac{\partial \mathbf{A}_{\alpha_\nu\beta}}{\partial x}, \mathbf{B}_{\alpha_\nu\beta}\right\rangle + \langle \mathbf{H}_4\mathbf{A}_{\alpha_\nu\beta}, \mathbf{B}_{\alpha_\nu\beta}\rangle\right]. \tag{2.86}$$

Continuous spectrum

Eigenfunctions of the continuous spectra oscillate at $y \to \infty$ as $\exp(\pm iky)$, and the analysis requires a modification. Instead of a single mode, we consider a narrow wave packet of width Δk around $k = k_l$. Therefore, solution for the narrow wave packet is considered in the form

$$\begin{aligned}\mathbf{A}_\beta(x, X, y) = \Bigg[&\int_{k_l-\Delta k/2}^{k_l+\Delta k/2} D_j(X,k)\,\mathbf{A}_{\alpha_j\beta}(X,y)\,e^{i\int\alpha_j(X,k)dx}dk \\ &+ \varepsilon\int_{k_l-\Delta k/2}^{k_l+\Delta k/2}\mathbf{A}^{(1)}_{\alpha_j\beta}(X,y)\,e^{i\int\alpha_j(X,k)dx}dk + \ldots\Bigg],\end{aligned} \tag{2.87}$$

where $\mathbf{A}_{\alpha_j\beta}$ is an eigenfunction of the continuous spectra satisfying Eq. (2.82). We substitute Eq. (2.87) into Eq. (2.78) and consider the equation in order $O(\varepsilon)$. Evaluation of the dot product with adjoint eigenfunction $\mathbf{B}_{\alpha^l_j\beta}$ satisfying Eq. (2.83) at $\alpha^l_j = \alpha_j(k_l)$ and integration of the result with respect to y from 0 to ∞ lead to the ordinary differential equation for D_j, as follows

$$i\alpha_{np} = \frac{d\ln D_j(X,k_l)}{dx} = -\Gamma^{-1}\lim_{\Delta k\to 0}\int_{k_l-\Delta k/2}^{k_l+\Delta k/2}\left[\left\langle \mathbf{H}_2\frac{\partial \mathbf{A}_{\alpha_j\beta}}{\partial x}, \mathbf{B}_{\alpha^l_j\beta}\right\rangle + \left\langle \mathbf{H}_4\mathbf{A}_{\alpha_j\beta}, \mathbf{B}_{\alpha^l_j\beta}\right\rangle\right]dk. \tag{2.88}$$

In the limit $\Delta k \to 0$, the integrals in Eq. (2.88) lead to evaluation of terms like $\int_0^\infty \exp(i(k-k_l)y)\,dy = \pi\delta(k-k_l)$ (see [Tum03]), and the result can be evaluated using asymptotic solutions outside of the boundary layer.

Multimode solution in a weakly nonparallel flow

In the case of a multimode solution, we are presenting our result as

$$\begin{aligned}\mathbf{A}_\beta(x,X,y) = &\sum_\nu D_\nu(X)\,\mathbf{A}_{\alpha_\nu\beta}(X,y)\,e^{i\int\alpha_\nu(X)dx} + \\ &\sum_j\int_0^\infty D_j(X,k)\,\mathbf{A}_{\alpha_j\beta}(X,y)\,e^{i\int\alpha_j(X,k)x}dk + O(\varepsilon), \\ &D_\nu(0) = d_\nu, \\ &D_j(0,k) = d_j(k).\end{aligned} \tag{2.89}$$

One should keep in mind that the multi-mode form of solution, Eq. (2.89) admits a mechanism of inter-modal exchange due to the weakly nonparallel flow effect. An example of this phenomenon was illustrated by Zhigulev and Fedorov[ZF87], who considered generation of

an unstable discrete mode by an acoustic wave. Although the effect is weak when the wave numbers of the modes are different, the exponential amplification of the unstable mode leads to its relatively large amplitude. In the present work, we neglect such inter-modal exchange.

The initial values d_ν and d_j in Eq. (2.89) are to be determined from the receptivity problem solution[Tum06b]. In the case of a roughness element, the linearized wall-boundary condition for the streamwise velocity component may be written as follows:

$$y = 0: \qquad u = -f(x,z)\, U'_w, \tag{2.90}$$

where $U'_w = (\partial U_s/\partial y)_{y=0}$ is the derivative of the unperturbed flow velocity profile. For a localized hump, the nonparallel flow effects on the receptivity problem solution can be neglected in the leading approximation, and one can find[Tum06b]

$$\begin{aligned} & d_j(k) = \Lambda \varphi(\alpha_j, \beta), \\ & \Lambda = \frac{U'_w}{\Gamma}\left[B_{\alpha_j \beta 1}\right]_{y=0}, \\ & \varphi(\alpha_j, \beta) = \int_{-\infty}^{+\infty}\int_{-\infty}^{+\infty} f(x,z)\, e^{-i\alpha_j x - i\beta z} dz dx, \end{aligned} \tag{2.91}$$

where $[B_{\alpha_j \beta 1}]_{y=0}$ is the first component of the adjoint eigenfunction evaluated at the wall.

The nonparallel flow effects may be incorporated into the receptivity problem solution along the lines of the distributed receptivity model proposed by Choudhari[Cho94a]. It was shown in [Cho94a] that the cumulative effect of distributed wall perturbations can be evaluated using the parallel flow approximation for each piece of the actuator and integrating the result over the distributed actuator. In our case, the result (with the reference point at $x = 0$) will be written as follows:

$$d_j(k) = \int_{-\infty}^{+\infty}\int_{-\infty}^{+\infty} \Lambda(k,x)\, f(x,z)\, e^{-i\int_0^x \alpha_j(k,x')dx' - i\beta z} dz dx, \tag{2.92}$$

where $\Lambda(k,x)$ is defined in Eq. (2.91).

One should keep in mind that the linearized wall-boundary condition, Eq. (2.90), could be rigorously derived within the triple-deck asymptotic analysis when the height of the hump is small in comparison with the thickness of the viscous sublayer. At finite Reynolds numbers, we do not have criteria for height and length of the hump in order to specify limits when the linearized boundary conditions can be used. The results should be compared with direct numerical simulations and/or experiments in order to establish validity of the boundary condition.

Numerical results

Verification: discrete mode at M=4.5

In order to test the new block of the code, we repeated results of [Gap80] for a two-dimensional TS wave in a compressible boundary layer over a flat plate at the Mach number

4.5, at the local Reynolds number (based on the Blasius scale) 1550, and at the frequency parameter 130×10^{-6}. Figure 2.30 shows the local growth rate of the mass flux perturbation as a function of the dimensionless coordinate $\eta = \sqrt{\mu_e x/\rho_e U_e}$. Comparison of the mass-flux perturbation corresponding to the discrete mode is shown in figure 2.31.

Roughness array. M = 0.02

In the case of roughness-induced perturbations, there are no discrete modes; and only steady normal modes of the continuous spectra represent the perturbation. There are two vorticity modes ('A' and 'B'), entropy modes, and the acoustic modes (representing Mach waves in the limit $\omega \to 0$) [Tum07].

In the present work, we consider the same array of roughness elements as in [Tum06b]. An array of humps is placed at distance x_0 from the leading edge of a flat plate. The geometry of each hump is defined by the function:

$$f(x,z) = a\cos^3\left(\frac{\pi\Delta x}{l_x}\right)\cos^3\left(\frac{\pi\Delta z}{l_z}\right), \tag{2.93}$$

where Δx and Δz are measured from the center of the hump, amplitude a = 0.172, l_x = 27.36 and l_z = 22.37 (in $\sqrt{\mu_e x_0/\rho_e U_e}$ units). The parameters correspond to a hump having a length scale of about 5 times the boundary layer thickness. Therefore, one may expect that the receptivity of the flow can be analyzed within the quasi-parallel flow approximation. This issue will be addressed later. The local Reynolds number is Re= 697.37. The spanwise period of the array is L_z ($2\pi/L_z$ = 0.073). In what follows, we include only the first 12 harmonics with $\beta_n = n \times 0.073$.

In order to evaluate the most significant interval of the parameter k in the present example, we show in figure 2.32 the amplitude factor,

$$|\Lambda(k)\varphi(\alpha_j(k),\beta)\, e^{i\alpha_j(k)(x-x_0)}|, \tag{2.94}$$

for two vorticity modes at $x_{down} = x - x_0 = 6.48 l_x$, $\beta = \beta_1$, and $M = 0.02$. One can see that the main input at these parameters is associated with a k of about 2.

Figure 2.33 shows variation of normalized $|\Lambda|$ along the roughness element for two vorticity modes at $k = 2$, $\beta = \beta_1$, and $M = 0.02$. The variation of the coefficient is about 1%, and one can consider the receptivity problem within the parallel flow approximation.

Figure 2.34 illustrates contours of the streamwise velocity perturbation, u, at $x_{down} = 6.48 l_x$ in the boundary layer at $M = 0.02$ obtained including the nonparallel flow effects and using the vorticity modes only. The continuous spectrum was discretized at $0 \le k \le 5$ using 500 intervals. One can see that there is a wake region downstream from the hump, and there are high-speed streaks on both sides of the hump.

Figure 2.35 shows the difference between two contour plots: $u_{parallel} - u_{nonparallel}$. One can see that the difference is about 10% in the wake.

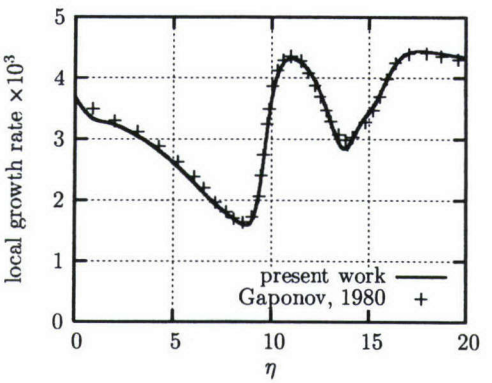

Figure 2.30: Local growth rate of the mass flux perturbation in the boundary layer over a flat plate.

In order to understand the source of the difference shown in figure 2.35, we plot real and imaginary parts of the integral,

$$N(k) = \int_{x_0}^{x_{down}} [\alpha(k) + \alpha_{np}(k,x)]\, dx, \tag{2.95}$$

in figure 2.36 for two vorticity modes together with the result stemming from the parallel flow approximation (in the parallel flow approximation, $N_r = 0$). One can see that the nonparallel flow effects do not have a significant effect on the integral. The latter means that the main source of the difference in figure 2.35 is associated with different shapes of the eigenfunctions evaluated at $x = x_0$ (parallel flow model) and at $x = x_0 + x_{down}$ (nonparallel flow consideration).

Roughness array. M = 0.5

In order to illustrate the nonparallel effects on the receptivity problem at $M = 0.5$, we present results at the temperature factor $T_w/T_{ad} = 0.5$ that are similar to the case $M = 0.02$.

Figure 2.37 shows the amplitude factor defined in Eq. (2.94) as a function of the parameter k.

Figure 2.38 shows variation of normalized $|\Lambda|$ along the roughness element for two vorticity modes and the entropy mode at $k = 2$, $\beta = \beta_1$, $M = 0.5$, and $T_w/T_{ad} = 0.5$. The variation of the coefficient is about 1%, as in the previous case, and one can consider the receptivity problem within the parallel flow approximation.

Figures 2.39 and 2.40 demonstrate the streamwise velocity contour plots in the case of an adiabatic wall at $M = 0.5$. The nonparallel flow effect on temperature perturbations at $M = 0.5$ (adiabatic wall) is illustrated by figures 2.41 and 2.42. Figures 2.43 through 2.46

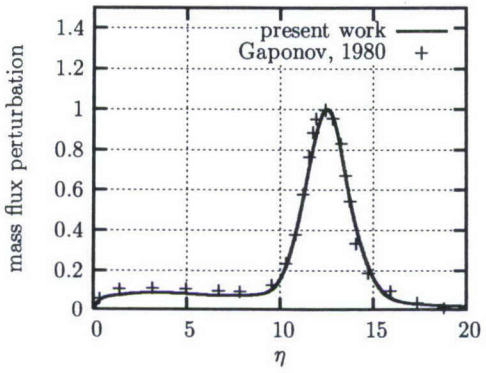

Figure 2.31: Mass-flux perturbation in the discrete mode.

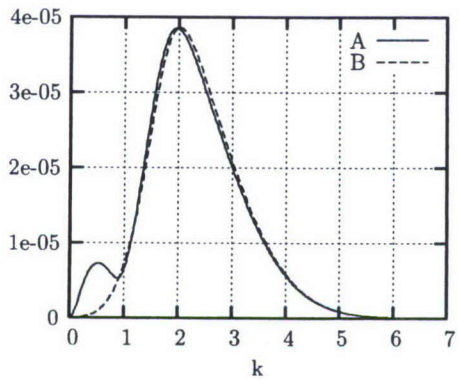

Figure 2.32: Amplitude factor [Eq.(2.94)] at $x_{down} = 6.48 l_x$. $M = 0.02$, adiabatic wall.

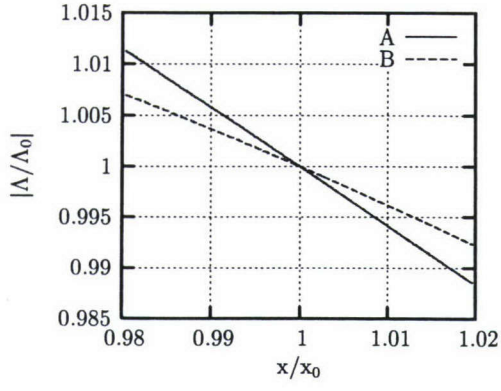

Figure 2.33: Variation of normalized $|\Lambda|$ along the roughness element for two vorticity modes. $M = 0.02$, adiabatic wall.

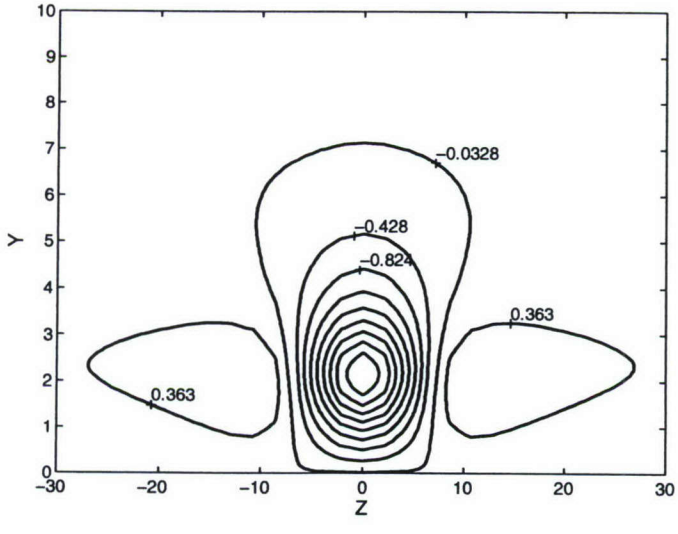

Figure 2.34: Contours of $u \times 10^4$ at $x_{down} = 6.48 l_x$. $M = 0.02$, adiabatic wall.

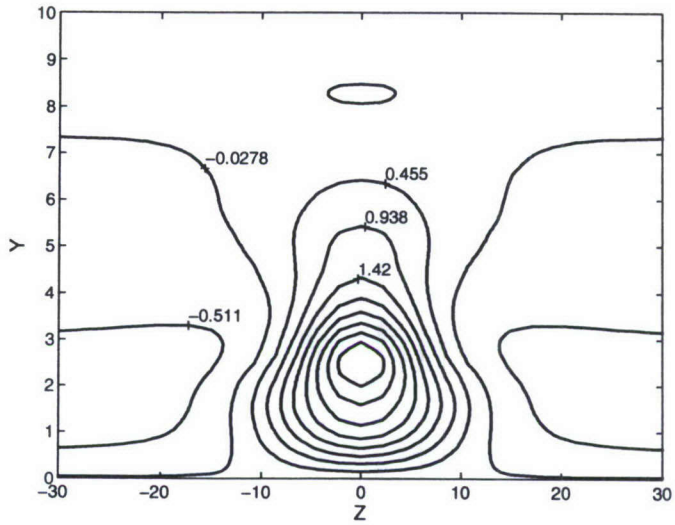

Figure 2.35: Difference (times 10^5) between streamwise velocity perturbations obtained within parallel and nonparallel flow models. $M = 0.02$, adiabatic wall.

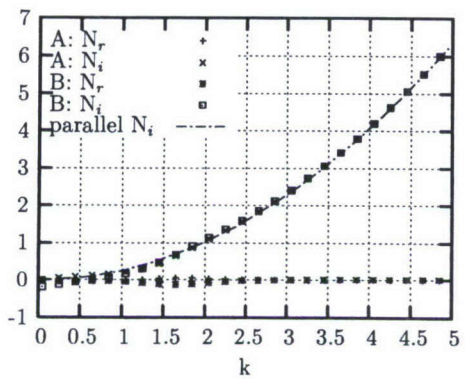

Figure 2.36: Integral N for two vorticity modes at $M = 0.02$, adiabatic wall.

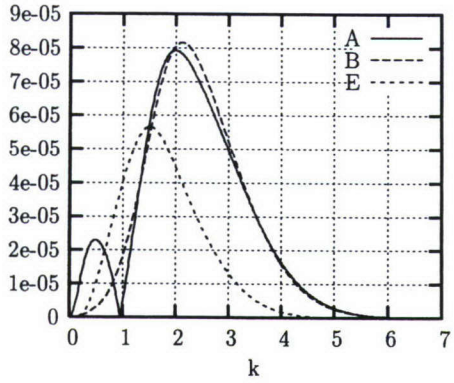

Figure 2.37: Amplitude factor [Eq.(2.94)] at $x_{down} = 6.48 l_x$. $M = 0.5$, $T_w/T_{ad} = 0.5$. A and B - two vorticity modes, E - entropy mode.

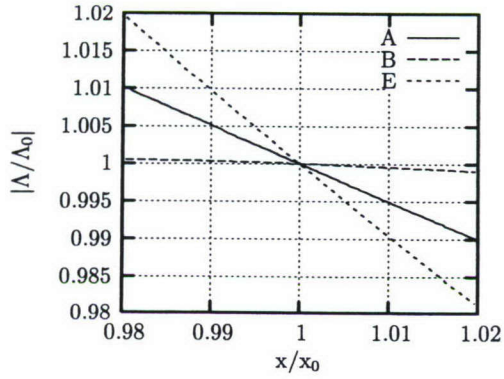

Figure 2.38: Variation of normalized $|\Lambda|$ along the roughness. $M = 0.5$, $T_w/T_{ad} = 0.5$. A and B - two vorticity modes, E - entropy mode.

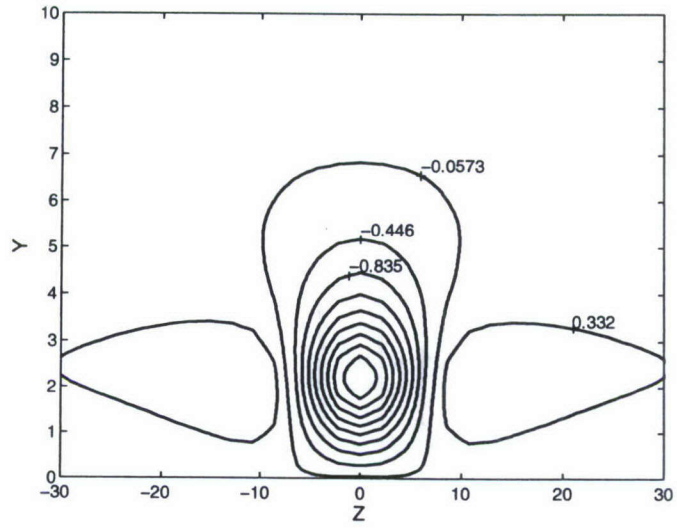

Figure 2.39: Contours of $u \times 10^4$ at $x_{down} = 6.48 l_x$. $M = 0.5$, adiabatic wall.

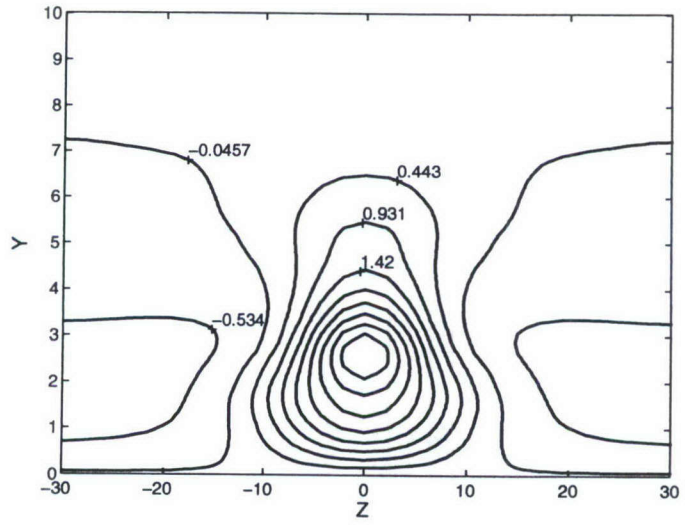

Figure 2.40: Difference (times 10^5) between streamwise velocity perturbations obtained within parallel and nonparallel flow models. $M = 0.5$, adiabatic wall.

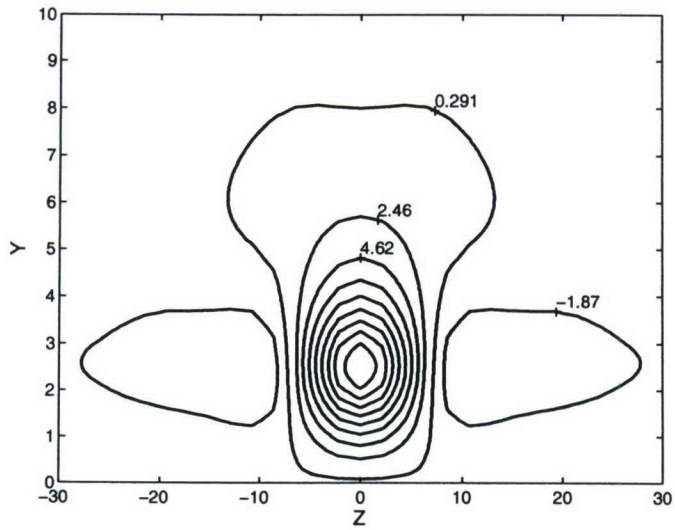

Figure 2.41: Contours of $\theta \times 10^6$ at $x_{down} = 6.48 l_x$. $M = 0.5$, adiabatic wall.

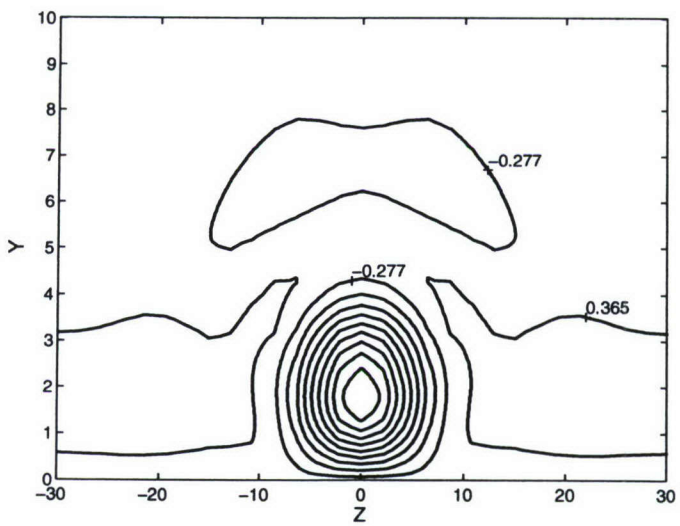

Figure 2.42: Difference (times 10^6) between temperature perturbations obtained within parallel and nonparallel flow models. $M = 0.5$, adiabatic wall.

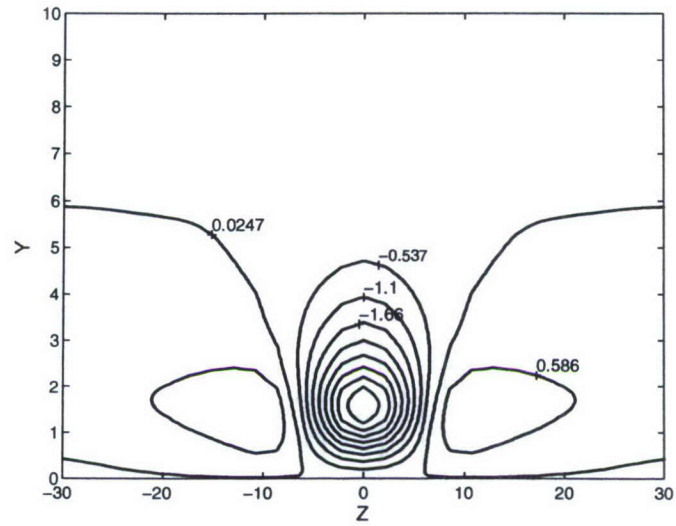

Figure 2.43: Contours of $u \times 10^4$ at $x_{down} = 6.48 l_x$. $M = 0.5$, $T_w/T_{ad} = 0.5$.

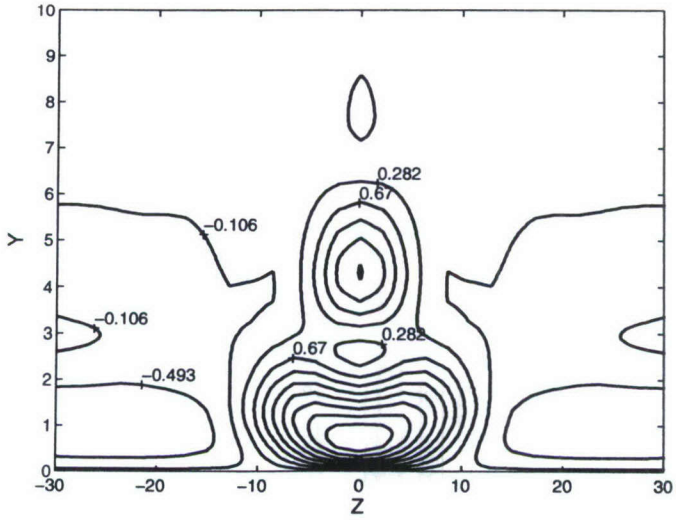

Figure 2.44: Difference (times 10^5) between streamwise velocity perturbations obtained within parallel and nonparallel flow models. $M = 0.5$, $T_w/T_{ad} = 0.5$.

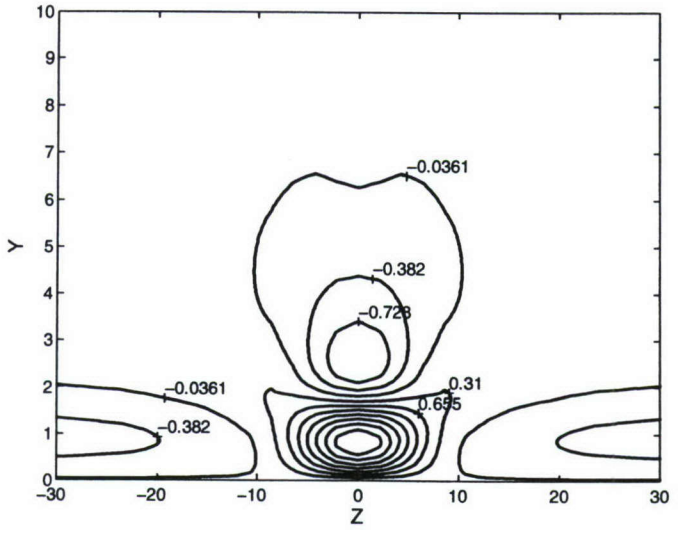

Figure 2.45: Contours of $\theta \times 10^4$ at $x_{down} = 6.48 l_x$. $M = 0.5$, $T_w/T_{ad} = 0.5$.

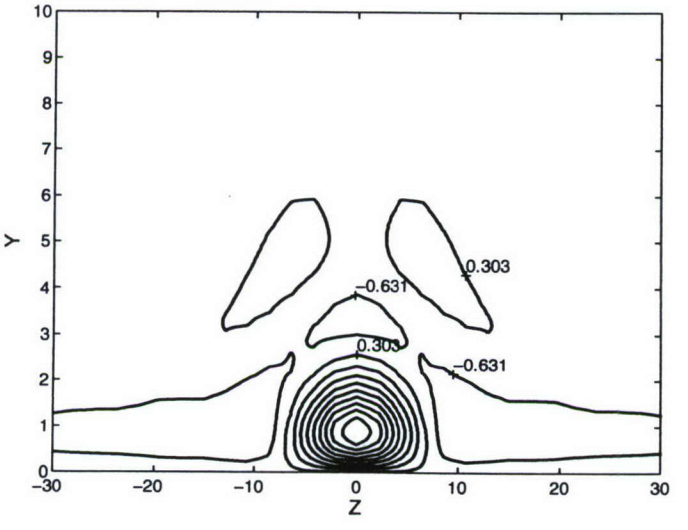

Figure 2.46: Difference (times 10^5) between temperature perturbations obtained within parallel and nonparallel flow models. $M = 0.5$, $T_w/T_{ad} = 0.5$.

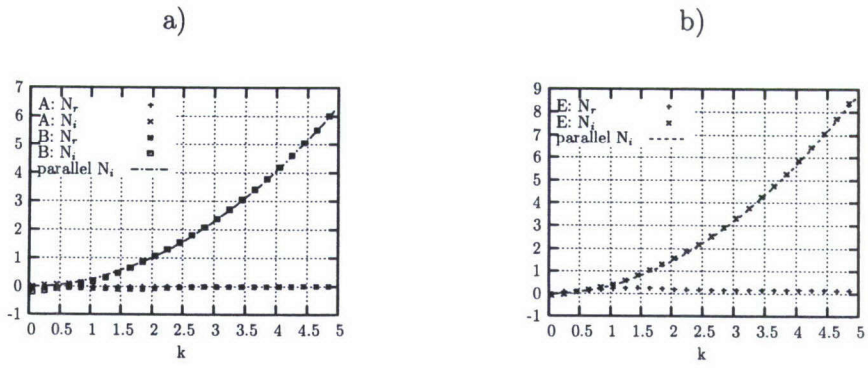

Figure 2.47: Integral N for two vorticity modes and the entropy mode at $M = 0.5$, $T_w/T_{ad} = 0.5$.

illustrate the nonparallel flow effect at $M = 0.5$ and the temperature factor 0.5. In these examples, the results were obtained using the vorticity and entropy modes. In order to avoid overlapping of the vorticity and entropy spectra and to simplify the computations, we use a small non-zero frequency ($\omega = 10^{-5}$) as was described in [Tum07].

Similarly to the example at $M = 0.02$, we plot in figure 2.47 integral N for two vorticity modes and the entropy mode at $M = 0.5$ and $T_w/T_{ad} = 0.5$. One can see that in this case the nonparallel flow effects also do not have a significant effect on the integral.

Conclusion

To our knowledge, this is the first example when the weakly nonparallel flow effects are considered for modes of the continuous spectra. Although the results obtained with nonparallel flow effects included are quantitatively different (up to 10% in the wake velocity perturbation) from the results obtained in [TR05] and [Tum06b] within the parallel flow approximation, the qualitative structure of the flow field downstream of the roughness element remains the same. Analysis of the nonparallel flow effects in subsonic boundary layers over a flat plate revealed that one can take them into account just by evaluation of the eigenfunctions at the local Reynolds number downstream from the hump.

2.4.1 Periodic-in-time actuators placed on the wall

Receptivity to periodic-in-time blowing-suction through the wall

As an example of a periodic-in-time actuator, we consider a point blowing-suction through the wall. For the purpose of illustration, we choose the two examples of flow past a flat plate analyzed by Balakumar and Malik [BM92]. In the first example, Mach number $M = 2$ and dimensionless angular frequency $\omega = 0.02$. In the second example, $M = 4.5$ and $\omega = 0.2$. The free-stream stagnation temperature of 311 K, adiabatic wall conditions, and Prandtl number, Pr, equal to 0.72 were used for both cases. Viscosity was computed in accordance with Sutherland's law. The free-stream velocity, density, and viscosity were used as the characteristic scales, together with the Blasius length scale, $(\nu_\infty x_0/U_\infty)^{1/2}$, where x_0 stands for distance from the leading edge.

Balakumar and Malik [BM92] evaluated the integral in (2.69) by closing the path in the upper half-plane α_v in order to represent the result as a sum of the residue values (input from the discrete spectrum) and integrals along three branch cuts representing input from the continuous spectrum. In the present method, we use (2.76) in order to find amplitudes of the discrete and continuous spectra and substitute them into (2.70). Because the shape function $v_w(x,z)$ in equation (2.63a) was chosen as $\delta(x-x_0)\,\delta(z)$, $\rho(\alpha,\beta) = 1$ and $C = G_v$ in (2.76).

Flat plate, M = 2. Balakumar and Malik [BM92] found the receptivity coefficients of the least stable discrete modes when the eigenfunction was normalized so that the maximum amplitude of the streamwise velocity component was equal to one. Their results for discrete modes and comparisons with the present method are presented in tables 2.1 and 2.2 for $\beta = 0$ and $\beta = 0.08$, respectively. One can see that results of the present work and of [BM92] agree well, except for the second discrete mode in table 2.2.

Table 2.1: Flat plate. $M = 2$, $T_0 = 311$ K, $Pr = 0.72$, $Re = 1000$, $\omega = 0.02$, $\beta = 0$.

Balakumar and Malik[BM92]		the present work	
α	$\lvert G_v \rvert$	α	$\lvert G_v \rvert$
$(3.733 \times 10^{-2}, -3.696d \times 10^{-4})$	2.2079×10^{-2}	$(3.733 \times 10^{-2}, -3.696d \times 10^{-4})$	2.2096×10^{-2}
$(2.841 \times 10^{-2}, 2.619 \times 10^{-2})$	1.1448	$(2.844 \times 10^{-2}, 2.617 \times 10^{-2})$	1.1242
$(-9.670 \times 10^{-2}, 4.206 \times 10^{-2})$	0.7527	$(-9.671 \times 10^{-2}, 4.206 \times 10^{-2})$	0.7535
$(4.366 \times 10^{-2}, 4.495 \times 10^{-2})$	4.7175×10^{-2}	$(4.366 \times 10^{-2}, 4.495 \times 10^{-2})$	4.7259×10^{-2}

Table 2.2: Flat plate. $M = 2$, $T_0 = 311$ K, $Pr = 0.72$, $Re = 1000$, $\omega = 0.02$, $\beta = 0.08$

Balakumar and Malik[BM92]		the present work	
α	$\lvert G_v \rvert$	α	$\lvert G_v \rvert$
$(4.077 \times 10^{-2}, -2.384 \times 10^{-3})$	0.2333	$(4.078 \times 10^{-2}, -2.384 \times 10^{-3})$	0.2335
$(2.035 \times 10^{-2}, 1.751 \times 10^{-2})$	11.9667	$(2.062 \times 10^{-2}, 1.699 \times 10^{-2})$	4.67364
$(4.382 \times 10^{-2}, 4.453 \times 10^{-2})$	0.2193	$(4.383 \times 10^{-2}, 4.453 \times 10^{-2})$	0.2191
$(-6.637 \times 10^{-2}, 7.634 \times 10^{-2})$	0.7404	$(-6.638 \times 10^{-2}, 7.634 \times 10^{-2})$	0.7406

Figure 2.48 shows the real and imaginary parts of the eigenvalue, $\alpha_r(\beta)$ and $\alpha_i(\beta)$, respectively, together with the receptivity coefficient $G_v(\beta)$ for the unstable mode at $Re = 1000$. One can compare the results with figure 6 of [BM92] to conclude that there is a good agreement. The method of the Section 2.3.2 is also convenient for parametric studies. Figure 2.49 shows the contour plot of the receptivity coefficient for a perturbation having frequency parameter $F = \omega/Re = 20 \times 10^{-6}$. The contour plots of α_r and α_i in the (Re, β) plane are presented in figure 2.50.

It is interesting to compare the results for continuous spectra obtained within the present work with the results of [BM92]. The eigenmodes of the continuous spectrum are oscillating outside the boundary layer. Their asymptotic behavior is $\sim \exp(\pm iky)$, where k is a real parameter. Figure 2.51 shows the branch cuts in the complex plane α associated with the continuous spectrum. Branch cuts 1 and 3 in figure 2.51 represent the fast (FA) and slow (SA) acoustic modes, respectively. Branch cut 2 actually represents (indistinguishable in the plot scale) two branch cuts associated with the entropy and vorticity modes [Tum06c].

Numerical evaluation of integrals in (2.70) associated with the acoustic modes was done with the help of the trapezoidal formula on a finite interval $[0, k_{max}]$ with 320-640 steps. The parameter k_{max} was varied up to 6 to verify independence of the results from the interval and number of steps. Figure 2.52 shows inputs from the fast and slow acoustic modes (branch cuts 1 and 3, respectively) to the real part of the normal velocity component, v_r, at distances $x - x_0 = 250$, 500, and 750. The peaks in the velocity distributions correspond to the Mach wave. One can compare the results of figure 2.52 with the results in figures 19 and 21 of [BM92] and conclude that they are in agreement. One can also notice from figure 19 of [BM92] that there are oscillations of the solution above the Mach wave, whereas our results in figure 2.52 demonstrate a quiet region above the Mach wave. We attribute the oscillations

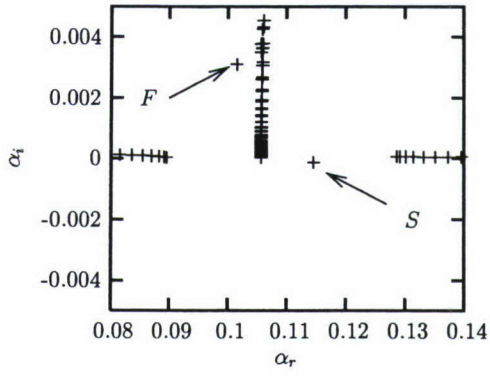

Figure 2.48: Eigenvalues α and receptivity coefficient $|G_v|$ at $M = 2$, $\omega = 0.02$, $Re = 1000$.

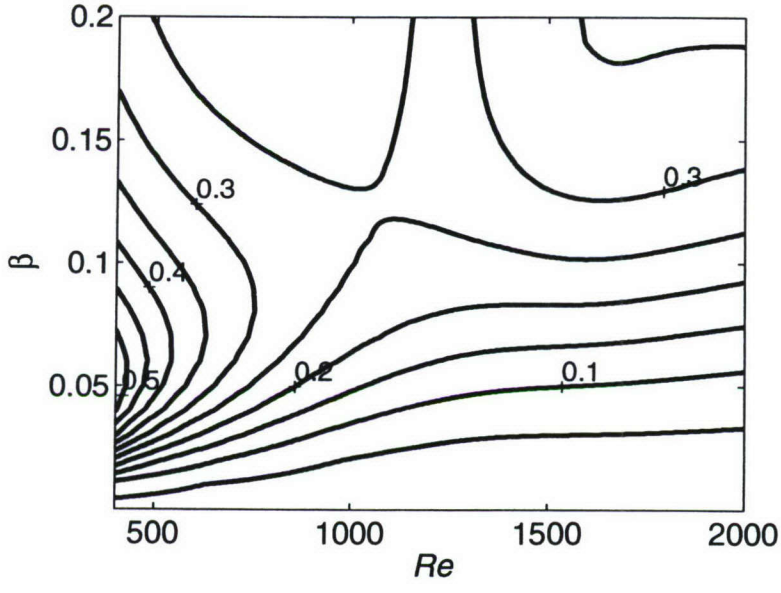

Figure 2.49: Contour plot of the receptivity coefficient, $|G_v|$, at $M = 2$, $F = 20 \times 10^{-6}$.

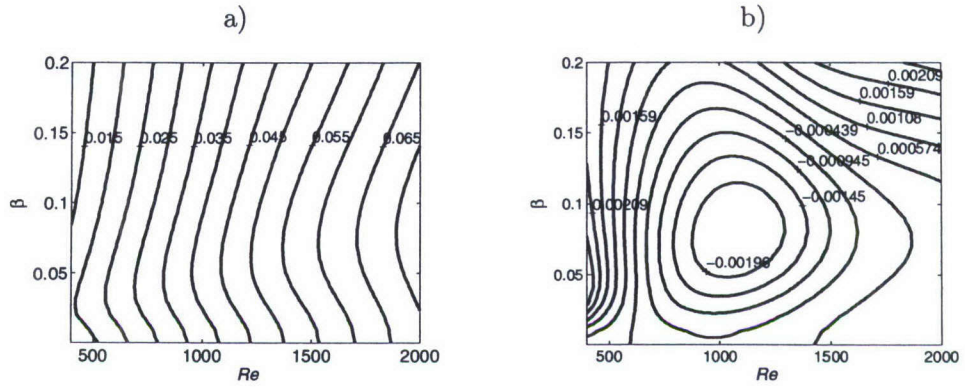

Figure 2.50: Contour plots of real (a) and imaginary (b) parts of the eigenvalue, α, at $M = 2$, $F = 20 \times 10^{-6}$.

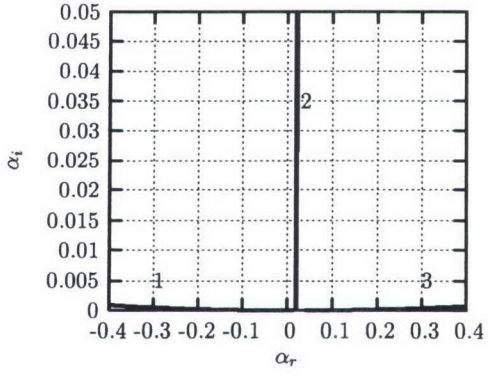

Figure 2.51: Branch cuts in the complex plane α at $M = 2$, $\omega = 0.02$, $Re = 1000$, $\beta = 0$.

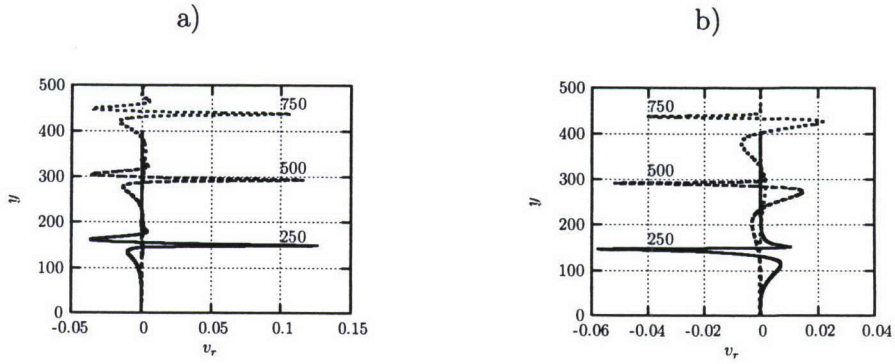

Figure 2.52: Real part of the normal velocity component resulting from the fast (a) and slow (b) acoustic waves at $x - x_0$ locations 250, 500, and 750. $M = 2$, $Re = 1000$, $\omega = 0.02$, and $\beta = 0$.

Table 2.3: Flat plate. $M = 4.5$, $T_0 = 311$ K, $Pr = 0.72$, $Re = 1000$, $\omega = 0.2$, $\beta = 0$

Balakumar and Malik[BM92]		the present work	
α	$\lvert G_v \rvert$	α	$\lvert G_v \rvert$
$(0.220, -3.091 \times 10^{-3})$	1.7537×10^{-2}	$(0.220, -3.091 \times 10^{-3})$	1.7537×10^{-2}
$(0.221, 1.569 \times 10^{-2})$	9.9071×10^{-2}	$(0.221, 1.569 \times 10^{-2})$	4.8394×10^{-2}
$(-0.565, 5.559 \times 10^{-2})$	0.3878	$(-0.565, 5.560 \times 10^{-2})$	0.3880
$(0.560, 5.659 \times 10^{-1})$	6.5089	$(0.561, 5.659 \times 10^{-1})$	6.5166

in [BM92] to not long enough pieces of the branch cuts being included in the evaluation of the integrals. As it was pointed out in [BM92], the main input to the perturbation is associated with the fast acoustic modes. Figure 2.53 shows the receptivity coefficients of the fast and slow acoustic modes as functions of the parameter k. The coefficients correspond to the normalization when the streamwise velocity derivative on the wall is $(\partial u/\partial y)_w = 1$. One can see that the receptivity coefficients are higher for the fast acoustic mode.

Inputs from the entropy modes and vorticity modes are shown in figure 2.54. Note that the perturbations have maxima in the vicinity of the boundary layer edge, and they are very small. These results are different from those reported in [BM92]. They obtained input from branch cut 2 as a standing-wave-type pattern in the y-direction spreading far away above the Mach wave (figure 20 of [BM92]). The result is, probably, also attributed to the short piece of the branch cut used in evaluating of the integrals.

Flat plate, M = 4.5. In this example, we consider perturbations having the frequency parameter $F = 200 \times 10^{-6}$. Tables 2.3 and 2.4 provide comparisons of the receptivity coefficients of the least stable discrete modes obtained in [BM92] and in the present work. The agreement is also good, except for the second mode in table 2.3.

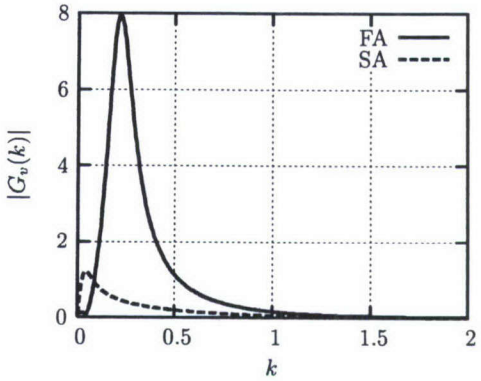

Figure 2.53: Receptivity coefficients of the fast, FA, and the slow, SA, acoustic modes. $M = 2$, $\omega = 0.02$, $Re = 1000$, $\beta = 0$, $(\partial u/\partial y)_w = 1$.

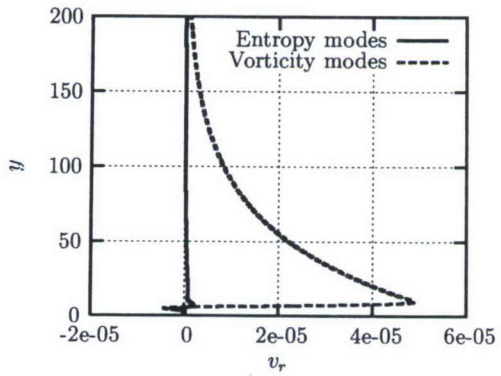

Figure 2.54: Real part of the normal velocity component resulting from the entropy and vorticity modes at $x - x_0$ location 750. $M = 2$, $Re = 1000$, $\omega = 0.02$, and $\beta = 0$.

Table 2.4: Flat plate. $M = 4.5$, $T_0 = 311$ K, $Pr = 0.72$, $Re = 1000$, $\omega = 0.2$, $\beta = 0.12$

Balakumar and Malik[BM92]		the present work	
α	$\lvert G_v\rvert$	α	$\lvert G_v\rvert$
$(0.2181, 2.969 \times 10^{-4})$	1.5405×10^{-2}	$(0.2181, 2.974 \times 10^{-4})$	1.5413×10^{-2}
$(0.2124, 1.288 \times 10^{-2})$	6.1334×10^{-2}	$(0.2124, 1.288 \times 10^{-2})$	6.1341×10^{-2}
$(-0.5498, 5.684 \times 10^{-2})$	0.3862	$(-0.5499, 5.685 \times 10^{-2})$	0.3864

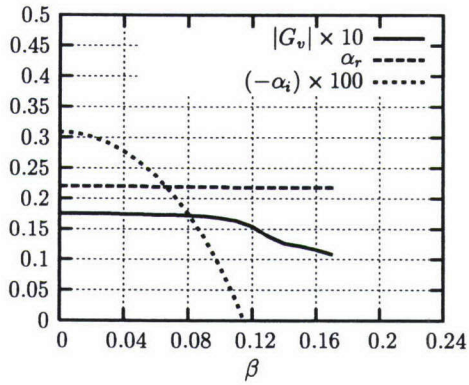

Figure 2.55: Eigenvalues α and receptivity coefficient $|G_v|$ at $M = 4.5$, $\omega = 0.2$, $Re = 1000$.

Figure 2.55 shows the real and imaginary parts of the eigenvalue, $\alpha_r(\beta)$ and $\alpha_i(\beta)$, respectively, together with the receptivity coefficient $G_v(\beta)$ for the unstable mode at $Re = 1000$. One can compare the results with figure 7 of [BM92] to conclude that the results are in good agreement. Figures 2.56 and 2.57 show the contour plots of the receptivity coefficient and the eigenvalues, α_r and α_i, in the (Re, β,) plane, respectively.

Figure 2.58 shows inputs from the fast and slow acoustic modes at $M = 4.5$ (branch cuts 1 and 3, respectively) to the real part of the normal velocity component, v_r, at distances $x - x_0 = 250$, 500, and 750. The receptivity coefficient of the fast acoustic mode is shown in figure 2.59. One can compare the result with figure 2.53 to see that in this case, the maximum is shifted toward the higher values of the parameter k.

Inputs of the entropy and vorticity modes to the velocity perturbation at $x = 500$ are shown in figure 2.60. Similarly to the case of $M = 2$, the inputs are small and the maxima are located at the edge of the boundary layer.

Discussion of the results

The receptivity of compressible boundary layers to three-dimensional wall perturbations was solved with the help of the biorthogonal eigenfunction system. The method allows finding amplitudes of the discrete and continuous spectra. The main result of the present work is associated with inclusion of the continuous spectra in compressible boundary layers into the receptivity analysis within the scope of the biorthogonal eigenfunction expansion. In the case of a periodic-in-time actuator or an array of roughness elements, the continuous spectra provide correct representation of the Mach waves in supersonic flows. Although each mode of the continuous spectra is oscillating at $y \to \infty$, their sum represents zero perturbations above the Mach wave. The example with an array of roughness elements in Section 2.3.2 at M=0.5 illustrates how the modes of the continuous spectra (vorticity and entropy modes)

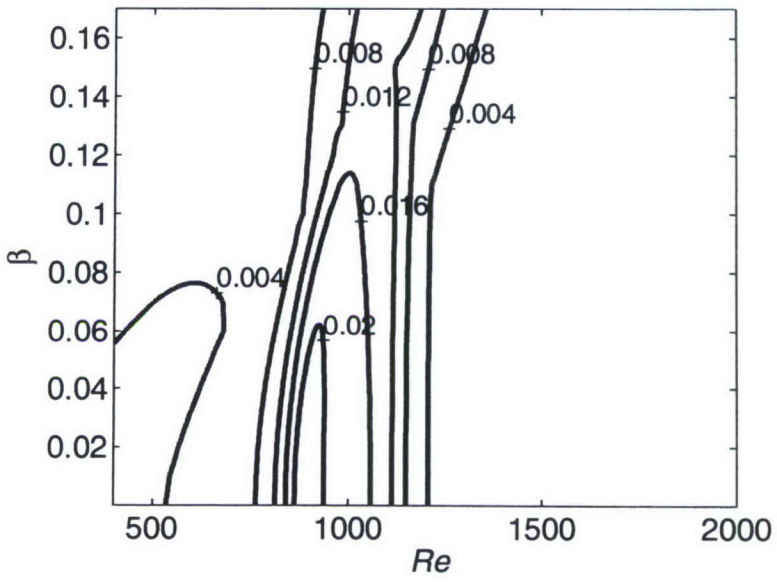

Figure 2.56: Contour plot of the receptivity coeficient, $|G_v|$, at $M = 4.5$, $F = 200 \times 10^{-6}$.

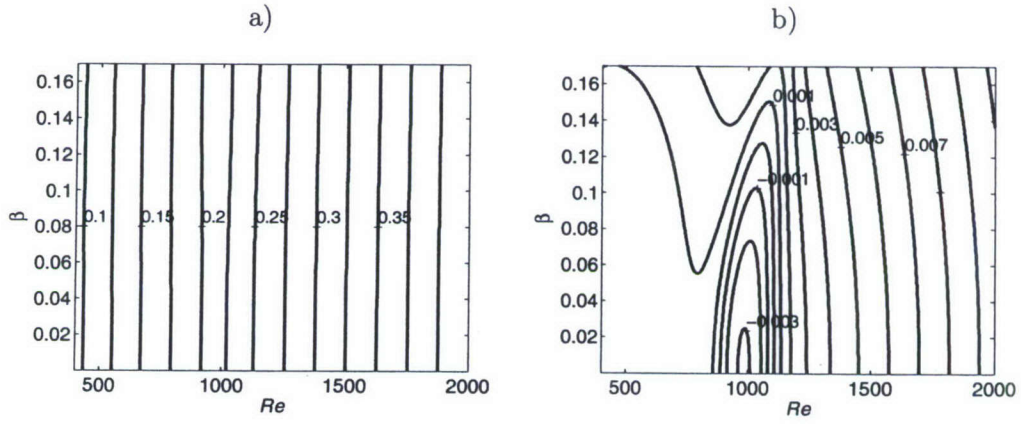

Figure 2.57: Contour plots of real (a) and imaginary (b) parts of the eigenvalue, α, at $M = 4.5$, $F = 200 \times 10^{-6}$.

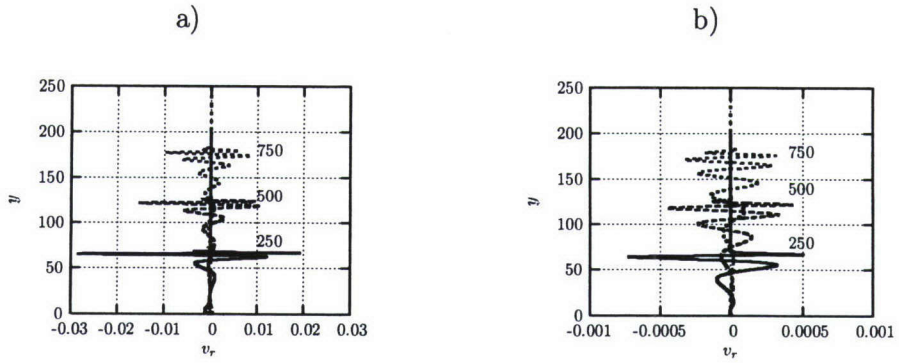

Figure 2.58: Real part of the normal velocity component resulting from the fast (a) and slow (b) acoustic waves at $x - x_0$ locations 250, 500, and 750. $M = 4.5$, $Re = 1000$, $\omega = 0.2$, and $\beta = 0$.

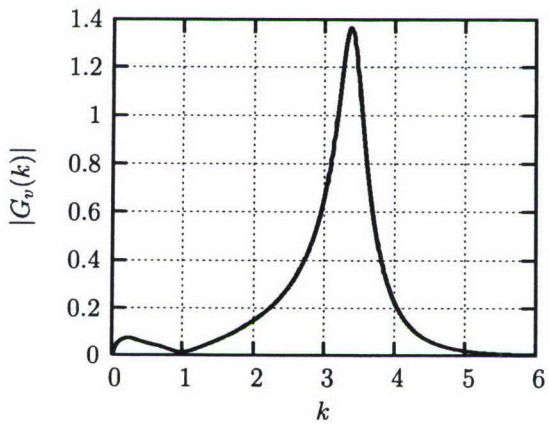

Figure 2.59: Receptivity coefficients of the fast acoustic mode. $M = 4.5$, $\omega = 0.2$, $Re = 1000$, $\beta = 0$, $(\partial u/\partial y)_w = 1$.

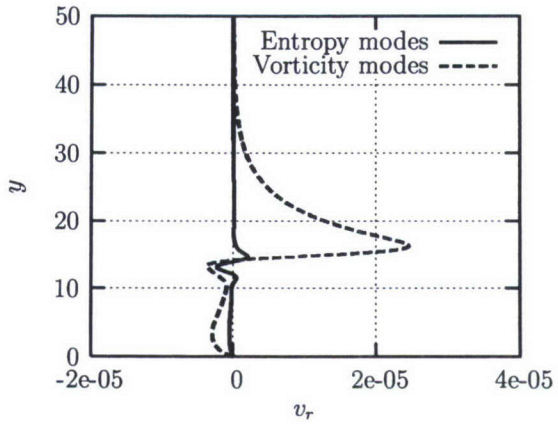

Figure 2.60: Real part of the normal velocity component resulting from the entropy and vorticity modes at $x - x_0$ location 500. $M = 4.5$, $Re = 1000$, $\omega = 0.2$, and $\beta = 0$.

represent streamwise vortices localized inside the boundary layer. It is also worthwhile to mention that the results demonstrate that a roughness element on a cold wall creates a low-speed streak above the wake region. To our knowledge, this phenomenon has not been addressed in asymptotical or CFD studies. This phenomenon might be associated with a secondary instability mechanism, and it has to be addressed in the future.

The solution in the present work is based on the parallel flow approximation. This approximation is valid when the characteristic scale of the perturbation (wave length) is much smaller than the characteristic scale of the unperturbed flow in the downstream direction. This condition is violated when the actuator is located close to the leading edge. Tumin, Wang and Zhong [TWZ06] analyzed results of a direct numerical simulation when perturbations were introduced into a hypersonic boundary layer by periodic-in-time blowing and suction through a slot. Comparison of theoretical and numerical results for amplitudes of discrete modes generated by the actuator revealed their discrepancy when the slot was located close to the leading edge.

In the case of three-dimensional boundary layers, roughness elements may generate a crossflow instability mode (see [RS89, Bip99, SRW03]). Comparison of the receptivity prediction for the discrete mode within the scope of the parallel flow approximation with the Navier–Stokes solution revealed that nonparallel flow effects reduce the initial amplitude [CL99]. In order to take into account the nonparallel flow effects, Bertolotti [Ber00] suggested an approach based on the Taylor series for the mean flow in the vicinity of the roughness element. Comparison of the receptivity coefficients obtained with the help of the model with the values obtained from the solution of linearized Navier–Stokes solutions demonstrated their good agreement. In principle, this approach can be incorporated into

the method discussed in the present work.

Results of the present work are also based on the assumption that the denominator in (2.72) is not equal to zero. Fedorov and Khokhlov [FK01] showed that the denominator is equal to zero at the branching point of discrete modes. They also showed [FK02] that it might be of practical importance in high-speed boundary layers on a cold wall. In this case, the nonparallel flow effects are to be taken into account in order to resolve the singularity.

In the present method, an adjoint solution serves as a filter to find the amplitude of a mode (see equation 2.72). Hill [Hil96] and Herbert [Her97] suggested using adjoint parabolized stability equations (APSE) for receptivity prediction when the nonparallel flow effects are essential. Luchini and Bottaro [LB98] used the same idea for analysis of the receptivity of the Görtler instability. They calculated Green's function from the solution of the parabolic adjoint problem by marching upstream. Later on, a number of publications (see [AWB00, CD00, DC00, Air00, PAHH00, AWB02]) demonstrated how the APSE can be used to predict the receptivity of boundary layers to a variety of forcing. The method is suitable to determine the amplitude of an instability mode (the leading mode) that is usually of interest. However, as was discussed by Fedorov and Khokhlov [FK01], decaying modes in high-speed boundary layers may be an important element of the laminar-turbulent transition scenario as well. At the present time, it is not clear how accuratly the APSE approach can determine the amplitudes of the decaying modes. In addition, the APSE method in its present formulation does not provide a tool for the prediction of amplitudes of modes belonging to continuous spectra, whereas the adjoint method in the parallel-flow approximation has the capability to address decaying modes of discrete and continuous spectra. The local parallel approximation, together with the extension suggested by Bertolotti [Ber00], probably will be an adequate tool to analyze the decaying discrete modes and modes of the continuous spectra when the nonparallel flow effects are significant.

2.5 Multimode decomposition of perturbations in a compressible boundary layer

This section is based on the paper published in collaboration with P. Gaydos [GT04].

2.5.1 Introduction

The progress being made in computational fluid dynamics (CFD) provides an opportunity for reliable simulation of such complex phenomenon as laminar-turbulent transition. The dynamics of flow transition depends on the instability of small perturbations excited by external sources. CFD provides complete information about the flow field, which would be impossible to measure in real experiments. However, this increase in available information does not furnish a physical insight of the transition because the leading mechanisms still remain hidden behind a messy disturbance field. Sometimes, a flow possesses a few instability modes that are equally significant in the transition process, and it might be desirable to distinguish the dynamics of each mode in the complex non-steady flow field. Figure 2.61 illustrates the dependence of the real parts of wave numbers of the first and the second discrete modes on the local Reynolds number, $R = \sqrt{\rho_e U x/\mu_e}$, in a hypersonic boundary layer over a sharp cone, where ρ_e, μ_e, and U_e are density, viscosity, and mean velocity at the edge of the boundary layer. The coordinate x is measured along the surface of the cone, and the wave numbers are dimensionless with the help of the length scale $\sqrt{\mu_e x/\rho_e U_e}$. In this example and what follows, the boundary layer solution was obtained with Mangler transformation from a planar to a conical configuration. The frequency parameter is $F = 150 \times 10^{-6}$, and the Mach number is equal to 5.6. One can see that there is a synchronism of these two modes in the vicinity of $R = 1600$. The synchronism is not absolute because the eigenvalues, α, have small but different imaginary parts. Nevertheless, the complex wave numbers are very close, and figure 2.62 demonstrates that the mode shapes are very close as well. In simple words, one has to recognize these modes in the presence of acoustic, vorticity and entropy modes and separate them from one another. Consequently, the problem of decomposing the flow fields into normal modes arises. Because CFD provides complete information about the flow field, one can expect that the decomposition may be formulated as a rigorous procedure.

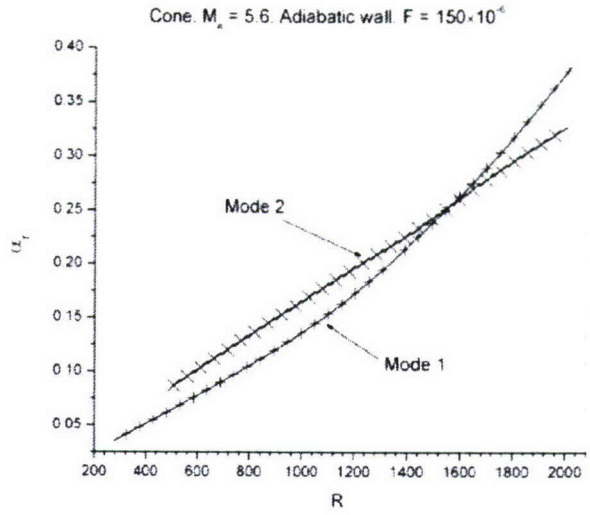

Figure 2.61: Wave numbers of two discrete modes.

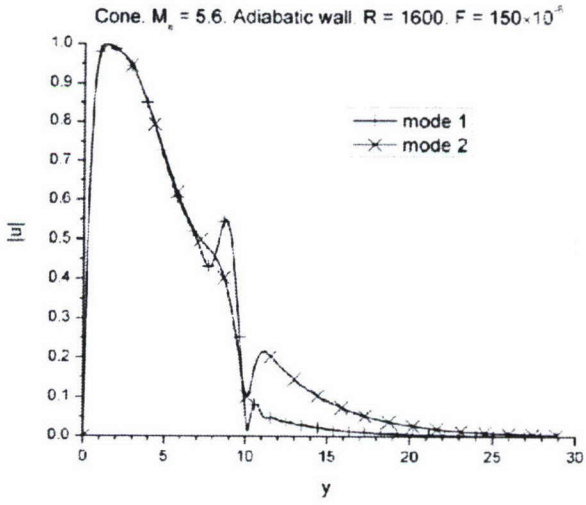

Figure 2.62: Profiles (normalized to 1) of the discrete modes at R = 1600. Eigenvalues of the first and the second modes are $\alpha_1 = 0.2627 + i0.02269$ and $\alpha_2 = 0.2603 - i0.00494$, respectively.

2.5.2 Outline of the method

Governing equations and formal solution to the spatial Cauchy problem

We analyze two-dimensional perturbations in a two-dimensional compressible boundary layer, and the boundary layer is considered in the parallel flow approximation. After Fourier transform with respect to time, the linearized Navier-Stokes equations are recast in the following matrix form:

$$\frac{\partial}{\partial y}\left(L_0\frac{\partial \mathbf{A}}{\partial y}\right) + L_1\frac{\partial \mathbf{A}}{\partial y} = H_1\mathbf{A} + H_2\frac{\partial \mathbf{A}}{\partial x} \tag{2.96}$$

where L_0, L_1, H_1, and H_2 are 9×9 matrices. Their non-zero elements are presented in A.4. The vector-function, $\mathbf{A}(x, y)$, is defined with the help of the streamwise and normal velocity perturbations, u and v, respectively, pressure perturbation, π, and temperature perturbation, θ.

$$\mathbf{A} = (u, \partial u/\partial y, v, \pi, \theta, \partial\theta/\partial y, \partial u/\partial x, \partial v/\partial x, \partial\theta/\partial x)^T \tag{2.97}$$

The boundary conditions are a no-slip condition on the wall and decaying perturbations outside the boundary layer.

For the purpose of clarity, we briefly recapitulate the main ideas of [TF83b]. The Cauchy problem for (2.96) with initial data at $x = 0$ is ill-posed. The latter is associated with possible upstream influence of the downstream boundary of the domain. However, if there is no evidence of the upstream impact, one can assume that the solution has a finite growth rate along the coordinate x.

Assuming that the solution has a finite growth rate, we apply the Laplace transform with respect to x:

$$\mathbf{A_p}(\mathbf{y}) = \int_0^\infty \mathbf{A}(\mathbf{x}, \mathbf{y})\, \mathbf{e}^{-\mathbf{px}} \mathbf{dx} \tag{2.98}$$

As a result, we arrive at the following inhomogeneous system of ordinary differential equations:

$$\begin{aligned} &\frac{d}{dy}\left(L_0\frac{d\mathbf{A_p}}{dy}\right) + L_1\frac{d\mathbf{A_p}}{dy} - H_1\mathbf{A}_p - pH_2\mathbf{A_p} = \mathbf{F} \\ &\mathbf{F} = -H_2\mathbf{A_0} \end{aligned} \tag{2.99}$$

where vector-function $\mathbf{A_0}$ stands for the initial data at $x = 0$. A homogeneous system of equations corresponding to (2.99) can be recast in the form

$$\frac{d\mathbf{z}}{dy} = H_0\mathbf{z} \tag{2.100}$$

where H_0 is a 6×6 matrix (see A.4) and $\mathbf{z}$ is a vector-function comprised of the first six elements of vector-function $\mathbf{A}_p$. The system of equations (2.100) has six fundamental solutions, $\mathbf{z}_1(y)$, $\mathbf{z}_2(y)$,..., $\mathbf{z}_6(y)$. Because their properties will be used in further analysis, we shall discuss them in detail.

Classification of the fundamental solutions stems from their behavior outside the boundary layer, where $U_s(y) \equiv 1$, $T_s(y) \equiv 1$, and derivatives of the mean flow profiles are equal to zero. Solutions of (2.100) outside the boundary layer have an exponential form as $\mathbf{z}_j^0 \exp(\lambda_j y)$. For $y \to \infty$, the characteristic equation

$$\det \|H_0 - \lambda \mathbf{I}\| = 0 \tag{2.101}$$

can be written in the explicit form

$$\begin{aligned}
&\left(b_{11} - \lambda^2\right) \times \left[\left(b_{22} - \lambda^2\right)\left(b_{33} - \lambda^2\right) - b_{23}b_{32}\right] = 0, \\
&b_{11} = H_0^{21}, \\
&b_{22} = H_0^{42}H_0^{24} + H_0^{43}H_0^{34} + H_0^{46}H_0^{64}, \\
&b_{23} = H_0^{42}H_0^{25} + H_0^{43}H_0^{35} + H_0^{46}H_0^{65}, \\
&b_{32} = H_0^{64}, \\
&b_{33} = H_0^{65}
\end{aligned} \tag{2.102}$$

where elements of matrix H_0 are evaluated at $y \to \infty$. The roots of equation (2.102) are

$$\begin{aligned}
\lambda_{1,2}^2 &= b_{11} = \alpha^2 + iR\left(\alpha - \omega\right), \\
\lambda_{3,4}^2 &= \frac{b_{22} + b_{33}}{2} - \frac{1}{2}\sqrt{\left(b_{22} - b_{33}\right)^2 + 4b_{23}b_{32}}, \\
\lambda_{5,6}^2 &= \frac{b_{22} + b_{33}}{2} + \frac{1}{2}\sqrt{\left(b_{22} - b_{33}\right)^2 + 4b_{23}b_{32}}
\end{aligned} \tag{2.103}$$

Solution of the inhomogeneous system of differential equations (2.99) can be expressed in terms of the fundamental solutions $\mathbf{z}_1(y)$, $\mathbf{z}_2(y)$,..., $\mathbf{z}_6(y)$ with coefficients depending on the initial data $\mathbf{A}_0$. The inverse Laplace transform could be presented as a sum of residue values at poles corresponding to the modes of discrete spectrum and a sum of integrals along branch-cuts in the complex plane p. These branch-cuts are associated with the continuous spectrum, and they can be found from equations

$$\lambda_j^2 = -k^2, \quad j = 1, ..., 6 \tag{2.104}$$

where k is a positive parameter. In the case of the spatially growing disturbances, there are seven branches of the continuous spectrum. This number stems from the fact that the characteristic equation represents a polynomial of seventh order with respect to the wave number, $\alpha = ip$ (the continuity equation has the first derivative with respect to x, the two momentum equations and the energy equation have second derivatives with respect to x). Particularly, indices $j = 1$ and 2 correspond to the vorticity modes, whereas the others correspond to the acoustic and entropy modes [depending on the branch of the square root in Eq. (2.103)]. The classification of the modes follows from their properties outside the boundary layer (one can find discussion of the properties of vorticity, entropy and acoustic modes in [Pie89]).

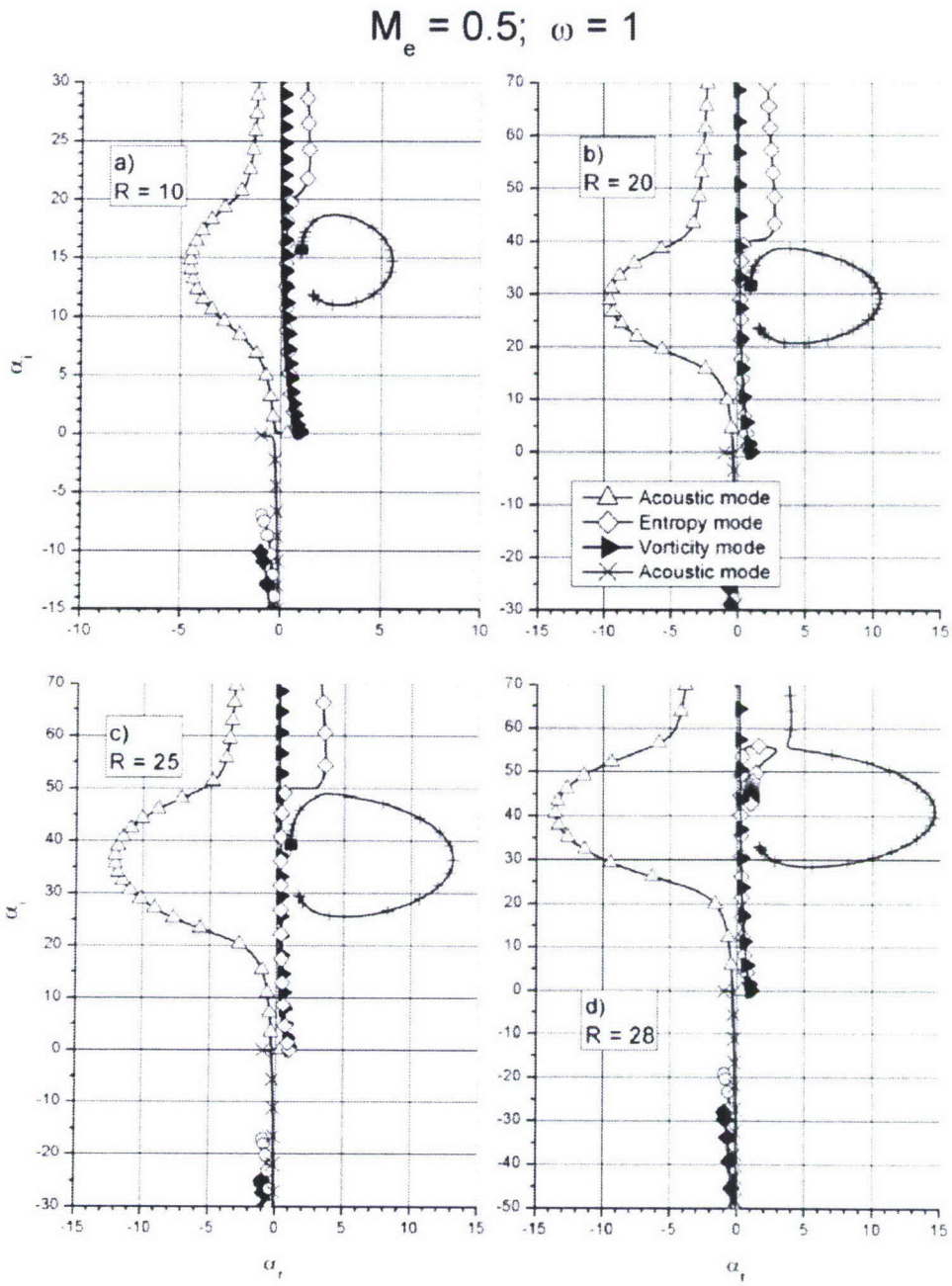

Figure 2.63: Branches of the continuous spectrum in the complex plane α.

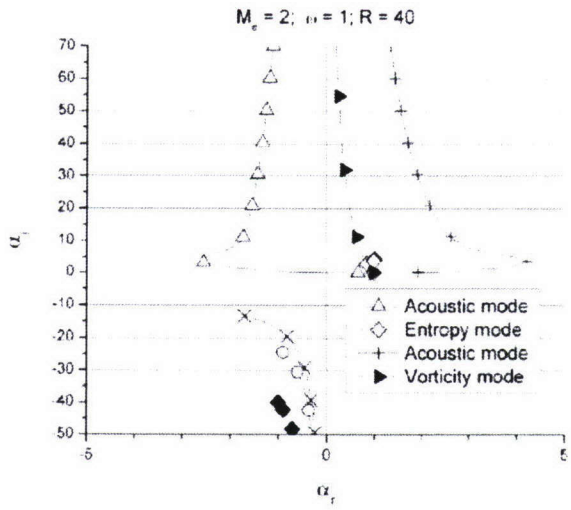

Figure 2.64: Branches of the continuous spectrum in the complex plane α.

Figure 2.63 demonstrates branches of the continuous spectrum at local Mach number $M_e = 0.5$ in the complex plane $\alpha = ip$. Figure 2.64 shows the branches in the case of a supersonic flow ($M_e = 2$). In both examples the dimensionless frequency was chosen equal to 1. The relatively small Reynolds numbers are chosen for purpose of the illustration only (the Mach numbers on the illustrations are the same as in [TF83b]). One can see that there are three modes having negative imaginary parts of α. They are associated with upstream perturbations. The other four modes correspond to the downstream modes. One of the branches has a limiting point as parameter k tends to infinity. Although the limiting point exists at significantly high positive values of α_i that are usually not of interest, we demonstrate the structure of the branches for completeness of the illustration. The branches can be interpreted as acoustic, entropy, and vorticity modes in accordance with their properties outside the boundary layer. Note that the branch having a limiting point in the upper half-plane was calculated incorrectly in [TF83b]. The correct behavior of this branch was found by D. E. Ashpis (private communication, 1993). However, the error was associated with strongly decaying modes, and it did not affect the main result and conclusions of [TF83b].

Biorthogonal eigenfunction system

It was shown in [TF83b] that the formal solution of the spatial initial-value problem could be represented as a sum of the continuous and discrete spectra. The direct and the adjoint

problems corresponding to these modes ($\mathbf{A}_\alpha$ and $\mathbf{B}_\alpha$, respectively) are the following:

$$\begin{cases} \dfrac{d}{dy}\left(L_0\dfrac{d\mathbf{A}_\alpha}{dy}\right) + L_1\dfrac{d\mathbf{A}_\alpha}{dy} = H_1\mathbf{A}_\alpha + i\alpha H_2\mathbf{A}_\alpha \\ y = 0: \quad A_{\alpha 1} = A_{\alpha 3} = A_{\alpha 5} = 0 \\ y \to \infty: \quad |A_{\alpha j}| < \infty \end{cases} \tag{2.105}$$

$$\begin{cases} \dfrac{d}{dy}\left(L_0^T\dfrac{d\mathbf{B}_\alpha}{dy}\right) - L_1^T\dfrac{d\mathbf{B}_\alpha}{dy} = H_1^T\mathbf{B}_\alpha + i\alpha H_2^T\mathbf{B}_\alpha \\ y = 0: \quad B_{\alpha 2} = B_{\alpha 4} = B_{\alpha 6} = 0 \\ y \to \infty: \quad |B_{\alpha j}| < \infty \end{cases} \tag{2.106}$$

In the definition of the adjoint problem, we do not introduce the complex conjugate due to the convenience associated with a numerical realization. The subscript α indicates that the mode is associated with the wave number.

The system of equations (2.105) can be recast in the form of Eq. (2.100), whereas Eq. (2.106) can be recast as

$$-\frac{d\mathbf{Y}}{dy} = H_0^T\mathbf{Y} \tag{2.107}$$

We have found relationships between components of vectors $\mathbf{B}$ and $\mathbf{Y}$ with the help of *Mathematica* [Wol99] (see A.5).

The following orthogonality condition exists:

$$\langle H_2\mathbf{A}_\alpha, \mathbf{B}_{\alpha'}\rangle \equiv \sum_{j=1}^{9}\int_0^\infty (H_2\mathbf{A}_\alpha)_j\, B_{\alpha' j}\, dy = Q\Delta_{\alpha,\alpha'} \tag{2.108}$$

where $\Delta_{\alpha,\alpha'}$ is the Kronecker symbol if α or α' belongs to the discrete spectrum, and $\Delta_{\alpha,\alpha'} = \delta(\alpha - \alpha')$ is the delta function if both α and α' belong to the continuous spectrum. The coefficient Q on the right-hand side of (2.108) depends on normalization of $\mathbf{A}_\alpha(y)$ and $\mathbf{B}_\alpha(y)$.

If we have a vector function $\mathbf{A}_0(y)$ (for example, from a computational study), we can find the amplitude of a mode as follows:

$$C_\alpha = \langle H_2\mathbf{A}_0, \mathbf{B}_\alpha\rangle \,/\, \langle H_2\mathbf{A}_0, \mathbf{B}_\alpha\rangle \tag{2.109}$$

An example of two discrete modes is given in figure 2.62. Examples of the acoustic modes in the boundary layer over a cone $R = 1600$ and $F = 150 \times 10^{-6}$ are shown in figure 2.65. The parameter k in these examples is equal to 1 and the normalization of the modes was defined by the equation $\partial u/\partial y = 1$ on the wall.

Examples of the multimode decomposition

We consider two examples. The first one is an emulation of the analysis of a flow field obtained by means of a computational method, i.e. all parameters of the flow are assumed to be known at a prescribed station x. The second example will be an emulation of the decomposition of 'experimental' data. Details of the numerical methods are presented in [FT03].

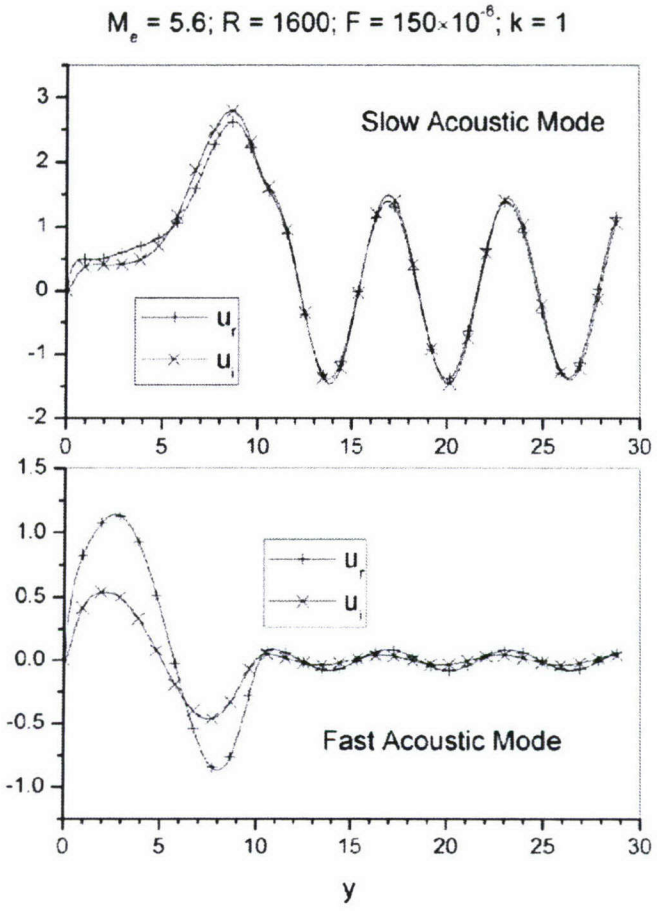

Figure 2.65: Streamwise velocity component of acoustic modes.

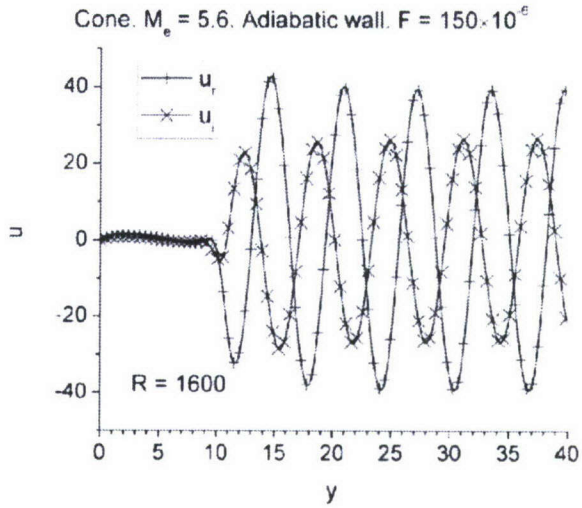

Figure 2.66: Real and imaginary parts of the combined flowfield (two discrete modes, vorticity and acoustic).

'CFD' Flow Field

Figure 2.66 gives an example of a flow field, $\mathbf{A}_0(y)$, comprised of two discrete modes (figure 2.62) with amplitudes $C_1 = 1$ and $C_2 = -1$, acoustic and vorticity modes, respectively. The sum of the discrete modes only is shown in figure 2.67. It is very difficult to imagine presence of the discrete modes in the total flow field. The phase shift between the modes was chosen to illustrate how interpretation of the flow field might be complicated. The decomposition procedure, Eq. (2.109), leads to the coefficients $C_1 = 1.0018 + i1.58e-03$ and $C_2 = -0.9997 - i1.59e-04$. The negligible discrepancy with the actual values is attributed to the accuracy of the numerical evaluation of the integrals.

Evaluation of the coefficient Q in Eq. (2.108) in the case of the discrete spectrum is straightforward: numerical integration on the interval $[0, y_{\max}]$ and analytical calculation on the interval $[y_{\max}, \infty)$. In the case of the continuous spectra, the coefficient Q can be found with the help of the asymptotic solutions outside of the boundary layer. An outline of the evaluation is given in [Tum03]. We would like to point out that the coefficient Q and, therefore coefficients C_j, depend on the normalization of the biorthogonal eigenfunction system. However, the product of the coefficients and the eigenfunctions $\mathbf{A}_\alpha$ is invariant with respect to the normalization.

'Experimental' Flow Field

In the previous example, all components of the vector $\mathbf{A}_0(y)$ were known. If, for some reason, one can expect that only a few modes are responsible for the total signal measured in the

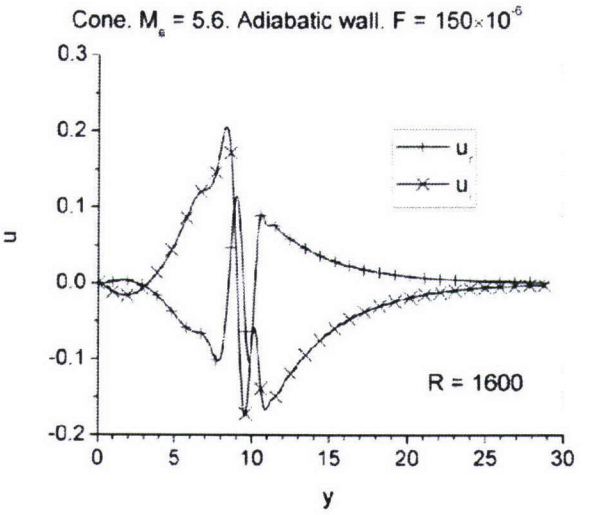

Figure 2.67: Real and imaginary parts of the combined flowfield (two discrete modes only). Compare magnitudes of the functions in figures 2.66 and 2.67.

experiment, this *a priori* information also can be helpful in decomposing the experimental flow field. The assumption about the main input from specific modes actually allows recovery of the other components in the vector $\mathbf{A}_0(y)$ with unknown coefficients. For example, we have 'experimental' data for the x-velocity component as in figures 2.68 and 2.69 (amplitude and phase of the streamwise velocity perturbation corresponding to figure 2.67). If there is *a priori* information that the data are comprised of two discrete modes associated with wave numbers α_1 and α_2, one can represent the vector $\mathbf{A}_0(y)$ as follows:

$$\begin{aligned}\mathbf{A}_0(y) = (u, &C_1A_{\alpha_1} + C_2A_{\alpha_2 1}, C_1A_{\alpha_1 2} + C_2A_{\alpha_2 2}, C_1A_{\alpha_1 3} + C_2A_{\alpha_2 3},\\ &C_1A_{\alpha_1 4} + C_2A_{\alpha_2 4}, C_1A_{\alpha_1 5} + C_2A_{\alpha_2 5}, C_1A_{\alpha_1 6} + C_2A_{\alpha_2 6},\\ &C_1A_{\alpha_1 7} + C_2A_{\alpha_2 7}, C_1A_{\alpha_1 8} + C_2A_{\alpha_2 8}, C_1A_{\alpha_1 9} + C_2A_{\alpha_2 9})\end{aligned} \tag{2.110}$$

where $A_{\alpha_j m}$ stands for the m-th component of the vector $\mathbf{A}_{\alpha_j}$. At the same time, the *a priori* information suggests that the vector $\mathbf{A}_0(y)$ can be represented also as a sum of these two modes

$$\mathbf{A}_0(y) = C_1\mathbf{A}_{\alpha_1}(y) + C_2\mathbf{A}_{\alpha_2}(y) \tag{2.111}$$

From the orthogonality condition, one can obtain

$$\begin{aligned}\langle H_2\mathbf{A}_0, \mathbf{B}_{\alpha_1}\rangle &= C_1\langle H_2\mathbf{A}_{\alpha_1}, \mathbf{B}_{\alpha_1}\rangle\\ \langle H_2\mathbf{A}_0, \mathbf{B}_{\alpha_2}\rangle &= C_2\langle H_2\mathbf{A}_{\alpha_2}, \mathbf{B}_{\alpha_2}\rangle\end{aligned} \tag{2.112}$$

Substitution of $\mathbf{A}_0(y)$ from Eq. (2.110) into Eq. (2.112) leads to a system of algebraic equations for C_1 and C_2. This decomposition procedure has been applied to data in figures

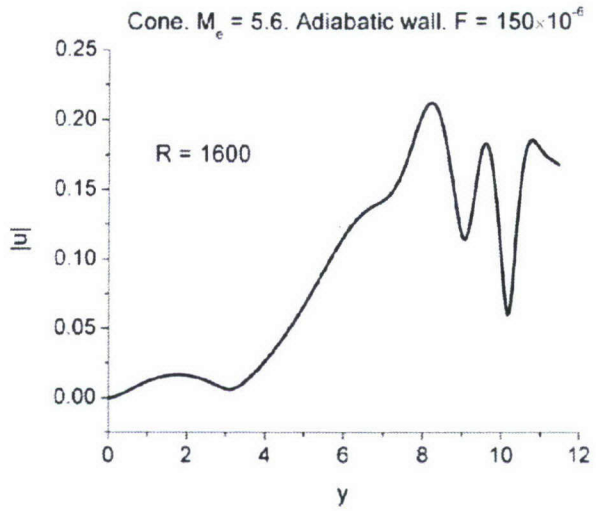

Figure 2.68: Experimental streamwise velocity disturbance amplitude distribution across the boundary layer.

2.68 and 2.69 and the coefficients C_1 and C_2 were found as $1.00002 + i1.16e-04$ and $-0.999996 + i1.65e-06$, respectively. Because the experimental data might be contaminated by noise or by other modes that were not included into the decomposition, one has to carry out *a posteriori* comparison of the measured and recovered profiles in order to estimate consistency of the decomposition with the *a priori* information/assumption.

Conclusion

The formulated method of multimode decomposition might be very helpful for the analysis of computational results related to laminar-turbulent transition in compressible boundary layers. Although the present formulation deals with two-dimensional disturbances and two-dimensional boundary layers, the orthogonality relationship can be easily extended to a general case of three-dimensional perturbations when the boundary layer flow is independent of the spanwise coordinate (for example, infinite swept wing flow). In this case, the Fourier transform with respect to the spanwise coordinate can be employed and the orthogonality condition can be formulated for the modes having the same spanwise wave number. The method might be also useful in the analysis of real experimental data when *a priori* information about the modes is available.

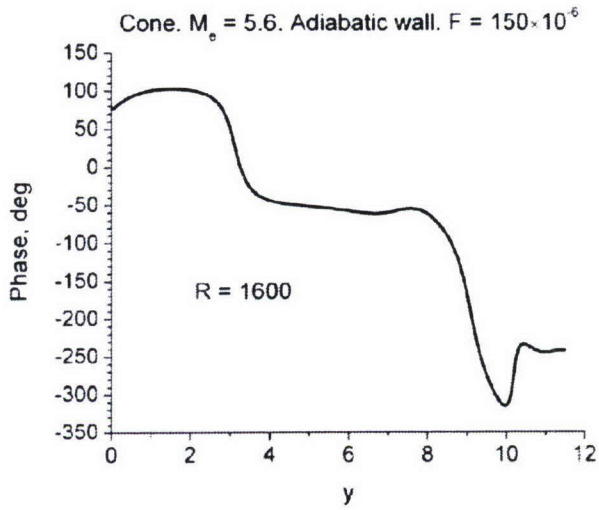

Figure 2.69: Experimental streamwise velocity disturbance phase distribution across the boundary layer.

2.5.3 Application of the decomposition to DNS results

This section is based on the paper published in collaboration with X. Wang and X. Zhong [TWZ07].

Introduction

The objective of the present section is to demonstrate how the multimode decomposition may serve as a tool for gaining insight into the computational results and to validating them as well. As an example, the direct numerical simulations (DNS) of high-speed boundary layer receptivity to wall blowing-suction are chosen for the analysis [WZ05]. The perturbation flow field obtained in the DNS is projected onto the spatially growing/decaying modes of discrete and continuous spectra at a prescribed frequency. In addition, the filtered-out amplitudes of two discrete normal modes and of the fast acoustic modes are compared with ones predicted by the linear receptivity theory.

Numerical approach

A numerical simulation was carried out by Wang and Zhong [WZ05] to determine the receptivity of a Mach 8.0 flow over a sharp wedge to wall blowing-suction through a slot on the wedge surface. The wedge had a half-angle of 5.3°. The freestream parameters were: velocity $U_\infty = 1181.7$ m/s, density $\rho_\infty = 0.0247$ kg/m^3, and temperature $T_\infty = 54.78$ K. Such a hypersonic boundary-layer flow had been numerically studied by other researchers. Malik *et al.* [MLS99] solved the linearized Navier–Stokes equations to investigate the responses of the flow to three types of external forcing. Ma and Zhong [MZ03c] studied receptivity mechanisms of the same flow to various freestream disturbances by solving the two-dimensional compressible Navier-Stokes equations. In the current simulation, we extend the study to the receptivity mechanism of the hypersonic boundary layer to wall blowing-suction disturbances.

In our simulation, the Mach 8 flow is assumed to be thermally and calorically perfect. The governing equations for the simulation are the two-dimensional Navier-Stokes equations in the conservative form, i.e.,

$$\frac{\partial \mathbf{U}}{\partial t} + \frac{\partial}{\partial x_1}(\mathbf{F}_{1i} + \mathbf{F}_{1v}) + \frac{\partial}{\partial x_2}(\mathbf{F}_{2i} + \mathbf{F}_{2v}) = 0, \tag{2.113}$$

where $\mathbf{U}$ is a vector containing the conservative variables of mass, momentum, and energy, i.e.,

$$\mathbf{U} = \{\rho, \rho u_1, \rho u_2, e\}. \tag{2.114}$$

The flux vector in (2.113) is divided into its inviscid and viscous components, because the two components are discretized with two finite difference schemes: $\mathbf{F}_{1i}$ and $\mathbf{F}_{2i}$ are inviscid flux vectors, whereas $\mathbf{F}_{1v}$ and $\mathbf{F}_{2v}$ are viscous flux vectors. The flux vectors can be expressed

as

$$\mathbf{F}_{ji} = \begin{bmatrix} \rho u_j \\ \rho u_1 u_j + p\delta_{1j} \\ \rho u_2 u_j + p\delta_{2j} \\ u_j(e+p) \end{bmatrix}, \tag{2.115}$$

$$\mathbf{F}_{jv} = \begin{bmatrix} 0 \\ -\tau_{1j} \\ -\tau_{2j} \\ -\tau_{nj}u_n - \kappa\frac{\partial T}{\partial x_j} \end{bmatrix}, \tag{2.116}$$

with $j, n \in \{1, 2\}$. In the perfect gas assumption, pressure and energy are given by

$$p = \rho RT, \tag{2.117}$$

$$e = \rho c_v T + \frac{\rho}{2}(u_1^2 + u_2^2), \tag{2.118}$$

where c_v is the specific heat at constant volume. For compressible Newtonian flow, the viscous stress tensor can be written as

$$\tau_{ij} = \mu(\frac{\partial u_i}{\partial x_j} + \frac{\partial u_j}{\partial x_i}) - \frac{2}{3}\mu\frac{\partial u_n}{\partial x_n}\delta_{ij}, \tag{2.119}$$

for $i, j, n \in \{1, 2\}$. In the simulation, the viscosity coefficient, μ, and the heat conductivity coefficient, κ, are calculated using Sutherland's law together with a constant Prandtl number, $Pr = 0.72$.

The fifth-order shock-fitting method of Zhong [Zho98] is used to solve the two-dimensional Navier–Stokes equations in a domain bounded by the bow shock and the wedge surface. The bow shock is treated as a boundary of the computational domain, which makes it possible for the Navier–Stokes equations to be spatially discretized by high-order finite difference methods. Specifically, a fifth-order upwind scheme is used to discretize the inviscid flux derivatives. Meanwhile, the viscous flux derivatives are discretized by a sixth-order central scheme. The Rankine-Hugoniot relation across the shock and a characteristic compatibility relation from the downstream flow field are combined to solve the flow variables behind the shock. By using the shock-fitting method, the interaction between the unsteady perturbations and the bow shock is solved as part of the solutions, with the position and velocity of the shock front being taken as unknown flow variables. A three-stage semi-implicit Runge-Kutta method is used for temporal integration, where the time step size is obtained based on CFL number and grid size.

The steady base flow is computed by solving (2.113) with a combination of the fifth-order shock-fitting method and a second-order TVD scheme. In the leading edge region, there exists a singular point at the tip of the wedge, which will introduce numerical instability if the fifth-order shock-fitting method is used to simulate the flow. Therefore, the computational domain for the shock-fitting simulation starts from a very short distance downstream of

the leading edge. A second-order TVD scheme is used to simulate the steady base flow in a small region including the leading edge to supply inlet conditions for the shock-fitting simulation. The steady base flow simulation is advanced in time until the last pair of solutions separated by a finite time interval can be considered as identical within a specified tolerance. For unsteady simulations, blowing-suction disturbances are introduced in a downstream region where the shock-fitting method is used. The subsequent responses of the hypersonic boundary layer are simulated with the fifth-order shock-fitting method to achieve a periodic-in-time flow field (large time asymptote of perturbation calculations).

For the simulation of steady base flow, the wall is adiabatic, and the physical boundary condition of velocity on the wedge surface is the non-slip condition. When periodic-in-time blowing-suction disturbances are enforced on the steady base flow, the isothermal temperature condition is applied on the wall. This temperature condition is a standard boundary condition for theoretical and numerical studies of high-frequency disturbances. Meanwhile, a non-slip condition is applied on the wall, except for the forcing region. Inlet conditions are specified, while high-order extrapolation is used for outlet conditions because the flow is supersonic at the exit boundary, except for a small region near the wedge surface.

In the current study, the coordinate x is defined as the distance measured from the tip of the wedge, whereas the coordinate y is the normal distance from the wall. The blowing-suction slot is simulated by the periodic-in-time boundary conditions for the perturbation of the mass flux on the wall, which can be written as follows:

$$\rho v = q_0 g(l) \sum_{n=1}^{15} \sin(\omega_n t), \tag{2.120}$$

where q_0 is an amplitude parameter and ω_n is the circular frequency of multi-frequency perturbations. In (2.120), $g\,(l)$ is the profile function defined as

$$g\,(l) \begin{cases} 20.25l^5 - 35.4375l^4 + 15.1875l^2, & (l \leq 1)\,; \\ -20.25\,(2-l)^5 + 35.4375\,(2-l)^4 - 15.1875\,(2-l)^2\,, & (l > 1)\,. \end{cases} \tag{2.121}$$

The variable l in (2.121) is a non-dimensional coordinate defined within the blowing-suction slot:

$$l\,(x) = \frac{2\,(x - x_i)}{(x_e - x_i)}, \qquad x_i \leq x \leq x_e; \tag{2.122}$$

where x_i and x_e are the coordinates of the leading and the trailing edges of the slot, respectively. The amplitude distribution, $g\,(l)$, is shown in figure 2.70. Numerical simulations reveal that there is no difference in the results if surface blowing-suction is specified by the perturbation in the y-velocity only. This is due to the fact that the weak perturbation is in the linear region. The corresponding velocity perturbation at $y = 0$ is

$$v(x,t) = v_w(x) \sum_{n=1}^{15} \sin(\omega_n t) = \frac{q_0}{\rho_{sw}} g(l) \sum_{n=1}^{15} \sin(\omega_n t), \tag{2.123}$$

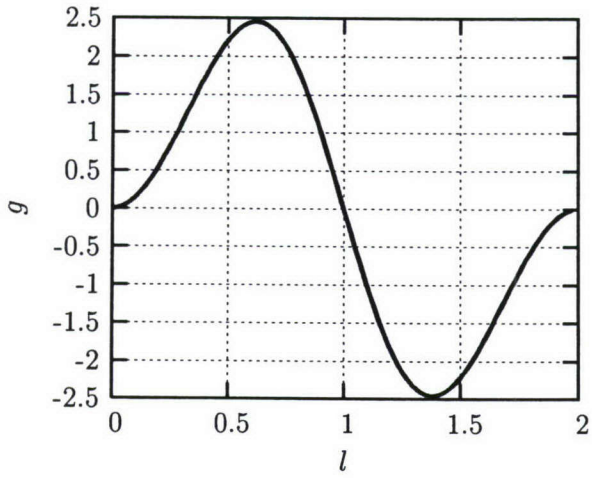

Figure 2.70: Amplitude distribution of the blowing-suction slot.

where ρ_{sw} is density of the unperturbed flow on the wall. In the theoretical analysis we utilize (2.123) as the boundary condition simulating the actuation.

As had been mentioned above, the steady base flow is simulated with a combination of a fifth-order shock-fitting finite difference method and a second-order TVD scheme. In the leading edge region, there exists a singular point at the tip of the wedge, which will introduce numerical instability if the fifth-order shock-fitting method is used to simulate the flow. Therefore, the computational domain for the fifth-order shock-fitting method starts at $x = 0.00409$ m and ends at $x = 1.48784$ m. In actual simulations, the computational domain is divided into 30 zones, with a total of 5936 grid points in the streamwise direction and 121 grid points in the wall-normal direction. Forty-one points are used in the buffering region between two neighboring zones, which proved to be sufficient to make the solution accurate and smooth within the whole domain. An exponential stretching function is used in the wall-normal direction to cluster more points inside the boundary layer. On the other hand, the grid points are uniformly distributed in the stream-wise direction.

For the first zone of the shock-fitting calculations, the inlet conditions are obtained from the results of the second-order TVD shock-capturing scheme, which is used to simulate the steady base flow in a small region including the leading edge. For other zones, inlet conditions are interpolated from the results of the previous zone. Figure 2.71 shows the wall-normal velocity and density contours near the leading edge of the steady base flow obtained by the second-order TVD scheme and the fifth-order shock-fitting method. The flow field including the leading edge is simulated by the TVD scheme, while the flow field after $x = 0.00409$ m is simulated by the shock-fitting method. It shows that wall-normal velocity and density contours have good agreement within the buffering region, which indicates that the TVD

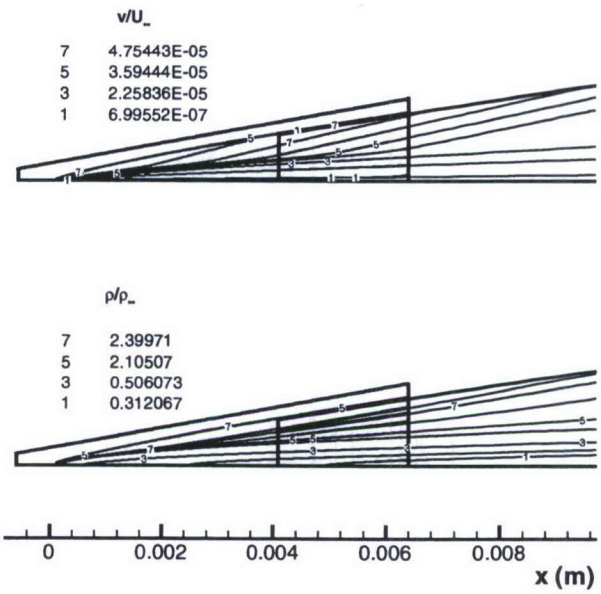

Figure 2.71: Wall-normal velocity and density contours near the leading edge of the steady base flow obtained by a combination of a fifth-order shock-fitting method and a second-order TVD scheme.

solutions are accurate for use as inlet conditions for the fifth-order shock-fitting simulation in the first zone.

In our simulations, three sets of grid structures are tested to check the grid independence of the numerical results. As an example, figure 2.72 compares the temperature contours of the steady base flow in zone 10, simulated using the three sets of grids. It shows that the three contours agree well in the domain despite the increases in grid points. This figure indicates that the simulation results are converged in both the x and y directions. Figure 2.73 shows the streamwise velocity and temperature profiles in the wall-normal direction at the location of $x = 0.62784$ m. The current numerical solutions are compared with the self-similar boundary-layer solutions. In the figure, velocity and temperature are non-dimensionalized by corresponding freestream values, while the y coordinate is non-dimensionalized by $\sqrt{x\mu_\infty/\rho_\infty U_\infty}$. This figure shows that the properties of the current numerical simulation agree very well with those of the self-similar boundary-layer solution. In unsteady simulations, the amplitude of blowing-suction is at least one order of magnitude larger than the maximum numerical noise and it is small enough to preserve the linear properties of the disturbances. Figure 2.74 compares dimensionless amplitude along the wedge surface of a pressure perturbation at the frequency of 149.2 kHz. The solid line and trian-

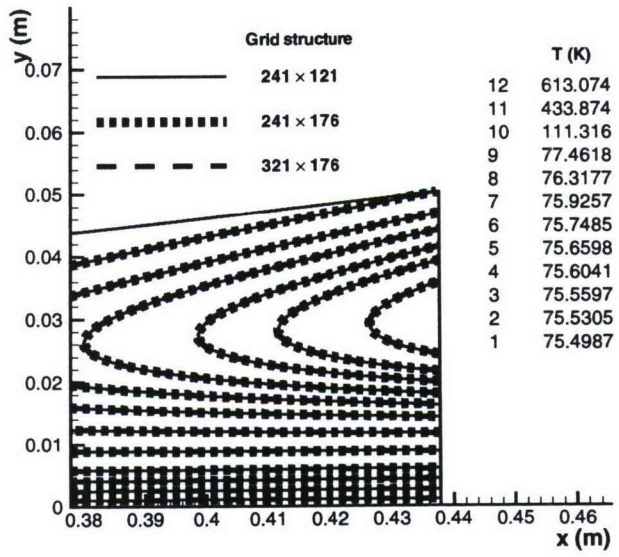

Figure 2.72: Comparison of temperature contours of the steady base flow in zone 10 simulated using the three sets of grids.

gular symbol represent the numerical results simulated using grid structures of 241 × 176 and 241 × 121, respectively. The agreement between the two distributions of perturbation amplitude indicates that the grid independence of unsteady simulation is achieved. All these three figures show that the grid structure of 241 × 121 used in the current simulation is enough to ensure grid-independent numerical simulations.

For the purpose of the multimode decomposition, fast Fourier transform (FFT) of the perturbation field is carried out downstream from the slot at distance x_{data}. The time duration of simulation data used for FFT analysis is one period of the base frequency. Seven cases with different x_i, x_e, and x_{data} are considered in the present work. In all cases, the width of the slot, $w = x_e - x_i$, is kept equal to 1.2 cm. Coordinates of the slot center, x_c, and the coordinates x_{data} are presented in table 2.5.

Figure 2.75 shows an example of the streamwise velocity amplitude distributions obtained in the numerical simulation for case 1. The velocity is scaled with the edge velocity, U_e = 1167.3 m/s, and the distance from the wall is scaled with $H = 0.1251$ mm. The length scale H is defined as $\sqrt{x_{data}\mu_\infty/\rho_\infty U_\infty}$.

The boundary layer thickness δ_{99} (distance from the wall where the local velocity $U = 0.99U_e$) is given in table 2.5. As follows from the table, the ratio δ_{99}/H is about 19.5 in all cases.

The contours of the instantaneous pressure perturbation induced by blowing-suction disturbance at frequency 5 × 14.92 kHz are shown in figure 2.76 (case 2). After the blowing-

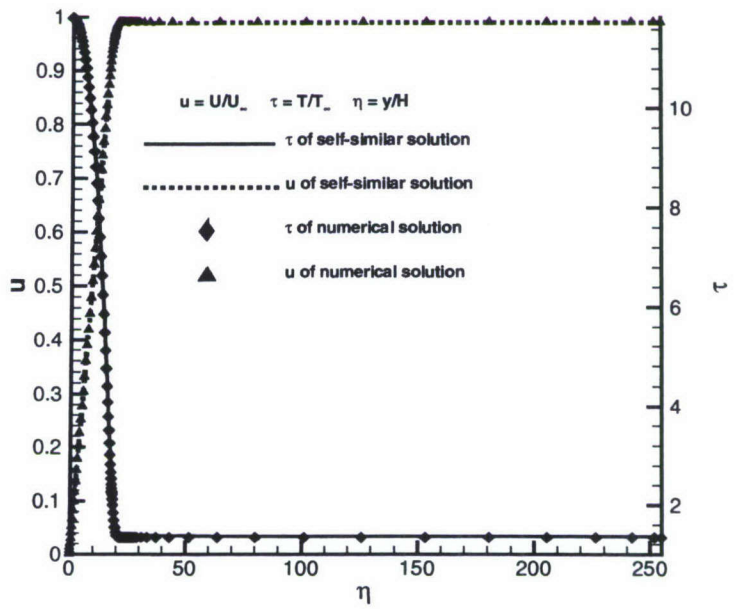

Figure 2.73: Profiles of streamwise velocity and temperature in the wall-normal direction at the location of $x = 0.62784$ m.

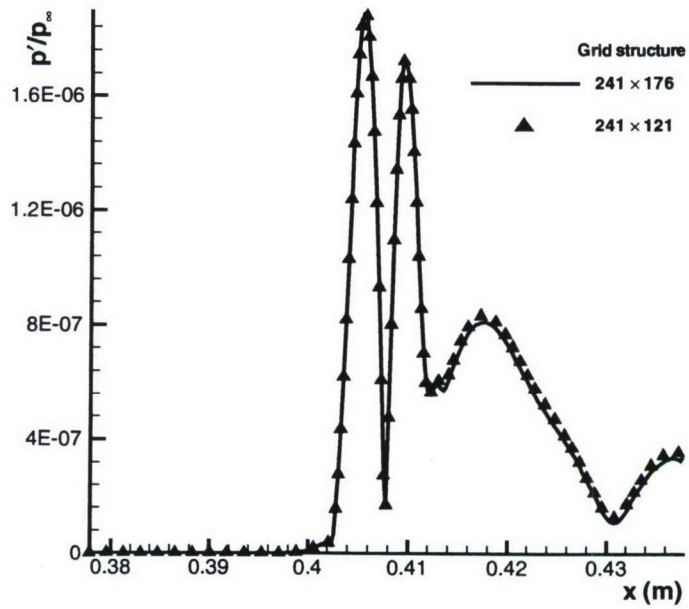

Figure 2.74: Comparison of dimensionless amplitude along the wedge surface of pressure perturbation at the frequency of 149.2 kHz.

Case	x_c (m)	x_{data} (m)	$q_0 \times 10^5$ (kg/s m^2)	H (mm)	δ_{99} (mm)	N	$\alpha_{Sr}H$ $\alpha_{Si}H$	$\alpha_{Fr}H$ $\alpha_{Fi}H$
1	0.10772	0.12784	0.125188	0.1251	2.437	11	$+1.07 \times 10^{-1}$	$+9.91 \times 10^{-2}$
							-3.38×10^{-4}	$+2.73 \times 10^{-3}$
2	0.40784	0.42784	0.054453	0.2289	4.452	7	$+1.17 \times 10^{-1}$	$+1.15 \times 10^{-1}$
							-1.98×10^{-3}	$+6.92 \times 10^{-3}$
3	0.05784	0.07784	0.214139	0.09764	1.901	11	$+8.54 \times 10^{-2}$	$+7.19 \times 10^{-2}$
							$+5.77 \times 10^{-6}$	$+8.16 \times 10^{-4}$
4	0.15784	0.17784	0.096130	0.1476	2.875	10	$+1.13 \times 10^{-1}$	$+1.09 \times 10^{-1}$
							-1.14×10^{-3}	$+6.75 \times 10^{-3}$
5	0.20784	0.22784	0.080666	0.1670	3.250	9	$+1.14 \times 10^{-1}$	$+1.10 \times 10^{-1}$
							-1.28×10^{-3}	$+6.63 \times 10^{-3}$
6	0.25784	0.27784	0.070759	0.1845	3.590	8	$+1.10 \times 10^{-1}$	$+1.05 \times 10^{-1}$
							-6.05×10^{-4}	$+6.89 \times 10^{-3}$
7	0.30784	0.32784	0.063745	0.2004	3.900	8	$+1.19 \times 10^{-1}$	$+1.19 \times 10^{-1}$
							-2.43×10^{-3}	$+7.55 \times 10^{-3}$

Table 2.5: Coordinates of the slot center, x_c, and of the station, x_{data}, where data were provided for the decomposition; the amplitude parameter q_0 in (2.120); the length scale H corresponding to the considered examples; the local boundary layer thickness, δ_{99}; the real and imaginary parts of the eigenvalues corresponding to the slow and fast discrete modes, α_S and α_F, respectively. The presented eigenvalues correspond to frequencies $(N-1) \times 14.92$ kHz, where N is given in the table.

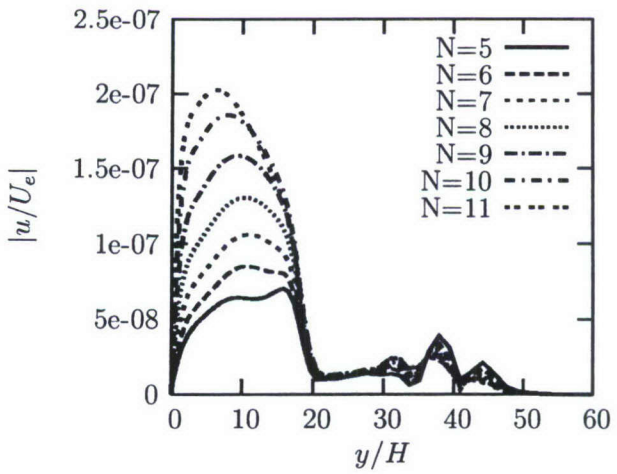

Figure 2.75: Amplitude distribution of the streamwise velocity component at $x = x_{data}$ and frequency $(N-1) \times 14.92$ kHz for case 1.

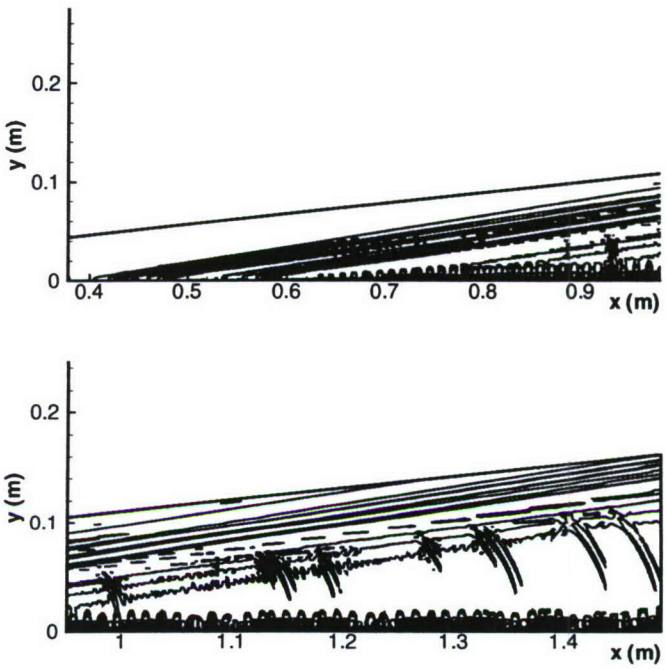

Figure 2.76: Contours of the instantaneous pressure perturbation induced by blowing-suction disturbance at frequency 5×14.92 kHz for case 2.

suction slot, the excited pressure perturbations are divided into two branches: one branch penetrates the boundary layer and propagates along the Mach lines (acoustic waves) while the other branch stays within the boundary layer, which is the instability mode (mode S in terminology of the results' part of this section), indicated by the typical wave structures near the wall.

Theoretical analysis

The theoretical analysis of the numerical results in the present work includes two steps. The first one is the decomposition of the perturbation field obtained in the computational part of the work into normal modes (projection onto the basis comprised of the eigenfunctions of the continuous and discrete spectra). The second step is the receptivity problem solution with the blowing-suction on the wall defined by (2.123) and comparison of the found amplitudes with those filtered out from the computational results.

The multimode decomposition of two-dimensional perturbations in compressible boundary layers was introduced by Guydos and Tumin [GT04] (Section 2.5.2), and it can be utilized for analysis of the present problem. Alternatively, one can use the results for three-dimensional perturbations [Tum06c] when the spanwise wave number, β, is very small. Similarly, the receptivity problem solution for three-dimensional perturbations introduced on the wall (see Section 2.3.2 and 2.4.1) can be utilized for analysis of the two-dimensional problem by using $\beta \to 0$. For clarity of the method description, we recapitulate the receptivity problem solution in a form adequate for two-dimensional perturbations in a compressible boundary layer [Fed84]. One can find a historical perspective of the method and relevant bibliography in Sections 2.3.2 and 2.7.

In the parallel flow approximation, we write down the governing equations for a two-dimensional periodic-in-time perturbation in the matrix notation of Section 2.5.2,

$$\frac{\partial}{\partial y}\left(\mathbf{L}_0 \frac{\partial \mathbf{A}}{\partial y}\right) + \mathbf{L}_1 \frac{\partial \mathbf{A}}{\partial y} = \mathbf{H}_1 \mathbf{A} + \mathbf{H}_2 \frac{\partial \mathbf{A}}{\partial x}, \tag{2.124}$$

where $\mathbf{L}_0$, $\mathbf{L}_1$, $\mathbf{H}_1$, and $\mathbf{H}_2$ are 9×9 matrices. Their non-zero elements are given in Section 2.5.2. Vector $\mathbf{A}$ is comprised of the perturbation profiles and their derivatives,

$$\mathbf{A} = \left(u, \partial u/\partial y, v, \pi, \theta, \partial \theta/\partial y,\ \partial u/\partial x, \partial v/\partial x, \partial \theta/\partial x\right)^T, \tag{2.125}$$

where u and v are x- and y-velocity components, respectively; π is the pressure perturbation; θ is the temperature perturbation; and T stands for transposed. In the case of blowing-suction through a slot, the boundary conditions in the slot domain are inhomogeneous, $A_3(x, 0) = v_w(x)$, and A_8 can be found from A_3 by the definition. The solution of (2.124) is decaying outside the boundary layer. For simplicity, we assume that the perturbation frequency is subcritical, and one can employ the Fourier transform with respect to x.

$$\mathbf{A}_v(\alpha_v, y) = \int_{-\infty}^{+\infty} \mathbf{A}(x, y)\, e^{-i\alpha_v x} dx. \tag{2.126}$$

In the case of a supercritical frequency, one has to refer to Briggs' method in order to include the unstable mode (exponentially growing downstream mode) in the inverse Fourier transform [AR90, BM92].

Vector-function $\mathbf{A}_v(\alpha_v, y)$ satisfies the following equation and boundary conditions

$$\frac{d}{dy}\left(\mathbf{L}_0\frac{d\mathbf{A}_v}{dy}\right)+\mathbf{L}_1\frac{d\mathbf{A}_v}{dy}=\mathbf{H}_1\mathbf{A}_v+i\alpha_v\mathbf{H}_2\mathbf{A}_v, \tag{2.127}$$

$$y=0: \quad A_{v1}=0, \quad A_{v3}=\varphi(\alpha_v), \quad A_{v5}=0, \tag{2.128a}$$

$$y\to\infty: \quad |A_{vj}|\to 0, \qquad (j=1,...,9), \tag{2.128b}$$

where

$$\varphi(\alpha_v)=\int_{-\infty}^{+\infty} v_w(x)\,e^{-i\alpha_v x}dx. \tag{2.129}$$

Equation (2.127) has three fundamental solutions decaying outside the boundary layer. One can write down the solution of the inhomogeneous boundary-value problem as follows:

$$\mathbf{A}_v=C_1\mathbf{Z}_1+C_3\mathbf{Z}_3+C_5\mathbf{Z}_5, \tag{2.130}$$

where $\mathbf{Z}_1$, $\mathbf{Z}_3$, and $\mathbf{Z}_5$ are the decaying fundamental solutions. The coefficients C_j in (2.130) are found from the boundary conditions (2.128a) on the wall. The formal solution of (2.124) satisfying the boundary conditions can be written as follows

$$\mathbf{A}(x,y)=\frac{1}{2\pi}\int_{-\infty}^{+\infty}\mathbf{A}_v(\alpha_v,y)\,e^{i\alpha_v x}d\alpha_v. \tag{2.131}$$

It was shown in [TF83b] and [Tum06c] that the periodic-in-time solution of the linearized Navier–Stokes equations can be expanded into the normal modes of continuous and discrete spectra,

$$\mathbf{A}(x,y)=\sum_j\int_0^\infty C_j(k)\mathbf{A}_\alpha(y,k)e^{i\alpha_j(k)x}dk+\sum_m C_m\mathbf{A}_{\alpha_m}(y)\,e^{i\alpha_m x}, \tag{2.132}$$

where the eigenfunctions $\mathbf{A}_\alpha$ are found as solutions of the following problem:

$$\frac{d}{dy}\left(\mathbf{L}_0\frac{d\mathbf{A}_\alpha}{dy}\right)+\mathbf{L}_1\frac{d\mathbf{A}_\alpha}{dy}=\mathbf{H}_1\mathbf{A}_\alpha+i\alpha\mathbf{H}_2\mathbf{A}_\alpha, \tag{2.133}$$

$$y=0: \quad A_{\alpha1}=A_{\alpha3}=A_{\alpha5}=0, \tag{2.134a}$$

$$y\to\infty: \quad |A_{\alpha j}|<\infty, \qquad (j=1,...,9). \tag{2.134b}$$

The first term in (2.132) represents summation over the modes of the continuous spectrum (such as entropy, vorticity, and acoustic modes), and the second term represents input of the discrete modes. Eigenfunctions of the discrete modes decay outside the boundary layer, whereas eigenfunctions of the continuous spectra have asymptotic behavior $\sim exp(\pm iky)$ at $y \to \infty$, where k is a real parameter ($k > 0$). This parameter also serves as a coordinate along the branches of the continuous spectra in (2.132).

Vectors $\mathbf{A}_\alpha$ together with the solution of the adjoint problem, $\mathbf{B}_\alpha$,

$$\frac{d}{dy}\left(\mathbf{L}_0^T \frac{d\mathbf{B}_\alpha}{dy}\right) - \mathbf{L}_1^T \frac{d\mathbf{B}_\alpha}{dy} = \mathbf{H}_1^T \mathbf{B}_\alpha + i\alpha \mathbf{H}_2^T \mathbf{B}_\alpha, \tag{2.135}$$

$$y = 0: \quad B_{\alpha 2} = B_{\alpha 4} = B_{\alpha 6} = 0, \tag{2.136a}$$

$$y \to \infty: \quad |B_{\alpha j}| < \infty, \qquad (j = 1, ..., 9), \tag{2.136b}$$

represent the biorthogonal eigenfunction system $\{\mathbf{A}_\alpha, \mathbf{B}_\alpha\}$. There is the following orthogonality relation

$$\langle \mathbf{H}_2 \mathbf{A}_\alpha, \mathbf{B}_{\alpha'} \rangle \equiv \sum_{j=1}^{9} \int_0^\infty (\mathbf{H}_2 \mathbf{A}_\alpha)_j \, B_{\alpha' j} dy = Q \Delta_{\alpha,\alpha'}, \tag{2.137}$$

where $\Delta_{\alpha,\alpha'}$ is the Kronecker delta if α or α' belongs to the discrete spectrum, and $\Delta_{\alpha,\alpha'} = \delta(\alpha - \alpha')$ is the delta function if both α and α' belong to the continuous spectrum. The coefficient Q in the right-hand side of (2.137) depends on the normalization of $\mathbf{A}_\alpha(y)$ and $\mathbf{B}_\alpha(y)$. Evaluation of the coefficient in the case of the discrete spectrum is straightforward. In the case of the continuous spectrum, the coefficient can be found with the help of the fundamental solutions outside the boundary layer [Tum03, Tum06c].

The orthogonality relation (2.137) provides a tool to find coefficients C_j and C_m in the formal solution (2.131). With the help of the orthogonality relation (2.137), one can find the initial amplitude of a mode entering in the formal solution $\mathbf{A}(x, y)$:

$$C = \frac{\langle \mathbf{H}_2 \mathbf{A}(x, y), \mathbf{B}_\alpha(y) \rangle}{Q} e^{-i\alpha x}. \tag{2.138}$$

If we consider a dot product of $\mathbf{B}_\alpha$ and (2.127), and integrate with respect to y over the interval $[0, \infty)$, we arrive at the following identity (we take into account explicit forms of matrices $\mathbf{L}_0$ and $\mathbf{L}_1$):

$$\begin{aligned} &\left[L_0^{43} A_{v3} \frac{dB_{\alpha 4}}{dy} - A_{v3} B_{\alpha 3}\right]_{y=0} + \left\langle \mathbf{A}_v, \frac{d}{dy}\left(\mathbf{L}_0^T \frac{d\mathbf{B}_\alpha}{dy}\right)\right\rangle \\ &- \left\langle \mathbf{A}_v, \mathbf{L}_1^T \frac{d\mathbf{B}_\alpha}{dy}\right\rangle = \langle \mathbf{A}_v, \mathbf{H}_1^T \mathbf{B}_\alpha \rangle + i\alpha_v \langle \mathbf{A}_v, \mathbf{H}_2^T \mathbf{B}_\alpha \rangle, \end{aligned} \tag{2.139}$$

where L_0^{43} stands for the element of matrix $\mathbf{L}_0$ having indices $(4, 3)$. Taking into account the adjoint equation (2.135), one can substitute the formal solution (2.131) in (2.138) and find

with the help of (2.139) the following result:

$$C = \frac{1}{2\pi}\frac{1}{Q}\int_{-\infty}^{+\infty} e^{i(\alpha_v-\alpha)x}\varphi(\alpha_v)\frac{\left[L_0^{43}\frac{dB_{\alpha 4}}{dy} - B_{\alpha 3}\right]_{y=0}}{i(\alpha_v-\alpha)}d\alpha_v. \tag{2.140}$$

By closing the path of the integral in the upper half plane, we find the theoretical coefficient as the residue value at the pole $\alpha_v = \alpha$:

$$C = \frac{\varphi(\alpha)}{Q(\alpha)}\left[L_0^{43}\frac{dB_{\alpha 4}}{dy} - B_{\alpha 3}\right]_{y=0}. \tag{2.141}$$

On the other hand, we have results of the direct numerical simulation (DNS) in the form of the vector-function $\mathbf{A}_{DNS}$ at $x = x_{DNS}$. One can find from (2.138) the initial amplitude, C_{DNS}, of the mode as follows:

$$C_{DNS} = \frac{\langle \mathbf{H_2 A}_{DNS}(x_{DNS}, y), \mathbf{B}_\alpha\rangle}{Q(\alpha)} e^{-i\alpha x_{DNS}}. \tag{2.142}$$

According to the definition of coefficients in (2.132), C in (2.141) and C_{DNS} in (2.142) are the complex amplitudes at $x = 0$. In order to interpret the complex weight C in (2.141) as initial amplitude and phase of the normal mode generated by the slot, the origin, $x = 0$, is chosen at the slot center. Therefore, x_{DNS} in (2.142) means the distance $x_{data} - x_c$, where x_{data} and x_c are given in table 2.5 for each case. Because the distance x_{DNS} in all considered examples is less than $11\delta_{99}$, the nonparallel effects in the growing/decaying of the perturbations on the interval x_{DNS} are ignored. If one is interested in the local amplitude of a mode at $x = x_{DNS}$, the origin of the coordinate should be at this point. In other words, $x_{DNS} = 0$ in (2.142).

Finally, one can compare the filtered-out coefficient C_{DNS} in (2.142) with the predicted C in (2.141).

Results

Discrete modes

One can find the details of the numerical method used for computation of the eigenvalues and eigenfunctions of the direct and adjoint problems elsewhere [Tum06c]. In all cases, eigenvalues and eigenfunctions of the discrete and continuous spectra are computed using the velocity, temperature, and viscosity profiles obtained from the direct numerical simulation at $x = x_{data}$.

Figure 2.77 shows the discrete and continuous spectra at frequency $f = 134.28$ kHz. One can see in figure 2.77 slow (S) and fast (F) discrete modes, and branches of the continuous spectra. There are two horizontal branches representing the slow and fast acoustic modes. Their branching points correspond to phase velocities $c = 1 \mp 1/M$, where M is the local Mach

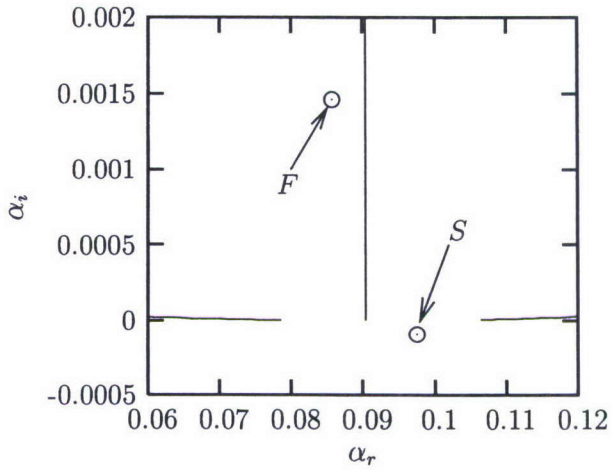

Figure 2.77: Continuous and discrete spectra at 134.28 kHz for case 1.

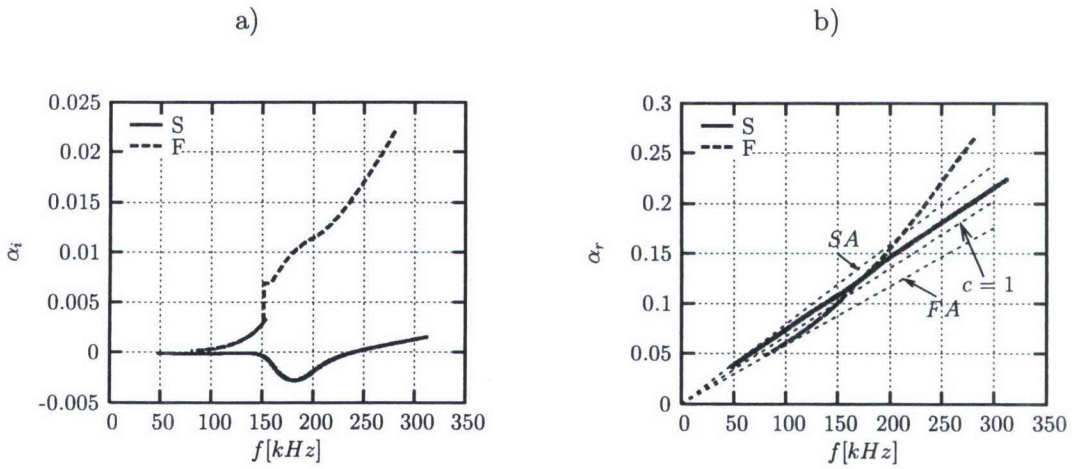

Figure 2.78: Imaginary (a) and real (b) parts of the wave number, case 1.

number at the edge of the boundary layer. At this scale, the vertical branch is comprised of two indistinguishable branches of entropy and vorticity modes [Tum06c].

Figure 2.78 shows the imaginary and real parts of the wave number α for the discrete modes as functions of frequency, ω. Lines SA and FA in figure 2.78*b* represent the branching points ($k = 0$) of the slow and fast acoustic modes, respectively. One discrete mode (mode F) is synchronized with the fast acoustic mode at low frequencies, whereas the other discrete mode (mode S) is synchronized with the slow acoustic mode.

At $f \approx 150$ kHz, mode F is synchronized with the vorticity and entropy modes ($c = 1$). This synchronization is accompanied by a discontinuity in α_i. The phenomenon may be illustrated as a sequence of figures 2.77 at different frequencies. When frequency increases, the vertical branch in figure 2.77 is moving from left to right with speed $d\alpha_r/d\omega = 1$, whereas the eigenvalue corresponding to the fast discrete mode moves from left to right with $d\alpha_r/d\omega > 1$. At some frequency, the discrete mode coalesces with the branch of the continuous spectrum. As was discussed in [FT03], the discrete mode coalesces with the continuous spectrum from one side of the branch cut and reappears on the other side at another point. Mathematically, the eigenvalue associated with mode F approaches one side of the branch cut on the complex α plane. As the pole on the plane coalesces with the branch cut, it moves to the upper Riemann sheet while, simultaneously, the pole that was on the lower Riemann sheet moves into the complex α plane at another point. Actually, one should interpret these poles as two different modes. Historically, they are discussed as one mode having the discontinuity.

At higher frequency, $f \approx 170$ kHz, there is a synchronism between mode F and mode S. However, there is no coalescence of the eigenvalues. A model of two-mode synchronism considered by Fedorov and Khokhlov [FK91, FK01] explained the branching of the modes at the point of synchronism. At this point, one of the modes becomes unstable, whereas the other one moves toward positive α_i. Although in this example the modes have the same phase velocity $c = \omega/\alpha_r$ at $f \approx 170$ kHz, the minimum of $|\alpha_F - \alpha_S|$ exists in the vicinity of $f \approx 150$ kHz, and, actually, this is the point where we observe the modes' branching.

Both the slow and fast discrete modes could be involved in the laminar-turbulent transition scenario. For example, the decaying mode could be generated by the entropy or vorticity modes of the continuous spectra. At the point of synchronism between the fast and slow modes, the decaying mode can give rise to the unstable mode (switching of the modes), which may lead to the transition. The scenario suggested by Fedorov and Khokhlov [FK01] means that both the stable and unstable modes are of interest for understanding transition mechanisms. Later on, switching of the modes was observed in direct numerical simulations of perturbations in high-speed boundary layers [MZ03b]. These features of the fast and slow discrete modes explain why we need accurate simulations of the decaying mode as well.

Figure 2.79 shows a comparison of the theoretical receptivity coefficient with the amplitude filtered out from the computational results in accordance with (2.142). Results in figure 2.79 and what follows for the discrete modes correspond to normalization of the eigenfunctions when the maximum of the mass flux perturbation in the boundary layer is equal to one. Figures 2.80 through 2.85 demonstrate comparisons of theoretical and numerical results

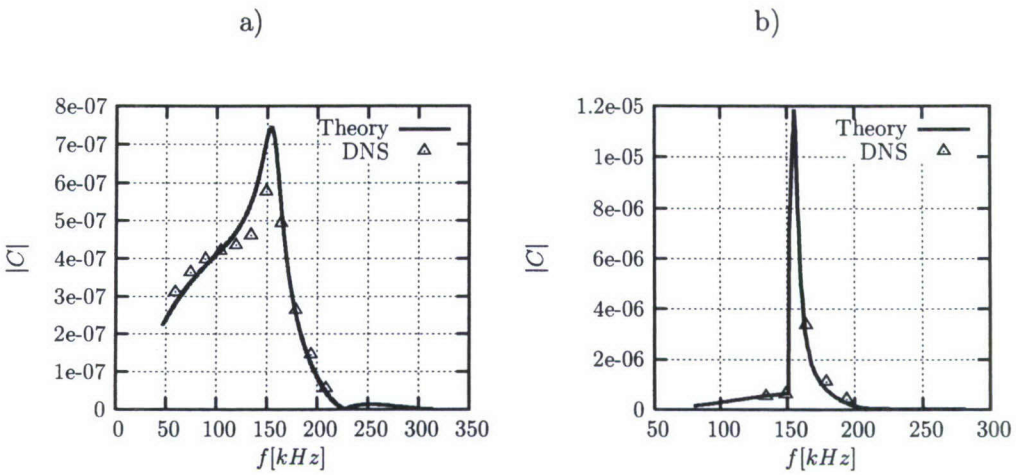

Figure 2.79: Comparison of the theoretical prediction for the receptivity coefficient in case 1 with data filtered out from the computational results: a) mode S and b) mode F.

for cases 2 through 7, respectively.

One can see from the figures that there is a good agreement between amplitudes calculated with the help of the receptivity model of the theoretical part of this section and those obtained from the numerical results as a projection onto the normal modes.

One can also notice that the shape of the function $|C(f)|$ for mode S in case 3 (figure 2.81a) is qualitatively different from the other cases, and agreement between the theoretical prediction and the numerical results is not as good. Case 3 corresponds to the closest location of the slot to the wedge's tip. The slot has a width of about 1.2 cm, whereas the distance from the tip is about 5 cm, and one should expect nonparallel flow effects, which were neglected in the present model. The nonparallel flow effects may be incorporated into the receptivity problem solution with the help of the multiple scales method along the lines of the distributed receptivity model proposed by Choudhari [Cho94a]. Another approach to receptivity problems with nonparallel flow effects was suggested by Bertolotti [Ber00]. Because the main objective of the present work was decomposition of the DNS results, we do not pursue the nonparallel flow effects in the theoretical solution of the receptivity problem.

The most significant discrepancy between the theory and the computational results is observed for mode F in case 6 at $f = 104.44$ kHz (figure 2.84b). This example corresponds to the eigenvalue $\alpha = 0.1047 + i6.894 \times 10^{-3}$ located very close to the branch cut representing the vorticity/entropy modes having $\alpha_r \approx 0.1036$. In order to illustrate the qualitative difference between the mode eigenfunctions when a mode is approaching the branch cut, we show in figure 2.86 streamwise velocity perturbations of the neighboring discrete modes at 89.52 kHz and 119.36 kHz (phase velocities, c, of the modes in figures 2.86a and 2.86b are equal to 1.059 and 0.926, respectively). The streamwise velocity of mode F at $f = 104.44$ kHz is shown in

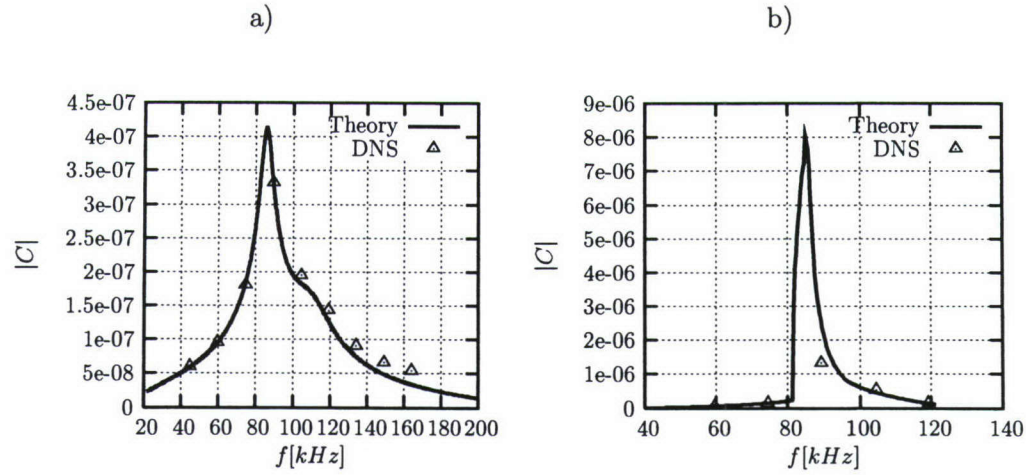

Figure 2.80: Comparison of the theoretical prediction for the receptivity coefficient in case 2 with data filtered out from the computational results: a) mode S and b) mode F.

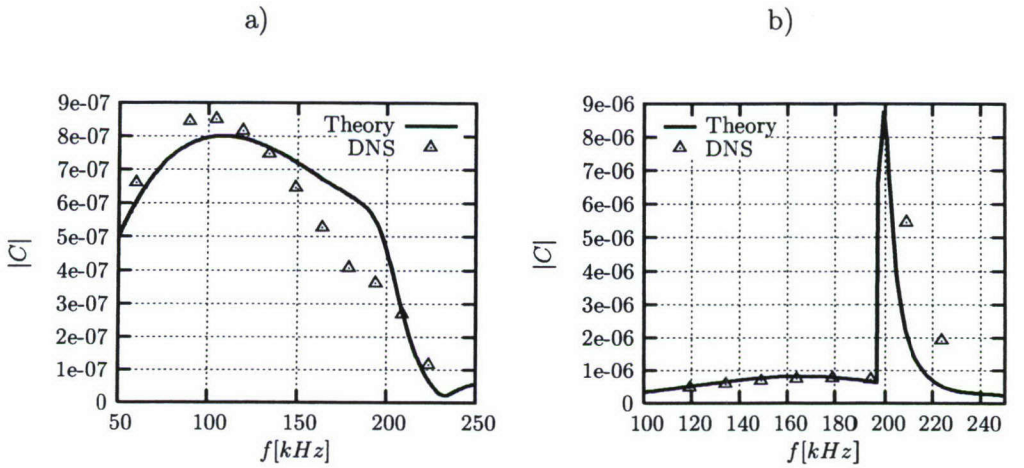

Figure 2.81: Comparison of the theoretical prediction for the receptivity coefficient in case 3 with data filtered out from the computational results: a) mode S and b) mode F.

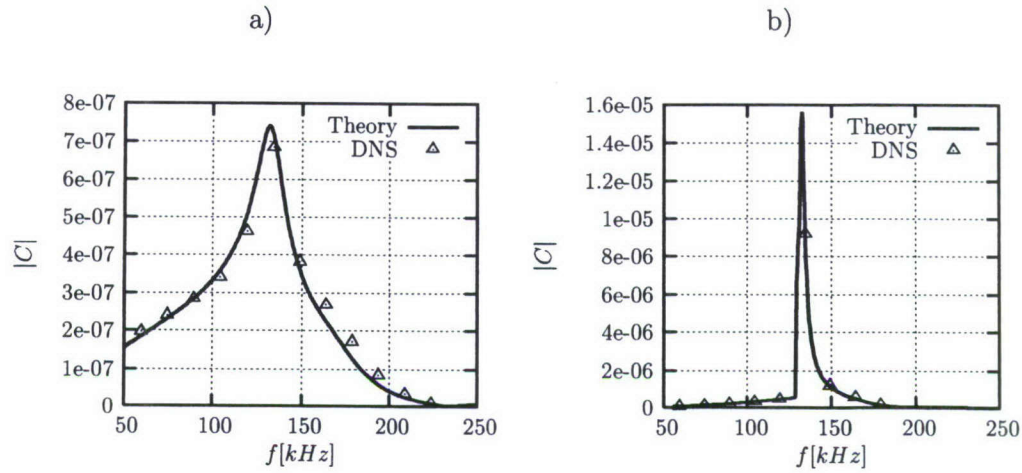

Figure 2.82: Comparison of the theoretical prediction for the receptivity coefficient in case 4 with data filtered out from the computational results: a) mode S and b) mode F.

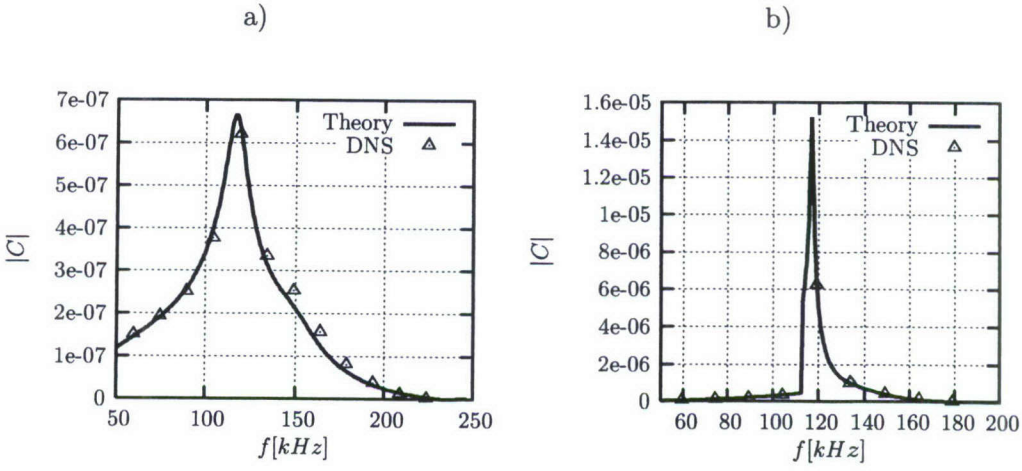

Figure 2.83: Comparison of the theoretical prediction for the receptivity coefficient in case 5 with data filtered out from the computational results: a) mode S and b) mode F.

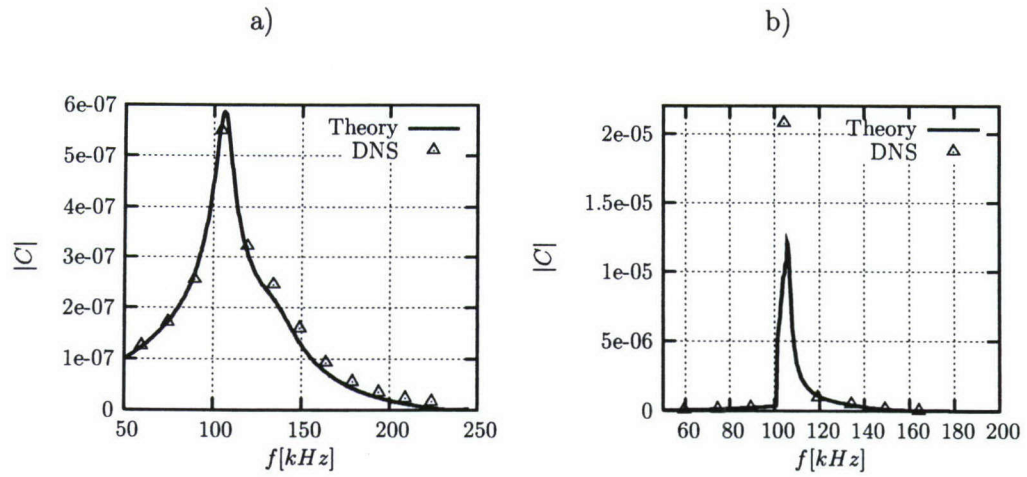

Figure 2.84: Comparison of the theoretical prediction for the receptivity coefficient in case 6 with data filtered out from the computational results: a) mode S and b) mode F.

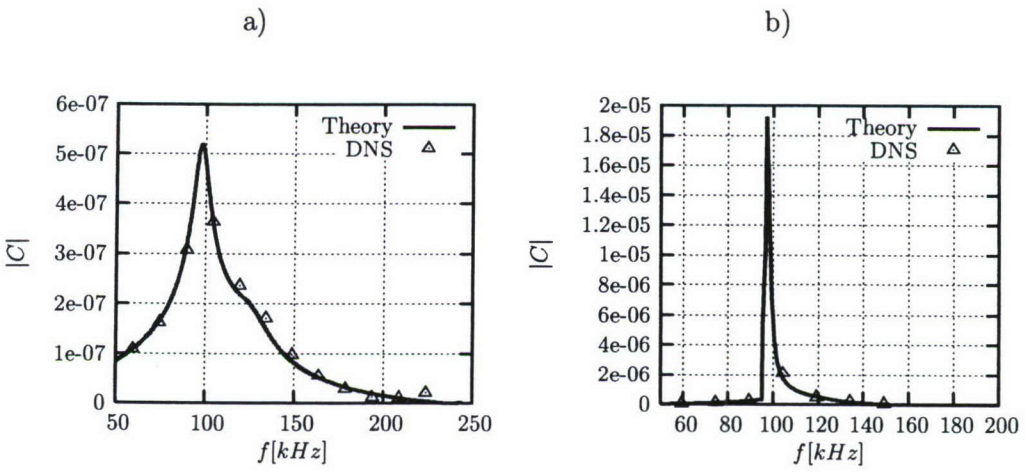

Figure 2.85: Comparison of the theoretical prediction for the receptivity coefficient in case 7 with data filtered out from the computational results: a) mode S and b) mode F.

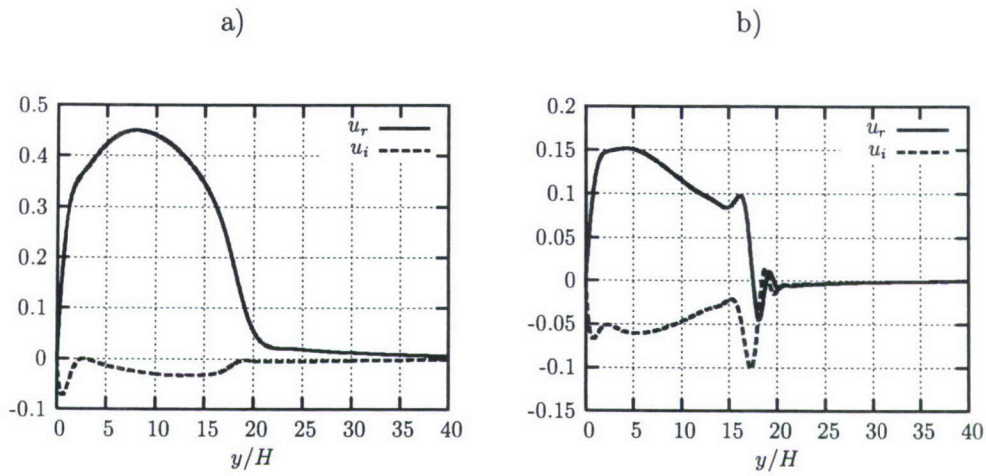

Figure 2.86: Streamwise velocity perturbation in discrete mode F: a) 89.52 kHz ($c = 1.059$) and b) 119.36 kHz ($c = 0.926$).

figure 2.87 ($c = 0.99$). One can see that although the amplitude of the mode decays outside the boundary layer, as it has to for a discrete mode, there are oscillations in the amplitude distribution in y typical for modes of continuous spectra. The closer the location of the eigenvalue is to the branch cut, the more similarity with the continuous spectra should be observed.

Fedorov and Khokhlov [FK02] considered the receptivity problem when a synchronism between two discrete modes is possible. They showed that in this case $Q = \langle \mathbf{H}_2 \mathbf{A}_\alpha, \mathbf{B}_\alpha \rangle \to 0$, and the analysis has to include both modes simultaneously, together with the nonparallel flow effects. In our example, we have a synchronism between a discrete mode and the continuous spectrum. Figure 2.88 shows the magnitude $|Q|$ for modes F and S as functions of frequency. One can see that in the case of mode F, Q is very close to zero at $f = 104.44$ kHz. This means that the theoretical model based on the parallel flow approximation is not adequate, and the extension of the model [FK02] to the case of a continuous spectrum is required.

Acoustic modes

The biorthogonal eigenfunction expansion also provides a tool for analysis of the input from continuous spectra in the computational results. Examples of boundary layers at $M = 2$ and 4.5 considered by Balakumar and Malik [BM92] and Tumin [Tum06b] (see Sections 2.3.2 and 2.4.1) indicate that input from entropy and vorticity modes due to blowing-suction through the wall is small in comparison to the acoustic modes. Therefore, we are considering the fast and slow acoustic modes only (the horizontal branches in figure 2.77).

In the case of two-dimensional perturbations, eigenfunctions corresponding to the acoustic modes are comprised of four fundamental solutions [TF83b, GT04]. Two of them decay exponentially outside the boundary layer, whereas the other two fundamental solutions be-

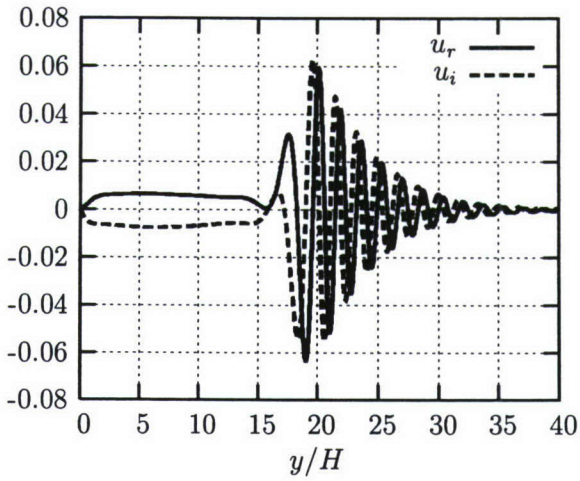

Figure 2.87: Streamwise velocity perturbation in discrete mode F at $f = 104.44$ kHz ($c = 0.99$).

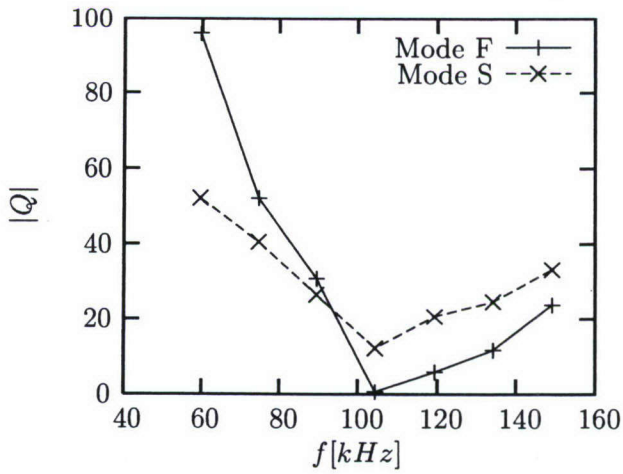

Figure 2.88: Magnitude of the denominator in (2.142),case 6.

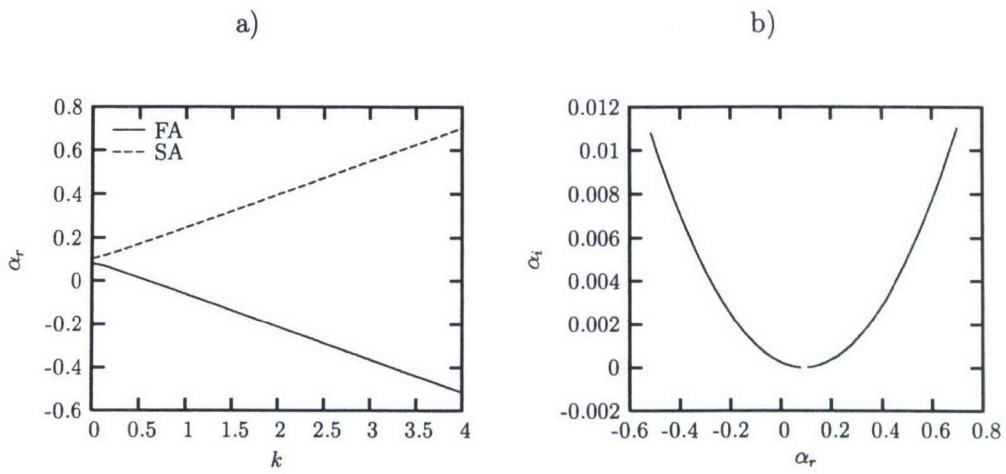

Figure 2.89: Streamwise wave numbers of the fast (FA) and slow (SA) acoustic modes, case 1 (134.28 kHz).

have as $\exp(\pm iky)$ at $y \to \infty$. One can interpret these fundamental solutions at $k \neq 0$ as incident and reflected acoustic waves.

In the inviscid limit, the wavenumbers of the fast and slow acoustic waves (α_{FA} and α_{SA}, respectively), can be found analytically as follows:

$$\alpha_{FA} = \frac{\omega M^2}{M^2-1} - \frac{\sqrt{k^2 + \frac{\omega^2 M^2}{M^2-1}}}{\sqrt{M^2-1}}, \tag{2.143a}$$

$$\alpha_{SA} = \frac{\omega M^2}{M^2-1} + \frac{\sqrt{k^2 + \frac{\omega^2 M^2}{M^2-1}}}{\sqrt{M^2-1}}, \tag{2.143b}$$

At the finite Reynolds number, the wave numbers α_{FA} and α_{SA} are found numerically from the characteristic equation for fundamental solutions outside the boundary layer at prescribed parameter k [GT04, Tum06c]. Figure 2.89*a* shows dimensionless real parts of α_{FA} and α_{SA} as functions of the parameter k in case 1 corresponding to the frequency 134.28 kHz. Branches of the acoustic spectrum in the complex plane α are presented in figure 2.89*b*.

Projection of the computational data onto the eigenfunction system allows evaluation of the amplitudes of the modes and, therefore, revealation of the underlying physics. Figure 2.90 shows the computational (input) data for the streamwise velocity perturbation corresponding to the frequency 134.28 kHz in case 1 at $x = x_{data}$, the reconstructed input of two discrete modes (S and F), and the acoustic modes ('A' stands for sum of the slow and fast acoustic modes). In this example, amplitudes of the modes are determined from the computational results with the help of the orthogonality relation (2.137). Integrals corresponding to the continuous spectra in (2.132) are evaluated numerically with respect to k from 0 to 4 with

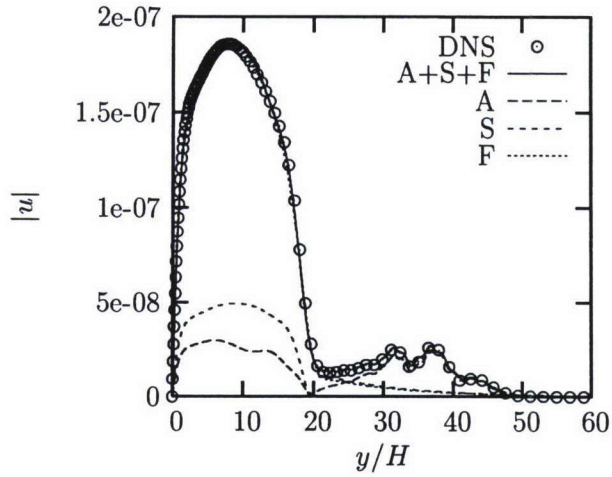

Figure 2.90: Input DNS data at $x = x_{data}$ and results of the projection onto modes of discrete spectrum (S and F), and the acoustic modes, case 1 (134.28 kHz).

the help of the trapezoidal formula resulting from 100 steps on the interval. Computations with larger number of steps and longer interval of the integration have not revealed a visible difference on the scale used in figure 2.90.

One can see that the acoustics provides the main input outside the boundary layer. The wiggles in the computational data (at $y/H \approx 35 - 45$) are associated with the acoustic perturbations emanating from the slot and propagating along the Mach lines outside the boundary layer. In this case, $M \approx 6.62$ and the Mach angle $\mu \approx 8.69°$. One can find width, Δy, of the perturbation strip propagating along the Mach lines as $\Delta y = w \tan \mu \approx 14.7H$, which is in agreement with the results in figure 2.90.

In the inviscid flow, the distance between the wall and the strip is $(x_{data} - x_c - 0.5w) \times \tan \mu \approx 17.25H$. As follows from figure 2.90, there is the boundary boundary layer flow effect, and the strip is displaced from the wall a distance of about δ_{99}.

At the parameters corresponding to the results in figure 2.90, the main input into the perturbation profile inside the boundary layer is associated with the fast (F) discrete mode. It is also found that the slow acoustic modes have small amplitudes in comparison with the fast modes, similar to the previous studies [BM92, Tum06b].

It is interesting to compare the amplitudes of the acoustic modes obtained with the help of the receptivity problem solution and their amplitudes obtained as a projection of the computational results. Figure 2.91*a* shows the theoretical amplitudes of the fast acoustic modes and the values filtered-out from the computational results. One can see that there is a discrepancy between them at $k \approx 1 - 1.5$. The discrepancy might be attributed to the grid in the DNS not being fine enough in the vicinity of the wiggles at $y/H \approx 35 - 45$ having the

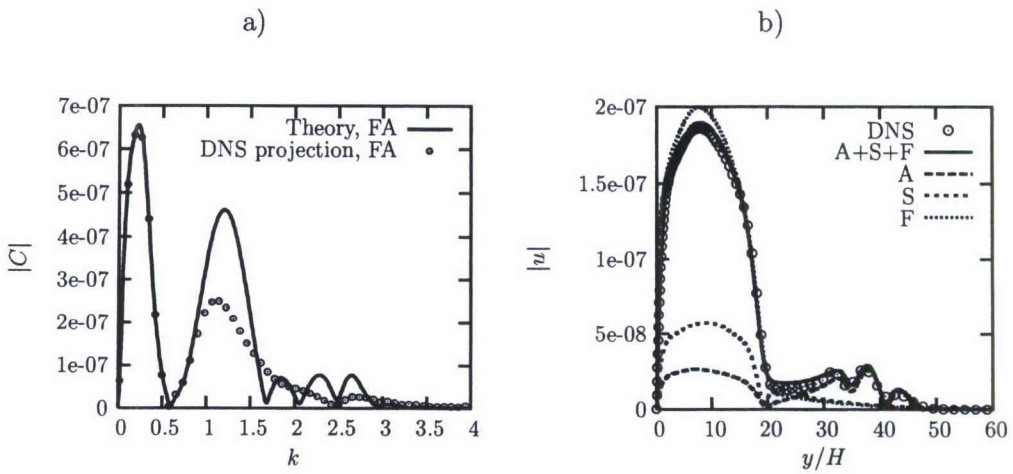

Figure 2.91: Amplitudes of the fast acoustic modes (a) and predicted velocity perturbation profiles (b), case 1 (134.28 kHz).

length scale $\leq 2\pi$.

Figures 2.92 through 2.95 show comparisons of the theoretical prediction for amplitudes of the fast acoustic modes and their amplitudes found as a projection of the computational results, together with the reconstructed profiles of the velocity perturbations in case 1 at frequencies 149.2 kHz, 164.12 kHz, 179.04 kHz, and 193.96 kHz, respectively.

Discussion of the results

The results of the present work serve as an illustration of how the biorthogonal eigenfunction system can provide an insight into computations. In order to be able to distinguish the modes, one needs amplitude and phase distributions for pressure, temperature, and velocity components, together with some of their derivatives, given at only one station x. The necessary information is always available in computational studies, and the described method allows finding the amplitudes of the modes from the discrete and continuous spectra. For example, the results illustrate how one can find amplitudes of the decaying modes in numerical simulations that could not be addressed at all in the past (only unstable modes dominating the perturbation field in a numerical simulation could be compared with predictions of the linear stability theory).

The solution in the present work is based on the parallel flow approximation. This approximation is valid when the characteristic scale of the perturbation (wave length) is much smaller than the characteristic scale of the unperturbed flow in the downstream direction. This condition is violated when the actuator is located close to the leading edge (see case 3 in the results' part). Results of the present work are also based on the assumption that the denominator in (2.142) is not equal to zero. Fedorov and Khokhlov [FK02] showed that the denominator is equal to zero at the branching point of two discrete modes. In this case,

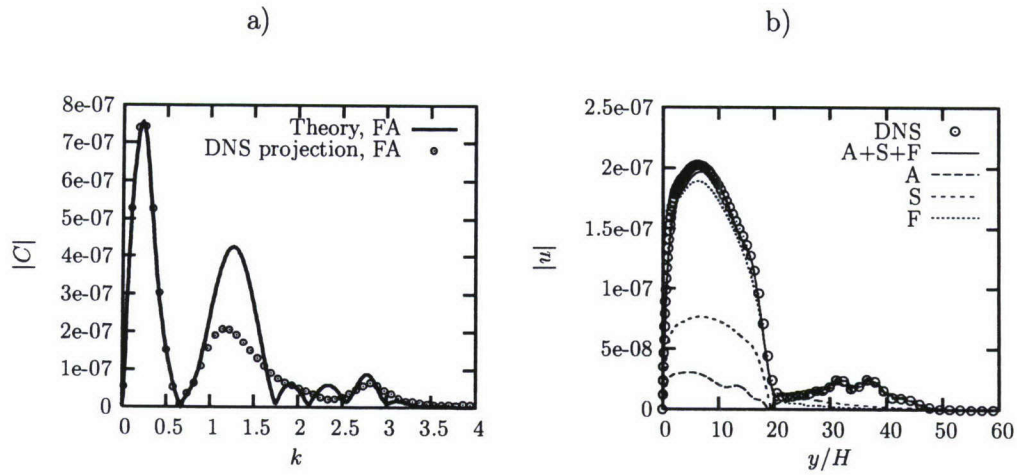

Figure 2.92: Amplitudes of the fast acoustic modes (a) and reconstructed velocity perturbation profiles (b), case 1 (149.2 kHz).

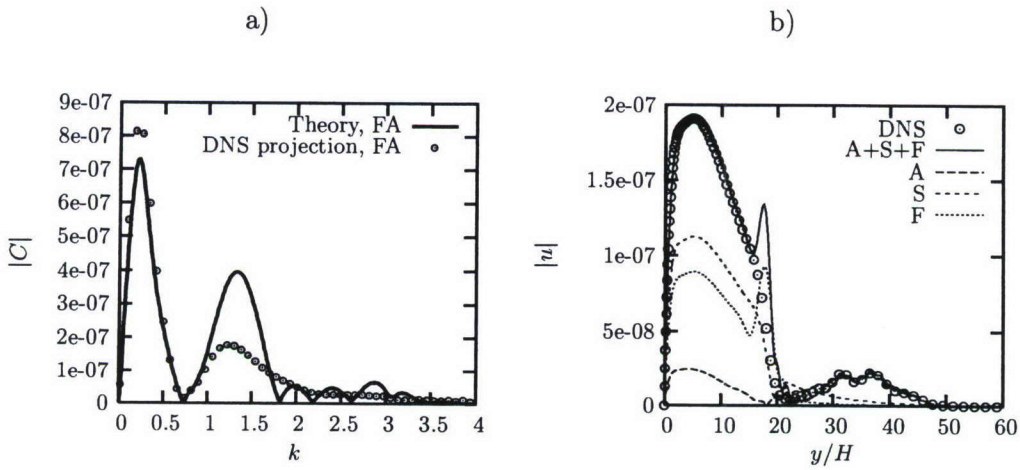

Figure 2.93: Amplitudes of the fast acoustic modes (a) and reconstructed velocity perturbation profiles (b), case 1 (164.12 kHz).

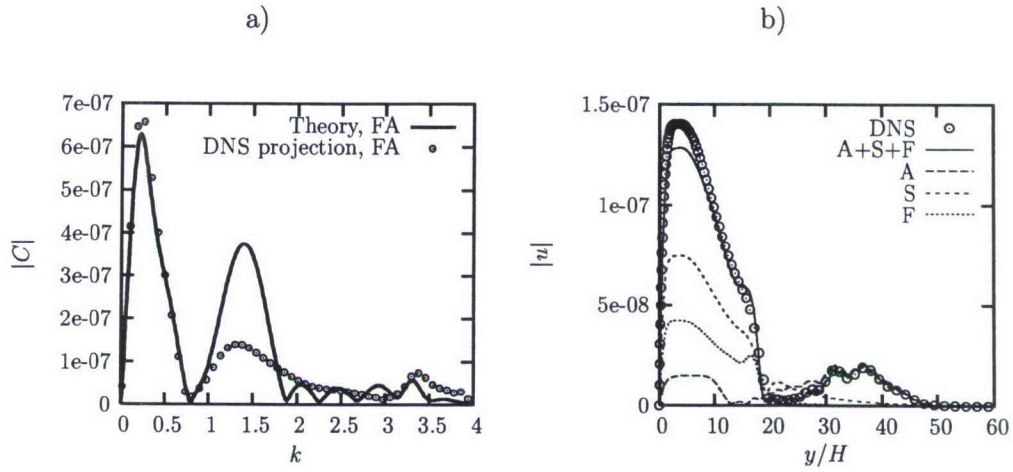

Figure 2.94: Amplitudes of the fast acoustic modes (a) and reconstructed velocity perturbation profiles (b), case 1 (179.04 kHz).

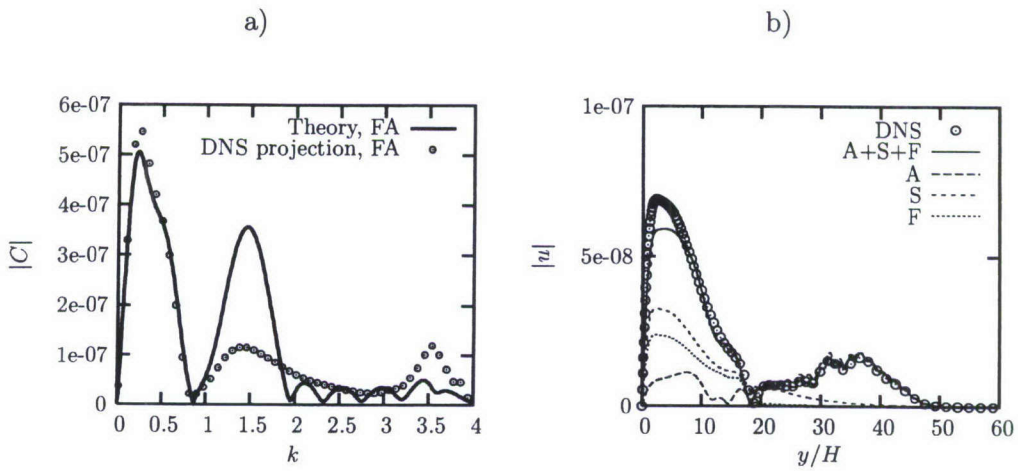

Figure 2.95: Amplitudes of the fast acoustic modes (a) and reconstructed velocity perturbation profiles (b), case 1 (193.96 kHz).

the nonparallel flow effects are to be taken into account in order to resolve the singularity. Analysis of case 6 ($f \approx 104$ kHz) showed that the denominator tends to zero in the case of synchronism between the discrete mode and the continuous spectra. Therefore, an extension of the theoretical model of [FK02] to the case of continuous spectra is required.

Decomposition of perturbations when only partial information is available is an ill-posed problem. Nevertheless, it is still possible to analyze the flow field if some additional information about the data is available. Tumin *et al.* [TACZ96, Tum03, GT04, Tum06c] discussed examples where the perturbations could be decomposed into the normal modes when only partial information was available. Further development of this approach might be especially helpful in analysis of experimental data in high-speed boundary layers.

2.6 Biorthogonal eigenfunction system for supersonic inviscid flow past a flat plate

This section is based on the paper published in collaboration with C. Chiquete [sAT07].

The objective of the present section is to illustrate the main ideas of the multimode decomposition using a study case where all steps of the method are accompanied by analytical solutions. The problem of perturbations in inviscid uniform flow past a flat plate provides the opportunity to formulate the biorthogonal eigenfunction system in analytical form.

Spatial Cauchy problem

The first step in the method is to demonstrate that periodic-in-time solutions of linearized Euler's equations can be presented as an expansion into normal modes. This problem is analogous to analysis of perturbations in boundary layers in [Tum03, Tum06c], and [TF83b].

Consider two-dimensional perturbations in an inviscid uniform supersonic flow past a flat plate. Axis x is chosen in the flow direction; coordinate y stands for the distance from the plate. The governing equations for the perturbations are the linearized Euler equations, which can be written in dimensionless form as follows:

$$\begin{aligned}
&\frac{\partial \rho}{\partial t}+\frac{\partial \rho}{\partial x}+\frac{\partial u}{\partial x}+\frac{\partial v}{\partial y}=0\\
&\frac{\partial u}{\partial t}+\frac{\partial u}{\partial x}=-\frac{\partial \pi}{\partial x}\\
&\frac{\partial v}{\partial t}+\frac{\partial v}{\partial x}=-\frac{\partial \pi}{\partial y}\\
&\frac{\partial \theta}{\partial t}+\frac{\partial \theta}{\partial x}=(\gamma-1)M^2\left(\frac{\partial \pi}{\partial t}+\frac{\partial \pi}{\partial x}\right)
\end{aligned} \tag{2.144}$$

where u, v, π, ρ, and θ are perturbations of the x and y velocities, pressure, density and temperature, respectively. The free-stream velocity U_∞, density ρ_∞, and temperature T_∞ are chosen as the characteristic scales in (2.144). The pressure is scaled with the help of $\rho_\infty U_\infty^2$. The coordinates x and y are scaled with a length scale L, whereas the time scale is L/U_∞. M and γ in (2.144) are the free-stream Mach number and the specific heats ratio, respectively. In addition, one can find from the linearized equation of state that

$$\rho=\gamma M^2\pi-\theta \tag{2.145}$$

We consider periodic-in-time solutions of the governing equations in the complex form $q(x,y,t)=\hat{q}(x,y)\exp(-i\omega t)$. As a result, the equations (2.144) are recast with the help of

the equation of state (2.145) (we omit ' ^ '):

$$
\begin{aligned}
&-i\omega\left(\gamma M^2\pi-\theta\right)+\frac{\partial}{\partial x}\left(\gamma M^2\pi-\theta\right)+\frac{\partial u}{\partial x}+\frac{\partial v}{\partial y}=0\\
&-i\omega u+\frac{\partial u}{\partial x}=-\frac{\partial \pi}{\partial x}\\
&-i\omega v+\frac{\partial v}{\partial x}=-\frac{\partial \pi}{\partial y}\\
&-i\omega\theta+\frac{\partial \theta}{\partial x}=(\gamma-1)M^2\left(-i\omega\pi+\frac{\partial \pi}{\partial x}\right)
\end{aligned}
\tag{2.146}
$$

The system of four equations can be written in the matrix-vector form with the help of the vector function $\mathbf{A}(x,y)=(u,v,\theta,\pi)^T$, where T refers to the matrix transpose.

$$
\begin{aligned}
&\mathbf{E}\frac{\partial \mathbf{A}}{\partial y}=\mathbf{H}_1\mathbf{A}+\mathbf{H}_2\frac{\partial \mathbf{A}}{\partial x}\\
&\mathbf{E}=\begin{pmatrix}0&0&0&0\\0&1&0&0\\0&0&0&0\\0&0&0&1\end{pmatrix},\ \mathbf{H}_1=\begin{pmatrix}i\omega&0&0&0\\0&0&-i\omega&i\omega\gamma M^2\\0&0&i\omega&-i\omega(\gamma-1)M^2\\0&i\omega&0&0\end{pmatrix}\\
&\mathbf{H}_2=\begin{pmatrix}-1&0&0&-1\\-1&0&1&-\gamma M^2\\0&0&-1&(\gamma-1)M^2\\0&-1&0&0\end{pmatrix}
\end{aligned}
\tag{2.147}
$$

Solution of (2.147) is subject to the following boundary conditions on the wall ($y=0$) and at $y\to\infty$:

$$y=0:\quad A_2=0 \tag{2.148}$$

$$y\to\infty:\quad |A_j|\to 0,\ (j=1,...,4) \tag{2.149}$$

At $x=0$, the initial data for the amplitude functions are provided:

$$x=0:\quad \mathbf{A}=\mathbf{A}_0(y)=(u_0(y),v_0(y),\theta_0(y),\pi_0(y))^T \tag{2.150}$$

where the initial data vector $\mathbf{A}_0(y)$ is assumed to decay at $y\to\infty$. This defines the spatial Cauchy problem.

Solution of the problem, (2.147) - (2.150), can be found with the use of the Laplace transform with respect to x:

$$\mathbf{A}_s(y)=\int_0^\infty \mathbf{A}(x,y)e^{-sx}ds \tag{2.151}$$

The transformation leads to the following boundary-value problem for inhomogeneous ordinary differential equations:

$$\begin{aligned} &\mathbf{E}\frac{d\mathbf{A}_s}{dy} - \mathbf{H}_1\mathbf{A}_s - s\mathbf{H}_2\mathbf{A}_s = \mathbf{F} \\ &y = 0: \quad A_{s,2} = 0 \\ &y \to \infty: \quad |A_{s,j}| \to 0 \end{aligned} \tag{2.152}$$

where $\mathbf{F} = -\mathbf{H}_2\mathbf{A}_0$. A fundamental solution of the corresponding homogeneous system of (2.152) can be found as $\propto \exp(-\lambda y)$, where λ is a root of the characteristic polynomial

$$-(s - i\omega)^2(-\lambda^2 + M^2(s - i\omega)^2 - s^2) = 0 \tag{2.153}$$

There are two distinct roots

$$\begin{aligned} &\lambda_{1,2}(s) = \pm\mu(s) \\ &\mu(s) = \sqrt{M^2(s - i\omega)^2 - s^2} \end{aligned} \tag{2.154}$$

where the root branch is chosen to have $\mathcal{R}e(\mu) > 0$. This defines two fundamental solutions

$$\mathbf{z}_1 = \left(-\frac{s}{s - i\omega}, \frac{\mu}{s - i\omega}, M^2(\gamma - 1), 1\right)^T \tag{2.155}$$

and

$$\mathbf{z}_2 = \left(-\frac{s}{s - i\omega}, -\frac{\mu}{s - i\omega}, M^2(\gamma - 1), 1\right)^T \tag{2.156}$$

The non-homogeneous system given by (2.152) has a solution expressed in the form

$$\begin{aligned} &\mathbf{A}_s(y) = \mathbf{M}\mathbf{Q}(y) + \mathbf{G}(y) \\ &\mathbf{G} \equiv (F_1/(s - i\omega), 0, F_3/(s - i\omega), 0)^T \end{aligned} \tag{2.157}$$

where $\mathbf{M} = [[\mathbf{z}_1 \exp(-\mu y), \mathbf{z}_2 \exp(\mu y)]]$ is the matrix of fundamental solutions, and the vector of coefficients $\mathbf{Q}(y) = (Q_1(y), Q_2(y))^T$ has to be found. Applying (2.157) to (2.152), we arrive at the following reduced 2×2 system:

$$\begin{aligned} &\mathbf{m}\frac{d\mathbf{Q}}{dy} = \mathbf{f}(y), \\ &\mathbf{f} = \left(F_2 + F_3 - \frac{s}{s - i\omega}F_1, F_4\right)^T \end{aligned} \tag{2.158}$$

where $\mathbf{m}$ is a 2×2 matrix: One can solve the algebraic equations (2.158) and write down the solution of (2.152) as follows

$$\mathbf{A}_s(y) = \left(\int_0^y C_1(y'; s)dy' - c_1(s)\right)\mathbf{z}_1 e^{-\mu y} + \left(\int_\infty^y C_2(y'; s)dy'\right)\mathbf{z}_2 e^{\mu y} + \mathbf{G}(y) \tag{2.159}$$

where

$$
\begin{aligned}
c_1(s) &= \int_0^\infty C_2(y';s)dy' \\
C_1(y;s) &= \frac{e^{\mu y}}{2\mu}\left[\mu v_0 - i\omega u_0 + \left(\left[M^2(s-i\omega)-s\right)\pi_0\right]\right. \\
C_2(y;s) &= \frac{e^{-\mu y}}{2\mu}\left[\mu v_0 + i\omega u_0 - \left(\left[M^2(s-i\omega)-s\right)\pi_0\right]\right. \\
\mathbf{G}(y) &= \left(\frac{\pi_0+u_0}{s-i\omega}, 0, -\frac{M^2(\gamma-1)\pi_0-\theta_0}{s-i\omega}, 0\right)^T
\end{aligned}
\tag{2.160}
$$

Finally, the solution of the spatial Cauchy problem can be written as the inverse Laplace transform

$$
\mathbf{A}(x,y) = \frac{1}{2\pi i}\int_\Gamma \mathbf{A}_s(y)e^{sx}ds \tag{2.161}
$$

where Γ indicates a vertical path in the complex plane of s to the right of any singularities of the integrand. There is a pole located at $s = i\omega$ and two branch points, $s = i\omega M/(M \pm 1)$. In order to have solution (2.159) decaying at $y \to \infty$ everywhere in the complex plane s, we choose two vertical branch cuts (defined by the equation $\mathcal{R}e(\mu) = 0$) as shown in figure 2.96.

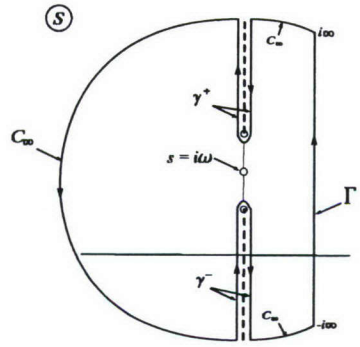

Figure 2.96: A sketch of the complex plane of s.

The path of integration, Γ, can also be closed, as in figure 2.96. By Cauchy's residue theorem, the contour integral over the closed path is equivalent to the residue of the integrand at $s = i\omega$, i.e.,

$$
\frac{1}{2\pi i}\left(\int_\Gamma \cdots + \int_{\gamma^-} \cdots + \int_{\gamma^+} \cdots + \int_{C_\infty} \ldots\right) = \mathrm{Res}(\mathbf{A}_s e^{sx})_{s=i\omega} \tag{2.162}
$$

Because the integral vanishes along the contour C_∞, we can represent the contour integral over Γ as a sum of residues derived from the poles of the integrand, and two contour integrals along the branch cuts γ^+ and γ^-.

One can find explicitly the residue of $\mathbf{A}_s(y)\exp(sx)$ at $s = i\omega$:

$$\mathrm{Res}(\mathbf{A}_s e^{sx})_{s=i\omega} = e^{i\omega x}\begin{pmatrix} -i\omega\left\{e^{-\omega y}[f_1(y)+f_2(0)]+e^{\omega y}f_2(y)\right\}+\pi_0+u_0 \\ \omega\left\{e^{-\omega y}[f_1(y)+f_2(0)]-e^{\omega y}f_2(y)\right\} \\ \theta_0 - M^2(\gamma-1)\pi_0 \\ 0 \end{pmatrix} \tag{2.163}$$

where

$$f_1(y) = \int_0^y \frac{e^{\omega y'}}{2}\left[v_0 - i(u_0+\pi_0)\right]dy' \tag{2.164a}$$

$$f_2(y) = \int_\infty^y \frac{e^{-\omega y'}}{2}\left[v_0 + i(u_0+\pi_0)\right]dy' \tag{2.164b}$$

Then solution of the spatial Cauchy problem is given by

$$\mathbf{A}(x,y) = \mathrm{Res}(\mathbf{A}_s e^{sx}) - \frac{1}{2\pi i}\left(\int_{\gamma^-}\mathbf{A}_s e^{sx}ds + \int_{\gamma^+}\mathbf{A}_s e^{sx}ds\right) \tag{2.165}$$

This defines the formal solution to the initial value problem. However, the branch cut integral can be simplified by parameterizing the complex variable s along the branch cut contours. This procedure will facilitate the proof of the equivalence of the formal solution and the expansion in the biorthogonal eigenfunction system.

In the following the integrals in (2.165) along either path (γ^+ or γ^-) are considered at once, and denoted as $\gamma^\pm$. Then writing the explicit path along the branch cuts gives

$$-\frac{1}{2\pi i}\int_{\gamma^\pm}\ldots ds = -\frac{1}{2\pi i}\left(\int_{s_\pm^*}^{\pm i\infty}\mathbf{A}_s(y)e^{sx}ds + \int_{\pm i\infty}^{s_\pm^*}\mathbf{A}_s(y)e^{sx}ds\right) \tag{2.166}$$

where $s_+^* = i\omega M/(M-1)$ is the upper branch point of the function $\mu(s)$ and $s_-^* = i\omega M/(M+1)$ is the lower branch point. The vector function $\mathbf{A}_s(y)$ is discontinuous across the branch cut, i.e., if we parameterize $\mu(s) = \pm ik$ for $k > 0$ on the right-hand side of the branch cut, then $\mu(s) = \mp ik$ on the left-hand side. On each branch cut, we have $s = s_m(k)$ $(m = 1, 2)$, where we solve

$$\mu(s) = \sqrt{M^2(s-i\omega)^2 - s^2} = \pm ik$$

for s. Two solutions for s can be found and are denoted $s_{1,2}(k)$,

$$\begin{aligned} s_1(k) &= i\left(\frac{M^2\omega + \sqrt{(M^2-1)k^2 + M^2\omega^2}}{M^2-1}\right), \\ s_2(k) &= i\left(\frac{M^2\omega - \sqrt{(M^2-1)k^2 + M^2\omega^2}}{M^2-1}\right) \end{aligned} \tag{2.167}$$

Figure 2.97 illustrates the path of integration and values of $\mu(k)$ on the sides of the branch cuts.

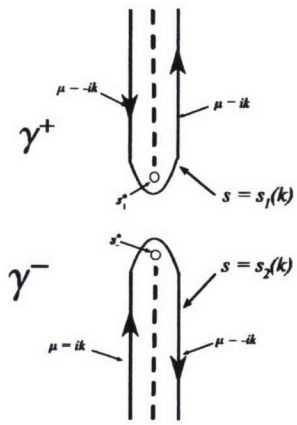

Figure 2.97: The change of variable scheme.

Integrals along the sides of the branch cuts in (2.166) are then recast as integrals with respect to the parameter k via the transformation $s = s_m(k)$ and so $ds = (ds_m/dk)dk$:

$$\begin{aligned}
-\frac{1}{2\pi i}\int_{\gamma^\pm} \ldots ds = -\frac{1}{2\pi i}\Bigg(&\int_0^\infty [\mathbf{A}_s(y)]^{\mu=-ik}_{s=s_m(k)}\, e^{s_m(k)x}\frac{ds_m}{dk}dk \ldots \\
&+ \int_\infty^0 [\mathbf{A}_s(y)]^{\mu=ik}_{s=s_m(k)}\, e^{s_m(k)x}\frac{ds_m}{dk}dk\Bigg) \\
&= \frac{1}{2\pi i}\int_0^\infty \left([\mathbf{A}_s(y)]^{\mu=ik}_{s=s_m(k)} - [\mathbf{A}_s(y)]^{\mu=-ik}_{s=s_m(k)}\right) e^{s_m(k)x}\frac{ds_m}{dk}dk
\end{aligned}$$

Writing the full solution,

$$\mathbf{A}(x,y) = \mathrm{Res}(\mathbf{A}_s e^{sx}) + \frac{1}{2\pi i}\sum_{m=1,2}\int_0^\infty \left([\mathbf{A}_s(y)]^{\mu=ik}_{s=s_m(k)} - [\mathbf{A}_s(y)]^{\mu=-ik}_{s=s_m(k)}\right) e^{s_m(k)x}\frac{ds_m}{dk}dk$$

Explicitly evaluating the vector valued factor in the integrand,

$$[\mathbf{A}_s(y)]^{\mu=ik}_{s=s_m(k)} - [\mathbf{A}_s(y)]^{\mu=-ik}_{s=s_m(k)} = D_m(k)\left[e^{iky}\mathbf{z}_1\left(^{\mu=ik}_{s=s_m(k)}\right) + e^{-iky}\mathbf{z}_2\left(^{\mu=ik}_{s=s_m(k)}\right)\right], \quad (2.168a)$$

$$D_m(k) = \int_0^\infty \left[iv_0 \sin ky' - \left(\frac{\omega u_0}{k} + i\frac{(M^2(s_m(k) - i\omega) - s_m(k))}{k}\pi_0\right)\cos ky'\right]dy' \quad (2.168b)$$

The final form of the formal solution is therefore as follows:

$$\begin{aligned}
&\mathbf{A}(x,y) = \mathrm{Res}(\mathbf{A}_s e^{sx}) + \\
&\quad \frac{1}{2\pi i}\sum_{m=1,2}\int_0^\infty D_m(k)\left(e^{iky}\mathbf{z}_1\left(^{\mu=ik}_{s=s_m(k)}\right) + e^{-iky}\mathbf{z}_2\left(^{\mu=ik}_{s=s_m(k)}\right)\right)e^{s_m(k)x}\frac{ds_m}{dk}dk
\end{aligned} \quad (2.169)$$

It will be shown that this formal solution can be recast as an eigenfunction expansion.

Biorthogonal eigenfunction system

The idea that any disturbance governed by the linearized Navier-Stokes equations can be considered as a superposition of vorticity, entropy, and acoustic modes was expressed a long time ago (see, for example, [Pie89], pp. 519 and 524). A proof for an ideal gas having Prandtl number 3/4 was given by Wu in [Wu05]. In the case of an inviscid gas without heat conduction, the acoustic modes have non-zero velocity, pressure, and temperature perturbations, whereas there are no vorticity and entropy perturbations. The entropy modes have non-zero entropy and temperature perturbations, whereas the velocity and pressure perturbations are absent. The vorticity modes have non-zero velocity and vorticity perturbations, and there are no pressure, entropy, and temperature perturbations.

In the present section, we introduce a biorthogonal eigenfunction system that can serve as a tool for projection of the perturbation field onto the normal modes, i.e., for decomposition into vorticity, entropy, and acoustic modes.

We define the following biorthogonal eigenfunction system $\{\mathbf{A}_\alpha, \mathbf{B}_\alpha\}$

$$\begin{aligned} &\mathbf{E}\frac{d\mathbf{A}_\alpha}{dy} - \mathbf{H}_1\mathbf{A}_\alpha - i\alpha\mathbf{H}_2\mathbf{A}_\alpha = 0 \\ &y = 0: \quad A_{\alpha,2} = 0 \\ &y \to \infty: \quad |A_{\alpha,j}| < \infty \end{aligned} \tag{2.170}$$

$$\begin{aligned} &-\mathbf{E}\frac{d\mathbf{B}_\alpha}{dy} - \mathbf{H}_1^H\mathbf{B}_\alpha + i\alpha\mathbf{H}_2^H\mathbf{B}_\alpha = 0 \\ &y = 0: \quad B_{\alpha,4} = 0 \\ &y \to \infty: \quad |B_{\alpha,j}| < \infty \end{aligned} \tag{2.171}$$

The superscript H in (2.171) stands for the Hermitian transpose.

Fundamental solutions of the equations (2.170) can be found in the form $\sim \exp(\lambda y)$, which yields the following characteristic equation for λ:

$$-(\alpha-\omega)^2(\lambda^2 + (M^2-1)\alpha^2 - 2M^2\omega\alpha + M^2\omega^2) = 0 \tag{2.172}$$

leads to four roots of α at a given λ. In order to ensure the boundary conditions at $y = 0$ and $y \to \infty$ are satisfied, we impose $\lambda = \pm ik$ (where k is a positive real number), and construct the eigenfunction as a sum of two fundamental solutions $\propto \exp(\pm iky)$. Therefore, one can find from (2.172)

$$\alpha_{1,2} = \frac{M^2\omega \pm \sqrt{(M^2-1)k^2 + M^2\omega^2}}{M^2-1} \tag{2.173a}$$

$$\alpha_{3,4} = \omega \tag{2.173b}$$

Each root $\alpha(k)$ corresponds to the following four distinct eigenfunctions representing the normal modes. The first of these modes we define as the slow acoustic mode, i.e.,

$$\mathbf{A}_{ac1}(y;k) = \begin{pmatrix} \frac{\alpha_1}{k} \\ 1 \\ \frac{M^2(\gamma-1)(\omega-\alpha_1)}{k} \\ \frac{\omega-\alpha_1}{k} \end{pmatrix} e^{iky} - \begin{pmatrix} -\frac{\alpha_1}{k} \\ 1 \\ -\frac{M^2(\gamma-1)(\omega-\alpha_1)}{k} \\ -\frac{\omega-\alpha_1}{k} \end{pmatrix} e^{-iky} \tag{2.174}$$

The phase speed of the slow acoustic mode at $k = 0$ is equal to $c = 1 - 1/M$.

The fast acoustic mode is found similarly,

$$\mathbf{A}_{ac2}(y;k) = \begin{pmatrix} \frac{\alpha_2}{k} \\ 1 \\ \frac{M^2(\gamma-1)(\omega-\alpha_2)}{k} \\ \frac{\omega-\alpha_2}{k} \end{pmatrix} e^{iky} - \begin{pmatrix} -\frac{\alpha_2}{k} \\ 1 \\ -\frac{M^2(\gamma-1)(\omega-\alpha_2)}{k} \\ -\frac{\omega-\alpha_2}{k} \end{pmatrix} e^{-iky} \tag{2.175}$$

The phase speed of the fast acoustic mode at $k = 0$ is equal to $c = 1 + 1/M$.

We define the following as the vorticity mode,

$$\mathbf{A}_v(y;k) = \begin{pmatrix} 1 \\ -\frac{\omega}{k} \\ 0 \\ 0 \end{pmatrix} e^{iky} + \begin{pmatrix} 1 \\ \frac{\omega}{k} \\ 0 \\ 0 \end{pmatrix} e^{-iky} \tag{2.176}$$

where $\alpha_v = \omega$. This mode is denoted as the vorticity mode since it produces a non-zero vorticity.

Finally, the entropy mode is given by

$$\mathbf{A}_e(y;k) = \begin{pmatrix} 0 \\ 0 \\ 1 \\ 0 \end{pmatrix} e^{iky} \pm \begin{pmatrix} 0 \\ 0 \\ 1 \\ 0 \end{pmatrix} e^{-iky} \tag{2.177}$$

where $\alpha_e = \omega$. Because the boundary condition on the wall is satisfied for each fundamental solution corresponding to the entropy mode, both of them can be considered as independent entropy modes. Instead of dealing with the fundamental solutions as modes, we construct symmetric and antisymmetric eigenfunctions by choosing $+$ or $-$ in (2.177).

The adjoint solution corresponding to the slow acoustic mode is given by

$$\mathbf{B}_{ac1}(y;k) = \begin{pmatrix} -\frac{\alpha_1}{k} \\ -\frac{\omega-\alpha_1}{k} \\ -\frac{\omega-\alpha_1}{k} \\ 1 \end{pmatrix} e^{-iky} - \begin{pmatrix} \frac{\alpha_1}{k} \\ \frac{\omega-\alpha_1}{k} \\ \frac{\omega-\alpha_1}{k} \\ 1 \end{pmatrix} e^{iky} \tag{2.178}$$

Similarly, the adjoint solution corresponding to the fast acoustic mode is

$$\mathbf{B}_{ac2}(y;k) = \begin{pmatrix} -\frac{\alpha_2}{k} \\ -\frac{\omega-\alpha_2}{k} \\ -\frac{\omega-\alpha_2}{k} \\ 1 \end{pmatrix} e^{-iky} - \begin{pmatrix} \frac{\alpha_2}{k} \\ \frac{\omega-\alpha_2}{k} \\ \frac{\omega-\alpha_2}{k} \\ 1 \end{pmatrix} e^{iky} \tag{2.179}$$

There is an associated adjoint vorticity mode,

$$\mathbf{B}_v(y;k) = \begin{pmatrix} \frac{k}{\omega} \\ 0 \\ 0 \\ 1 \end{pmatrix} e^{-iky} - \begin{pmatrix} -\frac{k}{\omega} \\ 0 \\ 0 \\ 1 \end{pmatrix} e^{iky} \tag{2.180}$$

Finally, the adjoint solution associated with the entropy mode is of the form

$$\mathbf{B}_e(y;k) = \begin{pmatrix} 0 \\ 0 \\ 1 \\ 0 \end{pmatrix} e^{-iky} \pm \begin{pmatrix} 0 \\ 0 \\ 1 \\ 0 \end{pmatrix} e^{iky} \tag{2.181}$$

To derive vectors (2.178) - (2.181), we used the theorem [Kam59] about the relationship between fundamental solutions of the adjoint system (2.171) and the matrix of fundamental solutions of the direct problem (2.170). The j-th fundamental solution of Eq. (2.171) can be obtained as a vector comprised of cofactors of the j-th column of the matrix of fundamental solutions for the direct problem, Eq. (2.170).

One can establish the following orthogonality relation for the modes of the continuous spectra [Tum03]:

$$\langle \mathbf{H}_2 \mathbf{A}_{\alpha'}(y;k'), \mathbf{B}_\alpha(y;k) \rangle = Q_\alpha \delta(k-k') \tag{2.182}$$

where $\delta(k-k')$ is the Dirac delta function and Q_α is a constant, which depends on the normalization of the eigenfunctions ($Q_\alpha = 0$ if α and α' belong to different normal modes or belong to different symmetries in the case of the entropy modes).

For the particular normalizations of $\mathbf{A}_\alpha(y;k)$ and $\mathbf{B}_\alpha(y;k)$ used above, one can find

$$\begin{aligned} Q_{ac1} &= -4\pi \frac{\omega-\alpha_1}{k} \left[\frac{d\alpha_1}{dk}\right]^{-1} \\ Q_{ac2} &= -4\pi \frac{\omega-\alpha_2}{k} \left[\frac{d\alpha_2}{dk}\right]^{-1} \\ Q_v &= -2\pi \left(\frac{\omega}{k} + \frac{k}{\omega}\right) \\ Q_e &= -2\pi \end{aligned} \tag{2.183}$$

The coefficients of the expansion

In the present section, we are going to show that the solution (2.165) can be written as an expansion into the eigenfunctions so that

$$\mathbf{A}(x,y) \equiv \sum_{\alpha'} \int_0^\infty C_{\alpha'}(k')\mathbf{A}_{\alpha'}(y;k')e^{i\alpha' x}dk' \tag{2.184}$$

One can recognize that the input from the residue value in (2.165) is associated with the entropy and vorticity modes, whereas the integrals along the branch cuts lead to the fast and slow acoustic modes in (2.184).

Using the orthogonality condition in (2.182) and that $\mathbf{A}_0(y)$ is a given vector function in (2.150), it follows that

$$C_\alpha(k) = \frac{\langle \mathbf{H}_2\mathbf{A}_0(y), \mathbf{B}_\alpha(y;k)\rangle}{Q_\alpha} \tag{2.185}$$

In order to confirm that the eigenfunction system representation (2.184) together with (2.185) is equivalent to (2.165), we proceed with the discussion of the modes separately.

Vorticity modes

The vorticity mode has two non-zero components (u and v) and therefore its contribution to the solution involves only these two components. Using the definition for the vorticity coefficient defined in (2.185), we will show that the contribution of the vorticity mode is equivalent to the residue value of these two components in (2.163). The coefficient of the expansion for the vorticity mode is given by Eq. (2.185), therefore,

$$C_v(k) = \frac{k^2}{\pi(k^2+\omega^2)}\int_0^\infty (u_0+\pi_0)\cos ky'dy' + \frac{i\omega k}{\pi(k^2+\omega^2)}\int_0^\infty v_0 \sin ky'dy' \tag{2.186}$$

The contribution to the solution from the vorticity mode can be evaluated as the following integral:

$$\tilde{\mathbf{A}}_v(x,y) = \int_0^\infty C_v(k)\mathbf{A}_v(y;k)e^{i\alpha_v x}dk = e^{i\omega x}\int_0^\infty C_v(k)\mathbf{A}_v(y;k)dk \tag{2.187}$$

The first component of $\tilde{\mathbf{A}}_v(x,y)$ is $\exp(i\omega x)u_v(y)$ where $u_v(y)$ is determined by the following integral:

$$\begin{aligned} u_v(y) &= 2\int_0^\infty C_v(k)\cos kydk \\ &= \frac{2}{\pi}\int_0^\infty \left(\int_0^\infty \frac{k^2(u_0+\pi_0)}{k^2+\omega^2}\cos ky'dy'\right)\cos kydk \\ &+ \frac{2}{\pi}\int_0^\infty \left(\int_0^\infty \frac{i\omega k v_0}{k^2+\omega^2}\sin ky'dy'\right)\cos kydk \end{aligned} \tag{2.188}$$

Since the integrand of both double integrals is a bounded function of k and y', we can exchange the order of integration,

$$\begin{aligned} u_v(y) = &\frac{2}{\pi}\int_0^\infty (u_0+\pi_0)\left(\int_0^\infty \frac{k^2}{\omega^2+k^2}\cos ky\cos ky'dk\right)dy' \\ &+\frac{2}{\pi}\int_0^\infty iv_0\left(\int_0^\infty \frac{\omega k}{\omega^2+k^2}\cos ky\sin ky'dk\right)dy' \end{aligned} \tag{2.189}$$

The integrals inside the parentheses can be evaluated explicitly [GR00]:

$$\begin{aligned} \int_0^\infty \frac{k^2}{\omega^2+k^2}\cos ky\cos ky'dk &= \frac{\pi}{2}\delta(y-y') - \frac{\omega\pi}{2}\begin{cases} e^{-\omega y}\cosh\omega y', & y'<y \\ e^{-\omega y'}\cosh\omega y, & y'>y \end{cases} \\ \int_0^\infty \frac{\omega k}{\omega^2+k^2}\cos ky\sin ky'dk &= \frac{\omega\pi}{2}\begin{cases} -e^{-\omega y}\sinh\omega y', & y'<y \\ e^{-\omega y'}\cosh\omega y, & y'>y \end{cases} \end{aligned} \tag{2.190}$$

Therefore, one can obtain from (2.189)

$$\begin{aligned} u_v(x,y) = &(\pi_0+u_0) - \omega e^{-\omega y}\int_0^y \left[(u_0+\pi_0)\cosh\omega y' + iv_0\sinh\omega y'\right]dy' \ldots \\ &-\omega\cosh wy\int_y^\infty e^{-\omega y'}\left[-iv_0+(u_0+\pi_0)\right]dy' \end{aligned} \tag{2.191}$$

Expanding each of the hyperbolic sine and cosine functions and regrouping terms lead to the following result:

$$\begin{aligned} u_v(x,y) &= (\pi_0+u_0) - i\omega e^{-\omega y}\int_0^y \left[v_0\sinh\omega y' - i(u_0+\pi_0)\cosh\omega y'\right]dy' \ldots \\ &\quad + i\omega\cosh wy\int_y^\infty e^{-\omega y'}\left[v_0+i(u_0+\pi_0)\right]dy' \\ &= (u_0+\pi_0) - i\omega\left(e^{-\omega y}\left[\int_0^y \frac{e^{\omega y'}}{2}[v_0-i(\pi_0+u_0)]dy' \ldots\right.\right. \\ &\quad \left.\left. -\int_0^\infty \frac{e^{-\omega y'}}{2}[v_0+i(u_0+\pi_0)]dy'\right] - e^{wy}\int_y^\infty \frac{e^{-\omega y'}}{2}[v_0+i(u_0+\pi_0)]dy'\right) \end{aligned} \tag{2.192}$$

Finally, Eq. (2.192) can be recast as

$$u_v(x,y) = e^{i\omega x}\{(u_0+\pi_0) - i\omega\left[e^{-\omega y}[f_1(y)+f_2(0)] + e^{\omega y}f_2(y)\right]\} \tag{2.193}$$

where $f_1(y)$ and $f_2(y)$ are defined in (2.164a) and (2.164b), respectively.

The same procedure is used to derive the second component of $\tilde{\mathbf{A}}_v(x,y)$, which is defined

as $\exp(i\omega x)v_v(y)$. In order to determine $v_v(y)$, we write that

$$\begin{aligned} v_v(y) &= -2i\int_0^\infty \frac{\omega}{k}C_v(k)\sin ky'dy' \\ &= \frac{2}{\pi}\int_0^\infty v_0\left(\int_0^\infty \frac{\omega^2}{k^2+\omega^2}\sin ky\sin ky'dk\right)dy' \\ &- \frac{2}{\pi}\int_0^\infty i(\pi_0+u_0)\left(\int_0^\infty \frac{\omega k}{k^2+\omega^2}\sin ky\cos ky'dk\right)dy' \end{aligned}$$

The integrals in parentheses can be found explicitely [GR00], i.e.,

$$\begin{aligned} \int_0^\infty \frac{\omega^2}{k^2+\omega^2}\sin ky\sin ky'dk &= \frac{\omega\pi}{2}\begin{cases} e^{-\omega y}\sinh\omega y', & y'<y \\ e^{-\omega y'}\sinh\omega y, & y'>y \end{cases} \\ \int_0^\infty \frac{\omega k}{k^2+\omega^2}\sin ky\cos ky'dk &= \frac{\omega\pi}{2}\begin{cases} e^{-\omega y}\cosh\omega y', & y'<y \\ -e^{-\omega y'}\sinh\omega y, & y'>y \end{cases} \end{aligned} \tag{2.194}$$

Expanding of the hyperbolic functions and regrouping the terms lead to

$$\begin{aligned} v_v(y) = \omega\Bigg[e^{-\omega y}\int_0^y \frac{e^{\omega y'}}{2}[v_0 - i(u_0+\pi_0)]dy' \ldots \\ - e^{-\omega y}\int_0^y \frac{e^{-\omega y'}}{2}[v_0 + i(u_0+\pi_0)]dy' + e^{\omega y}\int_0^\infty \frac{e^{-\omega y'}}{2}[v_0 + i(u_0+\pi_0)]dy'\Bigg] \end{aligned} \tag{2.195}$$

Finally, Eq. (2.195) can be recast as

$$v_v(x,y) = \omega e^{i\omega x}\left[e^{-\omega y}[f_1(y)+f_2(0)] + e^{\omega y}f_2(y)\right]$$

There are no other non-zero terms in $\mathbf{A}_v$, therefore the contribution to the solution from the vorticity mode is

$$\tilde{\mathbf{A}}_v(x,y) = e^{i\omega x}\begin{pmatrix} (u_0+\pi_0) - i\omega\left[e^{-\omega y}[f_1(y)+f_2(0)] + e^{\omega y}f_2(y)\right] \\ \omega\left[e^{-\omega y}[f_1(y)+f_2(0)] + e^{\omega y}f_2(y)\right] \\ 0 \\ 0 \end{pmatrix} \tag{2.196}$$

If we refer to Eq. (2.163), the vorticity contribution is exactly equivalent to the first two components of the residue value of $\mathbf{A}_s(y)\exp(sx)$ at $s = i\omega$. In the following we shall show that the third component of the residue value is represented by the entropy mode.

Entropy modes

For brevity of the discussion, we assume that the initial data allow expansion only into the symmetric entropy mode. The entropy mode coefficient is calculated using Eq. (2.185), and so we obtain

$$C_e(k) = \frac{1}{\pi}\int_0^\infty (\theta_0 - M^2\gamma\pi_0)\cos ky'dy' \tag{2.197}$$

The entropy mode has only one non-zero component, i.e., $A_{e3}(y;k) = 2\cos ky$. Its contribution, $\exp(i\omega x)\theta_e(y)$, can be evaluated as the following integral:

$$\begin{aligned}\theta_e(y) &= 2\int_0^\infty C_e(k)\cos kydk \\ &= \frac{2}{\pi}\int_0^\infty \left(\int_0^\infty [\theta_0 - M^2(\gamma-1)\pi_0]\cos ky'dy'\right)\cos kydy \\ &= \frac{2}{\pi}\int_0^\infty [\theta_0 - M^2(\gamma-1)\pi_0]\left(\int_0^\infty \cos ky\cos ky'dk\right)dy'\end{aligned} \tag{2.198}$$

The integral in parentheses can be found to be proportional to the Dirac delta function, specifically,

$$\int_0^\infty \cos ky\cos ky'dk = \frac{\pi}{2}\delta(y-y') \tag{2.199}$$

Consequently,

$$\theta_e(y) = \theta_0 - M^2(\gamma-1)\pi_0$$

Now it is clear that the contribution from the entropy and vorticity modes to the solution $\mathbf{A}(x,y)$ is the same as the contribution from the residue value at $s = i\omega$ in the formal solution, Eq. (2.165),

$$\begin{aligned}\mathrm{Res}(\mathbf{A}_s(y)e^{sx}) &= \int_0^\infty C_v(k)\mathbf{A}_v(y;k)e^{i\alpha_v x}dk + \int_0^\infty C_e(k)\mathbf{A}_e(y;k)e^{i\alpha_e x}dk \\ &= \begin{pmatrix} -i\omega\left\{e^{-\omega y}[f_1(y)+f_2(0)] + e^{\omega y}f_2(y)\right\} + (\pi_0+u_0) \\ \omega\left\{e^{-\omega y}[f_1(y)+f_2(0)] - e^{\omega y}f_2(y)\right\} \\ \theta_0 - M^2(\gamma-1)\pi_0 \\ 0\end{pmatrix}\end{aligned} \tag{2.200}$$

Fast and slow acoustic modes

It will be shown the integrals along the branch cut in figure 2.96 that have been parameterized by $k > 0$ in (2.169), can be represented via the fast and slow acoustic modes. The equivalence will follow from first expressing the expansion into the acoustic modes, and subsequently showing the acoustic mode expansion to be equivalent to the integrals that appear in the formal solution in (2.169). First, the expansion into the acoustic modes using the coefficients defined in (2.185) for the slow and fast modes is given by

$$\mathbf{A}_{ac}(x,y) = \sum_{m=1,2}\int_0^\infty C_{acm}(k)\mathbf{A}_{acm}(y;k)e^{i\alpha_m x}dk \tag{2.201}$$

where the coefficients are found from (2.185) as

$$C_{acm}(k) = \frac{1}{2\pi}\frac{k}{\omega-\alpha_m}\frac{d\alpha_m}{dk}C_m(k) \tag{2.202a}$$

$$C_m(k) = \int_0^\infty iv_0\sin kydy - \int_0^\infty \left(\frac{\omega}{k}u_0 + \frac{M^2(\omega-\alpha_m)+\alpha_m}{k}\pi_0\right)\cos kydy \tag{2.202b}$$

The wave numbers $\alpha_m(k)$ $(m = 1, 2)$ in (2.202) are defined by (2.173a).

From (2.167) it is clear that in fact $s_m(k) = i\alpha_m(k)$, and the acoustic mode coefficients is recast as:

$$C_{acm}(k) = \frac{1}{2\pi} \frac{k}{i\omega - s_m} \frac{ds_m}{dk} C_m(k) \tag{2.203a}$$

$$C_m(k) = \int_0^\infty iv_0 \sin kydy - \int_0^\infty \left(\frac{\omega}{k} u_0 + \frac{M^2(s_m - i\omega) - s_m}{k} \pi_0 \right) \cos kydy \tag{2.203b}$$

Also, we can show that the acoustic mode vector can be represented in terms of the fundamental solutions of the Laplace transform solution in (2.169),

$$\mathbf{A}_{acm}(y,k) = \frac{i\omega - s_m(k)}{k} \frac{1}{i} \left[e^{iky} \mathbf{Z}_1 \left(\begin{smallmatrix} \mu = ik \\ s = s_m(k) \end{smallmatrix} \right) + e^{-iky} \mathbf{Z}_2 \left(\begin{smallmatrix} \mu = ik \\ s = s_m(k) \end{smallmatrix} \right) \right]$$

And therefore the contribution of the acoustic modes is equivalent to

$$\begin{aligned} \mathbf{A}_{ac}(x,y) &= \sum_{m=1,2} \int_0^\infty C_{acm}(k) \mathbf{A}_{acm}(y;k) e^{i\alpha_m x} dk \\ &= \frac{1}{2\pi i} \sum_{m=1,2} \int_0^\infty C_m(k) \left[e^{iky} \mathbf{Z}_1 \left(\begin{smallmatrix} \mu = ik \\ s = s_m(k) \end{smallmatrix} \right) + e^{-iky} \mathbf{Z}_2 \left(\begin{smallmatrix} \mu = ik \\ s = s_m(k) \end{smallmatrix} \right) \right] \frac{ds_m}{dk} e^{s_m(k)} dk \end{aligned}$$

Given that $D_m(k) = C_m(k)$ where $D_m(k)$ is defined in (2.168), the acoustic mode component is exactly equal to the integrals that appear in the formal solution in (2.169). Therefore, it is concluded that integrals over γ^+ and γ^- can be represented by the fast and slow acoustic modes, i.e.,

$$-\frac{1}{2\pi i} \left(\int_{\gamma^-} \dots ds + \int_{\gamma^+} \dots ds \right) = \sum_{m=1,2} \int_0^\infty C_{acm}(k) \mathbf{A}_{acm}(y;k) e^{i\alpha_m x} dk \tag{2.204}$$

with the coefficients defined from Eq. (2.202). Analysis of the branches corresponding to the slow and fast acoustic modes ends the proof of the equivalence of the Cauchy problem formal solution (2.165) and eigenfunction expansion (2.184).

Two examples of BES application

Projection of computational results onto the normal modes

The biorthogonal eigenfunction system can be used to obtain insight into computational results by decomposition of the perturbations into the normal modes. For the purpose of illustration, we analyze computational results for the receptivity problem involving a periodic-in-time actuator placed on a flat plate in uniform supersonic inviscid flow. This part of the work is similar to the analysis of acoustic perturbations in [TWZ07].

The actuator is emulated by the inhomogeneous boundary condition on the wall:

$$v(x, y = 0, t) = v_w(x,t) = \varepsilon g(x) \sin \omega t \tag{2.205}$$

For the numerical example the following dimensionless parameters are chosen: freestream Mach number $M = 6.62$; angular frequency of the perturbations $\omega = 0.1$, the actuator's length $w = 100$, and the specific heats ratio $\gamma = 1.4$. These parameters are close to the local parameters in the direct numerical simulation of perturbations emanating from the wall of a wedge in supersonic flow in [WZ05].

The actuator shape function $g(x)$ is given by

$$g(x) = \begin{cases} 20.25l^5 - 35.4375l^4 + 15.1875l^2, \ (l \leq 1) \\ -20.25(2.0 - l)^5 + 35.4375(2.0 - l)^4 - 15.1875(2.0 - l)^2 \ (l \geq 1) \end{cases} \tag{2.206}$$

where $l(x) = 2x/w$. A plot of the shape function is shown in figure 2.98. The actuator amplitude ε is chosen as 10^{-4}.

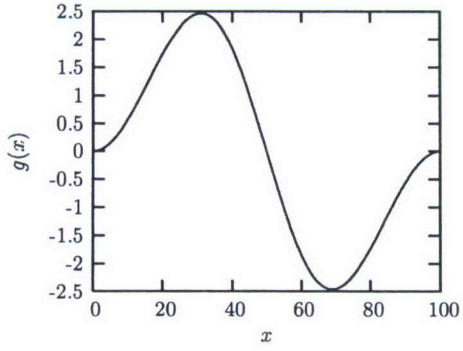

Figure 2.98: The shape function $g(x)$.

The nonlinear Euler equations are solved with the help of code based on the Conservation Element/Solution Element (CE/SE) Euler method introduced by Chang *et al.* [CWC99].

For the problem at hand, we use the following computational domain: $0 \leq x \leq 200$ and $0 \leq y \leq 35$. Two grids, $N_x \times N_y$, having N_x and N_y intervals in the x and y directions, respectively, were used in order to check the numerical convergence:

- Coarse Grid: 250×200 ,
- Fine Grid: 500×400.

The time steps were $\tau = 0.1$ and 0.05 for the coarse and fine grids, respectively.

The CE/SE method uses two alternating grids, Ω_1 and Ω_2. These are shown in figure 2.99. The method begins with grid Ω_2 at $t = 0$, intermediately finds a solution on grid Ω_1 at $t = \tau/2$, and finishes on grid Ω_2 at $t = \tau$, and so forth. We notice that at certain x-coordinates, the grid uses points slightly above and below the wall. The actuator boundary condition (2.205) is applied at these points in spite of their shift from $y = 0$ in order to simplify the algorithm. We can estimate the effect of the simplified boundary conditions by comparing the fine and coarse grid solutions in the vicinity of the wall. Downstream of the

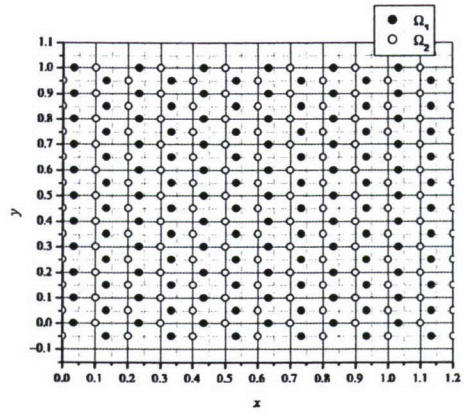

Figure 2.99: The alternating grids Ω_1 and Ω_2.

actuator, the no-penetration boundary condition is imposed at the wall, $y = 0$, following [CWC99]. The boundary conditions at the right and the upper sides of the domain are the non-reflecting boundary conditions used in [CWC99]. On the left-hand side of the domain, the no-perturbation boundary condition was used.

The CE/SE scheme includes three additional parameters: α and β (both related to the control of oscillations resulting from discontinuities such as shock waves) and ε_0 (serving to control effects of numerical viscosity). In this case, $\alpha = \beta = 0$ and $\varepsilon_0 = 0.3$. The value for ε_0 was chosen after experiments with the parameter and was found to mostly affect the layer close to the wall.

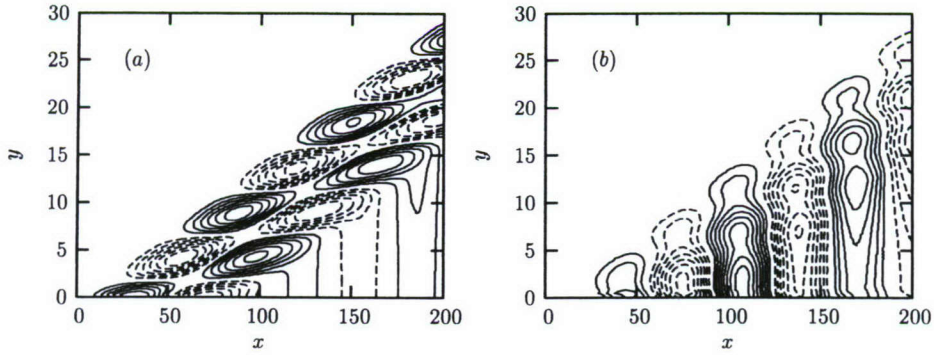

Figure 2.100: Coarse grid result for the (a) pressure perturbation (increment of $.5 \times 10^{-5}$ between the contours) and (b) streamwise velocity perturbation (increment 1×10^{-5})

The numerical results for the pressure field, π, and streamwise velocity field, u, at $t = 200$, are shown in figure 2.100. The dashed contours represent negative contours while the solid lines represent the positive contours. Each contour represents an increase or decrease of the indicated increment. For example, the outermost positive contour in figure 2.100(a) has

value 0.5×10^{-5}, and the innermost positive contour has value 3.0×10^{-5}. These results were produced using the coarse grid.

Comparison of the numerical results with $\varepsilon = 2 \times 10^{-4}$ in (2.205) demonstrated that $\varepsilon = 10^{-4}$ is small enough that the perturbations can be interpreted as linear.

Figure 2.101 shows the pressure perturbation and streamwise velocity as function of y at $x = 160$ for both coarse and fine grids. The results show nearly perfect agreement. In the

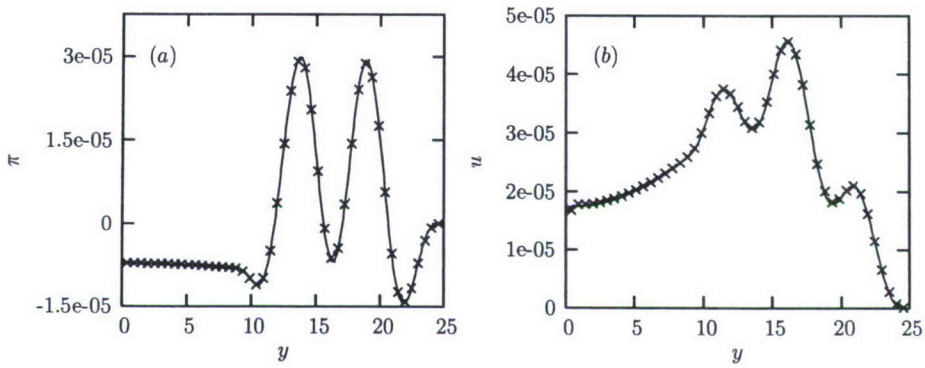

Figure 2.101: Coarse (crosses) and fine (solid-line) grid comparison for $x = 160$ and $t = 200$ for the (a) pressure perturbation and (b) streamwise velocity perturbation

case of the streamwise velocity, there is a relatively larger difference between the coarse and fine grid solutions in the vicinity of the wall, which we attribute to the inaccuracy in the application of the actuator boundary condition at the staggered points in the vicinity of the wall.

As an example of the BES application, one can use the computational results together with (2.185) in order to find a projection onto the normal modes at a prescribed coordinate x. Figure 2.102 shows the amplitudes of the slow and fast acoustic modes as functions of the parameter k. Because there is no dissipation, the amplitude distributions shown in figure 2.102 are independent of x. One can see that the fast acoustic mode amplitude is a magnitude larger than the slow acoustic mode. The BES technique reveals this insight, which otherwise would remain hidden from view if one knew the numerical solution only.

It is worthwhile to compare the computational results and their projection onto the fast and slow acoustic modes presented in this section with the results of [TWZ07]. The results are very close qualitatively. The latter means that the main features of the numerical results for acoustic modes observed in [TWZ07] have an inviscid character.

Projection of the analytical result onto the normal modes: the receptivity problem solution

The receptivity problem that was solved numerically in the preceding section has an analytical solution [AL65]. It can be found as a solution of the linearized velocity potential equation with inhomogeneous boundary condition on the wall. The solution provides the

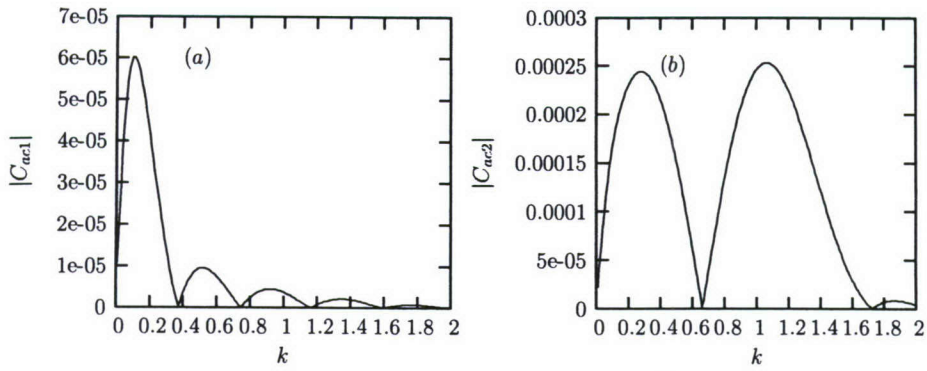

Figure 2.102: Projection result for the (a) slow acoustic mode (C_{ac1}) and (b) fast acoustic mode (C_{ac2})

perturbation flow field, and it does not reveal anything about the amplitudes of the fast and slow acoustic modes. Using the BES, one can decompose the analytical solution as was done for the numerical result. Instead of the decomposition of the available analytical result, we are going to show how the BES can be used to find the receptivity problem solution as an expansion into the normal modes directly. (This part of the work is similar to the receptivity problem solution in [Tum06b], within the scope of the linearized Navier-Stokes equations.) After that, one can prove that the solution is equivalent to the result of [AL65].

Assuming that the solutions of linearized Euler equations are proportional to $\exp(-i\omega t)$, the governing equations are identical to (2.147) except for differing boundary conditions on the wall.

$$\begin{aligned} &\mathbf{E}\frac{\partial \mathbf{A}}{\partial y} = \mathbf{H}_1\mathbf{A} + \mathbf{H}_2\frac{\partial \mathbf{A}}{\partial x} \\ &y = 0: \quad A_2(x,0) = v_w(x) \\ &y \to \infty: \quad |A_j| \to 0 \end{aligned} \tag{2.207}$$

where $v_w(x) = \varepsilon g(x)$ as defined in (2.206).

To find the formal solution of the problem, we begin with the Fourier transform with respect to x,

$$\mathbf{A}_f(y) = \int_{-\infty}^{\infty} \mathbf{A}(x,y)e^{-i\alpha_f x}ds \tag{2.208}$$

As a result, the problem (2.207) is transformed to the following boundary-value problem for ordinary differential equations:

$$\begin{aligned} &\mathbf{E}\frac{d\mathbf{A}_f}{dy} - \mathbf{H}_1\mathbf{A}_f - i\alpha_f\mathbf{H}_2\mathbf{A}_f = 0 \\ &y = 0: \quad A_{f,2} = \rho(\alpha_f) \\ &y \to \infty: \quad |A_{f,j}| \to 0 \end{aligned} \tag{2.209}$$

where

$$\rho(\alpha_f) = \int_{-\infty}^{\infty} v_w(x) e^{-i\alpha_f x} dx \tag{2.210}$$

One can find the solution of the problem (2.209) as follows:

$$\mathbf{A}_f(y) = \rho(\alpha_f) \left(-\frac{i\alpha_f}{\mu}, 1, \frac{iM^2(\gamma-1)(\alpha_f-\omega)}{\mu}, \frac{i(\alpha_f-\omega)}{\mu} \right)^T e^{-\mu y} \tag{2.211}$$

where

$$\mu(\alpha_f) = \sqrt{\alpha_f^2 - M^2(\alpha_f-\omega)^2} \tag{2.212}$$

and the positive branch of the square root, $\mathcal{R}e(\mu) > 0$ is chosen.

Finally, one can write the formal solution of problem (2.207)

$$\mathbf{A}(x,y) = \frac{1}{2\pi} \int_{-\infty}^{+\infty} \mathbf{A}_f(y) e^{i\alpha_f x} d\alpha_f \tag{2.213}$$

The formal solution can be presented as a sum of the normal modes with coefficients

$$\begin{aligned} C_\alpha(k) &= \frac{\langle \mathbf{H}_2 \mathbf{A}(y), \mathbf{B}_\alpha(y;k) \rangle}{Q_\alpha} \\ &= \frac{\int_{-\infty}^{+\infty} \langle \mathbf{H}_2 \mathbf{A}_f, \mathbf{B}_\alpha \rangle e^{i(\alpha_f-\alpha)x} d\alpha_f}{2\pi Q_\alpha} \end{aligned} \tag{2.214}$$

Using the dot product of Eq. (2.207) and $\mathbf{B}_\alpha$, together with integration by parts, one can derive

$$\langle \mathbf{H}_2 \mathbf{A}_f, \mathbf{B}_\alpha \rangle = -\frac{\rho(\alpha_f) B_{\alpha 2}(y=0;k)}{i(\alpha_f - \alpha(k))}$$

Therefore,

$$C_\alpha(k) = -\frac{B_{\alpha 2}(y=0;k)}{Q_\alpha(k)} \left(\frac{1}{2\pi i} \int_L \frac{\rho(\alpha_f) e^{i(\alpha_f-\alpha(k))x}}{\alpha_f - \alpha(k)} d\alpha_f \right) \tag{2.215}$$

The integral in (2.215) can be evaluated explicitly as the residue value at $\alpha_f = \alpha(k)$ by completing the path in the upper half-plane α_f. As a result, we arrive at

$$C_\alpha(k) = -\frac{\rho(\alpha(k))}{Q_\alpha(k)} B_{\alpha 2}(y=0;k) \tag{2.216}$$

If we refer to the equations defining the adjoint modes, it is clear from Eqs. (2.180) and (2.181) that the entropy and vorticity mode coefficients are zero since the second component of both modes is zero, i.e., $B_{e2} = 0$ and $B_{v2} = 0$. This result explains the observation in [Tum06b] that amplitudes of the entropy and vorticity modes are very small in the case of a periodic-in-time actuator placed at the bottom of the boundary layer.

For the slow and fast acoustic modes, the second component at $y = 0$ is non-zero for both modes, i.e., $B_{acm2} = -2(\omega - \alpha_m)/k$, and one can find explicitly amplitudes of the slow, $C_{ac1}(k)$, and fast, $C_{ac2}(k)$, modes as follows:

$$C_{ac1}(k) = -\frac{k\rho(\alpha_1(k))}{2\pi\sqrt{(M^2-1)k^2 + M^2\omega^2}} \tag{2.217}$$

$$C_{ac2}(k) = \frac{k\rho(\alpha_2(k))}{2\pi\sqrt{(M^2-1)k^2 + M^2\omega^2}} \tag{2.218}$$

The Fourier transform $\rho(\alpha)$ for the particular case of $v_w(x)$ was found the help of Mathematica, [Wol99] yielding

$$\rho(\alpha) = \frac{2i\varepsilon e^{-i\alpha w/2}}{w^5\alpha^6}(8w\alpha(48a_2 + a_3w^2\alpha^2)\cos\frac{w\alpha}{2} - 3840a_1\sin\frac{w\alpha}{2} + 384(5a_1 - a_2)w\alpha - 8(10a_1 - 6a_2 + a_3)w^3\alpha^3 + (a_1 - a_2 + a_3)w^5\alpha^5)$$

with $a_1 = 20.25$, $a_2 = -35.4375$, and $a_3 = 15.1875$.

We are now able to compare the amplitudes, (2.217) and (2.218), with the amplitudes derived from the projection of the numerical results for the slow and fast acoustic modes (see figure 2.103). The close agreement of the results serves as validation for the numerical method

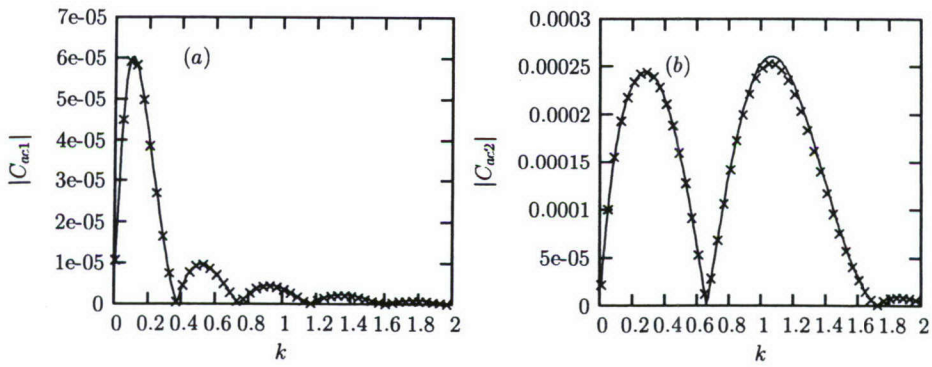

Figure 2.103: Comparison for the projection (crosses) and theoretical result (solid line) for the (a) slow acoustic mode (C_{ac1}) and (b) fast acoustic mode (C_{ac2}).

that was employed in solving the Euler equations for the receptivity problem. Figure 2.104 is a comparison of the theoretical and computational results for pressure and streamwise velocity perturbations at $x = 160$, $t = 200$.

Conclusions

The practical use of the BES technique with respect to analysis of computational data was illustrated by considering the receptivity problem of a periodic-in-time actuator on the

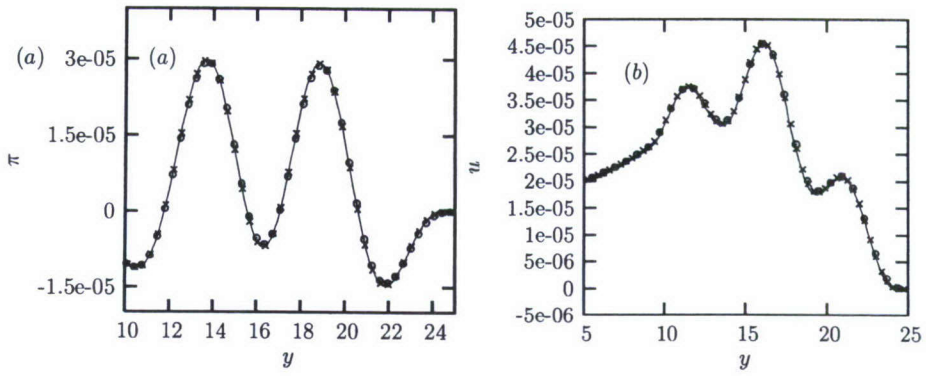

Figure 2.104: Comparison of the theory (solid-line) with the coarse (circle) and fine (cross) results for the (a) pressure and (b) streamwise velocity

wall in uniform flow. A numerical method derived from [CWC99] was used to solve the problem numerically. The computational data were projected onto the normal modes of the continuous spectra (slow and fast acoustic modes). As a result, it was found that the slow and fast acoustic modes compose the perturbation field found through the numerical method. Thus, The BES system helps to reveal the physical structure of the flow.

The receptivity problem was solved analytically, as well. With the help of the BES technique, it was shown that the actuator does not excite vorticity or entropy modes. We compared the theoretical and numerical amplitudes of the fast and slow acoustic modes, finding a close agreement between the predictions derived from our theory and the projection of the computational results. This type of analysis can be used for validation of numerical methods in other problems.

2.7 Biorthogonal eigenfunction system in the triple-deck limit

Introduction

Many problems in fluid dynamics at high Reynolds numbers are associated with different length scales. This is an obstacle for computational methods because the resolution of very different scales imposes heavy demands on computing resources. In this case, asymptotic methods might serve as an efficient complementary tool for understanding the flow structure. Modern asymptotic theories are associated with the triple-deck theory introduced in [Nei69], [SW69] and [Mes70]. One can find a large number of references relevant to the triple-deck theory in monographs [SRSK98] and [NBDL04], and in a recent review [RS98]. Initially, theoretical models dealt with steady perturbations like humps or other imperfections of the surface (see for example [BN71, BN77, SSB77, BL85, Bog86, Bog87, Bog88]). Non-steady perturbations were considered within the triple-deck theory in [Sch74, Dan75, RT77, ZR78, Ter78, ZR79, Smi79]. This extension of the triple-deck theory included problems of stability of boundary-layer flows (Tollmien-Schlichting waves) in the modern asymptotic framework (one can find the main references relevant to the predecessors of the applications of asymptotic methods to the hydro-dynamic stability theory in the monograph by [DR81]).

The first results on the generation of TS waves within the scope of asymptotic methods (the triple-deck theory) for an actuator on the plate surface were obtained by [Ter81, Ter84, Ter85]. [Gol83] utilized an asymptotic analysis for the problem of TS wave generation by acoustic waves interacting with a plate leading edge. Using a similar approach, [Gol85] and [Rub85b, Rub85a] analyzed the excitation of TS waves by acoustic waves scattered by a roughness element. Publications relevant to the asymptotic analysis of boundary-layer receptivity in succeeding years can be found in [Cho98] and [SRK02].

The objective of this section is to establish the equivalence between the receptivity problem solutions obtained within the scope of the biorthogonal eigenfunction system and those obtained with the help of the asymptotic methods at the limit of high Reynolds numbers.

Receptivity problem solution via biorthogonal eigenfunction system

Problem formulation

For the purpose of clarity, we repeat the main results relevant to the receptivity problem solution within the scope of the biorthogonal eigenfunction technique. The consideration will be restricted only by incompressible two-dimensional boundary layer flow and by two-dimensional perturbations in the parallel flow approximation. The linearized Navier-Stokes equations after Fourier transform with respect to time are written in dimensionless form as a system of four partial differential equations

$$\frac{\partial \mathbf{A}(x,y)}{\partial y} = H_1 \mathbf{A}(x,y) + H_2 \frac{\partial \mathbf{A}(x,y)}{\partial x} \tag{2.219}$$

$$H_1 = \begin{pmatrix} 0 & 0 & 0 & 1 \\ 0 & 0 & -i\omega & 0 \\ 0 & 0 & 0 & 0 \\ i\omega Re & 0 & U'Re & 0 \end{pmatrix}; \quad H_2 = \begin{pmatrix} 0 & 0 & 1 & 0 \\ 0 & 0 & -U & -Re^{-1} \\ -1 & 0 & 0 & 0 \\ URe & Re & 0 & 0 \end{pmatrix}$$

The vector-function is defined as follows: $\mathbf{A} = (u, p, v, \partial u/\partial y - \partial v/\partial x)^T$, where T stands for transposed; $U(y)$ is the unperturbed velocity profile; $U' = dU/dy$; u and v are the streamwise and normal velocity components of the perturbation, respectively; p is the pressure perturbation; and Re is the Reynolds number. The velocity perturbations in Eq. (2.219) are scaled with the free stream velocity, U_∞; pressure is scaled with ρU_∞^2, where ρ is the density; and the coordinates x and y are scaled with the scale L having the order of magnitude of the distance from the flat plate leading edge.

Assuming that there is a localized actuator on the wall, the linearized boundary conditions are as follows:

$$\begin{aligned} &y = 0: \qquad u = -U'_w h f(x); \quad v = i\omega h f(x) \\ &y \to \infty: \quad |A_j| \to 0 \quad (j = 1, ..., 4) \end{aligned} \tag{2.220}$$

where $U'_w = (dU/dy)_{y=0}$, $f(x)$ is the actuators shape function, $\max_x f = 1$, and h is the amplitude parameter. The linearized boundary conditions on the wall (2.220) are applicable if the amplitude parameter, h, is very small with respect to the thickness of the viscous sublayer [Ter84]. For simplicity, we consider a subcritical frequency, i.e. the perturbation decays downstream from the actuator. In the particular case of steady perturbation, $\omega = 0$, the problem corresponds to the case of a two-dimensional hump placed on the wall.

Formal solution

With the help of the Fourier transform with respect to the coordinate x, we arrive at the following system of ordinary differential equations with inhomogeneous boundary conditions:

$$\frac{d\mathbf{A}_v(y)}{dy} = H_1 \mathbf{A}_v(y) + i\alpha_v H_2 \mathbf{A}_v(y) \tag{2.221}$$

$$\begin{aligned} &y = 0: \qquad A_{v1} = -U'_w h \rho(\alpha_v); \quad A_{v3} = i\omega h \rho(\alpha_v) \\ &y \to \infty: \quad |A_j| \to 0 \quad (j = 1, ..., 4) \end{aligned} \tag{2.222}$$

where

$$\begin{aligned} \mathbf{A}_v(y) &= \frac{1}{2\pi} \int_{-\infty}^{+\infty} \mathbf{A}(x, y) e^{-i\alpha_v x} dx \\ \rho(\alpha_v) &= \frac{1}{2\pi} \int_{-\infty}^{+\infty} f(x) e^{-i\alpha_v x} dx \end{aligned} \tag{2.223}$$

The system of ODE (2.221) has four fundamental solutions, $\mathbf{Z}_1(y), ..., \mathbf{Z}_4(y)$. Their asymptotic behavior outside the boundary layer can be easily found as $\sim \exp(\lambda_j y)$, with

complex numbers $\lambda_j(\alpha_v)$, $j = 1, ..., 4$

$$\lambda_{1,2} = \pm\alpha_v; \quad \lambda_{3,4} = \mp\sqrt{\alpha_v^2 + iRe\,(\alpha_v + \omega)} \tag{2.224}$$

In the general case, two fundamental solutions are decaying outside the boundary layer, and the other two solutions are exponentially growing. To be specific, we choose $\mathbf{Z}_1(y)$ and $\mathbf{Z}_3(y)$ as the decaying solutions at $y \to \infty$. In this case, we choose branch $\text{Real}(\lambda_3) < 0$, and the choice of $\mathbf{Z}_1(y)$ as decaying at $y \to \infty$ solution implies that $\text{Real}(\alpha_v) < 0$.

Explicitly, the fundamental solutions outside the boundary layer are written as follows

$$\begin{gathered}
\mathbf{Z}_1 = \begin{pmatrix} -\frac{\alpha}{\alpha+\omega} \\ 1 \\ \frac{i\alpha}{\alpha+\omega} \\ 0 \end{pmatrix} e^{\alpha y}; \quad \mathbf{Z}_2 = \begin{pmatrix} -\frac{\alpha}{\alpha+\omega} \\ 1 \\ -\frac{i\alpha}{\alpha+\omega} \\ 0 \end{pmatrix} e^{-\alpha y}; \\
\mathbf{Z}_3 = \begin{pmatrix} \frac{i\mu}{Re(\alpha+\omega)} \\ 0 \\ -\frac{\alpha}{Re(\alpha+\omega)} \\ 1 \end{pmatrix} e^{-\mu y}; \quad \mathbf{Z}_4 = \begin{pmatrix} -\frac{i\mu}{Re(\alpha+\omega)} \\ 0 \\ -\frac{\alpha}{Re(\alpha+\omega)} \\ 1 \end{pmatrix} e^{\mu y}; \\
\mu = \sqrt{\alpha^2 + iRe\,(\alpha+\omega)}
\end{gathered} \tag{2.225}$$

For $\text{Real}(\alpha_v) < 0$, the solution of system (2.221) satisfying the boundary conditions (2.222) can be written as follows:

$$\begin{gathered}
\mathbf{A}_v(y) = \frac{h\rho(\alpha_v)}{E_{13}}\left(-i\omega z_{13} - U_w' z_{33}\right)_{y=0} \mathbf{Z}_1(y) + \frac{h\rho(\alpha_v)}{E_{13}}\left(U_w' z_{31} + i\omega z_{11}\right)_{y=0} \mathbf{Z}_3(y) \\
E_{ij} = \det \begin{pmatrix} z_{1i} & z_{1j} \\ z_{3i} & z_{3j} \end{pmatrix}_{y=0}
\end{gathered} \tag{2.226}$$

where z_{ij} stands for the i-th component of vector $\mathbf{Z}_j$, and the formal solution is obtained as the inverse Fourier transform

$$\mathbf{A}(x, y) = \int_{-\infty}^{+\infty} \mathbf{A}_v(y)\, e^{i\alpha_v x} d\alpha_v \tag{2.227}$$

Biorthogonal eigenfunction system

We introduce the following biorthogonal eigenfunction system $\{\mathbf{A}_\alpha, \mathbf{B}_\alpha\}$:

$$\begin{gathered}
\frac{d\mathbf{A}_\alpha}{dy} = H_1 \mathbf{A}_\alpha + i\alpha H_2 \mathbf{A}_\alpha \\
y = 0: \qquad A_{\alpha 1} = A_{\alpha 3} = 0 \\
y \to \infty: \quad |A_{\alpha j}| < \infty, \quad (j = 1, ..., 4)
\end{gathered} \tag{2.228}$$

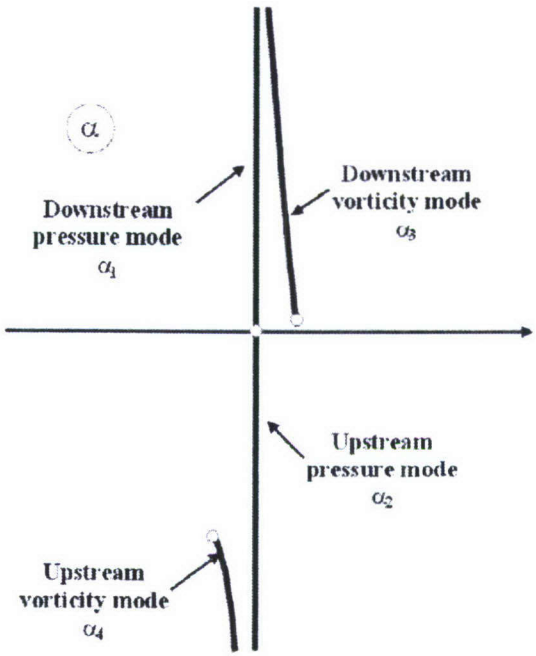

Figure 2.105: Branches of the continuous spectrum.

$$
\begin{aligned}
&-\frac{d\mathbf{B}_\alpha}{dy} = H_1^T \mathbf{B}_\alpha + i\alpha H_2^T \mathbf{B}_\alpha \\
&y = 0: \qquad B_{\alpha 2} = B_{\alpha 4} = 0 \\
&y \to \infty: \quad |B_{\alpha j}| < \infty, \quad (j = 1, ..., 4)
\end{aligned}
\tag{2.229}
$$

where α is a complex number, and the subscript 'α' indicates the corresponding solution [actually, Eqs. (2.229) define a complex conjugate of the conventional adjoint problem].

Following the analysis of the fundamental solutions, we arrive at the conclusion that the eigenvalues α belong to the discrete or continuous spectrum. In the case of the continuous spectrum, α is found from $\lambda_m^2 = -k^2$, $m = 1, ..., 4$, where k is a real parameter ($k > 0$) and $\lambda_m(\alpha)$ are defined in Eqs. (2.224). The branches of the continuous spectrum on the complex plane α are shown in figure 2.105. There are two pressure and two vorticity modes. The modes associated with the upper half-plane α are the downstream modes, whereas the other pair of modes represents the upstream ones. For the purpose of further analysis, we are interested in the downstream modes only.

The pressure modes can be found as follows:

$$
\mathbf{A}_\alpha(y) = \mathbf{Z}_1(y) + \frac{E_{31}}{E_{23}}\mathbf{Z}_2(y) + \frac{E_{12}}{E_{23}}\mathbf{Z}_3(y) \tag{2.230}
$$

where $\alpha = ik$, ($k > 0$) and the coefficients E_{ij} are defined in (2.226). At $y \to \infty$, the mode (2.230) has a non-zero pressure perturbation, whereas the vorticity perturbation is equal to

zero. Similarly, one can find for the vorticity mode

$$\mathbf{A}_\alpha(y) = \mathbf{Z}_1(y) + \frac{E_{41}}{E_{34}}\mathbf{Z}_3(y) + \frac{E_{13}}{E_{34}}\mathbf{Z}_4(y) \tag{2.231}$$

where $\alpha = -0.5iR\left(1 - \sqrt{1 + 4\left(k^2 + i\omega R\right)/R^2}\right)$, $(k > 0)$. At $y \to \infty$, the mode (2.231) has non-zero vorticity perturbation, whereas the pressure perturbation is equal to zero. In the case of the discrete spectrum, all characteristic numbers λ_m have a non-zero real part and only two fundamental solutions can be used to represent the mode. In the case of $\mathrm{Real}(\alpha_v) < 0$, one can find the discrete mode as follows:

$$\mathbf{A}_\alpha(y) = \mathbf{Z}_1(y) - \frac{z_{11}(0)}{z_{13}(0)}\mathbf{Z}_3(y) \tag{2.232}$$

where subscript 'α' means that the solution is evaluated at α as a root of the equation $E_{13}(\alpha) = 0$. Fundamental solutions of Eqs. (2.229) outside the boundary layer can be written as follows

$$\begin{aligned}
\mathbf{Y}_1 &= \begin{pmatrix} 0 \\ 1 \\ \frac{i(\alpha+\omega)}{\alpha} \\ \frac{i}{Re} \end{pmatrix} e^{\alpha y}; \quad \mathbf{Y}_2 = \begin{pmatrix} 0 \\ 1 \\ -\frac{i(\alpha+\omega)}{\alpha} \\ -\frac{i}{Re} \end{pmatrix} e^{-\alpha y}; \\
\mathbf{Y}_3 &= \begin{pmatrix} \frac{2i\alpha}{\alpha+\omega} \\ \frac{2i\alpha^2}{(\alpha+\omega)^2} \\ 0 \\ \frac{2\alpha\mu}{Re(\alpha+\omega)^2} \end{pmatrix} e^{-\mu y}; \quad \mathbf{Y}_4 = \begin{pmatrix} -\frac{2i\alpha}{\alpha+\omega} \\ -\frac{2i\alpha^2}{(\alpha+\omega)^2} \\ 0 \\ \frac{2\alpha\mu}{Re(\alpha+\omega)^2} \end{pmatrix} e^{\mu y}
\end{aligned} \tag{2.233}$$

One may consider the dot-product of Eq. (2.228) and $\mathbf{B}_{\alpha'}$, and integrate the result with respect to y on the interval $[0, \infty)$. With the help of integration by parts and Eq. (2.229), the following orthogonality relation may be derived:

$$\langle H_2\mathbf{A}_\alpha, \mathbf{B}_{\alpha'}\rangle = \int_0^\infty (H_2\mathbf{A}_\alpha, \mathbf{B}_{\alpha'})\, dy = Q\Delta_{\alpha\alpha'} \tag{2.234}$$

where $\Delta_{\alpha\alpha'}$ is the Kronecker symbol if α or α' belongs to the discrete spectrum, and $\Delta_{\alpha\alpha'} = \delta(\alpha - \alpha')$ is the Dirac delta function if both α and α' belong to the continuous spectrum. Coefficient Q in the right-hand side of (2.233) depends on the normalization of $\mathbf{A}_\alpha(y)$ and $\mathbf{B}_\alpha(y)$.

Contribution of the modes in the formal solution

The eigenfunction system is complete (see [Tum03]), i.e., a spatially growing/decaying solution of linearized Navier-Stokes equations can be presented as an expansion into the eigenfunction system) as follows:

$$\mathbf{A}(x, y) = \sum_\nu c_\nu \mathbf{A}_{\alpha_\nu} e^{i\alpha_\nu x} + \sum_j \int_0^\infty c_j(k)\mathbf{A}_{\alpha_j}(y)\, e^{i\alpha_j(k)x} dk \tag{2.235}$$

where $\sum_j$ stands for summation over the downstream pressure and vorticity modes and $\sum_\nu$ represents summation over the discrete modes.

With the help of the orthogonality condition (2.234), one can find from Eq. (2.235) for modes of discrete and continuous spectrum at some distance x

$$c_{\nu,j}(k)e^{i\alpha_{\nu,j}x} = \frac{\langle H_2\mathbf{A}, \mathbf{B}_{\alpha_{\nu,j}}\rangle}{Q_{\nu,j}} \tag{2.236}$$

where subscripts ν and j refer to the discrete and continuous spectra respectively. If we consider, for example, the dot-product of Eq. (2.221) and $\mathbf{B}_{\alpha_j}$ and integrate with respect to y over the interval $[0,\infty)$, we arrive at the following relationship:

$$\langle H_2\mathbf{A}_\nu, \mathbf{B}_{\alpha_j}\rangle = \frac{\left(A_{\nu 1}B_{\alpha_j 1} + A_{\nu 3}B_{\alpha_j 3}\right)_{y=0}}{i\left(\alpha_j - \alpha_\nu\right)} \tag{2.237}$$

Substitution of the formal solution (2.227) into Eq. (2.236) together with Eq. (2.237) leads to the following result

$$c_j(k) = -\frac{1}{Q_j}\int_{-\infty}^{+\infty} e^{i(\alpha_\nu-\alpha_j)x}\frac{\left(A_{\nu 1}B_{\alpha_j 1} + A_{\nu 3}B_{\alpha_j 3}\right)_{y=0}}{i\left(\alpha_\nu - \alpha_j\right)}d\alpha_\nu \tag{2.238}$$

By closing the path of integration in the upper half-plane, one can find the coefficient as the residue value at $\alpha_\nu = \alpha_j$

$$c_j(k) = -\frac{2\pi}{Q_j}\left(A_{\nu 1}B_{\alpha_j 1} + A_{\nu 3}B_{\alpha_j 3}\right)_{y=0} = \frac{2\pi h\rho\left(\alpha_j\right)}{Q_j}\left(U_w' B_{\alpha_j 1} - i\omega B_{\alpha_j 3}\right)_{y=0} \tag{2.239}$$

The coefficients c_ν corresponding to the discrete modes are obtained from (2.239) with α_j replaced by α_ν. Finally, substituting the coefficients $c_j(k)$ and c_ν into Eq. (2.235) provides the solution of the receptivity problem as an expansion into the normal modes.

The biorthogonal eigenfunction system in the triple-deck limit

In order to derive the triple-deck limit of (2.235), one has to find the eigenfunction system $\{\mathbf{A}_\alpha, \mathbf{B}_\alpha\}$ and the coefficient Q in the orthogonality condition (2.234) in the limit of high Reynolds number and scaling corresponding to the triple-deck theory.

Assuming that the dimension of the actuator in the x direction has the order of magnitude $\varepsilon^3 L$, where $\varepsilon = Re^{-1/8} \ll 1$ is the small parameter, we arrive at the triple-deck structure of the flow (see figure 2.106). The coordinate y in the outer deck has to be scaled with $\varepsilon^3 L$; the scale in the main deck is $\varepsilon^4 L$, and the lower deck (viscous sublayer) has a scale of $\varepsilon^5 L$. In the case of unsteady perturbations, the time is scaled with $\varepsilon^2 L/U_\infty$. We are going to consider the introduced normal modes in the triple-deck limit. The derivation of the asymptotic governing equations starts with the linearized Navier-Stokes equations (in the triple-deck theory, the linearization is utilized in the analysis of the lower deck, whereas the equations

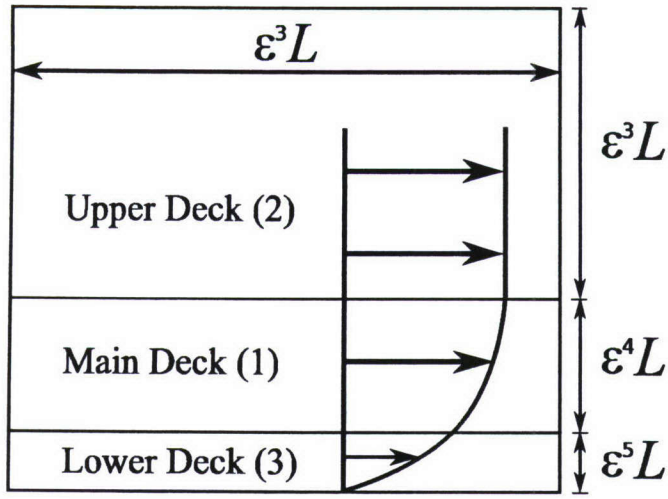

Figure 2.106: Triple-deck structure.

in the leading order of magnitude in the other decks are linear). Because the downstream vorticity mode has $\alpha \sim \omega/U_\infty \sim (\varepsilon^2 L)^{-1}$, it remains out of the triple-deck scaling and will be of no interest in the present section. In order to establish the equivalence of the solution (2.235) and asymptotic solutions of the receptivity problems, we have to find an asymptotic representation for the pressure and the discrete modes. They could be composed of two (discrete mode) or three (pressure mode) fundamental solutions. The triple-deck limit of the fundamental solutions is presented in A.6.

In the triple-deck limit, we obtain with help of the fundamental solutions from the A.6 the following result for $\bar{E}_{13}(\bar{\alpha}) = E_{13}/\varepsilon^4$:

$$\begin{aligned}\bar{E}_{13}(\bar{\alpha}) = &-\left(\frac{i\bar{\alpha}}{\bar{U}'_w} - i\omega\frac{\lambda}{\bar{\alpha}^2}\right)\left(i\bar{\alpha}\bar{U}'_w\right)^{-1/3}\int_\infty^\Omega \mathrm{Ai}(\zeta)\,d\zeta \\ &+\frac{\lambda}{\bar{\alpha}^2}\bar{U}'_w\frac{\left(i\bar{\alpha}\bar{U}'_w\right)^{1/3}}{\bar{U}'_w}\left[\mathrm{Ai}'(\Omega) - \Omega\int_\infty^\Omega \mathrm{Ai}(\zeta)\,d\zeta\right]\end{aligned} \tag{2.240}$$

where $\bar{\alpha} = \alpha/\varepsilon^3$, $\bar{\omega} = \omega\varepsilon^2$, $\bar{U}'_w = \varepsilon^4 U'_w$, and $\lambda = \pm\bar{\alpha}$ (depending on the sign of Real $(\bar{\alpha})$), and $\Omega = i^{1/3}\bar{\omega}\left(\bar{\alpha}\bar{U}'_w\right)^{-2/3}$. For a discrete mode, it has to be $\bar{E}_{13}(\bar{\alpha}) = 0$, and Eq. (2.240) leads to the dispersion relation as follows:

$$\begin{aligned}\frac{\mathrm{Ai}'(\Omega)}{I_0 - I_1(\Omega)} &= -\lambda\frac{\left(i\bar{\alpha}\bar{U}'_w\right)^{1/3}}{(\bar{U}'_w)^2} \\ I_0 = \int_0^\infty \mathrm{Ai}(\zeta)\,d\zeta = \frac{1}{3};&\quad I_1(\Omega) = \int_0^\Omega \mathrm{Ai}(\zeta)\,d\zeta\end{aligned} \tag{2.241}$$

One can find that the dispersion relation is equivalent to the one presented in [Ter81]. With the help of the asymptotic results for vectors $\mathbf{Z}_1$ and $\mathbf{Z}_3$, we can find from (2.232) the velocity components and pressure perturbations for the discrete mode in the viscous sublayer as follows

$$\mathbf{A}_\alpha = \mathbf{Z}_1 - \frac{z_{11}(0)}{z_{13}(0)}\mathbf{Z}_3 \tag{2.242}$$

where $\bar{\alpha}$ has to be found from Eq. (2.241). Explicitly, the velocity and pressure perturbations of the discrete mode in the main order of magnitude are recast in the lower deck as follows

$$\varepsilon^{-1}u = -\frac{\lambda \bar{U}'_w}{\bar{\alpha}^2}\left[1 - \frac{\int_\infty^\zeta \mathrm{Ai}(\zeta)\,d\zeta}{\int_\infty^\Omega \mathrm{Ai}(\zeta)\,d\zeta}\right], \tag{2.243a}$$

$$\varepsilon^{-3}v = \frac{\lambda}{\bar{\alpha}} i\bar{U}'_w y_3 - \frac{i\bar{\alpha}}{\bar{U}'_w} + \frac{i\bar{\omega}\lambda}{\bar{\alpha}^2} + \frac{\lambda}{\bar{\alpha}^2}\frac{\left(i\bar{\alpha}\bar{U}'_w\right)^{2/3}}{\int_\infty^\Omega \mathrm{Ai}(\zeta)\,d\zeta}\left(\mathrm{Ai}'(\zeta) - \zeta\int_\infty^\zeta \mathrm{Ai}(\eta)\,d\eta\right), \tag{2.243b}$$

$$\varepsilon^{-2}p = 1 \tag{2.243c}$$

In the case of flow perturbation downstream from a hump, we need expressions for the pressure modes at $\bar{\alpha} = i\bar{k}$ ($\bar{k}$ is a positive parameter) and $\bar{\omega} = 0$ ($\Omega = 0$). In the latter case, the pressure mode is presented similarly to Eq. (2.230)

$$\mathbf{A}_p = \mathbf{Z}_1 + C_2\mathbf{Z}_2 + C_3\mathbf{Z}_3 \tag{2.244}$$

where $\mathbf{Z}_1$ corresponds to $\lambda = \bar{\alpha} = i\bar{k}$ in the outer layer solution, and $\mathbf{Z}_2$ corresponds to the asymptotic solution with $\lambda = -\bar{\alpha} = -i\bar{k}$. The coefficients C_2 and C_3 are determined from the no-slip condition. Because we are going to consider the pressure modes in the steady case, $\bar{\omega} = 0$, we arrive at the equations

$$C_2\frac{\bar{U}'_w}{\bar{\alpha}} - C_3\frac{1}{3}\left(i\bar{\alpha}\bar{U}'_w\right)^{-1/3} = \frac{\bar{U}'_w}{\bar{\alpha}}, \tag{2.245a}$$

$$-C_2 i\bar{\alpha} + C_3\left(i\bar{\alpha}\bar{U}'_w\right)^{1/3}\mathrm{Ai}'(0) = i\bar{\alpha} \tag{2.245b}$$

Particularly, one can find C_2 as follows:

$$C_2 = \frac{3\bar{U}'_w\left(i\bar{\alpha}\bar{U}'_w\right)^{1/3}\mathrm{Ai}'(0) + i\bar{\alpha}^2\left(i\bar{\alpha}\bar{U}'_w\right)^{-1/3}}{3\bar{U}'_w\left(i\bar{\alpha}\bar{U}'_w\right)^{1/3}\mathrm{Ai}'(0) - i\bar{\alpha}^2\left(i\bar{\alpha}\bar{U}'_w\right)^{-1/3}} \tag{2.246}$$

Finally, the pressure perturbation in the viscous sublayer (corresponding to the pressure mode) can be presented as

$$\varepsilon^{-2}p_w = 1 + C_2 = -\frac{2}{\bar{\alpha}\left[-\frac{1}{\bar{\alpha}} + \bar{\alpha}^2\gamma^{-4/3}\left(i\bar{\alpha}\bar{U}'_w\right)^{-5/3}\right]}, \tag{2.247}$$

$$\gamma = \left(-3\mathrm{Ai}'(0)\right)^{3/4} = 0.8272$$

For a discrete mode, the adjoint problem solution can be written as the sum of two fundamental solutions

$$\mathbf{B}_\nu = \mathbf{g}_1 + D_3\mathbf{g}_3 \tag{2.248}$$

evaluated at $\bar{\alpha} = \bar{\alpha}_\nu$ as a root of the dispersion relation (2.241); and where $\mathbf{g}_1$ is the fundamental solution having in the outer deck the asymptotic behavior as $\sim \exp(\lambda y_2)$ ($\lambda = \pm\bar{\alpha}$), whereas $\mathbf{g}_3$ represents the fundamental solution localized in the viscous sublayer. The coefficient D_3 can be found from the boundary conditions on the wall.

In the case of the pressure mode, the adjoint problem solution is a sum of three fundamental solutions

$$\mathbf{B}_p = \mathbf{g}_1 + D_2\mathbf{g}_2 + D_3\mathbf{g}_3 \tag{2.249}$$

where $\mathbf{g}_1$ corresponds to $\lambda = \bar{\alpha} = i\bar{k}$ in the outer deck solution, $\mathbf{g}_2$ corresponds to the asymptotic solution with $\lambda = -\bar{\alpha} = -i\bar{k}$, and $\mathbf{g}_3$ stands for the fundamental solution localized in the viscous sublayer. The coefficients D_2 and D_3 are determined from the wall boundary condition. Because we are going to consider the pressure modes in the steady case, $\bar{\omega} = 0$, we arrive at the equations

$$g_{21}^{(3+)} + D_2 g_{21}^{(3-)} + D_3 g_{21}^{(3,sub)} = 0, \tag{2.250a}$$

$$g_{41}^{(3+)} + D_2 g_{41}^{(3-)} + D_3 g_{41}^{(3,sub)} = 0 \tag{2.250b}$$

where $g_{21}^{(3\pm)}$ and $g_{41}^{(3\pm)}$ are defined in Eqs. (A.60). The superscripts '$\pm$' stand for $\lambda = \pm\bar{\alpha}$ respectively, whereas the superscript '*sub*' stands for the solution (A.61) corresponding to $\mathbf{g}_3$. After substituting the solutions into Eqs. (2.250), one can obtain the algebraic system of equations in the following form:

$$-\frac{\pi k_2^+}{3}\mathrm{Bi}\,(0) + 1 + D_2\frac{\pi k_2^+}{3}\mathrm{Bi}\,(0) + D_2 + D_3\mathrm{Ai}\,(0) = 0, \tag{2.251a}$$

$$\frac{\pi k_2^+}{3}\mathrm{Bi}'\,(0) - D_2\frac{\pi k_2^+}{3}\mathrm{Bi}'\,(0) - D_3\mathrm{Ai}'\,(0) = 0, \tag{2.251b}$$

$$k_2^+ = \frac{\left(i\bar{\alpha}\bar{U}_w'\right)^{1/3}}{(\bar{U}_w')^2}\bar{\alpha} \tag{2.251c}$$

It is straightforward to find from (2.251) that

$$D_2 = -C_2 \tag{2.252}$$

where C_2 is defined in Eq. (2.246).

The receptivity problem solution in the triple-deck limit

Two-dimensional hump

In the case of a hump ($\bar{\omega} = 0$), there are no downstream discrete modes. The solution will be represented by the continuous spectrum. Moreover, because the vorticity modes are not

presented in the triple-deck limit, we have to analyze pressure modes only. For the purpose of brevity, we consider only pressure perturbation on the wall that can be easily evaluated within the triple-deck theory.

The pressure perturbation on the wall corresponding to the pressure mode was found in Eq. (2.247). This result has to be multiplied by the receptivity coefficient

$$\varepsilon^3 \left. \frac{2\pi \bar{h}\bar{\rho}\left(\bar{\alpha}\right)}{\bar{Q}_j} \bar{U}'_w \bar{B}_{\alpha 1} \right|_{y=0} p_w \tag{2.253}$$

where $\bar{h} = h/\varepsilon^5$, $\bar{\rho} = \rho/\varepsilon^3$, $\bar{B}_{\alpha_j 1} = B_{\alpha_j 1}/\varepsilon$, and $\bar{Q}_j = Q_j/\varepsilon^2$; p_w stands for the pressure perturbation corresponding to the eigenfunction of the pressure mode and evaluated on the wall [Eq. (2.247)]. Therefore, the induced pressure on the wall is recast as follows:

$$\varepsilon^{-2}\hat{P}_w = -\frac{4\pi \bar{h}\bar{\rho}\left(\bar{\alpha}\right)\bar{U}'_w \bar{B}_{\alpha 1 w}}{\bar{\alpha}\bar{Q}_j\left[-\frac{1}{\bar{\alpha}} + \bar{\alpha}^2\gamma^{-4/3}\left(i\bar{\alpha}\bar{U}'_w\right)^{-5/3}\right]}\varepsilon^3 \tag{2.254}$$

The next step is to find the asymptotic expressions for $\bar{B}_{\alpha 1 w}$ and Q_j. One can find from the fundamental solutions in the lower deck (A.60)

$$\bar{B}_{\alpha 1 w} = \frac{\bar{\alpha}}{\bar{U}'_w} - D_2\frac{\bar{\alpha}}{\bar{U}'_w} = \frac{\bar{\alpha}}{\bar{U}'_w}\left(1 + C_2\right) \tag{2.255}$$

The coefficient Q_j in the orthogonality condition (2.234) for the continuous spectrum can be found with the help of the asymptotic solutions outside the boundary layer (in the upper deck) [Tum03].

$$Q_j = \pi\left[D_2\left(H_2\mathbf{Z}_1, \mathbf{Y}_2\right) + C_2\left(H_2\mathbf{Z}_2, \mathbf{Y}_1\right)\right]^{(outerdeck)} \tag{2.256}$$

In the outer deck, one can use the explicit form of the matrix H_2 and fundamental solutions to arrive at the following result

$$\bar{Q}_j = \frac{Q_j}{\varepsilon^2} = 4\pi i C_2 \tag{2.257}$$

Finally, the pressure perturbation on the wall due to the hump is found from Eq. (2.254) as follows:

$$\begin{aligned}\varepsilon^{-2}\hat{P}_w\left(\bar{\alpha}\right) &= \frac{2i\bar{h}\bar{\rho}\left(\bar{\alpha}\right)\varepsilon^3}{\bar{\alpha}}\frac{1}{\left[-\frac{1}{\bar{\alpha}} + \bar{\alpha}^2\gamma^{-4/3}\left(i\bar{\alpha}\bar{U}'_w\right)^{-5/3}\right]\left[\frac{1}{\bar{\alpha}} + \bar{\alpha}^2\gamma^{-4/3}\left(i\bar{\alpha}\bar{U}'_w\right)^{-5/3}\right]} \\ &= \frac{i\bar{h}\bar{\rho}\left(\bar{\alpha}\right)\varepsilon^3}{\left[-\frac{1}{\bar{\alpha}} + \bar{\alpha}^2\gamma^{-4/3}\left(i\bar{\alpha}\bar{U}'_w\right)^{-5/3}\right]} - \frac{i\bar{h}\bar{\rho}\left(\alpha\right)\varepsilon^3}{\left[\frac{1}{\bar{\alpha}} + \bar{\alpha}^2\gamma^{-4/3}\left(i\bar{\alpha}\bar{U}'_w\right)^{-5/3}\right]}\end{aligned} \tag{2.258}$$

where $\bar{\alpha} = i\bar{k}$. In accordance with the solution (2.235), we have to integrate (2.258) with respect to $k = \bar{k}/\varepsilon^3 = -i\bar{\alpha}/\varepsilon^3$. Therefore, the pressure perturbation in the physical space may be found as the following integral

$$\varepsilon^{-2}P_w\left(x_3\right) = \int\limits_{\bar{\alpha}=i0}^{\bar{\alpha}=i\infty}\left\{\frac{\bar{h}\bar{\rho}\left(\bar{\alpha}\right)e^{i\bar{\alpha}x_3}}{\left[-\frac{1}{\bar{\alpha}} + \bar{\alpha}^2\gamma^{-4/3}\left(i\bar{\alpha}\bar{U}'_w\right)^{-5/3}\right]} - \frac{\bar{h}\bar{\rho}\left(\bar{\alpha}\right)e^{i\bar{\alpha}x_3}}{\left[\frac{1}{\bar{\alpha}} + \bar{\alpha}^2\gamma^{-4/3}\left(i\bar{\alpha}\bar{U}'_w\right)^{-5/3}\right]}\right\}d\bar{\alpha} \tag{2.259}$$

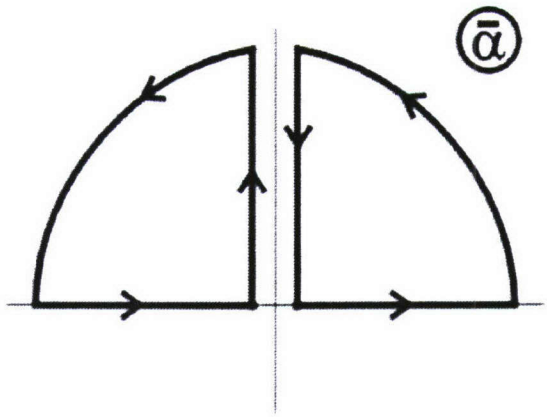

Figure 2.107: Paths of integration leading to transformation of Eq. (2.261) to Eq. (2.259).

This result was found as the triple deck limit of the solution derived with the help of the biorthogonal eigenfunction system, and we are going to show that it is identical to the result obtained from the triple-deck theory.

In the case of a 2D hump, one can find from [SSB77] (as the 2D limit of the 3D solution).

$$\varepsilon^{-2}\hat{P}_w\left(\bar{\alpha}\right) = \frac{\bar{\rho}\left(\bar{\alpha}\right)}{-\frac{1}{|\bar{\alpha}|} + \bar{\alpha}^2\gamma^{-4/3}\left(i\bar{\alpha}\bar{U}'_w\right)^{-5/3}} \tag{2.260}$$

The inverse Fourier transform might be found as the following integral:

$$\begin{aligned}\int\limits_{-\infty}^{+\infty} \varepsilon^{-2}\hat{P}_w\left(\bar{\alpha}\right)e^{i\bar{\alpha}x_3}d\bar{\alpha} = &\int\limits_{-\infty}^{0} \frac{\bar{\rho}\left(\bar{\alpha}\right)e^{i\alpha x_3}}{\left[\frac{1}{\bar{\alpha}} + \bar{\alpha}^2\gamma^{-4/3}\left(i\bar{\alpha}\bar{U}'_w\right)^{-5/3}\right]}d\bar{\alpha} \\ &+ \int\limits_{0}^{+\infty} \frac{\bar{\rho}\left(\bar{\alpha}\right)e^{i\alpha x_3}}{\left[-\frac{1}{\bar{\alpha}} + \bar{\alpha}^2\gamma^{-4/3}\left(i\bar{\alpha}\bar{U}'_w\right)^{-5/3}\right]}d\bar{\alpha}\end{aligned} \tag{2.261}$$

The two integrals on the right-hand side of Eq. (2.261) can be recast as integrals along the imaginary axis by closing the paths of integration as shown in figure 2.107, and one can arrive at the conclusion that (2.261) is identical to (2.259) at $\bar{h} = 1$.

Two-dimensional actuator

In the case of an unsteady actuator, we are interested in the amplitude of a discrete mode (Tollmien-Schlichting wave). The pressure perturbation on the wall follows from Eq. (2.239)

$$P_w = \frac{2\pi h\rho\left(\alpha\right)}{Q}\left(U'_w B_{\alpha 1} - i\bar{\omega}B_{\alpha 3}\right)\Big|_{y=0} p_w \tag{2.262}$$

where p_w stands for the pressure perturbation corresponding to the eigenfunction of the discrete mode and evaluated on the wall. Taking into account the difference in the definition of vector $\mathbf{A}_\alpha$ in Eq. (2.242) of the present work and in Eq. (21) of [TA97], one can derive from Eq. (2.262) (with the help of Eqs. (27) and (28) of [TA97]) the following result for pressure perturbation on the wall

$$P_w = -\frac{2\pi i h \rho(\alpha)}{\frac{\partial E_{13}}{\partial \alpha}} \left[z_{33} U_w' + i\omega z_{13} \right]_{y=0} p_w \tag{2.263}$$

After taking into account solutions in the viscous sublayer, we arrive at the following result

$$\varepsilon^{-2} P_w = -\frac{2\pi i \bar{h} \bar{\rho}(\bar{\alpha})}{\frac{\partial \bar{E}_{13}}{\partial \bar{\alpha}}} \left[\bar{z}_{33} \bar{U}_w' + i\bar{\omega} \bar{z}_{13} \right]_{y=0} \tag{2.264}$$

With the help of explicit solutions on the wall,

$$\bar{z}_{11}(0) = -\frac{\bar{U}_w' \lambda}{\bar{\alpha}^2}, \tag{2.265a}$$

$$\bar{z}_{31}(0) = -\left(\frac{i\bar{\alpha}}{\bar{U}_w'} - \frac{i\bar{\omega}\lambda}{\bar{\alpha}^2} \right), \tag{2.265b}$$

$$\bar{z}_{13}(0) = \left(i\bar{\alpha} \bar{U}_w' \right)^{-1/3} \int_\infty^\Omega \mathrm{Ai}(\eta)\, d\eta, \tag{2.265c}$$

$$\bar{z}_{33}(0) = \frac{\left(i\bar{\alpha} \bar{U}_w' \right)^{1/3}}{\bar{U}_w'} \left[\mathrm{Ai}'(\Omega) - \Omega \int_\infty^\Omega \mathrm{Ai}(\eta)\, d\eta \right] \tag{2.265d}$$

where eigenvalue $\bar{\alpha}$ has to be found from Eq. (2.241), one can find

$$\left[\bar{z}_{33} \bar{U}_w' + i\bar{\omega} \bar{z}_{13} \right]_{y=0} = \left(i\bar{\alpha} \bar{U}_w' \right)^{1/3} \mathrm{Ai}'(\Omega), \tag{2.266a}$$

$$\frac{\partial \bar{E}_{13}}{\partial \bar{\alpha}} = \frac{2i}{3\bar{U}_w'} \left(i\bar{\alpha} \bar{U}_w' \right)^{-1/3} \left[2 \int_\infty^\Omega \mathrm{Ai}(\zeta)\, d\zeta - \Omega \mathrm{Ai}(\Omega) \left(1 - \frac{\lambda \bar{\omega} \bar{U}_w'}{\bar{\alpha}^3} \right) \right] \tag{2.266b}$$

Substituting these results into Eq. (2.264) yields

$$\varepsilon^{-2} P_w = \frac{3\pi \bar{h} \bar{\rho}(\bar{\alpha}) \bar{U}_w' \left(i\bar{\alpha} \bar{U}_w' \right)^{2/3} \mathrm{Ai}'(\Omega)}{2(I_0 - I_1) + \Omega \mathrm{Ai}(\Omega) \left(1 - \frac{\lambda \bar{\omega} \bar{U}_w'}{\bar{\alpha}^3} \right)} \tag{2.267}$$

For positive frequency ($\bar{\omega} > 0$), the discrete mode has Real$(\bar{\alpha}) < 0$, and we have to choose $\lambda = \bar{\alpha}$. One can find that the result (2.267) is the same as in [Ter81].

Conclusion

By consideration of two examples (two-dimensional actuator placed on the wall and a two-dimensional hump), we have proved that the receptivity problem solution found with the help of the biorthogonal eigenfunction system is equivalent to the asymptotic results when the triple-deck scaling is assumed and the Reynolds number tends to infinity.

The biorthogonal eigenfunction system allows filtering out modes of continuous and discrete spectra, and the present results illustrate how this technique could be extended to asymptotic solutions of linearized Navier-Stokes equations.

Chapter 3

Three-dimensional wave packets in a compressible boundary layer

3.1 Introduction

This section is based on the papers published in collaboration with E. Forgoston and M Veirgutz [FT05, FVT06].

The transition process from laminar to turbulent flow in hypersonic boundary layers has been studied for many years. However, our understanding of this phenomenon is still very poor compared to the low speed case [Res94]. Several reasons exist for this difference. For example, experimental conditions are severe in hypersonic wind tunnels. Because of high levels of free-stream noise, it is difficult to perform experiments with controlled disturbances. Unlike the low speed case [SS47], it is difficult to design perturbers that can generate high-frequency artificial disturbances of individual modes. Instead, wave trains and wave packets are generated. Therefore, interpretation of experimental data is not straightforward, and this issue leads to the need for close coordination between theoretical modeling and experimental design and testing [FT03].

Experiments with controlled disturbances could provide insight into the governing mechanisms associated with hypersonic laminar-turbulent transition, with a sharp cone being a good candidate for transition studies due to its relatively simple geometry. Several methods for excitation of artificial disturbances in a hypersonic boundary layer are available. These methods could be used to generate either two-dimensional or three-dimensional wave packets of a broad frequency band.

Additionally, due to advances in computational fluid dynamics, it is possible to perform reliable simulations of laminar-turbulent transition. Ma and Zhong [MZ03a, MZ03b] and Zhong and Ma [ZM02] have performed direct numerical simulations to better understand the mechanisms leading to hypersonic boundary layer transition.

Accompanying these experiments, both wind-tunnel and numerical, should be theoretical modeling and studies of the development of wave packets in hypersonic boundary layers.

Gustavsson [Gus79] solved a two-dimensional (2D) initial-value problem for incompressible boundary layer flows. Fedorov and Tumin [FT03] analyzed a 2D initial-value problem in a compressible boundary layer. However, the problem for three-dimensional (3D) wave packets has not yet been considered.

The spatial analysis of the 2D instability modes in hypersonic flows [Fed03a] revealed the following: (1) in the region of the leading edge, two discrete modes, Mode F and Mode S (we use Fedorov's [Fed03a] terminology), are synchronized with fast and slow acoustic waves respectively; (2) at a downstream location, Mode F is synchronized with the entropy and vorticity waves; (3) further downstream, Mode F and Mode S could also become synchronized [FK01]. It is important to understand these features due to the role they may have in the transition process. Later on, similar features of Mode F and Mode S were seen in the 2D temporal problem [FT03].

The objective of this chapter is to solve the initial-value problem for a three-dimensional wave packet in a compressible boundary layer flow. Additionally, we will use a numerical example to illustrate features of the spectrum that are associated with the 3D character of the problem.

3.2 Initial-value problem for three-dimensional perturbations in a compressible boundary layer

Problem formulation

We consider a three-dimensional parallel boundary layer flow of a calorically perfect gas. At the initial time, $t = 0$, a three-dimensional localized disturbance is introduced into the flow. The problem is to describe the downstream evolution of the perturbation. The hydrodynamic and thermodynamic characteristics of the flow are expressed as a superposition $Q_s(y) + q(x, y, z, t)$, where Q_s is a mean-flow quantity and q is its disturbance. The streamwise, normal and spanwise spatial coordinates, given respectively by x, y, z, are nondimensionalized using a length scale L^*, and time is nondimensionalized as L^*/U_e^*, where U_e^* is the streamwise mean velocity at the upper boundary layer edge. The mean-flow velocity components are referenced to U_e^*, while temperature, density and viscosity are referenced to their respective quantities at the upper boundary layer edge. Pressure is made nondimensional using the dynamic pressure, $\rho_e^* (U_e^*)^2$. We denote u, v, and w to be respectively the streamwise, normal and spanwise velocity disturbances, and θ, π, ρ, and μ to be respectively the temperature, pressure, density and viscosity disturbances. The linearized, dimensionless, governing equations for the disturbances are:

$$\frac{\partial \rho}{\partial t} + \rho_s \frac{\partial u}{\partial x} + U_s \frac{\partial \rho}{\partial x} + \frac{\partial}{\partial y}(\rho_s v) + \rho_s \frac{\partial w}{\partial z} + W_s \frac{\partial \rho}{\partial z} = 0 \tag{3.1a}$$

$$\rho_s \left(\frac{\partial u}{\partial t} + U_s \frac{\partial u}{\partial x} + v \frac{\partial U_s}{\partial y} + W_s \frac{\partial u}{\partial z} \right) = -\frac{\partial \pi}{\partial x} + \frac{1}{Re} \left\{ \frac{\partial}{\partial x} \left[\mu_s \left(r \frac{\partial u}{\partial x} + m \frac{\partial v}{\partial y} + m \frac{\partial w}{\partial z} \right) \right] \right.$$
$$\left. + \frac{\partial}{\partial y} \left[\mu_s \left(\frac{\partial u}{\partial y} + \frac{\partial v}{\partial x} \right) + \mu \left(\frac{\partial U_s}{\partial y} \right) \right] + \frac{\partial}{\partial z} \left[\mu_s \left(\frac{\partial w}{\partial x} + \frac{\partial u}{\partial z} \right) \right] \right\} \tag{3.1b}$$

$$\rho_s \left(\frac{\partial v}{\partial t} + U_s \frac{\partial v}{\partial x} + W_s \frac{\partial v}{\partial z} \right) = -\frac{\partial \pi}{\partial y} + \frac{1}{Re} \left\{ \frac{\partial}{\partial x} \left[\mu_s \left(\frac{\partial u}{\partial y} + \frac{\partial v}{\partial x} \right) + \mu \left(\frac{\partial U_s}{\partial y} \right) \right] \right.$$
$$\left. + \frac{\partial}{\partial y} \left[\mu_s \left(m \frac{\partial u}{\partial x} + r \frac{\partial v}{\partial y} + m \frac{\partial w}{\partial z} \right) \right] + \frac{\partial}{\partial z} \left[\mu_s \left(\frac{\partial v}{\partial z} + \frac{\partial w}{\partial y} \right) + \mu \left(\frac{\partial W_s}{\partial y} \right) \right] \right\} \tag{3.1c}$$

$$\rho_s \left(\frac{\partial w}{\partial t} + U_s \frac{\partial w}{\partial x} + v \frac{\partial W_s}{\partial y} + W_s \frac{\partial w}{\partial z} \right) = -\frac{\partial \pi}{\partial z} + \frac{1}{Re} \left\{ \frac{\partial}{\partial x} \left[\mu_s \left(\frac{\partial w}{\partial x} + \frac{\partial u}{\partial z} \right) \right] \right.$$
$$\left. + \frac{\partial}{\partial y} \left[\mu_s \left(\frac{\partial v}{\partial z} + \frac{\partial w}{\partial y} \right) + \mu \left(\frac{\partial W_s}{\partial y} \right) \right] + \frac{\partial}{\partial z} \left[\mu_s \left(m \frac{\partial u}{\partial x} + m \frac{\partial v}{\partial y} + r \frac{\partial w}{\partial z} \right) \right] \right\} \tag{3.1d}$$

$$\rho_s \left[\frac{\partial \theta}{\partial t} + U_s \frac{\partial \theta}{\partial x} + v \frac{\partial T_s}{\partial y} + W_s \frac{\partial \theta}{\partial z} \right] = (\gamma - 1) M_e^2 \left[\frac{\partial \pi}{\partial t} + U_s \frac{\partial \pi}{\partial x} + W_s \frac{\partial \pi}{\partial z} + \frac{1}{Re} \Phi \right]$$
$$+ \frac{1}{RePr} \left[\frac{\partial}{\partial x} \left(\mu_s \frac{\partial \theta}{\partial x} \right) + \frac{\partial}{\partial y} \left(\mu_s \frac{\partial \theta}{\partial y} + \mu \frac{\partial T_s}{\partial y} \right) + \frac{\partial}{\partial z} \left(\mu_s \frac{\partial \theta}{\partial z} \right) \right] \tag{3.1e}$$

$$\Phi = \mu_s \left\{ 2 \left(\frac{\partial u}{\partial y} + \frac{\partial v}{\partial x} \right) \left(\frac{\partial U_s}{\partial y} \right) + 2 \left(\frac{\partial v}{\partial z} + \frac{\partial w}{\partial y} \right) \left(\frac{\partial W_s}{\partial y} \right) \right\}$$
$$+ \mu \left\{ \left(\frac{\partial U_s}{\partial y} \right)^2 + \left(\frac{\partial W_s}{\partial y} \right)^2 \right\} \tag{3.1f}$$

$$\frac{\pi}{P_s} = \frac{\theta}{T_s} + \frac{\rho}{\rho_s} \tag{3.1g}$$

where Re is the Reynolds number, Pr is the Prandtl number, and γ is the specific heat ratio. Additionally, $r = 2(e+2)/3$, $m = 2(e-1)/3$ where $e = 0$ corresponds to the Stokes hypothesis. $U_s(y)$, $W_s(y)$, $T_s(y)$, and $\mu_s(y)$ are mean flow profiles.

Denoting $\mathbf{A} = (u, \partial u/\partial y, v, \pi, \theta, \partial \theta/\partial y, w, \partial w/\partial y)^T$ as the disturbance vector function, it is possible to rewrite the system of equations (3.1a-3.1f) in the following matrix operator form:

$$\frac{\partial}{\partial y} \left(\mathbf{L}_0 \frac{\partial \mathbf{A}}{\partial y} \right) + \frac{\partial \mathbf{A}}{\partial y} = \mathbf{H}_{10} \frac{\partial \mathbf{A}}{\partial t} + \mathbf{H}_{11} \mathbf{A} + \mathbf{H}_2 \frac{\partial \mathbf{A}}{\partial x} + \mathbf{H}_3 \frac{\partial^2 \mathbf{A}}{\partial x \partial y} + \mathbf{H}_4 \frac{\partial^2 \mathbf{A}}{\partial x^2}$$
$$+ \mathbf{H}_5 \frac{\partial \mathbf{A}}{\partial z} + \mathbf{H}_6 \frac{\partial^2 \mathbf{A}}{\partial x \partial z} + \mathbf{H}_7 \frac{\partial^2 \mathbf{A}}{\partial y \partial z} + \mathbf{H}_8 \frac{\partial^2 \mathbf{A}}{\partial z^2} \tag{3.2}$$

where $\mathbf{L}_0$, $\mathbf{H}_{10}$, $\mathbf{H}_{11}$, $\mathbf{H}_2$, $\mathbf{H}_3$, $\mathbf{H}_4$, $\mathbf{H}_5$, $\mathbf{H}_6$, $\mathbf{H}_7$ and $\mathbf{H}_8$ are 8×8 matrices, whose non-zero elements are presented in the Electronic Physics Auxiliary Publication Service (EPAPS) (see EPAPS Document No. E-PHFLE6-17-005509 for the non-zero elements of the matrices in

Eqs. (3.2) and (3.8); a direct link to this document may be found in the online articles HTML reference section; the document may also be reached via the EPAPS homepage (http://www.aip.org/pubservs/epaps.html) or from ftp.aip.org in the directory /epaps; see the EPAPS homepage for more information). At the initial time, $t = 0$, the disturbance vector is denoted as

$$\mathbf{A}(x, y, z, 0) = \mathbf{A}_0(x, y, z) \tag{3.3}$$

The boundary conditions are

$$\begin{aligned} y = 0: &\quad u = v = w = \theta = 0 \\ y \to \infty: &\quad |A_j| \to 0, \quad (j = 1, ..., 8) \end{aligned} \tag{3.4}$$

These boundary conditions correspond to the no-slip condition and zero temperature disturbance on the wall, and all disturbances decaying to zero far outside the boundary layer.

Solution of the initial-value problem

The three-dimensionality of both the boundary layer flow and the disturbance adds complexity to the problem. However, the problem can be solved using a similar approach to the one used in [FT03] for the two-dimensional wave packet. The problem is solved using a Fourier transform with respect to the streamwise coordinate, x, a Fourier transform with respect to the spanwise coordinate, z, and a Laplace transform with respect to time, t:

$$\mathbf{A}_{p\alpha\beta}(y) = \frac{1}{2\pi} \int_0^\infty e^{-pt} \int_{-\infty}^{\infty} e^{-i\alpha x} \int_{-\infty}^{\infty} e^{-i\beta z} \mathbf{A}(x, y, z, t) dz dx dt \tag{3.5}$$

By applying the transforms given by Eq. (3.5) to the problem (Eqs. 3.2-3.4), we arrive at a system of non-homogeneous ordinary differential equations for the amplitude vector $\mathbf{A}_{p\alpha\beta}$:

$$\begin{aligned} &\frac{d}{dy}(\mathbf{L}_0 \frac{d\mathbf{A}_{p\alpha\beta}}{dy}) + \frac{d\mathbf{A}_{p\alpha\beta}}{dy} = \mathbf{H}_{10} p \mathbf{A}_{p\alpha\beta} - \mathbf{H}_{10} \mathbf{A}_{0\alpha\beta} + \mathbf{H}_{11} \mathbf{A}_{p\alpha\beta} \\ &+ i\alpha \mathbf{H}_2 \mathbf{A}_{p\alpha\beta} + i\alpha \mathbf{H}_3 \frac{d\mathbf{A}_{p\alpha\beta}}{dy} - \alpha^2 \mathbf{H}_4 \mathbf{A}_{p\alpha\beta} + i\beta \mathbf{H}_5 \mathbf{A}_{p\alpha\beta} \\ &- \alpha\beta \mathbf{H}_6 \mathbf{A}_{p\alpha\beta} + i\beta \mathbf{H}_7 \frac{d\mathbf{A}_{p\alpha\beta}}{dy} - \beta^2 \mathbf{H}_8 \mathbf{A}_{p\alpha\beta} \end{aligned} \tag{3.6}$$

where $\mathbf{A}_{0\alpha\beta}(y)$ is the Fourier transform (with respect to both x and z) of $\mathbf{A}_0(x, y, z)$, the initial disturbance vector. The solution of Eq. (3.6) satisfies the boundary conditions

$$\begin{aligned} y = 0: &\quad \mathrm{A}_{p\alpha\beta 1} = A_{p\alpha\beta 3} = A_{p\alpha\beta 5} = A_{p\alpha\beta 7} = 0 \\ y \to \infty: &\quad |A_{p\alpha\beta j}| \to 0 \quad (j = 1, ..., 8) \end{aligned} \tag{3.7}$$

The non-homogeneous term in Eq. (3.6) is the term containing the Fourier transform of the initial disturbance, $\mathbf{A}_{0\alpha\beta}$. The remainder of the terms form the homogeneous part of

Eq. (3.6). This homogeneous equation can be recast as the following system of ordinary differential equations:

$$\frac{d\mathbf{A}_{p\alpha\beta}}{dy} = \mathbf{H}_0 \mathbf{A}_{p\alpha\beta} \tag{3.8}$$

where $\mathbf{H}_0$ is an 8×8 matrix, whose non-zero elements are presented in EPAPS. There are eight fundamental solutions, $\mathbf{z}_1, ..., \mathbf{z}_8$, of the homogeneous system of equations given by Eq. (3.8). Outside the boundary layer ($y \to \infty$), $\mathbf{H}_0$ is a matrix of constant coefficients, and thus each fundamental solution has an exponential asymptotic behavior $\exp(\lambda_j y)$, where $\lambda_1, ..., \lambda_8$ are determined from the characteristic equation

$$\det \|\mathbf{H}_0 - \lambda \mathbf{I}\| \tag{3.9}$$

For ($y \to \infty$), Eq. (3.9) can be written as

$$\left(b_{11} - \lambda^2\right) \times \left(b_{41} - \lambda^2\right) \times \left[\left(b_{22} - \lambda^2\right)\left(b_{33} - \lambda^2\right) - b_{23}b_{32}\right] = 0 \tag{3.10}$$

where

$$\begin{aligned}
b_{11} &= H_0^{21}, \\
b_{41} &= H_0^{87} = H_0^{21} = b_{11}, \\
b_{22} &= H_0^{42}H_0^{24} + H_0^{43}H_0^{34} + H_0^{46}H_0^{64} + H_0^{48}H_0^{84}, \\
b_{23} &= H_0^{42}H_0^{25} + H_0^{43}H_0^{35} + H_0^{46}H_0^{65} + H_0^{48}H_0^{85}, \\
b_{32} &= H_0^{64}, \\
b_{33} &= H_0^{65}
\end{aligned}$$

with H_0^{ij} denoting the (i, j) element of matrix $\mathbf{H}_0$.

The roots of Eq. (3.10) are

$$\begin{aligned}
\lambda_{1,2}^2 &= b_{11} = \alpha^2 + \beta^2 + iRe\left(\alpha + \beta W_{se} - ip\right), \\
\lambda_{3,4}^2 &= \left(b_{22} + b_{33}\right)/2 + \frac{1}{2}\sqrt{\left(b_{22} - b_{33}\right)^2 + 4b_{23}b_{32}}, \\
\lambda_{5,6}^2 &= \left(b_{22} + b_{33}\right)/2 - \frac{1}{2}\sqrt{\left(b_{22} - b_{33}\right)^2 + 4b_{23}b_{32}}, \\
\lambda_{7,8}^2 &= b_{41} = \alpha^2 + \beta^2 + iRe\left(\alpha + \beta W_{se} - ip\right)
\end{aligned} \tag{3.11}$$

where W_{se} is the mean-flow spanwise velocity at the upper boundary layer edge. The root branches are chosen to have $\text{Real}(\lambda_1, \lambda_3, \lambda_5, \lambda_7) < 0$ and we define a matrix of fundamental solutions

$$\mathbf{Z} = \|\mathbf{z}_1, ..., \mathbf{z}_8\| \tag{3.12}$$

The non-homogeneous system given by Eq. (3.6) has a solution expressed in the form

$$\mathbf{A}_{p\alpha\beta} = \mathbf{Z}\mathbf{Q}(y) \tag{3.13}$$

where the vector of coefficients $\mathbf{Q}(y)$ is found using the method of variation of parameters:

$$2\mathbf{L}_0 \frac{d\mathbf{Z}}{dy}\frac{d\mathbf{Q}}{dy} + \mathbf{L}_0\mathbf{Z}\frac{d^2\mathbf{Q}}{dy^2} + \frac{d\mathbf{L}_0}{dy}\mathbf{Z}\frac{d\mathbf{Q}}{dy} + \mathbf{Z}\frac{d\mathbf{Q}}{dy} - i\alpha\mathbf{H}_3\mathbf{Z}\frac{d\mathbf{Q}}{dy} - i\beta\mathbf{H}_7\mathbf{Z}\frac{d\mathbf{Q}}{dy} = \mathbf{F} \tag{3.14}$$

where $\mathbf{F} = -(\mathbf{H}_{10}\mathbf{A}_{0\alpha\beta})$. Since $\mathbf{Z}$ is the matrix of fundamental solutions of the homogeneous system of equations, it follows that $d\mathbf{Z}/dy = \mathbf{H}_0\mathbf{Z}$. Substitution of this relationship into Eq. (3.14) yields the system of equations

$$2\mathbf{L}_0\mathbf{H}_0\mathbf{Z}\frac{d\mathbf{Q}}{dy} + \mathbf{L}_0\mathbf{Z}\frac{d^2\mathbf{Q}}{dy^2} + \frac{d\mathbf{L}_0}{dy}\mathbf{Z}\frac{d\mathbf{Q}}{dy} + \mathbf{Z}\frac{d\mathbf{Q}}{dy} - i\alpha\mathbf{H}_3\mathbf{Z}\frac{d\mathbf{Q}}{dy} - i\beta\mathbf{H}_7\mathbf{Z}\frac{d\mathbf{Q}}{dy} = \mathbf{F} \tag{3.15}$$

Let us consider the individual equations of Eq. (3.15). Denoting z_{ij} to be the ith component of vector $\mathbf{z}_j$, Q_j to be the jth component of vector $\mathbf{Q}$, and F_j to be the jth component of vector $\mathbf{F}$, then the first, third, fifth, sixth and seventh equations of Eq. (3.15) are respectively:

$$z_{1j}\frac{dQ_j}{dy} = 0 \tag{3.16}$$

$$z_{3j}\frac{dQ_j}{dy} = F_3 \tag{3.17}$$

$$z_{5j}\frac{dQ_j}{dy} = 0 \tag{3.18}$$

$$z_{6j}\frac{dQ_j}{dy} = F_6 \tag{3.19}$$

$$z_{7j}\frac{dQ_j}{dy} = 0 \tag{3.20}$$

The second and eighth equations of Eq. (3.15) are respectively:

$$z_{2j}\frac{dQ_j}{dy} - i\alpha H_3^{23} z_{3j}\frac{dQ_j}{dy} = F_2 \tag{3.21}$$

$$z_{8j}\frac{dQ_j}{dy} - i\beta H_7^{83} z_{3j}\frac{dQ_j}{dy} = F_8 \tag{3.22}$$

Substitution of Eq. (3.17) into Eq. (3.21) and Eq. (3.22) leads to the following forms:

$$z_{2j}\frac{dQ_j}{dy} = F_2 + i\alpha H_3^{23} F_3 \tag{3.23}$$

$$z_{8j}\frac{dQ_j}{dy} = F_8 + i\beta H_7^{83} F_3 \tag{3.24}$$

The fourth equation of Eq. (3.15) is

$$2L_0^{43} H_0^{3i} z_{ij}\frac{dQ_j}{dy} + L_0^{43} z_{3j}\frac{d^2Q_j}{dy^2} + z_{4j}\frac{dQ_j}{dy} + \frac{dL_0^{43}}{dy} z_{3j}\frac{dQ_j}{dy} = F_4 \tag{3.25}$$

By considering only the non-zero elements of H_0^{3i}, Eq. (3.25) can be rewritten as

$$z_{4j}\frac{dQ_j}{dy} = \frac{F_4 - L_0^{43} H_0^{33} F_3 - \frac{d\left(L_0^{43} F_3\right)}{dy}}{1 + L_0^{43} H_0^{34}} \tag{3.26}$$

Therefore, the non-homogeneous system (3.15) can be rewritten as

$$\mathbf{Z}\frac{d\mathbf{Q}}{dy} = \varphi \tag{3.27}$$

with

$$\begin{aligned}
\varphi_1 &= 0, \\
\varphi_2 &= -\left(\mathbf{H}_{10}\mathbf{A}_{0\alpha\beta}\right)_2 - i\alpha H_3^{23}\left(\mathbf{H}_{10}\mathbf{A}_{0\alpha\beta}\right)_3, \\
\varphi_3 &= -\left(\mathbf{H}_{10}\mathbf{A}_{0\alpha\beta}\right)_3, \\
\varphi_4 &= \frac{1}{1+L_0^{43}H_0^{34}}\left\{-\left(\mathbf{H}_{10}\mathbf{A}_{0\alpha\beta}\right)_4 + L_0^{43}H_0^{33}\left(\mathbf{H}_{10}\mathbf{A}_{0\alpha\beta}\right)_3 + \frac{d\left(L_0^{43}\left(\mathbf{H}_{10}\mathbf{A}_{0\alpha\beta}\right)_3\right)}{dy}\right\}, \\
\varphi_5 &= 0, \\
\varphi_6 &= -\left(\mathbf{H}_{10}\mathbf{A}_{0\alpha\beta}\right)_6, \\
\varphi_7 &= 0, \\
\varphi_8 &= -\left(\mathbf{H}_{10}\mathbf{A}_{0\alpha\beta}\right)_8 - i\beta H_7^{83}\left(\mathbf{H}_{10}\mathbf{A}_{0\alpha\beta}\right)_3
\end{aligned}$$

The formal solution of Eq. (3.27) is expressed as

$$\mathbf{A}_{\mathrm{p}\alpha\beta} = \sum_{j=1}^{8}\left(a_j + \int_{y_j}^{y}\frac{dQ_j}{dy}dy\right)\mathbf{z}_j \tag{3.28}$$

where the constants a_j and y_j are determined using the boundary conditions given by Eq. (3.7). Using properties of determinants, we obtain the following solution:

$$\mathbf{A}_{p\alpha\beta} = \left(a_1 + \int_0^y \frac{dQ_1}{dy}dy\right)\mathbf{z}_1 + \int_\infty^y \frac{dQ_2}{dy}dy\mathbf{z}_2 + \left(a_3 + \int_0^y \frac{dQ_3}{dy}dy\right)\mathbf{z}_3 + \int_\infty^y \frac{dQ_4}{dy}dy\mathbf{z}_4 \quad (3.29a)$$
$$+ \left(a_5 + \int_0^y \frac{dQ_5}{dy}dy\right)\mathbf{z}_5 + \int_\infty^y \frac{dQ_6}{dy}dy\mathbf{z}_6 + \left(a_7 + \int_0^y \frac{dQ_7}{dy}dy\right)\mathbf{z}_7 + \int_\infty^y \frac{dQ_8}{dy}dy\mathbf{z}_8$$

$$a_1 = \frac{c_2E_{2357} + c_4E_{4357} + c_6E_{6357} + c_8E_{8357}}{E_{1357}}, \quad (3.29b)$$

$$a_3 = \frac{c_2E_{1257} + c_4E_{1457} + c_6E_{1657} + c_8E_{1857}}{E_{1357}}, \quad (3.29c)$$

$$a_5 = \frac{c_2E_{1327} + c_4E_{1347} + c_6E_{1367} + c_8E_{1387}}{E_{1357}}, \quad (3.29d)$$

$$a_7 = \frac{c_2E_{1352} + c_4E_{1354} + c_6E_{1356} + c_8E_{1358}}{E_{1357}}, \quad (3.29e)$$

$$c_j = \int_0^\infty \frac{dQ_j}{dy}dy, \quad (3.29f)$$

$$E_{ijkl} = \det \left\| \begin{matrix} z_{1i} & z_{1j} & z_{1k} & z_{1l} \\ z_{3i} & z_{3j} & z_{3k} & z_{3l} \\ z_{5i} & z_{5j} & z_{5k} & z_{5l} \\ z_{7i} & z_{7j} & z_{7k} & z_{7l} \end{matrix} \right\|_{y=0} \quad (3.29g)$$

Inverse Laplace transform

The inverse Laplace transform of Eq. (3.29a) is

$$\mathbf{A}_{\alpha\beta}(y,t;\alpha,\beta) = \frac{1}{2\pi i}\int_{p_0-i\infty}^{p_0+i\infty} \mathbf{A}_{p\alpha\beta}(y;p,\alpha,\beta)e^{pt}dp \quad (3.30)$$

Figure 3.1 shows a schematic of an appropriate integration contour for the inverse Laplace transform, which is determined by poles (relevant to the discrete spectrum) and by branch cuts (relevant to the continuous spectrum).

By integrating along the contour shown in figure 3.1, Eq. (3.30) can be written as a sum of integrals along the sides, γ^+ and γ^-, of each branch cut and a sum of residues resulting from the poles of Eq. (3.29a) given by the equation $E_{1357}(p) = 0$, i.e.

$$\mathbf{A}_{\alpha\beta} = -\frac{1}{2\pi i}\sum_m \left(\int_{\gamma_m^+} \mathbf{A}_{p\alpha\beta}e^{pt}dp + \int_{\gamma_m^-} \mathbf{A}_{p\alpha\beta}e^{pt}dp\right) + \sum_n \mathrm{Res}_n\left(\mathbf{A}_{p\alpha\beta}\ e^{pt}\right) \quad (3.31)$$

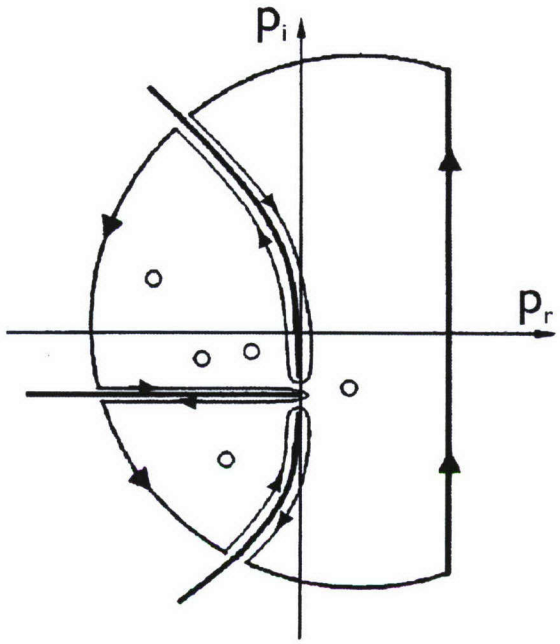

Figure 3.1: Integration contour for the inverse Laplace transform.

Discrete spectrum

Modes of the discrete spectrum correspond to poles of Eq. (3.29a), which are roots of $E_{1357}(p) = 0$, where E_{1357} is defined by Eq. (3.29g). Discrete modes arise from the situation when all the roots of Eq. (3.11) have non-zero real parts and are given by the poles' contribution to the inverse Laplace transform, i.e. the residues shown in Eq. (3.31). These residues have the form

$$\mathrm{Res}_n \left(\mathbf{A}_{p\alpha\beta} \, e^{pt} \right) = \mathbf{A}_n(y; p_n, \alpha, \beta) e^{p_n t} \tag{3.32}$$

with

$$\mathbf{A}_n = [a_1 \mathbf{z}_1 + a_3 \mathbf{z}_3 + a_5 \mathbf{z}_5 + a_7 \mathbf{z}_7] \times \left[\frac{\partial E_{1357}}{\partial p} (p_n) \right]^{-1} \tag{3.33}$$

where a_1, a_3, a_5 and a_7 are given by Eqs. (3.29b-3.29e). If the eigenvalue $p_n = -i\omega_n$ belongs to the discrete spectrum, then the associated eigenfunction $\mathbf{A}_n$ decays exponentially outside the boundary layer ($y \to \infty$).

To illustrate features of the spectrum, we consider a boundary layer over an adiabatic sharp cone at zero angle of attack. The length scale is $L^* = \sqrt{(\mu_e^* x^* / \rho_e^* U_e^*)}$ and the Reynolds number is $Re = \sqrt{(\rho_e^* U_e^* x^* / \mu_e^*)}$. Using the Lees-Dorodnitsyn transformation [Jr.89], we solve the conical problem with boundary layer profiles for a flat plate. Accordingly, all conical results presented hereafter can be adjusted to the flat plate boundary layer by dividing the parameters Re, α, β and ω by $\sqrt{3}$.

The standard form for the direct problem given by Eq. (3.8) was used for the numerical evaluations. The numerical scheme performs the integration of Eq. (3.8) for four fundamental solutions (discrete spectrum) or for five fundamental solutions (continuous spectrum). A fourth order Runge-Kutta integration method with constant step (301 points) was used to integrate from outside the boundary layer ($y_{\max} = 25$) toward the wall using the Gram-Schmidt orthonormalization procedure.

When analyzing the continuous spectrum, k is a parameter, and the frequency ω is calculated using $\lambda_j^2 = -k^2$, where λ_j are given by Eq. (3.11). When analyzing the discrete spectrum, ω is calculated using Newton's iteration method. This iteration method depends on the initial approach to ω. A two-domain Chebyshev spectral collocation method [Mal90] was used to determine the initial approach.

To maintain consistency with the 2D problem analyzed in [FT03], we choose the following parameter values: $M = 5.6$, $Re = 1219.5$, $Pr = 0.7$, $\gamma = 1.4$, $e = 0$ with an adiabatic wall and stagnation temperature $T_0 = 470K$.

Two discrete modes are of interest. One of the discrete modes will be referred to as "Mode F", where "F" stands for "fast"; this is the mode whose phase speed approaches that of the fast acoustic mode as $\alpha \to 0$ (2D case). Another discrete mode will be referred to as "Mode S", where "S" stands for "slow"; this is the mode whose phase speed approaches that of the slow acoustic mode as $\alpha \to 0$ (2D case). Even though in the 3D case, synchronism with the fast and slow acoustic modes as $\alpha \to 0$ may no longer occur, the behavior of each Mode curve (3D) is similar to the behavior of the corresponding 2D Mode curve. Thus, it should not be confusing to refer to the 3D curves as "Mode F" and "Mode S".

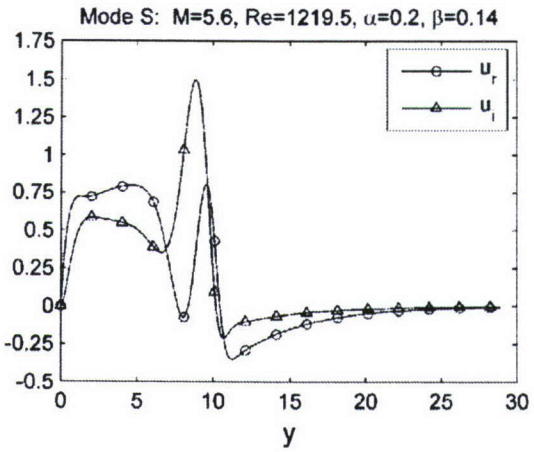

Figure 3.2: Streamwise velocity disturbance of Mode S.

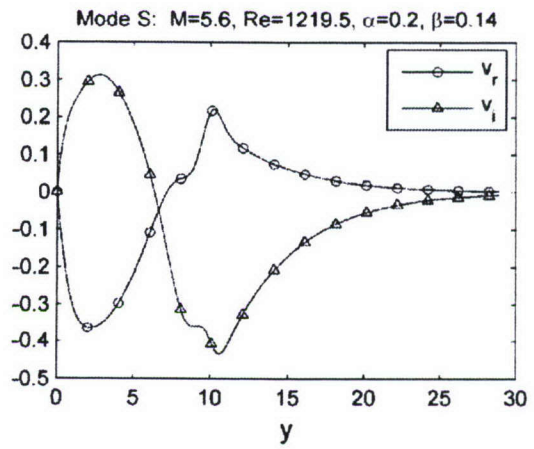

Figure 3.3: Normal velocity disturbance of Mode S.

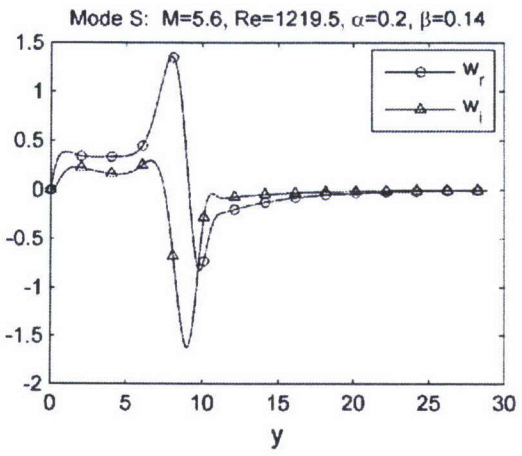

Figure 3.4: Spanwise velocity disturbance of Mode S.

As an example, figures 3.2, 3.3 and 3.4 show the distribution for the streamwise, normal and spanwise velocity disturbances corresponding to Mode S for $\alpha = 0.2$, $\beta = 0.14$, with complex-valued eigenvalue $\omega = 0.18291 + i3.95 \times 10^{-5}$ (this choice of parameters corresponds to a disturbance propagation angle of $\psi \approx 35°$, where $\tan\psi = \beta/\alpha$). Figures 3.5 and 3.6 show respectively the pressure and temperature disturbances corresponding to this mode.

Continuous spectrum

Modes of the continuous spectrum correspond to branch cuts of Eq. (3.29a). Solutions of the continuous spectrum arise from the situation when a characteristic number λ_j given by Eq. (3.11) is purely imaginary ($\lambda_j^2 = -k^2$, $k > 0$, $j = 1, ..., 8$). As in the two-dimensional case discussed in [FT03], the first pure oscillatory solution corresponds to $\lambda_{1,2}^2 = -k^2$. This equation, along with Eq. (3.11), leads to the following (different from the 2D case) relation:

$$p_{c,1} = -i\left(\alpha + \beta W_{se}\right) - \left(k^2 + \alpha^2 + \beta^2\right)/Re \tag{3.34}$$

As in the 2D case, this solution is interpreted as a vorticity branch, where the vorticity disturbances are propagating with a phase speed of $c = 1$. The equation

$$\left(b_{22} - \lambda^2\right)\left(b_{33} - \lambda^2\right) - b_{23}b_{32} = 0 \tag{3.35}$$

is a third degree polynomial in p and has three roots at $\lambda^2 = -k^2$. These roots ($p_{c,2}$, $p_{c,3}$, $p_{c,4}$) were computed numerically for the case when $W_{se} = 0$ (2D mean flow). Figure 3.7 shows the results for $\alpha = 0.2$, $\beta = 0.14$. The horizontal branch in figure 3.7 has a finite limiting point and is interpreted as an entropy branch, where the entropy disturbances are propagating with a phase speed of $c = 1$. The vorticity branch given by Eq. (3.34) overlaps the entropy branch. The upper and lower branches in figure 3.7 are associated with fast and slow acoustic waves. These waves travel with the respective phase speeds $c = 1 \pm \frac{\sqrt{1+\beta^2/\alpha^2}}{M_e}$.

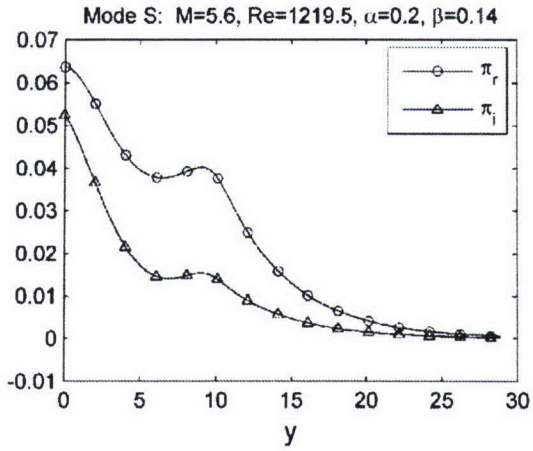

Figure 3.5: Pressure disturbance of Mode S.

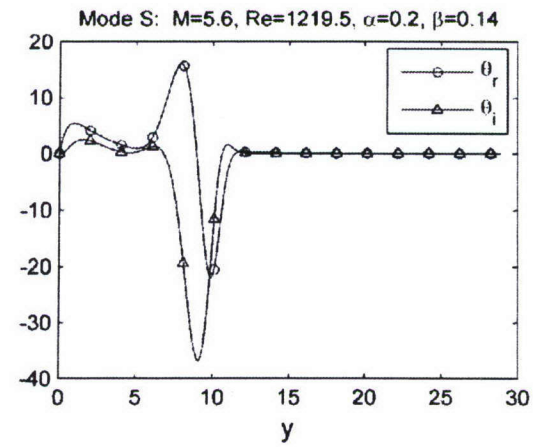

Figure 3.6: Temperature disturbance of Mode S.

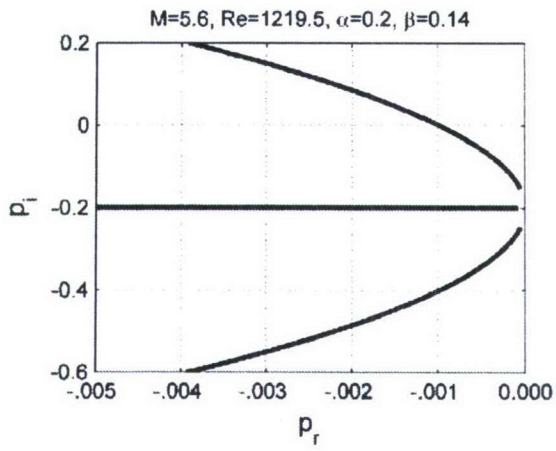

Figure 3.7: Branch cuts of the continuous spectrum in the complex plane $p = -i\omega$.

The fifth pure oscillatory solution is an additional solution not found for the 2D case. The equation, $\lambda_{7,8}^2 = -k^2$, along with Eq. (3.11), leads to the relation:

$$p_{c,5} = -i\left(\alpha + \beta W_s\right) - \left(k^2 + \alpha^2 + \beta^2\right)/Re \tag{3.36}$$

Eq. (3.36) is identical to Eq. (3.34). The fifth relation is also interpreted as a vorticity branch, where the vorticity disturbances are propagating with a phase speed of $c = 1$. The existence of two vorticity modes reflects the three-dimensionality of the perturbations.

As in the 2D case, it is possible to find compact forms for the solutions of the various regions of the continuous spectrum. Using a similar technique to that used in [FT03], we denote one side of each branch cut as '+' and the other side of the branch cut as '−' in accordance with the asymptotic behavior of the type of disturbance being considered. By relating $\mathbf{z}_j^+$ to $\mathbf{z}_j^-$ and dQ_j^+/dy to dQ_j^-/dy, the integrals along the branch cut sides γ^+ and γ^- can be written as one integral of the difference $\mathbf{A}_{p\alpha\beta}^+ - \mathbf{A}_{p\alpha\beta}^-$.

Solutions for the acoustic waves include five fundamental vector functions, three of which decay outside the boundary layer, and two of which oscillate as $e^{\pm iky}$. $\mathbf{A}_{p\alpha\beta}^+ - \mathbf{A}_{p\alpha\beta}^-$ can be written solely in terms of the functions on the '+' side of the branch cut as

$$\begin{aligned}\mathbf{A}_{p\alpha\beta}^+ - \mathbf{A}_{p\alpha\beta}^- = &\left(\frac{c_2 E_{1275}}{E_{1753}E_{1754}} + \frac{c_3 E_{1753}}{E_{1753}E_{1754}} + \frac{c_4 E_{1754}}{E_{1753}E_{1754}} + \frac{c_6 E_{1756}}{E_{1753}E_{1754}} + \frac{c_8 E_{7185}}{E_{1753}E_{1754}}\right) \times \\ &\left(E_{5734}\mathbf{z}_1 + E_{1754}\mathbf{z}_3 + E_{7153}\mathbf{z}_4 + E_{7134}\mathbf{z}_5 + E_{1534}\mathbf{z}_7\right)\end{aligned} \tag{3.37}$$

The horizontal branch cut in the 2D case has a region of overlapping vorticity and entropy disturbances. The remainder of the branch cut is a region of vorticity disturbances. In the 3D problem, the entire branch cut contains a region of overlapping vorticity modes, and there is a region of the branch cut that has entropy disturbances overlapping the two vorticity modes.

In the region of overlapping vorticity modes, there is an uncertainty. There are six fundamental solutions (four oscillating and two decaying) in this region; however, this number of fundamental solutions is larger than is needed to satisfy the boundary conditions. This difficulty is resolved using the technique described above in obtaining Eq. (3.37). The solution can be expressed as a sum of two stand-alone vorticity modes as follows

$$\mathbf{A}^{+}_{p\alpha\beta} - \mathbf{A}^{-}_{p\alpha\beta} = \mathbf{A}_{c,1} + \mathbf{A}_{c,5} \tag{3.38}$$

where

$$\begin{aligned}\mathbf{A}_{c,1} = &\left(\frac{c_1 E_{1753}}{E_{1753}E_{2753}} + \frac{c_2 E_{2753}}{E_{1753}E_{2753}} + \frac{c_4 E_{4753}}{E_{1753}E_{2753}} + \frac{c_6 E_{6753}}{E_{1753}E_{2753}} + \frac{c_8 E_{8753}}{E_{1753}E_{2753}}\right) \times \\ &(E_{2753}\mathbf{z}_1 - E_{1753}\mathbf{z}_2 + E_{1275}\mathbf{z}_3 + E_{1723}\mathbf{z}_5 + E_{1253}\mathbf{z}_7)\end{aligned} \tag{3.39}$$

and

$$\begin{aligned}\mathbf{A}_{c,5} = &\left(\frac{c_1 E_{1253}}{E_{2753}E_{2853}} + \frac{c_4 E_{5234}}{E_{2753}E_{2853}} + \frac{c_6 E_{2563}}{E_{2753}E_{2853}} + \frac{c_7 E_{7253}}{E_{2753}E_{2853}} + \frac{c_8 E_{8253}}{E_{2753}E_{2853}}\right) \times \\ &(E_{7853}\mathbf{z}_2 + E_{2785}\mathbf{z}_3 - E_{2783}\mathbf{z}_5 - E_{2853}\mathbf{z}_7 + E_{2753}\mathbf{z}_8)\end{aligned} \tag{3.40}$$

Both Eq. (3.39) and Eq. (3.40) satisfy the boundary conditions on the wall.

In the region of three overlapping modes (two vorticity and entropy), there also exists an uncertainty. There are seven fundamental solutions in this region (six oscillating and one decaying). Again, this number of fundamental solutions is larger than is needed to satisfy the boundary conditions. This difficulty is resolved using the technique described above in obtaining Eq. (3.37), and since the region of three overlapping modes has not been encountered before, we shall show the derivation of the solution. In this overlapping region, we denote one side of the branch cut as '+' and the other side of the branch cut as '−' in accordance with the asymptotic behavior:

$$\mathbf{z}_1^+ \sim e^{iky},\ \mathbf{z}_1^- \sim e^{-iky},\ \mathbf{z}_2^+ \sim e^{-iky}, \tag{3.41a}$$

$$\mathbf{z}_2^- \sim e^{iky},\ \mathbf{z}_3^+ \sim e^{\lambda_3 y},\ \mathbf{z}_3^- \sim e^{\lambda_3 y}, \tag{3.41b}$$

$$\mathbf{z}_4^+ \sim e^{\lambda_4 y},\ \mathbf{z}_4^- \sim e^{\lambda_4 y},\ \mathbf{z}_5^+ \sim e^{ik_1 y}, \tag{3.41c}$$

$$\mathbf{z}_5^- \sim e^{-ik_1 y},\ \mathbf{z}_6^+ \sim e^{-ik_1 y},\ \mathbf{z}_6^- \sim e^{ik_1 y}, \tag{3.41d}$$

$$\mathbf{z}_7^+ \sim e^{iky},\ \mathbf{z}_7^- \sim e^{-iky},\ \mathbf{z}_8^+ \sim e^{-iky},\ \mathbf{z}_8^- \sim e^{iky} \tag{3.41e}$$

where k and k_1 are real, positive parameters, and $\lambda_{3,4}$ are given by Eq. (3.11). It is possible

to obtain the relations

$$\mathbf{z}_1^- = \mathbf{z}_2^+,\ \mathbf{z}_2^- = \mathbf{z}_1^+,\ \mathbf{z}_3^- = \mathbf{z}_3^+,\ \mathbf{z}_4^- = \mathbf{z}_4^+, \tag{3.42a}$$

$$\mathbf{z}_5^- = \mathbf{z}_6^+,\ \mathbf{z}_6^- = \mathbf{z}_5^+,\ \mathbf{z}_7^- = \mathbf{z}_8^+,\ \mathbf{z}_8^- = \mathbf{z}_7^+, \tag{3.42b}$$

$$\frac{dQ_1}{dy}^- = \frac{dQ_2}{dy}^+,\ \frac{dQ_2}{dy}^- = \frac{dQ_1}{dy}^+, \tag{3.42c}$$

$$\frac{dQ_3}{dy}^- = \frac{dQ_4}{dy}^+,\ \frac{dQ_4}{dy}^- = \frac{dQ_3}{dy}^+, \tag{3.42d}$$

$$\frac{dQ_5}{dy}^- = \frac{dQ_6}{dy}^+,\ \frac{dQ_6}{dy}^- = \frac{dQ_5}{dy}^+, \tag{3.42e}$$

$$\frac{dQ_7}{dy}^- = \frac{dQ_7}{dy}^+,\ \frac{dQ_8}{dy}^- = \frac{dQ_8}{dy}^+, \tag{3.42f}$$

The integrals along the branch cut sides γ^+ and γ^- can be written as one integral of the difference

$$\begin{aligned}
\mathbf{A}^+_{p\alpha\beta} - \mathbf{A}^-_{p\alpha\beta} = &\left(a_1^+ + \int_0^y \frac{dQ_1}{dy}^+ dy\right)\mathbf{z}_1^+ + \int_\infty^y \frac{dQ_2}{dy}^+ dy\mathbf{z}_2^+ + \left(a_3^+ + \int_0^y \frac{dQ_3}{dy}^+ dy\right)\mathbf{z}_3^+ \\
&+ \int_\infty^y \frac{dQ_4}{dy}^+ dy\mathbf{z}_4^+ + \left(a_5^+ + \int_0^y \frac{dQ_5}{dy}^+ dy\right)\mathbf{z}_5^+ + \int_\infty^y \frac{dQ_6}{dy}^+ dy\mathbf{z}_6^+ + \left(a_7^+ + \int_0^y \frac{dQ_7}{dy}^+ dy\right)\mathbf{z}_7^+ \\
&+ \int_\infty^y \frac{dQ_8}{dy}^+ dy\mathbf{z}_8^+ - \left(a_1^- + \int_0^y \frac{dQ_1}{dy}^- dy\right)\mathbf{z}_1^- - \int_\infty^y \frac{dQ_2}{dy}^- dy\mathbf{z}_2^- - \left(a_3^- + \int_0^y \frac{dQ_3}{dy}^- dy\right)\mathbf{z}_3^- \\
&- \int_\infty^y \frac{dQ_4}{dy}^- dy\mathbf{z}_4^- - \left(a_5^- + \int_0^y \frac{dQ_5}{dy}^- dy\right)\mathbf{z}_5^- + \int_\infty^y \frac{dQ_6}{dy}^- dy\mathbf{z}_6^- - \left(a_7^- + \int_0^y \frac{dQ_7}{dy}^- dy\right)\mathbf{z}_7^- \\
&- \int_\infty^y \frac{dQ_8}{dy}^- dy\mathbf{z}_8^-
\end{aligned} \tag{3.43}$$

After substitution of the relations given in Eqs. (3.41a-3.41e) and (3.42a-3.42f), simplification leads to the following expression

$$\begin{aligned}
\mathbf{A}^+_{p\alpha\beta} - \mathbf{A}^-_{p\alpha\beta} = &\left(a_1^+ + c_1^+\right)\mathbf{z}_1^+ - \left(c_2^+ + a_1^-\right)\mathbf{z}_2^+ + \left(a_3^+ - a_3^-\right)\mathbf{z}_3^+ + \left(a_5^+ + c_5^+\right)\mathbf{z}_5^+ \\
&- \left(a_5^- + c_6^+\right)\mathbf{z}_6^+ + \left(a_7^+ + c_7^+\right)\mathbf{z}_7^+ - \left(c_8^+ + a_7^-\right)\mathbf{z}_8^+
\end{aligned} \tag{3.44}$$

Equation (3.44) can be expressed in the compact form

$$\mathbf{A}^+_{p\alpha\beta} - \mathbf{A}^-_{p\alpha\beta} = \mathbf{A}_{c,1} + \mathbf{A}_{c,2} + \mathbf{A}_{c,5} \tag{3.45}$$

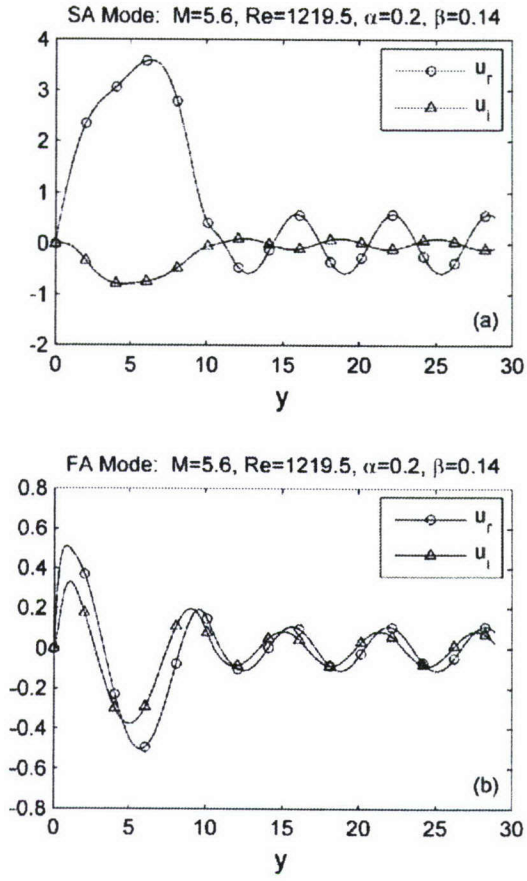

Figure 3.8: Streamwise velocity disturbance of the acoustic mode - (a) slow (b) fast.

where $\mathbf{A}_{c,1}$ and $\mathbf{A}_{c,5}$ are given by Eqs. (3.39) and (3.40) and with

$$\mathbf{A}_{c,2} = \left(\frac{c_1 E_{1283}}{E_{2853} E_{2863}} - \frac{c_4 E_{2834}}{E_{2853} E_{2863}} + \frac{c_5 E_{2853}}{E_{2853} E_{2863}} + \frac{c_6 E_{2863}}{E_{2853} E_{2863}} - \frac{c_7 E_{2783}}{E_{2853} E_{2863}} \right) \times \\ (E_{8563}\mathbf{z}_2 + E_{2856}\mathbf{z}_3 + E_{2863}\mathbf{z}_5 - E_{2853}\mathbf{z}_6 - E_{2563}\mathbf{z}_8) \tag{3.46}$$

Each term in Eq. (3.45) satisfies the boundary conditions on the wall and can be interpreted as a stand-alone mode.

As an example, figures 3.8 and 3.9 show the distribution of the streamwise and spanwise velocity for both slow and fast acoustic disturbances.

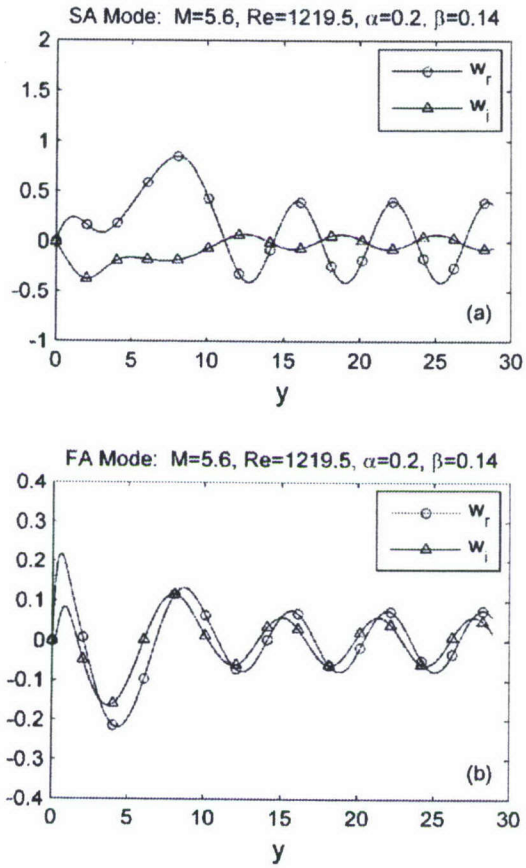

Figure 3.9: Spanwise velocity disturbance of the acoustic mode - (a) slow (b) fast.

Summary

We can now express the inverse Laplace transform given by Eq. (3.31) as

$$\mathbf{A}_{\alpha\beta}(y,t;\alpha,\beta) = -\frac{1}{2\pi i}\sum_{m=1}^{5}\int_{0}^{\infty}\mathbf{A}_{c,m}(y;k,\alpha,\beta)e^{p_{c,m}(k)t}\frac{dp_{c,m}}{dk}dk + \sum_{n}\mathbf{A}_{n}(y;p_n,\alpha,\beta)e^{p_n t} \tag{3.47}$$

where $m = 1$ corresponds to one vorticity wave, with $p_{c,1}$ and $\mathbf{A}_{c,1}$ given by Eqs. (3.34) and (3.39) respectively; $m = 2$ corresponds to the entropy wave, with $p_{c,2}$ and $\mathbf{A}_{c,2}$ given by Eqs. (3.35) and (3.46) respectively; $m = 3,4$ correspond to slow and fast acoustic waves, with $p_{c,3,4}$ and $\mathbf{A}_{c,3,4}$ given by Eqs. (3.35) and (3.37) respectively; $m = 5$ corresponds to the second vorticity wave, with $p_{c,5}$ and $\mathbf{A}_{c,5}$ given by Eqs. (3.36) and (3.40) respectively; p_n is a root of $E_{1357}(p) = 0$, and $\mathbf{A}_n$ is given by Eq. (3.33).

Biorthogonal system of eigenfunctions

Following [SG81], it is possible to express a solution of the initial-value problem (Eq. (3.47)) as an expansion in the biorthogonal eigenfunction system $\{\mathbf{A}_\omega, \mathbf{B}_\omega\}$, where the vector $\mathbf{A}_\omega$ is a solution of the direct problem and the vector $\mathbf{B}_\omega$ is a solution of the adjoint problem. There is an orthogonality relation associated with the biorthogonal eigenfunction system. This orthogonality relation, along with the Fourier transform of the initial data, can be used to compute the coefficients associated with each of the discrete and continuous modes. Further details can be found in B.1.

Synchronism of Mode S and Mode F with acoustic waves

In the 2D problem, Mode S and Mode F are synchronized respectively with the slow and fast acoustic modes for a wave number $\alpha \to 0$. Figure 3.10 shows numerical results for eigenvalues ω_r of Mode F for a fixed choice of spanwise wave number β. Included in figure 3.10 are lines of constant phase speed. One of these is a line of phase speed $c = 1$, the speed at which the entropy and vorticity disturbances travel. The other lines are associated with fast acoustic modes (FA Mode) and slow acoustic modes (SA Mode) for $\beta = 0.0001$ (2D) and $\beta = 0.1601$. The fast/slow acoustic waves travel with phase speed $c = 1 \pm \frac{\sqrt{1+\beta^2/\alpha^2}}{M_e}$. Figure 3.10 shows that Mode F for both $\beta = 0.0001$ and $\beta = 0.1601$ is a subsonic disturbance relative to the free stream for $\alpha < 0.37$ and is a supersonic disturbance relative to the free stream for $\alpha > 0.37$. Furthermore, although it is not shown in any figure, these disturbances are everywhere decaying. To obtain a clearer picture of what is occurring at the lower wave numbers, figure 3.11 shows a section of figure 3.10.

As can be seen in figure 3.11, just as Mode F at $\beta = 0.0001$ is synchronized with the $\beta = 0.0001$ fast acoustic mode at a wave number $\alpha < 0.1$, Mode F at $\beta = 0.1601$ is synchronized with the $\beta = 0.1601$ fast acoustic modes at a wave number $\alpha < 0.1$.

Figure 3.12 shows numerical results for eigenvalues ω_r of Mode S for a fixed choice of spanwise wave number. Also included in figure 3.12 are lines of constant phase speed for

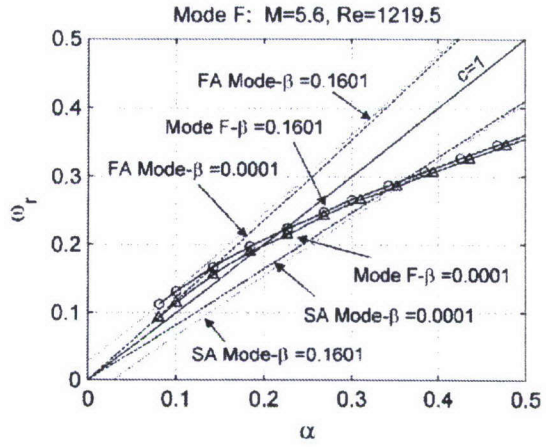

Figure 3.10: Eigenvalues for Mode F for $\beta = 0.0001$ and $\beta = 0.1601$.

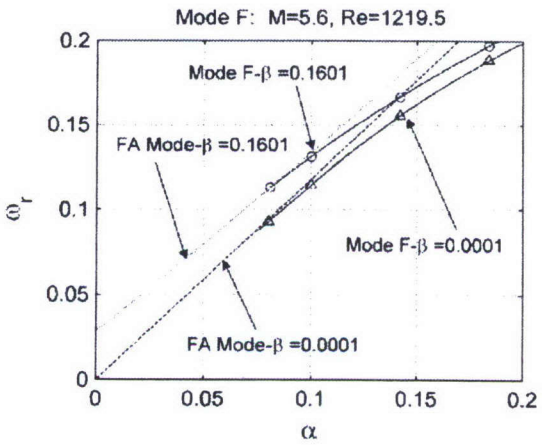

Figure 3.11: Figure 3.10 at low wave number.

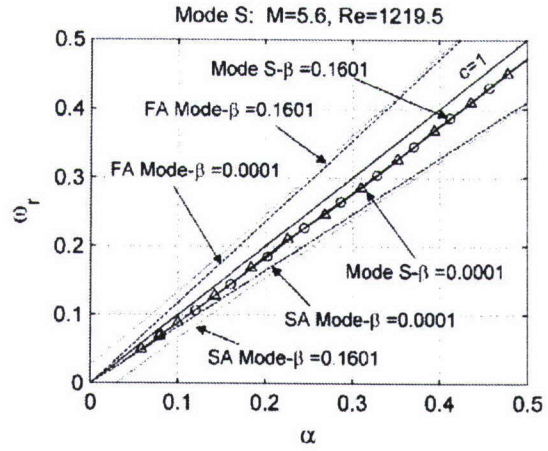

Figure 3.12: Eigenvalues for Mode S for $\beta = 0.0001$ and $\beta = 0.1601$.

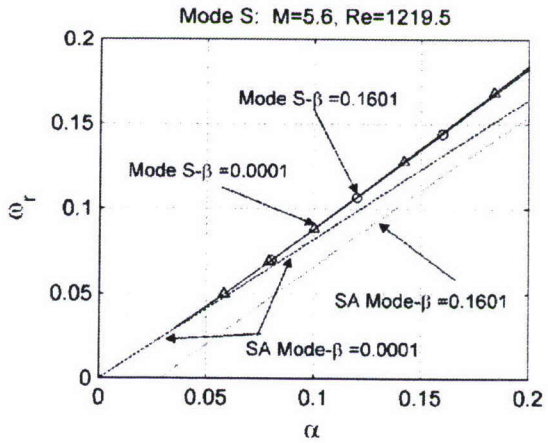

Figure 3.13: Figure 3.12 at low wave number.

the FA Mode and SA Mode for $\beta = 0.0001$ and $\beta = 0.1601$. The two Mode S curves are virtually overlapping. In order to gain a clearer view of what is occurring at the lower wave numbers, figure 3.13 shows a section of figure 3.12.

In contrast to Mode F, figure 3.13 clearly shows that Mode S for both choices of β is asymptotically approaching the SA Mode for $\beta = 0.0001$. We have observed this behavior at every choice of β that we have checked. Even though Mode S for various choices of β (3D) approach the SA Mode for $\beta = 0.0001$, there is no synchronism between the two. The primary synchronism of Mode S with acoustic waves for $\alpha < 0.1$ is two-dimensional (2D Mode S with the 2D SA Mode).

Synchronism of Mode F with entropy and vorticity waves

Figure 3.14 shows eigenvalues of Mode F for $\psi = 0°$ and $\psi = 60°$. One can see that for $\psi = 0°$, Mode F is subsonic relative to the free stream for $\alpha < 0.35$ and is supersonic relative to the free stream for $\alpha > 0.35$. However, for $\psi = 60°$, Mode F is subsonic relative to the free stream for this entire range of α. It can also be seen that Mode F for both angles of disturbance propagation is everywhere decaying.

Furthermore, figure 3.14 shows the synchronism between the 2D Mode F and the entropy and vorticity modes of the phase speed $c = 1$. In the 2D case, as the discrete mode coalesces with the continuous spectrum from one side of the branch cut, it reappears on the other side at another point. Mathematically, the pole associated with Mode F approaches one side of the branch cut on the complex p plane. At the same time, another pole, located on the lower Riemann sheet, approaches the branch cut from the opposite side. As the pole on the plane coalesces with the branch cut, it moves to the upper Riemann sheet, while simultaneously, the pole that was on the lower Riemann sheet moves into the complex p plane at another point [FT03]. This leads to a jump in ω_i. As the angle increases, the synchronism continues, but the jump-size decreases, until it is seen that for $\psi = 60°$, there is neither a synchronism, nor a jump in ω_i, at least for this interval of wave number α. Figure 3.15 shows contours of ω_i in the $\alpha - \beta$ wave number plane. One can see the jump location for choices of α and β. Also plotted in the figure is a small region bounding the branch cut. This region is denoted by the dashed lines. We have done this in lieu of plotting the branch cut, since the branch cut plot obscures the jumps in ω_i. It is clear that the discontinuity of ω_i is associated with the synchronism of Mode F and the entropy and vorticity waves. For large values of β, it appears that no jump is seen in figure 3.15 at the location of the branch cut. A jump does in fact exist, but the size of the jump is small enough so that it cannot be seen on the scale of this figure.

By plotting lines of constant angle, it is seen that the synchronism between Mode F and the entropy and vorticity waves vanishes for large enough angles.

Synchronism of Mode S with Mode F

Figure 3.16 shows the eigenvalue curves for Mode S and Mode F for $\psi = 30°$. The Mode S curve given by the imaginary part of the eigenvalue ω_i contains two regions of instability.

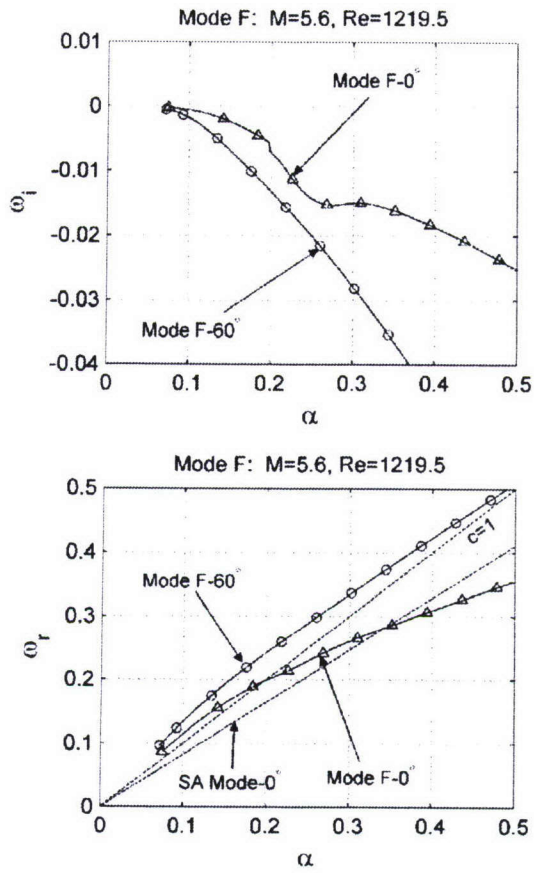

Figure 3.14: Eigenvalues for Mode F for $\psi = 0°$ and $\psi = 60°$.

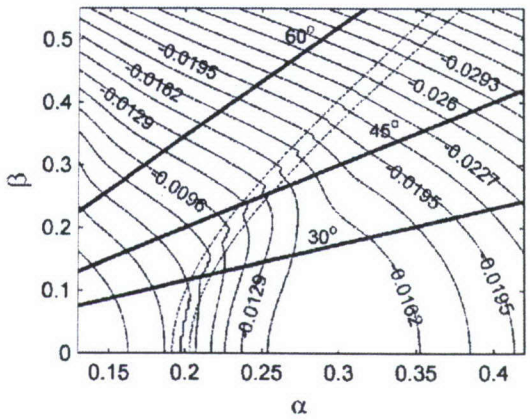

Figure 3.15: Contours of ω_i in the $\alpha - \beta$ plane.

The unstable region located at $\alpha = 0.12$ is equivalent to Mack's first mode. The unstable region located at $\alpha = 0.26$ is equivalent to Mack's second mode. Further details regarding the relation between Mode S and Mode F and Macks acoustic modes can be found in the Discussion paragraph. The range of α is extended to $\alpha = 0.5$ in order to show the decaying behavior of both Mode S and Mode F for larger values of α.

In the 2D case, Mode F is synchronized with Mode S. This synchronism is indicative of the fact that the discrete spectrum has a branch point at α^* in the complex α plane. True synchronism (Mode S and Mode F have the same value of ω_i as well as the same value of ω_r) occurs at α^*, which may have a different real part from where Mode S's value of ω_r is equal to Mode F's value of ω_r. At values of $\alpha > \alpha_r^*$, the disturbance spectrum branches out: Mode S becomes unstable while Mode F becomes more stable (the topological pattern may be sensitive to the mean flow parameters, such as Mach number, Prandtl number and temperature factor; further details can be found in [FK01]).

As seen in figure 3.16, this Mode S instability continues for a disturbance propagating at $\psi = 30°$ (near $\alpha \approx 0.23$). For larger angles, though, even though there is still synchronism between Mode S and Mode F, the synchronism is no longer accompanied by a Mode S instability. This behavior can be seen for a disturbance propagating at $\psi = 45°$ in figure 3.17. Even though it cannot be seen in figure 3.17, plots of the pressure disturbance indicate that there is a switch from the Mack first mode to the Mack second mode. However, for this disturbance propagation angle, there is no amplified Mack second mode.

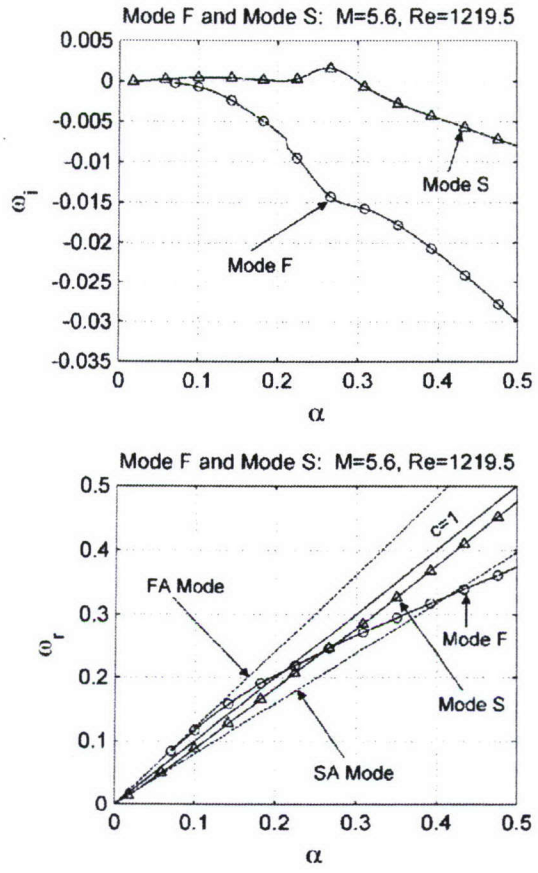

Figure 3.16: Eigenvalues for Mode F and Mode S for $\psi = 30°$.

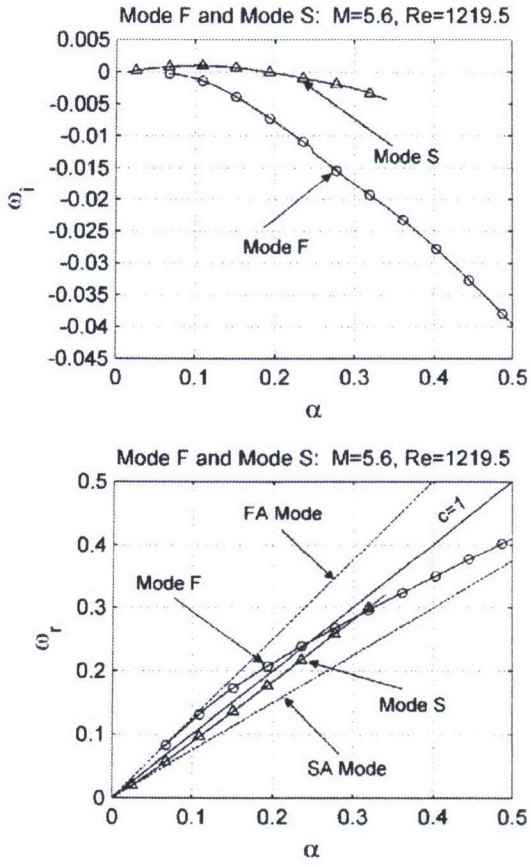

Figure 3.17: Eigenvalues for Mode F and Mode S for $\psi = 45°$.

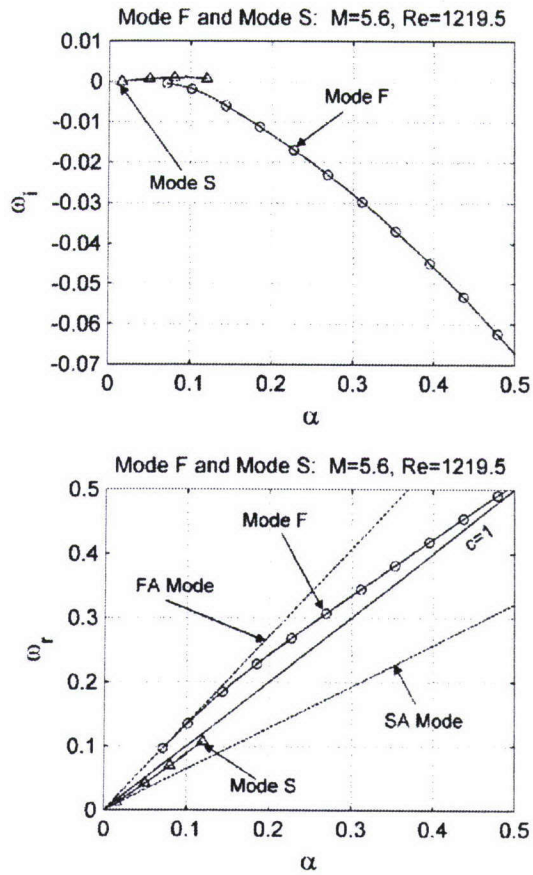

Figure 3.18: Eigenvalues for Mode F and Mode S for $\psi = 60°$.

In figure 3.18, one can see that at even higher angles of disturbance propagation, there is no synchronism between Mode S and Mode F. Additionally, at this angle, the Mode S curve consists entirely of the Mack first mode.

Discussion

In order to avoid confusion, we now discuss Mack's [Mac69, Mac84] results and how they relate to Mode S and Mode F. Mack first considered inviscid perturbations and computed eigenvalue curves or families for various choices of parameters. Each of these families contains an unstable region corresponding to one of the higher Mack modes (first mode, second mode, third mode, etc.), and each amplification rate curve represents a distinct discrete mode. Using asymptotic analysis, [GF89] also captured the feature that each amplified first mode, second mode, etc. represents a separate solution.

Mack then considered viscous perturbations and computed families of eigenvalues for finite Reynolds numbers and compared the eigenvalue curves with the inviscid ones. For one of Mack's choices of parameters, there were two "separate inviscid amplification rate curves for the first and second modes" (page 12-24 of [Mac69]) (i.e. two inviscid normal modes), but "only a single amplification rate curve at the finite Reynolds number shown" (page 12-24 of [Mac69]) (i.e. one viscous normal mode). This one viscous solution was comprised of both the first mode and the second mode. This viscous family is analogous to the Mode S mentioned in prior sections. Mode S in our analysis is a single discrete mode that corresponds to a single pole in the complex p plane. Furthermore, Mode S is comprised of Macks amplified first, second and possibly higher modes.

Additionally, Mack explained how "the inviscid solutions are to be the $\mathrm{Re} \to \infty$ limit of the viscous solutions" (page 12-25 of [Mac69]) through "the existence of multiple viscous solutions" (page 12-25 of [Mac69]). For the Reynolds number of his example, this additional viscous solution is damped, and it is analogous to the Mode F mentioned in prior sections. We would like to point out that [MZ03a, MZ03b] and [ZM02] refer to Mode F as Mode I and refer to Mode S, not as a single family, but rather to the parts that comprise the family (Mack's first mode, second mode, etc.).

Mack used a nomenclature for these viscous families that was based on his inviscid nomenclature. However, at the time, the receptivity problem was not understood, and the decomposition of the solutions of the linearized Navier-Stokes equations had not been developed. We therefore suggest keeping the terminology corresponding to the normal mode analysis. The normal modes, Mode S and Mode F, are represented by separate poles in the complex plane, and they may be synchronized with slow and fast acoustic waves at a wave number $\alpha \to 0$.

Conclusions

In this Section we solve the three-dimensional initial-value problem for disturbances propagating in a compressible boundary layer in the parallel flow approximation. After resolving the issue with overlapping branch cuts, we showed that the solution can also be expressed as an expansion in a biorthogonal eigenfunction system. A numerical example that is used to investigate the spectrum of three-dimensional disturbances in a two-dimensional high speed boundary layer flow leads to the following conclusions:

1. Mode S and Mode F are eigenvalue curves that correspond to separate solutions. Mathematically, each curve is the trajectory of a single pole in the complex p plane.

2. Mode S contains regions of Mack first and second modes. Our results are consistent with Mack's [Mac69, Mac84] in so far as the Mode S region comprised of Mack's second mode is most unstable to 2D disturbances, and the Mode S region comprised of Mack's first mode is most unstable to a 3D disturbance.

3. The discrete spectrum can change dramatically depending on the angle of the disturbance propagation.

4. Eigenvalue plots for choices of fixed spanwise wave number, β, show that the synchronism of Mode S with the slow acoustic mode is primarily two-dimensional.

5. At a sufficiently high angle of disturbance propagation, Mode F ceases to synchronize with the entropy and vorticity modes.

6. At a sufficiently high angle of disturbance propagation, the synchronism of Mode S and Mode F is no longer accompanied by a Mode S instability. At even higher angles, there is no synchronism between Mode S and Mode F.

The synchronism observed in the example means that the phase velocities of the modes are the same. However, their complex eigenvalues are different. When the parallel flow assumption is used, as it has been for this analysis, the normal modes are orthogonal to one another and therefore do not interact with each other. However, this analysis may be extended to the case of non-parallel flow through the use of multiple scale methods. There will be a slow and a fast scale. At the level of the fast scale, the analysis shown here for parallel flow will be valid. At the level of the slow scale, the normal modes will interact and hence, one mode may be generated by another mode at the point of synchronism. Analysis of a non-parallel boundary layer flow was performed by [FK01] for the spatial stability problem. They showed that Mode F may be generated by the vorticity/entropy modes. This decaying Mode F may then effectively generate an unstable Mode S. Additionally, this behavior has been seen in numerical studies for the spatial stability problem. Therefore, the features of the 3D spectrum found in our analysis of the initial-value problem might have a significant impact on the transition scenario in high speed boundary layers. All the features discussed must be taken into account when designing transition experiments in hypersonic flows.

3.3 Three-dimensional wave packets

This section is devoted to the application of the developed solution of the initial-value problem.

Receptivity to a Temperature Spot

As an example of an initial disturbance, we consider a temperature spot localized at a distance Y_0 from the wall. For the 3D initial-value problem, this disturbance will have the form

$$\theta(x,y,z) = \delta(x)\delta(y-Y_0)\delta(z) \quad \text{at} \quad t=0. \tag{3.48}$$

The orthogonality condition given by Eq. (B.15) allows one to determine the weights of the modes generated by the temperature spot. For Mode F and Mode S, the weight is given by

$$c(\alpha,\beta) = \frac{\langle \boldsymbol{H}_{10}\boldsymbol{A}_{0\alpha\beta}, \boldsymbol{B}_{\omega}\rangle}{\Gamma}, \tag{3.49}$$

where $\omega(\alpha,\beta)$ corresponds to the eigenvalue for the mode of interest. For a temperature spot of the form given by Eq. (3.48), it is possible to use the definition of $\boldsymbol{H}_{10}$ to obtain from Eq. (3.49) the expression

$$c(\alpha,\beta) = \frac{H_{10}^{35}(Y_0)\,\boldsymbol{B}_{\omega 3}(Y_0) + H_{10}^{65}(Y_0)\,\boldsymbol{B}_{\omega 6}(Y_0)}{\Gamma}, \tag{3.50}$$

with H_{10}^{ij} denoting the (i,j) element of matrix $\boldsymbol{H}_{10}$.

The coefficient $c(\alpha,\beta)$ depends on the normalization of the eigenfunction $\boldsymbol{A}_{\omega}$. However, the product $c(\alpha,\beta)\,\boldsymbol{A}_{\omega}$ is independent of the choice of normalization. We would like to normalize the eigenfunction so that the maximum value of u is 1. However, for our choice of parameters, there are two local maxima. We therefore choose to normalize the eigenfunction so that the value of the inner maximum is 1 (i.e. we normalize $\boldsymbol{A}_{\omega}$ as $u_{\max}$ = inner maximum of $u(y) = 1$). The normalized value of the outer maximum may be greater than 1. With this normalization, c is the amplitude of the maximum streamwise velocity component $u_{\max}$ associated with the appropriate mode.

As a limiting case, as $\beta \to 0$, one obtains the receptivity coefficient associated with the 2D initial-value problem [FT03].

Inverse Fourier Transform - 2D

The solution (before application of the two inverse Fourier transforms) is denoted as $\boldsymbol{A}_{\alpha\beta}$ and is given by Eq. (B.16). In the 2D case, the solution (before application of one inverse Fourier transform) is denoted as $\boldsymbol{A}_{\alpha}$ and will have a form similar to that of the 3D case. The 2D inverse Fourier transform is given by

$$\int_{-\infty}^{\infty} c(\alpha)\,\boldsymbol{A}_{\alpha}(\alpha,y)\,e^{i(\alpha x-\omega(\alpha)t)}\,d\alpha. \tag{3.51}$$

As an example, we consider the streamwise velocity component, u, of the disturbance vector, $\boldsymbol{A}$. The transform we are therefore interested in is given as

$$\int_{-\infty}^{\infty} c(\alpha)\, u(\alpha, y)\, e^{i(\alpha x - \omega(\alpha) t)}\, d\alpha, \tag{3.52}$$

where the coefficient $c(\alpha)$ is, for this example, the amplitude of the maximum streamwise velocity component $u_{\max}$. Expression (3.52) is transformed using a symmetry argument. Using the direct and complex conjugate matrix operator equations, when α is replaced by $-\alpha$, i.e., when $\alpha \rightarrow -\alpha$, it can be shown that $\omega \rightarrow -\overline{\omega}$, $c \rightarrow \overline{c}$, and $u \rightarrow \overline{u}$, where the overbar stands for complex conjugate. Therefore, (3.52) can be rewritten as

$$\int_{-\infty}^{\infty} c(\alpha)\, u(\alpha, y)\, e^{i(\alpha x - \omega(\alpha) t)}\, d\alpha = \tag{3.53a}$$

$$2 \int_{0}^{\infty} \text{Real}\left\{ c(\alpha)\, u(\alpha, y)\, e^{i(\alpha x - \omega(\alpha) t)} \right\} d\alpha. \tag{3.53b}$$

In the computation, we ignore the factor of 2. For the purpose of analysis, the Mode F and Mode S wave packets are considered separately.

Mode F

Figure 3.19(a) shows the imaginary part of the eigenvalue ω_i for Mode F. Figure 3.19(b) shows the maximum streamwise velocity amplitude, $u_{\max}$, at $t = 0$ for Mode F, which is generated by α components of the temperature spot located at varying normal distances Y_0 from the wall. One can see from figure 3.19(b) that there is little to no receptivity to a temperature spot located at $Y_0 < 5$ and $Y_0 > 11$.

The integral given by (3.53b) is numerically computed from $\alpha = 0.1$ to $\alpha = 0.5$. We were unable to calculate the Mode F eigenvalues below $\alpha \approx 0.08$ (figure 3.19(a)). However, for a finite time, the input into the integral for $\alpha < 0.1$ is not significant since the receptivity coefficient, $u_{\max}$, is close to 0 for this range of α (figure 3.19(b)). Beyond this finite time, the main input into the integral will come from the piece of Mode F with the largest values of ω_i (as $\alpha \rightarrow 0$), and this range of α should be considered.

Figure 3.19(b) also shows that the largest values of $u_{\max}$ occur near $\alpha \approx 0.27$. This fact, coupled with the fact that Mode F is everywhere decaying, suggests that there will not be much input into the integral for $\alpha > 0.5$ if a sufficiently large time, t, is chosen.

There is a synchronism between Mode F and the entropy and vorticity modes. As the discrete mode coalesces with the continuous spectrum from one side of the branch cut, it reappears on the other side at another point. This leads to the jump in ω_i seen in figure 3.19(a).

Figure 3.20 shows contours of ω_i in the complex α plane. One can see the jumps in ω_i along a nearly vertical line. As (3.53b) is integrated from $\alpha = 0.1$ to $\alpha = 0.5$, we must consider the continuous spectrum along with Mode F at the point of coalescence. To make the

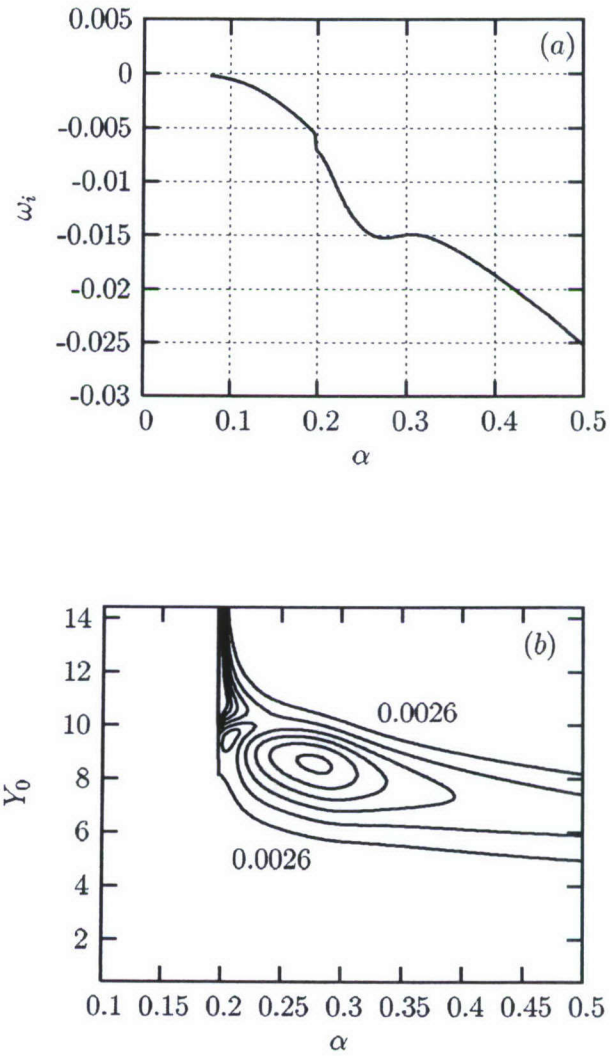

Figure 3.19: (a) Imaginary part of the eigenvalue for Mode F and (b) contours of $u_{\max}$ at $t = 0$ generated by α components of the temperature spot located at Y_0. The contour levels in (b) range from 0.0026 to 0.0156 in increments of 0.0026.

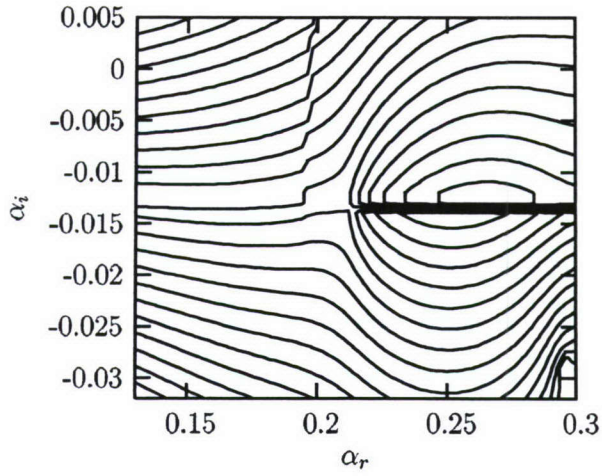

Figure 3.20: Contours of ω_i in the complex α plane. The contours range from -0.0298 at the bottom of the figure to 0.0028 at the top of the figure in increments of 0.0015.

analysis less complicated, we analytically continue the path of integration into the complex α plane in order to avoid the discontinuities associated with the coalescence of Mode F with the continuous spectrum. Therefore, the computed result is obtained using only Mode F. However, had we considered the sum of Mode F and the continuous spectrum and integrated along the real α axis, we would obtain the same result. Figure 3.21 is a schematic of an appropriate integration path. Due to the analyticity of the function being integrated, the result should be independent of the path of integration.

Using $Y_0 = 8.9$ (the edge of the boundary layer is located at $y \approx 10$), $t = 50$ and the integration path, Path 1, (3.53b) is integrated. Using the letters found in figure 3.21 (with points A, B, E and F located on the real axis), Path 1 is given explicitly as the following: At point A, $\alpha = 0.1$. At point B, $\alpha = 0.17$. At point C, $\alpha = 0.17 - 0.015i$. At point D, $\alpha = 0.2 - 0.015i$. At point E, $\alpha = 0.2$, and at point F, $\alpha = 0.5$.

The result is shown in figure 3.22(a) as contours of u in the $x - y$ plane. To better illustrate the Mode F wave packet, figure 3.22(b) shows a slice of figure 3.22(a) taken at $y = 2.02$.

To illustrate the decay of the wave packet in time, (3.53b) is integrated again using Path 1 and $Y_0 = 8.9$ for $t = 200$. Figure 3.23 shows the result taken at the slice $y = 2.02$. When figure 3.23 is compared to figure 3.22(b), one sees that u is an order of magnitude smaller for $t = 200$ than for $t = 50$. This order of magnitude decrease in amplitude is consistent with $\omega_i \approx -0.015$ (figure 3.19(a)). Additionally, the wave packet is seen to have moved downstream with the increase in time. By comparison of figure 3.23 to figure 3.22(b), one can also estimate the Mode F wave packet group velocity to be $\partial\omega_r/\partial\alpha \approx 0.65$. One can

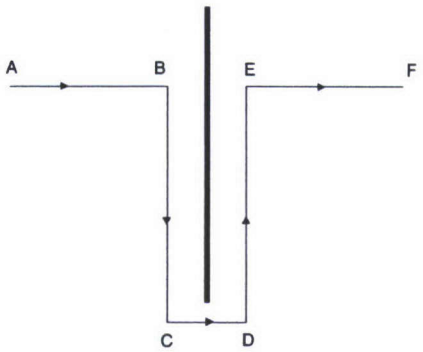

Figure 3.21: Schematic picture of an integration path around the branch cut.

see from figure 3.10 (Mode F eigenvalue curve for $\beta = 0.0001$ (2D)) in Section 3.2 that the group velocity estimate is very reasonable.

For the two times considered, we expect the main input into the integral to come from the receptivity coefficient. Figure 3.24 shows the amplitude spectrum for Mode F for both $t = 50$ and $t = 200$. This figure shows that the main input for both $t = 50$ and $t = 200$ occurs at an α value that corresponds favorably with the maximum values of $u_{\max}$ for a temperature spot located at $Y_0 = 8.9$ (figure 3.19(b)). As time increases, the main input to the integral will no longer come from the receptivity coefficient, but rather from the $e^{-i\omega(\alpha)t}$ component of the integrand at low α. Therefore, we expect the amplitude peak to be located at low values of α for large times. For $t = 200$, figure 3.24 shows that the amplitude peak has begun this shift to lower values of α. Also, figure 3.24 clearly shows the decay of Mode F in time.

To ensure that these results are independent of the choice of path of integration, the results shown for $Y_0 = 8.9$ at $t = 50$ using Path 1 are compared with results found using three other paths of integration. Using the letters found in figure 3.21, Paths 2,3 and 4 are given as follows:
Path 2 - At point A, $\alpha = 0.1$. At point B, $\alpha = 0.15$. At point C, $\alpha = 0.15 - 0.015i$. At point D, $\alpha = 0.2 - 0.015i$. At point E, $\alpha = 0.2$, and at point F, $\alpha = 0.5$.
Path 3 - At point A, $\alpha = 0.1$. At point B, $\alpha = 0.15$. At point C, $\alpha = 0.15 - 0.015i$. At point D, $\alpha = 0.21 - 0.015i$. At point E, $\alpha = 0.21$, and at point F, $\alpha = 0.5$.
Path 4 - At point A, $\alpha = 0.1$. At point B, $\alpha = 0.17$. At point C, $\alpha = 0.17 - 0.031i$. At point D, $\alpha = 0.2 - 0.031i$. At point E, $\alpha = 0.2$, and at point F, $\alpha = 0.5$.
To compare the results, figure 3.25 shows the wave packet at the slice $y = 2.02$ for each choice of integration path.

There is good agreement between the results obtained using the four different integration paths. A portion of each path of integration passes through a region of the complex α plane where $\alpha_i < 0$. This leads to numerical error associated with growth from the $e^{i\alpha x}$ term in the integrand. Since Path 3 has a longer portion of its path in the negative complex α plane, this

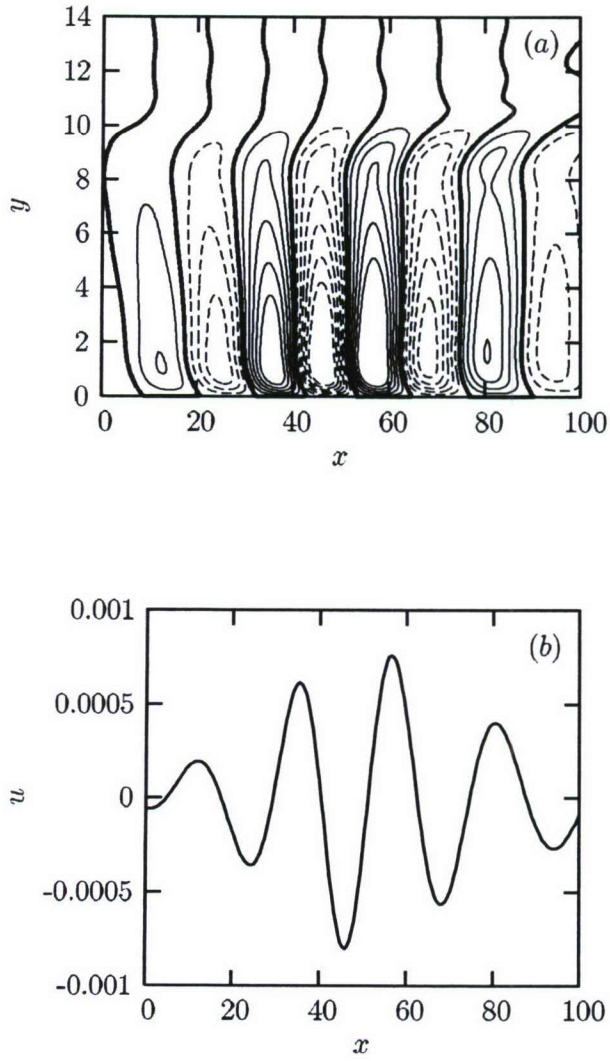

Figure 3.22: (a) Contours of u in the $x-y$ plane and (b) streamwise velocity disturbance, u, at $y = 2.02$ for $t = 50$. The contour levels in (a) are spaced in increments of 0.0001. The solid contours are positive; the dashed contours are negative; the bold contours are 0.

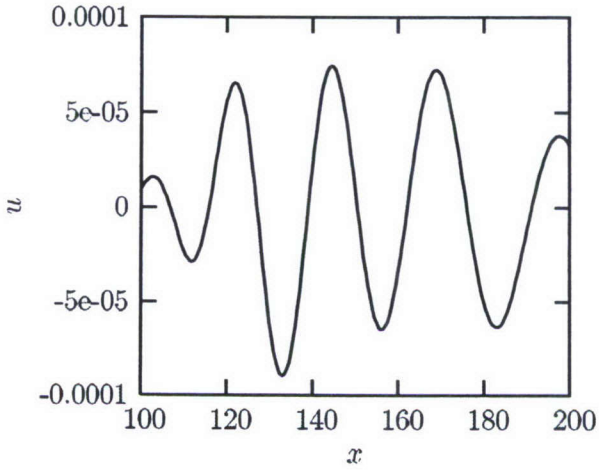

Figure 3.23: Streamwise velocity disturbance, u, at $y = 2.02$ for $t = 200$.

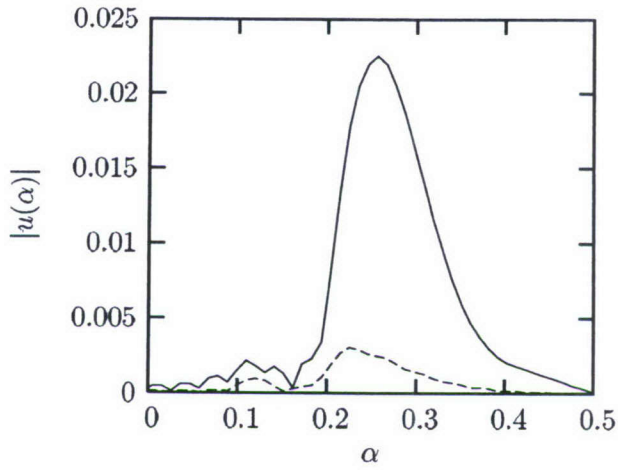

Figure 3.24: Amplitude spectrum of Mode F for $t = 50$ (solid line) and $t = 200$ (dashed line).

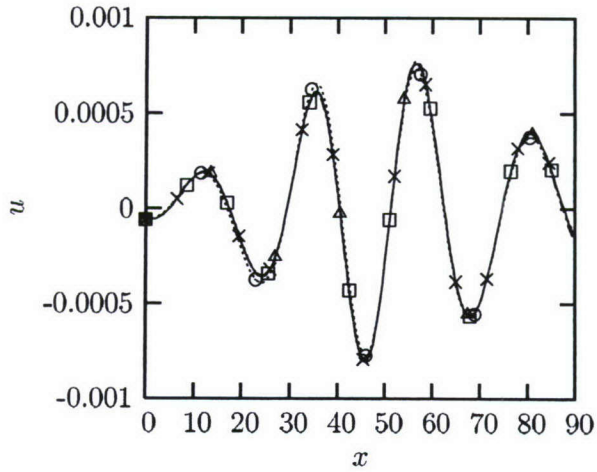

Figure 3.25: Streamwise velocity disturbance, u, at $y = 2.02$ for $t = 50$ for 4 paths of integration. The Path 1 result is denoted with "cross" markers; the Path 2 result with "square" markers; the Path 3 result with "circle" markers; the Path 4 result with "triangle" markers.

phenomena explains why the Path 3 result differs from the other three results (this deviation is difficult to see at the scale used for figure 3.25).

Mode S

Figure 3.26(a) shows the imaginary part of the eigenvalue ω_i for Mode S. Figure 3.26(b) shows the maximum streamwise velocity amplitude, $u_{\max}$, at $t = 0$ for Mode S, which is generated by α components of the temperature spot located at varying normal distances Y_0 from the wall.

The integral given by (3.53b) is numerically computed from $\alpha = 0.1$ to $\alpha = 0.5$. The greatest input into the integral will be from the region of $\alpha \approx 0.2$ to $\alpha \approx 0.3$. It is in this region that the receptivity coefficient, $u_{\max}$, is the highest, and it is also in this region where ω_i attains its largest value. Beyond $\alpha = 0.5$, Mode S is decaying, so that for sufficiently large times, there will not be significant input into the integral for $\alpha > 0.5$.

Unlike the Mode F case, there is no need to deform the path of integration to compute the Mode S inverse Fourier transform. The result for $Y_0 = 8.9$ at $t = 500$ is shown in figure 3.27(a) as contours of u in the $x - y$ plane. To better illustrate the Mode S wave packet, figure 3.27(b) shows a slice of figure 3.27(a) taken at $y = 2.02$.

We expect that the main input into the integral will come from the Gaussian shaped growth portion of the Mode S eigenvalue plot (figure 3.26(a)). Figure 3.28 shows the

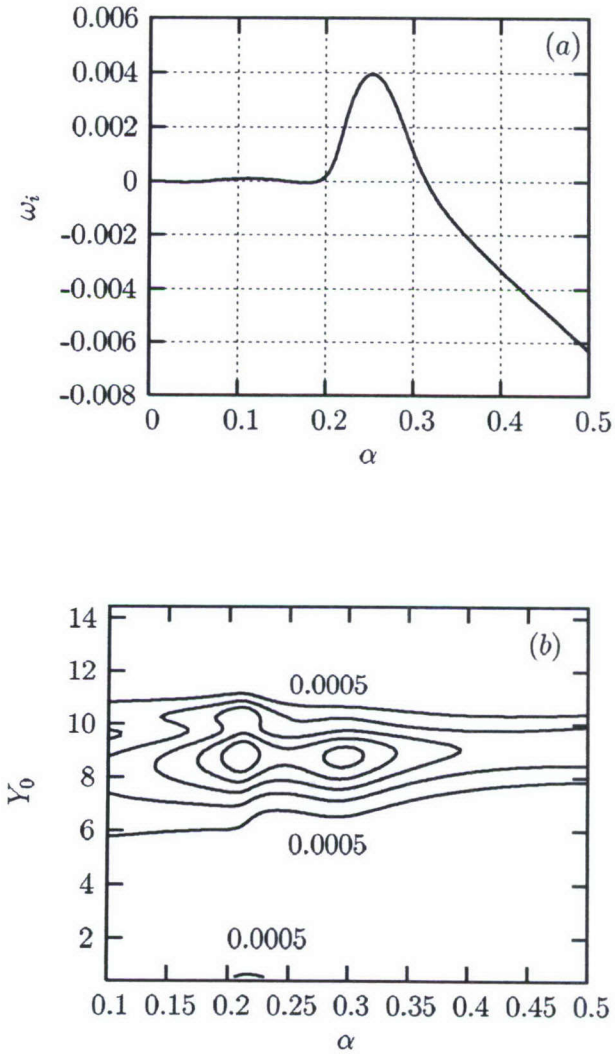

Figure 3.26: (a) Imaginary part of the eigenvalue for Mode S and (b) contours of $u_{\max}$ at $t = 0$ generated by α components of the temperature spot located at Y_0. The contour levels in (b) range from 0.0005 to 0.0025 in increments of 0.0005.

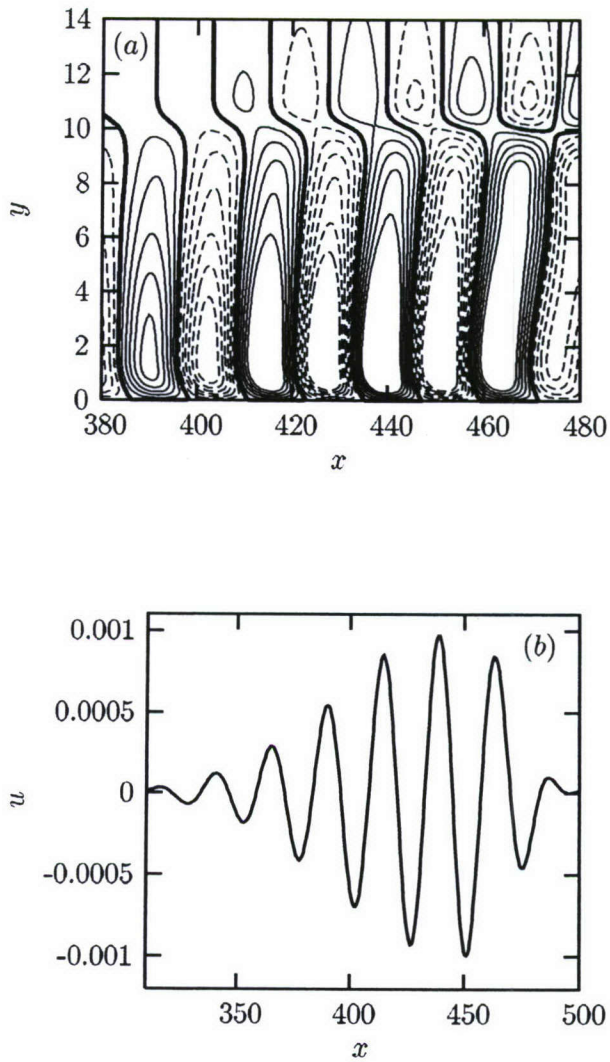

Figure 3.27: (a) Contours of u in the $x - y$ plane and (b) streamwise velocity disturbance, u, at $y = 2.02$ for $t = 500$. The contour levels in (a) are spaced in increments of 0.0001. The solid contours are positive; the dashed contours are negative; the bold contours are 0.

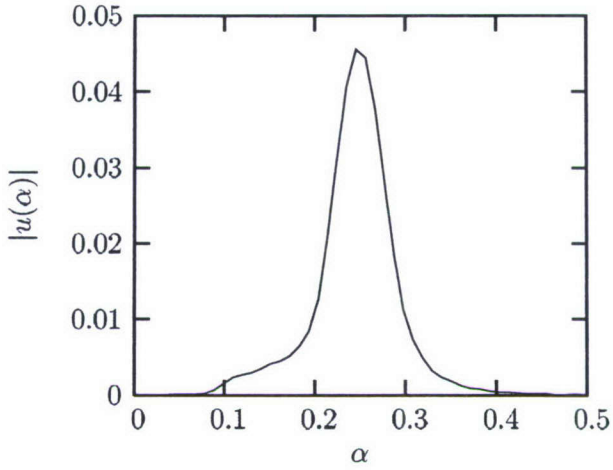

Figure 3.28: Amplitude spectrum of Mode S for $t = 500$.

amplitude spectrum of Mode S for $t = 500$. This figure shows that the main input occurs at an α value that compares favorably with the location of the Gaussian peak (figure 3.26(a)).

Asymptotic approximation with Taylor series expansion of $\omega(\alpha)$

Because the eigenvalue plot for Mode S contains a region where $\omega_i > 0$, the Mode S wave packet, unlike the Mode F wave packet, will grow in time (and downstream). It is useful to compare the Mode S computed inverse Fourier transform with an asymptotic approximation of the Fourier integral.

The development of 2D and 3D wave packets comprised of spatially growing discrete modes for incompressible boundary layer flows (parallel and non-parallel) has been considered previously by Gaster [Gas81, Gas82, Gas68]. In particular, Gaster used the method of steepest descent to find the asymptotic representation of integrals of the form given by (3.53b). Starting with (3.53b), we have the following:

$$\int_{-\infty}^{\infty} c(\alpha)\, u(\alpha, y)\, e^{i(\alpha x - \omega(\alpha) t)}\, d\alpha =$$
$$\int_{-\infty}^{\infty} c(\alpha)\, u(\alpha, y)\, e^{it\left(\alpha \frac{x}{t} - \omega(\alpha)\right)}\, d\alpha. \tag{3.54}$$

Assuming that the saddle point lies near the point $\alpha_{\max}$, we approximate $\omega(\alpha)$ as

$$\omega(\alpha) \approx \omega_{\max} + (\alpha - \alpha_{\max}) \left(\frac{\partial \omega}{\partial \alpha}\right)_{\max} + \frac{1}{2}(\alpha - \alpha_{\max})^2 \left(\frac{\partial^2 \omega}{\partial \alpha^2}\right)_{\max}, \tag{3.55}$$

where $(\partial\omega/\partial\alpha)_{\max}$ is real valued. To find the saddle point, α^*, at a prescribed x/t, we let $\phi(\alpha) = \alpha x/t - \omega(\alpha)$ and derive the following:

$$\left(\frac{\partial \phi}{\partial \alpha}\right)^* = \frac{x}{t} - \left(\frac{\partial \omega}{\partial \alpha}\right)_{\max} - (\alpha^* - \alpha_{\max}) \left(\frac{\partial^2 \omega}{\partial \alpha^2}\right)_{\max} = 0. \tag{3.56}$$

Solving for α^*, one obtains

$$\alpha^* = \alpha_{\max} + \frac{\frac{x}{t} - \left(\frac{\partial \omega}{\partial \alpha}\right)_{\max}}{\left(\frac{\partial^2 \omega}{\partial \alpha^2}\right)_{\max}}. \tag{3.57}$$

Equation (3.57) can be rewritten as

$$\alpha^* = \alpha_{\max} + \frac{x - x_{\max}}{t\left(\frac{\partial^2 \omega}{\partial \alpha^2}\right)_{\max}}, \tag{3.58}$$

where $x_{\max} = t\left(\partial\omega/\partial\alpha\right)_{\max}$.
Expression (3.54) can now be rewritten as

$$c(\alpha^*)\, u(\alpha^*, y) \int_L e^{it\left(\phi(\alpha^*) + \frac{1}{2}(\alpha - \alpha_{\max})^2 \phi''(\alpha^*)\right)} d\alpha = \tag{3.59a}$$

$$c(\alpha^*)\, u(\alpha^*, y) \sqrt{-\frac{2\pi}{it\phi''(\alpha^*)}} e^{it\phi(\alpha^*)} = \tag{3.59b}$$

$$c(\alpha^*)\, u(\alpha^*, y) \sqrt{\frac{2\pi}{it\left(\frac{\partial^2 \omega}{\partial \alpha^2}\right)_{\max}}} e^{it\phi(\alpha^*)}, \tag{3.59c}$$

where L is the contour of integration that has been deformed to pass through the saddle point, the prime ($'$) symbol denotes differentiation with respect to α, and $\phi'' = -\partial^2\omega/\partial\alpha^2$.

After substitution of α^* into (3.59c), the asymptotic representation of the original Fourier integral is given as:

$$c(\alpha^*)\ u(\alpha^*, y) \sqrt{\frac{2\pi}{it\left(\frac{\partial^2 \omega}{\partial \alpha^2}\right)_{\max}}} \times \exp\left(i\alpha_{\max} x + \frac{i(x - x_{\max})^2}{2t\left(\frac{\partial^2 \omega}{\partial \alpha^2}\right)_{\max}} - i\omega_{\max} t\right). \tag{3.60}$$

Actually, the use of a 2nd order Taylor series expansion of $\omega(\alpha)$ within the framework of the method of steepest descent is equivalent to Gaster's Gaussian model for a Fourier integral [Gas81, Gas82].

Using numerical results, the various quantities found in (3.60) can be determined. They are

$$\alpha_{\max} = 0.254, \quad \omega_{\max} = 0.2342 + 0.0039i$$
$$\left(\frac{\partial\omega}{\partial\alpha}\right)_{\max} = 0.86, \quad \left(\frac{\partial^2\omega}{\partial\alpha^2}\right)_{\max} = -0.2034 - 3.6431i.$$

Additionally, $c(\alpha^*)\,u(\alpha^*, y)$, the receptivity coefficient multiplied by the eigenfunction at the saddle point for the slice $y = 2.02$ is $0.00174 - 0.0011i$.

These values can be used to compare the computed inverse Fourier transform with the asymptotic approximation of the transform. Because we have used (3.53b) without the factor of 2 to compute the inverse Fourier transform, we will compare the computational result with the Real part of the asymptotic approximation given by (3.60). Though we expect good agreement between the two methods, especially for large times, there may be some differences between the "exact" result found numerically and the "approximate" result found with the method of steepest descent.

Figure 3.29(a) compares the wave packet found for $Y_0 = 8.9$ and $t = 500$ at the slice $y = 2.02$ with the asymptotic approximation at $t = 500$ given by (3.60) using the values given above. Figure 3.29(b) shows a similar comparison for $t = 1000$. One can see that as the time increases, the wave packet spreads out as it moves downstream. Furthermore, the amplitude of the perturbation increases with time. By comparing figure 3.29(a) to figure 3.29(b), one can estimate the Mode S wave packet group velocity to be $\partial\omega_r/\partial\alpha \approx 0.8$. This estimate is consistent with the group velocity value $(\partial\omega/\partial\alpha)_{\max} = 0.86$.

Overall, the asymptotic representation provides a good approximation to the computed wave packet. However, the "tails" of the two wave packets do not agree very well. This is particularly true for the front edge of the wave packet.

Asymptotic approximation with numerical computation of the saddle point

In an attempt to improve the asymptotic approximation of the wave packet at the "tails" of the wave packet, we numerically compute the location of the saddle point. To find the saddle point, α^*, at a prescribed x/t, we let $\phi(\alpha) = \alpha x/t - \omega(\alpha)$ and derive the following:

$$\left(\frac{\partial\phi}{\partial\alpha}\right)^* = \frac{x}{t} - \frac{\partial\omega}{\partial\alpha} = 0. \tag{3.61}$$

Therefore, the following relationships must be satisfied at α^*:

$$\frac{x}{t} = \frac{\partial\omega_r}{\partial\alpha} \quad \text{and} \quad 0 = \frac{\partial\omega_i}{\partial\alpha}. \tag{3.62}$$

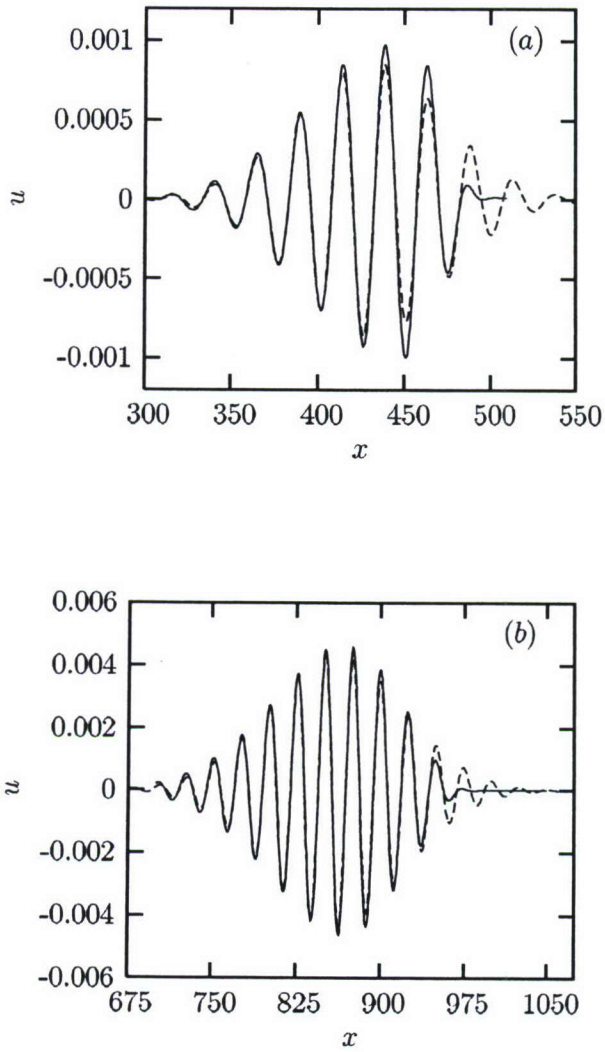

Figure 3.29: Comparison of computed integral (solid line) with the asymptotic approximation (using 2nd order Taylor series expansion of $\omega(\alpha)$) (dashed line) for (a) $t = 500$ and (b) $t = 1000$.

Using the method of steepest descent, the asymptotic representation of the inverse Fourier transform is given as:

$$c(\alpha^*)\ u(\alpha^*, y) \sqrt{\frac{2\pi}{it\left(\frac{\partial^2\omega}{\partial\alpha^2}\right)^*}} \times \exp\left(i\alpha^* x - i\omega^* t\right) \tag{3.63}$$

(Note that (3.63) is the same as (3.60) with $x = x_{\max}$ and all of the "max"-values replaced by "saddle point (*)"-values).

Using Eq. (3.62), α^*, ω^* and $(\partial^2\omega/\partial\alpha^2)^*$ are calculated. Figure 3.30(a) compares the "exact" computed wave packet found for $Y_0 = 8.9$ and $t = 500$ at the slice $y = 2.02$ with the asymptotic approximation at $t = 500$ given by (3.63) using the saddle point values. Figure 3.30(b) shows a similar comparison for $t = 1000$. There is now excellent agreement across the entire wave packet for both choices of time.

Inverse Fourier Transform - 3D for Fixed Spanwise Wave Number

For the streamwise velocity disturbance, u (of $\boldsymbol{A}_{\alpha\beta}$ given by Eq. (B.16)), the 3D inverse Fourier transform is given by

$$\int_{-\infty}^{\infty}\int_{-\infty}^{\infty} c(\alpha,\beta)\, u(\alpha,\beta,y)\, e^{i(\alpha x+\beta z-\omega(\alpha,\beta)t)}\, d\alpha\, d\beta. \tag{3.64}$$

Integration with respect to α for a prescribed β leads to

$$e^{i\beta z}\int_{-\infty}^{\infty} c(\alpha,\beta)\, u(\alpha,\beta,y)\, e^{i(\alpha x-\omega(\alpha,\beta)t)}\, d\alpha. \tag{3.65}$$

As for the 2D case, the integral of (3.65) can be transformed using a symmetry argument to an integral over the positive α half-plane. As before, for the purpose of computation, we ignore the factor of 2.

Figure 3.31(a) shows the imaginary part of the eigenvalue ω_i for Mode S for $\beta = 0.1001$. Figure 3.31(b) shows for Mode S at $t = 0$ the maximum streamwise velocity amplitude, $u_{\max}$, multiplied by the value of the eigenfunction at $y = 2.02$, which is generated by α and β components of the temperature spot located at the distance $Y_0 = 8.9$ from the wall.

The inverse Fourier transform given by (3.65) is numerically computed from $\alpha = 0.1$ to $\alpha = 0.5$ with $\beta = 0.1001$ and $z = 0$. Even though $\omega_i > 0$ for $\alpha < 0.1$, the receptivity coefficient (figure 3.31(b)) is near 0 in this region. The greatest input into the integral will be from the region of $\alpha \approx 0.2$ to $\alpha \approx 0.3$. It is in this region that the receptivity coefficient, $u_{\max}$, is the largest, and it is also in this region where ω_i attains its largest value. Beyond $\alpha = 0.5$, Mode S is decaying, so that for sufficiently large times, there will not be significant input into the integral for $\alpha > 0.5$.

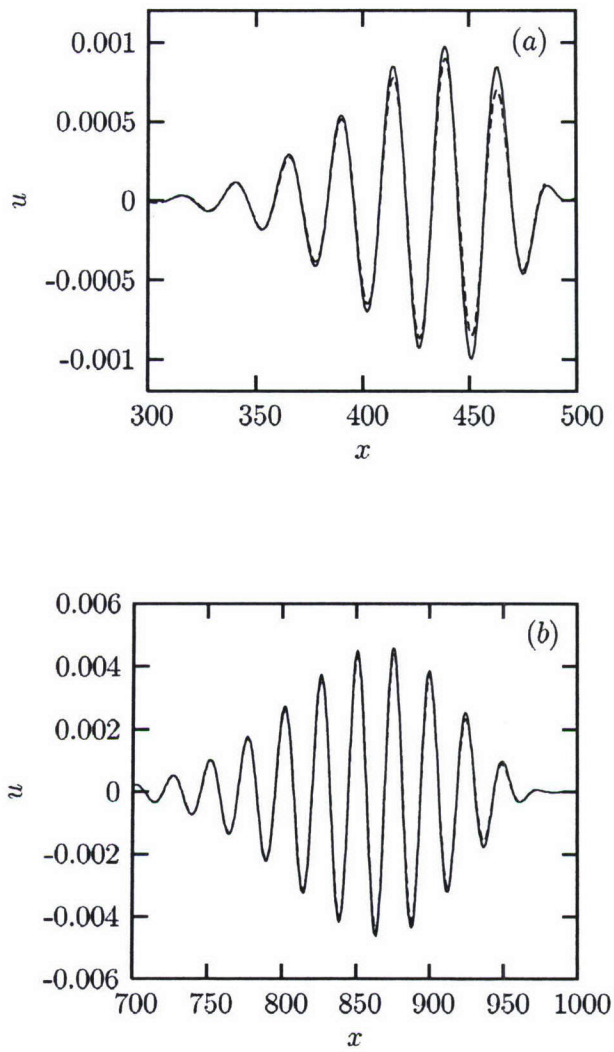

Figure 3.30: Comparison of computed integral (solid line) with the asymptotic approximation (using numerically computed saddle point values) (dashed line) for (a) $t = 500$ and (b) $t = 1000$.

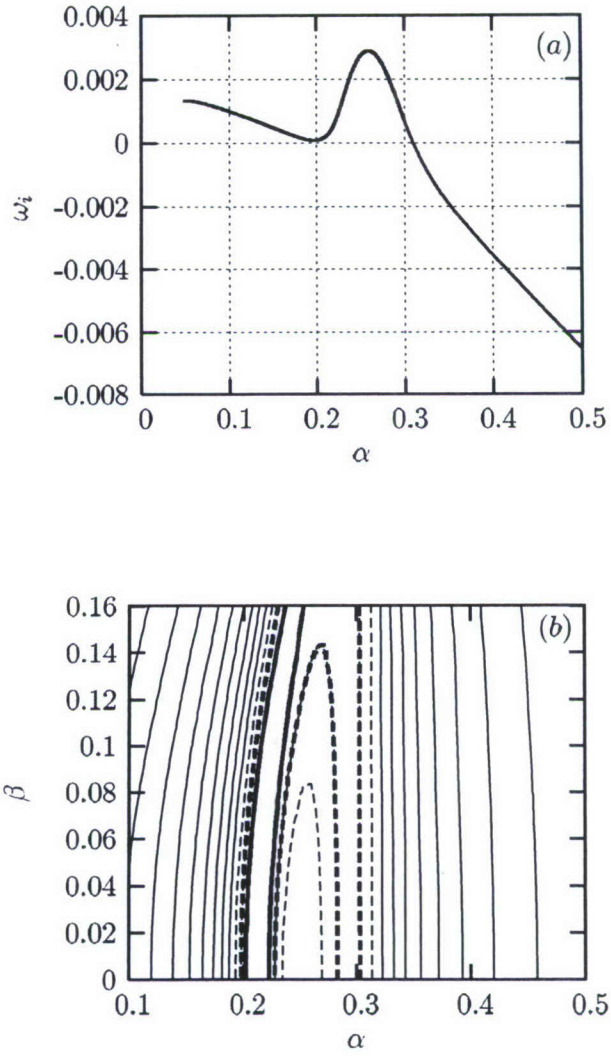

Figure 3.31: (a) Imaginary part of the eigenvalue for Mode S for $\beta = 0.1001$ and (b) contours of $c(\alpha, \beta)\, u$ at $y = 2.02$ at $t = 0$ generated by α and β components of a temperature spot located at $Y_0 = 8.9$. The contour levels in (b) increase in increments of 0.0002, beginning with 0.0004 on the left side of the figure and 0.0006 on the right side of the figure. The dashed contour is 0.0022, the bold dashed contour is 0.0024 and the bold solid contour is 0.0026.

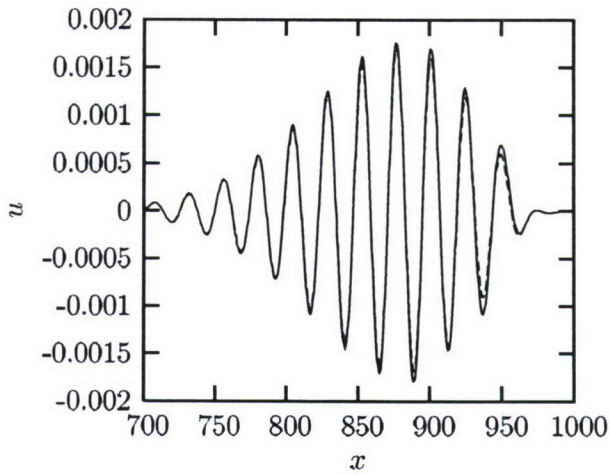

Figure 3.32: Comparison of computed integral (solid line) with the asymptotic approximation (using numerically computed saddle point values) (dashed line) for $\beta = 0.1001$, $z = 0$ and $t = 1000$.

Using the method of steepest descent, the asymptotic approximation of the inverse Fourier transform for a prescribed spanwise wave number β is given as

$$c(\alpha^*, \beta)\ u(\alpha^*, \beta, y) \sqrt{\frac{2\pi}{it\left(\frac{\partial^2\omega}{\partial\alpha^2}\right)^*}} \times \exp(i\beta z) \exp(i\alpha^* x - i\omega^* t)\,. \tag{3.66}$$

By numerically computing the saddle point quantities α^*, ω^*, and $(\partial^2\omega/\partial\alpha^2)^*$, and using the fact that $c(\alpha^*, \beta)\, u(\alpha^*, \beta, y)$, the receptivity coefficient multiplied by the eigenfunction at the saddle point for the slice $y = 2.02$ is $0.00159 - 0.00126i$, one can use (3.66) to find the asymptotic representation of the Fourier integral (as with the 2D case, the Real part of (3.66) is taken for the purpose of comparison with the computed result).

Figure 3.32 compares the wave packet computed for $\beta = 0.1001$, $z = 0$, $Y_0 = 8.9$ and $t = 1000$ at the slice $y = 2.02$ with the asymptotic approximation at $t = 1000$ given by (3.66). There is good agreement across the entire wave packet.

Inverse Fourier Transform - 3D

It was shown in Section VI that it was necessary to deform the path of integration of the 2D inverse Fourier transform for Mode F, but not for Mode S. Each inversion of the Fourier integral must be accompanied by an analysis of the spectrum to find a suitable integration

path. In order to perform the double integration of the 3D inverse Fourier transform, it is again necessary to understand the features of the spectrum so that an appropriate path of integration is used. Due to the complexities associated with the 3D spectrum, we will use an asymptotic approximation of the Fourier integral to compute the 3D wave packets.

For the streamwise velocity disturbance, u, the 3D inverse Fourier transform is given by (3.64). As in the 2D case, (3.64) can be transformed using a symmetry argument. Using the direct and complex conjugate matrix operator equations, when α is replaced by $-\alpha$, i.e. when $\alpha \rightarrow -\alpha$, it can be shown that $\beta \rightarrow -\beta$, $\omega \rightarrow -\overline{\omega}$, $c \rightarrow \overline{c}$, and $u \rightarrow \overline{u}$, where the overbar stands for complex conjugate. Therefore, (3.64) can be rewritten as:

$$\int_{-\infty}^{\infty}\int_{-\infty}^{\infty} c(\alpha,\beta)\, u(\alpha,\beta,y)\, e^{i(\alpha x+\beta z-\omega(\alpha,\beta)t)}\, d\alpha\, d\beta = \tag{3.67a}$$

$$2\int_{0}^{\infty}\int_{0}^{\infty} \text{Real}\left\{ c(\alpha,\beta)\, u(\alpha,\beta,y)\, e^{i(\alpha x+\beta z-\omega(\alpha,\beta)t)} \right\} d\alpha\, d\beta$$

$$+\, 2\int_{0}^{\infty}\int_{0}^{\infty} \text{Real}\left\{ c(\alpha,-\beta)\, u(\alpha,-\beta,y)\, e^{i(\alpha x-\beta z-\omega(\alpha,-\beta)t)} \right\} d\alpha\, d\beta. \tag{3.67b}$$

As before, the factor of 2 will be ignored.

At a first glance of (3.67b), it is tempting to think that there are two saddle points. The first saddle point, associated with the first double integral, must satisfy the following relations:

$$\frac{x}{t} = \frac{\partial \omega_r(\alpha,\beta)}{\partial \alpha} \quad \text{and} \quad 0 = \frac{\partial \omega_i(\alpha,\beta)}{\partial \alpha};$$

$$\frac{z}{t} = \frac{\partial \omega_r(\alpha,\beta)}{\partial \beta} \quad \text{and} \quad 0 = \frac{\partial \omega_i(\alpha,\beta)}{\partial \beta}. \tag{3.68}$$

The second saddle point, associated with the second double integral, must satisfy the following relations:

$$\frac{x}{t} = \frac{\partial \omega_r(\alpha,-\beta)}{\partial \alpha} \quad \text{and} \quad 0 = \frac{\partial \omega_i(\alpha,-\beta)}{\partial \alpha};$$

$$\frac{z}{t} = \frac{\partial \omega_r(\alpha,-\beta)}{\partial \beta} \quad \text{and} \quad 0 = \frac{\partial \omega_i(\alpha,-\beta)}{\partial \beta}. \tag{3.69}$$

Using the symmetry transformations along with properties of complex conjugation, it can be shown that Eq. (3.69) can be rewritten as

$$\frac{x}{t} = -\frac{\partial \omega_r(\alpha,\beta)}{\partial \alpha} \quad \text{and} \quad 0 = \frac{\partial \omega_i(\alpha,\beta)}{\partial \alpha};$$

$$\frac{z}{t} = \frac{\partial \omega_r(\alpha,\beta)}{\partial \beta} \quad \text{and} \quad 0 = \frac{\partial \omega_i(\alpha,\beta)}{\partial \beta}. \tag{3.70}$$

However, it can be shown numerically that no saddle point satisfies the relations given in Eq. (3.70), unless $x = 0$ and $z = 0$. Therefore, there is only one saddle point, and it is associated with the first double integral of (3.67b).

We follow Gaster [Gas68] to find the asymptotic representation of the 3D inverse Fourier transform. For a fixed β, the Fourier integral becomes

$$\int_{-\infty}^{\infty} e^{i\beta z} \int_{-\infty}^{\infty} e^{it\left(\alpha\frac{x}{t}-\omega(\alpha,\beta)\right)}\, d\alpha\, d\beta. \tag{3.71}$$

The asymptotic representation of the inner integral in (3.71) is known from the 2D case, and substitution of this representation leads to the following:

$$\sqrt{\frac{2\pi}{i}} \int_{-\infty}^{\infty} \frac{e^{it\left(\alpha^*(\beta)\frac{x}{t}+\beta\frac{z}{t}-\omega(\alpha^*(\beta),\beta)\right)}}{\sqrt{t\frac{\partial^2\omega}{\partial\alpha^2}(\alpha^*,\beta)}}\, d\beta. \tag{3.72}$$

If we let

$$\phi(\alpha^*,\beta) = i\left(\alpha^*(\beta)\frac{x}{t} + \beta\frac{z}{t} - \omega(\alpha^*(\beta),\beta)\right), \tag{3.73}$$

and expand ϕ about β^* so that

$$\phi(\alpha^*,\beta) \approx i\left[\phi(\alpha^*,\beta^*) + \frac{(\beta-\beta^*)^2}{2}\phi''(\alpha^*,\beta^*)\right], \tag{3.74}$$

then (3.71) can be written as:

$$\sqrt{\frac{2\pi}{it}} \frac{e^{it(\alpha^* x+\beta^* z-\omega(\alpha^*,\beta^*))}}{\sqrt{\frac{\partial^2\omega}{\partial\alpha^2}(\alpha^*,\beta^*)}} \times$$

$$\int_{-\infty}^{\infty} e^{it\frac{(\beta-\beta^*)^2}{2}\left(\frac{\partial^2\omega}{\partial\beta^2}+2\frac{\partial^2\omega}{\partial\alpha\partial\beta}\left(\frac{\partial\alpha}{\partial\beta}\right)+\frac{\partial^2\omega}{\partial\alpha^2}\left(\frac{\partial\alpha}{\partial\beta}\right)^2\right)^*} d\beta = \tag{3.75a}$$

$$\frac{2\pi}{it} \frac{e^{it(\alpha^* x+\beta^* z-\omega(\alpha^*,\beta^*))}}{\sqrt{\left(\frac{\partial^2\omega}{\partial\alpha^2}\frac{\partial^2\omega}{\partial\beta^2}-\left(\frac{\partial^2\omega}{\partial\alpha\partial\beta}\right)^2\right)^*}}. \tag{3.75b}$$

The asymptotic representation of the inverse Fourier transform given by (3.75b) can be derived more generally using a transformation of variables [BH86, Won01]. Starting with (3.64) with ϕ given as $\phi(\alpha,\beta) = \alpha x + \beta z - \omega(\alpha,\beta)\, t$, we approximate ϕ as:

$$\phi(\alpha,\beta) \approx \phi^* + \frac{(\alpha-\alpha^*)^2}{2}\phi^*_{\alpha\alpha} +$$

$$(\alpha-\alpha^*)(\beta-\beta^*)\phi^*_{\alpha\beta} + \frac{(\beta-\beta^*)^2}{2}\phi^*_{\beta\beta}, \tag{3.76}$$

where the α and β subscripts refer to first and second partial derivatives.

Using the change of variables

$$g = (\alpha - \alpha^*), \qquad h = (\beta - \beta^*),$$

$$\xi = g + \frac{\phi_{\alpha\beta}}{\phi_{\alpha\alpha}} h, \qquad \eta = h, \tag{3.77}$$

(3.64) is transformed to the following:

$$\int_{-\infty}^{\infty} \int_{-\infty}^{\infty} e^{\frac{t}{2}\left(\phi_{\alpha\alpha}\xi^2 + \frac{\left(\phi_{\alpha\alpha}\phi_{\beta\beta} - \phi_{\alpha\beta}^2\right)}{\phi_{\alpha\alpha}}\eta^2\right)} d\xi d\eta. \tag{3.78}$$

The integral given in (3.78) is an iterated integral where each integral is Gaussian. Evaluation of the iterated integral results in the asymptotic representation of the Fourier integral given by (3.75b).

The saddle point (α^*, β^*) and the various derivatives at the saddle point used in (3.75b) are numerically computed. Using the asymptotic approximation of the 3D inverse Fourier transform, the Mode S wave packet is calculated for $t = 1000$. Figure 3.34(a) is a surface plot of the streamwise velocity disturbance, u, taken at the slice $y = 2.02$ for $Y_0 = 8.9$ and $t = 1000$. Figure 3.34(b) is a rotation of figure 3.34(a) in order to see the underside of the wave packet. To have a clearer sense of the amplitude values, figure 3.34(c) shows contours of u for $y = 2.02$, $Y_0 = 8.9$, and $t = 1000$. It is clear from these figures that the wave packet is essentially 2D. Furthermore, it is possible to compare figure 3.34(a)-(c) with figure 3.33 (3D Mode S wave packet for $t = 500$) and see that the 3D Mode S wave packet group velocity is very similar to the 2D Mode S wave packet group velocity.

Conclusions

The previously solved 2D and 3D initial-value problems were used along with features of the discrete and continuous spectrum for one set of parameters to study the evolution of wave packets for two discrete modes, Mode S and Mode F. The biorthogonal eigenfunction system provides a method for the determination of the weights of individual modes given a specific initial disturbance. Using the specific disturbance of an initial temperature spot, we computed the 2D inverse Fourier transform for both Mode F and Mode S. Additionally the 3D inverse Fourier transform was computed for a fixed value of spanwise wave number β.

As shown in [FT03] and [FT05] (see Section 3.2), Mode F and Mode S are eigenvalue curves that correspond to the trajectory of poles in the complex p plane, while continuous modes correspond to branch cuts in the complex p plane. It is possible for various modes to be synchronized, and therefore it is crucial to fully understand the behavior of the spectrum before computing the inverse Fourier transform. For the 2D case, due to the synchronism between Mode F and entropy/vorticity waves, the path of integration is deformed around the branch cut associated with this synchronism. This allows us to compute the inverse Fourier

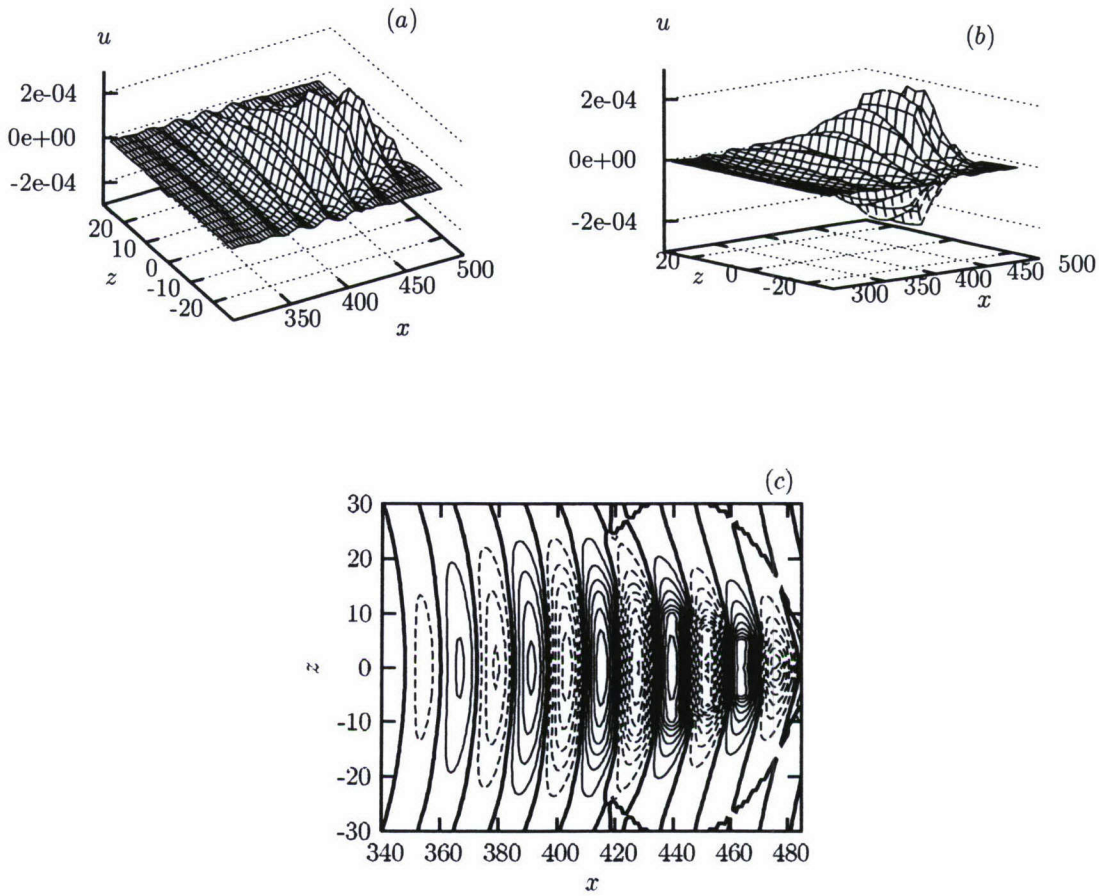

Figure 3.33: Surface (view 1) (a), surface (view 2) (b) and contours (c) of u for $y = 2.02$, $Y_0 = 8.9$, and $t = 500$. The contour levels in (c) are spaced in increments of 0.000025. The solid contours are positive; the dashed contours are negative; the bold contours are 0.

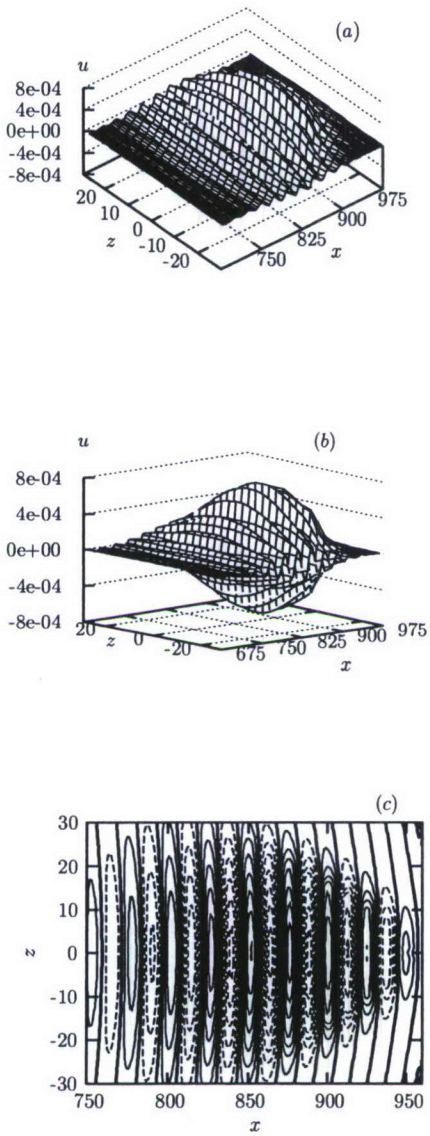

Figure 3.34: (a) Surface (view 1), (b) surface (view 2) and (c) contours of u for $y = 2.02$, $Y_0 = 8.9$, and $t = 1000$. The contour levels in (c) are spaced in increments of 0.0001. The solid contours are positive; the dashed contours are negative; the bold contours are 0.

transform using only Mode F. The result is equal to that found by considering Mode F and the continuous spectrum together and integrating along the real α axis. Since the integrand associated with the sum of Mode F and the continuous spectrum is analytic, the choice of the integration path should not affect the result, and in fact, the numerical results for four choices of integration path agree very well.

For the 2D and 3D (fixed β) cases, the results for Mode S were compared with an asymptotic approximation of the Fourier integral. The first approximation used a Taylor series expansion of ω. Generally, this approximation compared favorably with the computed results. However, there is a significant discrepancy at the wave packet "tails". The asymptotic approximation was improved using numerically computed saddle point values. From a computational point of view, it is much faster to compute the wave packet using the asymptotic approximation with numerically computed saddle point values than it is to compute the inverse Fourier transform.

Additionally, the full 3D inverse Fourier transform was found for Mode S. Since the 3D spectrum is so complex, rather than compute the inverse Fourier transform, we have used an asymptotic approximation of the Fourier integral, with numerically computed saddle point values. A key feature of the 3D wave packet is its 2D nature. As discussed in Section 3.2, Mode S is a single discrete mode that corresponds to a single pole in the complex p plane. This single mode is comprised of Mack's first and second modes, and for this set of parameters, the most unstable section of Mode S is associated with Mack's second mode, whose maximum growth rate is associated with 2D disturbances. Thus, it is not surprising that for sufficiently large time, the 3D wave packet will have a 2D appearance. One should note that a comparison of figure 3.26(a) and figure 3.31(a) shows that the spanwise wave number has little effect on the growth rate. This is a hint of the two-dimensionality of the 3D wave packet.

The previous analysis has been performed under a parallel flow assumption. However, this analysis may be extended to the case of weakly non-parallel flows through the use of multiple scales methods. Discussion of this extension may be found in Section 3.2. For strongly non-parallel flows, one should consider a BiGlobal stability problem formulation [The03]. Unlike the present analysis, the BiGlobal stability problem deals with a 2D PDE based generalized eigenvalue problem. However, it should be noted that the biorthogonal eigenfunction system formulation can be used in the analysis of BiGlobal instability problems (e.g. separated flow), and that we believe this is a worthwhile area of exploration.

Chapter 4

Transient growth of perturbations in compressible boundary layers

This section is based on the papers published in collaboration with E. Reshotko, S. Zuccher, and I. Shalaev [ZTR06, ZSTR07].

4.1 Introduction

The problem of optimal disturbances, in the context of bypass transition to turbulence, has been of great interest during the last decade. This interest is motivated by the fact that there are many applications where transition to turbulence occurs without the classical exponential growth, allowing a large transient growth of the disturbance energy in flows that are stable to wave-like perturbations (Tollmien–Schlichting waves).

Today it is clear that transient growth arises from the coupling between slightly damped, highly oblique Orr-Sommerfeld (OS) and Squire modes. This can lead to an algebraic growth followed, in viscous flows, by exponential decay in subcritical regions outside the Tollmien-Schlichting (TS) neutral curve. A weak transient growth can also occur for two-dimensional modes since the OS operator and its compressible counterpart are not self-adjoint, and therefore their eigenfunctions are not strictly orthogonal [Res01, SH01].

Historically, the first approach to nonmodal disturbances was in the inviscid limit. [EP75] found that the streamwise disturbance velocity amplitude may grow algebraically in time, even though the basic flow does not posses an inflection point. This growth mechanism was labeled "lift-up" [Lan75]. Later on, [Lan80] showed that all parallel inviscid shear flows are unstable to a wide class of three-dimensional disturbances and the result is independent of whether or not the shear flow is unstable to exponential growth. The temporal analysis involving resonance between OS and Squire modes was employed for the study of Couette flow [GH80], Poiseuille flow [Gus81] and boundary layers [HG81, BG81, JBG86], revealing a viscous decay following initial algebraic growth of the disturbance, otherwise known as transient growth. Meanwhile, the transient growth phenomenon was intensively studied in

meteorology [Far82, Far84, Far86, Far87].

[Far88a, Far88b] was the first to use the term optimal perturbations to denote the initial flow disturbances that produced the maximum gain, defined as the ratio between the perturbation kinetic energies at the final and initial time. A similar concept had, however, already been introduced for flow in a pipe by [BB88]. The first quantitative calculation of three–dimensional optimal perturbations with respect to temporal growth for a parallel approximation of the Blasius boundary layer was performed by [BF92]. Other works [Gus91, RH93, TTRD93], carried out more than a decade ago, recognized the great potential of nonmodal growth for explaining bypass transition.

Optimal perturbations in the spatial framework have only more recently been considered. The spatial Cauchy problem within the scope of the linearized Navier–Stokes equations is, however, radically different from the temporal one and is ill posed. This is the main obstacle in applying to the spatial analysis the same optimization methods used in the temporal case. The problem rises from the presence of modes with a negative imaginary part of the streamwise wavenumber α. These are modes decaying upstream and associated with the downstream boundary conditions. [TR01] pointed out that if the downstream boundary is moved far away, the upstream decaying modes can be neglected and the optimization can be carried out within the scope of the Cauchy problem, similarly to the temporal analysis. The ill-posedness of the spatial Cauchy problem was first overcome by considering the (linearized) boundary layer equations [ABH99, Luc00] instead of the Navier–Stokes equations. In addition, [ABH99] and [Luc00] included nonparallel effects. It was found that the optimal initial disturbance is composed of stationary streamwise vortices whereas the induced velocity field is dominated by streamwise streaks. For example, in the case of incompressible boundary layer past a flat plate, the maximum amplification occurs in the steady case (frequency $\omega = 0$) and for a non-zero value of the spanwise wavenumber $\beta = 0.45$ (scaled with $l = \sqrt{\nu L/U_\infty}$, ν being the kinematic viscosity, U_∞ the freestream velocity and L the longitudinal distance from the leading edge to the location where output energy is maximized). For the spatial problem, [ZBL06] computed the optimal perturbations in the nonlinear case.

The compressible counterpart of the aforementioned works has also been considered. Temporal [HSH96, HH98] and spatial [RT00, TR01, TR04a] analyses of the transient growth phenomenon have been carried out within the scope of the parallel flow approximation. [TR03] developed a model for transient growth including non-parallel effects in the compressible boundary layer past a flat plate.

Compressible optimal perturbations calculated by including surface curvature effects and non-parallel growth of the boundary layer are still missing and can actually be of great importance to explain the long-standing blunt body paradox [RT00].

Depending on the choice of the norm, which states what quantity will be maximized, constrained optimization in the framework of optimal perturbation can lead to quite different results. With reference to the incompressible case, [ABH99] maximized a full energy norm including all velocity components, whereas [Luc00] considered the energy of the streamwise component only. On the other hand, the choice of the initial condition (i.e. the choice of the norm at the inlet) may contribute as well to the result. In the incompressible framework,

the full inlet energy norm [ABH99] and the energy norm including only the spanwise and wall-normal velocity components [Luc00] were employed. In [ABH99] both norms at the inlet and at the outlet depend on the Reynolds number Re. However, in the limit $Re \rightarrow \infty$ (practically for $Re > 10^4$) results collapse onto those obtained by [Luc00].

The choice of the energy norm, therefore, can be a delicate issue, especially in the compressible case where effects due to compressibility should be taken into account through the inclusion of density and temperature. The physics of transient growth is mainly dominated by streamwise vortices [ABH99, Luc00] and therefore the choice of an initial energy excluding the streamwise velocity component, in the fashion proposed by [Luc00], is satisfactory. The choice of an outlet norm including only temperature and the component of the velocity in the streamwise direction, however, might not represent completely the structure of the flow field if the flow is not dominated by streamwise streaks. This could be the case of a blunt body, for which there are some indications that the largest transient growth is located close to the stagnation point [RT04]. Due to the short interval in the streamwise direction, a flow field mainly dominated by streaks might not be completely established and thus the contribution of the wall-normal and spanwise velocity components to the energy norm at the outlet could be non negligible.

4.2 Spatial transient growth, problem formulation

Governing equations

Governing equations for the steady, three-dimensional disturbance in a compressible flow are derived from the linearized Navier–Stokes equations.

A small parameter $\epsilon = H_{\text{ref}}/L_{\text{ref}}$ is introduced for scaling purposes, where $H_{\text{ref}} = \sqrt{\nu_{\text{ref}} L_{\text{ref}}/U_{\text{ref}}}$ is a typical boundary layer length in the wall-normal direction y and L_{ref} is a typical scale of the geometry (length of the flat plate L, radius of the sphere R, etc.), U_{ref} and ν_{ref} are respectively the reference scaling velocity and kinematic viscosity. In the case of the flat plate $H_{\text{ref}} = l = \sqrt{\nu_\infty L/U_\infty}$ (the subscript ∞ stands for freestream parameters, outside the boundary layer), while for the sphere $H_{\text{ref}} = \sqrt{\nu_{\text{ref}} R/U_{\text{ref}}}$ where the reference quantities are the values at the edge of the boundary layer at a certain downstream location x_{ref}, x being the streamwise direction. The scaling parameter ϵ is thus strictly related to the Reynolds number Re. For the flat plate $\epsilon = Re^{-1/2}$, where $Re = U_\infty L/\nu_\infty$ is the Reynolds number based on the length of the plate and freestream conditions, while for the sphere $\epsilon = Re_{\text{ref}}^{-1/2}$, where $Re_{\text{ref}} = U_{\text{ref}} R/\nu_{\text{ref}}$ is the reference Reynolds number based on the radius of the sphere R and reference parameters.

As it follows from previous works regarding optimal perturbations in both incompressible and compressible boundary layers [Luc00, CL00, TR04a, ZLB04, ZBL06], the disturbance flow is expected to be dominated by streamwise vortices and therefore the following scaling is employed. The streamwise coordinate x is normalized with L_{ref}, whereas the wall-normal coordinate y and the spanwise coordinate z are scaled with ϵL_{ref}. The streamwise velocity component u is scaled with U_{ref}, wall-normal velocity v and spanwise velocity w with ϵU_{ref}, temperature T with T_{ref} and pressure p with $\epsilon^2 \rho_{\text{ref}} U_{\text{ref}}^2$. Density ρ is eliminated through the state equation.

Due to the scaling adopted, the second derivative with respect to the streamwise coordinate x is smaller than the other terms, and is therefore neglected. This leads to a change in the nature of the equations from elliptic (Navier–Stokes equations) to parabolic.

For the flat plate, perturbations are assumed to be periodic in z, so that a general variable can be expressed as $q(x,y)\exp(\mathrm{i}\beta z)$, where $q(x,y)$ is the amplitude, which depends on x and y, β is the spanwise wavenumber and i is the imaginary unit. Similarly, for the sphere, perturbations are assumed to be periodic in the azimuthal direction ϕ as $\exp(\mathrm{i}m\phi)$, where m is the azimuthal index.

If the vector of perturbations is $\mathbf{f} = [u, v, w, T, p]^{\mathrm{T}}$ (where the superscript $^{\mathrm{T}}$ denotes the transpose), and $w = \mathrm{i}\tilde{w}$ ($\tilde{w}$ being the amplitude of the spanwise velocity component), the governing equations can be written as follows [TR03]:

$$(\boldsymbol{A}\mathbf{f})_x = (\boldsymbol{D}\mathbf{f}_y)_x + \boldsymbol{B}_0\mathbf{f} + \boldsymbol{B}_1\mathbf{f}_y + \boldsymbol{B}_2\mathbf{f}_{yy}. \tag{4.1}$$

This form of the governing equations is general and can be derived for different geometries such as flat plate, sphere, sharp cone or blunt-nose cone. Nonzero elements of the 5 by 5 real matrices $\boldsymbol{A}$, $\boldsymbol{B}_0$, $\boldsymbol{B}_1$, $\boldsymbol{B}_2$ and $\boldsymbol{D}$ for the flat plate are defined in the appendix of [TR03], while for the sphere they are reported in Appendix C.1.

As far as boundary conditions are concerned, all perturbations are required to be zero at the wall except for p, while in the freestream all perturbations vanish except for v:

$$\begin{aligned} y = 0: &\quad u = 0; v = 0; w = 0; T = 0 \\ y \to \infty: &\quad u \to 0; w \to 0; p \to 0; T \to 0. \end{aligned} \tag{4.2}$$

In order to isolate the derivative with respect to x, system (4.1) can be recast in a simple form as

$$(\boldsymbol{H}_1 \mathbf{f})_x + \boldsymbol{H}_2 \mathbf{f} = 0 \tag{4.3}$$

where operators $\boldsymbol{H}_1$ and $\boldsymbol{H}_2$ are still 5 by 5 real matrices and contain the dependence on x and y due to the basic flow:

$$\boldsymbol{H}_1 = \boldsymbol{A} - \boldsymbol{D}(\cdot)_y; \qquad \boldsymbol{H}_2 = -\boldsymbol{B}_0 - \boldsymbol{B}_1(\cdot)_y - \boldsymbol{B}_2(\cdot)_{yy}. \tag{4.4}$$

System (4.3) is parabolic in nature and can be solved by means of a downstream marching procedure with initial data specified at the inlet section of the domain $x = x_{\text{in}}$.

It is worth noting that, due to the normalization chosen, the disturbance equations for the flat plate are Reynolds-number independent, i.e. the Reynolds number Re does not enter explicitly in the equations, while for the sphere they are not Reynolds-number independent due to the parameter ϵ in the scaling, which is associated with curvature effects.

Constrained optimization and adjoint discrete equations

As stated in the introduction, we are interested in finding initial optimal disturbances for the compressible boundary layer over a flat plate and a sphere. The term "optimal" here refers to the initial condition that is able to produce the worst possible scenario as far as transition is concerned. It is clear that the choice of a specific quantity that can measure this worst possible scenario is neither easy nor unique. In previous works dealing with optimal perturbations in the incompressible framework [ABH99, Luc00, CL00, ZLB04, ZBL06], the kinetic energy of the disturbance field has always been the choice.

Once the objective function has been identified, the Lagrangian multiplier technique is employed in order to solve the constrained optimization problem. In doing so the costate (or adjoint) equations are derived. If this is applied to the discrete equations, the discrete version of the adjoint problem is obtained. The procedure is outlined for a general case, as done in the section with governing equations.

The objective function

In problems related to boundary-layer transition, the quantity that monitors the instability development is typically the kinetic energy. In optimal perturbation studies the latter is usually maximized at the outlet of the computational domain, but in other cases the integral of the kinetic energy over the whole domain has been considered, especially for optimal control problems [see CL00, ZLB04]. Since one of the goals of the present study is to check how the use of a "full energy norm" at the outlet can influence the results, the expression

we choose to maximize is Mack's energy norm [Mac69] including the perturbation kinetic energy and temperature in the outlet plane. After employing the scaling in the governing equations' section, the latter reads

$$E_{\text{out}} = \int_0^\infty \left[\rho_{s\text{out}} \left(u_{\text{out}}^2 + \epsilon^2 (v_{\text{out}}^2 + w_{\text{out}}^2) \right) + \frac{\rho_{\text{out}}^2 T_{s\text{out}}}{\gamma \rho_{s\text{out}} M^2} + \frac{T_{\text{out}}^2 \rho_{s\text{out}}}{\gamma(\gamma-1) T_{s\text{out}} M^2} \right] dy. \tag{4.5}$$

Expression (4.5) was derived for perturbations in the boundary layer over a flat plate within the temporal framework and is here utilized for the spatial one, as done by [TR03] (for the sphere, the integration generates a slightly different expression for the energy norm, which can be found in Appendix C.1). After employing the equation of state for the basic flow and for the perturbation, the norm reads

$$E_{\text{out}} = \int_0^\infty \left[\rho_{s\text{out}} \left(u_{\text{out}}^2 + \epsilon^2 (v_{\text{out}}^2 + w_{\text{out}}^2) \right) + \frac{p_{s\text{out}} T_{\text{out}}^2}{(\gamma-1) T_{s\text{out}}^2 M^2} \right] dy \tag{4.6}$$

and can be more compactly recast in matrix form as

$$E_{\text{out}} = \int_0^\infty \left(\mathbf{f}_{\text{out}}^T \widetilde{\boldsymbol{M}}_{\text{out}} \mathbf{f}_{\text{out}} \right) dy \tag{4.7}$$

where the linear operator $\widetilde{\boldsymbol{M}}_{\text{out}}$ is a diagonal 5×5 matrix

$$\widetilde{\boldsymbol{M}}_{\text{out}} = \begin{bmatrix} \rho_{s\text{out}} & 0 & 0 & 0 & 0 \\ 0 & \epsilon^2 \rho_{s\text{out}} & 0 & 0 & 0 \\ 0 & 0 & \epsilon^2 \rho_{s\text{out}} & 0 & 0 \\ 0 & 0 & 0 & \dfrac{p_{s\text{out}}}{(\gamma-1) T_{s\text{out}}^2 M^2} & 0 \\ 0 & 0 & 0 & 0 & 0 \end{bmatrix}. \tag{4.8}$$

The initial condition for the compressible boundary-layer equations is not arbitrary, but only three of the five variables can be imposed at x_{in} [Tin65]. However, in the incompressible case and for $Re \to \infty$, [Luc00] observed that the choice $u_{\text{in}} = 0$, $p_{\text{in}} = 0$, v_{in} and w_{in} related by the continuity equation guarantees the maximum gain in an input-output fashion (in the incompressible case the number of independent initial conditions is two; see also [LB98, Luc00, ZBL06]). This choice also corresponds to the physical mechanism, observed in transitional boundary layer flows, known as the lift-up effect [Lan80], according to which streamwise vortices lift low-momentum flow up (from the wall) and push down high-momentum flow causing streaks that eventually break down to turbulence. Led by these considerations, here we focus on initial perturbations with only v and w nonzero, which correspond to steady, streamwise vortices. It should be noticed, however, that in the case of

finite Reynolds number, for example $Re = 1000$, and for the incompressible boundary layer past a flat plate, the choice of a full energy norm at both inlet and outlet guarantees the largest gain in the optimization [ABH99].

The kinetic energy of the optimal disturbance $\mathbf{f}_{\text{in}}$, if only v_{in} and w_{in} are nonzero, is therefore:

$$E_{\text{in}} = \int_0^\infty \left[\rho_{s\text{in}} \epsilon^2 (v_{\text{in}}^2 + w_{\text{in}}^2)\right] dy, \tag{4.9}$$

or more compactly

$$E_{\text{in}} = \int_0^\infty \left(\mathbf{f}_{\text{in}}^T \widetilde{\boldsymbol{M}}_{\text{in}} \mathbf{f}_{\text{in}}\right) dy \tag{4.10}$$

where $\widetilde{\boldsymbol{M}}_{\text{in}}$ is a 5×5 diagonal matrix

$$\widetilde{\boldsymbol{M}}_{\text{in}} = \begin{bmatrix} 0 & 0 & 0 & 0 & 0 \\ 0 & \epsilon^2 \rho_{s\text{in}} & 0 & 0 & 0 \\ 0 & 0 & \epsilon^2 \rho_{s\text{in}} & 0 & 0 \\ 0 & 0 & 0 & 0 & 0 \\ 0 & 0 & 0 & 0 & 0 \end{bmatrix} \tag{4.11}$$

The quantity to be maximized is $G = E_{\text{out}}/E_{\text{in}}$, the ratio between the outlet and inlet norms. However, in order to allow direct comparison with previous works, $G\epsilon^2$ will be presented in the results section. Combining expressions (4.6) and (4.9) leads to

$$G\epsilon^2 = \frac{\displaystyle\int_0^\infty \left[\rho_{s\text{out}} \left(u_{\text{out}}^2 + \epsilon^2 (v_{\text{out}}^2 + w_{\text{out}}^2)\right) + \frac{p_{s\text{out}} T_{\text{out}}^2}{(\gamma - 1) T_{s\text{out}}^2 M^2}\right] dy}{\displaystyle\int_0^\infty \left[\rho_{s\text{in}} (v_{\text{in}}^2 + w_{\text{in}}^2)\right] dy}, \tag{4.12}$$

which reduces, in the $Re \to \infty$ limit ($\epsilon \to 0$), to the expression maximized by [TR03] for the compressible case and by [Luc00] for the incompressible one. Since the problem is linear, an arbitrary normalization for the initial disturbance at x_{in} can be chosen, e.g. $E_{\text{in}} = E_0 = 1$, so that the maximization of (4.12) turns out to be equivalent to the maximization of expression (4.7).

From the above discussion it is clear that the whole problem of finding optimal perturbations reduces to a "constrained optimization", in which we seek the initial conditions for the disturbance equations (4.3) that maximize (4.7) and that satisfy the constraint $E_{\text{in}} = E_0$ at x_{in} together with the direct equations (4.3) and boundary conditions (4.2) at each $x \in (x_{\text{in}}; x_{\text{out}})$.

Constrained optimization

The classical Lagrange multiplier technique is one of the most known tools to solve constrained optimization problems. As applied to optimal perturbations, numerous examples can be found in the literature regarding the continuous version of such an approach, which leads to the so-called adjoint equations in a continuous fashion. Rigorously speaking, in the theory of linear operators the adjoint equations are derived by satisfying an equality involving an inner product [NS00, Kre89]. Therefore their form is not necessarily related to constrained optimization problems. On the contrary, when the adjoint equations are derived from a constrained optimization (as in our case) only if the objective function includes exclusively quantities at the boundaries of the domain then their form is the same as those derived from an inner product equality. In fact, if we try to maximize the integral of the energy over the whole domain (as opposed to the outlet energy only), a source term arises in the adjoint equations [CL00, ZLB04, ZBL06]. As opposed to the continuous version of the Lagrange multiplier approach, less numerous are the examples where this technique is applied directly to the discrete equations [LB98, LB01, Luc00, CL00, ZLB04, ZBL06].

The adjoint methodology for the calculation of optimal perturbations, and in particular its discrete implementation, was introduced by [FM92] in the context of oceanic flows. The use of the discrete approach has several advantages among which the necessity of an "ad hoc" adjoint code is avoided and a foolproof test is available by comparing the results of the direct and adjoint calculations, which must match up to machine accuracy for any step size and not only in the limit of step size tending to zero [ZBL06]. This is due to the conservation of a quantity which depends on x only [LB98, Luc00]. For a thorough discussion on the issue of continuous versus discrete adjoints the reader is referred to [Gun00].

The numerical discretization of a general parabolic system of partial differential equations such as (4.3) can always be recast as

$$\boldsymbol{C}_{n+1}\mathbf{f}_{n+1} = \boldsymbol{B}_n\mathbf{f}_n \tag{4.13}$$

where n denotes the n-th grid point in the streamwise direction x, $\mathbf{f}$ is the vector of unknowns (not with only 5 elements but with $5 \times N_y$, where N_y is the number of grid points in the wall-normal direction y) and matrices $\boldsymbol{C}$ and $\boldsymbol{B}$ depend on x (as the basic flow does) and account for the discretization in both x and y. The solution is found by marching forward in space from $n = 0$ (x_{in}), given the initial condition $\mathbf{f}_0$, to $n = N$ (x_{out}). The boundary conditions at the wall and for $y \to \infty$ are already included in the matrices rows. The discrete objective function we aim to maximize is $\mathcal{J} = \mathbf{f}_N^{\mathrm{T}}\boldsymbol{M}_N\mathbf{f}_N$, where $\boldsymbol{M}_N$ is the discrete version of $\widetilde{\boldsymbol{M}}_{\text{out}}$ as defined in (4.8) and accounts for the discretization of the integral in y.

The augmented functional $\mathcal{L}$, which contains the objective function $\mathcal{J} = E_{\text{out}}$, the constraints (4.13) and $E_{\text{in}} = E_0$, and the Lagrange multipliers, is written as

$$\mathcal{L}(\mathbf{f}_0, \ldots, \mathbf{f}_N) = \mathbf{f}_N^{\mathrm{T}}\boldsymbol{M}_N\mathbf{f}_N + \sum_{n=0}^{N-1}\left[\mathbf{p}_n^{\mathrm{T}}\left(\boldsymbol{C}_{n+1}\mathbf{f}_{n+1} - \boldsymbol{B}_n\mathbf{f}_n\right)\right] + \lambda_0[\mathbf{f}_0^{\mathrm{T}}\boldsymbol{M}_0\mathbf{f}_0 - E_0] \tag{4.14}$$

where $\mathbf{p}_n$ is the vector of Lagrangian multipliers, which depends on the streamwise location n and $\boldsymbol{M}_0$ is the discrete version of $\widetilde{\boldsymbol{M}}_{\text{in}}$ as defined in (4.11), in the same fashion as $\boldsymbol{M}_N$. Only

the dependence on $\mathbf{f}_n$ $(n = 0, \ldots, N)$ has been emphasized in $\mathcal{L}$ because its derivative with respect to the Lagrangian multipliers (which is needed to impose $\delta\mathcal{L} = 0$) would lead to the constraints, that are already known. The summation between 0 and $N-1$ in (4.14) involving $\mathbf{p}_n$ reflects the integral along x. The integration by parts (which would be performed in the continuous case) is here replaced by adding and subtracting $\mathbf{p}_{n+1}^{\mathrm{T}}\boldsymbol{B}_{n+1}\mathbf{f}_{n+1}$ in the summation so that the terms can be rearranged as

$$\begin{aligned}\sum_{n=0}^{N-1}\left[\mathbf{p}_n^{\mathrm{T}}\left(\boldsymbol{C}_{n+1}\mathbf{f}_{n+1} - \boldsymbol{B}_n\mathbf{f}_n\right)\right] &= \sum_{n=0}^{N-1}\left[\mathbf{p}_n^{\mathrm{T}}\boldsymbol{C}_{n+1}\mathbf{f}_{n+1} - \mathbf{p}_{n+1}^{\mathrm{T}}\boldsymbol{B}_{n+1}\mathbf{f}_{n+1}\right] + \\ &\quad \sum_{n=0}^{N-1}\left[\mathbf{p}_{n+1}^{\mathrm{T}}\boldsymbol{B}_{n+1}\mathbf{f}_{n+1} - \mathbf{p}_n^{\mathrm{T}}\boldsymbol{B}_n\mathbf{f}_n\right] \\ &= \sum_{n=0}^{N-1}\left[\mathbf{p}_n^{\mathrm{T}}\boldsymbol{C}_{n+1}\mathbf{f}_{n+1} - \mathbf{p}_{n+1}^{\mathrm{T}}\boldsymbol{B}_{n+1}\mathbf{f}_{n+1}\right] + \\ &\quad \mathbf{p}_N^{\mathrm{T}}\boldsymbol{B}_N\mathbf{f}_N - \mathbf{p}_0^{\mathrm{T}}\boldsymbol{B}_0\mathbf{f}_0,\end{aligned}$$

and expression (4.14) can be rewritten as

$$\begin{aligned}\mathcal{L}(\mathbf{f}_0, \ldots, \mathbf{f}_N) &= \mathbf{f}_N^{\mathrm{T}}\boldsymbol{M}_N\mathbf{f}_N + \sum_{n=0}^{N-1}\left[\mathbf{p}_n^{\mathrm{T}}\boldsymbol{C}_{n+1}\mathbf{f}_{n+1} - \mathbf{p}_{n+1}^{\mathrm{T}}\boldsymbol{B}_{n+1}\mathbf{f}_{n+1}\right] + \\ &\quad \mathbf{p}_N^{\mathrm{T}}\boldsymbol{B}_N\mathbf{f}_N - \mathbf{p}_0^{\mathrm{T}}\boldsymbol{B}_0\mathbf{f}_0 + \lambda_0[\mathbf{f}_0^{\mathrm{T}}\boldsymbol{M}_0\mathbf{f}_0 - E_0].\end{aligned} \tag{4.15}$$

As in the continuous case, the stationary condition is found when $\delta\mathcal{L} = 0$

$$\frac{\delta\mathcal{L}}{\delta\mathbf{f}_0}\delta\mathbf{f}_0 + \sum_{n=0}^{N-2}\left[\frac{\delta\mathcal{L}}{\delta\mathbf{f}_{n+1}}\delta\mathbf{f}_{n+1}\right] + \frac{\delta\mathcal{L}}{\delta\mathbf{f}_N}\delta\mathbf{f}_N = 0,$$

which, in order to be satisfied for any arbitrary $\mathbf{f}_0$, $\mathbf{f}_{n+1}$ and $\mathbf{f}_N$, leads to

$$\frac{\delta\mathcal{L}}{\delta\mathbf{f}_0} = -\mathbf{p}_0^{\mathrm{T}}\boldsymbol{B}_0 + 2\lambda_0\mathbf{f}_0^{\mathrm{T}}\boldsymbol{M}_0 = 0 \tag{4.16}$$

$$\frac{\delta\mathcal{L}}{\delta\mathbf{f}_{n+1}} = \mathbf{p}_n^{\mathrm{T}}\boldsymbol{C}_{n+1} - \mathbf{p}_{n+1}^{\mathrm{T}}\boldsymbol{B}_{n+1} = 0, \quad n = 0, \ldots, N-1 \tag{4.17}$$

$$\frac{\delta\mathcal{L}}{\delta\mathbf{f}_N} = 2\mathbf{f}_N^{\mathrm{T}}\boldsymbol{M}_N + \mathbf{p}_N^{\mathrm{T}}\boldsymbol{B}_N = 0 \tag{4.18}$$

Equation (4.16) furnishes the optimality condition to be satisfied at x_{in} and equation (4.17) leads to

$$\mathbf{p}_n^{\mathrm{T}}\boldsymbol{C}_{n+1} - \mathbf{p}_{n+1}^{\mathrm{T}}\boldsymbol{B}_{n+1} = 0, \tag{4.19}$$

which is the discrete form of the adjoint equations to be solved by marching backwards from x_{out} to x_{in} with the initial condition provided by equation (4.18) solved for $\mathbf{p}_N$.

Outlet conditions

From expression (4.18) follows

$$\boldsymbol{B}_N^{\mathrm{T}}\mathbf{p}_N = -2\boldsymbol{M}_N^{\mathrm{T}}\mathbf{f}_N \tag{4.20}$$

where $\boldsymbol{B}_N$ is the discrete representation of $\boldsymbol{H}_{1\text{out}}$ and is singular due to the fact that the fifth column in $\boldsymbol{H}_1$ is made of zeros as $p_x = 0$ in this approximation (the last column of matrix $\boldsymbol{A}$ is made of zeros). This implies that the solution cannot be found unless the solvability condition is satisfied. The singularity of $\boldsymbol{H}_1$ is not simply a practical numerical problem for the solution of (4.20) but contains deeper information and insights regarding the initial condition for the adjoint variables. The impossibility to determine a unique solution of (4.20) translates into the fact that at least one out of five adjoint variables is free at $x = x_{\text{out}}$ and therefore can be chosen arbitrarily. For sake of simplicity, we set p_5 (the fifth adjoint variable) to zero.

Inlet conditions

By imposing $\delta\mathcal{L}/\delta\mathbf{f}_{\text{in}} = 0$ condition (4.16) was obtained. The operator $\boldsymbol{M}_0$ is the discrete counterpart of $\boldsymbol{M}_{\text{in}}$ and is singular (as $\boldsymbol{M}_{\text{out}}$) so $\boldsymbol{M}_0^{-1}$ does not exist and (4.16) can not be solved. However, $\boldsymbol{M}_0$ is diagonal and therefore the j-th element of $\mathbf{f}_0$ corresponding to $\boldsymbol{M}_{0jj} \neq 0$ can be retrieved by

$$\mathbf{f}_{0j} = \begin{cases} \dfrac{(\mathbf{p}_0^T \boldsymbol{B}_0)_j}{2\lambda \boldsymbol{M}_{0jj}} & \text{if} \quad \boldsymbol{M}_{0jj} \neq 0 \\ \\ 0 & \text{if} \quad \boldsymbol{M}_{0jj} = 0 \end{cases} \tag{4.21}$$

The multiplier λ is found by imposing the constraint $E_0 = E_{\text{in}}$.

An optimization algorithm

The constrained optimization developed above has enabled us to write a set of equations and boundary conditions that must be satisfied simultaneously. More specifically, we first need to solve system (4.13) from $x = x_{\text{in}}$ ($n = 0$) to $x = x_{\text{out}}$ ($n = N - 1$) with initial conditions at x_{in} expressed by (4.21). We refer to this as the direct or forward problem. Then we need to solve system (4.19) from $x = x_{\text{out}}$ ($n = N - 1$) to $x = x_{\text{in}}$ ($n = 0$), with initial conditions derived from (4.20) and provided at $x = x_{\text{out}}$. We call this the adjoint or backward problem.

A quite large system of linear equations supplemented by initial and boundary conditions has to be solved. Instead of doing it in one shot, however, we employ the intrinsic parabolic nature of the equations to efficiently solve separately the two coupled problems. Such an algorithm can be outlined in the following few steps:

1. a guessed initial condition $\mathbf{f}_{\text{in}}^{(0)}$ is provided at the beginning of the optimization procedure

2. the forward problem (4.13) is solved at the i-th iteration with the initial condition $\mathbf{f}_{\text{in}}^{(i)}$

3. the objective function $\mathcal{J}^{(i)} = E_{\text{out}}^{(i)}$ is computed at the end of the forward iteration and compared to the objective function $\mathcal{J}^{(i-1)} = E_{\text{out}}^{(i-1)}$ at the end of the previous forward iteration. If $|\mathcal{J}^{(i)}/\mathcal{J}^{(i-1)} - 1| < \epsilon_t$ (where ϵ_t is the maximum tolerance accepted to stop the optimization) then the optimization is considered converged

4. if $|\mathcal{J}^{(i)}/\mathcal{J}^{(i-1)} - 1| > \epsilon_t$ the initial conditions for the backward problem (4.20) are assigned at the outlet and derived from the direct solution at $x = x_{\text{out}}$

5. the backward problem (4.19) is solved from $x = x_{\text{out}}$ to $x = x_{\text{in}}$

6. a new initial condition for the forward problem $\mathbf{f}_{\text{in}}^{(i+1)}$ is obtained from the solution of the backward problem at $x = x_{\text{in}}$ employing (4.21)

7. the loop is repeated from step 2 on.

A similar iterative approach was first introduced by [FM92] for obtaining the most rapidly growing perturbations in oceanic flows.

It should be noted that the above procedure does not necessarily guarantee convergence. If there is an attractor for the solution, then the procedure will capture it and this happens quite fast (2-3 forward-backward iterations) when the norm proposed by [Luc00] is used. On the other hand, it was observed that when the full energy norm is employed the convergence is generally much slower, depending on the wavenumber β, reaching the fastest convergence in the proximity of the optimal β.

Discretization

A finite difference discretization scheme has been implemented to numerically solve equations (4.3) with boundary conditions (4.2). For sake of generality, grid points in x and y are not necessarily equally spaced. A staggered grid is introduced in the wall-normal direction, with variables u, v, w and T known at the grid points, and p known at the mid-grid (staggered) points. All equations are satisfied at the grid points except for continuity, which is satisfied in the mid-grid points. The use of the uneven grid in y allows us to cluster more nodes close to the wall so as to take into account the large gradients of boundary layer quantities in this region.

The last point of the y-grid is located far enough from the wall to allow us to specify there the boundary conditions for $y \to \infty$.

Fourth-order non-compact finite differences are used for the y discretization, employing six points so as to allow 4th order accuracy for the second derivative. By using six points, the first derivative is automatically 5th order accurate and the function (when interpolated due to the staggered grid) is 6th order accurate.

Also the discretization in the streamwise direction is based on uneven grid. Since the system of boundary layer equations is parabolic, a second order backward discretization is chosen, which requires the solution at two previous steps to be known. For the first step, however, a first order scheme is used because only the initial condition is available.

After the discretization, the original system of partial differential equations (4.3) can be re-written in the following form:

$$\left[C^0_{n+1}\boldsymbol{H}^1_{n+1} + \boldsymbol{H}^2_{n+1}\right]\mathbf{f}_{n+1} = -C^1_{n+1}\boldsymbol{H}^1_n\mathbf{f}_n - C^2_{n+1}\boldsymbol{H}^1_{n-1}\mathbf{f}_{n-1} \tag{4.22}$$

where coefficients C^0_{n+1}, C^1_{n+1} and C^2_{n+1} account for the streamwise discretization and matrices $\boldsymbol{H}^1_{n+1}$ and $\boldsymbol{H}^2_{n+1}$ are the discretized version of respectively $\boldsymbol{H}_1$ and $\boldsymbol{H}_2$ introduced in the governing equations' section. The solution is thus completely determined once the initial condition $\mathbf{f}_0 = \mathbf{f}_{\text{in}}$ is given at x_{in}. Clearly, for the first step in x a first-order approximation is used for the derivative since data are available only at one point upstream, not two.

Equation (4.22) can be easily rewritten in a form similar to (4.13)

$$\boldsymbol{C}_{n+1}\mathbf{f}_{n+1} = C^1_{n+1}\boldsymbol{B}_n\mathbf{f}_n + C^2_{n+1}\boldsymbol{B}_{n-1}\mathbf{f}_{n-1} \tag{4.23}$$

where $\boldsymbol{C}_{n+1} = \left[C^0_{n+1}\boldsymbol{H}^1_{n+1} + \boldsymbol{H}^2_{n+1}\right]$ and $\boldsymbol{B}_n = -\boldsymbol{H}^1_n$

Contrary to the simple form (4.13), which refers to a scheme where the new solution $\mathbf{f}_{n+1}$ depends on $\mathbf{f}_n$ only, the discrete equation (4.22) depends on $\mathbf{f}_n$ and $\mathbf{f}_{n-1}$ due to the second order approximation in x. Therefore, the discrete adjoint system is slightly different from (4.19). More specifically, by repeating the same steps as in constrained optimization section, the constraint $\boldsymbol{C}_{n+1}\mathbf{f}_{n+1} - C^1_{n+1}\boldsymbol{B}_n\mathbf{f}_n - C^2_{n+1}\boldsymbol{B}_{n-1}\mathbf{f}_{n-1} = 0$ is left multiplied by the vector of Lagrangian multipliers $\mathbf{p}_n$ and then all terms are included in the summation on n (in the streamwise direction) to form the functional for the constrained optimization. Within this summation, we first add and subtract the quantity $\mathbf{p}^{\mathrm{T}}_{n+1}\left[C^1_{n+2}\boldsymbol{B}_{n+1}\mathbf{f}_{n+1} + C^2_{n+2}\boldsymbol{B}_n\mathbf{f}_n\right]$ and rearrange the summation as $\sum \mathbf{p}^{\mathrm{T}}_n\left[\boldsymbol{C}_{n+1}\mathbf{f}_{n+1}\right] - \sum \mathbf{p}^{\mathrm{T}}_{n+1}\left[C^1_{n+2}\boldsymbol{B}_{n+1}\mathbf{f}_{n+1} + C^2_{n+2}\boldsymbol{B}_n\mathbf{f}_n\right]$ and then we add and subtract the quantity $\mathbf{p}^{\mathrm{T}}_{n+2}\left[C^1_{n+3}\boldsymbol{B}_{n+1}\mathbf{f}_{n+1}\right]$ so that the final form of the summation is $\sum \mathbf{p}^{\mathrm{T}}_n\left[\boldsymbol{C}_{n+1}\mathbf{f}_{n+1}\right] - \sum \mathbf{p}^{\mathrm{T}}_{n+1}\left[C^1_{n+2}\boldsymbol{B}_{n+1}\mathbf{f}_{n+1}\right] - \sum \mathbf{p}^{\mathrm{T}}_{n+2}\left[C^2_{n+3}\boldsymbol{B}_{n+1}\mathbf{f}_{n+1}\right]$. In this way, all terms are right multiplied by $\mathbf{f}_{n+1}$ so that the derivative of the functional $\mathcal{L}$ with respect to $\mathbf{f}_{n+1}$ leads to the adjoint discrete equation in the form

$$\mathbf{p}^{\mathrm{T}}_n\boldsymbol{C}_{n+1} - \mathbf{p}^{\mathrm{T}}_{n+1}C^1_{n+2}\boldsymbol{B}_{n+1} - \mathbf{p}^{\mathrm{T}}_{n+2}C^2_{n+3}\boldsymbol{B}_{n+1} = 0, \tag{4.24}$$

where the solution at step n is obtained by marching upstream in space from the outlet to the inlet and needs two steps downstream to be computed.

The basic-flow model

The basic flow for the flat plate is the same as in [TR03] and is obtained from a conventional similarity solution.

For the high-speed flow past a sphere, the streamwise velocity U_e at the edge of the boundary layer of the subsonic part of the flow can be approximated by

$$U_e = \left.\frac{dU_e}{d\theta}\right|_0 \theta,$$

where $dU_e/d\theta|_0$ is the derivative of the edge velocity with respect to the meridional coordinate θ evaluated at the stagnation point. This quantity can be calculated from the modified Newtonian pressure distribution [Jr.89] as

$$\frac{1}{U_\infty}\left.\frac{dU_e}{d\theta}\right|_0 = \sqrt{\frac{C_{p_{\max}}\rho_\infty}{\rho_0}}$$

with $C_{p_{\max}}$ (maximum pressure coefficient) and ρ_0 evaluated at the stagnation point for a calorically perfect gas with specific heat ratio $\gamma = 1.4$. Flow parameters at the edge of the boundary layer for the downstream locations can then be found from the isentropic relationships.

For the compressible boundary layer we consider the local-similarity approximation [Jr.89] and introduce the Levy-Lees-Dorodnitsyn variables

$$\xi = \int_0^\theta \rho_e \mu_e U_e R^3 (\sin\theta)^2 \, d\theta; \qquad \bar{\eta} = \frac{\rho_e U_e R \sin\theta}{\sqrt{2\xi}} \int_0^\eta \frac{\rho}{\rho_e} \, d\eta,$$

where $\eta = y/H_{\text{ref}}$, y being the coordinate in the wall-normal direction. After substituting these new variables ξ and $\bar{\eta}$, boundary-layer equations can be recast as

$$(Cf'')' + ff'' + \beta_H \left[\frac{\rho}{\rho_e} - (f')^2\right] = 0$$

$$\left(\frac{C}{Pr}\hat{g}'\right)' + f\hat{g}' + \frac{(\gamma-1)M_e^2}{1+\dfrac{\gamma-1}{2}M_e^2}\left[C\left(1-\frac{1}{Pr}\right)ff''\right]' = 0$$

where the prime ($'$) denotes the partial derivative with respect to $\bar{\eta}$, $C = (\rho\mu)/(\rho_e\mu_e)$ and $\beta_H = (2\xi/U_e)dU_e/d\xi$ is the Hartree parameter. These boundary layer equations are solved subject to the conventional boundary layer conditions on the wall and in the freestream [Jr.89]. The flow quantities are then retrieved from functions $f(\xi,\bar{\eta})$ and $\hat{g}(\xi,\bar{\eta})$, which are related to the velocity $U(\xi,\bar{\eta})$ and total enthalpy $I(\xi,\bar{\eta})$ according to the similarity laws

$$U(\xi,\bar{\eta}) = U_e(\xi) f'(\xi,\bar{\eta}); \qquad I(\xi,\bar{\eta}) = I_e \hat{g}(\xi,\bar{\eta}).$$

As proved in figures 4.1(a) and 4.1(b), for $\theta \leq 30°$ β_H lies within the interval $[0.5; 0.6]$ and the Mach number is a linear function of θ. Moreover, when the wall-normal distance is scaled with $H(\theta) = \sqrt{2\xi}/(\rho_e U_e R \sin\theta)$ profiles of U/U_e and T/T_e are almost independent of the Mach number M_e and Hartree parameter β_H, as shown in figures 4.2(a) and 4.2(b).

The dependence on the meridional angle θ enters the analysis only through the local velocity, temperature, density and pressure at the edge of the boundary layer, and through the local length scale $H(\theta)$, which is however a slow function of θ as figure 4.3 clearly shows.

For the present study we have chosen the scaled velocity and temperature profiles obtained for $M_e = 0.6$ and $\beta_H = 0.5$.

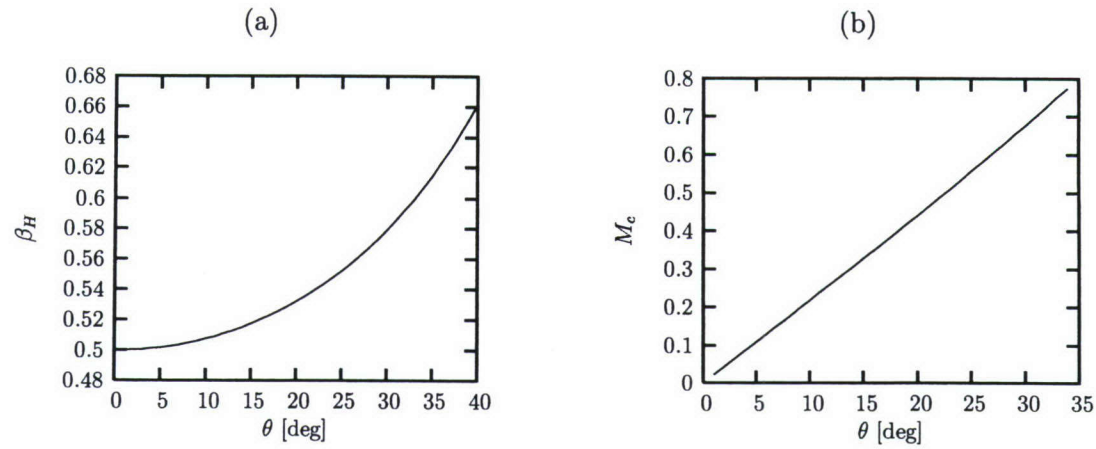

Figure 4.1: Hartree parameter β_H (a) and local Mach number M_e at the edge of the boundary layer (b) as a function of the the meridional angle θ.

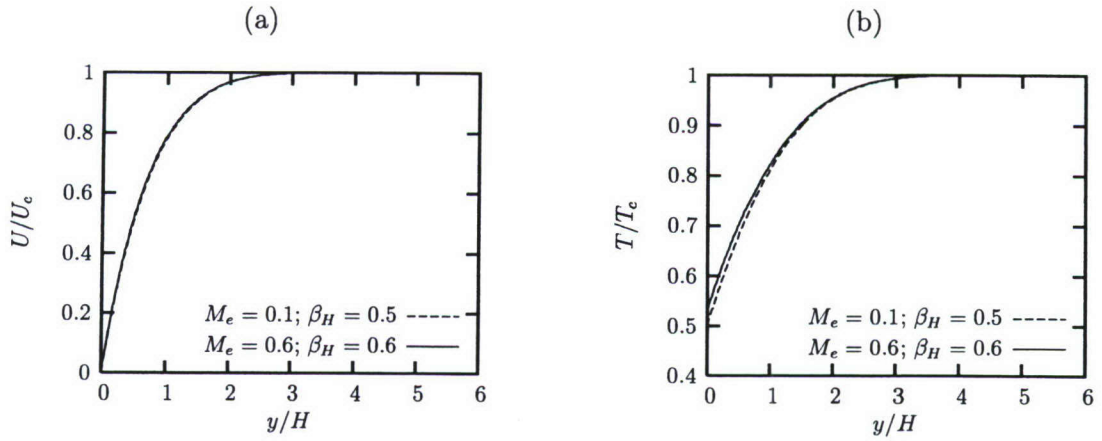

Figure 4.2: Effect of the Mach number M_e and Hartree parameter β_H on the basic flow profiles. (a) streamwise velocity, (b) temperature.

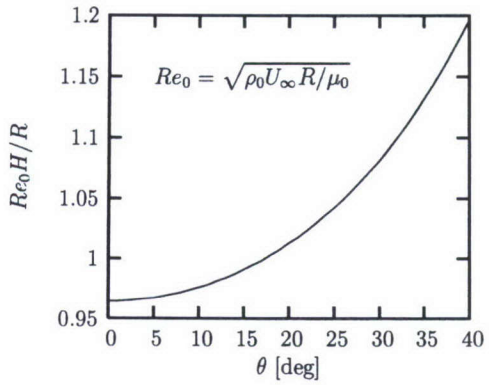

Figure 4.3: Boundary layer local length scale $Re_0 H/R$ as a function of the the meridional angle θ

Shortcoming of the iterative algorithm

As mentioned before, the choice of the norm is not unique. Here we discuss some limitations of the iterative algorithm due to the choice of the inlet norm and focus on the incompressible case, for which previously published results obtained with different norms are available.

[ABH99] employed the full norm including all components of velocity. By combining the continuity equation with the streamwise momentum equation (for the perturbations) and the continuity equation for the basic flow they derived a constraint that holds for each $x > 0$

$$(\beta^2 - V_y)u + Vu_y - u_{yy} + U_y v - Uv_y - \beta U w = 0, \tag{4.25}$$

but optimal disturbances were computed at the leading edge of the flat plate, $x_{\text{in}} = 0$. In order to avoid discontinuity of the solution at $x = 0$, [ABH99] required the optimal perturbation $[u_{\text{in}}, v_{\text{in}}, w_{\text{in}}]$ to satisfy the constraint (4.25) also at $x = 0^-$. However, since u, v and w at $x = 0^-$, as resulting from the application of the inlet conditions stemming from the adjoint-based iterative algorithm, do not satisfy (4.25), [ABH99] needed to solve a further least square problem seeking $[u_{\text{in}}, v_{\text{in}}, w_{\text{in}}]$ that simultaneously satisfy (4.25) and minimize the distance from the solution obtained by applying the inlet conditions (4.21).

It should be noticed that in [Luc00], where u_{in} was set to zero, no further constraints such as (4.25) were required because in that case v and w as resulting from the inlet conditions already satisfy the governing equations at $x_{\text{in}} = 0$, and there is no discontinuity in the solution.

From the point of view of optimization, what was done by [ABH99] corresponds to adding more constraints to the problem. Because of this, the optimization procedure locates a maximum with a value of the objective function lower than in the case where the optimal perturbation is not constrained by an equation at the inlet.

Here we propose a further analysis of this issue.

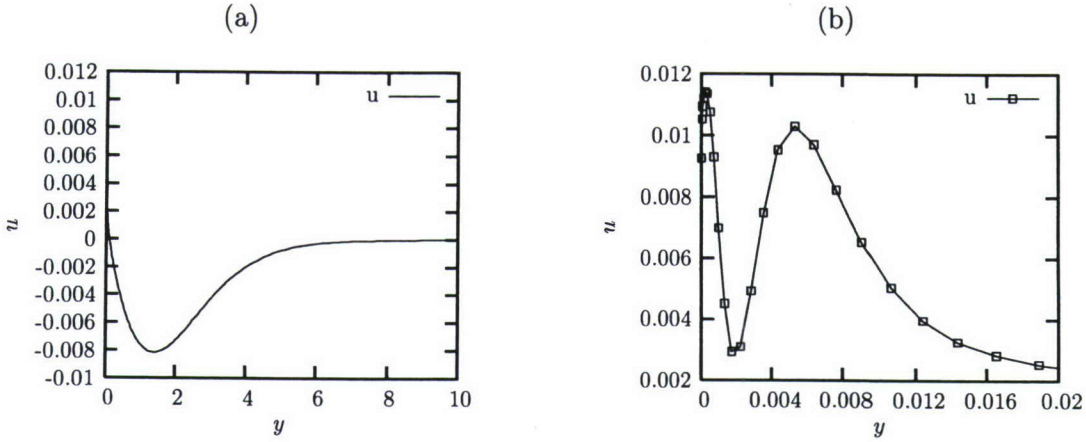

Figure 4.4: Profile of u_{in} as a function of y, no constraints on the initial condition, full energy norm at both inlet and outlet, $Re = 1000$. $M = 0.02$, $x_{\text{in}} = 0$ $x_{\text{out}} = 1.0$, $T_{\text{w}}/T_{\text{ad}} = 1$, $\beta = 0.55$. (a) Outer view. (b) Zoom in the proximity of the wall.

By writing explicitly the inlet conditions (4.21), it is easy to verify that v_{in} and w_{in} go to zero at the wall as long as the streamwise component of the basic flow does, because they originate from the adjoint solution multiplied by U. Therefore, even if the adjoint field is not homogeneous at the wall, since U satisfies the no-slip condition, v_{in} and w_{in} are zero at the wall. On the contrary, the expression for u_{in} does not guarantee $u = 0$ at the wall and thus a non homogeneous solution is allowed at the wall by the algorithm. However, this nonphysical solution guarantees the maximum gain in the optimization procedure.

We consider adiabatic wall conditions, $T_{\text{w}}/T_{\text{ad}} = 1$, and freestream Mach number $M = 0.02$. Figure 4.4 shows the streamwise component of the optimal perturbation obtained without any further constraint and using full energy norm at both input and output (FENI and FENO). The outer view, figure 4.4(a), indicates that u_{in} does not satisfy the no-slip condition at the wall. Zooming in on the proximity of $y = 0$, figure 4.4(b), the behavior of u_{in} is clearer, showing a few oscillations. The latter do not originate from the numerical scheme, as was proven by changing from 4th order to 2nd order finite differences in y. On the contrary, they originate from the fact that u_{in} is generated by a component of the adjoint solution that does not guarantee $u_{\text{in}} = 0$ at the wall.

Different possible choices are available to render u_{in} homogeneous at the wall so as to reconcile the optimization algorithm with the governing equations. Such a "smoothing", i.e. forcing $u_{\text{in}} = 0$ at the wall, avoids the discontinuity at $x_{\text{in}} = 0$ that would occur due to the fact that at $x = 0^+$ it must be $u = 0$ on the wall because of the no-slip condition.

The simplest approach is to substitute v_{in} and w_{in} as provided by the inlet conditions (4.21) into (4.25) and to obtain u_{in} from a boundary value problem where u_{in} is forced to be zero at the wall and in the free stream. By doing so, results reported in figure 4.5 are obtained. The order of magnitude of u is now much smaller than what was seen in figure 4.4,

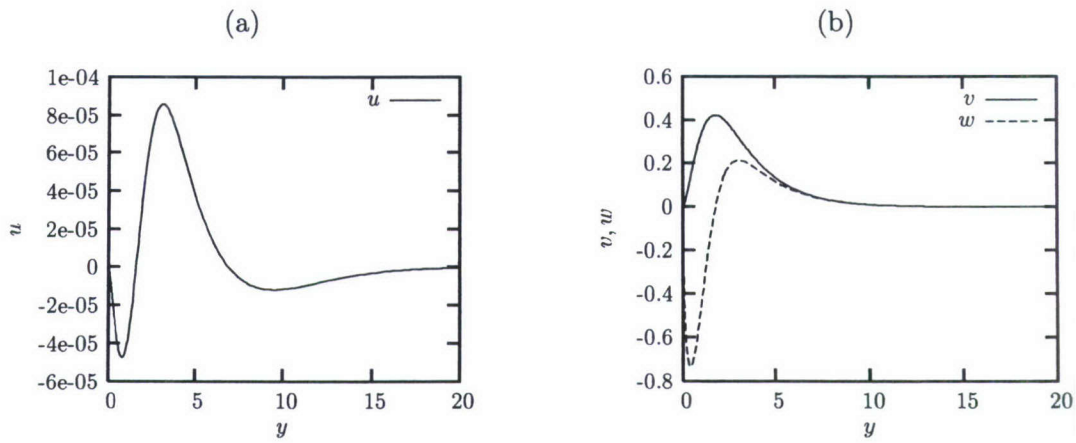

Figure 4.5: Profile of u_{in}, v_{in} and w_{in} as a function of y, physical, constrained solution. $M = 0.02$, $x_{\text{in}} = 0$ $x_{\text{out}} = 1.0$, $T_{\text{w}}/T_{\text{ad}} = 1$, $\beta = 0.55$. The constraint (4.25) is used where v_{in} and w_{in} are those originating from the inlet conditions (4.21) and u_{in} is calculated from the linear ordinary differential equation so obtained by imposing homogeneous boundary conditions at the wall and in the free stream. (a) u_{in}. (b) v_{in} and w_{in}.

while v_{in} and w_{in} remain on the same order as before. This choice of rendering u_{in} zero at the wall so as to avoid the discontinuity at x_{in}, therefore, leads to an initial perturbation very far from the one originally computed without additional constraints and generates a consequently much lower gain.

If the goal is to try to keep u_{in} on the same order of magnitude as the profile originating from the inlet conditions alone (the one in figure 4.4) but assuring the continuity at x_{in} by imposing the $u_{\text{in}} = 0$ on the wall, then infinite possibilities are available.

We chose to replace the oscillations in u_{in} visible in figure 4.4 with a smooth solution so as to keep u_{in} untouched from a certain $\hat{y}$ to y_{max} (where the boundary conditions for $y \to \infty$ are imposed) and to replace u_{in} with a smooth function that goes to zero with y for $y < \hat{y}$. Both $\hat{y}$ and the smooth function are arbitrary. For the function we need a choice that guarantees the continuity of u_{in} and its first and second derivative in $\hat{y}$ (to avoid discontinuities when u_{in} is substituted in (4.25)) and such that its second derivative is zero at the wall. The latter requirement is dictated by the constraint equation (4.25), from which it is easy to verify that at the wall $w = u_{yy}$. A 4th-order polynomial is used. The value $\hat{y}$ is chosen to be 80% of the position in y where v_{in} reaches its maximum. After u_{in} has been smoothed, the constraint (4.25) is used to compute w_{in} given u_{in} and v_{in}.

This choice of smoothing u_{in} and constraining it to be zero at the wall produces a small difference (in the profile of u_{in}) with respect to the free case reported in figure 4.4 (see figure 4.6(a)), with the discrepancy localized in the proximity of the wall. On the contrary, no significant differences are detectable in the profiles of v_{in} and w_{in} (figure 4.6(b)). Since the optimal perturbation remains almost unchanged, the difference in the gain between the

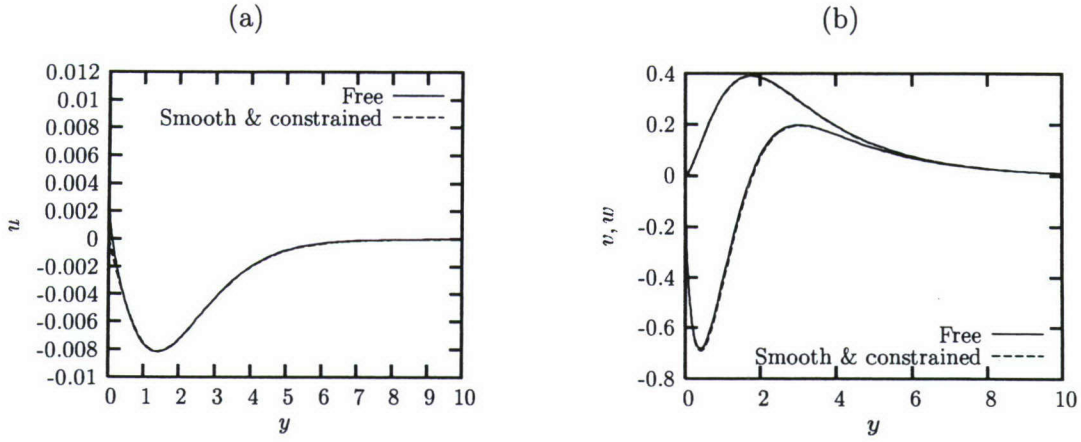

Figure 4.6: Profile of u_{in}, v_{in} and w_{in} as a function of y. Comparison between the "free" solution computed from the inlet conditions (4.21) and the physical solution obtained by smoothing u_{in} and constraining it to be zero at the wall. The constraint (4.25) is used to compute w_{in} given u_{in} and v_{in}. $M = 0.02$, $x_{\text{in}} = 0$ $x_{\text{out}} = 1.0$, $T_{\text{w}}/T_{\text{ad}} = 1$, $\beta = 0.55$. (a) u_{in}. (b) v_{in} and w_{in}.

"free" and "smooth and physical" cases is very tiny. For the smoothened case the gain is $G/Re = 2.52 \cdot 10^{-3}$ as opposed to $G/Re = 2.54 \cdot 10^{-3}$ in the free case. This difference is about 0.8%, even smaller than the tolerance (1%) which is required to end the forward-backward iteration in the optimization procedure presented in the algorithm section.

Such a result offers much better insights regarding the issue of the inlet norm. It shows that in the constrained case the gain is, as expected, smaller than in the free case but this difference is extremely tiny and within the tolerance of the scheme. The explanation resides in the order of magnitude of u_{in}. If it is kept on the same order as resulting from the application of the automatic inlet conditions (4.21) then the gain is practically the same as in the case of unconstrained u_{in}. On the contrary, when u_{in} is obtained by solving the ordinary differential equation (4.25) assuming v_{in} and w_{in} given, a much smaller u_{in} is obtained with a considerable difference in the gain.

A summary of the above discussion is graphically reported in figure 4.7, where different curves are reported.

Results by [ABH99] ($\times$) were obtained with full energy norm at both inlet and outlet and show the largest values of the gain. They differ only slightly from those obtained in the present work for the case of free optimization ($\square$) and for the case of smoothed and constrained inflow profile ($\circ$). The maximum discrepancy is on the order of 3% and it is believed to be due to different numerical schemes, as the same trend was observed in the case of infinite Reynolds number limit (figure 4.8). Although it is not clear how the problem of discontinuity in u_{in} at the wall for $x_{\text{in}} = 0$ was treated by [ABH99], our results illustrate that the energy gains are very close for constrained (smoothened u) and free optimizations.

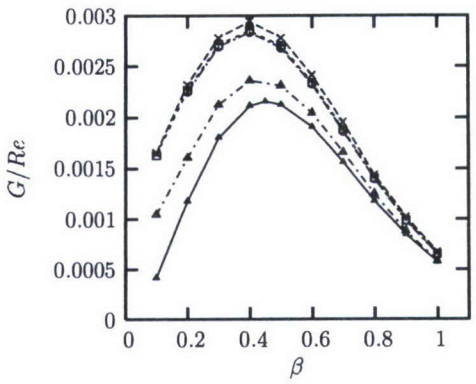

Figure 4.7: Comparison of G/Re between results obtained by [ABH99] and present work. $\times$, [ABH99], $Re = 1000$; $\square$, free optimization, $Re = 1000$; $\circ$, smooth and constrained, $Re = 1000$; $\triangle$, $u = 0$, $Re = 1000$; $\blacktriangle$, $Re \to \infty$. $M = 0.02$, $x_{\text{in}} = 0$ $x_{\text{out}} = 1.0$, $T_{\text{w}}/T_{\text{ad}} = 1$. Values of the gain are bounded between the free optimization results (upper limit - $\square$) and the Reynolds independent ones (lower limit - $\blacktriangle$). Any constraint on the initial perturbation produces an energy gain that is within these limits.

Instead of employing a constraint equation, one can simply impose $u = 0$ at x_{in} (symbols $\triangle$ in figure 4.7). This is one of the possible constraints to which the optimal perturbation can be required to obey. The gain obtained in this way is smaller than the previous ones (figure 4.7), but is still higher, at $Re = 1000$, than the Reynolds-independent case (solid line - $\blacktriangle$), which represents the lower limit for the gain.

The conclusion is therefore that the values of the gain are bounded between the free optimization results (upper limit) and the Reynolds independent ones (lower limit). Any constraint on the initial perturbation produces an energy gain that is within these limits.

Infinite choices are available to constrain the initial perturbation to be zero on the wall. Among those, we assume $u_{\text{in}} = 0$ and $T_{\text{in}} = 0$ (in the compressible case). This is more consistent with the scaling adopted in §4.5, according to which the leading mechanism is associated with the lift-up effect in the presence of streamwise vortices. Due to this choice, all results presented in §4.5 refer to partial energy norm at the inlet (PENI), as defined in expression (4.9).

From this analysis it is clear that the iterative algorithm described in the algorithm section and proposed as an efficient way to solve two coupled problems, which should be solved simultaneously, suffers some limitations at finite Reynolds number. The shortcoming is related to the choice of the energy norms, which change the coupling conditions at the inlet and/or outlet and therefore the solution of the complete optimization problem. When energy norms are those employed by [TR03] (i.e. PENI and PENO – the extension to the compressible regime of the norms proposed by [Luc00] for the incompressible case), which are Reynolds independent, the convergence of the iterative procedure on the attractor is fast

and usually does not require more than three forth-back iterations. On the contrary, the use of full energy norm at the outlet and partial one at the inlet (FENO and PENI), for $Re = 1000$, renders the convergence slower, requiring from five to ten iterations. If Reynolds number is increased so as to emulate the $Re \to \infty$ limit (e.g. $Re = 10^9$) results collapse on the Reynolds independent ones, as observed by [ABH99] in the incompressible case, and convergence is fast. Several iterations are still required at $Re = 1000$ when the full energy norm is employed at both inlet and outlet (FENI and FENO), whereas a fast convergence is restored by smoothing the optimal perturbation at the inlet so as to avoid the discontinuity at $x = 0$, as discussed above. This smoothing, however, is arbitrary and does not guarantee a solution independent of its choice.

The fact that the algorithm relies on the existence of an attractor, which changes depending on the choice of the norm because the latter affects directly the initial conditions of the direct and/or adjoint problems, raises the question about a more robust optimization algorithm.

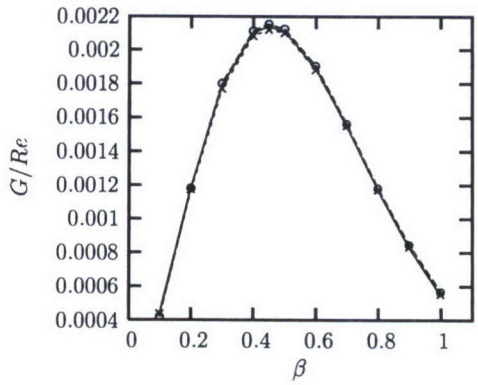

Figure 4.8: Comparison of G/Re as a function of the wavenumber β with previous results available in literature for the incompressible case in the limit $Re \to \infty$. Solid line, present; o, [ABH99]; ×, [TR03]. $M = 0.02$, $x_{\text{in}} = 0$ $x_{\text{out}} = 1.0$, $T_{\text{w}}/T_{\text{ad}} = 1$.

4.3 Spatial transient growth in a compressible boundary layer over a flat plate

In the first case the code was verified against incompressible [ABH99] and compressible [TR03] published works, in which spectral collocation methods (SCM) were employed.

In figure 4.8 the gain $G\epsilon^2 = G/Re$, where $G = E_{\text{out}}/E_{\text{in}}$, is shown in the limit $Re \to \infty$ as a function of the wavenumber β for the incompressible flow past a flat plate and compared with previous results available in the literature. The agreement is very good, even though present values of the gain are very slightly smaller than those obtained by [ABH99]. This might be due to the different numerical implementations.

In what follows, for the flat plate case, only results regarding the use of the full energy norm at the outlet (FENO), i.e. norm (4.6), are considered and compared to those obtained by [TR03], in which partial energy norm at the outlet (PENO) was employed (i.e. only u_{out} and T_{out} were nonzero, whereas v_{out} and w_{out} were excluded from (4.6)). In both cases the inlet energy norm is the one introduced by [Luc00] and extended to the compressible case as in (4.9). We refer to (4.9) as partial energy norm at the inlet (PENI), as it considers the contributions of v_{in} and w_{in} only. The choice of this inlet norm is further discussed in §4.2.

For the sphere case, the code for optimal perturbations was verified against [TR04a] (SCM) and results are later presented for both partial (PENO) and full (FENO) energy norm at the outlet, keeping the inlet norm fixed (PENI).

Here we consider a perfect gas with a specific heat ratio $\gamma = 1.4$, Prandtl number $Pr = 0.7$ and viscosity depending on T only, in accordance with the Sutherland law. The stagnation temperature T_0 is fixed and equal to 333 K.

As described in §4.2, the full energy norm at the outlet (FENO) includes not only u and T (as done in [TR03]) but also also v and w. At the inlet, PENI includes only v and w.

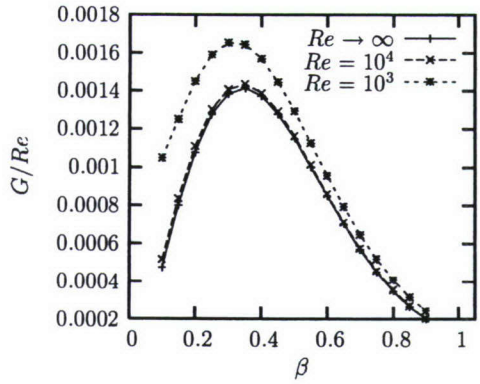

Figure 4.9: Objective function $\mathcal{J} = G/Re$: effect of Re and β for $M = 3$, $T_w/T_{ad} = 0.5$, $x_{in} = 0$ $x_{out} = 1.0$

Figure 4.9 shows the effect of the Reynolds number Re on G/Re when PENI and FENO are employed. The plot refers to the case Mach number $M = 3$, $T_w/T_{ad} = 0.5$ (T_w is the wall temperature and T_{ad} is the recovery temperature), initial station for the computation $x_{in} = 0$, and outlet station $x_{out} = 1.0$. It is clear that the Reynolds number has quite a strong influence only for $Re < 10^4$, while for values greater than this limit, results do not differ significantly from the Reynolds-independent case.

The effect of the norm (PENO versus FENO) for different temperature factors T_w/T_{ad} at $M = 0.5$ is reported in figure 4.10 ($x_{in} = 0$, $x_{out} = 1.0$). The Reynolds number for the case of full energy norm at the outlet (FENO) is $Re = 10^3$. It can be concluded that at low Mach number $M = 0.5$, though large enough to allow compressible effects, the choice of the norm does not produce a remarkable difference.

The conclusion drawn from figure 4.10 does not extend to larger values of Mach number. In figure 4.11, a moderate supersonic Mach number $M = 1.5$ is considered. The effect of increasing M is clearly to shift the maximum of the curves towards smaller values of β and to enhance the difference between results obtained with different norms. This is particularly true for $T_w/T_{ad} = 1.00$.

In the supersonic case, $M = 3$, reported in figure 4.12, a difference up to 17% can be detected when comparing PENO with FENO. This difference is remarkably higher for low values of the wavenumber β and is visible also in figure 2 of [ABH99] for $M = 0$.

It can thus be concluded that for the flat-plate case an energy norm including u, v, w and T at the outlet (FENO) provides a significant difference with respect to the case where only u and T are considered and that this effect increases with the Mach number.

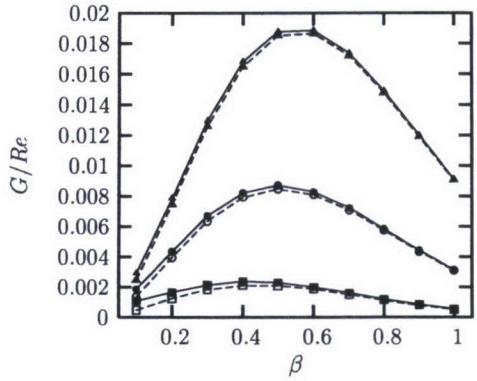

Figure 4.10: Objective function $\mathcal{J} = G/Re$: effect of β, T_w/T_{ad} and norm choice PENO (only u^2 and T^2 at x_{out}) versus FENO. PENI at the inlet (only v^2 and w^2 at x_{in}), $M = 0.5$, $Re = 10^3$, $x_{in} = 0$ $x_{out} = 1.0$. □, $T_w/T_{ad} = 1.00$; ○, $T_w/T_{ad} = 0.50$; △, $T_w/T_{ad} = 0.25$; full symbols and solid lines refer to FENO, empty symbols and dashed lines to PENO.

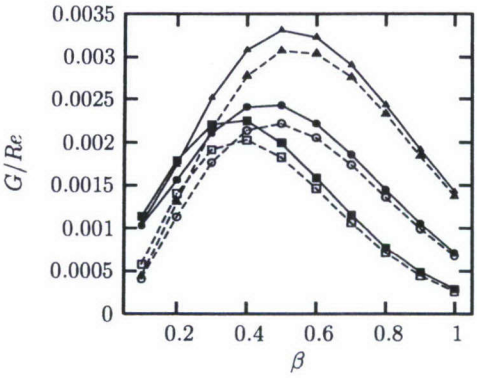

Figure 4.11: Objective function $\mathcal{J} = G/Re$: effect of β, T_w/T_{ad} and norm choice PENO (only u^2 and T^2 at x_{out}) versus FENO. PENI at the inlet (only v^2 and w^2 at x_{in}), $M = 1.5$, $Re = 10^3$, $x_{in} = 0$ $x_{out} = 1.0$. ×, PENO; □, $T_w/T_{ad} = 1.00$; ○, $T_w/T_{ad} = 0.50$; △, $T_w/T_{ad} = 0.25$; full symbols and solid lines refer to FENO, empty symbols and dashed lines to PENO.

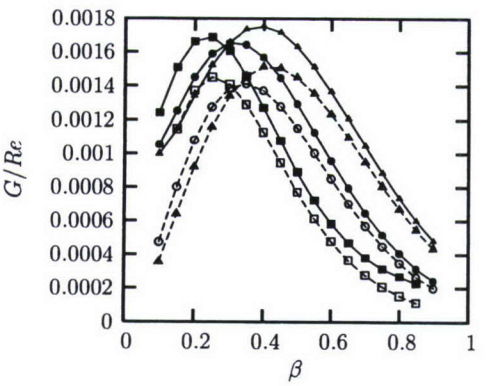

Figure 4.12: Objective function $\mathcal{J} = G/Re$: effect of β, T_w/T_{ad} and norm choice PENO (only u^2 and T^2 at x_{out}) versus FENO. PENI at the inlet (only v^2 and w^2 at x_{in}), $M = 3$, $Re = 10^3$, $x_{in} = 0$ $x_{out} = 1.0$. $\times$, PENO; $\square$, $T_w/T_{ad} = 1.00$; $\circ$, $T_w/T_{ad} = 0.50$; $\triangle$, $T_w/T_{ad} = 0.25$; full symbols and solid lines refer to FENO, empty symbols and dashed lines to PENO.

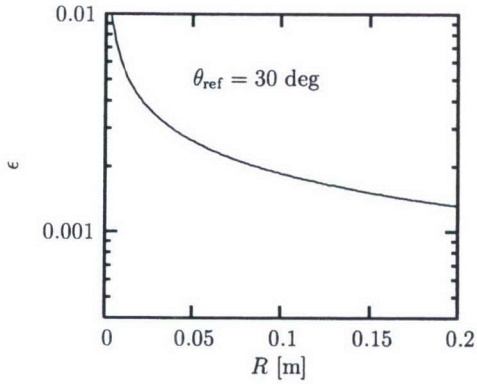

Figure 4.13: Estimate parameter ϵ at wind tunnel conditions. $M = 6$; $p_0 = 25$ bar; $T_0 = 750$ K.

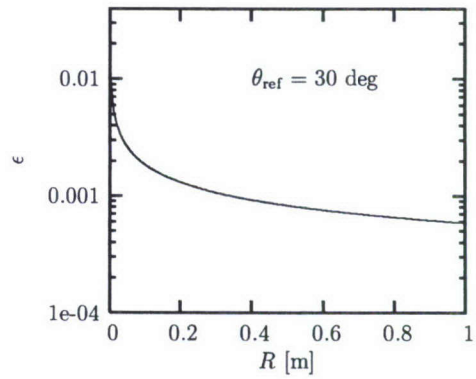

Figure 4.14: Estimate parameter ϵ at flight conditions. $M_\infty = 6$; $p_\infty = 0.0253$ bar; $T_\infty = 217$ K.

4.4 Spatial transient growth in a boundary layer over a sphere

In the case of the sphere, the solution of the governing equations is assumed to be proportional to $\exp(im\phi)$, where m is the azimuthal index and i the imaginary unit (see Appendix C.1).

In order to estimate the values of the small parameter ϵ that might be of interest to the analysis, we consider two examples at a freestream Mach number $M_\infty = 6$. The first one corresponds to typical wind tunnel conditions, $T_0 = 750$ K and $p_0 = 25$ bar. The second case is chosen as a flight condition, with $T_\infty = 217$ K and $p_\infty = 0.0253$ bar. Figures 4.13 and 4.14 illustrate typical values of ϵ as a function of the sphere radius R (in meters) and evaluated at the reference parameters corresponding to the edge of the boundary layer at $\theta_{ref} = 30°$. One can see that values of ϵ on the order or 10^{-3} correspond to realistic cases.

In what follows, the edge boundary layer parameters are defined at $\theta_{ref} = 30°$. This choice has an impact on the definition of ϵ, but the final result $G\epsilon^2 = E_{out}/E_{in}$ is independent of the reference point θ_{ref}.

The effect of ϵ on the gain G as a function of $\widetilde{m}$ ($\widetilde{m} = m\epsilon$) is shown in figure 4.15, where the partial energy norm is used at both inlet and outlet (PENI and PENO). Contrary to the parallel-flow formulation [RT04] where the Reynolds number and the curvature radius are independent, here the radius is strictly associated with the Reynolds number and not only with the curvature. Assuming that all reference parameters are constant, when the radius increases ϵ decreases ($\epsilon = \sqrt{\nu_{ref}/RU_{ref}}$) leading to an increases of the gain, as reported in figure 4.15.

The effect of wall temperature T_w/T_{ad} is illustrated in figure 4.16. Similarly to previous studies [RT00, TR01, TR03], the cooling of the wall destabilizes the flow with respect to the transient energy growth and the difference in G with respect to the adiabatic wall is about

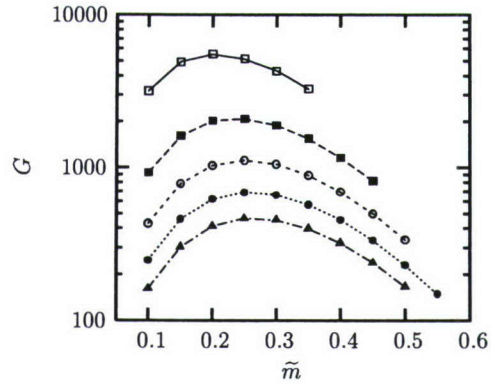

Figure 4.15: Objective function $\mathcal{J} = G$: effect of ϵ and $\widetilde{m} = m\epsilon$ for $\theta_{\text{in}} = 10.0°$, $\theta_{\text{out}} = 15.0°$, $\theta_{\text{ref}} = 30.0°$, $T_{\text{w}}/T_{\text{ad}} = 0.5$. Partial energy norm at both inlet and outlet (PENI and PENO). □, $\epsilon = 2.5 \cdot 10^{-4}$; ■, $\epsilon = 5.0 \cdot 10^{-4}$; ○, $\epsilon = 7.5 \cdot 10^{-4}$; ●, $\epsilon = 1.0 \cdot 10^{-3}$; △, $\epsilon = 1.25 \cdot 10^{-3}$.

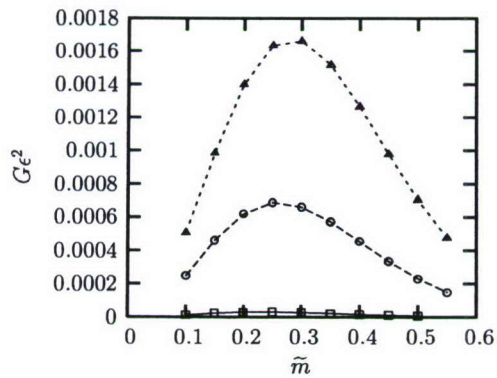

Figure 4.16: Objective function $\mathcal{J} = G\epsilon^2$: effect of wall temperature ratio $T_{\text{w}}/T_{\text{ad}}$ and $\widetilde{m} = m\epsilon$ for $\theta_{\text{in}} = 10.0°$, $\theta_{\text{out}} = 15.0°$, $\theta_{\text{ref}} = 30.0°$, $\epsilon = 10^{-3}$. Partial energy norm at both inlet and outlet (PENI and PENO). □, $T_{\text{w}}/T_{\text{ad}} = 1.00$; ○, $T_{\text{w}}/T_{\text{ad}} = 0.50$; △, $T_{\text{w}}/T_{\text{ad}} = 0.25$.

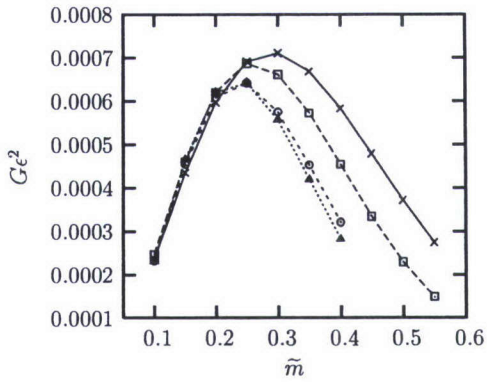

Figure 4.17: Objective function $\mathcal{J} = G\epsilon^2$: effect of outlet station θ_{out} and $\widetilde{m} = m\epsilon$ for $\theta_{\text{in}} = 10.0°$, $\theta_{\text{ref}} = 30.0°$, $T_{\text{w}}/T_{\text{ad}} = 0.5$, $\epsilon = 10^{-3}$. Partial energy norm at both inlet and outlet (PENI and PENO). ×, $\theta_{\text{out}} = 13°$; □, $\theta_{\text{out}} = 15°$; ○, $\theta_{\text{out}} = 20°$; △, $\theta_{\text{out}} = 25°$.

two orders of magnitude.

Figure 4.17 shows the effect of the outlet station θ_{out} and $\widetilde{m}$ for $\theta_{\text{in}} = 10.0°$, $\theta_{\text{ref}} = 30.0°$, $T_{\text{w}}/T_{\text{ad}} = 0.5$ and $\epsilon = 10^{-3}$. It is clear that the maximum transient growth is achieved for smallest intervals of the θ range, more specifically for $\theta \in [10°; 13°]$.

The trend observed in figure 4.17 can be found also in figure 4.18, where the same kind of plot is reported, but for $\theta_{\text{in}} = 15.0°$ instead of $\theta_{\text{in}} = 10.0°$. Again, the smallest range of meridional angles produces the largest energy growth.

Figure 4.19 provides better insights regarding the dependence of G on the choice of θ_{in} and θ_{out}. The difference $\theta_{\text{out}} - \theta_{\text{in}}$ is not the only factor that causes a larger energy growth. In fact, curves with the same $\theta_{\text{out}} - \theta_{\text{in}}$ (5°) but with different θ_{in} clearly show that the strongest transient growth is achieved close to the stagnation point.

The main outcome from the results presented up to this point and referred to the partial energy norm at both inlet and outlet (PENI and PENO) is a large transient energy growth in the proximity of the stagnation point. Moreover, this effect is much stronger when the difference $\theta_{\text{out}} - \theta_{\text{in}}$ is small. Due to the short downstream development of the flow, one issue is that maybe the optimal perturbation in the form of counter-rotating vortices still dominates the flow field and therefore the choice of the partial energy norm at the outlet could be misleading. On the contrary, the use of the full energy norm (which encompasses not only u and T but also v and w) at the outlet would clarify this issue.

Figure 4.20 shows the effect of norm choice and ϵ. Quite a number of curves are reported because comparisons of FENO have meaning depending on the value of ϵ, but results with the PENO change with ϵ as well. In all cases the inlet energy norm is fixed (PENI). The constant parameters are $\theta_{\text{in}} = 2.0°$, $\theta_{\text{out}} = 5.0°$ $\theta_{\text{ref}} = 30.0°$ and $T_{\text{w}}/T_{\text{ad}} = 0.5$. For $\epsilon = 10^{-3}$ there is basically no difference between using PENO and FENO. However, it is precisely in this range of ϵ that it is meaningful to investigate the behavior of the solution, since it

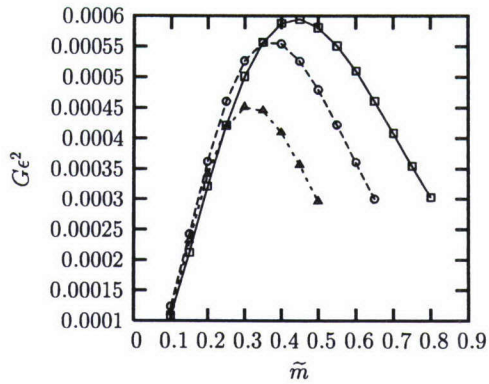

Figure 4.18: Objective function $\mathcal{J} = G\epsilon^2$: effect of outlet station θ_{out} and $\widetilde{m} = m\epsilon$ for $\theta_{\text{in}} = 15.0°$, $\theta_{\text{ref}} = 30.0°$, $T_{\text{w}}/T_{\text{ad}} = 0.5$, $\epsilon = 10^{-3}$. Partial energy norm at both inlet and outlet (PENI and PENO). □, $\theta_{\text{out}} = 18°$; ○, $\theta_{\text{out}} = 20°$; △, $\theta_{\text{out}} = 25°$.

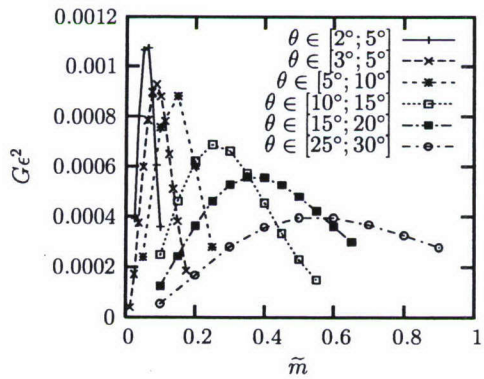

Figure 4.19: Objective function $\mathcal{J} = G\epsilon^2$: effect of interval location and $\widetilde{m} = m\epsilon$ for $\theta_{\text{ref}} = 30.0°$, $T_{\text{w}}/T_{\text{ad}} = 0.5$, $\epsilon = 10^{-3}$. Partial energy norm at both inlet and outlet (PENI and PENO).

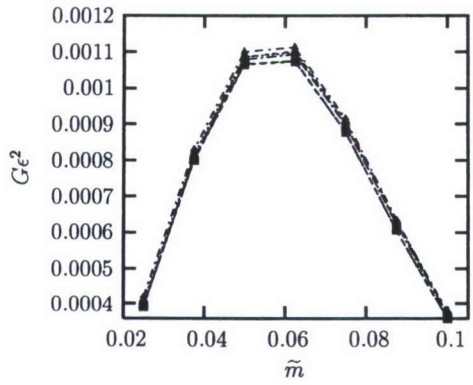

Figure 4.20: Objective function $\mathcal{J} = G\epsilon^2$: effect of ϵ, choice of the energy norm (FENO versus PENO, for PENI) and $\widetilde{m} = m\epsilon$ for $\theta_{\text{in}} = 2.0°$, $\theta_{\text{out}} = 5.0°$, $\theta_{\text{ref}} = 30.0°$, $T_{\text{w}}/T_{\text{ad}} = 0.5$. □, $\epsilon = 1 \cdot 10^{-3}$; ○, $\epsilon = 2 \cdot 10^{-3}$; △, $\epsilon = 3 \cdot 10^{-3}$; full symbols refer to FENO, empty ones to PENO.

corresponds to the estimated values for wind tunnel conditions and flight tests, as reported in figures 4.13 and 4.14. For higher values of ϵ ($2 \cdot 10^{-3}$ and $3 \cdot 10^{-3}$) the difference between the use of the two norms seems to be more evident.

The conclusion from figure 4.20 is, however, that the maximum appreciable difference is confined within about 1% of the parameters of interest.

Conclusions

Optimal perturbations in the compressible regime have been considered for both flat plate and sphere. An adjoint-based optimization technique is employed and the discrete costate problem is obtained from the discretized direct problem by applying the Lagrangian multipliers technique in the discrete framework. This simplifies the code, reduces the number of possible errors, and allows the automatic generation of coupling conditions at the inlet and outlet. The code has been verified against available results [TR03, TR04a].

The main contributions of the present work are the analysis including the full energy norm at the outlet and the fully discrete approach (including the coupling conditions), which considerably facilitates its implementation.

In the incompressible limit and for the flat plate (for which comparisons with the full energy norm at both inlet and outlet are available) it is found that the values of the gain are bounded by the free optimization results (the upper limit) and the Reynolds independent ones (the lower limit). Any constraint on the initial perturbation produces an energy gain that is within these limits.

The norm to be maximized at the outlet, in the compressible case, is extended to the complete Mack's norm, including not only u_{out} and T_{out} in the fashion proposed by [Luc00] but also v_{out} and w_{out}.

Results for the flat plate show that when the Reynolds number is on the order of 10^3, a significant difference in the energy growth (up to 17%) is found between the two choices of the outlet energy norm (full or partial). This is particularly true for supersonic values of the Mach number. On the other hand, when compressible effects are considerable but the basic flow is subsonic, the difference between the full and partial energy norms is not a critical factor. If the Reynolds number is greater than 10^4, v_{out} and w_{out} do not play a significant role even in supersonic flows.

Results for the sphere are first presented by considering the use of the partial energy norm only and secondly by comparing them with the full energy norm, in the most interesting case. The effect of the wall temperature is in agreement with previous finding based on the parallel flow model with curvature effects [TR01] and on the nonparallel flow model over a flat plate [TR03]. Particularly, the cooling of the wall destabilizes the flow with respect to the transient growth, with a difference up to two orders of magnitude when the adiabatic wall is compared to a cold wall ($T_{\text{w}}/T_{\text{ad}} = 0.25$). On the other hand, at fixed wall temperature, it is found that the energy growth is stronger in the proximity of the stagnation point, reinforcing what was found in the parallel flow approximation. In contrast with the latter, however, the present model includes a significant feature, the divergence of the flow. In the parallel flow approximation, the spanwise wavenumber β is a fixed parameter, whereas in this work the azimuthal index is kept constant so that the effective local spanwise wavenumber β is a function of the streamwise and radial coordinates. This divergence of the flow also leads to a modification of the energy norm resulting from the integration of the perturbation over a period in the azimuthal direction. Due to the scaling, the equations governing the perturbations on the sphere are not Reynolds-independent. This reflects the twofold role of the radius of the sphere in the transient growth phenomenon. Not only does it enter into the disturbance equations as the curvature parameter, but also in the Reynolds number through the small parameter ϵ. The overall effect is an increase of the energy growth with the sphere radius. The use of the full energy norm at the outlet was also investigated. This was done close to the stagnation point and for a small range of the meridional angle, since this is the region where the largest gain is observed for the sphere in the case of partial energy norm. Results reveal that, in the range of interesting values of Re_{ref} (related to the small parameter $\epsilon = (Re_{\text{ref}})^{-1/2}$) that are typical of wind tunnel tests or flight conditions, no significant role is played by v and w at the outlet. Despite the progress made in the present paper towards a better understanding of transient growth on blunt (spherical) noses, the ultimate elucidation of the blunt body paradox would require solving the receptivity problem, which would explain the origin of the perturbation. This issue will be addressed in a future work.

4.5 Transient growth phenomenon in a boundary layer over a sharp cone

Governing equations

The governing equations for steady, three-dimensional disturbances in the supersonic flow past a sharp cone are derived from the linearized Navier–Stokes equations, in the same fashion as in Section 4.2.

A small parameter $\epsilon = H_{\text{ref}}/L_{\text{ref}}$ is introduced for scaling purposes, where $H_{\text{ref}} = \sqrt{\nu_{\text{ref}} L_{\text{ref}}/U_{\text{ref}}}$ is a typical-boundary layer length in the wall-normal direction y and L_{ref} is a typical scale of the geometry (length of cone L in the present case). The scaling parameter ϵ is thus strictly related to the Reynolds number $\epsilon = Re_{\text{ref}}^{-1/2}$, where $Re_{\text{ref}} = U_{\text{ref}} L_{\text{ref}}/\nu_{\text{ref}}$ is the reference Reynolds number.

As it follows from previous works regarding optimal perturbations in both incompressible and compressible boundary layers [ZTR06, ZTR05, Luc00, ZBL06, TR04a, CL00, ZLB04], the disturbance flow is expected to be dominated by streamwise vortices and therefore the following scaling is employed (Section 4.2). The streamwise coordinate x is normalized with L_{ref}, whereas the wall-normal coordinate y is scaled with ϵL_{ref}. The azimuthal coordinate ϕ, being an angle, is not normalized. The streamwise velocity component u is scaled with U_{ref}, wall-normal velocity v and azimuthal velocity w with ϵU_{ref}, temperature T with T_{ref} and pressure p with $\epsilon^2 \rho_{\text{ref}} U_{\text{ref}}^2$. Density ρ is eliminated through the state equation.

Due to the scaling adopted, the second derivative with respect to the streamwise coordinate x and $\partial p/\partial x$ are smaller than the other terms, and are therefore neglected. This leads to a parabolic system of equations.

Perturbations are assumed to be periodic in the azimuthal direction ϕ as $\exp(\mathrm{i}m\phi)$, where m is the azimuthal index, so that the general unknown can be expressed as $q(x,y)\exp(\mathrm{i}m\phi)$, where $q(x,y)$ is the amplitude, which depends on x and y, and i is the imaginary unit.

If the vector of perturbations is $\mathbf{f} = [u, v, w, T, p]^{\mathrm{T}}$ (where the superscript $^{\mathrm{T}}$ denotes the transpose), with $w = \mathrm{i}\tilde{w}$ ($\tilde{w}$ being the amplitude of the spanwise velocity component), the governing equations can be written as follows:

$$(\boldsymbol{A}\mathbf{f})_x = (\boldsymbol{D}\mathbf{f}_y)_x + \boldsymbol{B}_0\mathbf{f} + \boldsymbol{B}_1\mathbf{f}_y + \boldsymbol{B}_2\mathbf{f}_{yy}. \tag{4.26}$$

This form of the governing equations is general and can be derived for different geometries such as flat plate, sphere, sharp cone or blunt-nose cone. Nonzero elements of the 5 by 5 real matrices $\boldsymbol{A}$, $\boldsymbol{B}_0$, $\boldsymbol{B}_1$, $\boldsymbol{B}_2$ and $\boldsymbol{D}$ are given in Appendix C.2. New terms, relative to the flat-plate case, arise in the equation due to the geometrical factors introduced by the half-angle of the cone tip θ.

As far as boundary conditions are concerned, all perturbations are required to be zero at the wall except for p, while in the freestream all perturbations vanish except for v:

$$\begin{aligned} y = 0: &\quad u = 0; v = 0; w = 0; T = 0 \\ y \to \infty: &\quad u \to 0; w \to 0; p \to 0; T \to 0 \end{aligned} \tag{4.27}$$

In order to isolate the derivative with respect to x, system (4.26) can be recast as

$$(\boldsymbol{H}_1\mathbf{f})_x + \boldsymbol{H}_2\mathbf{f} = 0, \tag{4.28}$$

where operators $\boldsymbol{H}_1$ and $\boldsymbol{H}_2$ are still 5 by 5 real matrices and contain the dependence on x and y due to the basic flow:

$$\boldsymbol{H}_1 = \boldsymbol{A} - \boldsymbol{D}(\cdot)_y; \qquad \boldsymbol{H}_2 = -\boldsymbol{B}_0 - \boldsymbol{B}_1(\cdot)_y - \boldsymbol{B}_2(\cdot)_{yy}. \tag{4.29}$$

System (4.28) is parabolic in nature and can be solved by means of a downstream marching procedure with initial data specified at the inlet section of the domain $x = x_{\text{in}}$.

It is worth noting that the disturbance equations are not Reynolds-number independent (contrary to the flat-plate case) because of the parameter ϵ in the scaling, which is associated with geometrical effects.

Formulation of the optimization problem

The problem of finding arbitrarily normalized optimal perturbations practically reduces to performing a constrained optimization. The constraints are the governing equations (4.28) and the normalization of the initial energy of the perturbation at the inlet, E_{in}. The objective function is a particular norm to be identified, and therefore arbitrary. However, it should be a measure of the flow conditions relevant to the transition process. This choice is neither easy nor unique. In previous works dealing with optimal perturbations in the incompressible framework [ABH99, Luc00, ZBL06, CL00, ZLB04], the kinetic energy of the disturbance field has always been the choice.

In the compressible case, in Section 4.2, we maximized Mack's energy norm [Mac69] of the perturbation kinetic energy, density, and temperature (or simply the part containing u and T) at the outlet plane,

$$E_{\text{out}} = \int_0^\infty \left[\rho_{s\text{out}} \left[u_{\text{out}}^2 + \epsilon^2 (v_{\text{out}}^2 + w_{\text{out}}^2) \right] + \frac{\rho_{\text{out}}^2 T_{s\text{out}}}{\gamma \rho_{s\text{out}} M^2} + \frac{T_{\text{out}}^2 \rho_{s\text{out}}}{\gamma(\gamma-1) T_{s\text{out}} M^2} \right] dy, \tag{4.30}$$

in which the scaling described in the governing equations' section is employed. Expression (4.30) was derived for perturbations developing in the boundary layer over a flat plate within the temporal framework, and is here utilized for the spatial case, as done in [TR03]. After employing the equation of state for the basic flow and for the perturbation, and observing that in the limit $\epsilon \to 0$ v and w can be neglected (Reynolds-independent approach, see [Luc00]), the norm reads

$$E_{\text{out}} = \int_0^\infty \left[\rho_{s\text{out}} u_{\text{out}}^2 + \frac{p_{s\text{out}} T_{\text{out}}^2}{(\gamma-1) T_{s\text{out}}^2 M^2} \right] dy, \tag{4.31}$$

or more compactly

$$E_{\text{out}} = \int_0^\infty \left(\mathbf{f}_{\text{out}}^T \widetilde{\boldsymbol{M}}_{\text{out}} \mathbf{f}_{\text{out}} \right) dy, \tag{4.32}$$

where the linear operator $\widetilde{\boldsymbol{M}}_{\text{out}}$ is the diagonal 5×5 matrix

$$\widetilde{\boldsymbol{M}}_{\text{out}} = \begin{bmatrix} \rho_{s\text{out}} & 0 & 0 & 0 & 0 \\ 0 & 0 & 0 & 0 & 0 \\ 0 & 0 & 0 & 0 & 0 \\ 0 & 0 & 0 & \dfrac{p_{s\text{out}}}{(\gamma-1)T_{s\text{out}}^2 M^2} & 0 \\ 0 & 0 & 0 & 0 & 0 \end{bmatrix}. \tag{4.33}$$

The initial condition for the compressible boundary-layer equations is not arbitrary, but only three of the five variables can be imposed at x_{in} [Tin65]. However, in the incompressible case and for $Re \to \infty$, it was observed that the choice $u_{\text{in}} = 0$, $p_{\text{in}} = 0$, v_{in} and w_{in} related by the continuity equation corresponds to the maximum gain in an input-output fashion [Luc00] (in the incompressible case the number of independent initial conditions is two; see also [Luc00, ZBL06, LB98]). This choice also corresponds to the physical mechanism, observed in transitional boundary-layer flows, known as the lift-up effect [Lan80], according to which streamwise vortices lift low momentum flow up (from the wall) and push down high momentum flow causing streaks that eventually break down to turbulence. Led by these considerations, here we focus on initial perturbations with only v and w nonzero, which correspond to steady, streamwise vortices.

The kinetic energy of the optimal disturbance $\mathbf{f}_{\text{in}}$, if only v_{in} and w_{in} are nonzero, is therefore:

$$E_{\text{in}} = \int_0^\infty \left[\rho_{s\text{in}} \epsilon^2 (v_{\text{in}}^2 + w_{\text{in}}^2)\right] dy, \tag{4.34}$$

or more compactly

$$E_{\text{in}} = \int_0^\infty \left(\mathbf{f}_{\text{in}}^T \widetilde{\boldsymbol{M}}_{\text{in}} \mathbf{f}_{\text{in}}\right) dy, \tag{4.35}$$

where $\widetilde{\boldsymbol{M}}_{\text{in}}$ is the 5×5 diagonal matrix

$$\widetilde{\boldsymbol{M}}_{\text{in}} = \begin{bmatrix} 0 & 0 & 0 & 0 & 0 \\ 0 & \epsilon^2 \rho_{s\text{in}} & 0 & 0 & 0 \\ 0 & 0 & \epsilon^2 \rho_{s\text{in}} & 0 & 0 \\ 0 & 0 & 0 & 0 & 0 \\ 0 & 0 & 0 & 0 & 0 \end{bmatrix}. \tag{4.36}$$

The quantity to be maximized is $G = E_{\text{out}}/E_{\text{in}}$, the ratio between the outlet and inlet norms. However, in order to allow direct comparison with previous works, $G\epsilon^2$ will be presented in the results section

$$G\epsilon^2 = \frac{\displaystyle\int_0^\infty \left[\rho_{s\text{out}} u_{\text{out}}^2 + \frac{p_{s\text{out}} T_{\text{out}}^2}{(\gamma-1)T_{s\text{out}}^2 M^2}\right] dy}{\displaystyle\int_0^\infty \left[\rho_{s\text{in}} (v_{\text{in}}^2 + w_{\text{in}}^2)\right] dy}. \tag{4.37}$$

Since the problem is linear, an arbitrary normalization for the initial disturbance at x_{in} can be chosen, e.g. $E_{\text{in}} = 1$, so that the maximization of (4.37) turns out to be equivalent to the maximization of expression (4.32), i.e. $\mathcal{J} = E_{\text{out}}$.

It should be clear now that the whole problem of finding optimal perturbations reduces to a constrained optimization, in which we seek the initial conditions for the disturbance equations (4.28) that maximize (4.32) and that satisfy the constraint $E_{\text{in}} = E_0$ at x_{in}, together with the direct equations (4.28) and boundary conditions (4.27) at each $x \in (x_{\text{in}}; x_{\text{out}})$.

The details of the constrained optimization procedure are reported in Section 4.2. The classical Lagrange multiplier technique is applied to the discrete version of problem (4.28), which can be recast as $\boldsymbol{C}_{n+1}\mathbf{f}_{n+1} = \boldsymbol{B}_n\mathbf{f}_n$, leading to the so-called adjoint equations [ZTR06, ZTR05, Luc00, ZBL06, CL00, ZLB04, LB98, LB01] (here n denotes the n-th grid node in the streamwise direction x, $\mathbf{f}$ is the vector of $5 \times N_y$ unknowns at each n station, N_y being the number of grid nodes in the wall-normal direction y; matrices $\boldsymbol{C}$ and $\boldsymbol{B}$ depend on x and y, as the basic flow does, and account for the discretization in both x and y).

The use of the discrete approach has several advantages among which the necessity of an "ad hoc" adjoint code is avoided and a foolproof test is available by comparing the results of the direct and adjoint calculation, which must match up to machine accuracy for any step size and not only in the limit of step size tending to zero [Luc00, ZBL06, LB98].

The augmented functional $\mathcal{L}$ contains the objective function $\mathcal{J} = E_{\text{out}}$, the constraints (4.28) and $E_{\text{in}} = E_0$, and the Lagrange multipliers (Section 4.2). The optimization imposes $\delta\mathcal{L} = 0$, which leads to the adjoint equations in the discrete form and coupling conditions between the direct and adjoint problems at the inlet (x_{in}) and outlet (x_{out}). These conditions can be written in a matrix form so that their application becomes straightforward. In order to retrieve the outlet conditions, a system needs to be solved where the coefficient matrix is singular (due to $\partial p/\partial x = 0$ in this approximation), reflecting the fact that at least one out of five adjoint variables is free at $x = x_{\text{out}}$ and therefore can be chosen arbitrarily. For sake of simplicity, we set the fifth adjoint variable equal to zero.

The constrained optimization formulation requires the simultaneous solution of a large, coupled system of direct equations, adjoint equations, boundary conditions and coupling conditions. Instead of doing it in one shot, however, we employ the intrinsic parabolic nature of the equations to efficiently solve separately the two coupled problems. Such an algorithm can be outlined in the following few steps. (1) a guessed initial condition $\mathbf{f}_{\text{in}}^{(0)}$ is provided at the beginning of the optimization procedure; (2) the forward problem is solved at the i-th iteration with the initial condition $\mathbf{f}_{\text{in}}^{(i)}$; (3) the objective function $\mathcal{J}^{(i)} = E_{\text{out}}^{(i)}$ is computed at the end of the forward iteration and compared to the objective function $\mathcal{J}^{(i-1)} = E_{\text{out}}^{(i-1)}$ at the end of the previous forward iteration. If $|\mathcal{J}^{(i)}/\mathcal{J}^{(i-1)} - 1| < \epsilon_t$ (where ϵ_t is the maximum tolerance accepted to stop the optimization) then the optimization is considered converged and the problem solved; (4) if $|\mathcal{J}^{(i)}/\mathcal{J}^{(i-1)} - 1| > \epsilon_t$ the initial conditions for the backward problem are assigned at the outlet and derived from the direct solution at $x = x_{\text{out}}$; (5) the backward problem is solved from $x = x_{\text{out}}$ to $x = x_{\text{in}}$; (6) a new initial condition for the forward problem $\mathbf{f}_{\text{in}}^{(i+1)}$ is obtained from the solution of the backward problem at $x = x_{\text{in}}$ employing the coupling condition at the inlet; (7) the loop is repeated from step (2) on until

it is eventually ended in step (3). It should be noted that this procedure does not necessarily guarantee convergence. If there is an attractor for the solution, then the procedure will capture it and this happens quite fast (2-3 forward-backward iterations).

Discretization

A finite difference discretization scheme has been implemented to numerically solve equations (4.28) with boundary conditions (4.27). For the sake of generality, grid nodes in x and y are not necessarily equally spaced. A staggered grid is introduced in the wall-normal direction, with variables u, v, w and T known at the grid nodes, and p known at the mid-grid (staggered) nodes. All equations are satisfied at the grid nodes except for continuity, which is satisfied in the mid-grid nodes. The use of the uneven grid in y allows us to cluster more nodes close to the wall so as to take into account the larger gradients of boundary layer quantities in this region. The last node of the y-grid is located far enough from the wall to allow satisfaction there of the boundary conditions for $y \to \infty$.

Fourth-order non-compact finite differences are used for the y discretization, employing six nodes so as to allow 4th order accuracy for the second derivative. By using six nodes, the first derivative is automatically 5th order accurate and the function (when interpolated due to the staggered grid) is 6th order accurate.

Also the discretization in the streamwise direction is based on an uneven grid. Since the system of boundary layer equations is parabolic, a second order backward discretization is chosen, which requires the solution at two previous steps to be known. For the first step, however, a first order scheme is used because only the initial condition is available.

Results

The basic flow for the sharp cone is obtained from the flat-plate case by rescaling the wall-normal coordinate y and its derivatives according to Mangler's transformation [HP59]. The local Mach number, M_{loc}, at the edge of the boundary layer was calculated assuming calorically perfect gas flow at free stream Mach number $M_\infty = 6$. Since the shock wave is assumed to be far away from the boundary layer (and perturbation), their mutual interaction is not considered. The calculations are performed for cone half-angles of $\theta = 15°$ and $25°$. The main goal in the presentation of the results is to discuss the effects originating from flow divergence induced by the geometry. The boundary-layer edge velocity,density, temperature, and viscosity at $x = L_{ref}$ are chosen as the reference parameters. All results are obtained at $\epsilon = 0.001$ unless otherwise stated.

Figure 4.21 shows the objective function $G\epsilon^2$ obtained from the optimization procedure for $\theta = 15°$. Adiabatic boundary conditions are used for the temperature at the wall, $T_{\text{w}}/T_{\text{ad}} = 1$, and the initial station is kept constant, $x_{\text{in}} = 0.2$, while changing the outlet station. Results show that there exists a location, downstream of $x_{\text{in}} = 0.2$, where the curve of the maximum energy growth as a function of modified azimuthal wavenumber, $\tilde{m} = \epsilon m$, reaches the largest value, after which the maximum of the curve decreases with increasing x_{out}. Among the computed curves, this maximum seems to be reached for $x_{\text{out}} = 0.3$.

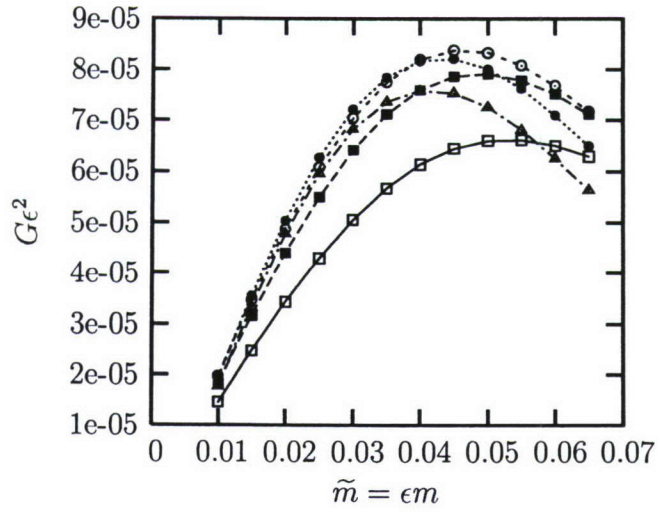

Figure 4.21: Objective function $G\epsilon^2$: effect of x_{out} and $\widetilde{m}$ for $\theta = 15°$, $M_\infty = 6$, $M_{\text{loc}} = 4.37$, $T_{\text{w}}/T_{\text{ad}} = 1$, $x_{\text{in}} = 0.2$. □, $x_{\text{out}} = 0.25$; ■, $x_{\text{out}} = 0.275$; ○, $x_{\text{out}} = 0.3$; ●, $x_{\text{out}} = 0.35$; △, $x_{\text{out}} = 0.4$.

However, a better estimate can be obtained by performing a parabolic interpolation of the data corresponding to the maxima for the three cases $x_{\text{out}} = 0.275$, $x_{\text{out}} = 0.3$ and $x_{\text{out}} = 0.35$. This leads to the optimal outlet location $x_{\text{out}} = 0.32$, from which the optimal interval $\Delta x = x_{\text{out}} - x_{\text{in}} = 0.12$ is obtained.

The shape of the optimal perturbation at x_{in} is very similar to what has been found so far in both incompressible and compressible studies [Luc00, TR03] and is shown in figure 4.22 for the largest gain observed in the previous figure, i.e. $\widetilde{m} = 0.045$ and $x_{\text{out}} = 0.3$. The maximum energy growth is determined by streamwise vortices generated by v- and w-perturbations that extend outside the boundary layer and decay at the same rate as a function of y. This type of perturbation is consistent with the assumptions employed in the scaling process.

By moving the inlet location further downstream to $x_{\text{in}} = 0.4$, results qualitatively similar to those shown in figure 4.21 are found. The corresponding estimated x_{out} that causes the maximum gain is $x_{\text{out}} = 0.64$ and the interval $\Delta x = x_{\text{out}} - x_{\text{in}} = 0.24$ is greater than the value $\Delta x = 0.12$ previously observed for $x_{\text{in}} = 0.2$. The conclusion is that divergence effects are stronger in the proximity of $x_{\text{in}} = 0$, as one could argue from geometrical considerations.

Figure 4.23 shows the objective function $G\epsilon^2$ computed for a larger cone half-angle, $\theta = 25°$, while keeping $x_{\text{in}} = 0.2$ fixed. The general trend of the results is as in figure 4.21. The estimated value of x_{out} that causes the maximum gain is $x_{\text{out}} = 0.32$, leading to $\Delta x = 0.12$. Remarkably, the latter is the same as for $\theta = 15°$ and $x_{\text{in}} = 0.2$.

By moving the inlet location to $x_{\text{in}} = 0.4$ (for $\theta = 25°$), the optimal estimated outlet location is $x_{\text{out}} = 0.64$ and thus $\Delta x = 0.24$, i.e. the same as for $\theta = 15°$. This suggests the

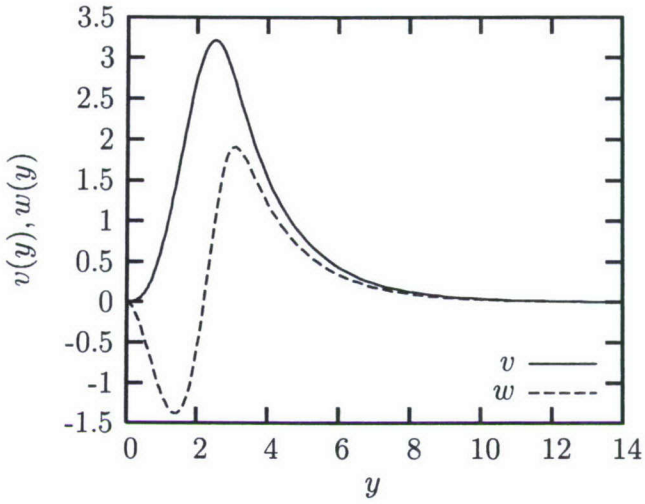

Figure 4.22: Optimal perturbation at x_{in} for $\theta = 15°$, $M_\infty = 6$, $M_{\text{loc}} = 4.37$, $T_{\text{w}}/T_{\text{ad}} = 1$, $x_{\text{in}} = 0.2$, $x_{\text{out}} = 0.3$ and $\widetilde{m} = 0.045$.

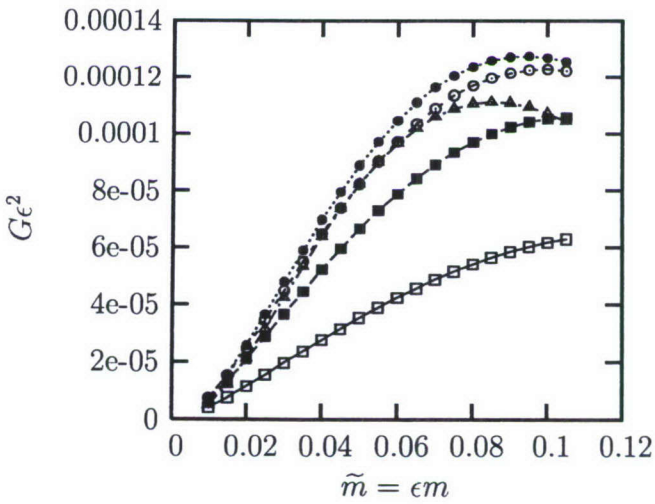

Figure 4.23: Objective function $G\epsilon^2$: effect of x_{out} and $\widetilde{m}$ for $\theta = 25°$, $M_\infty = 6$, $M_{\text{loc}} = 3.22$, $T_{\text{w}}/T_{\text{ad}} = 1$, $x_{\text{in}} = 0.2$. □, $x_{\text{out}} = 0.225$; ■, $x_{\text{out}} = 0.25$; ○, $x_{\text{out}} = 0.275$; ●, $x_{\text{out}} = 0.3$; △, $x_{\text{out}} = 0.4$.

possible insensitivity of $\Delta x = x_{\text{out}} - x_{\text{in}}$ to the nose-tip angle. However, as can be deduced by comparing figures 4.21 and 4.23, θ influences the values of $G\epsilon^2$, which are consistently higher for larger cone half-angles.

As opposed to the sharp-cone geometry, the flat-plate case has no effects due to the flow divergence. Therefore, by analyzing the results from the previous figures together with those obtained in the same fashion for the flat plate, more insights can be gained regarding the influence of the geometry. This is done in figure 4.24, where flat-plate results are shown

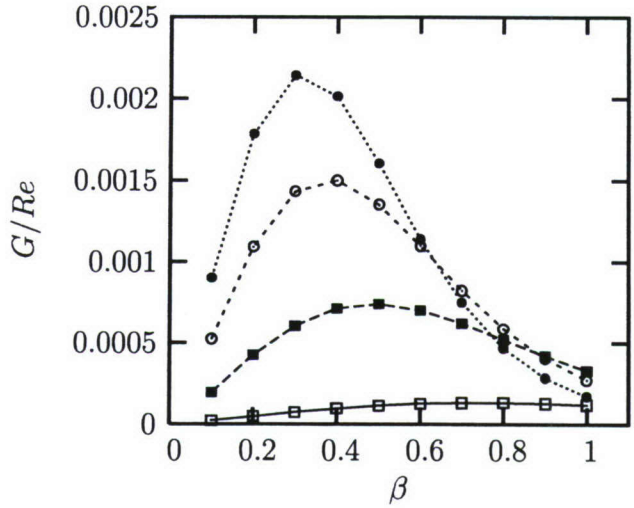

Figure 4.24: Objective function G/Re, flat plate: effect of x_{out} and β for $M = 3.22$, $T_w/T_{ad} = 1$, $x_{in} = 0.4$. □, $x_{out} = 0.45$; ■, $x_{out} = 0.6$; ○, $x_{out} = 0.8$; ●, $x_{out} = 1.0$;

for $M = 3.22$ (the local Mach number corresponding to the 25° cone), adiabatic wall and $x_{in} = 0.4$. It is clear that moving the outlet location downstream leads to a monotonic increase in the curve of maximum energy growth. A precise optimal outlet x_{out}, however, is not found. This is a new finding with respect to previous figures and to previously published results for the flat plate [TR03], in which only the inlet location x_{in} was changed, while keeping $x_{out} = 1.0$. The straightforward conclusion from the comparison between figure 4.24 and the previous ones is that, once the inlet location is fixed, divergence effects result in the existence of an optimal outlet location $x_{out} < 1$ for which the largest energy growth is reached. This behavior was also present in the sphere case (Section 4.4), corroborating the conjecture of being due to the flow divergence only.

Figure 4.25 plots the reverse case to what was seen before. The gain $G\epsilon^2$ is shown for the sharp-cone geometry, keeping the outlet fixed, $x_{out} = 1.0$, and changing the inlet x_{in}, for $\theta = 25°$ (the other parameters are $M_\infty = 6$, $M_{loc} = 3.22$, and $T_w/T_{ad} = 1$). An optimal inlet location is now found. By performing the same type of parabolic interpolation for the maxima as done before, the largest energy growth is obtained for an estimated $x_{in} = 0.72$, i.e. for $\Delta x = 0.28$. The latter is comparable with the value of Δx found for $x_{in} = 0.4$ while changing x_{out} for the 25° cone.

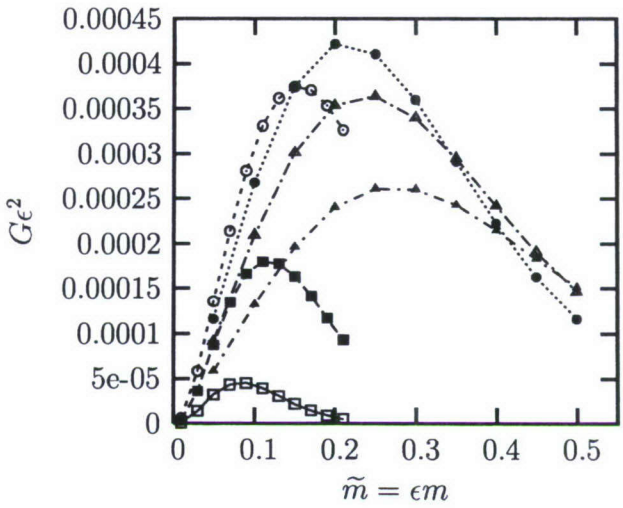

Figure 4.25: Objective function $G\epsilon^2$: effect of x_{in} and $\widetilde{m}$ for $\theta = 25°$, $M_\infty = 6$, $M_{\text{loc}} = 3.22$, $T_{\text{w}}/T_{\text{ad}} = 1$, $x_{\text{out}} = 1.0$. □, $x_{\text{in}} = 0.2$; ■, $x_{\text{in}} = 0.4$; ○, $x_{\text{in}} = 0.6$; ●, $x_{\text{in}} = 0.8$; △, $x_{\text{in}} = 0.85$; ▲, $x_{\text{in}} = 0.9$.

A quantitative comparison between flat-plate and sharp-cone results

Results presented in figure 4.24 certainly shed a new light on the differences between flat-plate and sharp-cone geometries that can be attributed to flow divergence. However, the order of magnitude of the gain reported in that figure differs quite remarkably from what is shown in the figures for the sharp cone. This allows only a qualitative comparison. In order to compare quantitatively the energy growth for flat plate and cone, both physics and scaling should be considered.

The physics suggests that the results for the sharp cone should reduce to those obtained for the flat plate in the limits $x_{\text{in}} \to x_{\text{out}}$ and $m \to \infty$. The first is dictated by the fact that divergence effects (which are the main difference between sharp-cone and flat-plate geometries) are negligible far from the cone tip (in the proximity of x_{out}). The second limit is due to the fact that the presence of many vortices in the azimuthal direction forces the flow to be less sensitive to divergence and, thus, to behave as in the flat-plate case. To emphasize the effects of divergence in the flow past the sharp cone, therefore, we focus on the limits $x_{\text{in}} \to x_{\text{out}}$ and $m \to \infty$. The outlet location $x_{\text{out}} = 1$ is kept constant, as for the flat-plate case, so as to allow direct comparison.

The scaling is important as well. The fact that the boundary layer thickness over the cone is $1/\sqrt{3}$ times that of the boundary layer thickness over the flat plate, and the same length scale L_{ref} is used in the definition of the Reynolds number in both cases, suggests that G/Re for the flat plate (Section 4.3) must be compared with $3G\epsilon^2$. On the other hand, the wavenumber $\beta z/H_{\text{ref plate}}$ must be compared with $m\phi = \dfrac{mz}{R} = \dfrac{mH_{\text{ref cone}}}{R}\dfrac{z}{H_{\text{ref cone}}}$,

where z is the transverse coordinate along the cone surface and R is the local radius. The comparison between $\beta z/H_{\text{ref plate}}$ and $m\phi$, therefore, reduces to the comparison between β and $mH_{\text{ref cone}}/R$. However, since $H_{\text{ref cone}} = H_{\text{ref plate}}/\sqrt{3}$ and $R = L_{\text{ref}} \sin\theta$, by taking into account that $\epsilon = H_{\text{ref plate}}/L_{\text{ref}}$, one gets

$$\frac{mH_{\text{ref cone}}}{R} = \frac{mH_{\text{ref plate}}}{\sqrt{3}R} = \frac{mH_{\text{ref plate}}}{\sqrt{3}L\sin\theta} = \frac{m\epsilon}{\sqrt{3}\sin\theta} = \frac{\widetilde{m}}{\sqrt{3}\sin\theta}.$$

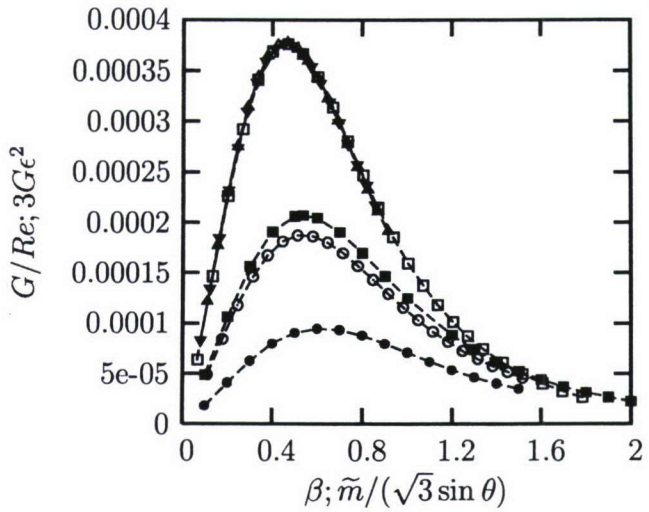

Figure 4.26: Objective function, comparison between G/Re (flat plate) and $3G\epsilon^2$ (sharp cone) as a function of β and $\widetilde{m}/(\sqrt{3}\sin\theta)$ respectively, effect of x_{in} and wavenumber. $M_{\text{loc}} = 3$, $T_{\text{w}}/T_{\text{ad}} = 1$, $x_{\text{out}} = 1.0$. □, $\theta = 15°$ and $x_{\text{in}} = 0.95$; △, $\theta = 15°$, $x_{\text{in}} = 0.95$ and $\epsilon = 0.0001$; ○, $\theta = 15°$ and $x_{\text{in}} = 0.97113$; ▽, $\theta = 25°$ and $x_{\text{in}} = 0.95$; ■, flat plate, $x_{\text{in}} = 0.913$; ●, flat plate, $x_{\text{in}} = 0.95$.

This rescaling is employed in figure 4.26 for the sharp-cone results in order to compare them with those for flat plate. Many conclusions can be deduced from these plots, obtained by changing θ and $\Delta x = x_{\text{out}} - x_{\text{in}}$. First, the scaling is correct in that all the results for the cone with $x_{\text{in}} = 0.95$ and $x_{\text{out}} = 1.0$ (□, △, ▽, ◇) collapse onto one curve, regardless of θ. Secondly, ϵ does not have any effect on the gain function ($3G\epsilon^2$), as is proved by comparison of the cases for $\epsilon = 0.001$ (□) and $\epsilon = 0.0001$ (△), both referring to $x_{\text{in}} = 0.95$, $x_{\text{out}} = 1.0$ and $\theta = 15°$. Third, the comparison between cone (empty symbols) and flat plate (full symbols) should be carried out with further care with respect to Δx. In fact, because of the difference in the boundary-layer thickness between flat plate and cone, distances Δx having about the same number of boundary-layer thicknesses should be considered. We suggest comparing Δx_{cone} with $\Delta x_{\text{plate}}/\sqrt{3}$, implying that the sharp-cone cases $x \in [0.95; 1]$ and $x \in [0.97113; 1]$ should be compared respectively with the flat-plate cases $x \in [0.913; 1]$, and $x \in [0.95; 1]$.

Figure 4.26 confirms this by showing that results for the sharp cone and flat plate collapse onto each other for $\widetilde{m} \to \infty$, when the correct intervals Δx are considered (see □ vs. ■ and ○ vs. ●).

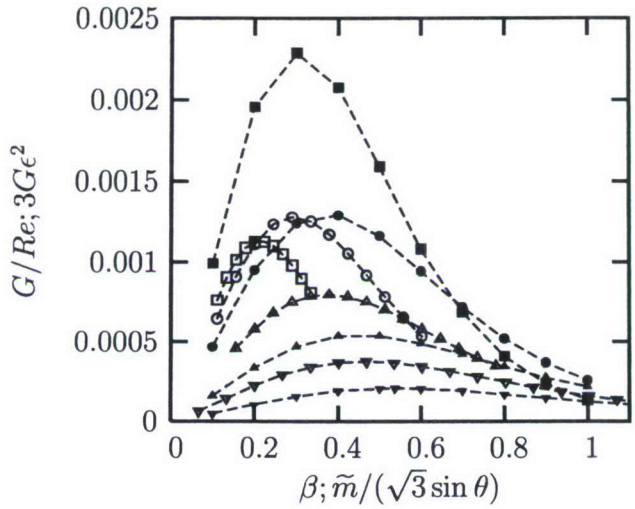

Figure 4.27: Objective function, comparison between G/Re (flat plate, full symbols) and $3G\epsilon^2$ (sharp cone, empty symbols) as a function of β and $\widetilde{m}/(\sqrt{3}\sin\theta)$ respectively, effect of x_{in} and wavenumber. $M_{\text{loc}} = 3$, $T_{\text{w}}/T_{\text{ad}} = 1$, $x_{\text{out}} = 1.0$. Sharp cone: □, $\theta = 15°$ and $x_{\text{in}} = 0.6$; ○, $\theta = 15°$ and $x_{\text{in}} = 0.8$; △, $\theta = 15°$ and $x_{\text{in}} = 0.9$; ▽, $\theta = 15°$ and $x_{\text{in}} = 0.95$. Flat plate: ■, $x_{\text{in}} = 0.30718$; ●, $x_{\text{in}} = 0.65359$; ▲, $x_{\text{in}} = 0.82679$; ▼, $x_{\text{in}} = 0.913$.

In order to investigate the intuitive idea that the difference in the energy growth between the two geometries should diminish as $x_{\text{in}} \to x_{\text{out}}$ and $m \to \infty$, in figure 4.27 we compare the sharp cone (empty symbols), $\theta = 15°$, and the flat plate (full symbols) at different x_{in}. The parameter Δx is properly rescaled so that □ compares with ■, ○ with ●, △ with ▲, and ▽ with ▼. Results confirm what is expected (see for example the sharp-cone case $x_{\text{in}} = 0.95$, ▽, compared to the flat-plate case $x_{\text{in}} = 0.913$, ▼).

Having the correct scaling, further comparisons between the two geometries can be carried out. The effect of wall temperature, which can either promote or delay transition in supersonic boundary layers, is shown in figure 4.28 in the limit $x_{\text{in}} \to x_{\text{out}}$. Empty symbols refer to the sharp cone ($\theta = 15°$) and full symbols to the flat plate. It can be noted that a cold wall, i.e. $T_{\text{w}}/T_{\text{ad}} = 0.5$ (○ and ▽ for sharp cone, corresponding to the cases ● and ▼ for the flat plate) enhances the energy growth, as already pointed out in previous sections. Moreover, not only is the gain larger for a cold wall, but the wavenumber for which the optimum is reached is also larger. For very large values of the wavenumber, results for the two geometries collapse onto each other, as a consequence of the $m \to \infty$ limit previously described. This behavior is consistent, for every case considered (see also □ vs. ■, and ▽ vs. ▼).

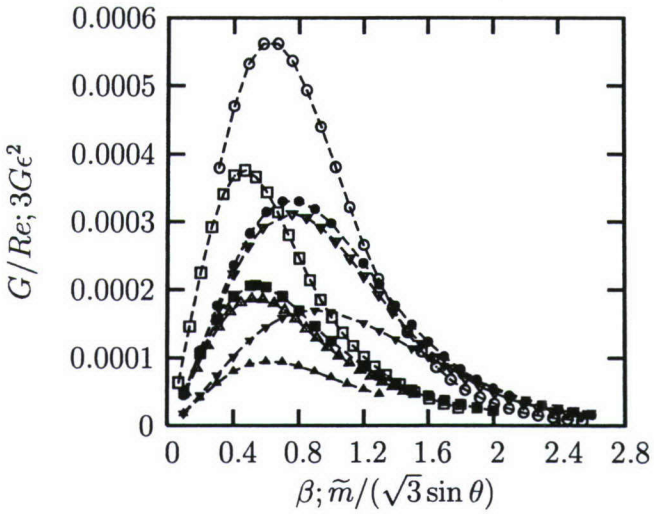

Figure 4.28: Objective function, comparison between G/Re (flat plate, full symbols) and $3G\epsilon^2$ (sharp cone, empty symbols) as a function of β and $\widetilde{m}/(\sqrt{3}\sin\theta)$ respectively, effect of x_{in}, wavenumber and $T_{\text{w}}/T_{\text{ad}}$. $M_{\text{loc}} = 3$, $x_{\text{out}} = 1.0$. Sharp cone: □, $\theta = 15°$, $T_{\text{w}}/T_{\text{ad}} = 1.0$ and $x_{\text{in}} = 0.95$; ○, $\theta = 15°$, $T_{\text{w}}/T_{\text{ad}} = 0.5$ and $x_{\text{in}} = 0.95$; △, $\theta = 15°$, $T_{\text{w}}/T_{\text{ad}} = 1.0$ and $x_{\text{in}} = 0.97113$; ▽, $\theta = 15°$, $T_{\text{w}}/T_{\text{ad}} = 0.5$ and $x_{\text{in}} = 0.97113$. Flat plate: ■, $x_{\text{in}} = 0.913$ and $T_{\text{w}}/T_{\text{ad}} = 1.0$; ●, $x_{\text{in}} = 0.913$ and $T_{\text{w}}/T_{\text{ad}} = 0.5$; ▲, $x_{\text{in}} = 0.95$ and $T_{\text{w}}/T_{\text{ad}} = 1.0$; ▼, $x_{\text{in}} = 0.95$ and $T_{\text{w}}/T_{\text{ad}} = 0.5$.

All considered examples demonstrate the growth factor G for the flat plate is larger than that for the cone leading to the conclusion that flow divergence has stabilizing effect.

Conclusion

Optimal disturbances originating in the supersonic boundary-layer flow past a sharp axisymmetric cone have been studied, motivated by several factors. Similar studies (Sections 4.2 - 4.4) report optimal perturbations for flat plate and sphere, but a direct comparison between them was complicated by the many effects present in the case of the sphere (flow divergence, pressure gradient, centrifugal forces and dependence of the edge parameters on the local Mach number). The sharp-cone geometry, on the other hand, is simpler than the spherical one and characterized by flow-divergence effects only, allowing us to identify them more easily when comparing flat plate, sharp cone and sphere. Moreover, in the development of the studies towards a more realistic three-dimensional supersonic case, the sharp-cone geometry is a natural step before the blunt-nose cone.

Equations are obtained from the linearized Navier–Stokes equations by employing a scaling that assumes the perturbation dominated by streamwise vortices. This leads to parabolic-in-x equations. The optimization is carried out in an iterative manner, relying on

the alternate solution of the direct and adjoint problems related by coupling conditions at the inlet and outlet.

A first set of results, obtained by keeping the inlet location fixed and changing the outlet location, provides interesting conclusions on flow divergence. An optimal distance Δx from the inlet ($\Delta x = x_{\text{out}} - x_{\text{in}}$) is found at $x_{out} < 1$, for which the curve of the maximum gain is the largest. The increase of Δx when the inlet location is moved downstream suggests that divergence effects are stronger in the proximity of the cone tip. On the other hand, increasing the cone half-angle does not seem to affect Δx. When these results are compared with the flat-plate case, it becomes clear that the presence of an optimal downstream location for the energy growth is a unique characteristic of flows dominated by geometrical divergence, such as those on sharp cones and spheres. For the case of the flat plate, in fact, for a given inlet station x_{in}, the curve of optimal energy gain reaches larger values monotonically as the outlet location, x_{out}, is moved downstream.

A second set of results is obtained by keeping the outlet location fixed and changing the inlet location. The gain, wavenumber and Δx are properly rescaled taking into account the half-cone angle θ and the fact that the boundary layer thickness on the sharp cone is $\sqrt{3}$ thinner than that over the flat plate. By comparing the two geometries, it is found that both the gain and the wavenumber scale fairly well and that results for the sharp cone collapse onto those for the flat plate in the limits $x_{\text{in}} \to x_{\text{out}}$ and $m \to \infty$.

Comparisons of growth factors for cones and flat plate demonstrate that the flow divergence has a stabilizing effect on transient growth. Results confirm also that a cold wall enhances transient growth.

4.6 Transient growth phenomenon in a boundary layer past a blunt cone

Despite the efforts done insofar, some issues regarding transition in supersonic flows are still open. One of them is the long-standing blunt-body paradox [RT00], according to which transition occurs in supersonic flows behind the detached bow shock, in a region that is subsonic and characterized by a favorable pressure gradient and therefore stable to TS-instability-like phenomena. Transient growth seems to be a promising mechanism to explain such a paradox (see Sections 4.1 - 4.4). However, the ultimate elucidation of the blunt-body paradox requires solving the roughness receptivity problem, which can explain the origin of the perturbation. The latter issue has not been addressed yet. The section presents the equations for analysis of optimal disturbances in the boundary layer over the blunt-nose cone at the angle of attack. The equations are derived for the stagnation line only.

We begin our derivation with full Navier-Stokes equations for axisymmetric system of coordinates [HCSP96]. Metric coefficients are the following: $h_x = 1 + \frac{y}{R}$, $h_y = 1$, $h_z = r + y\cos\theta$, where x is a streamwise coordinate, aligned to the envelope curve of the body, y is a coordinate which is normal to the surface, z represents the azimuthal angle ϕ, R is local radius of curvature in streamwise direction, r is local radius of curvature in spanwise direction, θ is the local angle between envelope curve and symmetry axis of the body. R, r and θ depend on streamwise coordinate x.

We use the same scaling as in the case of the sharp cone (section 4.5): the small parameter $\varepsilon = H_{ref}/L_{ref} = Re_{ref}^{-1/2}$, where $Re_{ref} = U_{ref}L_{ref}/\nu_{ref}$ is the reference Reynolds number, H_{ref} is a typical boundary layer length in the y-direction, L_{ref} is the typical scale of geometry. The radii of curvature, R and r, and x coordinate are scaled with L_{ref}, y coordinate is scaled with εL_{ref}, streamwise velocity component u is scaled with U_{ref}, normal and spanwise velocity components, v and w, are scaled with εU_{ref}, temperature T is scaled with T_{ref} and pressure p with $\varepsilon\rho_{ref}U_{ref}^2$ while density ρ is eliminated with the help of the equation of state.

We assume that perturbations are harmonic with respect to the transversal variable, $\propto \exp(im\phi)$ with azimuthal index m and use $w = i\tilde{w}$ as the spanwise velocity component.

In the vicinity of the spreading line ($\phi \to 0$) we can rewrite the z-component of base-flow velocity as $\bar{W} = \phi \left.\frac{\partial \bar{W}}{\partial \phi}\right|_{\phi=0} \to 0$ as $\phi \to 0$, and so the derivatives of $\bar{W}$ are zeros except $\frac{\partial \bar{W}}{\partial \phi} = \left.\frac{\partial \bar{W}}{\partial \phi}\right|_{\phi=0} \neq 0$ for $\phi \to 0$. The terms containing transversal velocity component of the base flow are though neglected.

The form of the equation needed to develop optimal perturbation analysis: $(\mathbf{Af})_x = (\mathbf{Df}_y)_x + \mathbf{B_0 f} + \mathbf{B_1 f}_y + \mathbf{B_2 f}_{yy}$, where $\mathbf{f} = (u,\ v,\ w,\ T,\ p)^T$, superscript T stands for transpose. The non-zero elements of matrices $\mathbf{A}$, $\mathbf{B_0}$, $\mathbf{B}_1$, $\mathbf{B}_2$ and $\mathbf{D}$ are given in the Appendix C.3.

Chapter 5

Conclusions

A comprehensive study of stability and receptivity of hypersonic boundary layers has been carried out under the support from the Air Force Office of Scientific Research, USAF under grant FA9550-05-101 monitored by Dr. J. D. Schmisseur.

The main results of the project:

- Mathematical method of the multimode decomposition for three-dimensional perturbations in compressible boundary layers has been developed. The method provides analysis of experimental and computational results for modes of discrete and continuous spectra.
- Theory of boundary-layer receptivity was developed for roughness-induced perturbations in incompressible and compressible boundary layers.
- The transient growth phenomenon in compressible boundary layers over flat plate, sphere, and sharp cone has been studied. The work was accompanied by development of solvers for these geometries. The solvers are described in Refs. [Zuc06a, Zuc06b, Zuc06c].[1]

[1]The reports have been delivered to AFRL at WPAFB and to the University of Minnesota

Appendix A

Appendices to Chapter 2

A.1 The matrix elements, Section 2.2

In what follows, U_s, T_s, and μ_s are velocity, temperature, and viscosity of the mean flow, respectively, and they are scaled with their values at the edge of the boundary layer. The pressure is scaled with $\rho_e U_e^2$, and $\mu_s' = d\mu/dT_s$, Re, Pr, and γ stand for the Reynolds number, Prandtl number, and specific heat ratio, respectively; M is the Mach number at the edge of the boundary layer; $D = d/dy$. The parameters r and m are defined as $r = 2(e+2)/3$ and $m = 2(e-1)/3$, and $2e/3$ is the ratio of the bulk viscosity to the dynamic viscosity. Particularly, Stokes' hypothesis corresponds to $e = 0$.

Nonzero elements of the matrices in (2.2) are

$$
\begin{aligned}
&L_0^{43} = -\frac{r\mu_s}{Re}, \\
&L_1^{11} = L_1^{22} = L_1^{33} = L_1^{44} = L_1^{55} = L_1^{66} = L_1^{77} = L_1^{88} = 1, \\
&L_1^{2,10} = L_1^{8,14} = m + 1.
\end{aligned}
$$

$$
\begin{aligned}
H_1^{12} &= 1, \\
H_1^{21} &= -\frac{i\omega Re}{T_s \mu_s}, \\
H_1^{22} &= -\frac{D\mu_s}{\mu_s}, \\
H_1^{23} &= \frac{Re\, DU}{T_s \mu_s}, \\
H_1^{25} &= -\frac{D\left(\mu_s' DU\right)}{\mu_s}, \\
H_1^{26} &= -\frac{\mu_s' DU}{\mu_s}, \\
H_1^{33} &= \frac{DT_s}{T_s}, \\
H_1^{34} &= i\omega\gamma M^2, \\
H_1^{35} &= -\frac{i\omega}{T_s}, \\
H_1^{43} &= i\omega\rho_s, \\
H_1^{56} &= 1, \\
H_1^{62} &= -2\left(\gamma - 1\right) Pr M^2 DU_s, \\
H_1^{63} &= \frac{RePr}{T_s \mu_s} DT_s, \\
H_1^{64} &= i\omega\left(\gamma - 1\right)\frac{RePr}{\mu_s} M^2, \\
H_1^{65} &= -i\omega\frac{RePr}{T_s \mu_s} - \left(\gamma - 1\right)\frac{Pr}{\mu_s} M^2 \mu_s' \left(\frac{\partial U_s}{\partial y}\right)^2 - \frac{D\left(\mu_s' DT_s\right)}{\mu_s}, \\
H_1^{66} &= -\frac{2D\mu_s}{\mu_s}, \\
H_1^{78} &= 1, \\
H_1^{87} &= -\frac{i\omega Re}{\mu_s T_s}, \\
H_1^{88} &= -\frac{D\mu_s}{\mu_s}, \\
H_1^{99} &= H_1^{10,10} = H_1^{11,11} = H_1^{12,12} = H_1^{13,13} = H_1^{14,14} = H_1^{15,15} = H_1^{16,16} = -1.
\end{aligned}
$$

$$
\begin{aligned}
H_2^{21} &= \frac{Re}{T_s \mu_s} U_s, \\
H_2^{23} &= -\frac{D\mu_s}{\mu_s}, \\
H_2^{24} &= \frac{Re}{\mu_s}, \\
H_2^{29} &= -r, \\
H_2^{31} &= -1, \\
H_2^{34} &= -\gamma U_s M^2, \\
H_2^{35} &= \frac{U_s}{T_s}, \\
H_2^{41} &= \frac{mD\mu_s}{Re}, \\
H_2^{42} &= (m+1)\frac{\mu_s}{Re}, \\
H_2^{43} &= -\frac{U_s}{T_s}, \\
H_2^{45} &= \frac{\mu_s'}{Re} DU_s, \\
H_2^{4,10} &= \frac{\mu_s}{Re}, \\
H_2^{63} &= -2(\gamma-1) Pr M^2 DU_s, \\
H_2^{64} &= -(\gamma-1)\frac{RePr}{\mu_s} M^2 U_s, \\
H_2^{65} &= \frac{RePr}{T_s \mu_s} U_s, \\
H_2^{6,11} &= -1, \\
H_2^{87} &= \frac{ReU_s}{\mu_s T_s}, \\
H_2^{8,12} &= -1, \\
H_2^{8,13} &= -(m+1), \\
H_2^{9,1} &= H_2^{10,3} = H_2^{11,5} = H_2^{12,7} = 1.
\end{aligned}
$$

$$
\begin{aligned}
H_3^{2,12} &= -(m+1), \\
H_3^{2,13} &= -1, \\
H_3^{37} &= -1, \\
H_3^{47} &= \frac{mD\mu_s}{Re}, \\
H_3^{48} &= (m+1)\frac{\mu_s}{Re}, \\
H_3^{4,14} &= \frac{\mu_s}{Re}, \\
H_3^{6,15} &= -1, \\
H_3^{83} &= -\frac{D\mu_s}{\mu_s}, \\
H_3^{84} &= \frac{Re}{\mu_s}, \\
H_3^{8,16} &= -r, \\
H_3^{13,1} &= H_3^{14,3} = H_3^{15,5} = H_3^{16,7} = 1.
\end{aligned}
$$

One can also find the nonzero elements of the matrix $\mathbf{H}_0$ in (A.3) and (A.4) from [Nay80] with the spanwise velocity of the mean flow equal to zero, $\alpha = -ip$, and

$$
\hat{\omega} = \omega - \alpha U_s, \qquad \chi = \left[\frac{Re}{\mu_s} - ir\gamma M^2\hat{\omega}\right]^{-1}.
$$

$$
\begin{aligned}
H_0^{12} &= H_0^{56} = H_0^{78} = 1, \\
H_0^{21} &= \alpha^2 + \beta^2 - i\hat{\omega}\frac{Re}{\mu_s T_s}, \\
H_0^{22} &= -\frac{D\mu_s}{\mu_s}, \\
H_0^{23} &= -i\alpha(m+1)\frac{DT_s}{T_s} - i\alpha\frac{D\mu_s}{\mu_s} + Re\frac{DU_s}{\mu_s T_s}, \\
H_0^{24} &= i\alpha\frac{Re}{\mu_s} + (m+1)\gamma M^2\alpha\hat{\omega}, \\
H_0^{25} &= -\alpha(m+1)\frac{\hat{\omega}}{T_s} - \frac{D(\mu_s' DU_s)}{\mu_s}, \\
H_0^{26} &= -\frac{\mu_s' DU_s}{\mu_s},
\end{aligned}
$$

$$
\begin{aligned}
H_0^{31} &= -i\alpha, \\
H_0^{33} &= \frac{DT_s}{T_s}, \\
H_0^{34} &= i\gamma M^2 \hat{\omega}, \\
H_0^{35} &= -\frac{i\hat{\omega}}{T_s}, \\
H_0^{37} &= -i\beta,
\end{aligned}
$$

$$
\begin{aligned}
H_0^{41} &= -i\chi\alpha \left(r\frac{DT_s}{T_s} + 2\frac{D\mu_s}{\mu_s} \right), \\
H_0^{42} &= -i\alpha\chi, \\
H_0^{43} &= \chi \left[-\alpha^2 - \beta^2 + i\frac{\hat{\omega} Re}{\mu_s T_s} + r\frac{D^2 T_s}{T_s} + r\frac{D\mu_s DT_s}{\mu_s T_s} \right], \\
H_0^{44} &= -i\chi r\gamma M^2 \left[\alpha DU_s - \hat{\omega}\frac{DT_s}{T_s} - \hat{\omega}\frac{D\mu_s}{\mu_s} \right], \\
H_0^{45} &= i\chi \left[r\frac{\alpha DU_s}{T_s} + \frac{\mu_s'}{\mu_s}\alpha DU_s - r\hat{\omega}\frac{D\mu_s}{\mu_s T_s} \right], \\
H_0^{46} &= -i\chi r\frac{\hat{\omega}}{T_s}, \\
H_0^{47} &= -i\chi\beta \left(r\frac{DT_s}{T_s} + 2\frac{D\mu_s}{\mu_s} \right), \\
H_0^{48} &= -i\beta\chi,
\end{aligned}
$$

$$
\begin{aligned}
H_0^{62} &= -2(\gamma - 1) M^2 Pr DU_s, \\
H_0^{63} &= -2i(\gamma - 1) M^2 Pr\alpha DU_s + RePr\frac{DT_s}{\mu_s T_s}, \\
H_0^{64} &= i(\gamma - 1) M^2 PrRe\frac{\hat{\omega}}{\mu_s}, \\
H_0^{65} &= \alpha^2 + \beta^2 - iRePr\frac{\hat{\omega}}{\mu_s T_s} - (\gamma - 1) M^2 Pr\mu_s'\frac{(DU_s)^2}{\mu_s} - \frac{D^2\mu_s}{\mu_s}, \\
H_0^{66} &= -2\frac{D\mu_s}{\mu_s},
\end{aligned}
$$

$$
\begin{aligned}
H_0^{83} &= -i\,(m+1)\,\beta\frac{DT_s}{T_s} - i\beta\frac{D\mu_s}{\mu_s},\\
H_0^{84} &= (m+1)\,\gamma M^2\beta\hat{\omega} + \frac{i\beta Re}{\mu_s},\\
H_0^{85} &= -\,(m+1)\,\frac{\beta\hat{\omega}}{T_s},\\
H_0^{87} &= \alpha^2 + \beta^2 - \frac{i\hat{\omega}Re}{\mu_s T_s},\\
H_0^{88} &= -\frac{D\mu_s}{\mu_s}.
\end{aligned}
$$

A.2 The biorthogonal eigenfunction system, Section 2.2

We introduce the following biorthogonal eigenfunction system $\{\mathbf{A}_{\alpha\beta}, \mathbf{B}_{\alpha\beta}\}$:

$$
\begin{aligned}
&\frac{\partial}{\partial y}\left(\mathbf{L}_0\frac{\partial \mathbf{A}_{\alpha\beta}}{\partial y}\right) + \mathbf{L}_1\frac{\partial \mathbf{A}_{\alpha\beta}}{\partial y} = \mathbf{H}_1\mathbf{A}_{\alpha\beta} + i\alpha\mathbf{H}_2\mathbf{A}_{\alpha\beta} + i\beta\mathbf{H}_3\mathbf{A}_{\alpha\beta},\\
&y = 0: \qquad A_{\alpha\beta 1} = A_{\alpha\beta 3} = A_{\alpha\beta 5} = A_{\alpha\beta 7} = 0,\\
&y \to \infty: \qquad |A_{\alpha\beta j}| < \infty,
\end{aligned}
\tag{A.1}
$$

$$
\begin{aligned}
&\frac{\partial}{\partial y}\left(\mathbf{L}_0^T\frac{\partial \mathbf{B}_{\alpha\beta}}{\partial y}\right) - \mathbf{L}_1^T\frac{\partial \mathbf{B}_{\alpha\beta}}{\partial y} = \mathbf{H}_1^T\mathbf{B}_{\alpha\beta} + i\alpha\mathbf{H}_2^T\mathbf{B}_{\alpha\beta} + i\beta\mathbf{H}_3^T\mathbf{B}_{\alpha\beta},\\
&y = 0: \qquad B_{\alpha\beta 2} = B_{\alpha\beta 4} = B_{\alpha\beta 6} = B_{\alpha\beta 8} = 0,\\
&y \to \infty: \qquad |B_{\alpha\beta j}| < \infty.
\end{aligned}
\tag{A.2}
$$

Actually, (A.2) defines the complex conjugate of the conventional adjoint problem. Equation (A.1) can be recast as a system of eight ODEs,

$$
\frac{d\mathbf{z}_{\alpha\beta}}{dy} = \mathbf{H}_0\mathbf{z}_{\alpha\beta}, \tag{A.3}
$$

where vector $\mathbf{z}_{\alpha\beta}$ is comprised of the first eight elements of the vector $\mathbf{A}_{\alpha\beta}$. The conventional adjoint problem in three-dimensional stability equations is found from the following system of ODEs:

$$
-\frac{d\mathbf{Y}_{\alpha\beta}}{dy} = \mathbf{H}_0\mathbf{Y}_{\alpha\beta}. \tag{A.4}
$$

One can establish correspondence between $\mathbf{B}_{\alpha\beta}$ and $\mathbf{Y}_{\alpha\beta}$ similar to the case of temporal three-dimensional normal modes (FT):

$$B_{\alpha\beta 1} = Y_{\alpha\beta 1} + \frac{i\alpha L_0^{43} Y_{\alpha\beta 4}}{(1 + L_0^{43} H_0^{34})}, \tag{A.5a}$$

$$B_{\alpha\beta 2} = Y_{\alpha\beta 2}, \tag{A.5b}$$

$$B_{\alpha\beta 3} = Y_{\alpha\beta 3} - i\alpha\,(m+1)\,Y_{\alpha\beta 2} - i\beta\,(m+1)\,Y_{\alpha\beta 8} - \frac{L_0^{43} H_0^{33} Y_{\alpha\beta 4}}{(1 + L_0^{43} H_0^{34})} + L_0^{43} \frac{d}{dy}\left[\frac{Y_{\alpha\beta 4}}{(1 + L_0^{43} H_0^{34})}\right], \tag{A.5c}$$

$$B_{\alpha\beta 4} = \frac{Y_{\alpha\beta 4}}{(1 + L_0^{43} H_0^{34})}, \tag{A.5d}$$

$$B_{\alpha\beta 5} = Y_{\alpha\beta 5} + H_0^{46} Y_4, \tag{A.5e}$$

$$B_{\alpha\beta 6} = Y_{\alpha\beta 6}, \tag{A.5f}$$

$$B_{\alpha\beta 7} = Y_{\alpha\beta 7} + \frac{i\beta L_0^{43} Y_{\alpha\beta 4}}{(1 + L_0^{43} H_0^{34})}, \tag{A.5g}$$

$$B_{\alpha\beta 8} = Y_{\alpha\beta 8}, \tag{A.5h}$$

$$B_{\alpha\beta 9} = -i\alpha r B_{\alpha\beta 2}, \tag{A.5i}$$

$$B_{\alpha\beta 10} = (m+1)\frac{dB_{\alpha\beta 2}}{dy} + i\alpha H_2^{4,10} B_{\alpha\beta 4}, \tag{A.5j}$$

$$B_{\alpha\beta 11} = -i\alpha B_{\alpha\beta 6}, \tag{A.5k}$$

$$B_{\alpha\beta 12} = -i\alpha B_{\alpha\beta 8} - i\beta\,(m+1)\,B_{\alpha\beta 2}, \tag{A.5l}$$

$$B_{\alpha\beta 13} = -i\alpha\,(m+1)\,B_{\alpha\beta 8} - i\beta B_{\alpha\beta 2}, \tag{A.5m}$$

$$B_{\alpha\beta 14} = (m+1)\frac{dB_{\alpha\beta 8}}{dy} + i\beta H_3^{4,14} B_{\alpha\beta 4}, \tag{A.5n}$$

$$B_{\alpha\beta 15} = -i\beta B_{\alpha\beta 6}, \tag{A.5o}$$

$$B_{\alpha\beta 16} = -i\beta r B_{\alpha\beta 8}, \tag{A.5p}$$

where r and m are defined in Appendix A.1.

The eigenfunction system $\{\mathbf{A}_{\alpha\beta}, \mathbf{B}_{\alpha\beta}\}$ has an orthogonality relation given as

$$\langle \mathbf{H_2 A}_{\alpha\beta}, \mathbf{B}_{\alpha'\beta} \rangle \equiv \int_0^\infty (\mathbf{H_2 A}_{\alpha\beta}, \mathbf{B}_{\alpha'\beta}) dy = \Gamma \Delta_{\alpha\alpha'}, \tag{A.6}$$

where Γ is a normalization constant; $\Delta_{\alpha\alpha'}$ is a Kronecker delta if either α or α' belongs to the discrete spectrum; $\Delta_{\alpha\alpha'}$ is a Dirac delta function if both α and α' belong to the continuous spectrum. Because Eq. (A.2) represents the complex conjugate of the conventional problem, the dot product $(,)$ in (A.6) does not involve complex conjugation. One can also establish the following equality:

$$\langle H_2 \mathbf{A}_{\alpha\beta}, \mathbf{B}_{\alpha\beta} \rangle = -i \left\langle \frac{\partial \mathbf{H}_0}{\partial \alpha} \mathbf{z}_{\alpha\beta}, \mathbf{Y}_{\alpha\beta} \right\rangle. \tag{A.7}$$

In our computations of the adjoint eigenfunctions, we find $\mathbf{Y}_{\alpha\beta}$ from (A.4) and restore $\mathbf{B}_{\alpha\beta}$ with the help of (A.5). Because derivation of asymptotic fundamental solutions of (A.4) at $y \to \infty$ is too complicated, we utilize the theorem [Kam59] that fundamental solutions of the adjoint system (A.4) can be found as vectors $\boldsymbol{\xi}_j$ comprised of cofactors of the jth column in the matrix of fundamental solution, $\mathbf{m}$, defined in (2.14). Therefore, we don't derive the asymptotics, but find them numerically with the help of the known asymptotic result for the matrix $\mathbf{m}$. Utilizing asymptotics for $\mathbf{z}_j$ (see Appendix A.3), one can find asymptotics $\boldsymbol{\xi}_j$ as follows:

$$\begin{aligned} \boldsymbol{\xi}_1 &= \boldsymbol{\xi}_1^0 e^{\lambda_2 y}, \quad \boldsymbol{\xi}_2 = \boldsymbol{\xi}_2^0 e^{\lambda_1 y}, \quad \boldsymbol{\xi}_3 = \boldsymbol{\xi}_3^0 e^{\lambda_4 y}, \quad \boldsymbol{\xi}_4 = \boldsymbol{\xi}_4^0 e^{\lambda_3 y}, \\ \boldsymbol{\xi}_5 &= \boldsymbol{\xi}_5^0 e^{\lambda_6 y}, \quad \boldsymbol{\xi}_6 = \boldsymbol{\xi}_6^0 e^{\lambda_5 y}, \quad \boldsymbol{\xi}_7 = \boldsymbol{\xi}_7^0 e^{\lambda_8 y}, \quad \boldsymbol{\xi}_8 = \boldsymbol{\xi}_8^0 e^{\lambda_7 y}. \end{aligned} \tag{A.8}$$

For each fundamental solution $\boldsymbol{\xi}_j$ having 8 components, one can restore fundamental solutions $\boldsymbol{\zeta}_j$ for the adjoint problem (A.2) comprised of 16 components with the help of (A.5). These steps allow computation of the adjoint eigenfunctions $\mathbf{B}_{\alpha\beta}$ of the discrete and continuous spectra.

One can find the following presentation of the adjoint eigenvectors $\mathbf{B}_c$ corresponding to the continuous spectra:

$$\mathbf{B}_{c,1} = \zeta_1 E_{1753} + \zeta_2 E_{2753} + \zeta_4 E_{4753} + \zeta_6 E_{6753} + \zeta_8 E_{8753}, \tag{A.9}$$

$$\mathbf{B}_{c,2} = \zeta_1 E_{1283} - \zeta_4 E_{2834} + \zeta_5 E_{2853} + \zeta_6 E_{2863} - \zeta_7 E_{2783}, \tag{A.10}$$

$$\mathbf{B}_{c,3} = \zeta_1 E_{6218} - \zeta_3 E_{2863} + \zeta_4 E_{2468} - \zeta_5 E_{6528} - \zeta_7 E_{6728}, \tag{A.11}$$

$$\mathbf{B}_{c,4} = \zeta_2 E_{1275} + \zeta_3 E_{1753} + \zeta_4 E_{1754} + \zeta_6 E_{1756} + \zeta_8 E_{7185}, \tag{A.12}$$

$$\mathbf{B}_{c,5} = \zeta_1 E_{1253} + \zeta_4 E_{5234} + \zeta_6 E_{2563} + \zeta_7 E_{7253} + \zeta_8 E_{8253}. \tag{A.13}$$

For the discrete modes, we find

$$\mathbf{B}_\nu = \zeta_2 E_{1257} + \zeta_4 E_{1457} + \zeta_6 E_{1765} + \zeta_8 E_{1578}. \tag{A.14}$$

One can see that the coefficients in (2.29),(2.31), (2.32), (2.34), (2.36), and (2.38), depending on the initial conditions, are associated with the adjoint eigenvectors, respectively, as follows:

$$\begin{aligned} &c_2 E_{1275} + c_3 E_{1753} + c_4 E_{1754} + c_6 E_{1756} + c_8 E_{7185} \sim \langle \mathbf{H_2 A}_0, \mathbf{B}_{c,4} \rangle, \\ &c_1 E_{1753} + c_2 E_{2753} + c_4 E_{4753} + c_6 E_{6753} + c_8 E_{8753} \sim \langle \mathbf{H_2 A}_0, \mathbf{B}_{c,1} \rangle, \\ &c_1 E_{1253} + c_4 E_{5234} + c_6 E_{2563} + c_7 E_{7253} + c_8 E_{8253} \sim \langle \mathbf{H_2 A}_0, \mathbf{B}_{c,5} \rangle, \\ &c_1 E_{1283} - c_4 E_{2834} + c_5 E_{2853} + c_6 E_{2863} - c_7 E_{2783} \sim \langle \mathbf{H_2 A}_0, \mathbf{B}_{c,2} \rangle, \\ &c_1 E_{6218} - c_3 E_{2863} + c_4 E_{2468} - c_5 E_{6528} - c_7 E_{6728} \sim \langle \mathbf{H_2 A}_0, \mathbf{B}_{c,3} \rangle, \\ &c_2 E_{1257} + c_4 E_{1457} + c_6 E_{1765} + c_8 E_{1578} \sim \langle \mathbf{H_2 A}_0, \mathbf{B}_\nu \rangle. \end{aligned} \tag{A.15}$$

Following [SG81], one can prove that the inverse Laplace transform (2.39) is an expansion into the biorthogonal eigenfunction system $\{\mathbf{A}_{\alpha\beta}, \mathbf{B}_{\alpha\beta}\}$.

The asymptotic vectors $\mathbf{Z}_j^0$ and $\boldsymbol{\zeta}_j^0$ are used to to calculate the normalization constant, Γ, in the orthogonality relation (A.6) for the continuous spectra. Evaluation of the normalization constant Γ for the continuous spectra can be found with the help of integrals like $\int_0^\infty \exp(i(k-k')y)\,dy = \pi\delta(k-k')$ [Tum03]. For example, one can find for an acoustic mode

$$\Gamma = \pi\left[\left(H_2\mathbf{Z}_5^0, \boldsymbol{\zeta}_5^0\right) + \left(H_2\mathbf{Z}_6^0, \boldsymbol{\zeta}_6^0\right)\right]. \tag{A.16}$$

A.3 Numerical method, Section 2.2

Two independent codes were used in the present work. The first one (SCM) was based on the single-domain Chebyshev spectral collocation method [Mal90]. Solution of the linearized Navier-Stokes equations for compressible gas is considered in the wave-like form

$$(u, v, w, \pi, \theta) = \left(\hat{u}(y), \hat{v}(y), \hat{w}(y), \hat{\pi}(y), \hat{\theta}(y)\right) e^{i(\alpha x + \beta z - \omega t)}. \tag{A.17}$$

In order to avoid the nonlinearity in α, we introduce the vector

$$\Phi = \left(\hat{u}, \hat{v}, \hat{w}, \hat{\pi}, \hat{\theta}, i\alpha\hat{u}, i\alpha\hat{v}, i\alpha\hat{w}, i\alpha\hat{\theta}\right)^T, \tag{A.18}$$

and the system of ODEs for the amplitude functions is written in the matrix form

$$(A_1 D^2 + A_2 D + A_3)\Phi = \alpha A_4 \Phi, \tag{A.19}$$

where $D = d/dy$; A_1, A_2, A_3, and A_4 are 9×9 matrices.

Homogeneous boundary conditions for (A.19) are formulated on the wall, $y = 0$, and at $y = y_{max}$,

$$y = 0 \quad \text{and} \quad y \to \infty: \qquad \Phi_j = 0, \qquad (j = 1, 2, 3, 5, \ldots, 9). \tag{A.20}$$

In the numerical implementation, the boundary conditions (A.20) were supplemented by the y-momentum equation at $y = 0$ and $y = y_{max}$.

An algebraic stretching was employed in order to map interval $[0, y_{max}]$ onto the Chebyshev interval $\xi \in [-1, +1]$,

$$y = d\frac{1+\xi}{b-\xi}, \tag{A.21}$$

where $b = 1 + 2d/y_{max}$ and $d = y_i y_{max}/(y_{max} - 2y_i)$. The parameter y_i is chosen to locate half of the grid points in the interval $(0, y_i)$. The Nth-order Chebyshev polynomials T_N were used with the collocation points

$$\xi_j = \cos(\pi j/N), \qquad j = 0, \ldots, N. \tag{A.22}$$

The unknown functions and their derivatives at the collocation points, y_j, are presented as sums of the Chebyshev polynomials, T_n, with unknown coefficients, a_n:

$$Q(y_j) = \sum_{n=0}^{N} a_n T_n(y_j), \tag{A.23}$$

As a result of the discretization, we arrive at the generalized eigenvalue problem

$$A_g \tilde{a} = \alpha B_g \tilde{a}, \tag{A.24}$$

where A_g and B_g are $9(N+1) \times 9(N+1)$ matrices, and $\tilde{a}$ is the vector comprised of $9(N+1)$ unknown coefficients. Because the rows of the matrix B_g corresponding to the boundary conditions (A.20) contain only zeros, we replace them by the corresponding rows of the matrix A_g divided by a large number, as was suggested by [HSH96]. This introduces eigenvalues that are located far away from the domain of interest in the complex plane α. The generalized eigenvalue problem (A.24) was solved with the help of standard routine DG6CCG from the IMSL FORTRAN Library.

[Mal90] reported eigenvalue $\alpha = 0.2534048 - i\,0.0024921$ for a two-dimensional perturbation in a boundary layer over a flat plate with an adiabatic wall. The following parameters were used: Mach number $M = 4.5$; the Reynolds number $Re = 1500$ was based on the Blasius scale; the stagnation temperature $T_0 = 611.11$ K; and the Prandtl number $Pr = 0.70$. For these parameters, we considered three-dimensional perturbations at $\beta = 10^{-4}$. At $N = 125$, $y_i = 5$, and $y_{max} = 100$, our result was $\alpha = 0.2534416 - i\,0.0027743$. Variation of y_i and y_{max} did not reveal a difference within six digits. Increasing N up to 175 revealed an effect only on the last digits of the real and imaginary parts of α. This code had an auxiliary role, and it served for verification of the other code that was based on the 4th-order Runge-Kutta solver for equations (A.3) and (A.4), and to provide an initial guess for the eigenvalues.

In the second code (RK), the fundamental solutions of equations (A.3) and (A.4) were found numerically by integration of the equations from y_{max} to the wall with the known analytical asymptotic solutions outside the boundary layer, $\mathbf{z}_j^0 \exp(\lambda_j y)$. One can find the asymptotic vectors $\mathbf{z}_j^0$ from (A.3) at $y \to \infty$. For vectors $\mathbf{z}_{1,2}^0$ and $\mathbf{z}_{7,8}^0$, we have

$$\mathbf{z}_{1,2}^0 = \left(1, \lambda_{1,2}, H_0^{31}/\lambda_{1,2}, 0, 0, 0, 0, 0\right)^T, \tag{A.25}$$

$$\mathbf{z}_{7,8}^0 = \left(0, 0, H_0^{37}/\lambda_{7,8}, 0, 0, 0, 1, \lambda_{7,8}\right)^T, \tag{A.26}$$

where the matrix elements H_0^{ij} are defined in Appendix A.1.

The nonzero elements z_{ij} of vectors $\mathbf{z}_j^0$ $(j = 3, \ldots, 6)$ were calculated as follows:

$$z_{1j}^0 = 1, \quad z_{2j}^0 = \lambda_j, \quad z_{4j}^0 = \left(\lambda_j^2 - H_0^{21}\right) b_{23}/b_{12}, \tag{A.27a}$$

$$z_{5j}^0 = -\left(b_{22} - \lambda_j^2\right)\left(\lambda_j^2 - H_0^{21}\right)/b_{12}, \quad z_{6j}^0 = \lambda_j z_{6j}^0, \tag{A.27b}$$

$$z_{7j}^0 = \left(H_0^{84} z_{4j}^0 + H_0^{85} z_{5j}^0\right) / \left(\lambda_j^2 - H_0^{87}\right), \quad z_{8j}^0 = \lambda_j z_{7j}^0, \tag{A.27c}$$

$$z_{3j}^0 = \left(H_0^{31} z_{1j}^0 + H_0^{34} z_{4j}^0 + H_0^{35} z_{5j}^0 + H_0^{37} z_{7j}^0\right)/\lambda_j, \tag{A.27d}$$

where $b_{12} = H_0^{24} b_{23} - H_0^{25}(b_{22} - \lambda_j^2)$, and b_{22} and b_{23} are defined in (2.12).

Asymptotic vectors $\boldsymbol{\xi}_j^0$ for the system (A.4) were found numerically from the matrix of the fundamental solutions $\mathbf{m}$ introduced in (2.14) (see discussion of properties of the adjoint system in Appendix A.2). The Gram-Schmidt orthonormalization procedure was employed in the computation of the fundamental solutions $\mathbf{z}_j$ and $\boldsymbol{\xi}_j$ during integration across the boundary layer.

[BM92], $\beta = 0$	the present work, $\beta = 10^{-4}$
$(0.220, -3.091 \times 10^{-3})$	$(0.220, -3.091 \times 10^{-3})$
$(0.221, 1.569 \times 10^{-2})$	$(0.221, 1.569 \times 10^{-2})$
$(-0.565, 5.559 \times 10^{-2})$	$(-0.565, 5.560 \times 10^{-2})$
$(0.560, 5.659 \times 10^{-1})$	$(0.561, 5.659 \times 10^{-1})$

Table A.1: Flat plate. $M = 4.5$, $T_0 = 311$ K, $Pr = 0.72$, $Re = 1000$, $\omega = 0.2$

[BM92]	the present work
$(0.2181, 2.969 \times 10^{-4})$	$(0.2181, 2.974 \times 10^{-4})$
$(0.2124, 1.288 \times 10^{-2})$	$(0.2124, 1.288 \times 10^{-2})$
$(-0.5498, 5.684 \times 10^{-2})$	$(-0.5499, 5.685 \times 10^{-2})$

Table A.2: Flat plate. $M = 4.5$, $T_0 = 311$ K, $Pr = 0.72$, $Re = 1000$, $\omega = 0.2$, $\beta = 0.12$

Finally, the eigenfunctions of the direct and adjoint problems could be obtained as a sum of the fundamental solutions with unknown coefficients that are to be determined from the boundary conditions on the wall. In the case of continuous spectra, the eigenfunctions are comprised of five fundamental solutions. The unknown coefficients could be found from four boundary conditions on the wall ($\hat{u} = \hat{v} = \hat{w} = \hat{\theta} = 0$) and the normalization condition $d\hat{u}/dy\,(0) = 1$. The wavenumbers α corresponding to the modes of the continuous spectra were found from the equation $\lambda_j^2 = -k^2$. For the problem of the discrete spectrum, the eigenfunctions are comprised of four fundamental solutions $\mathbf{z}_1$, $\mathbf{z}_3$, $\mathbf{z}_5$, and $\mathbf{z}_7$. The unknown four coefficients were determined from the boundary conditions $\hat{u} = \hat{v} = \hat{w} = 0$ and the normalization condition $d\hat{u}/dy\,(0) = 1$. The eigenvalue α was found with the help of the Newton method as a root of the equation $\theta(0) = 0$. The convergence criterion was chosen as $|\theta(0)| < \varepsilon$ with $\varepsilon \leq 10^{-5}$.

We tested the code with the example discussed above. The outer boundary was chosen as $y_{max} = 35$, with the uniform grid having $N = 601$ nodes and the convergence criterion $\varepsilon = 10^{-5}$. The spanwise wavenumber β was held at 10^{-4}. The found eigenvalue was $\alpha = 0.2534420 - i\,0.0027738$. The result remained the same for $N = 1201$, $\varepsilon = 10^{-5}$, and $N = 601$, $\varepsilon = 10^{-7}$.

In another test, we used the eigenvalues reported by [BM92] for a boundary layer over an adiabatic flat plate at Mach number $M = 4.5$, Prandtl number $Pr = 0.72$, stagnation temperature in the free stream $T_0 = 311$ K, Reynolds number $Re = 1000$, and dimensionless frequency $\omega = 0.2$. In table A.1, we compare our eigenvalues, α, obtained with help of the RK solver at $\beta = 10^{-4}$ and results from [BM92] at $\beta = 0$. A comparison of eigenvalues α corresponding to $\beta = 0.12$ is given in table A.2.

A.4 The non-zero elements of matrices in Eqs. (2.96) and (2.100), Section 2.5.2

The velocity, temperature, and viscosity are scaled using their values at the upper boundary-layer edge; the pressure is scaled using $\rho_e U_e^2$. Non-zero elements of the matrices in Eq. (2.96) are

$$
\begin{aligned}
L_0^{43} &= -\frac{r\mu_s}{R}, \\
L_1^{ij} &= 1, \ (i,j = 1,...,6), \\
L_1^{28} &= m + 1,
\end{aligned}
$$

$$
\begin{aligned}
H_1^{12} &= 1, \\
H_1^{21} &= -\frac{i\omega R}{\mu_s T_s}, \\
H_1^{22} &= -D\left(\ln \mu_s\right), \\
H_1^{23} &= \frac{R}{\mu_s T_s} DU_s, \\
H_1^{25} &= -\frac{D\left(\mu_s' DU_s\right)}{\mu_s}, \\
H_1^{26} &= -\frac{\mu_s'}{\mu_s} DU_s, \\
H_1^{33} &= \frac{DT_s}{T_s}, \\
H_1^{34} &= i\omega\gamma M_e^2, \\
H_1^{35} &= -\frac{i\omega}{T_s}, \\
H_1^{43} &= \frac{i\omega}{T_s}, \\
H_1^{56} &= 1, \\
H_1^{63} &= -2DU_s \,\mathrm{Pr}\,(\gamma - 1)\, M_e^2, \\
H_1^{64} &= i\omega \frac{R\,\mathrm{Pr}}{\mu_s}\,(\gamma - 1)\, M_e^2, \\
H_1^{65} &= -\frac{\mathrm{Pr}\,(\gamma - 1)\, M_e^2}{\mu_s} \mu_s' \left(DU_s\right)^2 - \frac{D\left(\mu_s' DT_s\right)}{\mu_s} - \frac{i\omega R\,\mathrm{Pr}}{T_s \mu_s}, \\
H_1^{66} &= -\frac{2\mu_s' DT_s}{\mu_s}, \\
H_1^{77} &= H_1^{88} = H_1^{99} = 1,
\end{aligned}
$$

$$
\begin{aligned}
H_2^{21} &= \frac{RU_s}{\mu_s T_s}, \\
H_2^{23} &= -D\left(\ln \mu_s\right), \\
H_2^{24} &= \frac{R}{\mu_s}, \\
H_2^{27} &= -r, \\
H_2^{31} &= -1, \\
H_2^{34} &= -\gamma M_e^2 U_s, \\
H_2^{35} &= \frac{U_s}{T_s}, \\
H_2^{41} &= \frac{mD\mu_s}{R}, \\
H_2^{42} &= (m+1)\frac{\mu_s}{R}, \\
H_2^{43} &= -\frac{U_s}{T_s}, \\
H_2^{45} &= \frac{\mu_s' DU_s}{R}, \\
H_2^{48} &= \frac{\mu_s}{R}, \\
H_2^{62} &= -2\,\mathrm{Pr}\,DU_s\left(\gamma-1\right)M_e^2, \\
H_2^{64} &= -\frac{R\,\mathrm{Pr}}{\mu_s}\left(\gamma-1\right)M_e^2 U_s, \\
H_2^{65} &= \frac{R\,\mathrm{Pr}}{T_s\mu_s}U_s, \\
H_2^{69} &= H_2^{71} = H_2^{83} = H_2^{95} = -1,
\end{aligned}
$$

$$
\begin{aligned}
H_0^{12} &= H_0^{56} = 1, \\
H_0^{21} &= \alpha^2 + i\left(\alpha U_s - \omega\right) R/\mu_s T_s, \\
H_0^{22} &= -D\mu_s/\mu_s, \\
H_0^{23} &= -i\alpha\left(m+1\right) DT_s/T_s - i\alpha D\mu_s/\mu_s + RDU_s/\mu_s T_s, \\
H_0^{24} &= i\alpha R/\mu_s - \left(m+1\right)\gamma M_e^2 \alpha\left(\alpha U_s - \omega\right), \\
H_0^{25} &= \alpha\left(m+1\right)\left(\alpha U_s - \omega\right)/T_s - D\left(\mu_s' DU_s\right)/\mu_s, \\
H_0^{26} &= -\mu_s' DU_s/\mu_s, \\
H_0^{31} &= -i\alpha, \\
H_0^{33} &= DT_s/T_s, \\
H_0^{34} &= -i\gamma M_e^2\left(\alpha U_s - \omega\right), \\
H_0^{35} &= i\left(\alpha U_s - \omega\right)/T_s, \\
\chi &= \left[\frac{R}{\mu_s} + ir\gamma M_e^2\left(\alpha U_s - \omega\right)\right]^{-1}, \\
H_0^{41} &= -i\alpha\chi\left(rDT_s/T_s + 2D\mu_s/\mu_s\right), \\
H_0^{42} &= -i\alpha\chi, \\
H_0^{43} &= \chi\left[-\alpha^2 - i\left(\alpha U_s - \omega\right) R/\mu_s T_s + rD^2 T_s/T_s + rD\mu_s DT_s/\mu_s T_s\right], \\
H_0^{44} &= -i\chi r\gamma M_e^2\left[\alpha DU_s + \left(\alpha U_s - \omega\right)\left(DT_s/T_s + D\mu_s/\mu_s\right)\right], \\
H_0^{45} &= i\chi\left[r\alpha DU_s/T_s + \alpha\mu_s' DU_s/\mu_s + r\left(\alpha U_s - \omega\right) D\mu_s/\mu_s T_s\right], \\
H_0^{46} &= ir\chi\left(\alpha U_s - \omega\right)/T_s, \\
H_0^{62} &= -2\left(\gamma - 1\right) M_e^2 \Pr DU_s, \\
H_0^{63} &= -2i\alpha\left(\gamma - 1\right) M_e^2 \Pr DU_s + R\Pr DT_s/\mu_s T_s, \\
H_0^{64} &= -iR\Pr\left(\gamma - 1\right) M_e^2\left(\alpha U_s - \omega\right)/\mu_s, \\
H_0^{65} &= \alpha^2 + iR\Pr\left(\alpha U_s - \omega\right)/\mu_s T_s - \left(\gamma - 1\right) M_e^2 \Pr \mu_s'\left(DU_s\right)^2/\mu_s - D^2\mu_s/\mu_s, \\
H_0^{66} &= -2D\mu_s/\mu_s.
\end{aligned}
$$

A.5 Correspondence between solutions of the adjoint problems, Eqs. (2.106) and (2.107), Section 2.5.2

$$
\begin{aligned}
B_1 &= Y_1 - \frac{i\alpha r Y_4}{\left[\frac{R}{\mu_s} + ir\gamma M_e^2\left(\alpha U_s - \omega\right)\right]}, \\
B_2 &= Y_2, \\
B_3 &= -i\alpha\left(m+1\right)Y_2 + Y_3 \\
&\quad + \frac{rDT_s}{T_s}\frac{Y_4}{\left[\frac{R}{\mu_s} + ir\gamma M_e^2\left(\alpha U_s - \omega\right)\right]} - \frac{r\mu_s}{R}\frac{d}{dy}\left(\frac{Y_4}{\left[1 + i\frac{r\mu_s}{R}\gamma M_e^2\left(\alpha U_s - \omega\right)\right]}\right), \\
B_4 &= \frac{Y_4}{\left[1 + i\frac{r\mu_s}{R}\gamma M_e^2\left(\alpha U_s - \omega\right)\right]}, \\
B_5 &= Y_5 + \frac{ir\left(\alpha U_s - \omega\right)}{T_s}\frac{Y_4}{\left[\frac{R}{\mu_s} + ir\gamma M_e^2\left(\alpha U_s - \omega\right)\right]}, \\
B_6 &= Y_6, \\
B_7 &= i\alpha r B_2, \\
B_8 &= -\left(m+1\right)\frac{dB_2}{dy} - i\alpha H_2 B_4, \\
B_9 &= i\alpha B_6.
\end{aligned}
$$

A.6 Fundamental solutions in the triple-deck limit, Section 2.7

Direct problem

The outer deck (2). Introducing the new variables $y_2 = y^*/\varepsilon^3 L$, $x_2 = x^*/\varepsilon^3 L$, and $t_2 = t^* U_\infty/\varepsilon^2 L$, where '*' stands for dimensional coordinate, the solutions of the linearized Navier-Stokes equations are considered proportional to $\exp[i(\bar{\alpha}x_2 + \bar{\omega}t_2)]$. One can find the following expansions for the amplitude functions of the velocities and the pressure perturbation in the outer deck:

$$u = \varepsilon^2 u_1^{(2)}\left(y_2\right) + \varepsilon^3 u_2^{(2)}\left(y_2\right) + \ldots \tag{A.28a}$$

$$v = \varepsilon^2 v_1^{(2)}\left(y_2\right) + \varepsilon^3 v_2^{(2)}\left(y_2\right) + \ldots \tag{A.28b}$$

$$p = \varepsilon^2 p_1^{(2)}\left(y_2\right) + \varepsilon^3 p_2^{(2)}\left(y_2\right) + \ldots \tag{A.28c}$$

where the superscript indicates the number of the deck. Because we deal with a linear problem, the solution can be normalized arbitrarily. However, we keep the triple-deck scaling

for the velocities and pressure perturbations in Eqs. (A.28) stemming from the general analysis of nonlinear problems. In the main order of magnitude, the governing equations are as follows:

$$i\bar{\alpha}u_1^{(2)} + \frac{dv_1^{(2)}}{dy_2} = 0 \tag{A.29a}$$

$$u_1^{(2)} + p_1^{(2)} = 0 \tag{A.29b}$$

$$i\bar{\alpha}v_1^{(2)} + \frac{dp_1^{(2)}}{dy_2} = 0 \tag{A.29c}$$

Solution of Eqs. (A.29) can be presented as

$$p_1^{(2)} = e^{\lambda y_2} \tag{A.30a}$$

$$u_1^{(2)} = -p_1^{(2)}(y_2) \tag{A.30b}$$

$$v_1^{(2)} = -\frac{1}{i\bar{\alpha}}\frac{dp_1^{(2)}}{dy_2} = -\frac{\lambda}{i\bar{\alpha}}p_1^{(2)}(y_2) \tag{A.30c}$$

where $\lambda = \pm\bar{\alpha}$. Because the procedure of finding the asymptotic solutions corresponding to the direct problem is well known, we skip details of finding the inner limit of the outer solution at $y_2 \to 0$, derivation of the matching conditions for the outer limit of the main deck solution, and other conventional details for the triple-deck analysis.

The main deck (1). In the main deck, the variables are defined as $x_1 = x_2$, $t_1 = t_2$, and $y_1 = y_2/\varepsilon$, and the amplitude functions have the following expansion:

$$u = \varepsilon u_1^{(1)}(y_1) + \varepsilon^2 u_2^{(1)}(y_1) + \ldots \tag{A.31a}$$

$$v = \varepsilon^2 v_1^{(1)}(y_1) + \varepsilon^3 v_2^{(1)}(y_1) + \ldots \tag{A.31b}$$

$$p = \varepsilon^2 p_1^{(1)}(y_1) + \varepsilon^3 p_2^{(1)}(y_1) + \ldots \tag{A.31c}$$

In the main order of magnitude, one can find

$$p_1^{(1)} = 1 \tag{A.32a}$$

$$v_1^{(1)} = -\frac{\lambda}{i\bar{\alpha}}U(y_1) \tag{A.32b}$$

$$u_1^{(1)} = -\frac{\lambda}{\bar{\alpha}^2}\frac{dU}{dy_1} \tag{A.32c}$$

$$v_2^{(1)} = DU(y_1) + iU(y_1)\int_1^{y_1}\left[\bar{\alpha} - \omega\frac{\lambda}{\bar{\alpha}^2}\frac{dU}{dy_1}\right]\frac{dy_1}{U^2} \tag{A.32d}$$

$$D = i\bar{\omega}\frac{\lambda}{\bar{\alpha}^2}\int_1^{\infty}\frac{dU}{dy_1}\frac{dy_1}{U^2} - i\bar{\alpha}\int_1^{\infty}\left[\frac{1}{U^2} - 1\right]dy_1 + i\bar{\alpha} \tag{A.32e}$$

The lower deck (3). In the lower deck, the variables are $x_3 = x_1 = x_2$, $t_3 = t_1 = t_2$, and $y_3 = y_1/\varepsilon$. The leading terms only of our interest and one can find their scaling from the matching condition as follows

$$u = \varepsilon u_1^{(3)}(y_3) + ... \tag{A.33a}$$

$$v = \varepsilon^3 v_1^{(3)}(y_3) + ... \tag{A.33b}$$

$$p = \varepsilon^2 p_1^{(3)}(y_3) + ... \tag{A.33c}$$

These amplitude function satisfy the following equations

$$i\bar{\alpha}u_1^{(3)} + \frac{dv_1^{(3)}}{dy_3} = 0 \tag{A.34a}$$

$$i\bar{\omega}u_1^{(3)} + i\bar{\alpha}u_1^{(3)}\bar{U}'_w y_3 + v_1^{(3)}\bar{U}'_w = -i\bar{\alpha}p_1^{(3)} + \frac{d^2u_1^{(3)}}{dy_3^2} \tag{A.34b}$$

$$\frac{dp_1^{(3)}}{dy_3} = 0 \tag{A.34c}$$

where $\bar{U}'_w = (dU/dy_1)_{y_1=0}$.

From the last equation of the system (A.34) and the matching condition with the solution in the outer deck, we have $p_1^{(3)} = 1$. Therefore, we derive from Eqs. (A.34)

$$i\bar{\alpha}u_1^{(3)} + \frac{dv_1^{(3)}}{dy_3} = 0 \tag{A.35a}$$

$$i\bar{\omega}u_1^{(3)} + i\bar{\alpha}u_1^{(3)}\bar{U}'_w y_3 + v_1^{(3)}\bar{U}'_w = -i\bar{\alpha} + \frac{d^2u_1^{(3)}}{dy_3^2} \tag{A.35b}$$

The solution of Eqs. (A.35) satisfying the matching condition in the outer limit, $y_3 \to \infty$, can be found as

$$u_1^{(3)} = -\frac{\lambda}{\bar{\alpha}^2}\bar{U}'_w \tag{A.36a}$$

$$v_1^{(3)} = -\left(\frac{\lambda}{i\bar{\alpha}}\bar{U}'_w y_3 + \frac{i\bar{\alpha}}{\bar{U}'_w} - i\bar{\omega}\frac{\lambda}{\bar{\alpha}^2}\right) \tag{A.36b}$$

This result completes the analysis of the fundamental solutions of Eqs. (2.228) having asymptotic behaviors $\sim \exp(\pm\bar{\alpha}y_2)$ outside the boundary layer.

Another fundamental solution [residue of the vector $\mathbf{Z}_3$ in (2.230) and (2.232)] can be found in the viscous sublayer. This solution has $p_1^{(3)} = 0$, and $u_1^{(3)}(y_3)$ satisfies the following equation:

$$\frac{d^3u_1^{(3)}}{dy_3^3} - i\left(\bar{\alpha}\bar{U}'_w y_3 - \bar{\omega}\right)\frac{du_1^{(3)}}{dy_3} = 0 \tag{A.37}$$

With the help of the new variable,

$$\zeta = \frac{i\bar{\omega}}{\left(i\bar{\alpha}\bar{U}'_w\right)^{2/3}} + \left(i\bar{\alpha}\bar{U}'_w\right)^{1/3} y_3 \tag{A.38}$$

where the branch is chosen to provide $|\arg\left(i\bar{\alpha}\bar{U}'_w\right)^{1/3}| < \pi/3$. Equation (A.37) is reduced to the Airy equation for $Q(\zeta) = du_1^{(3)}/dy_3$

$$Q'' - \zeta Q = 0 \tag{A.39}$$

The decaying at $y_3 \to \infty$ solution of Eq. (A.39) is the Airy function, $Q(\zeta) = \mathrm{Ai}(\zeta)$. Therefore, the velocity components and pressure perturbation corresponding to this fundamental solution are as follows:

$$u_1^{(3)} = \left(i\bar{\alpha}\bar{U}'_w\right)^{-1/3} \int_{\infty}^{\zeta} \mathrm{Ai}\,(\eta)\, d\eta \tag{A.40a}$$

$$v_1^{(3)} = \frac{\left(i\bar{\alpha}\bar{U}'_w\right)^{1/3}}{\bar{U}'_w} \left[\mathrm{Ai}'\,(\zeta) - \zeta \int_{\infty}^{\zeta} \mathrm{Ai}\,(\eta)\, d\eta\right] \tag{A.40b}$$

$$p_1^{(3)} = 0 \tag{A.40c}$$

Adjoint problem

Similar to the consideration of the direct problem, we are looking for the fundamental solutions of Eqs. (2.229). Because the adjoint problem has not been discussed in the triple-deck limit elsewhere, more details are included in the following derivations.

We employ the scaling of the streamwise coordinate and the frequency in accordance with the triple-deck theory, and recast the system of Eqs. (2.229) as follows

$$-\frac{dY_1}{dy} = i\bar{\alpha}\varepsilon^{-3}\left(-Y_3 + \varepsilon^{-8}UY_4\right) + i\bar{\omega}\varepsilon^{-10}Y_4 \tag{A.41a}$$

$$-\frac{dY_2}{dy} = i\bar{\alpha}\varepsilon^{-11}Y_4 \tag{A.41b}$$

$$-\frac{dY_3}{dy} = U'\varepsilon^{-8}Y_4 - i\bar{\omega}\varepsilon^{-2}Y_2 + i\bar{\alpha}\varepsilon^{-3}\left(Y_1 - UY_2\right) \tag{A.41c}$$

$$-\frac{dY_4}{dy} = Y_1 - \varepsilon^5 i\bar{\alpha}Y_2 \tag{A.41d}$$

The outer deck (2). We are looking for the solution in the outer deck in the following asymptotic expansion form:

$$Y_1 = g_{11}^{(2)}(y_2) + \varepsilon g_{12}^{(2)}(y_2) + ... \tag{A.42a}$$

$$Y_2 = g_{21}^{(2)}(y_2) + \varepsilon g_{22}^{(2)}(y_2) + ... \tag{A.42b}$$

$$Y_3 = g_{31}^{(2)}(y_2) + \varepsilon g_{32}^{(2)}(y_2) + ... \tag{A.42c}$$

$$Y_4 = \varepsilon^8 g_{41}^{(2)}(y_2) + \varepsilon^9 g_{42}^{(2)}(y_2) + ... \tag{A.42d}$$

where the first subscript stands for the component of the adjoint vector solution, $\mathbf{Y}$. In the main order of magnitude, one can find

$$g_{21}^{(2)} = \exp(\lambda y_2) \tag{A.43a}$$

$$g_{41}^{(2)} = -\frac{\lambda}{i\bar{\alpha}} \exp(\lambda y_2) \tag{A.43b}$$

$$g_{31}^{(2)} = -\frac{\lambda}{i\bar{\alpha}} \exp(\lambda y_2) \tag{A.43c}$$

$$g_{11}^{(2)} = 0 \tag{A.43d}$$

where $\lambda = \pm\bar{\alpha}$. At the limit $y_2 \to 0$

$$g_{21}^{(2)} \to 1 + \lambda y_2 + ... = 1 + \varepsilon\lambda y_1 + ... \tag{A.44a}$$

$$g_{41}^{(2)} \to -\frac{\lambda}{i\bar{\alpha}}[1 + \lambda y_2 + ...] = -\frac{\lambda}{i\bar{\alpha}}[1 + \varepsilon\lambda y_1 + ...] \tag{A.44b}$$

$$g_{31}^{(2)} \to -\frac{\lambda}{i\bar{\alpha}}[1 + \lambda y_2 + ...] = -\frac{\lambda}{i\bar{\alpha}}[1 + \varepsilon\lambda y_1 + ...] \tag{A.44c}$$

$$g_{11}^{(2)} = 0 \tag{A.44d}$$

Equations (A.44) will serve as the outer matching conditions for the solution in the main deck.

The main deck (1). We are looking for the solution in the main deck (1) as the following expansions:

$$Y_1 = g_{11}^{(1)}(y_1) + \varepsilon g_{12}^{(1)}(y_1) + ... \tag{A.45a}$$

$$Y_2 = g_{21}^{(1)}(y_1) + \varepsilon g_{22}^{(1)}(y_1) + ... \tag{A.45b}$$

$$Y_3 = g_{31}^{(1)}(y_1) + \varepsilon g_{32}^{(1)}(y_1) + ... \tag{A.45c}$$

$$Y_4 = \varepsilon^8 g_{41}^{(1)}(y_1) + \varepsilon^9 g_{42}^{(1)}(y_1) + ... \tag{A.45d}$$

In the main order of magnitude, the governing equations are

$$g_{11}^{(1)} = 0 \tag{A.46a}$$

$$g_{31}^{(1)} = U g_{41}^{(1)} \tag{A.46b}$$

$$\frac{dg_{21}^{(1)}}{dy_1} = 0 \tag{A.46c}$$

$$\frac{dg_{31}^{(1)}}{dy_1} = -\frac{dU}{dy_1} g_{41}^{(1)} \tag{A.46d}$$

The solutions of Eqs. (A.46) satisfying the matching condition at $y_1 \to \infty$ are found as

$$g_{21}^{(1)} = 1 \tag{A.47a}$$

$$g_{41}^{(1)} = -\frac{\lambda}{i\bar{\alpha}U^2} \tag{A.47b}$$

$$g_{31}^{(1)} = -\frac{\lambda}{i\bar{\alpha}U} \tag{A.47c}$$

$$g_{11}^{(1)} = 0 \tag{A.47d}$$

For the purpose of analyzing the viscous sublayer (lower deck), we need also $g_{22}^{(1)}$. Thus, we consider the equations in the next order and arrive at:

$$-\frac{dg_{22}^{(1)}}{dy_1} = i\bar{\alpha} g_{41}^{(1)} \tag{A.48}$$

On can find $g_{22}^{(1)}(y_1)$ from Eqs. (A.48)

$$g_{22}^{(1)} = \lambda \int_1^{y_1} \frac{1}{U^2} dy_1 + C_0 \tag{A.49}$$

where C_0 is a constant that has to be determined from the matching condition with the solutions (A.44)

$$C_0 = \lambda - \lambda \int_1^{\infty} \left[\frac{1}{U^2} - 1 \right] dy_1 \tag{A.50}$$

At the limit $y_1 \to 0$, one can find

$$g_{21}^{(1)} = 1 \tag{A.51a}$$

$$g_{41}^{(1)} \to -\frac{\lambda}{i\bar{\alpha}(U'_w)^2 y_1^2} = -\frac{\lambda}{i\bar{\alpha}(U'_w)^2 y_3^2} \frac{1}{\varepsilon^2} \tag{A.51b}$$

$$g_{31}^{(1)} \to -\frac{\lambda}{i\bar{\alpha}U'_w y_3} \frac{1}{\varepsilon} \tag{A.51c}$$

$$g_{22}^{(1)} \to -\frac{\lambda}{(U'_w)^2 y_1} = -\frac{\lambda}{\varepsilon(U'_w)^2 y_3} \tag{A.51d}$$

The lower deck (3). In the lower deck, scaling of the leading terms stem from the matching condition at $y_3 \to \infty$

$$Y_1 = \varepsilon g_{11}^{(3)}(y_3) + ... \tag{A.52a}$$

$$Y_2 = g_{21}^{(3)}(y_3) + ... \tag{A.52b}$$

$$Y_3 = \varepsilon^{-1} g_{31}^{(3)}(y_3) + ... \tag{A.52c}$$

$$Y_4 = \varepsilon^6 g_{41}^{(3)}(y_3) + ... \tag{A.52d}$$

where the amplitude functions satisfy the following equations

$$-\frac{dg_{11}^{(3)}}{dy_3} = i\bar{\alpha}\left(-g_{31}^{(3)} + \bar{U}'_w y_3 g_{41}^{(3)}\right) + i\bar{\omega} g_{41}^{(3)} \tag{A.53a}$$

$$-\frac{dg_{21}^{(3)}}{dy_3} = i\bar{\alpha} g_{41}^{(3)} \tag{A.53b}$$

$$-\frac{dg_{31}^{(3)}}{dy_3} = \bar{U}'_w g_{41}^{(3)} \tag{A.53c}$$

$$-\frac{dg_{41}^{(3)}}{dy_3} = g_{11}^{(3)} \tag{A.53d}$$

One can derive from Eqs. (A.53) the equation for $g_{21}^{(3)}(y_3)$

$$\frac{d^4 g_{21}^{(3)}}{dy_3^4} = 2i\bar{U}'_w \bar{\alpha} \frac{dg_{21}^{(3)}}{dy_3} + i\bar{\alpha}\bar{U}'_w y_3 \frac{d^2 g_{21}^{(3)}}{dy_3^2} + i\bar{\omega}\frac{d^2 g_{21}^{(3)}}{dy_3^2} \tag{A.54}$$

With the help of the variable ζ [see Eq. (A.38) at $\bar{\omega} = 0$], one can arrive at

$$\frac{d^4 g_{21}^{(3)}}{d\zeta^4} - \frac{d^2 \zeta g_{21}^{(3)}}{d\zeta^2} = 0 \tag{A.55}$$

The integration of Eq. (A.55) with respect to ζ leads to the inhomogeneous Airy equation

$$\frac{d^2 g_{21}^{(3)}}{d\zeta^2} - \zeta g_{21}^{(3)} = G(\zeta)$$

$$G(\zeta) = k_1 \zeta + k_2$$

where k_1 and k_2 are constants that have to be determined from the matching condition at $y_3 \to \infty$. The solution of Eq. (A.56) can be written as (see [AS72])

$$g_{21}^{(3)}(\zeta) = \pi \left[\mathrm{Bi}(\zeta) \int_{\infty}^{\zeta} G\mathrm{Ai} d\zeta - \mathrm{Ai}(\zeta) \int_{-\infty}^{\zeta} G\mathrm{Bi} d\zeta \right] \tag{A.56}$$

where $\mathrm{Ai}(\zeta)$ and $\mathrm{Bi}(\zeta)$ are two fundamental solutions of the Airy equation [AS72], and their Wronskian is

$$\mathrm{Ai}(\zeta) \times Bi'(\zeta) - \mathrm{Ai}'(\zeta) \times Bi(\zeta) = \frac{1}{\pi} \tag{A.57}$$

One can find that at $y_3 \to \infty$ ($\zeta \to \infty$)

$$g_{21}^{(3)}(\zeta) \to -\frac{G(\zeta)}{\zeta} \tag{A.58}$$

Therefore, the matching conditions lead to the result

$$k_1 = -1 \tag{A.59a}$$

$$k_2 = \frac{\left(i\bar{\alpha}\bar{U}_w'\right)^{1/3}}{\left(\bar{U}_w'\right)^2}\lambda \tag{A.59b}$$

After substituting $G(\zeta)$ with $k_1 = -1$, we arrive at the solution in the lower deck

$$g_{21}^{(3)} = \pi k_2 \left[\mathrm{Bi}(\zeta) \int_{\infty}^{\zeta} \mathrm{Ai} d\zeta - \mathrm{Ai}(\zeta) \int_{-\infty}^{\zeta} \mathrm{Bi} d\zeta\right] + 1 \tag{A.60a}$$

$$g_{41}^{(3)} = -\frac{\pi k_2}{i\bar{\alpha}} \left(i\alpha\bar{U}_w'\right)^{1/3} \left[\mathrm{Bi}'(\zeta) \int_{\infty}^{\zeta} \mathrm{Ai} d\zeta - \mathrm{Ai}'(\zeta) \int_{-\infty}^{\zeta} \mathrm{Bi} d\zeta\right] \tag{A.60b}$$

$$g_{31}^{(3)} = \frac{\bar{U}_w'}{i\bar{\alpha}} \left[g_{21}^{(3)} - 1\right] \tag{A.60c}$$

$$g_{11}^{(3)} = \frac{\pi\lambda}{\bar{U}_w'} \left[\mathrm{Bi}''(\zeta) \int_{\infty}^{\zeta} \mathrm{Ai} d\zeta - \mathrm{Ai}''(\zeta) \int_{-\infty}^{\zeta} \mathrm{Bi} d\zeta\right] + \frac{\lambda}{\bar{U}_w'} \tag{A.60d}$$

Solution (A.60) summarizes the asymptotic analysis of two fundamental solutions having asymptotic behavior outside the boundary layer $\exp(\pm\bar{\alpha}y_2)$. The third fundamental solution will be found as a decaying at the $\zeta \to \infty$ solution of the homogeneous equation (A.52) (Airy equation). Therefore, we obtain for the third fundamental solution the following result:

$$g_{21}^{(3)} = \mathrm{Ai}(\zeta) \tag{A.61a}$$

$$g_{41}^{(3)} = -\frac{\left(i\bar{\alpha}\bar{U}_w'\right)^{1/3}}{i\bar{\alpha}} \mathrm{Ai}'(\zeta) \tag{A.61b}$$

$$g_{11}^{(3)} = \frac{\left(i\bar{\alpha}\bar{U}_w'\right)^{2/3}}{i\bar{\alpha}} \mathrm{Ai}''(\zeta) \tag{A.61c}$$

$$g_{31}^{(3)} = \frac{\bar{U}_w'}{i\bar{\alpha}} \mathrm{Ai}(\zeta) \tag{A.61d}$$

Appendix B

Appendices to Chapter 3

B.1 Biorthogonal system of eigenfunctions, Section 3.2

It is possible to express a solution of the initial-value problem (Eq. (3.47)) as an expansion in the biorthogonal eigenfunction system $\{\mathbf{A}_\omega, \mathbf{B}_\omega\}$. The vector $\mathbf{A}_\omega$ is a solution of the direct problem

$$\begin{aligned}\frac{d}{dy}(\mathbf{L}_0\frac{d\mathbf{A}_\omega}{dy}) + \frac{d\mathbf{A}_\omega}{dy} = &-i\omega\mathbf{H}_{10}\mathbf{A}_\omega + \mathbf{H}_{11}\mathbf{A}_\omega + i\alpha\mathbf{H}_2\mathbf{A}_\omega + i\alpha\mathbf{H}_3\frac{d\mathbf{A}_\omega}{dy} - \alpha^2\mathbf{H}_4\mathbf{A}_\omega \\ &+ i\beta\mathbf{H}_5\mathbf{A}_\omega - \alpha\beta\mathbf{H}_6\mathbf{A}_\omega + i\beta\mathbf{H}_7\frac{d\mathbf{A}_\omega}{dy} - \beta^2\mathbf{H}_8\mathbf{A}_\omega\end{aligned} \tag{B.1}$$

$$\begin{aligned}&y = 0: \ \mathbf{A}_{\omega 1} = \mathbf{A}_{\omega 3} = \mathbf{A}_{\omega 5} = \mathbf{A}_{\omega 7} = 0, \\ &y \to \infty: \ |\mathbf{A}_{\omega j}| < \infty, \ j = 1, ..., 8.\end{aligned} \tag{B.2}$$

The vector $\mathbf{B}_\omega$ is a solution of the adjoint problem

$$\begin{aligned}\frac{d}{dy}(\mathbf{L}_0^*\frac{d\mathbf{B}_\omega}{dy}) - \frac{d\mathbf{B}_\omega}{dy} = &\, i\bar{\omega}\mathbf{H}_{10}^*\mathbf{B}_\omega + \mathbf{H}_{11}^*\mathbf{B}_\omega - i\alpha\mathbf{H}_2^*\mathbf{B}_\omega + i\alpha\mathbf{H}_3^*\frac{d\mathbf{B}_\omega}{dy} - \alpha^2\mathbf{H}_4^*\mathbf{B}_\omega \\ &- i\beta\mathbf{H}_5^*\mathbf{B}_\omega - \alpha\beta\mathbf{H}_6^*\mathbf{B}_\omega + i\beta\mathbf{H}_7^*\frac{d\mathbf{B}_\omega}{dy} - \beta^2\mathbf{H}_8^*\mathbf{B}_\omega\end{aligned} \tag{B.3}$$

$$\begin{aligned}&y = 0: \ \mathbf{B}_{\omega 2} = \mathbf{B}_{\omega 4} = \mathbf{B}_{\omega 6} = \mathbf{B}_{\omega 8} = 0, \\ &y \to \infty: \ |\mathbf{B}_{\omega j}| < \infty, \ j = 1, ..., 8.\end{aligned} \tag{B.4}$$

The asterisk in Eq. (B.3) denotes a Hermitian matrix, and the over bar denotes a complex conjugate value. The direct problem, Eqs. (B.1-B.2), can be expressed in the standard form given by Eq. (3.8). The adjoint problem, Eqs. (B.3-B.4), can be expressed in a similar fashion as

$$-\frac{d\mathbf{Y}}{dy} = \mathbf{H}_0^*\mathbf{Y} \tag{B.5}$$

$$\begin{aligned} &y = 0: \ \mathbf{Y}_2 = \mathbf{Y}_4 = \mathbf{Y}_6 = \mathbf{Y}_8 = 0, \\ &y \to \infty: \ |\mathbf{Y}_j| < \infty, \ j = 1, ..., 8. \end{aligned} \tag{B.6}$$

A correspondence can be found between $\mathbf{B}_\omega$ and $\mathbf{Y}$. These relationships are given as follows:

$$B_1 = Y_1 + \frac{i\alpha r Y_4}{Re/\mu_s - ir\gamma M_e^2 (\alpha U_s + \beta W_s - \bar{\omega})} \tag{B.7}$$

$$B_2 = Y_2 \tag{B.8}$$

$$\begin{aligned} B_3 = {} & i\alpha (m+1) Y_2 + Y_3 + \frac{rDT_s}{T_s} \frac{Y_4}{Re/\mu_s - ir\gamma M_e^2 (\alpha U_s + \beta W_s - \bar{\omega})} \\ & - \frac{r\mu_s}{Re} \frac{d}{dy} \left(\frac{Y_4}{1 - ir\gamma M_e^2 (\mu_s/Re) (\alpha U_s + \beta W_s - \bar{\omega})} \right) + i\beta (m+1) Y_8 \end{aligned} \tag{B.9}$$

$$B_4 = \frac{Y_4}{1 - ir\gamma M_e^2 (\mu_s/Re) (\alpha U_s + \beta W_s - \bar{\omega})} \tag{B.10}$$

$$B_5 = Y_5 - \frac{ir (\alpha U_s + \beta W_s - \bar{\omega})}{T_s} \frac{Y_4}{Re/\mu_s - ir\gamma M_e^2 (\alpha U_s + \beta W_s - \bar{\omega})} \tag{B.11}$$

$$B_6 = Y_6 \tag{B.12}$$

$$B_7 = Y_7 + i\beta r \frac{Y_4}{Re/\mu_s - ir\gamma M_e^2 (\alpha U_s + \beta W_s - \bar{\omega})} \tag{B.13}$$

$$B_8 = Y_8 \tag{B.14}$$

Solutions of the direct and adjoint problems given by Eqs. (B.1-B.2) and (B.3-B.4) belong to the discrete and continuous spectrum. Eqs. (3.37), (3.39), (3.40) and (3.46) are modes that satisfy the direct problem with weights (coefficients) that depend on the Fourier transform of the initial disturbance, $\mathbf{A}_{0\alpha\beta}$.

The eigenfunction system $\{\mathbf{A}_\omega, \mathbf{B}_\omega\}$ has an orthogonality relation given as

$$\langle \mathbf{H}_{10} \mathbf{A}_\omega, \mathbf{B}_{\omega'} \rangle \equiv \int_0^\infty (\mathbf{H}_{10} \mathbf{A}_\omega, \mathbf{B}_{\omega'}) \, dy = \Gamma \Delta_{\omega,\omega'} \tag{B.15}$$

where Γ is a normalization constant. $\Delta_{\omega,\omega'}$ is a Kronecker delta if either ω or ω' belong to the discrete spectrum. $\Delta_{\omega,\omega'} = \delta(\omega - \omega')$ is a Dirac delta function if both ω and ω' belong to the continuous spectrum.

The inverse Laplace transform can be expressed as an expansion in the biorthogonal eigenfunction system as follows:

$$\mathbf{A}_{\alpha\beta}(y,t) = \sum_\nu c_\nu \mathbf{A}_{\alpha\beta\omega_\nu}(y) e^{-i\omega_\nu t} + \sum_j \int_0^\infty c_j(k) \mathbf{A}_{\alpha\beta\omega_j}(y) e^{-iw_j(k)t} dk \tag{B.16}$$

where $\sum_\nu$ denotes a summation over the discrete spectrum and $\sum_j$ denotes a summation over the continuous spectrum. Using the Fourier transform of the initial disturbance, $\mathbf{A}_{0\alpha\beta}$, as well as the orthogonality relation (Eq. (B.15)), one can find the coefficients c_ν and c_j.

Appendix C

Appendices to Chapter 4

C.1 Matrices for compressible flow past a sphere, Section 4.4

Assuming that the basic flow is known, let r, θ and ϕ denote respectively the radial, meridional and azimuthal coordinate and v, u, w be the corresponding velocity field. Temperature T and pressure p are the other unknowns of the problem, while density ρ is related to T and p by the state equation and thus is not an explicit unknown. The radial coordinate $r = R+y$ includes the sphere radius R and the distance from the sphere surface y.

The scaling is as described in §4.2. The unknowns in the disturbance equations are only five and are assumed to be proportional to $\exp(\mathrm{i}m\phi)$, where m is the azimuthal index and i the imaginary unit.

The scaling adopted for the sphere leads to the following relationships between ρ, p and T (the subscript $\cdot_s$ stands for basic flow), which allow us to recast the equations in five variables only:

$$\rho = -\frac{\rho_s T}{T_s}; \qquad \rho_s = \frac{p_s}{T_s}.$$

In what follows viscosity μ_s is assumed to be a function of temperature only, and therefore μ_s' stands for the derivative $d\mu_s/dT_s$.

Transformations of the linearized equations lead to a system of partial differential equations

$$(\boldsymbol{A}\mathbf{f})_\theta = \boldsymbol{D}\mathbf{f}_{\theta\eta} + \boldsymbol{B}_0\mathbf{f} + \boldsymbol{B}_1\mathbf{f}_\eta + \boldsymbol{B}_2\mathbf{f}_{\eta\eta}, \tag{C.1}$$

where $\boldsymbol{A}$, $\boldsymbol{B}_0$, $\boldsymbol{B}_1$, $\boldsymbol{B}_2$ and $\boldsymbol{D}$ are 5×5 matrices and $\eta = y/H_{\mathrm{ref}}$ is the normalized distance from the wall. System (C.1) can be recast as

$$(\boldsymbol{H}_1\mathbf{f})_\theta + \boldsymbol{H}_2\mathbf{f} = 0, \tag{C.2}$$

where the parabolic dependence on θ should be more clear and operators $\boldsymbol{H}_1$ and $\boldsymbol{H}_2$ are still 5 by 5 matrices and contain the dependence on θ and η:

$$\boldsymbol{H}_1 = \boldsymbol{A} - \boldsymbol{D}(\cdot)_\eta; \qquad \boldsymbol{H}_2 = -\boldsymbol{B}_0 - [\boldsymbol{B}_1 - \boldsymbol{D}_\theta](\cdot)_\eta - \boldsymbol{B}_2(\cdot)_{\eta\eta}. \tag{C.3}$$

It should be noticed that system (C.1) is written in a different form than (4.1). However, by rearranging the matrices, the same final forms (C.2) and (4.4) are obtained.

The expression to be maximized is the integral in the wall-normal direction of the kinetic energy and temperature

$$E_{\text{out}} = \int_0^\infty (1+\epsilon\eta)\sin(\theta_{\text{out}}) \left[\rho_{s_{\text{out}}}[u_{\text{out}}^2 + \epsilon^2(v_{\text{out}}^2 + w_{\text{out}}^2)] + \frac{p_{s_{\text{out}}} T_{\text{out}}^2}{(\gamma-1)T_{s_{\text{out}}}^2 M^2}\right] d\eta, \qquad \text{(C.4)}$$

where the term $(1+\epsilon\eta)\sin(\theta_{\text{out}})$ comes from the integration over the whole domain, i.e. over the three independent variables.

The nonzero elements of the matrices are here reported. It should be noticed that, formally, in the limit $\epsilon \to 0$, the geometric factor $(1+\epsilon\eta)$ reduces to 1 and thus is automatically excluded from the denominator. The dependence on ϵ remains only in the terms associated with the centrifugal force such as B_0^{31}. However, in the present numerical implementation, the outer boundary $\eta_{\max}$ had to be chosen far away (on the order of 100) and $\epsilon = \mathcal{O}(10^{-3})$, leading to $\epsilon\eta = \mathcal{O}(10^{-1})$. Since $\epsilon\eta$ is not negligible, we keep the factor $(1+\epsilon\eta)$ in the governing equations.

The wavenumber β in the following terms is defined as $\beta = \dfrac{m\epsilon}{(1+\epsilon\eta)\sin\theta}$.

Continuity equation:

$$A^{11} = \frac{\rho_s}{(1+\epsilon\eta)};$$

$$A^{14} = -\frac{\rho_s U_s}{T_s(1+\epsilon\eta)};$$

$$B_0^{11} = -\frac{\rho_s \cot\theta}{(1+\epsilon\eta)};$$

$$B_0^{12} = -\frac{\partial\rho_s}{\partial\eta};$$

$$B_0^{13} = -\beta\rho_s;$$

$$B_0^{14} = \frac{\partial}{\partial\eta}\left(\frac{\rho_s V_s}{T_s}\right) + \frac{\rho_s U_s \cot\theta}{T_s(1+\epsilon\eta)};$$

$$B_1^{12} = -\rho_s;$$

$$B_1^{14} = \frac{\rho_s V_s}{T_s};$$

θ-momentum equation:

$$
\begin{aligned}
A^{21} &= \frac{2\rho_s U_s}{(1+\epsilon\eta)};\\
A^{24} &= -\frac{\rho_s U_s^2}{T_s(1+\epsilon\eta)};\\
B_0^{21} &= -\frac{\partial \rho_s V_s}{\partial \eta} - \mu_s \beta^2 - \frac{2\rho_s U_s \cot\theta}{(1+\epsilon\eta)};\\
B_0^{22} &= -\frac{\partial \rho_s U_s}{\partial \eta};\\
B_0^{23} &= -\beta \rho_s U_s;\\
B_0^{24} &= \frac{\partial}{\partial \eta}\left(\frac{\rho_s V_s U_s}{T_s}\right) + \frac{\partial}{\partial \eta}\left(\mu_s' \frac{\partial U_s}{\partial \eta}\right) + \frac{\rho_s U_s^2 \cot\theta}{T_s(1+\epsilon\eta)};\\
B_1^{21} &= \frac{\partial \mu_s}{\partial \eta} - \rho_s V_s;\\
B_1^{22} &= -\rho_s U_s;\\
B_1^{24} &= \frac{\rho_s U_s V_s}{T_s} + \mu_s' \frac{\partial U_s}{\partial \eta};\\
B_2^{21} &= \mu_s;
\end{aligned}
$$

r-momentum equation:

$$A^{31} = \frac{\rho_s V_s}{(1+\epsilon\eta)} + \frac{2}{3(1+\epsilon\eta)}\frac{\partial \mu_s}{\partial \eta};$$

$$A^{32} = \frac{\rho_s U_s}{(1+\epsilon\eta)};$$

$$A^{34} = -\frac{\rho_s U_s V_s}{T_s(1+\epsilon\eta)} - \frac{\mu_s'}{(1+\epsilon\eta)}\frac{\partial U_s}{\partial \eta};$$

$$B_0^{31} = \frac{2}{3(1+\epsilon\eta)}\frac{\partial^2 \mu_s}{\partial\eta\partial\theta} - \frac{\rho_s V_s \cot\theta}{(1+\epsilon\eta)} + \frac{2\rho_s U_s}{\epsilon(1+\epsilon\eta)} - \frac{2\cot\theta}{3(1+\epsilon\eta)}\frac{\partial \mu_s}{\partial \eta};$$

$$B_0^{32} = -2\frac{\partial \rho_s V_s}{\partial \eta} - \beta^2 \mu_s - \frac{\rho_s U_s \cot\theta}{(1+\epsilon\eta)};$$

$$B_0^{33} = -\beta\rho_s V_s - \frac{2\beta}{3}\frac{\partial \mu_s}{\partial \eta};$$

$$\begin{aligned} B_0^{34} = {} & \frac{2\rho_s V_s}{T_s}\frac{\partial V_s}{\partial \eta} + \frac{\partial \mu_s'}{\partial \eta}\left[\frac{4}{3}\frac{\partial V_s}{\partial \eta} - \frac{2}{3(1+\epsilon\eta)\sin\theta}\frac{\partial U_s \sin\theta}{\partial\theta}\right] \\ & + \mu_s'\frac{\partial}{\partial \eta}\left(\frac{4}{3}\frac{\partial V_s}{\partial \eta} - \frac{2}{3(1+\epsilon\eta)\sin\theta}\frac{\partial U_s \sin\theta}{\partial\theta}\right) \\ & + V_s^2\frac{\partial}{\partial \eta}\left(\frac{\rho_s}{T_s}\right) + \frac{\rho_s U_s V_s \cot\theta}{T_s(1+\epsilon\eta)} - \frac{\rho_s U_s^2}{\epsilon T_s(1+\epsilon\eta)} + \frac{\mu_s' \cot\theta}{(1+\epsilon\eta)}\frac{\partial U_s}{\partial \eta}; \end{aligned}$$

$$B_1^{31} = \frac{1}{(1+\epsilon\eta)}\frac{\partial \mu_s}{\partial\theta} + \frac{\mu_s \cot\theta}{3(1+\epsilon\eta)};$$

$$B_1^{32} = -2\rho_s V_s + \frac{4}{3}\frac{\partial \mu_s}{\partial \eta};$$

$$B_1^{33} = \frac{\beta\mu_s}{3(1+\epsilon\eta)};$$

$$B_1^{34} = \mu_s'\left[\frac{4}{3}\frac{\partial V_s}{\partial \eta} - \frac{2}{3(1+\epsilon\eta)\sin\theta}\frac{\partial U_s \sin\theta}{\partial\theta}\right] + \frac{\rho_s V_s^2}{T_s};$$

$$B_1^{35} = -1;$$

$$B_2^{32} = \frac{4}{3}\mu_s;$$

$$D^{31} = \frac{\mu_s}{3(1+\epsilon\eta)};$$

ϕ-momentum equation:

$$A^{43} = \frac{\rho_s U_s}{(1+\epsilon\eta)};$$

$$A^{44} = \frac{\mu_s \beta U_s}{3T_s(1+\epsilon\eta)};$$

$$B_0^{41} = \frac{\mu_s \beta}{3\rho_s(1+\epsilon\eta)}\frac{\partial \rho_s}{\partial \theta} - \frac{\beta}{(1+\epsilon\eta)}\frac{\partial \mu_s}{\partial \theta} - \frac{2\beta\mu_s \cot\theta}{(1+\epsilon\eta)};$$

$$B_0^{42} = \frac{\mu_s \beta}{3\rho_s}\frac{\partial \rho_s}{\partial \eta} - \beta\frac{\partial \mu_s}{\partial \eta};$$

$$B_0^{43} = -\beta^2\mu_s - \frac{\partial \rho_s V_s}{\partial \eta} - \frac{2\rho_s U_s \cot\theta}{(1+\epsilon\eta)};$$

$$B_0^{44} = \frac{\rho_s U_s \beta}{3T_s(1+\epsilon\eta)}\frac{\partial}{\partial\theta}\left(\frac{\mu_s}{\rho_s}\right) - \frac{2\mu_s' \beta U_s \cot\theta}{(1+\epsilon\eta)}$$
$$+ \mu_s'\frac{2\beta}{3}\left[\frac{\partial V_s}{\partial \eta} + \frac{1}{(1+\epsilon\eta)\sin\theta}\frac{\partial}{\partial\theta}(U_s \sin\theta)\right]$$
$$- \frac{\mu_s\beta}{3\rho_s}\frac{\partial}{\partial\eta}\left(\frac{\rho_s V_s}{T_s}\right) - \frac{\mu_s \beta U_s \cot\theta}{3T_s(1+\epsilon\eta)};$$

$$B_0^{45} = \beta;$$

$$B_1^{43} = -\rho_s V_s + \frac{\partial \mu_s}{\partial \eta};$$

$$B_1^{44} = -\frac{\beta\mu_s V_s}{3T_s};$$

$$B_2^{43} = \mu_s;$$

Energy equation:

$$A^{51} = \frac{\rho_s T_s}{(1+\epsilon\eta)};$$

$$B_0^{51} = \frac{\gamma-1}{\gamma(1+\epsilon\eta)}\frac{\partial p_s}{\partial\theta} - \frac{\rho_s T_s \cot\theta}{(1+\epsilon\eta)};$$

$$B_0^{53} = -\beta\rho_s T_s;$$

$$B_0^{54} = \mu_s'(\gamma-1)M_{\text{ref}}^2\left(\frac{\partial U_s}{\partial\eta}\right)^2 - \frac{\beta^2\mu_s}{Pr} + \frac{1}{Pr}\frac{\partial}{\partial\eta}\left(\mu_s'\frac{\partial T_s}{\partial\eta}\right);$$

$$B_1^{51} = 2(\gamma-1)M_{\text{ref}}^2\mu_s\frac{\partial U_s}{\partial\eta};$$

$$B_1^{52} = -\rho_s T_s;$$

$$B_1^{54} = \frac{2}{Pr}\frac{\partial\mu_s}{\partial\eta};$$

$$B_2^{54} = \frac{\mu_s}{Pr}.$$

C.2 Matrices for compressible flow past a sharp cone, Section 4.5

Assuming that the basic flow is known, let x, y and ϕ denote the three independent coordinates, where x is the streamwise distance from the nose tip, y the wall-normal distance and ϕ the azimuthal angle. With this notation, u, v, w are the corresponding velocity field, that together with temperature T and pressure p form the set of problem's unknowns. Density ρ is related to T and p by the state equation and thus is not an explicit unknown.

The scaling is as described in §4.2. The unknowns in the disturbance equations are only five and are assumed to be proportional to $\exp(im\phi)$, where m is the azimuthal index and i the imaginary unit.

In what follows viscosity μ_s is assumed to be a function of temperature only, and therefore μ_s' stands for the derivative $d\mu_s/dT_s$.

Transformations of the linearized equations lead to the system of partial differential equations

$$(\boldsymbol{A}\mathbf{f})_x = (\boldsymbol{D}\mathbf{f}_y)_x + \boldsymbol{B}_0\mathbf{f} + \boldsymbol{B}_1\mathbf{f}_y + \boldsymbol{B}_2\mathbf{f}_{yy}, \tag{C.5}$$

where $\boldsymbol{A}$, $\boldsymbol{B}_0$, $\boldsymbol{B}_1$, $\boldsymbol{B}_2$ and $\boldsymbol{D}$ are 5×5 matrices, and can be recast as

$$(\boldsymbol{H}_1\mathbf{f})_x + \boldsymbol{H}_2\mathbf{f} = 0. \tag{C.6}$$

Operators $\boldsymbol{H}_1$ and $\boldsymbol{H}_2$ are still 5×5 matrices and contain the dependence on x and y:

$$\boldsymbol{H}_1 = \boldsymbol{A} - \boldsymbol{D}(\cdot)_y; \qquad \boldsymbol{H}_2 = -\boldsymbol{B}_0 - \boldsymbol{B}_1(\cdot)_y - \boldsymbol{B}_2(\cdot)_{yy}. \tag{C.7}$$

The expression to be maximized, in the limit $\epsilon \to 0$ (i.e. $Re \to \infty$), is the integral in the wall-normal direction of the kinetic energy and temperature. After the transformations imposed by the geometry, E_{out} reads

$$E_{\text{out}} = \int_0^\infty \sin\theta(x + \epsilon y \cot\theta) \left[\rho_{s\text{out}} u_{\text{out}}^2 + + \frac{p_{s\text{out}} T_{\text{out}}^2}{(\gamma-1) T_{s\text{out}}^2 M^2}\right] dy, \tag{C.8}$$

where the term $\sin\theta(x + \epsilon y \cot\theta)$ stems from the integration over the whole domain, i.e. over the three independent variables.

The nonzero elements of the matrices are here reported, with the wavenumber β defined as $\beta = \widetilde{m}/(1 + \epsilon\eta)$, $\widetilde{m}$ being $\widetilde{m} = \epsilon m$.

Continuity equation:

$$
\begin{aligned}
A^{11} &= \rho_s; \\
A^{14} &= -\frac{\rho_s U_s}{T_s}; \\
B_0^{11} &= -\frac{\rho_s}{(1+\epsilon\eta)}; \\
B_0^{12} &= -\frac{\partial \rho_s}{\partial y}; \\
B_0^{13} &= -\beta \rho_s; \\
B_0^{14} &= \frac{\partial}{\partial y}\left(\frac{\rho_s V_s}{T_s}\right) + \frac{\rho_s U_s}{T_s(1+\epsilon\eta)}; \\
B_1^{13} &= -\rho_s; \\
B_1^{14} &= \frac{\rho_s V_s}{T_s};
\end{aligned}
$$

x-momentum equation:

$$
\begin{aligned}
A^{21} &= 2\rho_s U_s; \\
A^{24} &= -\frac{\rho_s U_s^2}{T_s}; \\
B_0^{21} &= -\frac{\partial \rho_s V_s}{\partial y} - \mu_s \beta^2 - \frac{2\rho_s U_s}{(1+\epsilon\eta)}; \\
B_0^{22} &= -\frac{\partial \rho_s U_s}{\partial y}; \\
B_0^{23} &= -\beta \rho_s U_s; \\
B_0^{24} &= \frac{\partial}{\partial y}\left(\frac{\rho_s V_s U_s}{T_s}\right) + \frac{\partial}{\partial y}\left(\mu_s' \frac{\partial U_s}{\partial y}\right) + \frac{\rho_s U_s^2}{T_s(1+\epsilon\eta)}; \\
B_1^{21} &= \frac{\partial \mu_s}{\partial y} - \rho_s V_s; \\
B_1^{22} &= -\rho_s U_s; \\
B_1^{24} &= \frac{\rho_s U_s V_s}{T_s} + \mu_s' \frac{\partial U_s}{\partial y}; \\
B_2^{21} &= \mu_s;
\end{aligned}
$$

y-momentum equation:

$$A^{31} = \rho_s V_s + \frac{2}{3}\frac{\partial \mu_s}{\partial y};$$

$$A^{32} = \rho_s U_s;$$

$$A^{34} = -\frac{\rho_s U_s V_s}{T_s} - \mu_s' \frac{\partial U_s}{\partial y};$$

$$B_0^{31} = \frac{2}{3}\frac{\partial}{\partial x}\left(\frac{\partial \mu_s}{\partial y}\right) + \frac{1}{(1+\epsilon\eta)}\left(-\frac{2}{3}\frac{\partial \mu_s}{\partial y} - \rho_s V_s\right);$$

$$B_0^{32} = -2\frac{\partial \rho_s V_s}{\partial y} - \beta^2 \mu_s - \frac{\rho_s U_s}{(1+\epsilon\eta)};$$

$$B_0^{33} = -\beta \rho_s V_s - \frac{2\beta}{3}\frac{\partial \mu_s}{\partial y};$$

$$B_0^{34} = \frac{1}{(1+\epsilon\eta)}\left[\frac{\rho_s U_s V_s}{T_s} + \frac{1}{3}\mu_s' \frac{\partial U_s}{\partial y} - \frac{2}{3}U_s \frac{\partial \mu_s'}{\partial y}\right] + \frac{\partial}{\partial y}\left(\frac{\rho_s V_s^2}{T_s}\right)$$
$$+ \frac{\partial \mu_s'}{\partial y}\left[\frac{4}{3}\frac{\partial V_s}{\partial y} - \frac{2}{3}\frac{\partial U_s}{\partial x}\right] + \mu_s'\left[-\frac{\partial}{\partial x}\left(\frac{\partial U_s}{\partial y}\right) + \frac{4}{3}\frac{\partial^2 V_s}{\partial y^2} + \frac{1}{3}\frac{\partial^2 U_s}{\partial x \partial y}\right];$$

$$B_1^{31} = \frac{\mu_s}{3(1+\epsilon\eta)} + \frac{2}{3}\frac{\partial \mu_s}{\partial x};$$

$$B_1^{32} = -2\rho_s V_s + \frac{4}{3}\frac{\partial \mu_s}{\partial y};$$

$$B_1^{33} = \frac{\beta \mu_s}{3};$$

$$B_1^{34} = \mu_s'\left[\frac{4}{3}\frac{\partial V_s}{\partial y} - \frac{2}{3}\frac{\partial U_s}{\partial x}\right] + \frac{\rho_s V_s^2}{T_s} - \frac{2U_s}{3(1+\epsilon\eta)}\mu_s';$$

$$B_1^{35} = -1;$$

$$B_2^{32} = \frac{4}{3}\mu_s;$$

$$D^{31} = \frac{\mu_s}{3};$$

ϕ-momentum equation:

$$
\begin{aligned}
A^{43} &= \rho_s U_s; \\
A^{44} &= \frac{\mu_s \beta U_s}{3T_s}; \\
B_0^{41} &= \frac{\mu_s \beta}{3\rho_s}\frac{\partial \rho_s}{\partial x} - \beta\frac{\partial \mu_s}{\partial x} - \frac{2\beta\mu_s}{(1+\epsilon\eta)}; \\
B_0^{42} &= \frac{\mu_s \beta}{3\rho_s}\frac{\partial \rho_s}{\partial y} - \beta\frac{\partial \mu_s}{\partial y}; \\
B_0^{43} &= -\beta^2\mu_s - \frac{\partial \rho_s V_s}{\partial y} - \frac{2\rho_s U_s}{(1+\epsilon\eta)}; \\
B_0^{44} &= -\frac{\beta\mu_s}{3\rho_s}\frac{\partial}{\partial y}\left(\frac{\rho_s V_s}{T_s}\right) + \frac{\rho_s U_s \beta}{3T_s}\frac{\partial}{\partial x}\left(\frac{\mu_s}{\rho_s}\right) - \frac{\mu_s U_s \beta}{3T_s(1+\epsilon\eta)} \\
&\quad + \frac{2\beta\mu_s'}{3}\frac{\partial U_s}{\partial x} + \frac{2\beta\mu_s'}{3}\frac{\partial V_s}{\partial x} - \frac{4\beta U_s \mu_s'}{3(1+\epsilon\eta)}; \\
B_0^{45} &= \beta; \\
B_1^{43} &= -\rho_s V_s + \frac{\partial \mu_s}{\partial y}; \\
B_1^{44} &= -\frac{\beta\mu_s V_s}{3T_s}; \\
B_2^{43} &= \mu_s;
\end{aligned}
$$

Energy equation:

$$
\begin{aligned}
A^{51} &= \rho_s T_s; \\
B_0^{51} &= \frac{\gamma-1}{\gamma}\frac{\partial p_s}{\partial x} - \frac{\rho_s T_s}{(1+\epsilon\eta)}; \\
B_0^{52} &= -\frac{\partial \rho_s T_s}{\partial y}; \\
B_0^{53} &= -\beta\rho_s T_s; \\
B_0^{54} &= \mu_s'(\gamma-1)M_{\text{ref}}^2\left(\frac{\partial U_s}{\partial y}\right)^2 - \frac{\beta^2\mu_s}{Pr} + \frac{1}{Pr}\frac{\partial}{\partial y}\left(\mu_s'\frac{\partial T_s}{\partial y}\right); \\
B_1^{51} &= 2(\gamma-1)M_{\text{ref}}^2\mu_s\frac{\partial U_s}{\partial y}; \\
B_1^{52} &= -\rho_s T_s; \\
B_1^{54} &= \frac{2}{Pr}\frac{\partial \mu_s}{\partial y}; \\
B_2^{54} &= \frac{\mu_s}{Pr}.
\end{aligned}
$$

C.3 Matrices for compressible flow past a blunt cone

The form of the equation needed to develop optimal perturbation analysis of compressible flow over a blunt cone: $(\mathbf{Af})_x = (\mathbf{Df}_y)_x + \mathbf{B_0 f} + \mathbf{B_1 f}_y + \mathbf{B_2 f}_{yy}$, where $\mathbf{f} = (u,\ v,\ w,\ T,\ p)^T$, superscript T stands for transpose. Rewriting equations in this form, we get the following non-zero elements of matrices $\mathbf{A}$, $\mathbf{B_0}$, $\mathbf{B}_1$, $\mathbf{B}_2$ and $\mathbf{D}$:

Continuity equation:

$$
\begin{aligned}
A^{11} &= R_\varepsilon \rho_s; \\
A^{14} &= -R_\varepsilon \frac{\rho_s U_s}{T_s}; \\
B_0^{11} &= \frac{\partial R_\varepsilon}{\partial x}\rho_s - \frac{R_\varepsilon}{r_\varepsilon}\frac{\partial r_\varepsilon}{\partial x}\rho_s; \\
B_0^{12} &= -\frac{\partial \rho_s}{\partial y}; \\
B_0^{13} &= -\beta \rho_s; \\
B_0^{14} &= -\frac{\partial R_\varepsilon}{\partial x}\frac{\rho_s U_s}{T_s} + \frac{R_\varepsilon}{r_\varepsilon}\frac{\partial r_\varepsilon}{\partial x}\frac{\rho_s U_s}{T_s} + \frac{\partial}{\partial y}\left(\frac{\rho_s V_s}{T_s}\right) + \frac{1}{r_\varepsilon}\frac{\rho_s}{T_s}\left(\frac{\partial W_s}{\partial \phi}\right)_{\phi=0}; \\
B_1^{12} &= -\rho_s; \\
B_1^{14} &= \frac{\rho_s V_s}{T_s};
\end{aligned}
$$

where $R_\varepsilon = \frac{R}{R+\varepsilon y}$, $r_\varepsilon = r + \varepsilon y \cos\theta$ and $\beta = \frac{\varepsilon m}{r_\varepsilon}$, .

x-momentum equation

$$A^{21} = 2R_\epsilon \rho_s U_s;$$

$$A^{24} = -R_\epsilon \frac{\rho_s U_s^2}{T_s};$$

$$B_0^{21} = \left(2\frac{\partial R_\epsilon}{\partial x} - 2\frac{R_\epsilon}{r_\epsilon}\frac{\partial r_\epsilon}{\partial x}\right)\rho_s U_s - \frac{\partial \rho_s V_s}{\partial y} - \beta^2 \mu_s - \frac{1}{r_\epsilon}\rho_s \left(\frac{\partial W_s}{\partial \phi}\right)_{\phi=0};$$

$$B_0^{22} = -\frac{\partial \rho_s U_s}{\partial y};$$

$$B_0^{23} = -\beta \rho_s U_s;$$

$$B_0^{24} = \left(\frac{R_\epsilon}{r_\epsilon}\frac{\partial r_\epsilon}{\partial x} - \frac{\partial R_\epsilon}{\partial x}\right)\frac{\rho_s U_s^2}{T_s} + \frac{\partial}{\partial y}\left(\frac{\rho_s U_s V_s}{T_s}\right) + \frac{\partial}{\partial y}\left(\frac{d\mu_s}{dT_s}\frac{\partial U_s}{\partial y}\right) + \frac{1}{r_\epsilon}\frac{\rho_s U_s}{T_s}\left(\frac{\partial W_s}{\partial \phi}\right)_{\phi=0};$$

$$B_1^{21} = -\rho_s V_s + \frac{\partial \mu_s}{\partial y};$$

$$B_1^{22} = -\rho_s U_s;$$

$$B_1^{24} = \frac{\rho_s U_s V_s}{T_s} + \frac{d\mu_s}{dT_s}\frac{\partial U_s}{\partial y};$$

$$B_2^{21} = \mu_s.$$

y-momentum equation

$$A^{31} = R_\varepsilon \rho_s V_s + \frac{2}{3} R_\varepsilon \frac{\partial \mu_s}{\partial y};$$

$$A^{32} = R_\varepsilon \rho_s U_s;$$

$$A^{34} = -R_\varepsilon \frac{\rho_s U_s V_s}{T_s} - R_\varepsilon \frac{d\mu_s}{dT_s} \frac{\partial U_s}{\partial y};$$

$$B_0^{31} = \frac{R_\varepsilon}{r_\varepsilon} \frac{\partial r_\varepsilon}{\partial x} \left(-\frac{2}{3} \frac{\partial \mu_s}{\partial y} - \rho_s V_s \right) + 2 \frac{1}{\varepsilon R_\varepsilon} \rho_s U_s + \frac{2}{3} \frac{\partial}{\partial x} \left(R_\varepsilon \frac{\partial \mu_s}{\partial y} \right) + \frac{\partial R_\varepsilon}{\partial x} \rho_s V_s;$$

$$B_0^{32} = -\frac{R_\varepsilon}{r_\varepsilon} \frac{\partial r_\varepsilon}{\partial x} \rho_s U_s - 2 \frac{\partial \rho_s V_s}{\partial y} - \beta^2 \mu_s + \frac{\partial R_\varepsilon}{\partial x} \rho_s U_s - \frac{1}{r_\varepsilon} \rho_s \left(\frac{\partial W_s}{\partial \phi} \right)_{\phi=0};$$

$$B_0^{33} = -\beta \rho_s V_s - \frac{2}{3} \frac{\partial \mu_s}{\partial y} \beta;$$

$$\begin{aligned} B_0^{34} = {} & \frac{1}{3} R_\varepsilon \frac{d\mu_s}{dT_s} \frac{\partial^2 U_s}{\partial x \partial y} - \frac{2}{3} R_\varepsilon \frac{\partial}{\partial y} \left(\frac{d\mu_s}{dT_s} \right) \frac{\partial U_s}{\partial x} + \frac{4}{3} \frac{d\mu_s}{dT_s} \frac{\partial^2 V_s}{\partial y^2} \\ & + \frac{4}{3} \frac{\partial V_s}{\partial y} \frac{\partial}{\partial y} \left(\frac{d\mu_s}{dT_s} \right) + \frac{\partial}{\partial y} \left(\frac{\rho_s V_s^2}{T_s} \right) - \frac{1}{\varepsilon R_\varepsilon} \frac{\rho_s U_s^2}{T_s} - \frac{d\mu_s}{dT_s} \frac{\partial}{\partial x} \left(R_\varepsilon \frac{\partial U_s}{\partial y} \right) \\ & - \frac{\partial R_\varepsilon}{\partial x} \frac{\rho_s U_s V_s}{T_s} + \frac{R_\varepsilon}{r_\varepsilon} \frac{\partial r_\varepsilon}{\partial x} \left(\frac{1}{3} \frac{d\mu_s}{dT_s} \frac{\partial U_s}{\partial y} - \frac{2}{3} \frac{\partial}{\partial y} \left(\frac{d\mu_s}{dT_s} \right) U_s + \frac{\rho_s U_s V_s}{T_s} \right) \\ & + \left(\frac{1}{r_\varepsilon} \frac{\rho_s V_s}{T_s} - \frac{2}{3} \frac{1}{r_\varepsilon} \frac{\partial}{\partial y} \left(\frac{d\mu_s}{dT_s} \right) \right) \left(\frac{\partial W_s}{\partial \phi} \right)_{\phi=0} + \frac{1}{3} \frac{1}{r_\varepsilon} \frac{d\mu_s}{dT_s} \frac{\partial}{\partial y} \left(\frac{\partial W_s}{\partial \phi} \right)_{\phi=0}; \end{aligned}$$

$$B_1^{31} = \frac{1}{3} \frac{R_\varepsilon}{r_\varepsilon} \frac{\partial r_\varepsilon}{\partial x} \mu_s + R_\varepsilon \frac{\partial \mu_s}{\partial x};$$

$$B_1^{32} = \frac{4}{3} \frac{\partial \mu_s}{\partial y} - 2\rho_s V_s; \quad B_1^{33} = \frac{1}{3} \beta \mu_s;$$

$$\begin{aligned} B_1^{34} = {} & -\frac{2}{3} \frac{R_\varepsilon}{r_\varepsilon} \frac{\partial r_\varepsilon}{\partial x} \frac{d\mu_s}{dT_s} U_s + \frac{2}{3} \frac{d\mu_s}{dT_s} \left(2 \frac{\partial V_s}{\partial y} - R_\varepsilon \frac{\partial U_s}{\partial x} \right) + \frac{\rho_s V_s^2}{T_s} \\ & - \frac{2}{3} \frac{1}{r_\varepsilon} \frac{d\mu_s}{dT_s} \left(\frac{\partial W_s}{\partial \phi} \right)_{\phi=0}; \end{aligned}$$

$$B_1^{35} = -1;$$

$$B_2^{31} = \frac{4}{3} \mu_s;$$

$$D^{31} = \frac{1}{3} R_\varepsilon \mu_s.$$

ϕ-momentum equation:

$$A^{43} = R_\epsilon \rho_s U_s;$$

$$A^{44} = \frac{1}{3} R_\epsilon \beta \mu_s \frac{U_s}{T_s};$$

$$B_0^{41} = \frac{1}{3} R_\epsilon \frac{\beta \mu_s}{\rho_s} \frac{\partial \rho_s}{\partial x} - 2 \frac{R_\epsilon}{r_\varepsilon} \frac{\partial r_\varepsilon}{\partial x} \beta \mu_s - R_\epsilon \beta \frac{\partial \mu_s}{\partial x};$$

$$B_0^{42} = \frac{1}{3} \frac{\beta \mu_s}{\rho_s} \frac{\partial \rho_s}{\partial y} - \beta \frac{\partial \mu_s}{\partial y};$$

$$B_0^{43} = \frac{\partial R_\epsilon}{\partial x} \rho_s U_s - 2 \frac{R_\epsilon}{r_\varepsilon} \frac{\partial r_\varepsilon}{\partial x} \rho_s V_s - \frac{\partial \rho_s V_s}{\partial y} - \beta^2 \mu_s - \frac{2}{r_\varepsilon} \rho_s \left(\frac{\partial W_s}{\partial \phi} \right)_{\phi=0};$$

$$\begin{aligned} B_0^{44} = {} & \frac{1}{3} R_\epsilon \beta \frac{\rho_s U_s}{T_s} \frac{\partial}{\partial x} \left(\frac{\mu_s}{\rho_s} \right) + \left(\frac{\partial R_\epsilon}{\partial x} - \frac{R_\epsilon}{r_\varepsilon} \frac{\partial r_\varepsilon}{\partial x} \right) \frac{1}{3} \beta \mu_s \frac{U_s}{T_s} \\ & - \frac{4}{3} \frac{R_\epsilon}{r_\varepsilon} \frac{\partial r_\varepsilon}{\partial x} \beta \frac{d\mu_s}{dT_s} U_s - \frac{1}{3} \beta \frac{\mu_s}{\rho_s} \frac{\partial}{\partial y} \left(\frac{\rho_s V_s}{T_s} \right) \\ & + \frac{2}{3} R_\epsilon \beta \frac{d\mu_s}{dT_s} \frac{\partial U_s}{\partial x} + \frac{2}{3} \beta \frac{d\mu_s}{dT_s} \frac{\partial V_s}{\partial y} - \frac{1}{3 r_\varepsilon} \beta \left(\frac{\mu_s}{T_s} + 4 \frac{d\mu_s}{dT_s} \right) \left(\frac{\partial W_s}{\partial \phi} \right)_{\phi=0}; \end{aligned}$$

$$B_0^{45} = \beta;$$

$$B_1^{43} = -\rho_s V_s + \frac{\partial \mu_s}{\partial y};$$

$$B_1^{44} = -\frac{1}{3} \beta \frac{\mu_s V_s}{T_s};$$

$$B_2^{43} = \mu_s.$$

Energy equation:

$$A^{51} = R_\epsilon \rho_s T_s;$$

$$B_0^{51} = \frac{\partial R_\epsilon}{\partial x} \rho_s T_s - \frac{R_\epsilon}{r_\varepsilon} \frac{\partial r_\varepsilon}{\partial x} \rho_s T_s + \frac{\gamma - 1}{\gamma} R_\epsilon \frac{\partial p_s}{\partial x};$$

$$B_0^{52} = -\frac{\partial \rho_s T_s}{\partial y} + \frac{\gamma - 1}{\gamma} \frac{\partial p_s}{\partial y}; \quad B_0^{53} = -\beta \rho_s T_s;$$

$$B_0^{54} = (\gamma - 1) M_r^2 \frac{d\mu_s}{dT_s} \left(\frac{\partial U_s}{\partial y} \right)^2 + \frac{1}{\mathrm{Pr}} \left(\frac{\partial}{\partial y} \left(\frac{d\mu_s}{dT_s} \right) \frac{\partial T_s}{\partial y} + \frac{d\mu_s}{dT_s} \frac{\partial^2 T_s}{\partial y^2} - \beta^2 \mu_s \right);$$

$$B_1^{51} = 2(\gamma - 1) M_r^2 \mu_s \frac{\partial U_s}{\partial y};$$

$$B_1^{52} = -\rho_s T_s;$$

$$B_1^{54} = \frac{1}{\mathrm{Pr}} \left(\frac{\partial \mu_s}{\partial y} + \frac{d\mu_s}{dT_s} \frac{\partial T_s}{\partial y} \right);$$

$$B_2^{54} = \frac{1}{\mathrm{Pr}} \mu_s.$$

where M_r is the reference Mach number.

Bibliography

[ABH99] P. Andersson, M. Berggren, and D. S. Henningson. Optimal disturbances and bypass transition in boundary layers. *Phys. Fluids*, 11:134–150, 1999.

[Air00] C. Airiau. Non-parallel acoustic receptivity of a Blasius boundary layer using an adjoint approach. *Flow, Turbul. Combust.*, 65:347–367, 2000.

[AL65] Holt Ashley and Marten Landahl. *Aerodynamics of Wings and Bodies*, pages 256–257. Addison-Wesley Publishing Company, Inc., Reading, Massachusetts, 1st. edition, 1965.

[AP79] L. B. Aizin and M. F. Polyakov. Acoustic generation of Tollmien–Schlichting waves over local unevenness of surface immersed in stream. Preprint 17, Akad. Nauk USSR, Siberian Div., Inst. Theor. Appl. Mech., 1979. (in Russian).

[AR90] D. Ashpis and E. Reshotko. The vibrating ribbon problem revisited. *J. Fluid Mech.*, 213:531–547, 1990.

[AS72] M. Abramowitz and A. Stegun. *Handbook of Mathematical Functions.* Dover Publications, 1972.

[AS87] M. S. Acarlar and C. R. Smith. A study of hairpin vortices in a laminar boundary layer. part 1. hairpin vortices generated by a hemisphere protuberance. *J. Fluid Mech.*, 175:1–41, 1987.

[AWB00] C. Airiau, S. Walther, and A. Bottaro. Non-parallel receptivity and the adjoint PSE. In H. F. Fasel and W. S. Saric, editors, *Laminar-Turbulent Transition*, pages 57–62. Springer, 2000. IUTAM Symposium, Sedona/AZ, 1999.

[AWB02] C. Airiau, S. Walther, and A Bottaro. Boundary layer sensitivity and receptivity. *C. R. Mecanique*, 330:259–265, 2002.

[BB88] L. Boberg and U. Brosa. Onset of turbulence in a pipe. *Z. Natursforschung*, 43a:697–726, 1988.

[Ber00] F. B. Bertolotti. Receptivity of three-dimensional boundary-layers to localized wall roughness and suction. *Phys. Fluids*, 12:1799–1809, 2000.

[BF92] K. M. Butler and B. Farrell. Three–dimensional optimal perturbations in viscous shear flow. *Phys. Fluids A*, 4:1637–1650, 1992.

[BG81] D. J. Benney and L. H. Gustavsson. A new mechanism for linear and nonlinear hydrodynamic instability. *Stud. Appl. Math.*, 64:185–209, 1981.

[BH86] Norman Bleistein and Richard A. Handelsman. *Asymptotic Expansions of Integrals*. Dover Publications, Inc., 1986.

[Bip99] H. Bippes. Basic experiments on transition in three-dimensional boundary layers dominated by crossflow instability. *Prog. Aerosp. Sci.*, 35:363–412, 1999.

[BL85] V. V. Bogolepov and I. I. Lipatov. Locally three-dimensional laminar flows. *J. Appl. Mech. Tech. Phys.*, 26:24–31, 1985.

[BM92] P. Balakumar and M. R. Malik. Discrete modes and continuous spectra in supersonic boundary layer. *J. Fluid Mech.*, 239:631–656, 1992.

[BN71] V. V. Bogolepov and V. Y. Neiland. Viscous gas motion near small irregularities. *Trans. TsAGI*, 1363, 1971. (in Russian).

[BN77] V. V. Bogolepov and V. Y. Neiland. Investigation of local perturbations in viscous supersonic flows. In *Aeromechanics*, pages 104–118, 1977. (in Russian); Translated in *Soviet Research–Fluid Mechanics*, 1980, pp. 84–95.

[Bog86] V. V. Bogolepov. General arrangement of regimes for spatial local flows. *J. Appl. Mech. Tech. Phys.*, 27:860–869, 1986.

[Bog87] V. V. Bogolepov. Perturbations of a laminar boundary layer. *J. Appl. Mech. Tech. Phys.*, 28:706–716, 1987.

[Bog88] V. V. Bogolepov. Analysis of flow regimes in vicinity of three-dimensional humps. *Trans. TsAGI*, 2376, 1988. (in Russian).

[Bou72] M. Bouthier. Stabilité lineairé des écoulements presque paralléles. *J. de Mecanique*, 11(4):599–621, 1972.

[BR82] E. V. Bogdanova and O. S. Ryzhov. Oscillator-generated perturbations in viscous fluid flow at supercritical frequencies. *J. Appl. Mech. Tech. Phys.*, 23:523–529, 1982.

[CD00] S. S. Collis and A. Dobrinsky. Evaluation of adjoint based methods for the prediction of receptivity. In H. F. Fasel and W. S. Saric, editors, *Laminar-Turbulent Transition*, pages 111–116. Springer, 2000. IUTAM Symposium, Sedona/AZ, 1999.

[Cho94a] M. Choudhari. Distributed acoustic receptivity in laminar flow control. *Phys. Fluids*, 6:489–506, 1994.

[Cho94b] M. Choudhari. Roughness-induced generation of crossflow vortices in three-dimensional boundary layers. *Theor. Comput. Fluid Dyn.*, 6:1–30, 1994.

[Cho98] M. Choudhari. Receptivity. In R. W. Johnson, editor, *The Handbook of Fluid Dynamics*, pages 13–25 – 13–40. CRC Press, 1998.

[CL99] S. S. Collis and S. K. Lele. Receptivity to surface roughness near a swept leading edge. *J. Fluid Mech.*, 380:141–168, 1999.

[CL00] P. Cathalifaud and P. Luchini. Algebraic growth in boundary layers: optimal control by blowing and suction at the wall. *Eur. J. Mech. B - Fluids*, 19:469–490, 2000.

[Cro92] J. D. Crouch. Localized receptivity of boundary layers. *Phys. Fluids A*, 4:1408–1414, 1992.

[Cro93] J. D. Crouch. Receptivity of three-dimensional boundary layers. AIAA Paper 1993–0074, 1993.

[CS92] M. Choudhari and C. L. Streett. A finite Reynolds-number approach for the prediction of boundary-layer receptivity in localized regions. *Phys. Fluids A*, 4:2495–2513, 1992.

[CWC99] Sin-Chung Chang, Xiao-Yen Wang, and Chuen-Yen Chow. The space-time conservation element and solution element method: A new high-resolution and genuinely multidimensional paradigm for solving conservation laws. *Journal of Computational Physics*, 156:89–136, 1999.

[Dan75] P. G. Daniels. The flow about the trailing edge of a supersonic oscillating airfoil. *J. Fluid Mech.*, 72:541–557, 1975.

[DC00] A. Dobrinsky and S. S. Collis. Adjoint parabolized stability equations for receptivity prediction. AIAA Paper 2000–2651, 2000.

[DR81] P. G. Drazin and W. H. Reid. *Hydrodynamic Stability.* Cambridge University Press, 1981.

[EB93] W. Eißler and H. Bestek. Spatial numerical simulations of nonlnear transition phenomena in supersonic boundary layers. In *Transitional and Turbulent Compressible Flows*, volume FED 151. ASME, 1993.

[EFN04] I. V. Egorov, A. V. Fedorov, and A. V. Nechaev. Receptivity of supersonic boundary layer on a blunt plate to acoustic disturbances. AIAA Paper 2004–0249, 2004.

[EFS05] I. V. Egorov, A. V. Fedorov, and V. G. Soudakov. Direct numerical simulation of supersonic boundary layer receptivity to acoustic disturbances. AIAA Paper 2005–0097, 2005.

[EH80] N. M. El-Hady. On the stability of three-dimensional, compressible nonparallel boundary layers. AIAA Paper 80–1374, 1980.

[EP75] T. Ellingsen and E. Palm. Stability of linear flow. *Phys. Fluids*, 18:487–488, 1975.

[Far82] B. Farrell. The initial growth of disturbances in a baroclinic flow. *J. Atmos. Sci.*, 39:1663–1686, 1982.

[Far84] B. Farrell. Modal and nonmodal baroclinic waves. *J. Atmos. Sci.*, 41:668–673, 1984.

[Far86] B. Farrell. Transient growth of damped baroclinic waves. *J. Atmos. Sci.*, 42:2718–2727, 1986.

[Far87] B. Farrell. Developing disturbances in shear. *J. Atmos. Sci.*, 44:2191–2199, 1987.

[Far88a] B. Farrell. Optimal excitation of neutral Rossby waves. *J. Atmos. Sci.*, 45:163–172, 1988.

[Far88b] B. Farrell. Optimal excitation of perturbations in viscous shear flow. *Phys. Fluids*, 31(8):2093–2102, 1988.

[FC04] P. Fisher and M. Choudhari. Numerical simulation of roughness-induced transient growth in a laminar boundary layer. AIAA Paper 2004–2539, 2004.

[Fed82] A. V. Fedorov. *Generation and Development of instability waves in a boundary layer of a compressible gas.* Phd thesis, Moscow Institute of Physics and Technology, 1982. (in Russian).

[Fed84] A. V. Fedorov. Excitation of Tollmien-Schlichting waves in a boundary layer by periodic external source located on the body surface. *Fluid Dyn.*, 19:888–893, 1984.

[Fed88] A. V. Fedorov. Excitation of waves of instability of the secondary flow in the boundary layer on a swept wing. *J. Appl. Mech. Tech. Phys.*, 29:643–648, 1988.

[Fed03a] A. V. Fedorov. Receptivity of a high-speed boundary layer to acoustic disturbances. *J. Fluid Mech.*, 491:101–129, 2003.

[Fed03b] A. V. Fedorov. Receptivity of hypersonic boundary layer to acoustic disturbances scattered by surface roughness. AIAA Paper 2003–3731, 2003.

[FK91] A. V. Fedorov and A. P. Khokhlov. Mode switching in a supersonic boundary layer. *J. Appl. Mech. Tech. Phys.*, 32:831–836, 1991.

[FK01] A. V. Fedorov and A. P. Khokhlov. Prehistory of instability in a hypersonic boundary layer. *Theor. Comp. Fluid Dyn.*, 14:359–375, 2001.

[FK02] A. V. Fedorov and A. P. Khokhlov. Receptivity of hypersonic boundary layer to wall disturbances. *Theor. Comp. Fluid Dyn.*, 15:231–254, 2002.

[FM92] B. F. Farrell and A. M. Moore. An adjoint method for obtaining the most rapidly growing perturbation to oceanic flows. *J. Phys. Ocean.*, 22:338–349, 1992.

[FT03] A. Fedorov and A. Tumin. Initial-value problem for hypersonic boundary layer flows. *AIAA J.*, 41:379–389, 2003.

[FT05] E. Forgoston and A. Tumin. Initial-value problem for three-dimensional disturbances in a hypersonic boundary layer. *Phys. Fluids*, 17, 2005. paper No. 084106.

[FVT06] E. Forgoston, M. Viergutz, and A. Tumin. Numerical and asymptotical study of three-dimensional wave packets in a compressible boundary layer. AIAA Paper 2006-3223, June 2006.

[Gap80] S. A. Gaponov. Influence of nonparallel flow on the development of disturbances in a supersonic boundary layer. *Fluid Dynamics*, 15:195–199, 1980.

[Gas65] M. Gaster. On the generation of spatially growing waves in a boundary layer. *J. Fluid Mech.*, 22:433–441, 1965.

[Gas68] M. Gaster. The development of three-dimensional wave packets in a boundary layer. *J. Fluid Mech.*, 32:173–184, 1968.

[Gas74] M. Gaster. On the effects of boundary layer growth on flow stability. *J. Fluid Mech.*, 66:465–480, 1974.

[Gas81] M. Gaster. Propagation of linear wave packets in laminar boundary layers. *AIAA J.*, 19(4):419–423, 1981.

[Gas82] M. Gaster. The development of a two-dimensional wavepacket in a growing boundary layer. *Proc. R. Soc. Lond.*, 384(1787):317–332, 1982.

[Gay04] P. Gaydos. Analysis of small perturbations in compressible boundary layers. MS Thesis, The University of Arizona, 2004.

[GF89] V. R. Gushchin and A. V. Fedorov. Asymptotic analysis of inviscid perturbations in a supersonic boundary layer. *J. Appl. Mech. Tech. Phys.*, 30:64–70, 1989.

[GGJ94] M. Gaster, C. E. Grosch, and T. L. Jackson. The velocity field created by a shallow bump in a boundary layer. *Phys. Fluids*, 6:3079–3085, 1994.

[GH80] L. H. Gustavsson and L. S. Hultgren. A resonance mechanism in plane Couette flow. *J. Fluid Mech.*, 98:149–159, 1980.

[Gol83] M. E. Goldstein. The evolution of Tollmien–Schlichting waves near a leading edge. *J. Fluid Mech.*, 127:59–81, 1983.

[Gol85] M. E. Goldstein. Scattering of acoustic waves into Tollmien–Schlichting waves by small streamwise variations in surface geometry. *J. Fluid Mech.*, 154:509–529, 1985.

[GR00] I. S. Gradshteyn and I. M. Ryzhik. *Table of Integrals, Series, and Products.* Academic Press, sixth edition, 2000. pages 1109-1110.

[GS78] C. E. Grosch and H. Salwen. The continuous spectrum of the Orr–Sommerfeld equation. Part 1. the spectrum and eigenfunctions. *J. Fluid Mech.*, 87:33–54, 1978.

[GT04] P. Gaydos and A. Tumin. Multimode decomposition in compressible boundary layers. *AIAA J.*, 42:1115–1121, 2004.

[Gun00] M. Gunzburger. Adjoint equation-based methods for control problems in incompressible, viscous flows. *Flow, Turb. & Comb.*, 65:249–272, 2000.

[Gus79] L. H. Gustavsson. Initial-value problem for boundary layer flows. *Phys. Fluids*, 22:1602–1605, 1979.

[Gus81] L. H. Gustavsson. Resonant growth of three-dimensional disturbances in plane poiseuille flow. *J. Fluid Mech.*, 112:253–264, 1981.

[Gus91] L. H. Gustavsson. Energy growth of three-dimensional disturbances in plane Poisuille flow. *J. Fluid Mech.*, 224:241–260, 1991.

[HCSP96] K. Hoffmann, S.T. Chiang, S. Siddiqui, and M. Papadakis. *Fundamental Equations of Fluid Mechanics.* Engineering Education System, 1996.

[Her97] T. Herbert. Parabolized stability equations. *Ann. Rev. Fluid Mech.*, 29:245–283, 1997.

[HG81] L. S. Hultgren and L. H. Gustavsson. Algebraic growth of disturbances in a laminar boundary layer. *Phys. Fluids*, 24(6):1000–1004, 1981.

[HH98] A. Hanifi and D. Henningson. The compressible inviscid algebraic instability for streamwise independent disturbances. *Phys. Fluids*, 10(8):1784–1786, 1998.

[Hil95] D. C. Hill. Adjoint systems and their role in the receptivity problem for boundary-layers. *J. Fluid Mech.*, 292:183–204, 1995.

[Hil96] D. C. Hill. Receptivity and control in non-parallel flows. *Bull. Am. Phys. Soc.*, 41:1777, 1996.

[HP59] W. D. Hayes and R. F. Probstein. *Hypersonic Flow Theory.* Academic Press, New York, 1959.

[HSH96] A. Hanifi, P. J. Schmid, and D. S. Henningson. Transient growth in compressible boundary layer flow. *Phys. Fluids*, 8:826–837, 1996.

[JBG86] P. S. Jang, D. J. Benney, and R. L. Gran. On the origin of streamwise vortices in a turbulent boundary layer. *J. Fluid Mech.*, 169:109–123, 1986.

[JG95] R. D. Joslin and C. E. Grosch. Growth characteristics downstream of a shallow bump: computation and experiment. *Phys. Fluids*, 7:3042–3047, 1995.

[Jr.89] J. D. Anderson Jr. *Hypersonic and High Temperature Gas Dynamics.* AIAA, Inc., 1989.

[Kam59] E. Kamke. *Differentialgleichungen. Lösungsmethoden und Lösungen.* Akademische Verlagsgesellschaft Geest & Portig, Leipzig, 1959.

[Kre89] E. Kreyszig. *Introductory functional analysis with applications.* John Wiley & Sons, 1989.

[Lan75] M. T. Landahl. Wave breakdown and turbulence. *SIAM J. Appl. Math.*, 28:735–756, 1975.

[Lan80] M. T. Landahl. A note on an algebraic instability of inviscid parallel shear flow. *J. Fluid Mech.*, 98:243–251, 1980.

[LB98] P. Luchini and A. Bottaro. Görtler vortices: a backward-in-time approach to the receptivity problem. *J. Fluid Mech.*, 363:1–23, 1998.

[LB01] P. Luchini and A. Bottaro. Linear stability and receptivity analyses of the Stokes layer produced by an impulsively started plate. *Phys. Fluids*, 13:1668–1678, 2001.

[Luc00] P. Luchini. Reynolds–number–independent instability of the boundary layer over a flat surface: optimal perturbations. *J. Fluid Mech.*, 404:289–309, 2000.

[Mac69] L. M. Mack. Boundary layer stability theory. JPL Report 900–277, Jet Propulsion Lab., California Institute of Technology, Pasadena, CA, USA, 1969.

[Mac84] L. M. Mack. Special course on stability and transition of laminar flow. AGARD Report 709, June 1984.

[Mal90] M. R. Malik. Numerical methods for hypersonic boundary layer stability. *J. Comput. Phys.*, 86:376–413, 1990.

[Man89] S. V. Manuilovich. Disturbances of a three-dimensional boundary layer generated by surface roughness. *Fluid Dyn.*, 24:764–769, 1989.

[Mes70] A. F. Messiter. Boundary layer flow near the trailing edge of a flat plate. *SIAM J. Appl. Mech.*, 18:241–257, 1970.

[MLS99] M. R. Malik, R. S. Lin, and R. Sengupta. Computation of hypersonic boundary-layer response to external disturbances. AIAA Paper 1999–0411, 1999.

[Mor69] M. V. Morkovin. Critical evaluation of transition from laminar to turbulent shear layers with emphasis on hypersonic traveling bodies. AFRL Report AFF DL–TR–68–149, Air Force Flight Dynamics Laboratory, Wright-Patterson AFB, OH, USA, 1969.

[MZ01] Y. Ma and X. Zhong. Numerical simulation of receptivity and stability of nonequilibrium reacting hypersonic boundary layers. AIAA Paper 2001–0892, 2001.

[MZ03a] Y. Ma and X. Zhong. Receptivity of a supersonic boundary layer over a flat plate. Part 1: Wave structures and interactions. *J. Fluid Mech.*, 488:31–78, 2003.

[MZ03b] Y. Ma and X. Zhong. Receptivity of a supersonic boundary layer over a flat plate. Part 2: Receptivity to freestream sound. *J. Fluid Mech.*, 488:79–121, 2003.

[MZ03c] Y. Ma and X. Zhong. Receptivity to freestream disturbances of mach 8 flow over a sharp wedge. AIAA Paper 2003–0788, 2003.

[MZ05] Y. Ma and X. Zhong. Receptivity of a supersonic boundary layer over a flat plate. Part 3: Effects of different types of free-stream disturbances. *J. Fluid Mech.*, 532:63–109, 2005.

[Nay80] A. H. Nayfeh. Stability of three-dimensional boundary layers. *AIAA J.*, 18:406–416, 1980.

[NBDL04] V. Y. Neiland, V. V. Bogolepov, G. N. Dudin, and I. I. Lipatov. *Asymptotic Theory of Viscous Gas Flows.* Nauka, Moscow, 2004. (in Russian).

[NC99] L. L. Ng and J. D. Crouch. Roughness-induced receptivity to crossflow vortices on a swept wing. *Phys. Fluids*, 11:432–438, 1999.

[Nei69] V. Y. Neiland. Towards a theory of separation of the laminar boundary layer in a supersonic stream. *Izv. Akad. Nauk SSSR Mekh. Zhidk. Gaza*, 4:33–35, 1969.

[NS00] A. W. Naylor and G. R. Sell. *Linear Operator Theory in Engineering and Science (Applied Mathematical Sciences, Vol 40).* Springer, 2000.

[PAHH00] J. O. Pralits, C. Airiau, A. Hanifi, and D. S. Henningson. Sensitivity analysis using adjoint parabolized stability equations for compressible flows. *Flow, Turbul. Combust.*, 65:321–346, 2000.

[Pie89] A. D. Pierce. *Acoustics.* The Acoustical Society of America, New York, 1989.

[PN79] A. R. Padhaye and A. H. Nayfeh. Nonparallel stability of three-dimensional flows. AIAA Paper 79–1281, 1979.

[Res76] E. Reshotko. Boundary-layer stability and transition. *Ann. Rev. Fluid Mech.*, 8:311–349, 1976.

[Res94] E. Reshotko. Boundary layer instability, transition and control. AIAA Paper 94–0001, 1994.

[Res01] E. Reshotko. Transient growth: a factor in bypass transition. *Phys. Fluids*, 13:1067–1075, 2001.

[RH93] S. C. Reddy and D. S. Henningson. Energy growth in viscous channel flows. *J. Fluid Mech.*, 252:209–238, 1993.

[RS89] H. L. Reed and W. S. Saric. Stability of three-dimensional boundary layers. *Ann. Rev. Fluid Mech.*, 21:235–284, 1989.

[RS98] A. P. Rothmayer and F. T. Smith. Incompressible triple-deck theory. In *The Handbook of Fluid Dynamics*. CRC Press, New York, 1998. Section 23.1.

[RT77] O. S. Ryzhov and E. D. Terent'ev. On unsteady boundary layer with self-induced pressure. *J. Appl. Math. Mech.*, 41:1024–1040, 1977.

[RT00] E. Reshotko and A. Tumin. The blunt body paradox – a case for transient growth. In *Laminar-Turbulent Transition*, pages 403–408. Springer–Verlag, Berlin, 2000. Paper presented at the 5th IUTAM Symposium on Laminar-Turbulent Transition, Sedona, USA, 1999.

[RT04] E. Reshotko and A. Tumin. The role of transient growth in roughness-induced transition. *AIAA J.*, 42(4):766–770, 2004.

[Rub85a] A. I. Ruban. On the generation of Tollmien–Schlichting waves by sound. *Fluid Dyn.*, 19:709–716, 1985.

[Rub85b] A. I. Ruban. On Tollmien–Schlichting wave generation by sound. In V. V. Kozlov, editor, *Laminar-Turbulent Transition*, pages 313 – 320. Springer, 1985. IUTAM Symposium, Novosibirsk/USSR, 1984.

[sAT07] C. Chiquete snd A. Tumin. Biorthogonal eigenfunction system for supersonic inviscid flow past a flat plate. AIAA Paper 2007–3982, 2007.

[Sch74] W. Schneider. Upstream propagation of unsteady disturbances in supersonic boundary layers. *J. Fluid Mech.*, 63:465–485, 1974.

[SG81] H. Salwen and C. E. Grosch. The continuous spectrum of the Orr–Sommerfeld equation. Part 2. eigenfunction expansion. *J. Fluid Mech.*, 104:445–465, 1981.

[SH01] P. J. Schmid and D. S. Henningson. *Stability and Transition in Shear Flows.* Springer, New York, 2001.

[Smi79] F. T. Smith. On the non-parallel flow stability of the blasius boundary layer. *Proc. Roy. Soc. London*, A366:91–109, 1979.

[SN75] W. S. Saric and A. H. Nayfeh. Nonparallel stability of boundary-layer flow. *Phys. Fluids*, 18(8):945–950, 1975.

[SN77] W. S. Saric and A. H. Nayfeh. Nonparallel stability of boundary layers with pressure gradients and suction. Technical Report AGARD-CP-224, 1977.

[SRK02] W. S. Saric, H. L. Reed, and E. J. Kerschen. Boundary-layer receptivity to free-stream disturbances. *Ann. Rev. Fluid Mech.*, 34:291–319, 2002.

[SRSK98] V. V. Sychev, A. I. Ruban, Vic. V Sychev, and G. L. Korolev. *Asymptotic Theory of Separated Flows*. Cambridge University Press, UK, 1998.

[SRW03] W. S. Saric, H. L. Reed, and E. B. White. Stability and transition of three-dimensional boundary layers. *Ann. Rev. Fluid Mech.*, 35:413–440, 2003.

[SS47] G. B. Schubauer and H. K. Skramstad. Laminar boundary-layer oscillations and stability of laminar flow. *J. Aero. Sci.*, 14, 1947.

[SSB77] F. T. Smith, R. I. Sykes, and P. W. Brighton. A two-dimensional boundary layer encountering a three-dimensional hump. *J. Fluid Mech.*, 83:163–176, 1977.

[SW69] K. Stewartson and P. G. Williams. Self-induced separation. *Proc. Roy. Soc. London*, A312:181–206, 1969.

[TA77] A. N. Tikhonov and V. Y. Arsenin. *Solutions of Ill-Posed Problems*. Wiley, New York, 1977.

[TA97] A. Tumin and L. Aizatulin. Instability and receptivity of laminar wall jets. *Theor. Comp. Fluid Dyn.*, 9:33–45, 1997.

[TACZ96] A. Tumin, M. Amitay, J. Cohen, and M. Zhou. A normal multi-mode decomposition method for stability experiments. *Phys. Fluids*, 8:2777–2779, 1996.

[Ter78] E. D. Terent'ev. Unsteady supersonic boundary layer with self-induced pressure near an oscillating wall. *Dokl. Akad. Nauk. SSSR*, 240:1046–1049, 1978.

[Ter81] E. D. Terent'ev. The linear problem of a vibrator in a subsonic boundary layer. *J. Appl. Math. Mech.*, 45:791–795, 1981.

[Ter84] E. D. Terent'ev. The linear problem of a vibrator performing harmonic oscillations at supercritical frequencies in a subsonic boundary layer. *J. Appl. Math. Mech.*, 48:184–191, 1984.

[Ter85] E. D. Terent'ev. The linear problem on vibration on a flat plate in subsonic boundary layer. In V. V. Kozlov, editor, *Laminar-Turbulent Transition*, pages 295–302. Springer, 1985. IUTAM Symposium, Novosibirsk/USSR, 1984.

[TF82] A. M. Tumin and A. V. Fedorov. On the weakly nonparallel flow effect on characteristics of flow stability. *Uchenye Zapiski TsAGI*, 13(6):91–96, 1982. (in Russian).

[TF83a] A. M. Tumin and A. V. Fedorov. Excitation of instability waves in a boundary layer on a vibrating surface. *J. Appl. Mech. Tech. Phys.*, 24:670–674, 1983.

[TF83b] A. M. Tumin and A. V. Fedorov. Spatial growth of disturbances in a compressible boundary layer. *J. Appl. Mech. Tech. Phys.*, 24:548–554, 1983.

[TF84] A. M. Tumin and A. V. Fedorov. Excitation of instability waves by a vibrator localized in the boundary layer. *J. Appl. Mech. Tech. Phys.*, 25:867–873, 1984.

[TGSY95] A. N. Tikhonov, A. V. Goncharski, V. V. Stepanov, and A. G. Yagola. *Numerical Methods for the Solution of Ill-Posed Problems.* Kluwer, London, 1995.

[The03] Vassilios Theofilis. Advances in global linear instability analysis of nonparallel and three-dimensional flows. *Prog. in Aero. Sci.*, 39(4):249–315, 2003.

[Tin65] L. Ting. On the initial conditions for boundary layer equations. *J. Math. Phys.*, 44:353–367, 1965.

[TR01] A. Tumin and E. Reshotko. Spatial theory of optimal disturbances in boundary layers. *Phys. Fluids*, 13(7):2097–2104, 2001.

[TR03] A. Tumin and E. Reshotko. Optimal disturbances in compressible boundary layers. *AIAA J.*, 42:2357–2363, 2003.

[TR04a] A. Tumin and E. Reshotko. Optimal disturbances in the boundary layer over a sphere. AIAA Paper 2004–2241, 2004.

[TR04b] A. Tumin and E. Reshotko. The problem of boundary-layer flow encountering a three-dimensional hump revisited. AIAA Paper 2004–0101, 2004.

[TR05] A. Tumin and E. Reshotko. Receptivity of a boundary-layer flow to a three-dimensional hump at finite reynolds numbers. *Phys. Fluids*, 17(9), 2005. paper No. 094101.

[TTRD93] L. N. Trefethen, Anne E. Trefethen, S. C. Reddy, and T. A. Driscoll. Hydrodynamic stability without eigenvalues. *Science*, 261:578–584, 1993.

[Tum83] A. Tumin. Excitation of Tollmien–Schlichting waves in a boundary layer on a vibrating surface of an infinitely swept wing. *J. Appl. Mech. Tech. Phys.*, 24:670–674, 1983.

[Tum96] A. Tumin. Receptivity of pipe Poiseuille flow. *J. Fluid Mech.*, 315:119–137, 1996.

[Tum98] A. Tumin. Subharmonic resonance in a laminar wall jet. *Phys. Fluids*, 10:1769–1771, 1998.

[Tum03] A. Tumin. Multimode decomposition of spatially growing perturbations in a two-dimensional boundary layer. *Phys. Fluids*, 15:2525–2540, 2003.

[Tum06a] A. Tumin. Biorthogonal eigenfunction system in the triple-deck limit. *Studies in Applied Mathematics*, 117:165–190, 2006.

[Tum06b] A. Tumin. Receptivity of compressible boundary layers to three-dimensional wall perturbations. AIAA Paper 2006–1110, 2006.

[Tum06c] A. Tumin. Three-dimensional spatial normal modes in compressible boundary layers. AIAA Paper 2006–1109, 2006.

[Tum07] A. Tumin. Three-dimensional spatial normal modes in compressible boundary layers. *J. Fluid Mech.*, 586:295–322, 2007.

[Tum08] A. Tumin. Nonparallel flow effects on roughness-induced perturbations in boundary layers. AIAA Paper 2008–0504, 2008.

[TWZ06] A. Tumin, X. Wang, and X. Zhong. Direct numerical simulation of receptivity in a hypersonic boundary layer: validation. AIAA Paper 2006–1108, 2006.

[TWZ07] A. Tumin, X. Wang, and X. Zhong. Direct numerical simulation and the theory of receptivity in a hypersonic boundary layer. *Phys. Fluids*, 19(1), 2007. paper 014101.

[WE97] E. B. White and F. G. Ergin. Receptivity and transient growth of roughness-induced disturbances. AIAA Paper 2003–4243, 1997.

[Whi02] E. B. White. Transient growth of stationary disturbances in a flat plate boundary layer. *Phys. Fluids*, 14:4429–4439, 2002.

[Wol99] S. Wolfram. *The Mathematica Book.* Wolfram Media and Cambridge University Press, Cambridge, 4 edition, 1999.

[Won01] R. Wong. *Asymptotic Approximations of Integrals.* Society for Industrial and Applied Mathematics, 2001.

[Wu05] T. Y. Wu. Small perturbations in the unsteady flow of a compressible viscous and heat conducting fluid. *Journal of Mathematics and Physics*, 35:13–27, 2005.

[WZ05] X. Wang and X. Zhong. Receptivity of a Mach 8.0 flow over a sharp wedge with half-angle 5.3° to wall blowing-suction. AIAA Paper 2005–5025, 2005.

[WZ07] X. Wang and X. Zhong. Numerical simulation if hypersonic boundary-layer receptivity to two and three-dimensional wall perturbations. AIAA Paper 2007–946, 2007.

[ZBL06] S. Zuccher, A. Bottaro, and P. Luchini. Algebraic growth in a blasius boundary layer: Nonlinear optimal disturbances. *Eur. J. Mech. B/Fluids*, 25:1–17, 2006.

[ZF87] V. N. Zhigulev and A. V. Fedorov. Boundary layer receptivity to acoustic disturbances. *J. Appl. Mech. Tech. Phys.*, 28:28–34, 1987.

[Zho98] X. Zhong. High-order finite-difference schemes for numerical simulation of hypersonic boundary-layer transition. *Journal of Computational Physics*, 144:662–709, 1998.

[ZLB04] S. Zuccher, P. Luchini, and A. Bottaro. Algebraic growth in a Blasius boundary layer: Optimal and robust control by mean suction in the nonlinear regime. *J. Fluid Mech.*, 513:135–160, 2004.

[ZM02] X. Zhong and Y. Ma. Receptivity and linear stability of Stetson's Mach 8 blunt cone stability experiments. AIAA Paper 2002–2849, 2002.

[ZR78] V. I. Zhuk and O. S. Ryzhov. A property of linearized boundary layer equations with self-induced pressure. *Dokl. Akad. Nauk. SSSR*, 240:1042–1045, 1978.

[ZR79] V. I. Zhuk and O. S. Ryzhov. Solutions of dispersion relationship in free-interacting boundary-layer theory. *Dokl. Akad. Nauk. SSSR*, 247:1085–1088, 1979.

[ZST80] V. N. Zhigulev, N. V. Sidorenko, and A. M. Tumin. Generation of instability waves in a boundary layer by external turbulence. *J. Appl. Mech. Tech. Phys.*, 21:774–778, 1980.

[ZSTR07] S. Zuccher, I. Shalaev, A. Tumin, and E. Reshotko. Optimal disturbances in the supersonic boundary layer past a sharp cone. *AIAA J.*, 45(2):366–373, 2007.

[ZT87] V. N. Zhigulev and A. M. Tumin. *Origin of Turbulence*. Nauka, Novosibirsk, 1987. (in Russian) [NASA TT-20340, October 1988 (translated)].

[ZTR05] S. Zuccher, A. Tumin, and E. Reshotko. Optimal disturbances in compressible boundary layers – complete energy norm analysis. AIAA Paper 2005-5314, 2005.

[ZTR06] S. Zuccher, A. Tumin, and E. Reshotko. Parabolic approach to optimal perturbations in compressible boundary layers. *J. Fluid Mech.*, 556:189–216, 2006.

[Zuc06a] S. Zuccher. 4th order finite difference solver for compressible optimal perturbations over a sharp cone. Contractor's report, Tucson, 2006.

[Zuc06b] S. Zuccher. 4th order finite difference solver for compressible optimal perturbations over an axisymmetric body of revolution. Contractor's report, Tucson, 2006.

[Zuc06c] S. Zuccher. General finite-difference solver for compressible optimal perturbations in supersonic flows. Contractor's report, Tucson, 2006.